Proceedings of NEWRAD 2014

Edited by

Seongchong Park, KRISS
Petri Kärhä, Aalto University
Erkki Ikonen, Aalto University / MIKES

FOREWORD

These Proceedings contain the extended abstracts of the NEWRAD 2014 Conference in Espoo, Finland, 24-27 June 2014. The oral and poster presentations are listed in the conference program at http://newrad2014.aalto.fi/programme.html

In addition, the NEWRAD Scientific Committee has invited the authors of the following extended abstracts to submit a related paper to the NEWRAD special issue of *Metrologia*:

DBA_OR_018, jag@justervesenet.no
DBA_OR_040, shaw@nist.gov
DBA_OR_022, george.eppeldauer@nist.gov
EAO_OR_004, swbrown@nist.gov
QOT_OR_007, i.degiovanni@inrim.it
QOT_OR_012, christopher.chunnilall@npl.co.uk
SBR_OR_020, timo.donsberg@aalto.fi
SBR_OR_002, peter.sperfeld@ptb.de
DBA_OR_014, ari.feldman@nist.gov
OPM_OR_004, khaled55eg@yahoo.com
QOT_OR_014, d.fukuda@aist.go.jp
OPM_OR_018, sara.pourjamal@aalto.fi
EAO_OR_016, l.lolli@inrim.it
EAO_OR_011, priit.jaanson@aalto.fi
EAO_OR_012, m.rajteri@inrim.it
OPM_OR_014, georgi.t.georgiev@nasa.gov
QOT_OR_011, g.brida@inrim.it
QOT_OR_010, ingmar.mueller@ptb.de
DBS_OR_019, lutz.werner@ptb.de
SSR_OR_001, hsuehling.yu@gmail.com
SSR_OR_007, benjamin.walter@pmodwrc.ch
DBS_OR_009, ian.littler@measurement.gov.au
SSR_OR_009, huang-xuebo@nmc.a-star.edu.sg

The above corresponding authors have agreed that they will submit the related article to *Metrologia* before 9 June 2014.

The extended abstracts of these proceedings are organized in numerical order under the following categories:

Invited talks;

INV-0, INV-1, ... , INV-9

Contributed papers;

EAO – Earth observation
SSR – Solar / stellar radiometry
QOT – Quantum optics technologies
SBR – Source-based radiometry
DBS – Detector-based radiometry: scale realisations
DBA – Detector-based radiometry: applications
OPM – Optical properties of materials / components
OT – Other topics

Table of Contents

Selected Topics of Radiometry Research in Finland

Erkki Ikonen[1,2]

[1]*Metrology Research Institute, Aalto University, and* [2]*Centre for Metrology and Accreditation (MIKES), Espoo, Finland*

The achievements of radiometry research in Finland are reviewed from a personal point of view, including links with the work presented at the NEWRAD 2014 Conference.

EARLY DEVELOPMENTS

An early achievement of optical precision measurements in Finland is the Väisälä white light interferometer which still today is the only instrument capable of measuring 1-km distances with an uncertainty of 0.1 mm [1]. That work created a favourable national tradition in optics. The actual radiometry work was started by a group of scientists at VTT with electrical metrology background developing the world's second cryogenic radiometer [2] a few years after NPL [3]. That radiometer served well for almost 20 years with good results in international comparison measurements [4,5].

Personally it has been interesting to see that my early research results from x-ray coincidences [6,7] have a link to present-day single-photon detector calibrations in correcting for the effect of multiple photon events with a synchrotron radiation source [8].

OPTICAL PROPERTIES OF MATERIALS

The development of national standards laboratory in radiometry and photometry started in 1990 to respond to a need of spectral transmittance measurements for visibility applications at airports by Vaisala Ltd, a company founded by the industrial branch of the Väisälä family. The device built for transmittance measurements of filters [9] and its successors [10-13] provide our largest number of calibration certificates.

Another equipment was developed for diffuse reflectance measurements [14,15] and later upgraded for fluorescence measurements, with the then surprising finding of non-Lambertian fluorescence [16]. In retrospect, that finding becomes well understood by models including the effect of refractive index difference between air and the fluorescent material [17,18].

SOURCES AND DETECTORS

Calibration facilities for radiometric and photometric properties of light sources were first developed in collaboration with the Swedish SP for visible [19] and with STUK for UV [20]. The leading idea was to use the Hamamatsu trap detector [21] in a filter radiometer to avoid interreflections between the detector and filter to allow separate calibration of the filter transmittance [9] and trap detector [4]. The method was later refined to a spectral irradiance scale over UV and visible regions using characterized filter radiometers directly with lamps [22,23], with special emphasis on solar UV where the continued collaboration with STUK and the Finnish Meteorological Institute has been important [24,25].

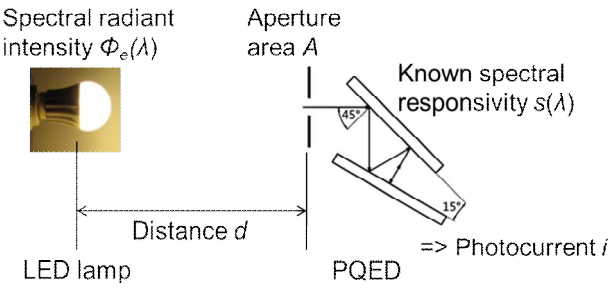

Figure 1. Setup for photometric measurements without $V(\lambda)$ filter. The accurately known spectral responsivity of the PQED allows the colour mismatch correction for white LEDs to be determined with lower uncertainty than that of the relative emission spectrum $\Phi_e(\lambda)/\Phi_e(\lambda_0)$ [48,49]. It is essential that LEDs emit very little outside the visible.

For photometry, the units of luminous intensity [26], luminance [27] and luminous flux [28] were realized using the most convenient methods available at that time for incandescent lamps. Recently, the work has been extended to LED [29,30] and OLED [31] light sources, including mesopic photometry [32]. The aperture area and effective distance between source and detector are important parameters for photometry. For both of these, original optical measurement methods have been developed [33-35], which have also been taken into use [36,37] and applied [38] by others.

In recent years a significant effort has been devoted to the development of the Predictable Quantum Efficient Detector (PQED) [39-47]. As shown in Fig. 1, the PQED consists of two special silicon photodiodes that have very low internal quantum deficiency and reflectance [39,40]. These features allow the PQED to be used as a primary

standard of optical power in the visible wavelength range [45] and for new type of photometry applicable with LED light sources as depicted in Fig. 1 [48,49].

The PQED development [50,51] and applications [52] continue in the EMRP's NEWSTAR project [53].

REFERENCES

1. Y. Väisälä, Die Anwendung der Lichtinterferenz zu Längenmessungen auf grösseren Distanzen, Publ. Finn. Geod. Inst**. 2**, 22 p. (1923).
2. T. Varpula et al. Optical Power Calibrator Based on a Stabilized Green He-Ne Laser and a Cryogenic Absolute Radiometer, IEEE Trans. Instrum. Meas. **38**, 558 (1989).
3. J. E. Martin et al. A Cryogenic Radiometer for Absolute Radiometric Measurements, Metrologia **21**, 147 (1985).
4. A. Lassila et al. Intercomparison of Cryogenic Radiometers using Silicon Trap Detectors, Meas. Sci. Technol. **8**, 123 (1997).
5. R. Goebel et al. Report on the International Comparison of Cryogenic Radiometers Based on Transfer Detectors, BIPM Report-2000/9 (2000).
6. E. Ikonen, Interference Effects between Independent Gamma Rays, Phys. Rev. Lett. **68**, 2759 (1992).
7. E. Ikonen and R. Rüffer, Correlated Gamma Rays in Synchrotron Radiation, Hyp. Interact. **92**, 1089 (1994).
8. I Müller et al. QOT_PO_009, NEWRAD 2014
9. F. Manoochehri and E. Ikonen, High-accuracy Spectrometer for Measurement of Regular Spectral Transmittance, Appl. Optics **34**, 3686 (1995).
10. A. Haapalinna et al. Precision Spectrometer for Measurement of Specular Reflectance, Rev. Sci. Instrum. **73**, 2237 (2002).
11. A. Haapalinna et al. Spectral Reflectance of Silicon Photodiodes, Appl. Optics **37**, 729 (1998).
12. A. Lamminpää et al. Characterization of Thin Films Based on Reflectance and Transmittance Measurements at Oblique Angles of Incidence, Appl. Optics **45**, 1392 (2006).
13. S. Pourjamal et al. OPM_OR_018, NEWRAD 2014
14. S. Nevas et al. Gonioreflectometer for Measuring Spectral Diffuse Reflectance, Appl. Optics **35**, 6391 (2004).
15. P. Jaanson et al. EAO_OR_011, NEWRAD 2014
16. S. Holopainen et al. Non-Lambertian Behaviour of Fluorescence Emission from Solid Amorphous Material, Metrologia **46**, S197 (2009).
17. T. Pulli et al. A Method for Optimizing the Cosine Response of Solar UV Diffusers, J. Geophys. Res. Atmos. **118**, 7897 (2013).
18. T. Pulli et al. SSR_OR_005, NEWRAD 2014
19. E. Ikonen et al. Radiometric Realization of the Candela with a Trap Detector, Metrologia **32**, 689 (1995/96).
20. P. Kärhä et al. Detector-Based Calibration Method for High-Accuracy Solar UV Measurements, Photochem. Photobiol. **64**, 340 (1996).
21. N. P. Fox, Trap Detectors and Their Properties, Metrologia **28**, 197 (1991)
22. P. Kärhä et al. Development of a Detector-Based Absolute Spectral Irradiance Scale in the 380–900 nm Spectral Range, Appl. Optics **36**, 8909 (1997).
23. T.Kübarsepp et al. Spectral Irradiance Measurements of Tungsten Lamps with Filter Radiometers in the Spectral Range 290 nm to 900 nm, Metrologia **37**, 305 (2000).
24. K. Lakkala et al. EAO_PO_003, NEWRAD 2014
25. P. Kärhä et al. Portable Detector-Based Primary Scale of Spectral Irradiance, J. Geophys. Res. **105**, 4803 (2000).
26. P. Toivanen et al, Realization of the Unit of Luminous Intensity at the HUT, Metrologia **37**, 131 (2000).
27. P. Toivanen et al. Realizations of the Units of Luminance and Spectral Radiance at the HUT, Metrologia **37**, 527 (2000).
28. J. Hovila et al. Realization of the Unit of Luminous Flux at the HUT Using the Absolute Integrating-Sphere Method, Metrologia **41**, 407 (2004).
29. T. Poikonen et al. Luminous Efficacy Measurement of Solid State Lamps, Metrologia **49**, S135 (2012).
30. T. Poikonen et al. OT_OR_011, NEWRAD 2014
31. M. Santaholma et al. SBR_OR_013, NEWRAD 2014
32. P. Kärhä et al. DBA_OR_042, NEWRAD 2014
33. A. Lassila et al. An Optical Method for Direct Determination of the Radiometric Aperture Area at High Accuracy, Meas. Sci. Technol. **8**, 973 (1997).
34. J. Hovila et al. Determination of the Diffuser Reference Plane for Accurate Illuminance Responsivity Calibrations, Appl. Optics **44**, 5894 (2005).
35. P. Manninen et al. Estimation of the Optical Receiving Plane Positions of Solar Spectroradiometers with Spherical Diffusers on the Basis of Spatial Responsivity Data, Opt. Lett. **34**, 3241 (2009).
36. M. Stock and R. Goebel, Practical Aspects of Aperture-Area Measurements by Superposition of Gaussian Laser Beams, Metrologia **37**, 633 (2000).
37. H. Shitomi, NMIJ, private communication.
38. J. Gröbner et al. Experimental Determination of the Reference Plane of Shaped Diffusers by Solar Ultra-violet Measurements, Opt. Lett. **32**, 80 (2007).
39. M. Sildoja et al. Reflectance Calculations for a Predictable Quantum Efficient Detector, Metrologia **46**, S151 (2009).
40. J. Gran et al. Simulations of a Predictable Quantum Efficient Detector with PC1D, Metrologia **49**, S130 (2012).
41. M. Sildoja et al. Predictable Quantum Efficient Detector: I. Photodiodes and Predicted Responsivity, Metrologia **50**, 385 (2013).
42. I. Müller et al. Predictable Quantum Efficient Detector: II. Characterization and Confirmed Responsivity, Metrologia **50**, 395 (2013).
43. M. Sildoja et al. Use of the Predictable Quantum Efficient Detector with Light Sources of Uncontrolled State of Polarization, Meas. Sci. Technol. **25**, 015203 (2014).
44. F. Manoocheri et al. Low-Loss Photon-to-Electron Conversion, Optical Review (in press).
45. T. Dönsberg et al. A Primary Standard of Optical Power Based on Induced-Junction Silicon Photodiodes Operated at Room Temperature, Metrologia (in press).
46. M. Sildoja et al. DBS_OR_020, NEWRAD 2014
47. T. Dönsberg et al. DBS_OR_016, NEWRAD 2014
48. T. Dönsberg et al. SBR_OR_020, NEWRAD 2014
49. H. Baumgartner et al. SBR_OR_019, NEWRAD 2014
50. I. Müller et al. DBS_PO_011, NEWRAD 2014
51. C. K. Tang et al. DBA_OR_012, NEWRAD 2014
52. J. Gran et al. DBA_OR_018, NEWRAD 2014
53. M. L. Rastello et al. DBS_OR_015, NEWRAD 2014

New integrating sphere-based absolute reflectance measurement with emphasis on the reflectance uniformity of the sphere wall

Hiroshi Shitomi

National Metrology Institute of Japan (NMIJ), AIST, Tsukuba, JAPAN
Corresponding e-mail address: h-shitomi@aist.go.jp

A new method for integrating sphere-based absolute reflectance measurement has been developed and applied to the establishment of the spectral diffuse reflectance standard in NMIJ from the UV to the near-IR (NIR) region. It focuses on the improvement of critical error factors such as reflectance non-uniformity by theoretical and instrumental modification by applying a specially designed integrating sphere. Recent CCPR-K5 comparison shows the good agreement that strongly supports the validity of the new approach discussed here.

INTRODUCTION

Spectral diffuse reflectance was assigned to a key comparison (CCPR-K5) in 1997 as the most fundamental quantities that can be used to underpin a lot of measurand relating to the optical properties of materials under the framework of CIPM MRA. Thus, realizing and maintaining the accurate spectral diffuse reflectance standard with appropriate traceability chain through calibration services are of high importance for national metrology institutes (NMIs).

National Metrology Institute of Japan (NMIJ) has been trying to establish the spectral diffuse reflectance standard from UV (down to 250 nm) to NIR (up to 2500 nm) region with a new integrating sphere-based approach. That is the integrated approach by modifying existing methods with respect to re-consideration of sphere-errors and by introducing a specially designed integrating sphere with emphasis on the reflectance uniformity. In this paper, a series of study on the development of the new method is summarized with the outline of theoretical and instrumental modification of existing methods, characterization of an integrating sphere specialized for the absolute reflectance measurement purposes and the validation of the method by means the international comparison (CCPR-K5).

PRINCIPLE AND INSTRUMENTATION

There are two prominent features in the new method. One is the theoretical and instrumental modification of Sharp-Little setup [1, 2] to improve critical sphere-errors discussed in the past [3]. Another one is development of a novel integrating sphere suitable for absolute reflectance measurements.

Fig.1 shows the schematic diagram of the modified Sharp-Little method, outlined in ref [4]. The spectral radiant flux $\Phi_0(\lambda)$ introduced into an integrating sphere irradiates a part of the sphere wall B. Radiance ($L_1(\lambda)$ and $L_2(\lambda)$) of another part of the sphere C is measured under two different geometries with respect to the position of a baffle X inside the sphere, which works to control the contribution of the first reflection component from B to C. The ratio $L_1(\lambda)/L_2(\lambda)$ corresponds to the average spectral reflectance of the sphere wall $\rho_{d:d}(\lambda)$ as follows.

$$\frac{L_1(\lambda)}{L_2(\lambda)} = \frac{\dfrac{\rho_{de:0}(\lambda)}{\pi}\left(\dfrac{\Phi_0(\lambda)}{S}\cdot\dfrac{\rho_{0:de}(\lambda)\cdot\rho_{d:d}(\lambda)}{1-\rho_{d:d}(\lambda)}\right)}{\dfrac{\rho_{de:0}(\lambda)}{\pi}\left(\dfrac{\Phi_0(\lambda)}{S}\cdot\dfrac{\rho_{0:de}(\lambda)}{1-\rho_{d:d}(\lambda)}\right)} = \rho_{d:d}(\lambda) \qquad (1)$$

where $\rho_{0:de}(\lambda)$ is the spectral diffuse reflectance of B and $\rho_{de:0}(\lambda)$ is spectral radiance factor of C, respectively. Apparent measurement principle is simple, and the main difference from the original Sharp-Little setup is that the measurement target is fixed whereas two positions on the sphere wall are measured in the original one. Fixing the measurement target is essential to decrease the error due to reflectance non-uniformity of the sphere wall and eliminate some critical approximation based on the "ideal sphere" applied in the original method, which is hard to be satisfied. In addition, the new method explicitly includes some correction factors regarding the imperfections of the integrating sphere and conversion of measurement geometries.

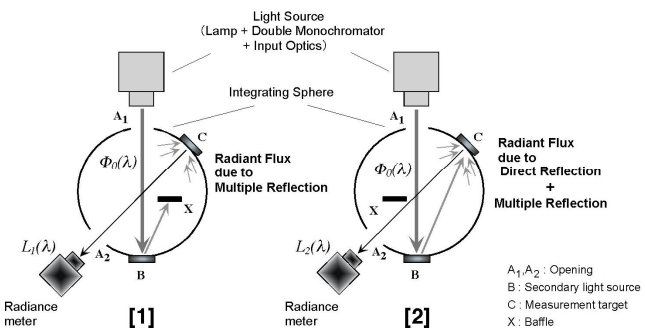

Figure 1. Outline of the modified Sharp-Little setup.

Another key development is the specially designed integrating sphere, whose basic concept was discussed in ref [5]. A series of study revealed that the most critical error factor is the reflectance non-uniformity of the sphere wall. That can basically be applied almost all the integrating sphere-based absolute methods proposed in the past [3]. We developed a PTFE-based integrating sphere (NMIJ sphere) that has excellent reflectance uniformity as shown in Fig.2. The reflectance non-uniformity of the NMIJ sphere from UV to NIR region evaluated as the distribution of relative spectral reflectance at each position of the sphere wall is 0.09 % to 0.66 % (2σ) depending on the wavelength, which is around one order of magnitude better than conventional integrating spheres with $BaSO_4$ paint surface.

RESULTS

By the combination of the modified Sharp-Little method and the NMIJ sphere, we successfully established the spectral diffuse reflectance standard and corresponded calibration capability with the relative expanded uncertainty of 0.30 % to 0.46 % (k=2) for the visible region.

NMIJ took part in the CCPR-K5, the comparison on the spectral diffuse reflectance measurements in the wavelength range from 360 nm to 820 nm, using the standard based on the new absolute reflectance measurement described in this paper. Fig.3 shows relative difference from the key comparison reference value (KCRV) [6]. The bar indicates the relative expanded uncertainty (k=2) NMIJ declared at each wavelength. A good agreement within the stated uncertainty was observed for the NMIJ's result, which is the strong evidence to show the validity of the new absolute reflectance measurement.

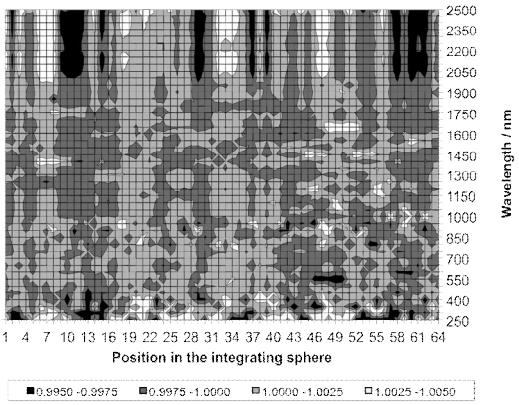

Figure 2. Relative reflectance distribution onto the sphere wall.

FHRTHER DEVELOPMENT

Further methodology, modified double-sphere method [7], has been applied to extend the calibration range with respect to the wavelength to both UV and NIR region. Using the known absolute reflectance obtained by the modified Sharp-Little method shown above, a critical parameter can be determined and the wavelength range is effectively extended as relative-like measurement with known absolute reflectance, which has a great advantage to overcome the difficulty in directly applying existing absolute reflectance measurements for UV and NIR regions.

SUMMARY

Based on the modifications of Sharp-Little method and double-sphere method and their effective integration with the PTFE-based integrating sphere with uniform reflectance, spectral diffuse reflectance standard from 250 nm to 2500 nm has been successfully realized in NMIJ, whose validity is supported by the result of CCPR-K5.

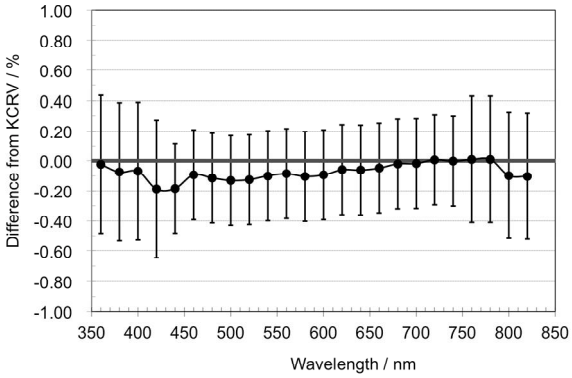

Figure 3. NMIJ's result shown in CCPR-K5.

REFERENCES

1. C. H. Sharp et al., Measurements of reflection factors, Trans. Illum. Eng. Soc., 15, 802-810, 1920.
2. W. Budde et al., Absolute measurements of diffuse reflectance in the d/0 geometry, Die Farbe, 19, 94-102, 1970.
3. A. Reule, Absolute reflectance measurement using integrating sphere goniophotometric corrections in the evaluation of results of different methods, Optik, 49, 499-504, 1978.
4. H. Shitomi et al., New Realization of Spectral Diffuse Reflectance Standard at NMIJ, Proc. 10th Congress of AIC, 523-526, 2005.
5. H. Shitomi et al., Development of a new integrating sphere with uniform reflectance for absolute diffuse reflectance measurements, Metrologia, 40, S185-S188, 2003.
6. M. Nadal et al., Final report on the key comparison CCPR-K5: Spectral diffuse reflectance, Metrologia, 50, Technical Supplement 02003, 2013.
7. H. Shitomi et al., A new absolute diffuse reflectance measurement in the near-IR region based on the modified double-sphere method, Metrologia, 46, S186-S190, 2009.

The Moon as an Absolute Radiometric Standard for Remote Sensing

Claire Cramer

National Institute of Standards and Technology, Gaithersburg, MD, USA
Corresponding e-mail address: claire.cramer@nist.gov

Establishing the Moon as an absolute spectral irradiance reference source has the potential to improve on-orbit calibrations of earth-observing instruments, especially across gaps in satellite data records. The Moon is of comparable brightness to the Earth when viewed from orbit, its surface reflectance is exceptionally stable, and it has the advantage of not being obscured by the Earth's atmosphere. Observations of the Moon have been used to track changes in satellite sensor response at the sub-percent level, relying on a model developed by the United States Geological Survey (USGS) that predicts the geometric dependence of the Moon's irradiance. The absolute scale of the USGS model, however, is not known accurately enough to allow the Moon to establish an absolute scale for instrument response.

The National Institute of Science and Technology (NIST) is currently engaged in an effort to improve the absolute calibration of lunar irradiance at reflected solar wavelengths from an accuracy of ~10 % to 1 % in the spectral range accessible with silicon detectors, with the intent to expand further into the infrared in subsequent years. Our prototype observation platform is a 4-inch telescope with an integrating sphere in the optical train at a position where the sphere aperture is slightly larger than the imaged lunar disk. The sphere is fiber-coupled to a laboratory-calibrated spectrometer with a resolution of 3 nm.

Our proof-of-principle measurement yielded an uncertainty below 1 % from 420 nm to 1000 nm. This measurement uncertainty meets the stability requirement for many climate data records derived from satellite images, including those for vegetation, aerosols, and snow and ice albedo. It therefore opens the possibility of using the Moon as a calibration standard to bridge gaps in satellite coverage and validate atmospheric retrieval algorithms. Our measurement technique also yields detailed information about the atmosphere at the measurement site, suggesting that lunar observations are a possible solution for aerosol monitoring during the polar winter and can provide night-time measurements to complement aerosol data collected with sun photometers.

I will review the context in which lunar calibration is useful for remote sensing, describe the NIST measurements, and outline an observing campaign that could establish the Moon as a useful exoatmospheric optical radiation standard traceable to the SI.

Radiometric Calibration of Limb Sounders for Traceable Measurement of Atmospheric Essential Climate Variables

C. Monte[1], B. Gutschwager[1], A. Adibekyan[1], M. Kehrt[1], F. Olschewski[2], P. Preusse[3], J. Ungermann[3], H. Oelhaf[4], F. Friedl-Vallon[4], and J. Hollandt[1]

[1]*Physikalisch-Technische Bundesanstalt, Abbestraße 2-12, 10587 Berlin, Germany*
[2]*University of Wuppertal, Atmospheric Physics, 42119 Wuppertal, Germany*
[3]*Research Centre Jülich GmbH, 52428 Jülich, Germany*
[4]*Karlsruhe Institute of Technology, 76131 Karlsruhe, Germany*
Christian.Monte@PTB.de

GLORIA is an airborne, imaging, infrared Fourier Transform spectrometer that applies the limb-sounding technique to perform trace gas and temperature measurements in the Earth's atmosphere with unprecedented 2-dimensional or even 3-dimensional resolution. To ensure the traceability of these measurements to the International Temperature Scale and thereby to an absolute radiance scale, GLORIA carries an on-board calibration system. We describe the radiometric and thermometric characterization and calibration of the in-flight calibration system at the Reduced Background Calibration Facility (RBCF) of the PTB with a standard uncertainty of less than 100 mK. Extensive investigations of the system concerning its absolute radiation temperature and spectral radiance, its temperature homogeneity, its short- and long-term stability and the traceability chain are discussed. The instrument has and will participate in numerous scientific aircraft campaigns addressing upper troposphere/lower stratosphere (UTLS) science. Exemplarily, results on atmospheric essential climate variables measured during the TACS/ESMVal-Campaign in 2012 on the German research aircraft HALO are presented.

INTRODUCTION AND BACKGROUND

The newly developed limb-imaging technique provides 3D observations of multiple trace gases, aerosols, and clouds in the UTLS with unprecedented resolution. The highly dynamic structure and chemical composition of the UTLS play an essential role in the earth's climate system, causing prominent changes in the surface temperature via changes in the atmospheric radiative forcing. The Gimballed Limb Observer for Radiance Imaging of the Atmosphere (GLORIA) [1,2] (Fig. 1) developed for operation on the German research aircraft HALO (High Altitude and LOng Range Research Aircraft) and the Russian M55-Geophysica is the first instrument that uses this technique and further applications on balloons and satellites are envisaged. The measurement of key climate variables requires these instruments to be stringently calibrated and recalibrated traceable to the International System of Units (SI).

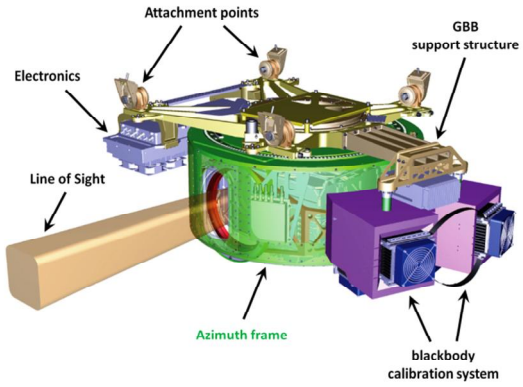

Figure 1. Gimbal-mounted GLORIA instrument with its on-board calibration sources.

GLORIA CALIBRATION SYSTEM

To ensure the traceability of the atmospheric measurements to the International Temperature Scale and thereby to an absolute radiance scale, GLORIA carries a sophisticated on-board calibration system [3]. It basically consists of two identical large area and high emissivity infrared radiators (GLORIA-Blackbodies: GBB-C and GBB-H) (Fig. 2), which can be continuously and independently operated at two adjustable temperatures in a range from -50 °C to 0 °C during flight. The limited resources in weight and electrical power provided in the instrument compartment of the aircraft, the harsh and rapidly changing environmental conditions during flight and the demanding calibration requirements of GLORIA meant a major challenge for the design and operation of the calibration system. The major radiometric and

thermometric requirements on the GLORIA calibration system are summarized as follows: Radiating area 126 mm x 126 mm, temperature of GBB-C at least 10 K below ambient temperature, temperature difference between GBB-C and GBB-H at least 40 K, standard uncertainty of surface radiation temperature < 100 mK, short-term stability better than 25 mK/min, temperature homogeneity better than 150 mK over full aperture.

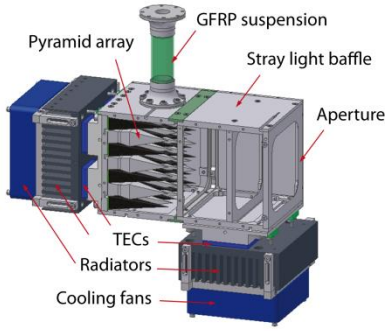

Figure 2. Schematic diagram of a GLORIA blackbody. A pyramid array forms the radiating area.

RADIOMETRIC CALIBRATION

The GLORIA calibration system has been comprehensively characterized at the RBCF in terms of its radiometric and thermometric requirements [4]. The RBCF serves as a facility for the measurement of spectral radiance and radiation temperature of radiation sources and the signal-temperature characteristic of radiation thermometers under reduced infrared background radiation in a temperature range from -170 °C to 450 °C traceable to the ITS-90. Furthermore, it allows the spectrally and angularly resolved measurement of the spectral emissivity from -40 °C to 600 °C. Measurements can be performed in air, under the pressure conditions of the upper atmosphere, and in vacuum. The calibration was performed by direct comparison of each GBB to the reference blackbodies of the RBCF via a vacuum radiation thermometer and a vacuum FTS from 7 µm to 16 µm. All measurements confirmed that the required short-term stability and spatial homogeneity (Fig. 3) over the full optical surface is achieved by both GBBs. The measured radiation temperatures showed no significant dependence with wavelength. All measurements confirmed that a high as well as spatially and spectrally homogeneous effective emissivity is achieved with the coated pyramid array.

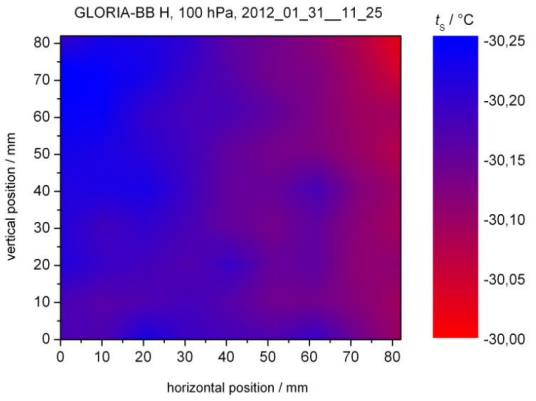

Figure 3. Radiation temperature distribution of GBB-H over its central area of 80 mm x 80 mm at -30 °C in a 100 hPa nitrogen environment.

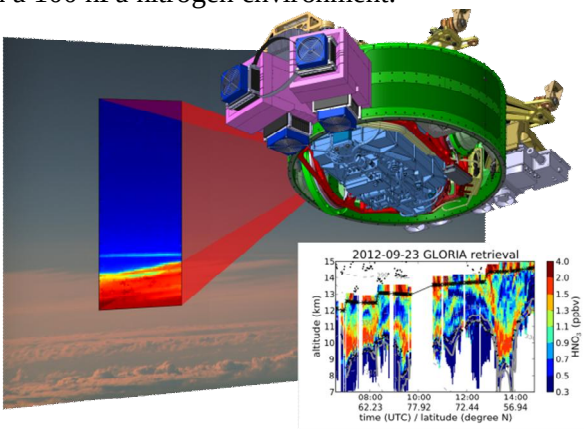

Figure 4. View of GLORIA on a cloud scenario taken from 14 km heights. The infrared image of GLORIA is given as a cutout in false colour (red/blue). It represents integrated radiation from 10.5 µm to 12.5 µm. Greenhouse gases can be identified by their spectral signatures. The graph in the lower right corner gives the atmospheric distribution of low concentrations of nitric acid recorded during a flight from southern Germany to northern Norway.

OUTLOOK

So far three calibration campaigns have been performed with the GBBs at the RBCF: In December 2010 about one year before the maiden flight of GLORIA, in January 2012 shortly after its successful test flight with the Geophysica during the ESA Sounder Campaign ESSenCe, and in January 2013 about four months after its first scientific campaign with HALO during the TACS/ESMVal Campaign (Fig. 4). The GLORIA calibration system will be regularly linked to the ITS-90 via the RBCF at PTB to provide traceability of the GLORIA atmospheric measurements as needed.

REFERENCES

1. M. Riese et al. Gimballed Limb Observer for Radiance Imaging of the Atmosphere (GLORIA) scientific objectives. *Atmos. Meas. Tech. Discuss., 7,* 1535–1572, 2014.
2. F. Friedl-Vallon et al. Instrument concept of the imaging Fourier transform spectrometer GLORIA, *Atmos. Meas. Tech. Discuss., 7,* 2301-2337, 2014.
3. F. Olschewski et al. The in-flight blackbody calibration system for the GLORIA interferometer on board an airborne research platform. Atmos. Meas. Tech., 6, 3067-3082, 2013.
4. C. Monte et al. Radiometric calibration of the in-flight blackbody calibration system of the GLORIA interferometer. Atmos. Meas. Tech., 7, 13-27, 2014.

Part of this work has been supported by the European Metrology Research Programme (EMRP).

Calibration of the reference spectroradiometer for the quality assurance of the terrestrial solar spectral ultraviolet radiation measurements in Europe

Saulius Nevas[1], Julian Gröbner[2], Michaela Schuster[1], Peter Sperfeld[1], Luca Egli[2], Gregor Hülsen[2], Armin Sperling[1], Peter Meindl[1], Stefan Pendsa[1], and Sven Pape[1]

[1] *Physikalisch-Technische Bundesanstalt (PTB), Braunschweig and Berlin, Germany,*
[2] *Physikalisch-Meteorologisches Observatorium Davos, World Radiation Center, Davos Dorf, Switzerland*
Corresponding e-mail address: saulius.nevas@ptb.de

Quality assurance of the terrestrial solar spectral ultraviolet radiation measurements at European UV monitoring sites is based on the reference spectroradiometer QASUME. Calibration of the instrument along a shortened traceability chain with reduced uncertainties was one of the key tasks within the EMRP solarUV project. This paper presents new developments within the project to reach these aims.

INTRODUCTION

Long-term trends in surface solar radiation due to atmospheric induced changes have demonstrated decadal changes of the order of 2% per decade over Europe [1]. These changes are currently explained by changes in the transparency of the atmosphere and possibly long-term changes in clouds. The effects on ultraviolet radiation have not yet been quantified due to the difficulty of observing these small changes over such long time scales. Future changes in UV radiation due to atmospheric changes are expected to be of the same order of magnitude and require measurements with significantly lower uncertainties of around 1% to 2% to detect such decadal changes. To address this challenge, not only significant improvements in the characterisation and operation of the solar UV instruments deployed at UV monitoring sites but also in the traceability to the primary reference standard operated by National Metrology Institutes are required.

Quality assurance of the solar spectral ultraviolet radiation measurements at the European UV monitoring sites and harmonisation of the results are based on a portable reference spectroradiometer, QASUME, operated by the Physikalisch-Meteorologisches Observatorium Davos/World Radiation Center (PMOD/WRC) [2]. Since the completion of the European Commission-funded project Quality Assurance of Spectral Ultraviolet Measurements in Europe through the Development of a Transportable Unit (QASUME), the calibration of the spectroradiometer has been carried out via a set of transfer standard lamps traceable to the spectral irradiance scale at the Physikalisch-Technische Bundesanstalt (PTB) realised by a high temperature blackbody [3, 4]. In 2011, a joint research project ENV03 "Traceability for surface spectral solar ultraviolet radiation" was started within the European Metrology Research Programme (EMRP) with ambitious goals to address the above mentioned challenges related to the solar UV radiation measurements. One of the goals of the project was to shorten the traceability chain and to reduce the associated transfer uncertainties. The talk will present the work carried out within the project following this aim and the results achieved.

FROM SOURCE- TO DETECTOR-BASED CALIBRATION

The traceability chain for the calibration of QASUME reference spectroradiometer has been mainly source-based: a high-temperature blackbody radiator as primary standard of spectral irradiance and transfer standard lamps were used for direct or subsidiary measurements (Figure 1, right side). Alternatively, a completely detector-based traceability chain allowing a calibration of the spectral responsivity of QASUME against a trap detector can be realised with the help of wavelength-tuneable lasers (Figure 1, left side). The motivation to follow this traceability route is to shorten the traceability chain to the primary standard of optical power, the cryogenic radiometer, and, thus, reduce the associated uncertainties. In order to enable this calibration scheme, however, a uniform and quasi monochromatic radiant field with sufficiently high irradiance needs to be generated. Within the framework of the mentioned EMRP solarUV project, the wavelength-tuneable laser facility at the PTB, TULIP, was upgraded by mode-locked fs-pulsed lasers and prepared for the operations throughout the solar UV spectral rage, 280 nm to 400 nm, and

beyond. To enable irradiance-mode calibrations at the TULIP facility in the UV spectral range, a laser monochromator has been set-up and an active stabilisation for the laser power has been implemented. Additionally, a beam conditioning unit providing a spatially homogeneous and depolarised field qualified for calibrations in the irradiance mode has been developed (see Figure 2). The traceability to the primary standard for radiant power, the cryogenic radiometer of the PTB, is provided by silicon trap detectors built and characterised for this purpose. The transfer to irradiance responsivity has been realized using a radiometric aperture with calibrated area.

Two measurement campaigns involving both the calibration of QASUME spectroradiometer at the TULIP facility against the trap detectors and a direct measurement of spectral irradiance by the high temperature blackbody were arranged, in spring of 2013 and of 2014. The second campaign was used to sort out systematic effects observed in the behaviour of QASUME spectroradiometer during the laser-based calibrations of the first campaign. Results of the calibrations will be presented during the talk.

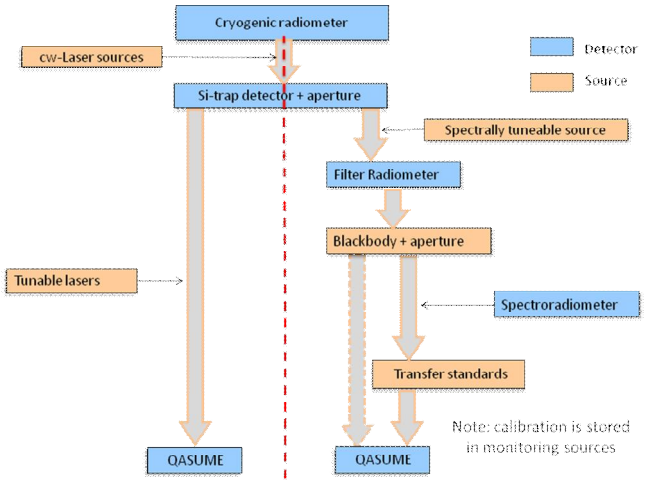

Figure 1. Traceability chain for the calibration of the reference spectroradiometer QASUME: it can be realised by means of calibration sources as shown to the right from the vertical line or by using a calibrated detector and wavelength-tuneable lasers.

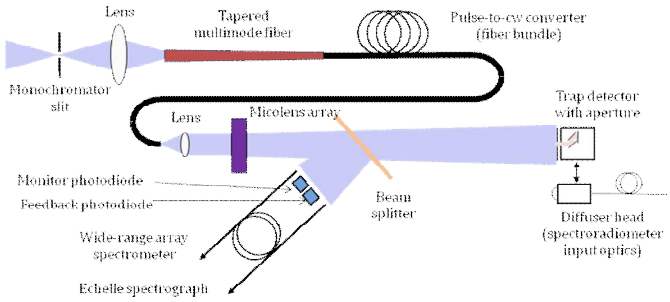

Figure 2. Schematic representation of a beam conditioning unit in the TULIP facility used to convert the beam of a mode-locked fs-pulsed tuneable laser into a uniform, stable and depolarised radiant field necessary for the irradiance-mode calibrations.

ACKNOWLEDGEMENT

Part of this work has been supported by the European Metrology Research Programme (EMRP) within the joint research project "Traceability for surface spectral solar ultraviolet radiation" (solarUV). The EMRP is jointly funded by the EMRP participating countries within EURAMET and the European Union.

REFERENCES

1. M. Wild, "Global dimming and brightening: A review," J. Geophys. Res., 114, doi: 10.1029/ 2008JD011470, 2009.
2. G. Hülsen and J. Gröbner, "One decade of QASUME site audits: 2002-2012," UVNews: The official newsletter of the Thematic Network for Ultraviolet Measurements, No. 9, 27-29, 2013.
3. J. Gröbner, J. Schreder, S. Kazadzis, A. F. Bais, M. Blumthaler, P. Görts, R. Tax, T. Koskela, G. Seckmeyer, A. R. Webb, and D. Rembges, "Traveling reference spectroradiometer for routine quality assurance of spectral solar ultraviolet irradiance measurements," Appl. Opt., 44, 5321-5331, 2005.
4. J. Gröbner and P. Sperfeld, "Direct traceability of the portable QASUME irradiance scale to the primary irradiance standard of the PTB,'' Metrologia, 42, 134—139, 2005.

MEMS tunable filters

Maurizio Tormen

CSEM – Centre Suisse d'Electronique et de Microtechnique, Neuchatel, Switzerland
Corresponding e-mail address: Maurizio.tormen@csem.ch

CSEM has developed miniaturized tunable filters, based on MEMS (Micro-Electro-Mechanical Systems) technology. The chip operates in different spectral regions (VIS, near-IR, Mid-IR) and has been introduced as tunable element in devices such as tunable external cavity lasers, monochromators and wavemeters.

CSEM filter is a 5 x 5 mm^2 chip comprising a position encoder for accurate tuning.

Key features are compactness, low power operation, light weight, scalability for mass production and low price, shock resistance up to 3000 g.

The optical systems based on such a chip require basic optical elements and do not require external moving parts, keeping the system optical alignment simple.

Applications of pulsed OPO laser systems for optical radiometry

Yuqin Zong and Ping-Shine Shaw

National Institute of Standards and Technology (NIST), Gaithersburg, Maryland, USA
Corresponding e-mail address: yuqin.zong@nist.gov

Automated kHz tuneable optical parametric oscillator (OPO) laser systems are new and powerful tools for optical radiometry. A method was developed in 2011 for calibration of broadband detectors for spectral responsivities with a small uncertainty based on measurement of the total energy of pulse OPO laser trains. This method was extended recently for calibration of spectroradiometers. OPO laser systems have also been used in other optical radiometry fields at NIST such as spectral characterization and calibration of imaging instruments, measurement of optical properties, and biological research.

1. INTRODUCTION

Newly developed kHz tuneable optical parametric oscillator (OPO) laser systems are new and valuable tools for optical radiometry. Such OPO laser systems are typically automated with wide tuneable spectral ranges and are relatively low cost compared to continuous wave (CW) tuneable lasers. Different from CW tuneable lasers, output power of a kHz OPO laser system fluctuates on the order of 10 %, and it is difficult to stabilize an OPO laser system using a laser power controller commonly used in CW laser systems. Furthermore, duty-cycle of a kHz OPO is very low ($\approx 10^{-5}$) which makes measurement of the laser power difficult using conventional trans-impedance amplifiers. However, these difficulties associated with the application of kHz OPO lasers in optical radiometry can be overcome by changing the measurement mode from the conventional optical power mode to an optical energy mode. We developed a method in 2011 for calibration of broadband detectors for spectral responsivity with an expanded uncertainty of 0.05 % (k = 2) using a kHz OPO laser system [1]. Recently we extended this method for calibration of spectroradiometers in order to achieve much smaller calibration uncertainties. OPO laser systems have also been used in other optical radiometry fields at NIST such as characterization and calibration of imaging instruments, measurement of optical properties, and biological research.

2. NEW DETECTOR-BASED CALIBRATION METHOD FOR SPECTRORADIOMETERS

Spectroradiometers are typically calibrated against broadband spectral standard sources (e.g., deuterium lamps for the ultraviolet (UV) spectral region and quartz tungsten halogen lamps for the visible and infrared regions). Using the conventional source-based calibration method, however, the calibration uncertainty for spectral irradiance/radiance responsivity is limited to on the order of 1 %. In the UV regions the calibration uncertainties are much larger due to relatively low spectral radiant power of the calibration source and spectral stray light inside the spectroradiometer [2]. To reduce the calibration uncertainties we developed a new, detector-based calibration method for spectroradiometers using a kHz OPO laser system.

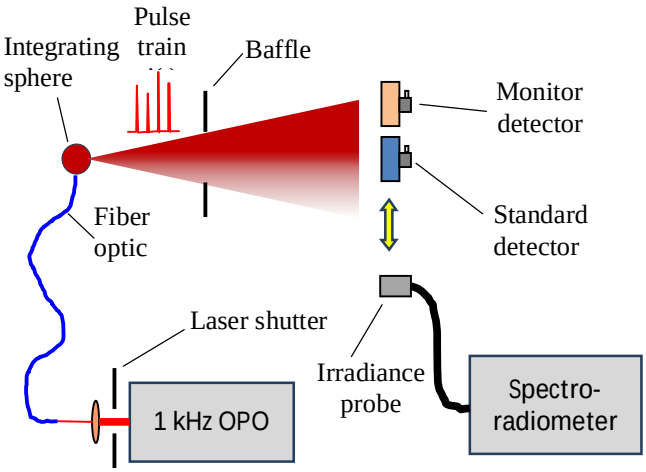

Figure 1. Schematic diagram of the detector-based method for calibration of spectroradiometers.

Similar to the calibration method developed for broadband detectors, the new method is based on simultaneous measurements of the total energy of a pulsed OPO laser train using the test spectroradiometer and a standard detector with a current integrator (also called charge amplifier). A schematic diagram of this method is shown in Figure 1.

The OPO laser beam is coupled into an integrating sphere through a multimode fiber optic to

form a uniform irradiance source. The spectroradiometer (or the standard detector) and the monitor detector measure a laser pulse train simultaneously. The laser shutter is used to control the length of a laser pulse train. Calibration of the test spectroradiometer is performed using a substitution method. The test spectroradiometer and the standard detector are aligned, in turn, to measure a pulsed OPO laser train over a period of time. The monitor detector is used to correct fluctuation of the pulsed OPO laser between the test spectroradiometer measurement and the standard detector measurement. The wavelength of the OPO laser is tuned across the entire spectral region of the spectroradiometer to determine the spectral responsivity of the spectroradiometer. The calibration process is fully automated.

The results and uncertainties using the new detector-based calibration method will be discussed and compared to those using the conventional source-based calibration method.

3. SPECTRAL CHARACTERIZATION AND CALIBRATION OF IMAGING INSTRUMEMTS

Imaging photometers and imaging radiometers are increasingly used in various applications. However, measurement uncertainties of such instruments are rather large compared to that of a single-element luminance meter or radiance meter. One of the causes resulting in large uncertainties is lack of a high-power wavelength-tuneable uniform spectral source such as an integrating sphere for spectral characterization and calibration. The kHz OPO laser based calibration system shown in Figure 1 is a powerful tool for this task, where the spectroradiometer is replaced with an imaging instrument. We have used this system for characterization of an imaging photometer for spectral responsivities.

4. MEASUREMENT OF OPTICAL PROPERTIES

A tuneable kHz OPO laser system is a great tool for measurement of optical properties such as spectral transmittance and reflectance. A tuneable kHz OPO laser system with a spectral range from 405 nm to 2500 nm is used for research of hyper-spectral medical imaging at NIST to measure optical property of various samples. Such a system has many advantages compared to a hyper-spectral camera in terms of spectral image quality and measurement uncertainty.

5. BIOLOGICAL RESEARCH

A kHz OPO laser system is also a valuable tool for biological research. As an example, a kHz UV OPO laser system is used at NIST for UV water treatment research to study action spectra of various microbes. The tuneable UV OPO laser system has many advantages compared to conventional mercury lamp based systems for biological research.

6. SUMMARY

Automated kHz tuneable OPO laser systems are new and powerful tools for optical radiometry. They have been used for calibration of broadband detectors and spectroradiometers for spectral responsivity with a small uncertainty. The OPO laser systems have also been used in other optical radiometry fields at NIST such as characterization and calibration of imaging instruments, measurement of optical properties, and biological research.

ACKNOWLEDGMENT

The authors would like to thank Thomas Larason, David Allen, John Woodward, Steven Brown, Keith Lykke, Yoshi Ohno, and Cameron Miller for their valuable contributions to this research.

REFERENCES

1. Y. Zong, S. W Brown, G. P. Eppeldauer, K. R. Lykke, and Y. Ohno, “A new method for spectral irradiance and radiance responsivity calibrations using kilohertz pulsed tunable optical parametric oscillators,” *Metrologia*, 49, S124–129. (2012).
2. Y. Zong, S. W. Brown, B. C. Johnson, K. R. Lykke, and Y. Ohno, “Simple spectral stray light correction method for array spectroradiometers,” *Appl. Opt.*, 45, 1111-1119, (2006).

Novel Lithographic Electrical-Substitution Radiometer

John Lehman[1], Solomon Woods[2], Malcolm White[1], and Nathan Tomlin[1]

[1]*The National Institute of Standards and Technology, Boulder, Colorado, USA*
[2]*The National Institute of Standards and Technology, Gaithersburg, Maryland, USA,*
Corresponding e-mail address: lehman@boulder.nist.gov

We have established a complete electrical-substitution radiometer fabricated from micro-machined silicon and vertically-aligned carbon nanotubes. Our present effort is directed toward fibre-coupled laser power measurements and, separately, Fourier transform spectrometer-based measurements of far infrared radiation. The essential variables relevant to detector operation are discussed with respect to physical properties and dimensions of the radiometer. The reduced size and complexity of the carbon nanotube-based radiometer compared to the conventional cryogenic radiometer presents the opportunity to reduce the cost and complexity while increasing the speed and versatility for a variety of NIST priorities.

INTRODUCTION

Carbon nanotube coatings are known to have high thermal diffusivity and extremely efficient optical absorption. In the past we have undertaken experiments to exploit carbon nanotubes for improved detectors for radiometry; primarily thermal detectors such as pyroelectrics, thermopiles and detectors for high-power laser measurements.[1,2,3] More recently, we have demonstrated the unique thermistor behaviour of vertically-aligned carbon nanotube arrays (VANTAs) at cryogenic temperatures.[4] Now, the VANTA is more than an optical coating. The large temperature coefficient of resistance presents the opportunity to build a greatly simplified electrical-substitution radiometer whereby the heater, thermistor and absorber are incorporated on a single chip. We describe the evolution of the carbon nanotube radiometer (CNTR), some theoretical basis for its design and measurement results that demonstrate the suitability for high accuracy measurements of electromagnetic radiation extending from the visible to the far infrared (VIS-FIR). The photograph in Fig. 1 depicts the CNTR described in this work. Fig. 2 is a schematic of the essential components.

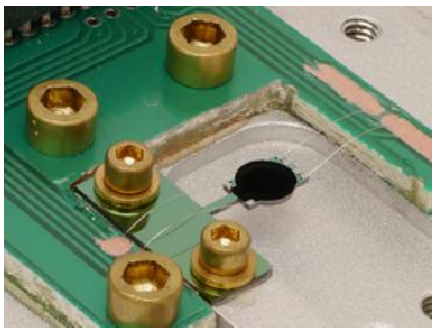

Figure 1. Photograph of the CNTR mounted mechanically with screws and electrically with wire bonding. The carbon nanotube forest is the ∅3 mm black circular area.

There are several important variables that must be considered in the radiometer chip's design. Conventionally, three of these four variables are designated α, distinguished by the subscript. The thermal diffusivity is $\alpha_{th} = k/\rho c$, where k is the thermal conductivity, ρ is the density and c is the specific heat capacity of the nanotube array. The thermal diffusivity of VANTAs was demonstrated with a carbon nanotube-coated pyroelectric detector.[2] In that work, the measured diffusivity $\alpha_{th} = 3 \times 10^{-4}$ m^2/s, was extremely high for a relatively low density ρ =7.6 kg/m^3 compared to other black coatings, which is an important consideration for coatings that are sufficiently thick for FIR absorption.

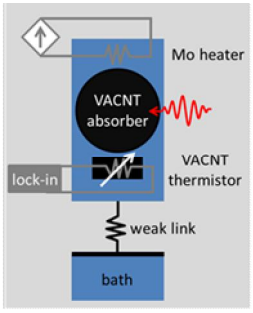

Figure 2. Schematic of the CNTR showing major components and readout.

Yang et al. first documented VANTAs as being "the world's darkest substance".[5] Since then, others have established that broad, uniform and highly efficient absorption, $\alpha_{opt} \sim 0.999$, in the VIS-FIR is attainable from a nanotube array.[6] The temperature

coefficient of resistance is $\alpha_{bol}=T/R(dR/dT)$, where R is the electrical resistance of the VANTA measured at temperature T. Tomlin et al., documented values of α_{bol} comparable to semiconductor thermistors.[4] The thermal conductance is determined by the silicon substrate on which the nanotubes are grown. In this instance, it is defined by $G = k_{sub}(wt/l)$, where k_{sub} is the thermal conductivity of the micromachined silicon substrate link having width w, thickness t and length l. Micromachining provides us with exquisite control of the substrate geometry (l, w and t).

DEVICE

The CNTR is lithographically fabricated on a ∅76.2 mm diameter silicon wafer. The processing steps consist of a molybdenum thin film deposition and wet etch, Al_2O_3 and Fe liftoff, micro-machined silicon etch, and VANTA growth. The VANTAs are ~100 µm tall and perform two functions: the absorber (a large circular patch) and the thermistor (a rectangular section with Mo leads).

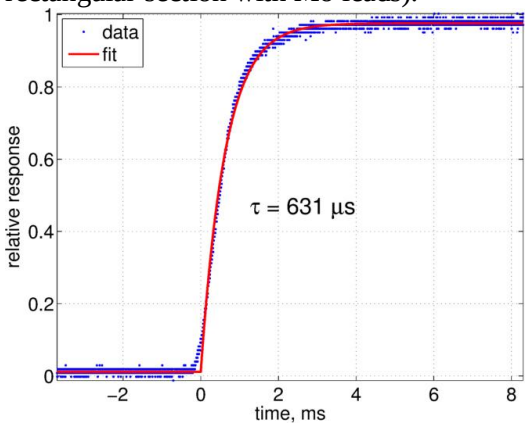

Figure 3. Temporal response of the CNTR due to optical heating. The switched optical power was ~450 µW.

The current CNTR was designed to be comparable to our existing cryogenic radiometer cavities and electronics, so that at 2 K, G ~ 150 µW/K, the Mo heater resistance is 90 Ohm, the thermistor resistance is ~10 kOhm, and the temperature coefficient α_{bol} ~ -2 (Table 1). One large difference, however, from conventional cryogenic radiometer cavities is the much shorter time constant (τ) less than 1 ms (Fig. 3).

The time response was measured with optical power applied to the CNTR by means of a standard 9 µm core, single-mode telecommunication fiber that is aligned at normal incidence to the center of the nanotube area. Optical powers were determined using electrical substitution to match the change in thermistor resistance for both optical and electrical power. To demonstrate the free-field operation of the CNTR, the spectral responsivity was measured by means of an infrared monochromator-based system, described elsewhere.[7] The results are consistent with independent reflectance measurements, which demonstrate the spectral uniformity of the CNTR.

CONCLUSION

The CNTR has potentially several great advantages over conventional cryogenic radiometers. Among the practical considerations is lower cost and smaller overall dimensions for a given detector area. The short time constant of the detector response is among the most desirable properties making the radiometer compatible with Fourier transform (FT) based measurements that would be impossible with slower detectors. In addition to FT-based FIR measurements, the technology might be exploited in the future for detector arrays and imaging where other detector technologies require unfavourable trade-offs.

Table 1. Summary of essential characteristics of the prototype CNTR.

Detector Attribute	Value
Area	∅ 3mm diameter
Time Constant, τ	1 ms
Wavelength Range	VIS > 25 µm
NEP	2×10^{-13} W/Hz$^{1/2}$
Operating Temperature	2-4 K
Thermistor Resistance, R	1-50 kΩ
Thermistor Sensitivity, α_{bol}	-2

REFERENCES

1. J. H. Lehman, C. Engtrakul, T. Gennett, and A. C. Dillon, Appl. Opt. 44 (4), 483-488 (2005).
2. J. H. Lehman, B. L., and E. N. Grossman, Applied Optics 50 (21), 4099-4104 (2011).
3. K. Ramadurai, L. Lewis, C. Cromer, R. L. Mahajan, K. E. Hurst, and J. H. Lehman, Proc. SPIE - Int. Soc. Opt. Eng. 6403-6408 (2006).
4. N. A. Tomlin and J. H. Lehman, Opt. Lett. **38** (2), 175-177 (2013).
5. Z. Yang, L. Ci, J. A. Bur, S. Lin, and P. M. Ajayan, Nano Lett. 8 (2), 446-451 (2008).
6. C. J. Chunnilall, J. H. Lehman, E. Theocharous, and A. Sanders, Carbon 50 (14), 5348-5350 (2012).
7. G. P Eppeldauer, J. Zeng, H. W. Yoon, B. Wilthan, T. C. Larason, and L M Hanssen, Metrologia 46 (4), S155 (2009).

Application of pulsed source for detector characterization

Kee-Suk Hong, Seongchong Park, and Dong-Hoon Lee*

Division of Physical Metrology, Korea Research Institute of Standards and Science (KRISS), Daejeon, Korea
Corresponding e-mail address: dh.lee@kriss.re.kr

We present our methodology for applying a pulsed source to characterize the response of optical detectors. The advantages and obstacles of the method are discussed based on our experimental realization of spectral responsivity scale from 250 nm to 1600 nm by using a tunable nanosecond-pulsed laser source.

Traditionally, optical radiometry is associated with continuous-wave (CW) radiation. Since most of the natural and artificial light sources in everyday life operate in the CW regime, optical detectors and sensors are characterized and calibrated for the corresponding conditions. In the CW regime, therefore, a source with high stability of output radiation was required for characterizing and calibrating optical detectors. Introduction of flickering or periodic modulation to a CW source improves the sensitivity of detection. However, the detector signal in this case is also proportional to the radiation power averaged over many cycles, and the requirement of source stability remains unchanged.

With the recent advance of the laser technology, a variety of pulsed sources with very high peak power and ultra-short pulse duration are available. A wavelength-tuneable monochromatic source covering a wide spectral range from UV to mid-IR can be easily realized based on a pulsed laser. In order to apply such a source for characterizing optical detectors, however, a new methodology needs to be developed considering various effects of detector response to high peak power, ultra-short pulse duration, and pulse-to-pulse energy fluctuation.

In this invited talk, we present the methodology developed in order to use a wavelength-tuneable pulsed laser for measuring spectral responsivity of photodiodes in a wide range from 250 nm to 1600 nm [1]. As a source, an optical parametric oscillator pumped at 355 nm is used, which provides pulses with a pulse duration of approximately 10 ns at a repetition rate of 1 kHz. Based on our method, we demonstrate a realization of the spectral responsivity scale traceable to the absolute cryogenic radiometer and to the spectral reflectance standards.

The main advantage of our method with a pulsed laser is that we can compare the signals of two detectors with a large sensitivity difference. In the realization of spectral responsivity, we compared a photodiode directly with a pyro-electric detector whose sensitivity is more than 3 orders of magnitude lower than a photodiode. Measurement of extreme values of ratios of two detector readings is made possible by the high peak power of the pulsed source. In addition, our method does not require a stable power output of the source. The ratio of detector readings is measured for each individual pulse so that the pulse-to-pulse energy fluctuation does not affect the measurement accuracy. We will show that such a fluctuation can be even beneficial to test the non-linearity of the test detector simultaneously with the responsivity measurement.

Our method also has several obstacles which should be carefully considered to achieve a high-accuracy measurement of detector responsivity. The most critical issue is how to produce a readout signal of detectors, which is proportional to the pulse energy. An optical pulse with duration of 10 ns can be regarded as a delta peak input for most of amplifiers and detectors under test, the time-dependent shape of the final reading of the detector output is limited by the combined bandwidth of amplifier and detector. However, the bandwidth of most of current amplifiers, especially operational amplifiers, depends on the input signal level, which results in a distortion of the pulse shape depending on the input pulse energy. This bandwidth-related nonlinearity of the detector reading should be carefully evaluated as an error or uncertainty component when a pulsed source is used.

The current status of realization of the spectral responsivity scale based on a pulsed tunable laser is that we could validate an agreement within 1 % with the results of the conventional realization. Further improvements of accuracy will be discussed in the talk.

REFERENCES

1. Kee-Suk Hong *et al.*, Realization of spectral responsivity scale from 250 nm to 1600 nm based on a pulsed tunable laser, in preparation.

Generation of narrowband single photons in the telecom band

Christoph Becher

Universität des Saarlandes, Saarbrücken, Germany
Corresponding e-mail address: christoph.becher@physik.uni-saarland.de

Single photon sources (SPS) with emission in one of the low-transmission loss windows of optical telecommunication (around 1.3 µm and 1.55 µm) are essential resources for many applications ranging from quantum information (e.g. quantum repeaters, quantum networks) to calibration of the detection efficiency of telecom single photon detectors.

In general, two major processes can be used for the generation of single telecom band photons: First, due to a current lack of deterministic SPS with direct emission in the telecom range, single photons from an emitter in the red or near-infrared spectral range (e.g. quantum dots, color centers) can be frequency converted by a nonlinear optical mixing process. The second option makes use of another nonlinear optical process, i.e. spontaneous parametric down conversion (SPDC) where a photon pair is produced and the detection of one of the produced photons may be used as herald of a single photon in the second channel.

For the first scheme, we here report on experiments on highly efficient (> 30%) frequency down-conversion of true single photons from quantum light sources in the visible or near-infrared to one of the telecom bands. As an example we demonstrate conversion of single photons from a semiconductor quantum dot (711 nm) to the telecom O-band (1313 nm) by difference frequency mixing with a strong classical field at 1550 nm. We measure the first and second order correlation of the single photons before and after conversion and prove the conservation of classical and non-classical properties [1]. In a second example we show frequency down-conversion of single photons from a frequency-degenerate photon pair source resonant with an atomic transition (854 nm) of Ca+ ions which are suitable as quantum repeater node. One photon of the pair is spectrally filtered to the linewidth of the atomic transition and used as a herald. By mixing with a pump field at 2.5 μm in a nonlinear waveguide the partner photon is converted to the telecom O-band at 1313 nm. We show that the temporal correlation between the photon pairs is preserved in the conversion process by measuring the photon correlation functions.

We further investigate generation of heralded telecom band single photons based on SPDC in a single-resonant optical parametric oscillator (OPO) operating far below oscillation threshold. The OPO is widely tunable from 810 nm to 955 nm in the signal mode and from 1200 nm to 1565 nm in the idler mode. We show that the signal could be tuned to an atomic resonance (e.g. Cs or Ca+) while the corresponding idler is located at telecom wavelengths. Using spectral filters we cut out one single line of the OPO-spectrum (44 MHz linewidth) and measure the spectral and temporal characteristics of the source including the signal-idler cross correlation and the heralding efficiency.

Combining SPDC sources with the technique of quantum frequency conversion will allow tailoring heralded single photons for application in long-range quantum networks and quantum metrology.

REFERENCES

1. S. Zaske, et al., Visible-to-Telecom Quantum Frequency Conversion of Light from a Single Quantum Emitter, Phys. Rev. Lett., 109, 147404, 2012.

Vacuum Radiance Temperature Standard Facility for Chinese Meteorological Satellite Infrared Remote Sensing

Xiaopeng Hao[1], Jian Song[1], Kang Xu[2], Zundong Yuan[1], and Jianping Sun[1]

[1]*Radiation Thermometry Laboratory, National Institute of Metrology, Beijing, China*

[2]*Chengdu University of Technology, Chengdu, China*

Corresponding e-mail address: haoxp@nim.ac.cn

The vacuum radiance temperature standard facility (VRTSF) for Chinese meteorological satellite infrared remote sensing is introduced in this paper. This facility as the national standard will be used to calibrate the big aperture blackbody for calibration the infrared remote-sensing instruments and the on-board blackbodies in the temperature range from 190 K to 340 K with the wavelength from 1-1000 μm in vacuum and reduced background chamber. The target uncertainty of this facility is 50 mK at 300 K and 10 μm wavelength. This facility will be finished at the end of 2015.

INTRODUCTION

Chinese meteorological satellites have been developed since 1970s in China. There are eight stars in four series until 2014. Chinese meteorological satellite is an important part of the world meteorological satellite detection system.

With climate change, environmental monitoring and forecast demanding more and more intense, the measurement accuracy become more and more important. For spectrally resolved thermal radiance and for sea-surface temperature datasets, they require an uncertainty of 0.1 K and a stability of 0.04 K per decade, corresponding to 0.01K stability in the IR spectral band of remote-sensing observations system from space [1].

The VNIIOFI of Russia has set up the standard facility which temperature 213 K – 353K at 2000 [2]. The RBCF of PTB is the very good standard facility for the calibration of the remote-sensing, the temperature range is from 100K-700K at 2009 [3].

The vacuum radiance temperature standard facility (VRTSF) for Chinese meteorological satellite infrared remote sensing has been started to setup at the national institute of metrology China (NIM) from 2013.

In this paper, the structure of VRTSF, vacuum standard blackbody and liquid nitrogen blackbody are introduced.

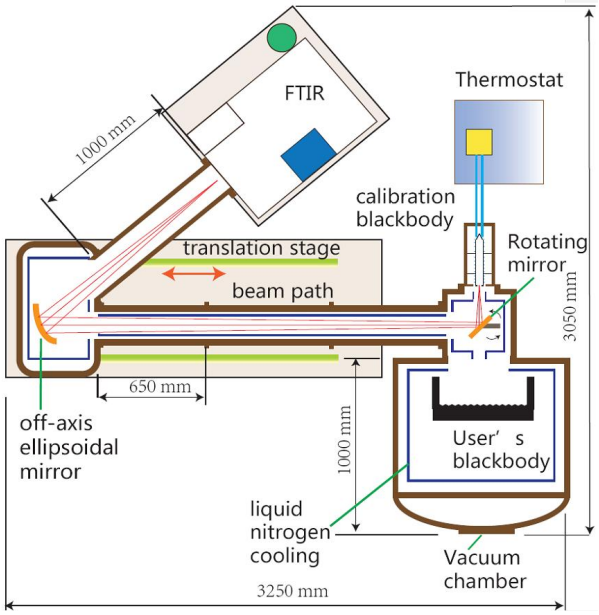

Figure 1. Layout of the VRTSF.

DESIGN OF VRTSF

The VRTSF is consisted of six parts, such as vacuum chamber for use's blackbody, FTIR spectrometer, standard blackbody, optical system, vacuum pumping and liquid nitrogen support system. The layout and specifications of the VRTSF is shown in figure 1 and listed in table 1. The vacuum chamber for user's blackbody is 1000 mm in diameter and 1000 mm in length included the heat sink cooling by liquid nitrogen. The maximum diameter for the calibrated user's blackbody is 650 mm.

The FTIR spectrometer is a Bruker VERTEX 80 V, the wavelength range of which is 1 μm-1000 μm by the InSb, MCT and Si-bolometer detectors.

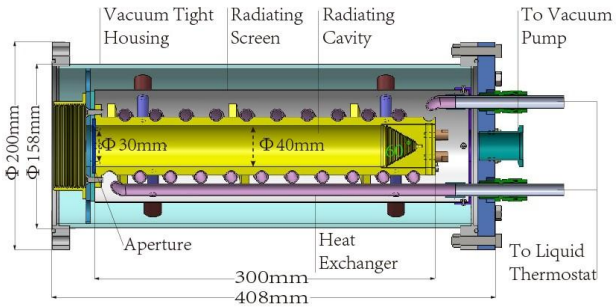

Figure 2. Cut view of the standard blackbody.

The standard blackbody is shown in figure 2. The temperature range is from 190K to 340K. The Lauda RP890C is used to control the temperature of the standard blackbody. The aperture of the cavity is 30 mm in diameter. The cavity is 300mm in depth, 40 mm in diameter. The surface of the cavity is coated by the Nextel Velvet-Coating 811-21. The bottom of the cavity is 60 º conical with V-groove. The normal cavity emissivity is 0.9999 calculated by STEEP 3 at the coating emissivity with 0.95[4].

Table 1. Specifications of the VRTSF.

Specification	Requirement
Temperature Range	190 K-340 K
Standard Blackbody Emissivity (190 K – 340 K)	0.9999
Diameter of Cavity	30 mm
Depth of Cavity	300 mm
Coating of Cavity	Nextel Velvet-Coating 811-21
FTIR spectrometer	Bruker Vertex 80V
Detector of FTIR	InSb, MCT and Si-Bolometer
Spectral Range	1-1000 μm
Vacuum Degree	5E-4 Pa
Vacuum Chamber	Diameter: 1000 mm; Length: 1000 mm
Diameter of the off-axis ellipsoidal mirror	160 mm
Customer Blackbody Outline Size Limited	Diameter: 650 mm; Length: 800 mm
Uncertainty (k=2)	50 mK@300K/10μm

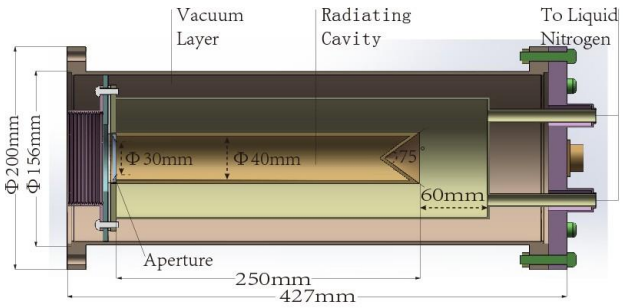

Figure 3. Cut view of the liquid nitrogen cooled blackbody.

The liquid nitrogen cooled blackbody is used to the zero reference for the FTIR. The aperture of the cavity is 30 mm in diameter. The cavity is 250 mm in depth, 40 mm in diameter. The surface of the cavity is coated by the Nextel Velvet-Coating 811-21. The bottom of the cavity is 75 º cone with V-groove. The emissivity is 0.9997 calculated by STEEP3.

FUTURE WORK

The design and simulation of the stray light of the optical system is the key research point in this facility. All the simulation result will direct the mechanical design. The establishment of the VRTSF will be finished in the autumn of 2014. This facility calibration service for use's blackbody will be start at the end of the 2015.

REFERENCES

1. G. Ohring, B. Wielicki, R. Spencer, B. Emery, R. Datla, Bull. Am. Meteorol. Soc. 86, 1303,2005.
2. V. S. Ivanov, B.E. Lisiansky, S. P. Morozova, V. I. Sapritsky, U. A. Melenevsky, L. Y. Xi, L. Pei, Medium-background radiometric facility for calibration of sources or sensors, Metrologia 37, 599-602, 2000.
3. C. Monte, B. Gutschwager, S. P. Morozova, J. Hollandt, Radiation thermometry and emissivity measurements under vacuum at the PTB, Int. J Thermophys. 30, 203-219, 2009.
4. S.P. Sapritsky, A. V. Prohorov, calculation of the effective emissivities of specular diffuse cavities by the Monte carlo method, Metrologia, 29, 9-14, 1992.

Satellite Sensor Calibrations using Tunable Laser Systems: the Suomi VIIRS Example

Keith R. Lykke[1], Steven W. Brown[1], Bruce Guenther[2], and Christopher Moeller[3]

[1]*National Institute of Standards and Technology, Gaithersburg, MD,* [2]*Stellar Solutions, Palo Alto, CA,*
[3]*University of Wisconsin, Madison, WI*
Corresponding e-mail address: swbrown@nist.gov

Current NASA radiometric calibration strategies, relying on the output of a lamp-monochromator system for relative spectral response measurements and lamp-illuminated integrating spheres for radiance responsivity calibrations, result in sensor uncertainties that are too large to support the uncertainty requirements of future Earth remote sensing missions. The high radiant flux available from tunable laser systems in laser-based radiometric calibration facilities enables consideration of unique and unusual calibration approaches to a wide variety of sensors ranging from microscopes to large aperture satellite sensors. In this work we discuss results of the calibration of the Suomi Visible Infrared Imaging Radiometer Suite (VIIRS) sensor using NIST's portable laser-based calibration system known as Traveling SIRCUS.

EXPERIMENTAL SETUP

VIIRS, a follow-on to NASA's Moderate Resolution Imaging Spectroradiometer (MODIS) sensors, is a scanning radiometer with 22 filter bands covering the spectral range from 412 nm to 12.013 μm. There are 16 detectors in each band at the focal plane. VIIRS data products include cloud and aerosol properties, ocean color and sea surface temperature, and land reflectance. Among other applications, VIIRS data are used to improve our understanding of global climate change.

Two laser-based calibration tests were undertaken for VIIRS: Test 1 was a spectral radiance responsivity test with the VIIRS telescope looking through the sensor's Earth viewport at a laser-illuminated integrating sphere; Test 2 was an irradiance responsivity test using a collimator pumped by SIRCUS lasers to illuminate the VIIRS sensor through its solar port. The radiance responsivities of 7 bands were measured, with nominal band center wavelengths ranging from 412 nm to 865 nm; the irradiance responsivity was measured for three bands centered at 412 nm, 742 nm, and 865 nm, respectively. The sources were placed in the Ball Aerospace and Technology Center's (BATC's) clean room while the tunable laser systems were kept outside the clean room area. Laser light was introduced into the sources using steel-jacketed fiber-optic cable. Figure 1 shows the two source configurations in front of VIIRS.

These tests represented the first time in the NASA Earth Observation MODIS/VIIRS time series that:

1. The response of a sensor was measured with monochromatic light under flood illumination conditions. Figure 2 shows the illumination pattern on the VIIRS focal plane for flood illumination and illumination by the lamp-monochromator system (called the SpMA). This enabled testing of cross-talk and relative spectral response simultaneously as well as a more accurate measurement of detector-to-detector differences within a band.
2. The source radiance was known to ~0.25 %, enabling the first laboratory calibration that met stringent ocean color uncertainty requirements (0.5 %).
3. The Solar Diffuser full aperture and the Solar Diffuser Stability Monitor were simultaneously illuminated enabling testing of the fundamental calibration approach at the full system level (rather than piece-parts).

RESULTS

Figure 3 shows the relative spectral radiance responsivities from the SIRCUS measurements and the SpMA measurements for VIIRS Band M7, Detector 8. The figure illustrates the good agreement between the two calibration approaches with the exception of the region around 650 nm. In this region, the SIRCUS measurements directly measure the cross-talk from Band M5.

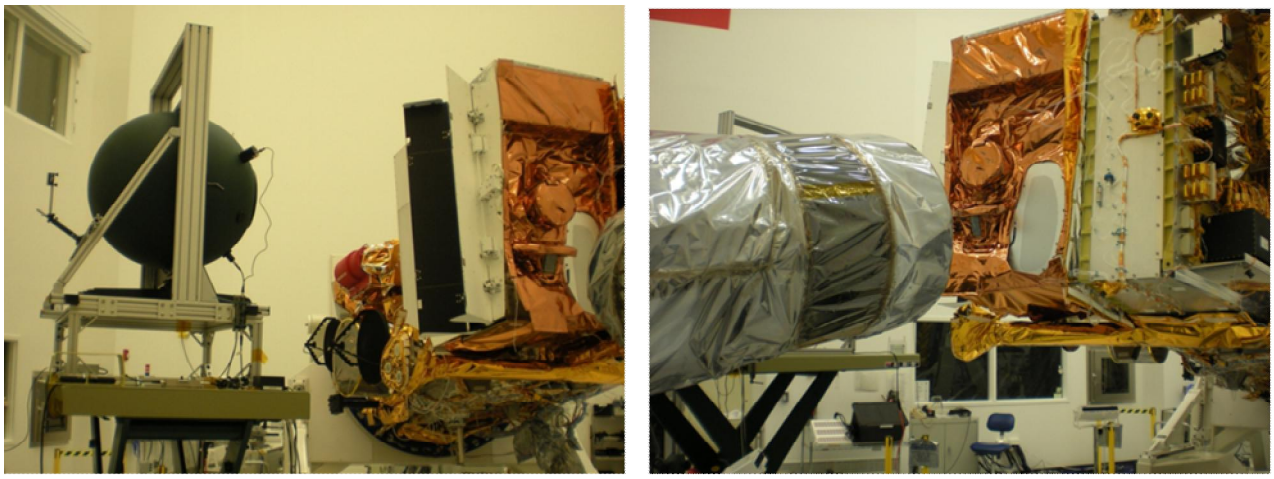

Figure 1. Experimental setup of (left) the integrating sphere in front of the VIIRS Earth viewport and (right) the collimator in front of the VIIRS solar diffuser port in the clean room at BATC.

Figure 4 shows the band center wavelengths for the 16 detectors in Band M7 measured using SIRCUS and the SpMA. Differences as large as 0.35 nm were observed. The SIRCUS-measured detector-to-detector differences, centered around Detector 9, are in good agreement with modelled detector-to-detector band centers.

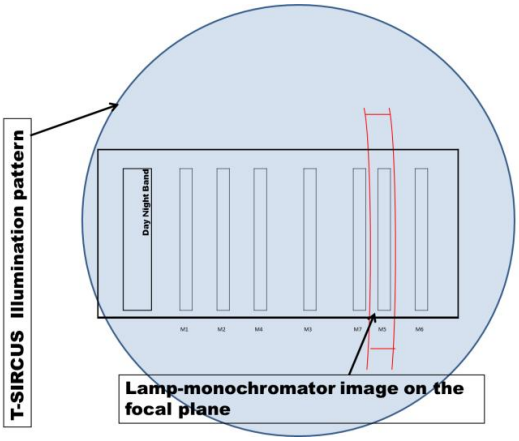

Figure 2. Image of T-SIRCUS and SpMA illumination patterns on the VIIRS focal plane.

CONCLUSIONS

These tests established baseline protocols for using laser-based systems to characterize and calibrate Earth observing satellite sensors. Lessons learned provide a path forward for further development of tunable laser systems and spacecraft sensor calibration targets as well as software for smooth integration with sensor acquisition software. For the Suomi VIIRS sensor, the tests provided the highest fidelity sensor characterization. The radiance responsivity measurements established the level of optical cross-talk between channels and provided the absolute spectral responsivity with uncertainties an order of magnitude lower than the current state-of-the-art using lamps as the source of radiant flux. The irradiance responsivity tests provided information about the sensor responsivity when illuminated through the solar viewport, enabling the first sensor comparison between measurements and modelled results.

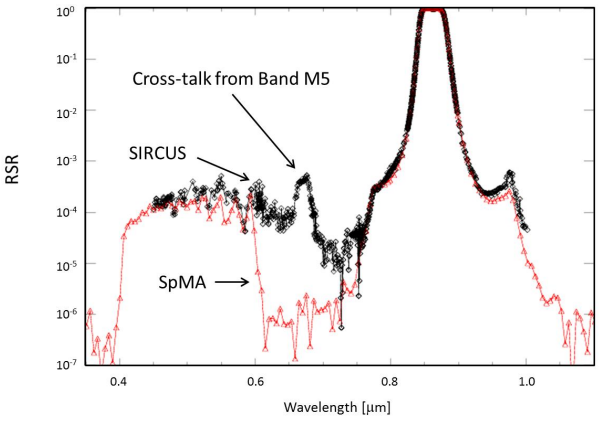

Figure 3. VIIRS Band M7 RSR comparison between the SIRCUS and the SpMA measurements.

Figure 4. Differences in Band M7 Band Center wavelengths measured by SIRCUS and the SpMA.

The growth of a vertically aligned carbon nanotube coating on aluminium substrates and its partial space qualification for EO applications

E. Theocharous[1], C. Chunnilall[1], R Mole[1], D. Gibbs[1], N. Fox[1], N. G. Shang[2], G. Howlett[2], B. Jensen[2], R. Taylor[3], J. R. Reveles[3], O. B. Harris[3], and N. Ahmed[3]

[1]NPL, Teddington, TW11 0LW, UK, [2]Surrey NanoSystems Ltd, Newhaven, BN9 0DQ, UK,
[3]EnerSys ABSL, Abingdon, OX14 3ED, UK
Corresponding e-mail address: e.theo@npl.co.uk

The fabrication of NanoTube Black, a Vertically Aligned carbon NanoTube Array (VANTA) on aluminium substrates is reported for the first time. The coating on aluminium was realised using a process that employs top down thermal radiation to assist growth, enabling deposition at temperatures below the substrate's melting point. The NanoTube Black coatings were shown to exhibit directional hemispherical reflectance values of typically less than 1% across wavelengths in the 2.5 µm to 15 µm range. VANTA-coated aluminium substrates were subjected to space qualification testing (mass loss, outgassing, shock, vibration and temperature cycling) before their optical properties were re-assessed. Within measurement uncertainty, no changes to the hemispherical reflectance were detected, confirming that NanoTube Black coatings on aluminium are good candidates for Earth Observation (EO) satellite applications.

INTRODUCTION

Blackbodies flown on Earth Observation (EO) satellite missions currently provide the means to calibrate instruments measuring thermal infrared radiance with the lowest uncertainties. As payload mass is a critical factor in any satellite-borne EO mission, minimising the weight of the blackbody calibration source cavity whilst retaining the required environmental integrity and optical performance necessarily leads to design trade-offs. Vertically Aligned carbon NanoTube Array (VANTA) coatings offer higher absorbance values in the infrared that those currently used [1]. VANTA coatings have already been used as black coatings for thermal detectors [2]. VANTA coatings offer the possibility of designing smaller, and consequently lighter, blackbody cavities than those that can be realised with lower-emissivity materials. However, the VANTA coating must be suited to application on lightweight engineering alloys to retain these benefits.

Aluminium is used almost exclusively in EO blackbody cavity applications as it combines low weight with high thermal conductivity. Unfortunately, conventional growth of VANTA coatings requires the substrate to be maintained at around 750 ^{o}C, which is beyond aluminium's 660 ^{o}C melting point. However, methods of synthesising VANTA coatings at substrate temperatures as low as 350 ^{o}C have been reported [3], which would be suitable for use with low melting point aluminium alloys. This paper reports the procedure developed for depositing a NanoTube Black VANTA coating on aluminium substrates intended for EO applications, and describes the partial space qualification of these coatings.

METHOD

A total of six NanoTube Black samples were prepared by Surrey NanoSystems (SNS) on 40 mm x 40 mm x 3 mm 6061-T6 aluminium alloy coupons, with a range of total VANTA thicknesses ranging from 22 µm to 44 µm. The coupons were chemically cleaned prior to the deposition of a multi-layer barrier/catalyst, designed to absorb IR energy from the radiation source whilst ensuring robust adhesion of the CNTs to the substrate. The samples were then subjected to an activation step under a reducing atmosphere at 450 °C. After catalyst activation, the samples were transferred to a CVD reactor configured for plasma-assisted, photo-thermal chemical vapour deposition (PTCVD). The PTCVD process provides rapid top-down heating of the catalysed surface of the sample, whilst maintaining the bulk of the coupon at a much lower temperature via cooling of its support platen. This technique allows the higher catalyst temperatures required for low defect, aligned growth at controllable CNT mass density, whilst preventing melting or gross

mechanical changes of the underlying alloy. CNT growth was initiated at reduced pressure using acetylene as the carbon source in a mixed carrier gas at a temperature of 425 °C. The growth time was varied to achieve different CNT lengths on the coupons.

The structure and morphology of the deposited CNT films on the aluminium coupons was characterised by Raman scattering and scanning electron microscopy.

The directional-hemispherical reflectance of these samples was measured using the NPL infrared hemispherical reflectance facility [4]. Five of the VANTA coated samples were then sent to ABSL where they were subjected to space qualification testing, whilst the sixth sample was retained by NPL as a control. On completion of space qualification testing, the NanoTube Black samples were returned to NPL for re-measurement of the hemispherical reflectance. The control was also re-measured at this time.

The space qualification tests included a mass loss test, an outgassing test, a vibration test, a shock test, and a thermal cycling test. The mass loss and outgassing test consisted of the samples being analysed under vacuum by a residual gas analyser. No molecular species were detected at significant levels other than water, which would be driven off by the preliminary bake-out. The vibration test was completed in a class 100 environment while the thermal cycling test involved the thermal cycling of the test samples between -100 ^{o}C and +100 ^{o}C for 6 full cycles. A calibrated residual gas analyser (RGA) and thermal-crystal quartz meter (TQCM) were used to monitor outgassing and changes in cleanliness levels during these tests.

RESULTS

Figure 1 shows the directional-hemispherical reflectance of test sample 5, measured before and after the space qualification tests. Figure 2 shows the absolute change in the directional-hemispherical reflectance of the same test sample, measured before and after the space qualification tests, respectively. All five samples evaluated gave comparable results.

DISCUSSION

The uncertainty in the measurement of hemispherical reflectance of the test samples was 0.0045 (k=2) [4]. The directional-hemispherical reflectance values of the samples before and after the space qualification tests are in good agreement. We can conclude that no changes in the hemispherical reflectance of these samples were observed as a result of the space qualification tests. Measurements on the control sample (the sample not subjected to the space qualification tests) confirm that there was no significant change in the reflectance data as a result of the space qualification tests.

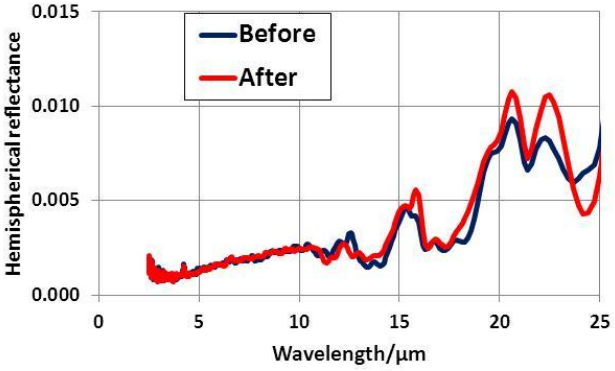

Figure 1. Hemispherical reflectance of sample 5 measured before and after the space qualification tests.

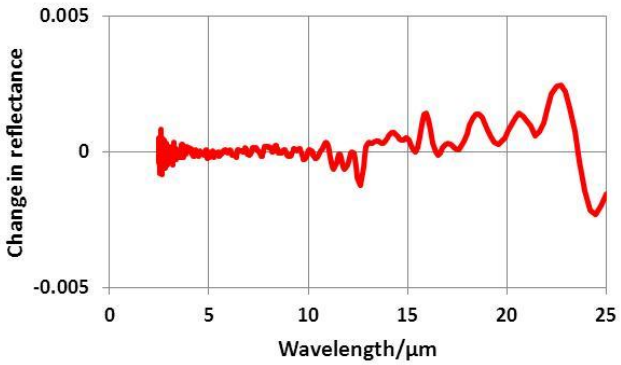

Figure 2. Absolute change in the hemispherical reflectance of sample 5 due to the space qualification tests.

The authors wish to thank TSB for the financial support to complete this project. Support from the National Measurement Office of the UK Department of Business, Innovation and Skills is also gratefully acknowledged.

REFERENCES

1. Z. P. Yang, M. L. Hsieh, J. A., Bur, L. Ci, L. M. Hanssen, B. Wilthan, P. M. Ajayan and S. Y. Lin, "Experimental observation of extremely weak optical scattering from an interlocking carbon nanotube array", Applied Optics, **50**, 1850-1854, 2011.
2. E. Theocharous, S. P. Theocharous and J. H. Lehman, "Assembly and evaluation of a pyroelectric detector

bonded to vertically aligned multiwalled carbon nanotubes over thin silicon", Applied Optics, **52**, 8054-8059, 2013.
3. N. G. Shang, Y. Y. Tan, V. Stolojan, P. Papakonstantinou P. and S. R. P. Silva, "High-rate low-temperature growth of vertically aligned carbon nanotubes" Nanotechnology, 21, 1-6, 2010.
4. C. Chunnilall, and E. Theocharous, "Infrared hemispherical reflectance measurements in the 2.5 μm to 50 μm wavelength region using an FT spectrometer" Metrologia, **49**, S73-S80, 2012.

Radiometric characterization of a large-aperture variable-radiance calibration source for remote sensing applications

R. D. Taubert, C. Baltruschat, S. Schiller, and J. Hollandt

Physikalisch-Technische Bundesanstalt (PTB), Berlin, Germany
Corresponding e-mail address: dieter.taubert@ptb.de

The increasing demand for traceable pre-and post-flight calibrations of airborne multi/hyper-spectral imagers has been met by the Physikalisch-Technische Bundesanstalt (PTB) with the development and characterization of a novel, integrating sphere based, large-aperture variable-radiance source (LAVRAS). LAVRAS was extensively characterized with respect to its temporal stability, lateral and angular radiance distribution, followed by an absolute calibration in terms of its spectral radiance over its entire dynamic radiance range of two orders of magnitude. The results obtained confirm that LAVRAS is particularly suitable for linearity investigations as well as for flat-field calibrations when homogeneity below 1% is required.

INTRODUCTION

A core activity within the framework of the European Metrology Research Program (EMRP) is to sustainably improve the SI-traceability and accuracy of the measurements of essential climate variables, which among others are retrieved by space- and airborne remote sensing instruments.

To significantly support this challenging objective, a three-year-duration EMRP Joint Research Project "European metrology for earth observation and climate – MetEOC" has been launched in 2011 [1]. One of its work packages includes the optimization, full radiometric characterization and application of a fit-to-purpose calibration transfer standard to be used in the wavelength range from 400 nm to 1000 nm for the flat-field and linearity pre- and post-flight calibration of a selected airborne multi-spectral camera system of the German Aerospace Center (DLR).

APARATUS

LAVRAS was jointly developed with the Czibula und Grundmann GmbH, Berlin. It is based on a barium sulphate coated integrating sphere of 1.2 m diameter with an aperture diameter of 40 cm. As optical radiation sources serve a number of 64 tungsten halogen lamps (50 W) with aluminium-coated reflectors and non-UV-blocking quartz glass bulbs (type OSRAM 64607 EFM). The lamps are grouped in pairs of two in 32 individual, actively air-cooled housings which are mounted symmetrically around the circumference of the sphere (Figure 1).

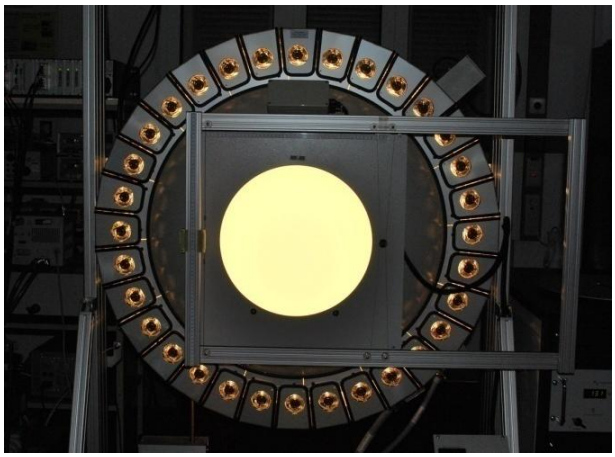

Figure 1. The integrating sphere based large-aperture variable-radiance source (LAVRAS) of PTB.

The optical radiation is coupled into the sphere via 32 synchronously adjustable apertures placed between the sphere and the 32 attached housings for the pairs of lamps. The open area of these apertures, and with it the radiance of the source, can be modified by a stepper motor operated control system. This concept, together with the possibility of individually turning on/off each pair of lamps, allows modifying the spectral radiance of the integrating sphere over more than two orders of magnitude while keeping the spectral shape of the radiance constant within a few percent. To monitor the spectral radiance during operation the integrating sphere is equipped with a temperature controlled detector unit, consisting of three broadband-filtered Si-detectors operating in the UV, VIS and NIR wavelength range.

RADIOMETRIC CHARACTERIZATION AND CALIBRATION

Prior to the radiometric characterization with respect to the lateral and angular radiance distribution and absolute spectral radiance calibration, the stability of

the integrating sphere was investigated by means of the integrated monitor diodes. Additionally, the radiance was monitored via an LP3 radiation thermometer operating as a narrow-band, radiance measuring instrument at a wavelength of 650 nm [2]. Within more than 60 hours of continuous operation, the relative radiance changed less than 1% in the VIS and up to 1.4% in the UV and NIR spectral range.

The homogeneity over the full aperture plane was measured by scanning with the LP3, alternately operated at 650 nm and 900 nm and applying a 5 mm × 5 mm grid, with the focus of the LP3 being set into the integrating sphere aperture plane (Figure 2). At both wavelengths the uniformity was found being better than ±1%.

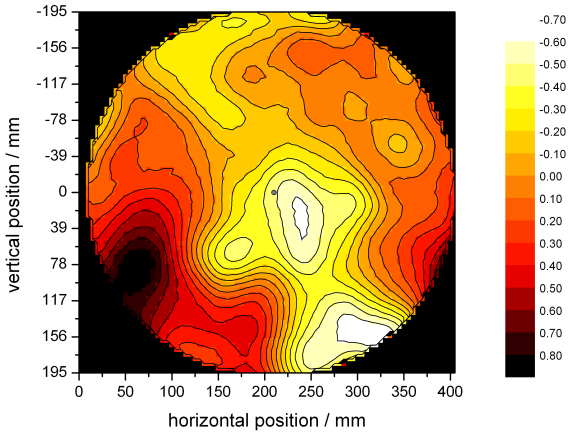

Figure 2. Relative spectral radiance distribution across the 40 mm aperture of the integrating sphere, measured at 650 nm and with a 32×2-lamps in operation configuration. One colour change corresponds to a 0.1% radiance change.

Additionally, the horizontal radiance distribution along the central line of the aperture was measured at 400 nm, 550 nm, 800 nm and 1000 nm for a symmetric 4-, 12-, 24- and 32-lamp pairs in operation configuration at the Spectral Radiance Comparator Facility (SRCF) [3] of the PTB.

For the measurement of the angular radiance distribution the LP3 was mounted on a dedicated kinematic stage with five degrees of freedom. This setup allows performing fully automatic radiance distribution measurements while keeping the focus point of the radiance measuring instrument fixed at a defined position i.e. at any point of the radiating aperture of the integrating sphere.

The angular radiance distribution measurement was carried out at 650 nm with the focus set in the centre of the radiating area for angles ranging from ±30° horizontally and ±10° vertically for seven different lamp operation configurations, including deliberately chosen asymmetric illuminations. All configurations displayed a Lambertian behaviour within ±2% within the investigated angular range.

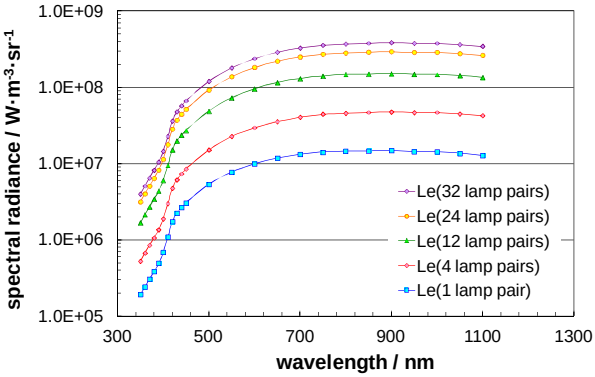

Figure 3. The calibrated spectral radiance of the PTB large aperture integrating sphere for five different lamp configurations.

The absolute spectral radiance of the integrating sphere has been calibrated in the wavelength range from 350 nm to 1100 nm at the SRCF of PTB by comparison with the Spectral Radiance Primary Standard, the High Temperature Blackbody HTBB 3200pg. The calibration comprised five different lamp configurations (1-, 4-, 12-, 24- and 32-lamp pairs in operation,) for a fixed aperture opening (Figure 3). Additionally, for the 31-lamp pairs in operation configuration the radiance calibration was performed for 5 different settings of the adjustable lamp apertures. Depending on wavelength, the spectral shape of the spectral radiance varies not more than 3% in the VIS and NIR and not more than 8% in the UV spectral range relative to the reference value at 650 nm with the number of lamps operated.

Product names cited are used for identification purposes only and do not constitute an endorsement by PTB.

The EMRP is jointly funded by the EMRP participating countries within EURAMET and the European Union.

REFERENCES

1. http://www.emceoc.org/
2. T. Keawprasert et al., Absolute Calibration of Spectral Responsivity for a Radiation Thermometer, Proc. NEWRAD 2008, ed. Dong-Hoon Lee, 287-288, KRISS, Daejeon, Korea, 2008.
3. R. D. Taubert et al., Traceable Calibration of Radiation Sources from the Visible to the Far Infrared for Space Borne Applications at PTB, Proc. SPIE Vol.7474, Sensors, Systems and Next Generation Satellites XIII, ed. R. Meynart, Bellingham, USA, 2009.

Standard radiometric facility for preflight calibration of space borne Earth observation instruments in IR spectral range

V.I. Sapritsky[1], A.A. Katysheva[1], V.N. Krutikov[1], B.E. Lisyansky[1], S.P. Morozova[1], S.A. Ogarev[1], A.S. Panfilov[1], N.A. Parfentyev[1], D.M. Karpunin[2], and E.V. Makolkin[2]

[1] *All-Russian Research Institute for Optical and Physical Measurements (VNIIOFI), Moscow, Russia*
[2] *Central Research Institute of Machine Building (TsNIIMash), Moscow, Russia)*
Corresponding e-mail address: ogarev-m4@vniiofi.ru

Preflight calibration of space borne Earth observation instruments (EOI) under conditions of cryo-vacuum chamber intended for space orbit environment modeling, is the requirement of information value in the Earth remote sensing (ERS). Paper describes the new Standard radiometric facility for preflight calibration of space borne EOI within IR spectral range (from 3 to 14 μm), on the basis of high-vacuum chamber. Layout determinations aimed at the solution of measuremental assurance task of radiometric calibration in IR spectral range of wide-aperture (up to 500 mm) EOI, are presented.

INTRODUCTION

Currently ERS is one of the most quickly developing fields of science and technology with a view to control Earth environment, monitor agricultural lands conditions, weather prediction, etc. Bearing in mind these tasks, evaluation of aerospace ERS data gains in importance [1]. Of a great necessity is to obtain an observation on the basis of EOI calibration. Comprehensive preflight radiometric calibration of ERS instruments can be carried out in corpore by means of complex ground based measurement facilities. Such calibration is generally connected with the usage of standard radiators in form of wide-aperture low temperature variable blackbodies (BB). Estimation of spectral radiance (SR) of these sources and its monitoring with time is a difficult task. In order to carry out proper radiometric calibration within IR range, one should perform transfer of SR size of unit, and measurement of relative spectral sesitivity of EOI under conditions of cryo-vacuum chamber equivalent to normal space orbital environment.

STANDARD RADIOMETRIC FACILITY

Standard Radiometric Facility (SRF) was designed and developed for the aims of carrying out preflight radiometric calibration of EOI in IR spectral range (from 3 to 14 μm). SRF represents a measurement complex on the basis of cryo-vacuum chamber modeling space environment conditions, supplying calibration services for EOI featuring optical lens with aperture diameter up to 500 mm.

In order to solve measurement problem of EOI calibration in IR range, i.e. to determine quantitatively a system response on the given input signal, one should define concretely a model of an object under measurement, formulate measuring equation, and determine measured quantity:

• model of object - extended uniform on radiance and spectral parameters orthotropic surface with unchangeable characteristics within measurement data acquisition time;

• measuring equation:

$$N = k\int_0^\infty L(\lambda)S(\lambda)d\lambda \,, \qquad (1)$$

where k – is calibration factor,

$L(\lambda)$ – is *SR* of an object under measurement,

$S(\lambda)$ – is relative spectral responsivity of EOI;

• measured quantity – effective spectral radiance

$$L = \int_0^\infty L(\lambda)S(\lambda)d\lambda \,. \qquad (2)$$

Technical basis of calibration must supply measurement of these radiometric quantities, relative spectral characteristics of EOI and calibration curves, in the process of which measurement, it is realized a transfer of SR size of unit from standard radiation sources to instrument under calibration. Such a technical basis must consist of: standard of unit of SR – blackbody model; standard of unit of spectral power of monochromatic radiation source (MRS) [2]; and cryogenic vacuumized chamber.

Paper presents feasible methodological and technical approaching pointed at the solution of a task of metrological assurance of radiometric calibration in IR spectral range. Optical schemes of standard

radiometric facility on the basis of cryo-vacuum chamber are presented. Figure 1 depicts general layout of SRF components: movable EOI under calibration, FTIR Fourier-spectrometer, MRS including monochromator and low temperature BB, set of different blackbody sources – fixed-point one on the basis of Gallium phase transition, LABB - wide-aperture flat, VTBB – variable temperature BB, LN_2BB – low-temperature, standard detector, and necessary optical components – mirrors, collimator, etc.

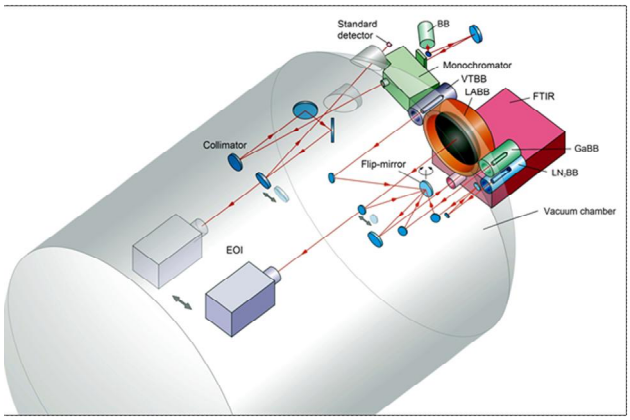

Figure 1. General layout of SRF complex.

The SRF complex is intended to carry out measurements, as follows:

• calibration of precise variable-temperature BB against GaBB on the basis of fixed point of phase transition temperature of Gallium melting/solidification;

• calibration of wide-aperture flat-surface (non-cavity type) on spectral radiance against precise BB with working temperature from 213 to 423 K;

• calibration of EOI on SR in IR spectral range with the usage of wide-aperture LABB radiation source;

• calibration of a monochromatic IR radiation source in the range from 3 to 14 μm on the relative spectral power by means of the standard detector which is in its turn calibrated on spectral responsivity (on the basis of the National radiometric Standard);

• measurement of relative spectral responsivity of EOI when its input pupil is being radiated by collimated light beam from MRS;

Arrangement of integrated national calibration center on the basis of cryo-vacuum chamber of SRF opens a possibility to uniformity of measurements required for obtaining of ERS data of high quality.

REFERENCES

1. V. I. Sapritsky, V. N. Krutikov, V. S. Ivanov, A. S. Panfilov, M. N. Pavlovich, A. A. Burdakin, V. V. Rakov, S. P. Morozova, B. E. Lisyansky, B. B. Khlevnoy, V. R. Gavrilov, S. A. Ogarev, A. V. Pusanov, M. L. Samoylov, M. V. Solodilov, A. A. Katysheva, N. A. Parfentyev and A. A. Stakharny Current activity of Russia in measurement assurance of Earth optical observation, Metrologia, 49, pp. S9–S16, 2012.
2. S.A. Ogarev, S.P. Morozova, A.A. Katysheva, A.S. Panfilov, B.E. Lisyansky, M.L. Samoylov, V.I. Sapritsky, E.V. Makolkin Blackbody-based IR monochromatic radiation source for preflight spectral radiance calibration facility, Abstracts book of TEMPMEKO'2013, October 14, 2013, Madeira, 2013, p.365.

Gonioreflectometric properties of metal surfaces

P. Jaanson[1,2], F. Manoocheri[1,2], H. Mäntynen[1], M. Gergely[3], J.-L. Widlowski[3], and E. Ikonen[1,2]

[1]Metrology Research Institute, Aalto University, Espoo, Finland; [2]Centre for Metrology and Accreditation (MIKES), Espoo, Finland; [3]European Commission DG Joint Research Centre, Ispra, Italy

Corresponding e-mail address: priit.jaanson@aalto.fi

Angularly resolved measurements of scattered light from surfaces can provide useful information in various fields of research and industry, such as computer graphics, satellite based earth observation etc. In practice, models are needed to interpolate the measurement results, because thorough characterization of the surfaces can be time consuming due to the many variables involved. In this work, plain and anodized metal samples were prepared and measured optically for BRDF and mechanically for surface roughness. The measured values are compared to the values predicted by the Torrance-Sparrow BRDF model. The predicted values are in better agreement with the measurement results for plain metal surfaces than for anodized surfaces.

INTRODUCTION

Satellite based observation of Earth in the visible and NIR wavelength range can provide crucial information to study climate change. In order to interpret the measured data a variety of Radiative Transfer (RT) codes have been developed, which simulate the propagation of radiation in the Earth's atmosphere by transmission, absorption and scattering [1]. Considerable effort is put into validation of these RT codes, one approach focusing on SI traceability using artificial targets is described in [2].

Many RT codes make use of models describing the light scattering from surfaces. The scattered light from a surface is usually described with a bidirectional reflectance distribution function (BRDF), which is defined as:

$$f(\Omega_i,\Omega_r)=\frac{dL_r(\Omega_i,\Omega_r)}{dE_i(\Omega_i)}, \quad (1)$$

where dL_r is the radiance of the sample in the direction Ω_r while illuminated by irradiance dE_i from the direction Ω_i. Due to many parameters associated with the BRDF, the measurements of real world surfaces can be time consuming. In order to save measurement time, various BRDF models have been developed mainly based on either geometrical optics or wave optics [3-5]. The results of measurements for plain and anodized aluminium surfaces can then be compared with the predicted values for example from the Torrance-Sparrow BRDF model [3,4,6].

INSTRUMENTS AND METHODS

In this work two types of metal surfaces have been produced: roughened plain aluminium and roughened aluminium anodized with a green pigment. The surfaces have been characterized for BRDF and surface roughness.

The measurements of BRDF have been carried out with the MIKES-Aalto gonioreflectometer [7]. The instrument is designed to perform angularly resolved spectrophotometric measurements. The source system and the beam guiding optics are explained in Fig. 1. The sample area contains a linear translator for spatial uniformity measurements and a turntable to adjust the angle of incident light on the sample. The collection system consists of a precision aperture, lens, a silicon photodetector and a low noise current preamplifier. The detector is mounted on a goniometer allowing the movement of the detector by nearly 360 degrees around the sample.

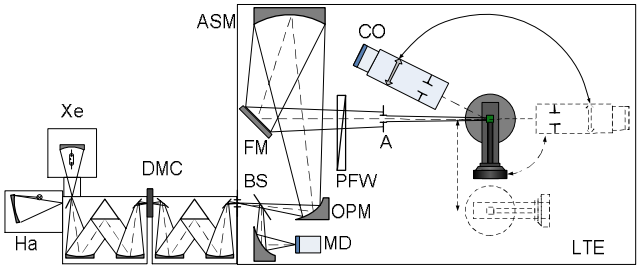

Figure 1. MIKES-Aalto gonioreflectometer. Xe – xenon arc lamp, Ha – halogen lamp, DMC – double monochromator, BS – beam splitter, MD – monitor detector, OPM – off-axis parabolic mirror, ASM – aspherical mirror, FM – flat mirror, PFW – polariser filter wheel, A – aperture, CO – collection optics, LTE – light tight enclosure.

The surface roughness has been characterized by measuring the surface height profiles in three lines across every surface.

The BRDFs of surfaces have been measured in the plane of incidence with the illumination zenith

angles ranging from 0° to 60° and the viewing zenith angles ranging from -60° to 80°. The measurements are conducted for both s- and p-polarised incident light. The BRDF for unpolarised light is evaluated on the basis of s- and p-polarised reflectance data.

In addition to the illumination and viewing directions indicated in equation (1), the BRDF model depends on the surface roughness parameter (root mean squared slope), complex refractive index and weights for the diffuse and specular components of the model. The surface roughness parameter is obtained from measurements and the refractive index for the plain aluminium surfaces is found from literature [8]. The only fitted parameters are the weights of the diffuse and specular components. In the case of the anodized surfaces also the complex refractive index is fitted.

RESULTS AND DISCUSSION

The measurement results and corresponding modelled values for the plain roughened aluminium surfaces are in reasonably good agreement as seen in Fig. 2. The sum of the squared residuals (*RSS*) is 0.995 (over five different surfaces). The differences are within a few percent near the specular peak and reach up to 30% further away from the specular angle.

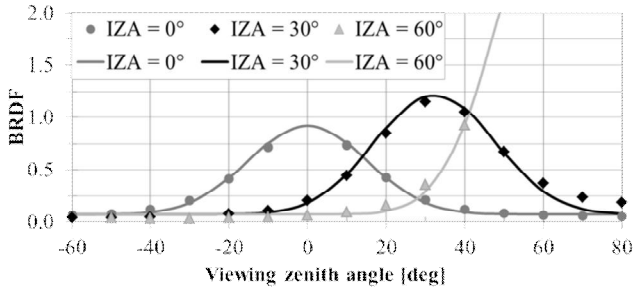

Figure 2. Measured (markers) and modelled (lines) BRDF values for the roughened plain aluminium surface.

The agreement is not as good for the anodized surfaces as for plain aluminium surfaces as seen in Fig. 3. The *RSS* value is 0.940 for five surfaces. The relative differences between the measurement results and modelled values range from 5% to 30%.

The higher deviation between the measured and the modelled values at large viewing angles may indicate that the Gaussian microfacet distribution is not a good approximation for these anodized surfaces under test. Therefore other microfacet distributions should be tested in the BRDF model or better manufacturing schemes need to be developed.

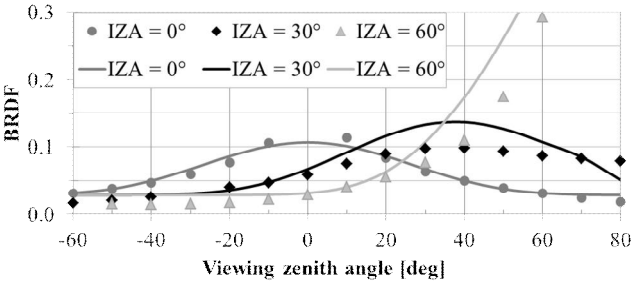

Figure 3. Measured (markers) and modelled (lines) BRDF values for the roughened anodized aluminium surface.

The relative expanded uncertainty ($k = 2$) of the BRDF measurement results is ranging from 2% near the specular peak to 10% at large viewing angles.

CONCLUSIONS

The BRDF values predicted by the Torrance-Sparrow model are in a reasonably good agreement with the measurement results for plain aluminium surfaces. For anodized surfaces some further development of the model is needed. A major source of uncertainty for the SI traceable validation of RT codes thus may be the choice/relevance of the scattering distribution models used in the setup of the environments for which RT simulations are to be generated.

This research was performed under the European Metrology Research Program project MetEOC (Metrology for Earth Observation and Climate).

REFERENCES

1. S. Clough et al, Atmospheric radiative transfer modeling: a summary of the AER codes, J. Quant. Spectrosc. Radiat. Transf., 91, 233–244, 2005.
2. A. Bialek et al, SI traceable validation of the Radiative Transfer codes, submitted to NEWRAD 2014.
3. E. M. Sparrow et al, Theory for Off-Specular Reflection From Roughened Surfaces, *J. Opt. Soc. Am.*, 57, 1105-1114, 1967.
4. R. Cook and K. Torrance, A reflectance model for computer graphics, ACM Trans. Graph., 1, 7–24, 1982.
5. M. W. Hyde et al, A geometrical optics polarimetric bidirectional reflectance distribution function for dielectric and metallic surfaces, *Opt. Express*, 17, 22138–53, 2009.
6. Y. Govaerts, A model of light scattering in three-dimensional plant canopies: a Monte Carlo ray tracing approach. Space Applications Institute, JRC, report EUR 16394 EN, 1996.
7. S. Nevas et al, Gonioreflectometer for measuring spectral diffuse reflectance, Appl. Opt., 43, 6391–6399, 2004.
8. A. Rakić, Algorithm for the determination of intrinsic optical constants of metal films: application to aluminum., Appl. Opt., 34, 4755–67, 1995.

Self-calibrating LED-based multi-band field radiometer for a sensor web vicarious-sites measurements

Emanuele Taralli[1], Roberto Filippo[1], Davide Corona[1], Marco Santiano[1], Giorgio Brida[1], Mauro Rajteri[1], Simon R.G. Hall [2], Agnieszka Bialek[2], Claire Greenwell[2], and Nigel Fox[2]

[1] INRiM, Torino, Italy, [2] NPL, Teddington UK

Corresponding e-mail address: m.rajteri@inrim.it

We have developed a multi-band radiometer sensing system based on light-emitting diodes (LEDs) to create a self-calibrating sensor web for land-based measurements. An autonomous prototype sensor web of 5 radiometers that could be geographically distributed over hundreds of metres has been realised. Temporally continuous measurement of the land reflectance in 4 spectral bands, from 350 nm to 900 nm, can be acquired. The system has the ability to regularly re-calibrate autonomously and in the field, communicating results to a remote home base.

INTRODUCTION

Remote monitoring of the earth system is crucial to enable better stewardship of the environment to provide the information to policy makers developing appropriate mitigation strategies for climate change. Global observations can only be made from space, and although such observations are being made, the harsh and challenging environment of space limits the uncertainty currently attainable. Satellites require improved uncertainty and traceability through all stages of data production: pre-flight and post-launch calibration and validation and all the intermediate processing steps.

These problems have been addressed within the European Metrology Research Program MetEOC (Metrology for Earth Observation and Climate) [1].

To perform autonomous SI traceable measurements of geographically distributed surface spectral reflectance/radiance for vicarious test sites, a prototype of a sensor web consisting of field radiometers based on Light-Emitting Diodes (LEDs) has been designed and built.

This paper provides information about the design of this multi-band radiometer sensing system and we report preliminary results on sensor web performance tested in field situations, uncertainty budget and self-calibration.

FIELD RADIOMETER DESCRIPTION

In addition to being a light source, an LED can also be applied as a wavelength selective photodetector whose response is related to its emission spectral profile. The advantages of an LED-based photodetector are: 1) its low cost, which becomes important when planning for development of a large number of instruments like a sensor web; 2) its intrinsic bandpass wavelength response without the need for additional optical filters, and 3) its compactness, which ensures minimal problems when deployed on test sites that undergo a wide range of weather conditions.

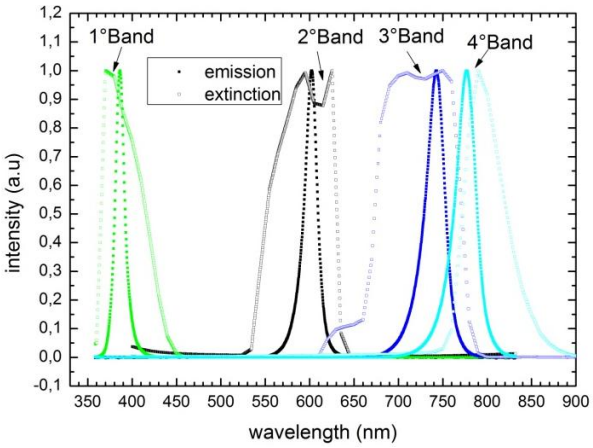

Figure 1. Emission and detection spectra of the selected LEDs.

The successful use of LED-based radiometers has been already demonstrated by various research groups as sun photometers [2,3] and field radiometers [4,5]. These LED radiometers are composed of a few separate LEDs and are calibrated either by being removed from the site, or by using a calibrating reflectance plate that is taken to the site and used for comparison, while our LED radiometer design is based on a self-calibrating capability [6].

If one reference LED is used as an emitter and another to detect this light, the crossover of the two spectral ranges sets the value of the measured current. With no degradation, this current should be constant,

while a correction factor can be determined if the LED detector performance has changed at all.

More than 20 LEDs with different properties (power, wavelength and activearea,) have been investigated both as emitters and detectors. Among these, four couples of LEDs in the spectral range from 350 nm to 900 nm have been selected and their spectral properties are shown in Figure 1.

The emission spectra of the LEDs were measured with a commercial array spectrophotometer, while the detection spectra were measured with a monochromator irradiating the LED and acquiring the output photocurrent by means of an electrometer.

The LED radiometer is composed of a cylinder that hosts the four LED detectors that measure the surface spectral reflectance/radiance and the four LED emitters used for the calibration. At the end of the cylinder, a shutter closes the radiometer to allow both the dark current measurement and the self-calibration procedure, and also protects the instrument from the external environment when it is not operative. One iris inside the cylinder, together with its end aperture, defines the radiometer field of view (FOV). The overlap of the single LED FOV has a diameter of 30 cm when the radiometer is mounted at 1 m height from the ground. A custom electronic main board manages the signal read-out, the self-calibration, power supply, shutter control and the wireless communication between the LED radiometers and the home base.

REFERENCES

1. http://www.emceoc.org/index.html.
2. Y.B. Acharya, A. Jayaraman, S. Ramachandran, and B. H. Subbaraya, Compact light-emitting-diode sun photometer for atmospheric optical depth measurements, Appl. Opt., 34, 1209-1214, 1995.
3. F.M. Mims III, Sun photometer with light-emitting diodes as spectrally selective detectors, Appl. Opt., 31, 6965-6967, 1992.
4. J.S. Czapla-Myers, K.J. Thome, and S.F. Biggar, Design, calibration and characterization of a field radiometer using light-emitting diodes as detectors, Appl. Opt., 47, 6753-6762, 2008.
5. M.C. Helmlinger, C.J. Bruegge, E.H. Lubka and H.N. Gross, LED Spectrometer (Lspec) autonomous vicarius calibration facility, Proceedings of SPIE, 6677, 2007.
6. D.A. Lock, S. R. G. Hall, A. D. Prins, B. G. Crutchley, S. Kynaston, and S.J. Sweeney “LED Junction Temperature Measurement Using Generated Photocurrent” Journal of Display Technology, Vol. 9, Issue 5, 396-401 (2013).

A handheld leaf goniometer for in situ spectro-directional measurements

Lapo Lolli[1], Marco Pisani[1], Mauro Rajteri[1], Marco Santiano[1], Jean-Luc Widlowski [2], Agnieszka Bialek [3], Claire Greenwell[3], and Nigel Fox [3]

[1] INRiM, Torino, Italy, [2] IES/JRC, Ispra, Italy, [3] NPL, Teddington UK
Corresponding e-mail address: l.lolli@inrim.it

A newly developed goniometer for in situ spectro–directional measurements of reflective and transmissive properties of individual leaves is presented. One diffuse and five directional illumination angles can be chosen. A multichannel spectrometer allows simultaneous detection of the scattered light at 80 angles in the spectral range from 400 nm to 1000 nm.

INTRODUCTION

The spectro-directional characterisation of foliage elements under controlled illumination conditions is typically carried out in laboratory settings [1]. During the time between leaf sample collection and goniometer measurements, the spectral properties of the leaf will change due to moisture loss (up to 20 % has been observed in water absorption bands of infrared region) [2].

Three-dimensional radiative transfer (RT) models require detailed mathematical formulations of the spectro-directional behaviour of individual foliage elements in order to simulate the response of satellite or in situ measuring devices. These expressions should be developed on the basis of ideally SI-traceable goniometer measurements acquired under controlled illumination conditions. In particular for the simulation of in situ measurement campaigns the specular component of foliage scattering becomes important. Relatively little information is currently available regarding the specular behaviour of foliage (in particular for large incident zenith angles) [3] and no studies have been carried out to assess the leaf transport time affects the measured specular signatures of leaves.

This problem has been addressed within the European Metrology Research Program MetEOC (Metrology for Earth Observation and Climate) by developing and building a portable leaf goniometer capable of measuring hyperspectral leaf scattering properties under controlled illumination conditions and within a short amount of time [4].

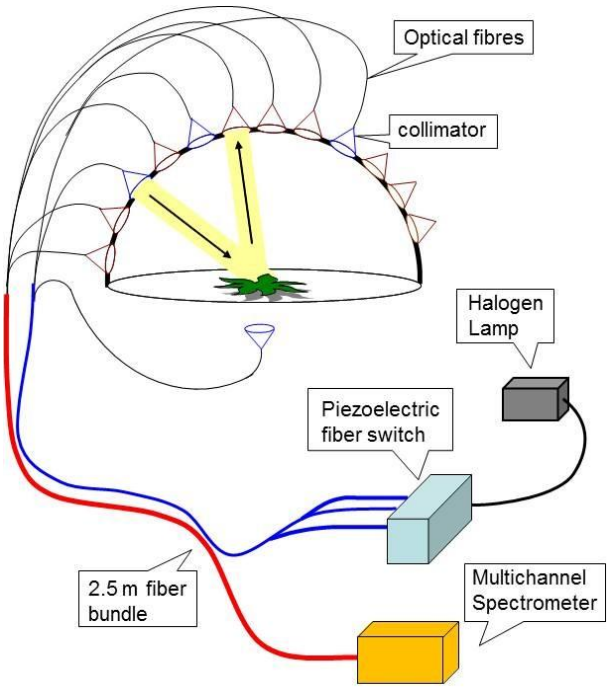

Figure 1. Sketch of the leaf goniometer.

This paper provides information about the design of the new hand-held spectrogoniometer for in situ measurements of single leaves and we report on the first results on calibrated targets.

GONIOMETER DESCRIPTION

The main function for the instrument is to measure, in the field, the multi-angular scattering properties of individual leaves with an acquisition time short enough to avoid the degradation of leaves.

These aims have been obtained by designing a prototype goniometer based on a multichannel spectral camera which simultaneously acquires the spectra of 80 channels in the range between 400 nm and 1000 nm. A sketch of the hand-held leaf goniometer is shown in Fig. 1.

Each channel receives the light from a 600 µm core optical fibre that detects the scattered light from an integration area of 6 mm through a collimator. The 80 detection angles are distributed across a 25 cm

diameter hemisphere enabling sufficient sampling of the principal and orthogonal plane as well as the forward scattering peak due to specular scattering from the leaf surface (black disks in Figure 2). Five directional illumination sources have been arranged in the hemisphere above the leaf (red disks in Figure 2) and one diffuse illumination source is placed below the leaf. The zenith angles of the five illumination sources were chosen such as to cover a range as large as possible, and, in theory should also provide the possibility to compute the Bi-hemispherical reflectance of the leaf target.

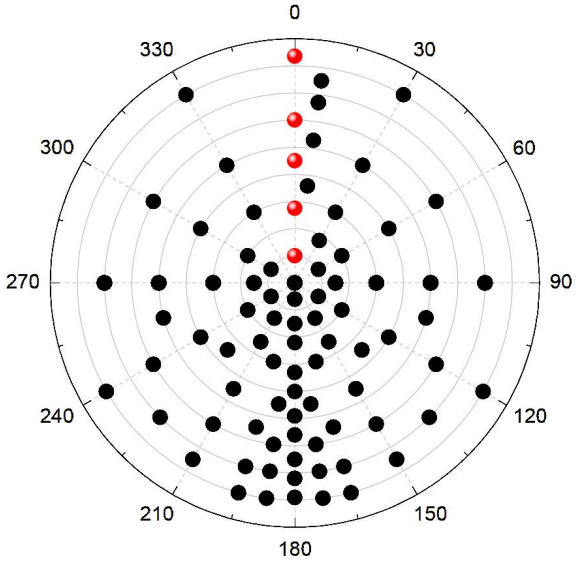

Figure 2. Overview of the illumination (red) and viewing (black) locations in polar coordinates.

The light source is a fibre coupled halogen lamp which, through a piezoelectric fibre switch, can reach either 5 collimators on the hemisphere for reflectance measurements or one on the bottom of the leaf for transmittance measurements.

A motorized leaf holder allows rotation of the sample around the zenith zero axis of the hemisphere. A black iris on the sample holder guarantees the same leaf active area for illuminators and detectors.

This instrument will be calibrated by a set of reflectance standards. Twelve matt ceramic tiles with 25 mm diameter are currently being calibrated at NPL. The tiles: white, mid-grey, pale-grey and black, will be used for instrument calibration, dark readings and detector linearity assessment. In addition, a green matt ceramic disc and a green glass transmittance disc are prepared as green references. Principal axes geometries will be calibrated using NPL National Reference Reflectometer (NRR) [4]. Reported uncertainties for 0º-45º geometry and 99 % reflectance targets for this facility are at the level of 0.3 % for the 400 nm-1000 nm wavelength range. All geometries out-of-plane and in-plane that characterise the hand-held spectrogoniometer has will be calibrated using an Imaging Sphere (a commercial instrument for Bidirectional Reflectance Distribution Function BRDF measurements).

Dedicated software has been developed to perform the data acquisition and analysis in field. It will take the binary output files from the camera and average the results from several frames. The data will be normalised using previously obtained dark and white reference files. The user will then be able to save the processed BRDF data. The software can also display the results as spectral and 3D BRDF graphs. Due to the time sensitive nature of the measurements, it will include a timer so that time elapsed during processing can be monitored.

The optical head will have a weight of about 10 kg. The device will be mounted on a rack which hosts the whole electronics and can be easily transported in a van to the measurement site.

CONCLUSION

A portable leaf goniometer has been designed and build that enables rapid acquisitions of spectro-directional leaf characteristics under controlled illumination conditions in the field. Data will be made available for RT modellers via a web interface.

REFERENCES

1. D. Combes et al., A new spectrogoniophotometer to measure leaf spectral and directional optical properties Remote Sensing of Environment, 109, 107-117, 2007.
2. D. Biliouris et al., A Compact Laboratory Spectro-Goniometer (CLabSpeG) to Assess the BRDF of Materials. Presentation, Calibration and Implementation on Fagus sylvatica L. Leaves, Sensors, 7, 1846-1870, 2007.
3. L. Bousquet et al., Leaf BRDF measurements and model for specular and diffuse components differentiation Remote Sensing of Environment, 98, 201-211, 2005
4. http://www.emceoc.org/index.html.
5. C.J. Chunnilall, et al., NPL scales for radiance factor and total diffuse reflectance, Metrologia, 40, S192-S195, 2003.

Hyper-Spectral Earth Observation Instrument and its Pre-flight Calibration

Nikolay Butiaykin[1], Victoriya Lin'ko[1], Marina Luzganova[1], Aleksandr Li[1], Boris Khlevnoy[2], Maxim Solodilov[2], Valeriy Gavrilov[2], Sergey Ogarev[2], Alexander Panfilov[2], Sergey Arkhipov[1], and Victor Sapritsky[2]

[1]*JSC «Krasnogorsky Zavod», Krasnogorsk, Russia,*
[2]*All-Russian Research Institute for Optical and Physical Measurements (VNIIOFI), Moscow, Russia*
Corresponding e-mail address: khlevnoy-m4@vniiofi.ru

A hyper-spectral instrument was designed and manufactured by the Scientific Centre JSC "Krasnogorsky Zavod" to be used for space-borne earth observation in the spectral range from 400 nm to 960 nm. The instrument was calibrated at VNIIOFI against an integrating-sphere spectral radiance source, which was compared with a high-temperature blackbody traceable to SI via a set of high-temperature fixed points. The expanded uncertainty of the instrument calibration is within 6.0%.

INTRODUCTION

Hyper-spectral Earth observation instrument GSA-RP intended for operation onboard the Resurs-P spacecraft was designed and manufactured by JSC «Krasnogorsky Zavod» under the contract with Space Rocket Center TsSKB-Progress.
The Resurs-P satellite was launched on 25 June 2013, and now is in operation since the date of flight tests finalizing at 01 October 2013.

DESIGN OF INSTRUMENT

The GSA-RP instrument is designed on the basis of a dual-channel autocollimation prism spectrometer and high-frequency frame-transfer CCD matrices.

Optical layout of GSA-RP is depicted in Figure 1. It consists of the following elements: Input lens (1) rendering an image of underlying surface to the spectrometer input slits plane (2), prism block (3) splitting the input beam into two channels (VR1 and VR2) of the spectrometer, lenses of the channels VR1 (4) and VR2 (8), dispersive prisms (5) and (9) of two channels, autocollimation mirrors (6) and (10), mirrors (7) and (11) projecting spectral images of the input slit onto the CCD matrix of the VR1 and VR2 channels.
Temperature of GSA-RP's housing is monitored and controlled with a system of thermo-gradient stabilization. Temperature monitoring function, including reading temperature sensors every 20 seconds, accumulation, analysis and transmission of data to the Earth, allows analyzing he apparatus temperature change in any desired time interval. On the base of analysis result the temperature control is switched on if necessary. The control is performed by means of turning on/off film heaters distributed over the GSA-RP body using a special algorithm. The control process may be interrupted when the average temperature and its distributing are reasonable.

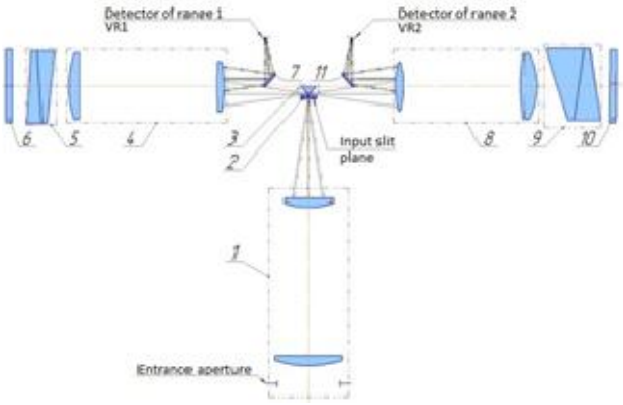

Figure 1. Optical layout of GSA instrument.

The GSA-RP includes a special calibration-check unit for periodical check of stability of the instrument responsivity and wavelength scale. The unit is assigned for illuminating the input lenses (1) and consists of the following elements (Fig.2): two miniature quarts halogen lamps (11), glass filters (12), lenses (13) and a diffuse reflector (14) located on the inner side of entrance window cover.

INSTRUMENT CHARACTERISTICS

The main technical characteristics of the instrument GSA-RP is presented in Table 1. GSA-RP is controlled by a control unit with commands generated by Resurs-P spacecraft controlling system.

The main operation modes of GSA-RP are: «work» and «Calibration»; At the «Calibration» mode the instrument measures spectral radiance of the check unit. This mode is used for in-flight monitoring of stability of GSA parameters, such as

responsivity and wavelength scale, and for making data files intended for computation of corresponding correction factors.

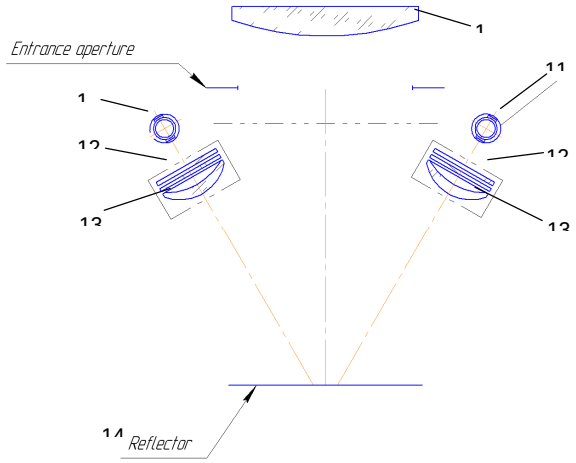

Figure 2. Layout of calibration-check unit.

PRE-FLIGHT CALIBRATION

GSA-RP was calibrated at VNIIOFI in terms of spectral radiance responsivity against a reference 600 mm aperture integrating sphere source (IS) included in the Standard Radiometric Facility for Earth Observation Instruments [1]. Calibration was done at 9 levels of IS intensity. Spectral radiance of IS at each level was measured by means of comparison with a precise blackbody with temperature of about 3020 K.

Table 1. Technical characteristics.

Item	value
Spectral range, μm	0.40-0.96
Number of spectral channels	75-130
Spectral resolution, nm	≤7.0
Span (in Nadir), km	30
Resolution (GSD), m	30
Signal to noise ratio	>230
Wavelength scale accuracy, nm	≤1.0
Number of digits of data, bit/pixel	14
Non-linearity of channels' calibration curve, %	<1.0
Signal irregularity at observation of uniform surface, %	<0.5

A radiation thermometer used for the blackbody temperature measurement was calibrated using tree high-temperature fixed points: Co-C (1598 K), Re-C (2748 K) WC-C (3021 K). The stability and reproducibility of the fixed points were confirmed in a set of investigations and international comparison, and their thermodynamic temperatures were measured accurately [2-4]. Standard uncertainty of the WC-C temperature is about 0.5 K, but reproducibility of this point is better than 0.1 K. Use of the fixt points guarantees reliable traceability to SI and high reproducibility of the calibration procedure.

Minimal intervals between the calibration steps allowed avoiding the long-term instability problem.

UNCERTAINTY

Standard uncertainty of IS spectral radiance measurement in the range 400 nm to 1000 nm varies from 0.5 % to 1.0 %. The main components of the uncertainty relates to blackbody temperature measurement, sphere source non-uniformity and instability, stray light, non-linearity, size-of-source effect and noise-to signal ration of a spectral comparator.

The main sources of the GSA-RP calibration uncertainty, besides the IS calibration uncertainty, were non-linearity and non-uniformity of the CCD, wavelength accuracy, stay light, interference of the CCD pixels and noise-to-signal of the instrument reading. Minimal intervals between the calibration steps allowed avoiding the long-term instability problem.

The combined expanded (k=2) uncertainty of the GSA-RP instrument in terms of spectral radiance responcivity is within 6%.

REFERENCES

1. V. Sapritsky e.a., Current activity of Russia in measurement assurance of Earth optical observations, Metrologia 49, S9–S16, 2012.
2. V. Gavrilov, B. Khlevnoy et al, Measurement of thermodynamic temperature of high temperature fixed points, AIP Conference Proceedings 1552, 329-334, 2013.
3. B. Khlevnoy, I. Grigoryeva and D. Otryaskin, Development and investigation of WC–C fixed-point cells, Metrologia 49, S59–S67, 2012.
4. B. Khlevnoy, Y. Yamada, I. Grigoryeva et al, Comparison of Re–C Fixed-Point Cells and Their T90 Temperatures Between NMIJ and VNIIOFI, Int. J. Thermophys 32, 1753–17622, 2011.

Back-calibration and Cross-calibration of Earth Observing Imagers Using the Moon as a Common Radiometric Reference

Thomas C. Stone

U. S. Geological Survey, Astrogeology Science Center, Flagstaff, Arizona, USA
Corresponding e-mail address: tstone@usgs.gov

The reflected light from the Moon can be used for radiometric calibration of Earth observing imager instruments at reflected solar wavelengths. The lunar radiometric reference is provided through computations of an analytic model for the spectral irradiance of the Moon, developed at the U.S. Geological Survey in Flagstaff, Arizona. The inherent stability of the lunar surface enables using this model reference for back-calibration and cross-calibration of instruments that have viewed the Moon, regardless of the times of the observations. Applying lunar calibration to the visible-channel imagers on geostationary meteorological satellites has led to the development of time-dependent calibration corrections for these sensors.

INTRODUCTION

The recognized importance of using environmental data records from Earth observing satellite instruments for climate change assessment has demonstrated the need for consistent and stable radiometric calibration. Much effort has been dedicated to validating on-board calibration systems at reflected solar wavelengths, e.g. to offset the well-known degradation of solar diffusing panels. The process of on-orbit calibration consists of comparing an instrument's response to a known reference source.

The Moon can be used as a radiometric reference, requiring no correction for an atmosphere between the sensor and the calibration target. To enable quantitative specification of the intensity of reflected light from the Moon, the reflectance properties of the lunar surface have been characterized at the U.S. Geological Survey (USGS) in Flagstaff, Arizona, using a multiple-year collection of ground-based observations acquired by the Robotic Lunar Observatory (ROLO). The USGS Lunar Calibration facility has developed the tools and techniques to use the spectral irradiance of the Moon as a radiometric reference [1]. The lunar irradiance measured by an instrument depends primarily on the relative positions of the Sun, the Moon and the sensor, and on the physical orientation of the Moon at the time of observation. Predicting the lunar irradiance corresponding to any particular set of geometric conditions of a spacecraft instrument's observations of the Moon requires querying an analytic model. Thus the lunar irradiance model is considered to be the radiometric reference standard.

Regarded as a diffuse reflecting surface, the Moon is photometrically stable to an exceptional level, changing less than one part in 10^8 per year [2]. An important implication of this inherent stability is that the predictions of the lunar irradiance model are valid for any observation time. This enables cross-calibration of any instruments that have viewed the Moon, even if their lunar observations were not simultaneous, and also back-calibration using lunar images found in archived data.

LUNAR CALIBRATION SYSTEM OPERATION

Realizing a lunar calibration for imager instruments consists of comparing lunar irradiance measurements from images of the Moon to the lunar model predictions corresponding to the Sun-Moon-Observer geometry of the instrument observations. The irradiance measurements E_{meas} are derived from summation of radiance pixels L_i, as

$$E_{meas}=\Omega_{pix}\Sigma L_i \qquad (1)$$

where Ω_{pix} is the angular acceptance (solid angle) of a pixel, and the summation covers the entire lunar disk image.

For the lunar model predictions, the geometry parameters of phase angle and the lunar librations for an observation are computed from the spacecraft position and solar and lunar ephemeris calculations; these parameters are the inputs to the lunar model. The raw model outputs are the disk-equivalent reflectance at the 32 ROLO band wavelengths. A representative lunar reflectance spectrum is fitted to these 32 values with a linear function of wavelength. This fitting step ensures spectral consistency over the full valid range of observation geometries. The

fitted spectrum is then convolved with the instrument band relative spectral response and the solar spectral irradiance functions to give the lunar irradiance at the band wavelengths. Finally, corrections are applied for the $1/r^2$ dependencies of the Sun-Moon and Moon-observer distances.

The final results are reference lunar irradiances E_{ref} suitable for direct comparison to the measurements from images. The ratio of measured to reference lunar irradiances E_{meas}/E_{ref} effectively normalizes the Moon brightness in the images, which can vary considerably from image to image. Consequently, the lunar model computations provide a consistent reference for the lunar irradiances corresponding to the instrument observations.

APPLICATION TO GEOSTATIONARY METEOROLOGICAL IMAGERS

The visible-channel imagers on geostationary meteorological satellites provide a notable example of a succession of instruments that have viewed the Moon somewhat regularly throughout their lifetimes, thus enabling cross-calibration against the common lunar radiometric reference. From geostationary orbit, images of the Moon are captured by chance (and sometimes by dedicated observations) in the corners and margins of a rectangular field of regard. Hundreds of Moon images have been found in the archives of meteorological data kept by satellite operating agencies, and processed to irradiance using

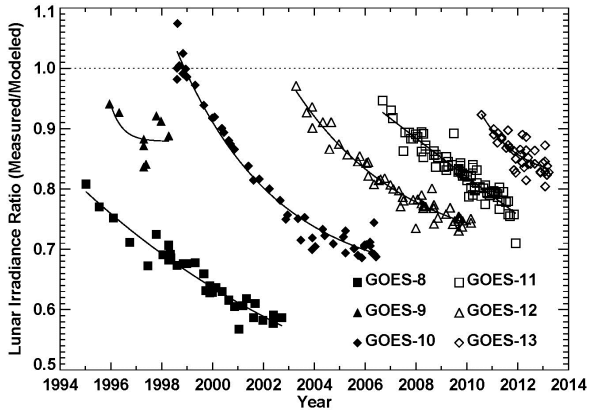

Figure 1. Time series of lunar irradiance comparisons for GOES-8 through GOES-13, given as ratios of measurements from images to lunar model computations. Fitted temporal trends are shown as solid lines through the data points.

Equation 1. Figure 1 shows time series of lunar irradiance comparisons (E_{meas}/E_{ref}) for the visible-channel imagers on GOES-8 through GOES-13. For this initial analysis, the GOES operational images were converted to radiance from raw sensor counts using constant (pre-launch) calibration coefficients for each imager, and the time series exhibit sensor response degradation trends.

The response trends shown in Figure 1 were used to develop time-dependent corrections to the pre-launch calibration coefficients, in the form of quadratic polynomial functions of the elapsed time from the satellite operational dates. Applying these corrections and re-computing the lunar irradiance measurements normalizes the time series of comparisons, as shown in Figure 2.

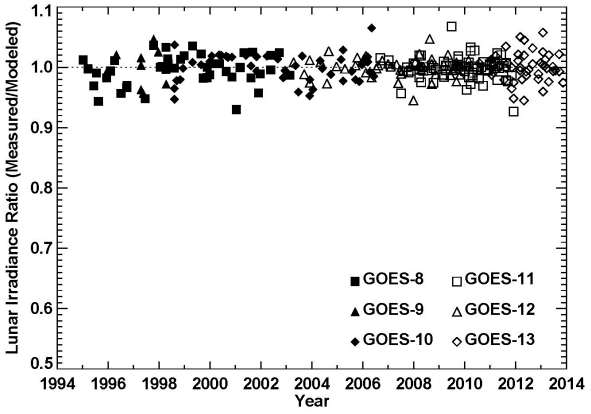

Figure 2. Time series of lunar irradiance comparisons for GOES-8 through GOES-13, where the radiance pixels used for the measurements from lunar images have had time-dependent calibration corrections applied. These corrections were developed from analysis of the sensor response trends shown in Figure 1.

The results in Figure 2 show the calibration corrections remove the temporal response trends, and place all six GOES imagers on the same radiometric scale, referenced to the USGS lunar irradiance model. This analysis demonstrates the application of lunar calibration to instruments long past their operational lifetimes, and the capability to cross-calibrate sensors using the Moon as a common radiometric reference source.

REFERENCES

1. H. H. Kieffer and T. C. Stone, The Spectral Irradiance of the Moon, Astronomical Journal, 129, 2887-2901, 2005.
2. H. H. Kieffer, Photometric Stability of the Lunar Surface, Icarus, 130, 323-327, 1997.

New possibilities for UV research by simultaneous spectral radiance measurements

Gunther Seckmeyer, Michael Schrempf, Stefan Riechelmann, and Ansgar Stührmann

Institute of Meteorology and Climatology, Leibniz University, Hannover, Germany
Corresponding e-mail address: Seckmeyer@muk.uni-hannover.de

The knowledge of the angular distribution of solar radiance and its spectral characteristics is required for many applications including solar energy and the impact of UV radiation on humans. Sky radiance has been found to be the dominant factor for the solar UV exposure of humans, both with respect to positive and negative effects of UV radiation. We recently developed a novel method to calculate the actual vitamin D3–weighted exposure of a human by using radiance instead of irradiance. In Addition a new non-scanning multidirectional spectroradiometer was developed to measure radiance simultaneously in a high temporal resolution.

INTRODUCTION

Measurements of spectral sky radiance are useful for many applications where knowledge of temporal and spatial information of the radiation field is necessary. Possible applications are the calculation of power yield of tilted solar cells [1] or the determination of spectral exposure objects like the human body [2]. Earlier exposure investigations are based on the irradiance, which not take into account the complex geometry of the radiation field. To calculate the actual vitamin D3–weighted exposure a novel method was developed, which integrates the incident solar spectral radiance over all relevant parts of the human body.

Since clouds play a crucial role in determining the actual exposure of humans and the yield of solar cells, new instruments that measure sky radiance in dependence of zenith and azimuth angle in more than 100 directions are needed.

The measurement of spectral sky radiance is a demanding task, since this four-dimensional unit depends on zenith angle, azimuth angle, wavelength and time. It is therefore commonly derived by sequentially measuring a set of directions in the sky using double monochromators or charged coupled device array spectroradiometer. Since the measuring time takes several minutes, new instruments have been developed in recent years. We developed a novel multidirectional spectroradiometer (MUDIS), which is capable of performing simultaneous spectral sky radiance measurements in the UV. Such instruments are expected to improve our understanding both with respect to solar energy and health effects of solar radiation.

DEVELOPEMENTS

Calculation of the Exposure:

The equation for the calculation of the actual exposure of a human is complex and due to numerous dependencies the calculation can be quite demanding. Therefore some simplifying assumptions have been made (e.g. skin areas treated as lambertian surfaces, skin areas have same sensitivity).

The complex geometry of the human is taken into account by deriving projection areas of the human body for each considered direction. To calculate a biologically weighted exposure, the radiance for all directions is weighted with a biological action spectrum and then multiplied with the projection area for the corresponding direction. Finally all weighted directions are integrated.

MUDIS Instrument:

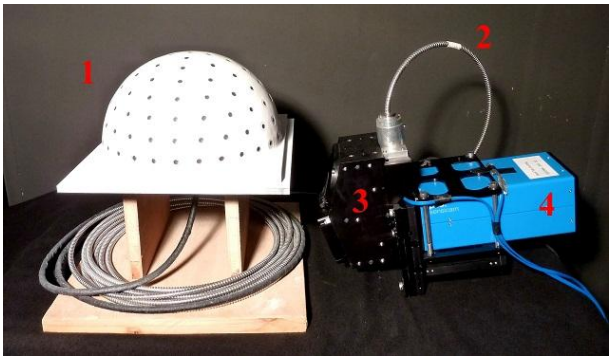

Figure 1. Main components of MUDIS: hemispherical entrance optics dome with weather protection (1), fibre bundle (2), Offner imaging spectrometer (3), UV-sensitive CCD camera (4).

The developed spectroradiometer is shown in figure 1. The main component of MUDIS is a

hyperspectral imager consisting of a UV-sensitive CCD camera and an Offner imaging spectrometer. A bundle of optical fibres are embedded in a hemispherical shaped dome and are evenly distributed in zenith and azimuth directions. A single measurement (sky capture) performed with MUDIS therefore simultaneously performs 113 sky radiance measurements in different zenith and azimuth directions. MUDIS is capable of measuring spectra from 250 to 600 nm with a bandwidth of approximately 2 nm and a sampling interval of 0.4 nm. Spectral sky radiance measurements were performed with MUDIS and a Scanning CCD spectroradiometer (SCCD) in Hannover, Germany on two days covering the two meteorological conditions cloudless and overcast.

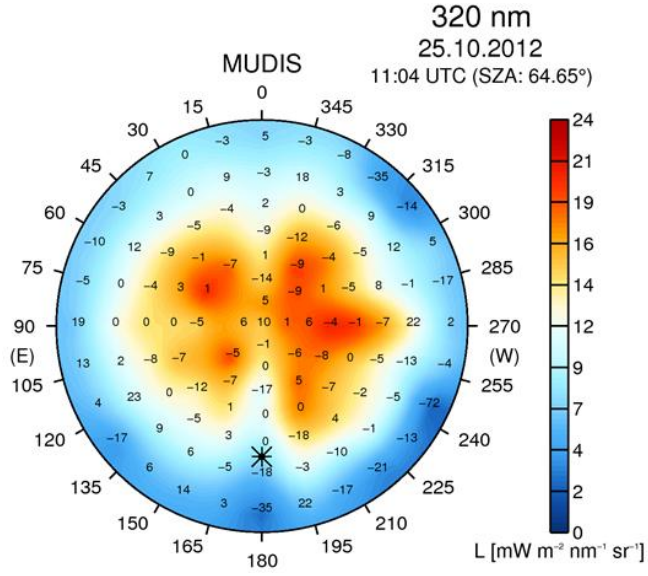

Figure 2. Spectral sky radiance as a function of zenith and azimuth angle measured with MUDIS for overcast sky on 25 October 2012 at 11:04 UTC. The plotted Numbers represent the difference between corresponding MUDIS and SCCD measuring points in per cent. The sun symbol marks the position of the sun at the beginning of the sky scan.

RESULTS AND DISCUSSION

Our new method to estimate the UV exposure for humans enables, in principle, to calculate the necessary exposure times to gain a healthy vitamin D status for various conditions taking into account the complex geometry of both the human body and the sky radiance. Our calculations show that the UV index (based on the unit irradiance) is not a good indicator for the exposure. At the winter solstice vitamin D cannot be obtained with realistic clothing both in the southern and the northern hemisphere, even if the exposure were extended to all daylight hours.

Figure 2 shows the spectral sky radiance distribution of the sky on October 25 covered with stratocumulus clouds at 320 nm measured with MUDIS.

For spectral comparisons between MUDIS and SCCD spectral actinic irradiances were calculated from measurements and the ratios are shown in figure 3 for cloudless and overcast conditions.

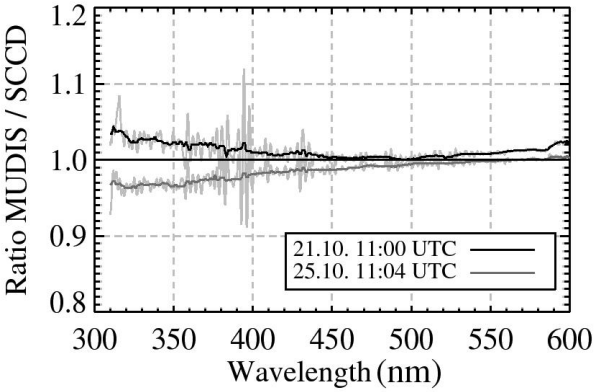

Figure 3. Median filtered ratios of spectral actinic irradiances measured with MUDIS and SCCD under cloudless sky on 21 October (black line) and under overcast sky on 25 October (dark grey line), 2012. The unfiltered ratios are plotted in light grey.

Actinic irradiance calculated from radiance measurements of both instruments shows a deviation of less than 6% under cloudless sky and less than 8% during overcast sky. Histograms of sky radiance measurements at two representative wavelengths (320 and 500 nm) show good agreement between both MUDIS and SCCD. Despite the inability to measure the circumsolar region with high spatial resolution, the MUDIS bare fibre entrance optics dome with a FOV of 10.6°–18.4° performs well compared to the 5◦ FOV SCCD entrance optics under various sky conditions. The development of a system capable of measuring sky radiance as a function of zenith and azimuth angle in seconds rather than minutes enables new possibilities to study the spectral influence of fast changing cloud conditions without the disadvantages of scanning processes [3].

REFERENCES

1. Beringer S., Schilke H., Lohse I., Seckmeyer G.: *Case study showing that the tilt angle of photovoltaic plants is nearly irrelevant*, Solar Energy, 85, pp. 470-476, February 2011.

2. Seckmeyer G., Schrempf M., Wieczorek A., Riechelmann S., Graw K., Seckmeyer S., Zankl M.: *A novel method to calculate solar UV exposure relevant to vitamin D production in humans*, Photochemistry & Photobiology, 89: 974–983, 2013.
3. Riechelmann S., Schrempf M., Seckmeyer G.: *Simultaneous measurement of spectral sky radiance by a non-scanning multidirectional spectroradiometer (MUDIS)*, Measurement Science and Technology, 24, 125501, http://dx.doi.org/10.1088/0957-0233/24/12/125501, 2013.

Vicarious Calibration of Imaging Spectrometers using Desert Sites: ARTEMIS Example

Ronald B. Lockwood[1], Joel McCorkel[2], Kurtis Thome[2], Nathan Leisso[3], Michael Brueggeman[4], and Thomas Cooley[4]

[1]MIT Lincoln Laboratory, Lexington, MA USA, [2]Goddard Space Flight Center, NASA, Greenbelt, MD USA, [3]National Ecological Observatory Network, Boulder, CO USA, Air Force Research Laboratory, Kirtland AFB, NM USA
Corresponding e-mail address: Ronald.lockwood@ll.mit.edu

The on-orbit calibration of the Advanced Tactically-Effective Military Imaging Spectrometer (ARTEMIS) relied entirely upon vicarious calibration techniques since the sensor lacked an on-board calibration source. The calibration technique developed for ARTEMIS combines results from reflectance-based vicarious calibration experiments conducted at Ivanpah Playa, with a series of measurements over a pseudo-invariant test site. A combined approach is necessary since the Ivanpah measurements did not sample the full swath-width of the imaging spectrometer. Data from the spatially uniform, invariant site allowed the transfer of the Ivanpah radiometric calibration to the remaining spatial-spectral pixels. The transfer approach consists of retrieving the average ground reflectance of the large, homogeneous site to build an accurate radiometric model of the at-aperture radiance that allows the derivation of the remaining calibration coefficients. Results from the application of the method to ARTEMIS are presented.

INTRODUCTION

The Air Force Research Laboratory recently completed the demonstration of a rapidly and inexpensively developed, but highly capable, imaging spectrometer for use in space. The ARTEMIS sensor consisted of a Ritchey-Chrétien telescope and an Offner-Chrisp imaging spectrometer [1]. One of the development goals was to achieve a high degree of spatial-spectral uniformity with the design having <5% non-uniformity [2]. The as-built sensor only slightly exceeded this goal. For example, the spatial non-uniformity for the spectral response functions corresponding to the 940 nm water atmospheric absorption feature had a variation of 0.2 % in the center values and 6.2% in the full-width-at-half-maximum (FWHM) values. The range of spectral response function variation was 0.06-0.4% for the center values and 5.7-6.4% for the FWHM values.

ARTEMIS did not have an on-board calibration source and vicarious calibration techniques were used throughout the mission to update and maintain the calibration coefficients. These techniques require the labor intensive characterization of appropriate ground site coincident with the acquisition of the spectral imagery from space. It is not possible to measure the entire cross-track swath width of the imagery without a prohibitively expensive ground truth effort. It is therefore necessary to somehow transfer the calibration from the portion of the swath width that is directly calibrated to the remaining, uncalibrated portion.

The calibration transfer is accomplished using imagery collected from a pseudo-invariant site. The radiance from such a site is known for that portion of the swath width that was previously calibrated from the Ivanpah Playa measurements and is transferred to those spatial-spectral samples that were not directly calibrated. This process would be relatively easy for an imaging spectrometer that has perfect spatial-spectral uniformity with identical spectral response functions for every spatial sample corresponding to a particular center wavelength. The calibration transfer in such a case would involve a simple ratio of the calibrated to the uncalibrated samples for a particular center wavelength. This process fails for any real imaging spectrometer with some degree of spatial-spectral nonuniformity. Given this failure, a method must be devised to transfer the radiometric calibration given the slight variation in the spectral response functions as a function of spatial sample.

VICARIOUS CALIBRATION RESULTS

The data calibration for ARTEMIS utilized the reflectance-based vicarious calibration method to generate at-aperture radiance [3,4]. Briefly, the approach relies upon a site that has a spatially and spectrally homogeneous reflectance that is measured using field spectrometers referenced to a NIST-

traceable reflectance standard during the sensor overpass. The atmosphere is also simultaneously characterized using a suite of atmospheric sensors with the primary instrument being an automated solar radiometer. These ground truth data sets are subsequently used to develop the inputs to a radiative transfer code such as MODTRAN®. The absolute uncertainty for this method is in the 3 to 5% range [4].

Ivanpah Playa was utilized for the vicarious calibration of ARTEMIS throughout the life of the sensor. For the work reported here, the at-aperture radiance corresponding to the ground reflectance measured in a rectangular area of about 320 m × 90 m was modeled using MODTRAN® for measurements made on October 19 and 23, 2011. Large blue tarps that were readily apparent in the imagery were used to mark the opposite corners on the diagonal of this rectangular area. The calibration coefficients corresponding to the characterized area were calculated for the two measurements and they agreed to better than 0.5%. This was true even though the solar zenith angle was quite different on the two days (47 and 62 degrees respectively) indicating the Lambertian nature of the playa reflectance. About 25% of the swath width was directly calibrated from the combined and overlapping measurements.

CROSS CALIBRATION USING A PSUEDO-INVARIENT SITE

There are several pseudo-invariant test sites that have been used to monitor the on-orbit calibration stability of spectral sensors built for scientific and commercial uses [5]. The sites share a variety of selection criteria such as high spatial uniformity, surface reflectance greater than 0.3 and near Lambertian, temporal invariance, high altitude, and minimum cloud cover [3]. The pseudo-invariant site that was selected for ARTEMIS use met these criteria.

The goal is to transfer the calibration to the uncalibrated portion of the swath width. The approach to accomplish this is to produce an at-aperture radiance model that matches the calibrated portion of the swath width under the assumption that, due to site uniformity, the rest of the scene shares the same radiance. Calibration coefficients are then produced in the same way that they were for the Ivanpah Playa data. This approach requires knowledge of the water content, the aerosol loading, and the surface reflectance in order to perform the radiative transfer modeling.

The first step in the process was to utilize the directly calibrated portion of the ARTEMIS swath width to evaluate the site. This subset of data was sorted to remove any outliers and the spectral radiance corresponding to each of the spatial samples was averaged in the along-track direction. This yielded average spectral radiance that had a non-uniformity that was less than 3% (1-σ). Less than 10% of the pixels were removed in the process. The uncalibrated portion of the cross-track spatial samples, in digital numbers, was similarly evaluated to remove the outliers.

The second step was to retrieve the water content as a function of spatial pixel from the calibrated portion of the swath width. The water content was estimated using the Continuum Interpolated Band Ratio (CIBR) method [6]. The method calculates a ratio between the radiance in the spectral channel centered on a water absorption feature, such as the one at 940 nm, to the weighted interpolation of the radiance within two reference bands on either side of the water absorption feature. The reference bands are outside of the water feature. This ratio is compared to the values calculated using MODTRAN® and stored in a look-up table. The calculation is performed for each of the spatial pixels that were not removed in the first step and a histogram of the retrieved water values was plotted. Additionally, the MODTRAN® modeled spectral radiance is compared to the ARTEMIS data for evaluation.

The third step was the aerosol retrieval. This is more difficult since the pseudo-invariant site data lack any “dark objects” of the kind that are typically used to estimate the aerosol loading. The aerosol estimation employed here again used a MODTRAN® model generated look-up table to compare to the calculated top of the atmosphere (TOA) reflectance from the scene data. The look-up table had a visibility range from 5 to 323.58 km and the scene visibility is calculated by interpolation between the table and the ARTEMIS derived TOA reflectance using a least-squares minimization.

The final step in the ground reflectance retrieval requires the solution of the radiative transfer equation. The total radiance is the sum of the components from the direct and diffuse illumination, the path radiance, and the adjacency radiance due to

multiple scattering. The Lambertian approximation is used to estimate the direct radiance term and the adjacency component is neglected since the site dimensions are much large than those of the scene data. The outputs of the MODTRAN® calculations include the diffuse radiance, the path radiance, and the atmospheric transmission terms. These terms are combined with the ARTEMIS measured total radiance and the spectral reflectance is calculated. This is compared to the MODIS derived reflectance product for validation.

From this information the MODTRAN® model of the at-aperture radiance was generated. The calibration coefficients are subsequently calculated for the uncalibrated portion of the cross-track spatial samples. This process is repeated for each of the several pseudo-invariant site datasets and the retrieved reflectance and calibration coefficients are compared for consistency.

CONCLUSIONS

A method to calibrate a space-based wide swath width imaging spectrometer has been developed. The approach combines traditional vicarious calibration techniques with spectral imagery of a pseudo-invariant site. This adds an additional uncertainty to the calibrated radiance. The final uncertainty is estimated to be from 4% to 6% (1-σ). Additionally, the pseudo-invariant site reflectance has been retrieved and is in good agreement with the MODIS derived values. It is expected that the technique is broadly applicable to spectral sensors in the reflective spectral range.

REFERENCES

1. R. B. Lockwood, T. W. Cooley, R. M. Nadile, J. A. Gardner, P. S. Armstrong, A. M. Payton, T. M. Davis, S. D. Straight, T. G. Chrien, E. L. Gussin, and D. Makowski, “Advanced Responsive, Tactically-Effective Military Imaging Spectrometer (ARTEMIS) Design,” in *Proc. 2006 IEEE Int. Geoscience and Remote Sensing Symp.*, Denver, CO, pp. 1228-1630, 2006.
2. Pantazis Mouroulis, Robert O. Green, and Thomas G. Chrien, “Design of pushbroom imaging spectrometers for optimum recovery of spectroscopic and spatial information,” Applied Optics, vol. 39, 2210-2220, 2000.
3. P. N. Slater, S. F. Biggar, R. G. Holm, R. D. Jackson, Y. Mao, M. S. Moran, J. M. Palmer and B. Yuan, “Reflectance- and radiance-based methods for the in-flight absolute calibration of multispectral sensors,” *Remote Sens. Environ.*, vol. 22, pp. 11-37, 1987.
4. K. J. Thome, “Absolute radiometric calibration of Landsat 7 ETM+ using the reflectance-based method,” *Remote Sens. Environ.*, vol. 78, pp. 27-38, 2001.
5. Gyanesh Chander, Xiaoxiong (Jack) Xiong, Taeyoung (Jason) Choi, and Amit Angal, “Monitoring on-orbit calibration stability of the Terra MODIS and Landsat 7 ETM+ sensors using pseudo-invariant test sites,” *Remote Sens. Environ.*, vol. 114, pp. 925-939, 2010.
4. D. Schläpfer, C. C. Borel, J. Keller, and K. I. Itten, “Atmospheric precorrected differential absorption technique to retrieve columnar water vapor,” *Remote Sens. Environ.*, vol. 65, pp. 353-366, 1998.

The On-orbit Absolute Radiance Standard for Infrared Satellite Validation

Jonathan Gero, Fred Best, Hank Revercomb, Joe Taylor, Doug Adler,
Robert Knuteson, Claire Pettersen, and David Tobin

Space Science and Engineering Center, University of Wisconsin—Madison, Madison, WI, USA
Corresponding e-mail address: jonathan.gero@ssec.wisc.edu

The On-orbit Absolute Radiance Standard (OARS) is blackbody designed for high-accuracy validation of satellite infrared sensors. The OARS has a light trapping cavity geometry with its interior coated with highly emissive black paint. It has embedded phase change cells and precise thermal control for temperature calibration, and an integrated Heated Halo broadband thermal source for cavity emissivity measurement on-orbit. The OARS achieves a combined uncertainty (*k*=3) of 0.045 K in radiance temperature and 0.04% in emissivity.

INTRODUCTION

The next generation of infrared remote sensing satellite instrumentation, including climate benchmark missions, will require better absolute measurement accuracy than is now available, and will most certainly rely on the emerging capability to fly SI-traceable standards on-orbit. As an example, the detection of spectral climate signatures requires measurements of thermal infrared radiance with uncertainties better than 0.1 K (*k*=3) in radiance temperature [1]. An On-orbit Absolute Radiance Standard (OARS) that can be used to meet these stringent requirements has been demonstrated at the University of Wisconsin, with support from the NASA Instrument Incubator Program and Earth Science Technology Office. This work culminated with an integrated subsystem used to provide end-to-end radiometric accuracy validation in the laboratory and vacuum environments for the flight prototype of a climate benchmark instrument. We present the new technologies that underlie the OARS and the results of the laboratory testing that demonstrate its accuracy.

APPARATUS

The key features of the OARS are illustrated in Fig. 1. The blackbody design is based on the on-board calibration system developed for the NASA Geosynchronous Imaging Fourier Transform Spectrometer [2]. A temperature controlled light-trapping blackbody cavity contains ultra-stable thermistor temperature sensors and miniature phase change cells containing small amounts (<1 g) of high-purity reference materials that provide on-orbit temperature calibration. The heatable conical frustum (heated halo) thermally isolated in front of the cavity provides a broadband source for periodic measurement of cavity emissivity.

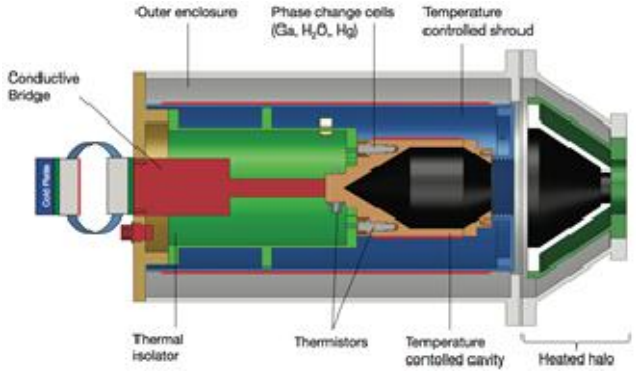

Figure 1. Cross sectional representation showing the key features of the OARS.

METHODOLOGY

A temperature calibration point is obtained by measuring the transient cavity temperature response to a small increase in power. Fig. 2 shows the sequence of events during a typical melt of gallium. After initial stabilization in the constant temperature mode, a constant power is used to transition through the melt plateau, where the phase change signature is observed. Various melt materials have been demonstrated, including H_2O, Hg, and a Ga-Sn eutectic. Using this technique, the thermistors embedded in the cavity can be calibrated to uncertainties of better than 5 mK (*k*=3). With the inclusion of all other error sources (type B), the combined uncertainty of the OARS blackbody effective temperature is 45 mK (*k*=3) [3].

Emissivity measurements are made with the spectroradiometer that normally views the cavity, but in this case it measures the reflected signal of the heated halo at an elevated temperature, typically 70 K hotter than the cavity temperature. With the

knowledge of the heated halo and effective background temperatures, and the solid angle view factor of the cavity view to the halo, the cavity emissivity can be calculated [4]. Laboratory measurements of an OARS type blackbody, with a spectral emissivity greater than 0.999, have been made with combined uncertainties (type B) less than 0.04% (k=3), and are in good agreement with model results as well as independent measurements [5].

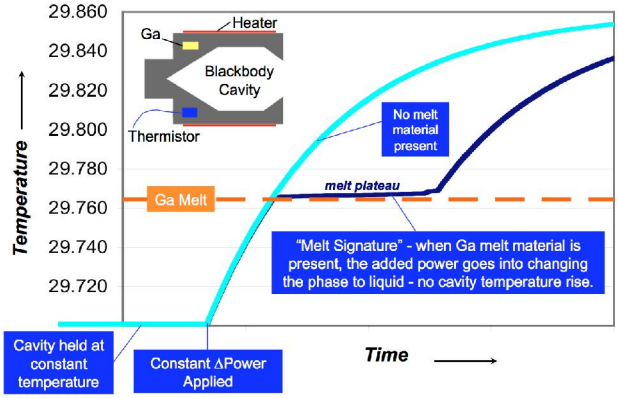

Figure 2. Key elements of a transient melt signature, shown for gallium. The melt plateau is approximately 4000 seconds in duration.

RESULTS AND DISCUSSION

By observing the OARS as an independent radiance source across a broad range of temperatures, the end-to-end radiometric uncertainty of a spaceborne spectroradiometer can be determined for the range of expected earth scene radiances. Such end-to-end validation is usually only performed on an instrument during pre-launch calibration, and launch into space breaks the traceability chain. In contrast, the OARS facilitates validation with traceability to the fixed points of the ITS-90 temperature scale throughout the lifetime of a mission.

The OARS has been used to validate the radiometric performance of the Absolute Radiance Interferometer (ARI), which is the flight prototype of a climate benchmark satellite instrument. End-to-end radiometric uncertainties better than 0.1 K (k=3) were demonstrated in both the laboratory and vacuum environment [6]. Based on these achieved uncertainties, Fig. 3 shows the expected radiometric performance that can be attained by a benchmark infrared satellite sensor that is validated on-orbit with the OARS. Thus the OARS can be used to improve the accuracy of the next generation satellite infrared remote sensors and to attain benchmark climate measurements from space.

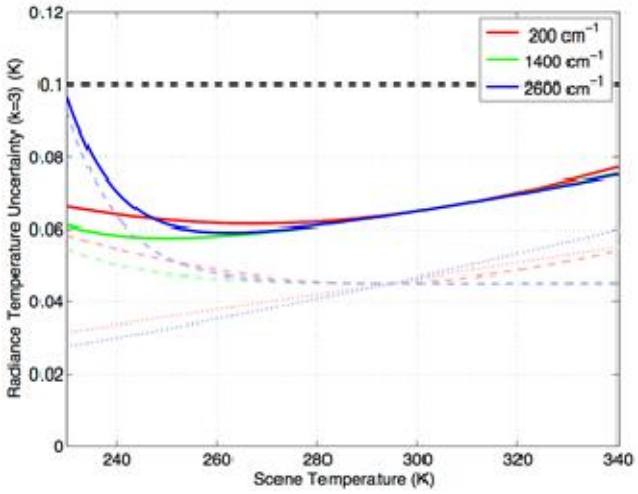

Figure 3. Predicted on-orbit radiometric performance: infrared sensor calibration uncertainty (dotted), OARS uncertainty (dashed), combined uncertainty (solid).

REFERENCES

1. National Research Council, Earth Science and Applications from Space: National Imperatives for the Next Decade and Beyond, National Academies Press, Washington D. C., 2007.
2. F. A. Best and Coauthors, Performance verification of the Geosynchronous Imaging Fourier Transform Spectrometer (GIFTS) on-board blackbody calibration system, in Proc. SPIE 6405, 64050I, 2006.
3. F. A. Best and Coauthors, On-orbit absolute radiance standard for the next generation of IR remote sensing instruments, in Proc. SPIE 8527, 85270N, 2012.
4. P. J. Gero and Coauthors, On-orbit absolute blackbody emissivity determination using the heated halo method, Metrologia, 49, S1-8, 2012.
5. P. J. Gero and Coauthors, The heated halo for space-based blackbody emissivity measurement, in Proc. SPIE 8527, 85270O, 2012.
6. J. K. Taylor and Coauthors, The University of Wisconsin Space Science and Engineering Center Absolute Radiance Interferometer (ARI): instrument overview and radiometric performance, in Proc. SPIE 8527, 85270P, 2012.

Diffusers, Properties and Performance in BSDF and Spectral Features

Bilgehan Gür[1,2], Hedser van Brug[1], Man Xu[1], and Elizabeth Vela[1]

[1]*TNO Delft, The Netherlands,*
[2]*S&T Delft, The Netherlands*
Corresponding e-mail address: Bilgehan.gur@tno.nl

A diffuser is a core element of calibration units in earth observation instruments. Its performance influences significantly the achievable accuracy of scientific observations. However, the performance, in particular the Bi-Directional Scattering Function BSDF and spectral features, depends on several parameters, such as surface properties, instrument configuration, observational conditions and further. This paper describes experimental activities to achieve a better understanding about the interaction between diffuser properties and performance and to provide an additional data base for theoretical modelling both on BSDF and spectral features.

INTRODUCTION

Diffusers are widely used in space instruments as parts of the on-board calibration unit. Its influence on the quality and accuracy of L2 products makes the adequate definition of diffuser properties to one of the key tasks in the design of on-board calibration units. Each instrument however, due to its possibly unique mission and configuration, requires an individual definition of a diffuser with regards to its surface properties, material, coating and further parameters. Previous activities have shown discrepancies in experimental and modelled performance, thus making it more difficult to design suitable components for future earth observation missions. The present paper describes our efforts in improving our understanding in the interaction of diffuser properties and according performance with regards to its scattering properties and spectral features, i.e. speckle induced non uniformities in the recorded spectra [1]. For a systematic approach a set of diffusers were manufactured with known surface properties and according experimental measurements performed. In this paper we present the latest experimental results, observed patterns in BSDF and speckle behaviour and discuss comparisons with latest theoretical models[2][3].

EXPERIMENTAL MEASUREMENTS

For the intended systematic approach a set of 24 diffusers (diameter 50mm, thickness 5mm) have been manufactured with different surface properties, i.e. with varying roughness parameters R_q. The used material was fused silica in order to allow measurements in the UV range. 12 diffusers were designed for transmission, the other 12 for reflection with Al coating on one side.

Table 1. Set of diffusers with different properties. The reflection diffusers were Al coated on one side.

Diffuser	Roughness (R_q in µm)
Transmission, 1 rough surface	0.5, 1.0, 1.5, 2.0, 2.5, 3.2
Transmission, 2 rough surfaces	0.5, 1.0, 1.5, 2.0, 2.5, 3.2
Reflection, 1 rough surface	0.5, 1.0, 1.5, 2.0, 2.5, 3.2
Reflection, 2 rough surfaces	0.5, 1.0, 1.5, 2.0, 2.5, 3.2

BSDF measurements have been performed in the "Absolute Radiometric Calibration Facility ARCF" at TNO, a unique setup for component characterisation for space applications. Two decoupled rotational stages allow variation of the angle of incidence and detection. Different wavelength ranges between 350nm and 1000nm, adjustable via a monochromator, have been used.

A further dedicated setup was used for speckle measurements. This setup basically consists of a monochromatic source, a diffuser holder and a line array. For the present measurements a source in the SWIR range at 2300nm was used. Diffuser and line array are placed on a rotational stage with sub-degree resolution. This way the angle of incidence was changed in small steps, while the angle of detection remained constant with respect to the diffuser normal. The value of interest to be determined is the so-called de-correlation angle, i.e. the angle where two speckle patterns are considered de-correlated. The resulting

averaging effect defines significantly the achievable relative radiometric accuracy in earth observation instruments.

RESULTS AND CONCLUSIONS

The experimental BSDF results show a systematic behaviour of the BSDF in dependence of the surface roughness.

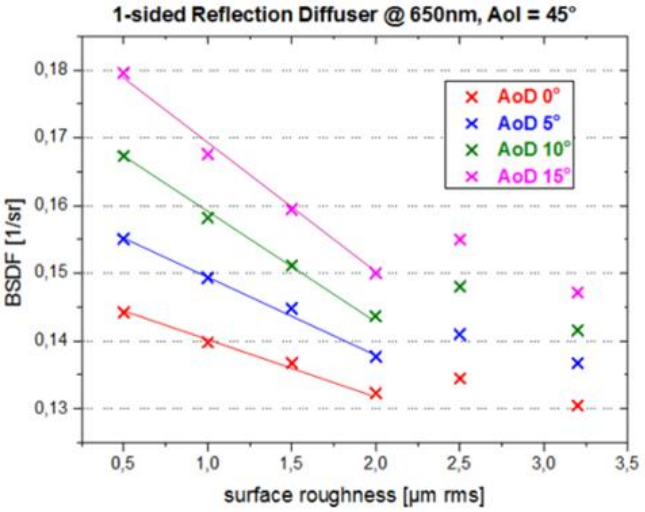

Figure 1. Example of systematic change of BSDF with surface roughness.

However, the dependency deviates from existing models, which predict a significant larger change in BSDF with varying surface roughness [2]. The cause is still to be investigated.

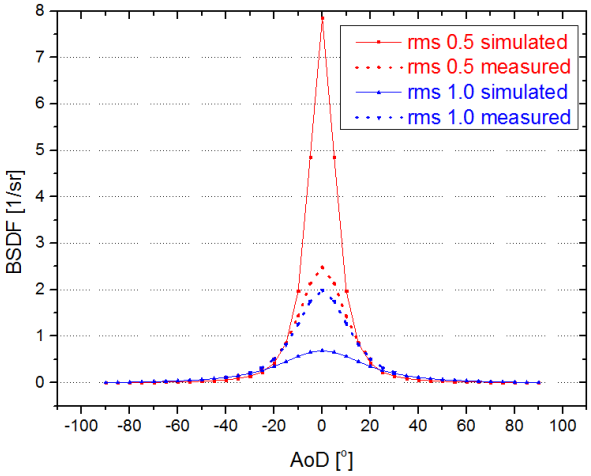

Figure 2. Comparison of simulated and measured BSDF values at different surface roughness.

A similar systematic pattern can be observed with speckle measurements. Figure 3 shows the correlation coefficients of different transmission diffusers with different surface properties. It shows expected faster de-correlation with higher surface roughness, a quantification of the effect is to be done.

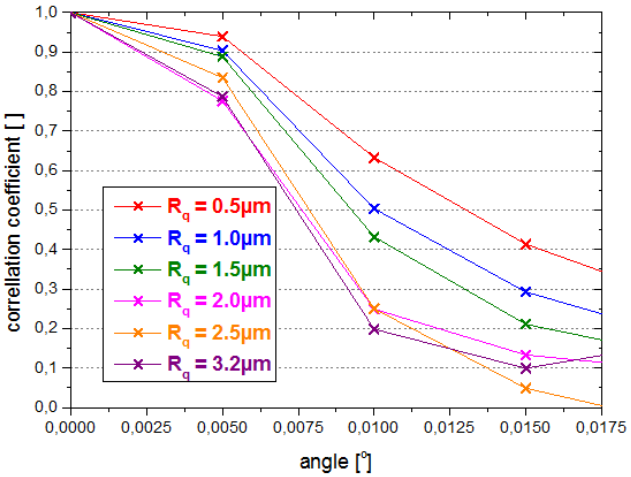

Figure 3. Example of de-correlation behaviour of diffusers with different surface properties.

REFERENCES

1. Hedser van Brug, Spectral Features due to on-board diffusers, Proc. SPIE 5882, Earth Observing Systems X, 588202, September 02, 2005.
2. L.G. Shirley, Laser Speckle from Thin and Cascaded Diffusers.
3. G. Bazalgette Courreges-Lacoste et al., Modeling of Spectralon diffusers for radiometric calibration in remote sensing, Optical Engineering, Vol. 42 No. 12, December 2003, 3600 – 3607.

3D hyperspectral target detection

Olli Nevalainen[1], Sanna Kaasalainen[1], Teemu Hakala [1], and Kati Anttila [1,2]

[1]*Finnish Geodetic Institute, Masala, Finland* [2]*Finnish Meteorological Institute, Helsinki, Finland*
Corresponding e-mail address: olli.nevalainen@fgi.fi

A prototype 8-channel full waveform active hyperspectral lidar (HSL) has been developed at the Finnish Geodetic Institute. This paper summarizes some of the new applications that demonstrate the potential of the instrument in hyperspectral 3D measurement.

THE INSTRUMENT

The hyperspectral lidar instrument (HSL) utilizes hyperspectral time-of-flight sensor and supercontinuum laser source which enables simultaneous 3D spatial and spectral measurements. Currently, the HSL measures with eight spectral channels between 500–1300 nm. More details on the instrument can be found in [1].

VEGETATION MAPPING

The new type of data has enabled completely new type of target identification processes, such as automatic tree species detection [2] or surveying the moisture condition, photosynthetic capacity, or physiological status of vegetation in a one-shot non-destructive measurement. The chlorophyll measurement was validated in the laboratory, and good correlation with the HSL measurement was found [3].

MINERALOGY

We have also carried out preliminary experiments to explore the potential of the instrument for distinguishing rock materials. A false colour RGB plot in Figure 1 demonstrates the separation of minerals in a rock sample.

SNOW COVER MONITORING

Detecting impurities in snow surfaces is important, because snow is a key factor in the Earth's climate system because of its high albedo [4]. The hyperspectral lidar is a promising tool for measuring the spatial distributions of impurities in the snowpack (Figure 2), because of the effect of these impurities in the spectral albedo of snow [5]. We have improved the instrument to include wavelength channels greater than 1000 nm to detect snow absorption lines, etc.

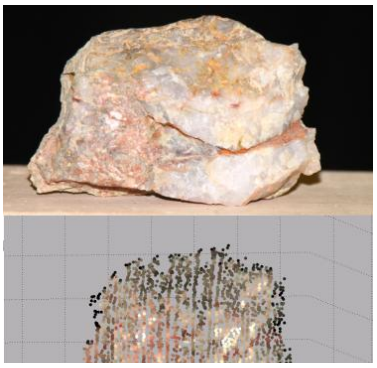

Figure 1. A hyperspectral point cloud (below) of a rock sample (above). Hyperspectral point cloud coloured using false colour RGB where R=2*691 nm, G= 2*554 nm and B=1,5*554 nm.

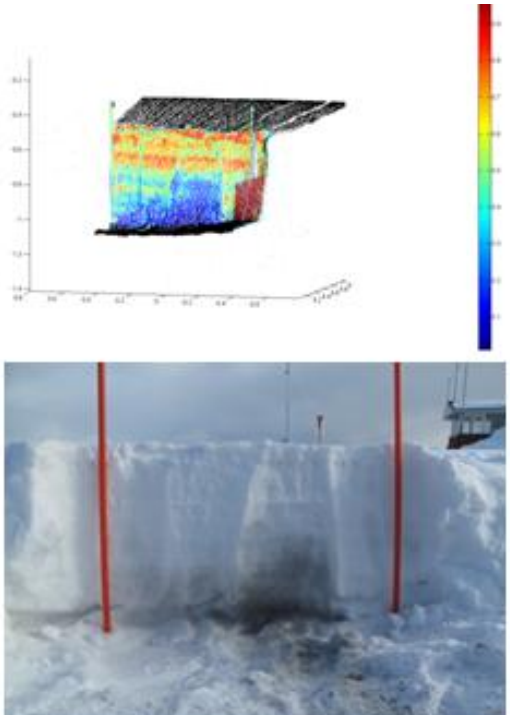

Figure 2. 3D distribution of exhaust gas in a snow surface (below) is visible in the hyperspectral point clouds of the target (above).

REFERENCES

1. T. Hakala, J. Suomalainen, S. Kaasalainen, Y. Chen. Full waveform hyperspectral LiDAR for terrestrial laser scanning. Optical Express 20, 7119–7127, 2012.
2. J.Vauhkonen, T. Hakala, J. Suomalainen, S. Kaasalainen, O. Nevalainen, M. Vastaranta, M.

Holopainen, and J. Hyyppä, Classification of Spruce and Pine Trees Using Active Hyperspectral LiDAR. IEEE Geoscience and Remote Sensing Letters, 10(5), 1138-1141, 2013.
3. O. Nevalainen, T. Hakala, J. Suomalainen, S. Kaasalainen, Nitrogen concentration estimation with hyperspectral LiDAR. ISPRS Annals of the Photogrammetry, Remote Sensing and Spatial Information Sciences Volume II-5/W2, ISPRS Workshop Laser Scanning 2013.
4. W. J. Wiscombe and S. G. Warren, A Model for the Spectral Albedo of Snow. I: Pure Snow, Journal of Atmospheric Sciences, 37, 2712-2733, 1981.
5. S. G. Warren and W. J. Wiscombe, A Model for the Spectral Albedo of Snow. II: Snow Containing Atmospheric Aerosols, Journal of Atmospheric Sciences, 37, 2734-2745, 1981.

Irradiance scale of long term UV measurements at Sodankylä and Jokioinen, Finland

Kaisa Lakkala[1], Tapani Koskela[2], and Petri Kärhä[3]

[1]Finnish Meteorological Institute, Arctic Resesarch Centre, Sodankylä, Finland, [2]Finnish Meteorological Institute, Jokioinen Observatory, Finland, [3]Aalto University, Espoo, Finland

Corresponding e-mail address: kaisa.lakkala@fmi.fi

The Finnish Meteorological Institute (FMI) measures spectral UV radiation with Brewer spectroradiometers since 1990. The long term irradiance scale is based on the scale provided by the national standards laboratory for optical quantities in Finland. 1-kW DXW lamps are used annually to transfer the irradiance scale to the working standard lamps at FMI. Each month, a calibration of the Brewer is performed at the optical laboratory of FMI to follow changes in the spectral responsivity of the spectroradiometer. Several lamps are used to distinguish the ageing of the lamp from a change in the instrument's responsivity. After careful analysis, taking into account lamp's ageing, the long term responsivity of the spectroradiometer can be calculated and used in processing the spectral UV time series.

INTRODUCTION

The Finnish Meteorological Institute (FMI) started to measure spectral UV radiation in 1990 and 1995 in Sodankylä and Jokioinen, respectively. In both places, a Brewer spectroradiometer with teflon diffuser was installed. In Sodankylä, a single monochromator Brewer is used with a spectral range of 290-325 nm. The step size is 0.5 nm and the bandwidth (FWHM) is 0.56 nm. In Jokioinen, a double monochromator Brewer measures from 286 nm up to 365 nm. The step size is 0.5 nm and the FWHM is 0.57 nm. The quality control and quality assurance procedures, as well as the data processing, are described in Lakkala et al. [1].

During the years, the instrument's spectral responsivity changes, and there is a need for regular calibrations in order to maintain the irradiance scale stable. Guidelines for the quality assurance and quality control [2,3] of spectral UV measurements include calibrations performed with several lamps on the measurement site in order to distinguish lamps' ageing from the drift of the spectral responsivity of the instrument.

MATERIAL AND METHODS

The spectral responsivity of a spectroradiometer is defined as

$$r(\lambda)=S_L(\lambda)/E_L(\lambda), \quad (1)$$

where $E_L(\lambda)$ is the spectral irradiance produced by the calibration source and $S_L(\lambda)$ is the signal of the spectroradiometer.

The spectral responsivities of the Brewer spectroradiometers of FMI are calculated using 1-kW DXW lamps. The irradiance scale is traceable to the national standards laboratory for optical quantities in Finland, MIKES / Aalto University [4]. The primary standard lamps of FMI are measured at Aalto each year, and the scale is transferred to the working standard lamps at FMI laboratories.

FMI's calibration laboratories were built in 1997 and 1998 at Jokioinen and Sodankylä, respectively. Since then, calibrations are performed each month. For the earlier years the calibration was re-calculated based on measurements made with 50W lamps to which the irradiance scale of MIKES was transferred retroactively from the 1-kW lamps.

At each calibration, three lamps are used. Those lamps are chosen from a set of five lamps so that each lamp is burned on a different basis. One lamp is burned only a couple of times during a year, one is used each time, and the others are operated between those two extremes. This allows us to identify the ageing of the lamps from the change in the responsivity of the spectroradiometer.

In Jokioinen, 50-W lamps are also measured between the laboratory calibrations with 1-kW lamps. They are measured at the operational site of the instrument, which is on the roof of the observatory. This allows following the stability of the instrument also between the calibrations.

RESULTS AND CONCLUSIONS

Each year, one year of calibration results is reprocessed afterwards, in order to correct for the

lamp drift and to exclude erroneous lamp measurements. The responsivity time series are interpolated, and running averages are calculated to get the spectral responsivities of the Brewers for each day. An example of the final responsivity time series is shown in Figure 1. Separate lamp measurements are also plotted in the figure during 2008-2011.

The spectral responsivity time series are used to calculate the spectral UV time series in Sodankylä and Jokioinen. Figure 2 shows the time series of the daily maximum UV indices in Sodankylä during 1990-2012. As part of the quality assurance, the UV irradiances are compared with independent measurements during international comparison campaigns or during the regular site audits of the European reference spectroradiometer from the World Calibration Centre (WCC-UV), Davos.

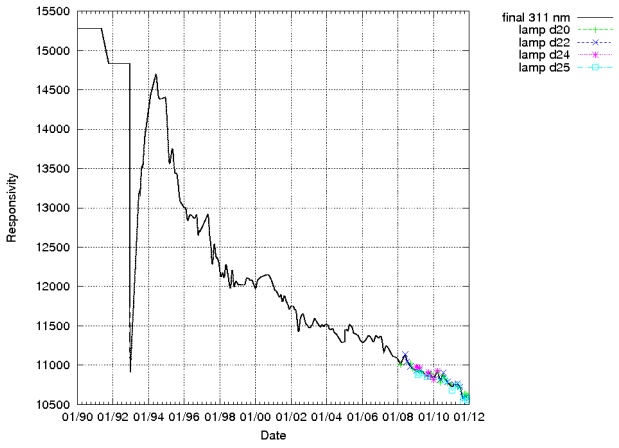

Figure 1. Final response time series at the wavelength of 311 nm during 1990-2011.

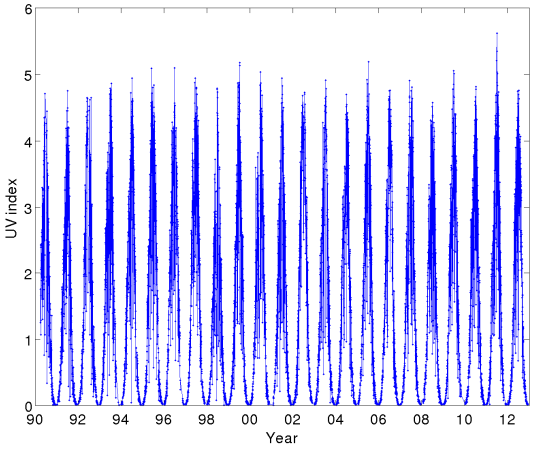

Figure 2. Final maximum UV index time series in Sodankylä, Finland, during 1990-2012.

REFERENCES

1. K. Lakkala, A. Arola, A. Heikkilä, J. Kaurola, T. Koskela, E. Kyrö, A. Lindfors, O. Meinander, A. Tanskanen, J. Gröbner and G. Hülsen, Quality assurance of the Brewer UV measurements in Finland, Atmos. Chem. Phys., 8, 3369-3383, 2008.
2. A. Webb, B. Gardiner, K., Leszczynski, V. Mohnen, P. Johnston, N. Harrison and D. Bigelow, Quality Assurance in Monitoring Solar Ultraviolet Radiation: The State of the Art, World Meteorological Organization (WMO), Global Atmosphere Watch report No. 146, 2003.
3. A. Webb, B. Gardiner, T. Martin, K. Leszcynski, J. Metzdorf and V. Mohnen, Guidelines for Site Quality Control of UV Monitoring, World Meteorological Organization (WMO), Global Atmosphere Watch report No. 126, 1998.
4. T. Kübarsepp, P. Kärhä, F. Manoocheri, S. Nevas, L. Ylianttila and E. Ikonen, Spectral irradiance measurements of tungsten lamps with filter radiometers in the spectral range 290 nm to 900 nm, Metrologia, 37, 305-312, 2000.

Stray light characterisation of a hyperspectral spectrometer for airborne remote sensing applications

Saulius Nevas[1], Stefan Nowy[1], Armin Sperling[1], Karim Lenhard[2], and Andreas Baumgartner[2]

[1] *Physikalisch-Technische Bundesanstalt (PTB), Braunschweig and Berlin, Germany,*

[2] *German Aerospace Center (DLR), Earth Observation Center (EOC), Remote Sensing Technology Institute (IMF), Oberpfaffenhofen, Germany*

Corresponding e-mail address: saulius.nevas@ptb.de

Stray light characterisation and correction of hyperspectral imagers are needed for their use in remote sensing applications. This presentation describes such a work carried out in collaboration between PTB and DLR. A hyperspectral instrument of DLR was characterised and corrected for the spectral-spatial stray light effects using the tuneable laser setup PLACOS at PTB.

INTRODUCTION

Hyperspectral sensors for airborne remote sensing of the Earth's surface have become a commercial commodity. As they are used for method development for spaceborne imagers, the same level of scrutiny needs to be applied to the calibration and characterization of the devices in both cases.

Large systematic errors caused by stray light have been reported for some hyperspectral instruments (ROSIS, SeaWIFS) [1, 2]. This information motivated an investigation of the stray light properties in flight geometry of a hyperspectral instrument operated by DLR in a way that would allow a subsequent correction of this effect in the measurement data [3, 4]. An instrument chosen for the studies was the HySpex VNIR-1600 of NEO [5], one of the two devices acquired for the development of physically-based inversion algorithms, atmospheric corrections, for calibration/validation activities as well as for the preparation of the EnMAP mission [6]. Furthermore, a quantification of the stray light properties is essential for an assessment of the measurement uncertainties.

In this contribution, measurements of the stray light characteristics of the instrument of DLR using the PLACOS facility at PTB [7] as well as a derivation of a correction tensor and the validation of the applied corrections will be discussed.

MATERIALS AND METHODS

The essential properties of the instrument with an expander lens that is normally used during airborne operations and approximately doubles the instrumental field-of-view (FOV) are listed in Table 1. Additional information about the sensor and other characterization results can be found in [8].

Table 1. Properties of the HySpex VNIR-1600 instrument with the FOV expander. The values for spectral bandwidth and the IFOVs are valid only at the center of the FOV and degrade toward the edges of the FOV.

	HySpex VNIR-1600
Detector technology	Si CCD
Spectral range	416 nm – 992 nm
Spectral sampling interval	3.6 nm
FOV	34.5°
IFOV (across track)	0.37 mrad
IFOV (along track)	0.5 mrad
Pixels	1600
Channels	160

To match the geometry requirements of the hyperspectral instrument during the stray light characterisation, a high quality mirror collimator with a focal length of 750 mm and a clear aperture of 100 mm was used. A 0.5 mm slit at the focal point of the collimator was irradiated by a fiber bundle (see Figure 1). The laser beam was coupled into the fiber using a micro-lens beam homogeniser. By turning the HySpex VNIR instrument and tuning the laser wavelength, any detector pixel within its FOV could be targeted (see Figure 2) yielding line spread functions (LSF) both in the spatial and the spectral domains (see Figures 3 and 4). The measurements were carried out at seven angular positions (spatial pixels) throughout the whole spectral range of the instrument. Based on the recorded LSFs, a tensor for the stray light correction was determined following the approach of [3, 4]. To cope with the large amounts of data, the 2D data of the hyperspectral sensor was interpolated and binned in the spatial domain reducing the dimensions of the data frames from 1600*160 to 16*160. Details on the necessary data processing steps and results of the validation measurements will be presented at the conference.

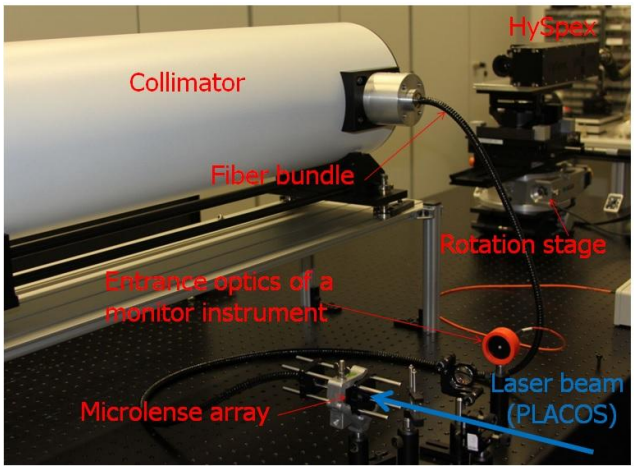

Figure 1. Arrangement of the instruments during the stray light characterisation of HySpex VNIR-1600.

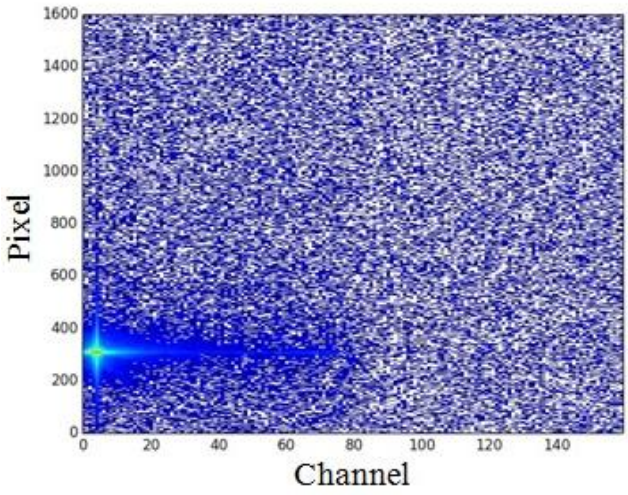

Figure 2. Dark value-corrected signal of the instrument; pixel No. 308 is irradiated at 430 nm.

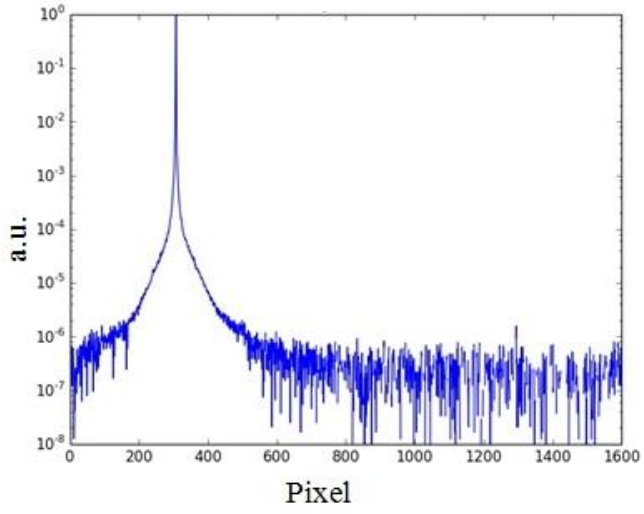

Figure 3. LSF of spectral channel No. 5 (430 nm) in the spatial domain.

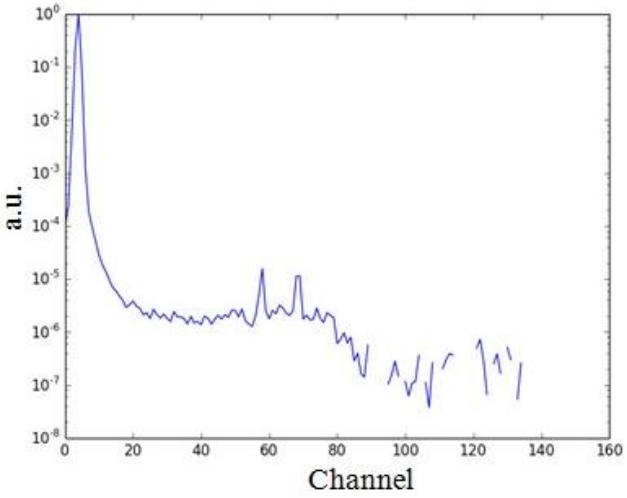

Figure 4. LSF of pixel 308 in the spectral domain.

ACKNOWLEDGEMENT

Part of this work has been supported by the European Metrology Research Programme (EMRP) within the joint research project Metrology for Earth Observation and Climate (MetEOC). The EMRP is jointly funded by the EMRP participating countries within EURAMET and the European Union.

REFERENCES

1. G. Acker, B. Hooker, R. Firestone, A. Barnes, W. Holmes, and E. Esaias, Stray Light in the SeaWiFS Radiometer, Memorandum SeaWiFS Volume 31. Nasa Technical Memorandum, 1995.
2. K. Lenhard, P. Gege, and M. Damm, Implementation of algorithmic correction of stray light in a pushbroom hyperspectral sensor, in Proceedings of 6th EARSeL Workshop on Imaging Spectroscopy, Tel Aviv, 2009.
3. Y. Zong, S. W. Brown, B. C. Johnson, K. R. Lykke, and Y. Ohno. Simple spectral stray light correction method for array spectroradiometers, Appl. Opt., 45, 1111–1119, 2006.
4. M. E. Feinholz, S. J. Flora, S. W. Brown, Y. Zong, K. R. Lykke, M. A. Yarbrough, B. C. Johnson, and D. K. Clark. Stray light correction algorithm for multichannel hyperspectral spectrographs, Appl. Opt., 51, 3631-3641, 2012.
5. Norsk Elektro Optikk. NEO HySpex website. http://www.hyspex.no/, Dec. 2013.
6. H. Kaufmann, K. Segl, S. Chabrillat, S. Hofer, T. Stuffler, and A. Mueller. EnMAP, A hyperspectral sensor for environmental mapping and analysis, in Proceedings of IGARSS, Denver, CO, USA, 2006.
7. S. Nevas, M. Lindemann, A. Sperling, A. Teuber, R. Maass, Colorimetry of LEDs with array spectroradiometers, MAPAN - Journal of Metrology Society of India, 24, 153-162, 2009.
8. K. Lenhard, A. Baumgartner, and T. Schwarzmaier, Independent laboratory characterization of NEO HySpex Imaging Spectrometers VNIR-1600 and SWIR-320M-E, *submitted to* IEEE TGRS, 2014.

Correction of gray-level- and integration time-related nonlinearities in a commercial field spectroradiometer

Javier Pacheco-Labrador[1], Alejandro Ferrero[2], and M. Pilar Martín[1]

[1] *Environ. Remote Sensing & Spectrosc. Lab. (SpecLab), Nat. Spanish Res. Council, Madrid, Spain,*
[2] *Instituto de Óptica, Consejo Superior de Investigaciones Científicas (CSIC), Spain.*
Corresponding e-mail address: javier.pacheco@cchs.csic.es

Commercial field spectroradiometers, commonly used in the study of earth surface properties, are typically assumed to have linear photoresponse or are corrected for non-linearity effects but only with those related with the measured gray level. However, their linearity can also be affected by the photoelectrons produced by the radiant flux on the sensor during the readout phase if they are added, in some extent, to the photoelectrons produced during the integration time. This causes a non-linearity effect which is more important the more comparable the integration and the readout times are. In this work, we propose a methodology to characterize and correct the two abovementioned types of non-linearity effects in spectroradiometers.

INTRODUCTION

Field spectroradiometers are commonly used to retrieve information about earth surface properties. However to assure data quality and comparability several instrumental issues, such as the non-linearity of detectors, need to be assessed. Most of the commercially available field spectroradiometers are reported to have a linear response, or apply a previously characterized correction function which exclusively depends on the gray level measured ($\Re_{GL}$), expressed in counts. However, this correction might be incomplete, since a photodiode sensor photoresponse is subject to other types of non-linearity [1].

We propose a new methodology to characterize and correct the non-linearity of spectroradiometers that depends on both, the gray level and also the integration time. The proposed method can be easily implemented since requires the same experimental setup than other generalized methods that characterize only $\Re_{GL}$ [2]: it is sampling radiance with different integration times from a constant radiation source.

METHOD

In this work we characterize and correct the non-linearity of a Unispec DC (SN 2038), a commercial dual channel field spectroradiometer (PP Systems, Amesbury, MA, USA). The non-linearity characterization experiment was carried out in the Environmental Remote Sensing and Spectroscopy Laboratory (SpecLab-CSIC) by acquiring radiance measurements at different integration times (t_{int}) from a homogeneous stabilized light source.

It was found that the relation between the measured non-linear and the corrected linear instrumental radiances (L^*_{meas} and L^*_{cor}) can be written as:

$$L_{cor}^* = L_{meas}^* / [\Re_{GL}(N_{meas,i})\,\Re_{IT}(t_{int})] - L_0^* \qquad (1)$$

where $\Re_{GL}(N_{meas,i})$ is the non-linearity correction factor exclusively dependent on $N_{meas,i}$ (gray level in counts); equivalently, $\Re_{IT}(t_{int})$ is the non-linearity correction factor exclusively dependent on t_{int}; and, finally, L_0^* is the instrumental radiance in dark conditions. $\Re_{IT}$ was defined as a hyperbolic function [1], whereas we used a polynomial to fit $\Re_{GL}$ [2-3]. To characterize $\Re_{IT}$, two parameters were fit for each pixel: *A*, which would represent the L^*_{meas} that the measurements should ideally show; and *B*, which is related to the readout time and the leakage and would represent the dependence of $\Re_{IT}$ on t_{int}:

$$L_{meas}^* = A \cdot (1 + B/t_{int}) \qquad (2)$$

RESULTS

Spectra acquired for the non-linearity characterization covered the radiometric range of the spectroradiometer. Maximum values were located in the pixels 126 and 128 in channel 1 and 2, respectively; these were very low (>4000 DN) for integration times lower than 38 ms. The signal decreased towards the extremes of the sensor up to almost dark signal levels.

Non-linearity characterization was done simultaneously adjusting $\Re_{GL}$ and $\Re_{IT}$. 5th and 7th

degree polynomials were used to $\Re_{GL}$ in channel 1 and 2, with RMSE of 0.0024 and 0.0023 respectively.

Unexpectedly, parameter B in Eq. 2 showed not being independent of the pixel position, which may be due to the different amount of radiant flux impinging on every pixel. We found that B was largely related with the gray level-corrected instrumental radiance; thus B was modeled as a function of this variable using all the pixels of the sensor together, except those with high noise corresponding to the lowest irradiances.

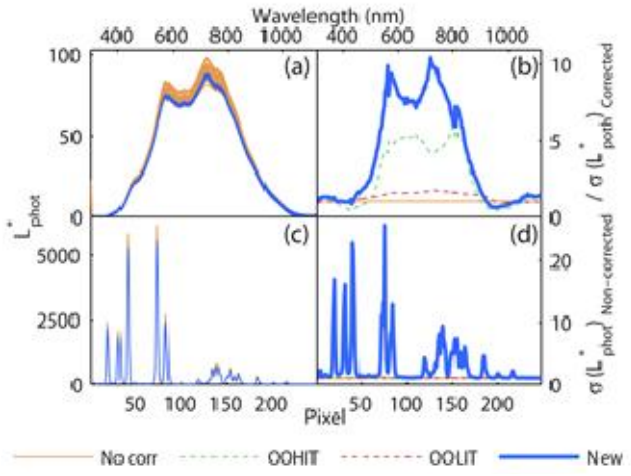

Figure 1. Non-linearity correction for the calibration and the validation datasets in channel 2.

Fig. 1 shows L^*_{phot} for different t_{int} and its standard deviation before and after applying the non-linearity correction with different methods. In the case of Figs. 1a and 1b, these are the same data used in the calibration; Figs. 1c and 1d show the spectra acquired from a mercury-argon lamp, at three integration times close to the sensor's readout time. Figs. 1a and 1c show the L^*_{phot} with and without the linearity correction. Figs. 1b and 1d show the ratio between the non-corrected and the corrected standard deviation of these L^*_{phot}, which is an index of the improvement produced by the two corrections methods compared: the one proposed here, and a commonly used method that only applies $\Re_{GL}$ functions [2-3]. In this case, we used two different functions which were characterized using spectra acquired with and without low integration times (OOLIT and OOHIT respectively in Fig. 1). As can be seen, the proposed method achieves a significant reduction of the L^*_{phot} variation for different integration times. The comparison with the models that only characterize $\Re_{GL}$ shows that this method achieves a better correction of non-linearities, both using the calibration dataset (Fig. 1b) and also with independent data (Fig. 1d). The standard deviation of L^*_{phot} was reduced, at maximum, 10.43 and 25.84 times (Fig. 1b and 1d, respectively) using the proposed method; whereas reduction of only 6.31, and 1.29, respectively, for OOHIT and 1.76, and 1.23 in the case of OOLIT were reached.

CONCLUSIONS

We report the existence of a type of non-linearity related with the integration time that can affect field spectroradiometers and propose a method to characterize and correct this effect in combination with others. This non-linearity was first detected in cameras, but correction was not possible [1]. To the best of the authors' knowledge this effect has been overlooked up to now in spectroradiometers, and can affect the characterization of other artifacts, such as the non-linearity related with the gray level. This stresses the need of matching the radiance levels used in the characterization of field spectroradiometers with those later found outdoors in order to achieve reliable field measurements. The non-linearity related with the integration time should be considered in the instrumentation design and characterization. The proposed method could not be applicable neither to every spectroradiometer nor to all radiation sensors, since pixels must be separately read out; however, in those cases the use of integration times close to the readout times could be avoided.

REFERENCES

1. A. Ferrero, J. Campos and A. Pons, "Apparent violation of the radiant exposure reciprocity law in interline CCDs," Applied Optics, 45(17), 3991-3997, 2006.
2. Ocean Optics, 2012. OOINLCorrect Loading Non-Linearity Correction Coefficients Instructions, URL: http://www.oceanoptics.com/technical/OOINLCorrect%20Linearity%20Coeff%20Proc.pdf, Ocean Optics Inc, Dunedin, Florida, USA (last date accessed: Dic, 2013).
3. J. Pacheco-Labrador and M.P. Martín, "Nonlinear Response in a Field Portable Spectroradiometer: Characterization and Effects on Output Reflectance," Geoscience and Remote Sensing, IEEE Transactions on, 52(2), 920-928, 2014.

Upcoming Space Experiments for Developing Space-Borne Low-Temperature Fixed-Point Blackbody

A. Burdakin[1], B. Khlevnoy[1], V. Krutikov[1], A. Panfilov[1], A. Puzanov[1], M. Samoylov[1], V. Sapritsky[1], E. Us[1]
A. Lysak[2], and M. Kudashkina[3]

[1] *All-Russian Institute for Opto-Physical Measurements (VNIIOFI), Moscow, Russia,*
[2] *TSNIIMASH, Korolev, Russia,* [3] *RSC "Energia", Korolev, Russia*
Corresponding e-mail address: burdakin-m4@vniiofi.ru

Two upcoming space experiments paving the way to development of the high-stable onboard low-temperature fixed-point blackbody are presented. One, space experiment "KALIBR" with onboard gallium fixed-point BB prototype tailored for on-orbit testing in an independent mode. Second, space experiment "REPER-KALIBR" aimed at in-depth study of melt/freeze phase transition of the eutectic alloys in zero-gravity environment.

UPCOMING SPACE EXPERIMENT "KALIBR"

Data acquisition on Sea surface temperature measured by space-borne infrared radiometric instruments within the temperature range ~ (280 ÷ 300) K is known to be of great importance for reliable climate change monitoring. The problem of delivering trustworthy long-term data on SST can be solved via the in-flight verification of pre-flight calibration characteristics of IR satellite instruments against perspective onboard low-temperature standard blackbodies of exceptionally high stability. In order to arrive at a space-borne calibration source possessing required long-term stability it is reasonable to suggest the integration of the phase transition phenomenon into traditional blackbody structure [1, 2].

The behaviour of phase-change materials (working substances) and operational characteristics of the onboard blackbody based upon phase transition may alter in zero-gravity environment. Thus, space experiments under the orbital conditions have become necessary.

The prototype of the novel high-stable space-borne radiation source - the gallium fixed-point blackbody with operational temperature ~ 302.9 K - has been manufactured for space experiment "KALIBR" in an independent mode on board the "Foton-M4" spacecraft. The space-borne fixed-point BB test model "KALIBR" (Fig. 1) is designed for operation in air, in conformity with environmental conditions onboard hermetically sealed spacecrafts of the "Foton" series (meant for research activities). This space experiment implies only contact temperature measurements (with PRT) of the blackbody's cavity radiating surface.

Figure 1. The gallium onboard fixed-point BB prototype "KALIBR" tailored for space experiment.

An opening of the BB (with no window) is 14 mm in diameter, an aperture size is 10 mm, cavity depth is 68 mm. The layer of working substance (Ga) surrounding the blackbody's cavity is 6 mm, the total mass of gallium is about 270 g. The Teflon cell with Ga is at atmospheric pressure, and properly sealed to avoid any leakage of melted gallium.

The cell is heated up/cooled down by means of thermoelectric modules; heat sinks are blown by air fan. Electrical power required to melt/freeze the gallium in a cell is about 50 Wt; duration of the melting (calibrating) plateaus is 1-2 hours.

Preliminary ground tests of the gallium fixed-point blackbody prototype have been quite satisfactory in terms of the grade of temperature stabilization within the cavity during the gallium melt phase transition [3]. Now the fixed-point BB prototype "KALIBR" is fully ready for space experiment; the launch of the "Foton-M4" spacecraft is expected in 2014.

UPCOMING SPACE EXPERIMENT "REPER-KALIBR"

Operational temperature of the gallium fixed-point BB is quite suitable in terms of calibration of the space-based instruments measuring radiance temperature of objects within the thermal infrared waveband. However, selection of some more proper working substances in addition to Ga can make a range of operational temperatures of the prospective onboard fixed-point blackbodies wider, and calibration - more accurate. Except Ga, the eutectic alloys on the basis of gallium also have the melt/freeze temperatures within the specified temperature range (Table 1). In compliance with the stated purpose of applying in the future on board the spacecrafts, the gallium and bimetallic eutectic alloys Ga-In, Ga-Sn, and Ga-Zn were studied earlier in small cells and showed rather high, in that context, characteristics as the melting fixed-point references [4].

The melting fixed points based upon the phase transition of the eutectic alloys are known to have obvious differences to the fixed points based on single-component substances. In short, they are more sensitive to external influences, both controlled and uncontrolled, including influence of gravitational force. The melting plateau shape and thus, the measured melting temperature (experimental value of the fixed point) may alter due to modification of the alloy structure in the course of crystallization under zero-gravity conditions.

The mechanism of heat-and-mass transfer through the liquid phase in a process of the eutectic phase transition undergoes significant changes in zero-gravity environment as well. This mechanism for the most part determines kinetics of the melt/freeze transition, and consequently also affects the melting plateau shape. All in all, space experiment aimed at studying the melt/freeze transition under zero-gravity conditions is of special importance in the case of eutectic alloys.

Currently such a space experiment "REPER-KALIBR" is being prepared for staging on board the ISS, in hermetic module. Related equipment is being developed for working in air, in the manual mode. The thermal chamber containing small-size Teflon cell with the investigated phase-change materials (weighing ~ 45 g) is heated/cooled by thermoelectric modules; heat sinks are blown by air fan. Electrical power required to melt/freeze the substances in a cell is about 15 Wt; duration of the melting plateaus is 1-1.5 h.

Table 1. Phase-change materials intended for space experiment "REPER-KALIBR".

Substance	Approximate melting temperature
Ga-In	288.8 K (15.7 °C)
Ga-Sn	293.6 K (20.5 °C)
Ga-Zn	298.3 K (25.2 °C)
Ga	302.9 K (29.76 °C)

CONCLUSION

The design of a novel high-stable space-borne BB presented here - with a cavity surrounded by phase-change material - may be arbitrarily called a "true" fixed-point blackbody in contrast to a variable temperature blackbody complemented by SI-traceable thermometry [2]. The "true" fixed-point blackbody has the important advantage of the method to guarantee the calibration source stability: the blackbody setpoint is fixed *directly* to immutable phase transition temperature of the working substance. So, the primary goal of space experiment "KALIBR" is to make sure that the gallium melting plateau - the blackbody setpoint - remains within the permissible limits under zero-gravity conditions.

Space experiment "REPER-KALIBR" is aimed at more thorough investigation of the impact of zero-gravity environment on the eutectic phase transition by example of gallium eutectics via data comparison for experiments under the ground and orbital conditions. If successful, it will pave the way to the development of a set of high-stable onboard low-temperature fixed-point blackbodies. Then, a variety of operational temperatures needed for more accurate calibration will be achieved with the use of different eutectic alloys as fixed-point BB's working substances.

REFERENCES

1. V. Krutikov, et al., The Global Earth Observation System of Systems (GEOSS) and Metrological Support for Measuring Radiometric Properties of Objects of Observations, Metrologia, 43, 94-97, 2006.
2. P. Gero, et al., A Blackbody Design for SI-Traceable Radiometry for Earth Observation, J. Atm. and Oceanic Tech., 25, 2046-2054, 2008.
3. V. Sapritsky, et al., Current activity of Russia in measurement assurance of Earth optical observations, Metrologia, 49, 9-16, 2012.
4. A. Burdakin et al., Melting points of gallium and of binary eutectics with gallium realized in small cells, Metrologia, 45, 75-82, 2008.

Calibration and Characterization of Remote Sensing Equipment

Ilmar Ansko[1], Riho Vendt[1], Joel Kuusk[1], Anu Reinart[1], and Madis Lepist[2]

[1]Tartu Observatory, Tõravere, Estonia, [2]Hohenheide OÜ, Põlvamaa, Estonia
Corresponding e-mail address: riho.vendt@to.ee

Earth observation methods usually involve measurements obtained by remote sensing radiometers. However, it is recognized, that calibration and characterization of remote sensing instrumentation is required for reliable interpretation of measurement data. For that purpose, a set of new facilities and methods is established at the Tartu Observatory in Tõravere, Estonia.

INTRODUCTION

In recent years continuously increasing attention is paid to monitoring and understanding the processes of the environment and climate on Earth. Climate studies rely largely on data collected by the methods of remote sensing. The quality of the methods is increased by comparison of the satellite products with in situ reference measurements. [1] However, the measurement capability has been still identified as one of the limiting factors in interpretation of this data. In order to obtain reliable and comparable measurements results, the instrumentation used for remote sensing has to be characterized and calibrated. For that purpose, new facilities dedicated to investigation of optical sensors used in remote sensing are established at the Tartu Observatory in Tõravere, Estonia.

ESTABLISHMENT AND APPLICATION OF THE RADIOMETRIC SCALE

In co-operation with Tarty Observatory and Hohenheide OÜ, two new filter radiometers have been developed allowing establishing the absolute radiometric scale for spectral irradiance and related quantities: spectral radiance, corresponding photometric quantities and optical power. The filter radiometers consist of a precise aperture, temperature stabilized bandpass filters, and three-element optical trap detector, all of which have been thoroughly tested and characterized. Relying on a few controllable parameters, the trap-based filter radiometers act as absolute irradiance detectors [2]. The radiometer for the wavelength region of (340…950) nm is based on three Si photodiodes, and the second one for the region of (950…1550) nm is based on three InGaAs photodiodes. The calibration wavelengths are defined by 16 narrow-band filters.

CHARACTERIZATION OF RADIOMETRIC SENSORS

In remote sensing applications, the absolute radiometric calibration of irradiance and radiance sensors are of the primary interest whereas additional characterization, e.g. stray-light and environmental properties, become more and more relevant. This kind of additional measurements are often needed to understand the behaviour of the remote sensing instruments and evaluate the calibration uncertainties. These measurements include: angular responsivity, spectral responsivity, out-of-band and stray light characterization, and temperature coefficients.

The calibration and characterization capabilities at the Tartu Observatory are listed in Table 1.

Table 1. List of calibration and characterization capabilities for radiometric sensors at Tartu Observatory.

Quantity, property, range	**Estimated exp. uncertainty**
Spectral responsivity, irradiance	
(340...950) nm; 100 nW/(m^2 nm)...500 mW/(m^2 nm)	1%...3%
(950...1500) nm; 5 µW/(m^2 nm)…500 mW/(m^2 nm)	3%...5%
Spectral responsivity, radiance	
(340...950) nm; 50 nW/(m^2 sr nm)...100 mW/(m^2 sr nm)	1%...3%
(950...1500) nm; 2 µW/(m^2 sr nm)…100 mW/(m^2 sr nm)	3%...5%
Spectral sensitivity, irradiance	
(250...1500) nm; >0.01 A/W; Bandwith < 10 nm	3%...5%
Angular responsivity, 0°...85°	1%
Uniformity of the flat-field view, <50 W/(m^2 sr)	0.5%...5%
Inherent stray light, 10^{-6}; (250...2500) nm	1%...10%

CONCLUSION

A set of dedicated calibration and characterization methods for remote sensing radiometers has been developed in order to increase the metrological credibility of Earth observations.

REFERENCES

1. G. Zibordi, K. Ruddick, I. Ansko, G. Moore, S. Kratzer, J. Icely, A. Reinart, In situ determination of the remote sensing reflectance: an intercomparison, Ocean Sci. Discuss. 9, 787-833, 2012.
2. T. Kübarsepp, P. Kärhä, F. Manoocheri, S. Nevas, L. Ylianttila, E., Ikonen, Spectral irradiance measurements of tungsten lamps with filter radiometers in the spectral range 290 nm to 900 nm, Metrologia, 37(4), 305-312, 2000.

Estimating the Uncertainty of Effective Radiance

Valeriy Gavrilov, Boris Khlevnoy, Alexander Panfilov, and Maxim Solodilov
All-Russian Research Institute for Optical and Physical Measurements (VNIIOFI), Moscow, Russia
Corresponding e-mail address: gavrilov@vniiofi.ru

The method for estimating uncertainty of the effective radiance during the Earth observation instrument calibration by use of standard source is proposed.

INTRODUCTION

Absolute radiometric calibration of the Earth observation instruments is accomplished by observing the instrument output in response to a standard source with known spectral radiance [1]. The measurement equation

$$r = R_L \cdot L_e \tag{1}$$

written for the broadband radiometer comprises the output signal r, absolute radiance responsivity R_L and effective radiance

$$L_e = \int_{\Lambda} L(\lambda) \cdot R(\lambda) \cdot d\lambda \tag{2}$$

Here $L(\lambda)$ is the spectral radiance of a standard source, $R(\lambda)$ stands for the relative spectral responsivity of the instrument and Λ is its spectral band.

Radiometric calibration implies determining the both $R(\lambda)$ and R_L [2]. To analyse the calibration uncertainty it is necessary to estimate the uncertainty associated with the effective radiance (2). Here we suggest a method for such estimating.

METHOD OF ESTIMATING

Suppose the spectral distributions $L(\lambda)$ and $R(\lambda)$ are measured at the wavelengths $\lambda_1,\ldots,\lambda_N$ in the interval $\Lambda=[\lambda_1,\lambda_N]$. We denote by L_i and R_i the estimated values of $L(\lambda_i)$ and $R(\lambda_i)$, respectively. Estimation of the effective radiance (2) may be approximately expressed by the linear quadrature rule:

$$L_e^{estim} = \sum_{i=1}^{N} w_i \, L_i \, R_i \tag{3}$$

with the weights w_i depending on the points λ_i. For simplicity we assume an uniform spacing of the points $h=(\lambda_N-\lambda_1)/(N-1)$. For instance, the trapezoidal rule implies: $w_2=\ldots=w_{N-1}=h$, $w_1=w_N=h/2$. Further we suppose that the expression (3) provides the estimated value of the integral (2) accurately enough.

Representation of the integral (2) in the form of sum by the linear quadrature rule allows to obtain the following estimation for the relative combined standard uncertainty

$$u_c^2(L_e) = \left(L_e^{estim}\right)^{-2} \cdot \sum_{k=1}^{N} w_k^2 \, L_k^2 \, R_k^2 \, \left\{u_c^2(L_k) + u_c^2(R_k)\right\} + \sum_{i \neq j} w_i w_j \left\{L_i \, L_j \, u(R_i, R_j) + R_i \, R_j \, u(L_i, L_j)\right\} \tag{4}$$

Here $u_c(L_i)$,and $u_c(R_i)$ are relative combined standard uncertainties and $u(L_i,L_j)$ $u(R_i,R_j)$ are the estimated covariances.

EXAMPLE OF APPLICATION

Here we apply the received formula (4) for the panchromatic remote-sensing instrument RDSA created by the JSC «Krasnogorsky Zavod». The results of measuring the instrument relative spectral responsivity for one particular panchromatic band are presented in Table 1.

Table 1. Relative spectral responsivity of the RDSA instrument and the corresponding relative standards uncertainties.

λ_k, nm	R_k	$u_A(R_k)$, %	$u_B(R_k)$, %	$u_c(R_k)$, %
510	0.02	9.88	0.34	9.89
520	0.05	4.34	0.34	4.36
530	0.58	0.76	0.34	0.83
540	0.79	0.47	0.34	0.58
550	0.94	0.35	0.34	0.49
560	0.98	0.31	0.35	0.47
570	0.77	0.42	0.36	0.55
580	0.89	0.33	0.37	0.49
590	0.17	1.66	0.35	1.70
600	0.01	8.83	0.34	8.84

As a standard source we consider the large aperture integrating sphere from VNIIOFI's standard radiometric facility [3]. The results of measuring the integrating sphere spectral radiance are summarised in Table 2.

The covariances in the formula (4) are evaluated as follows

$$u(L_i, L_j) = u_B(L_i) \; u_B(L_j) \; r_{ij}(L) \tag{5}$$

$$u(R_i, R_j) = u_B(R_i) \; u_B(R_j) \; r_{ij}(R) \tag{6}$$

where $r_{ij}(L)$ and $r_{ij}(R)$ are estimated correlation coefficients of systematic effect in measurements of the pairs $L(\lambda_i)$ and $L(\lambda_j)$, and $R(\lambda_i)$ and $R(\lambda_j)$, respectively. Type B uncertainties are shown in Table 1 and Table 2.

Table 2. Example of a table: page setting for the extended abstract.

λ_k, nm	L_k^{rel}	$u_A(L_k)$, %	$u_B(L_k)$, %	$u_c(L_k)$, %
510	0.54	0.30	0.64	0.71
520	0.59	0.29	0.63	0.69
530	0.65	0.28	0.62	0.68
540	0.71	0.27	0.61	0.66
550	0.76	0.26	0.60	0.65
560	0.81	0.24	0.59	0.64
570	0.86	0.23	0.58	0.62
580	0.91	0.22	0.56	0.61
590	0.96	0.21	0.55	0.59
600	1.00	0.20	0.54	0.58

The result of estimating is presented in Table 3 for the following two cases: zero correlation $r_{ij}(L)=r_{ij}(R)=0$ and strong positive correlation $r_{ij}(L)=r_{ij}(R)=0.99$.

Table 3. Relative combined standard uncertainty of the effective radiance for zero and strong positive correlation.

	Zero correlation	Strong positive correlation
$u_c(L_e)$, %	0.34	0.71

REFERENCES

1. C.L. Wyatt, V. Privalsky, R. Datla, Recommended Practice: Symbols, Terms, Units and Uncertainty Analysis for Radiometric Sensor Calibration, NIST Handbook 152, 1998.
2. V.R. Gavrilov, B.B. Khlevnoy, A.S. Panfilov, and M.V. Solodilov, Estimation of the uncertainty of the radiometric calibration of optical apparatus using an integrating sphere, Measurement Techniques, 56, No. 7, 783-790, 2013.
3. V.I. Sapritsky et al, Current activity of Russia in measurement assurance of Earth optical observation, Metrologia, 49, S9–S16, 2012.

SI traceable validation of Radiative Transfer codes

Agnieszka Bialek[1], Claire Greenwell[1], Priit Jaanson[2,4], Christopher Chunnilall[1], Nigel Fox[1], Mathias Gergely[3], and Jean-Luc Widlowski[3]

[1]NPL, Teddington, UK, [2] Centre for Metrology and Accreditation (MIKES), Espoo, Finland, European Commission DG Joint Research Centre, Ispra, Italy, [4]Aalto University, Espoo, Finland

Corresponding e-mail address: agnieszka.bialek@npl.co.uk

SI traceability is central to modern science and technology; moreover, it ensures the quality assurance of experimental data. Considerable effort is put into Earth Observation (EO) data quality assurance, which is achieved by continuous calibration and validation. Currently, there is a lack of SI traceable reference standards for radiative transfer (RT) models, which are essential to numerous EO products. We present an approach to RT model validation that uses a set of artefacts whose topographic and optical properties have been characterised by traceable measurements. The data obtained will be input into 3D Monte Carlo codes used for modelling RT in order to test their accuracy.

INTRODUCTION

State-of-the-art RT models simulate complicated solar radiation interactions with different objects, including natural environments such as the atmosphere, soil and vegetation canopies. In the context of canopy RT models validation activities have consisted primarily of ad hoc comparison with approximate in situ data. Systematic canopy RT model evaluations under perfectly controlled experimental conditions have been addressed by the RAdiation transfer Model Intercomparison (RAMI) effort [1,2]. This effort has identified a set of credible Monte Carlo ray-tracing models and development of a reference dataset that is now embedded in the RAMI Online Model Checker [3], which allows for model evaluation in quasi real-time.

As a first step towards SI traceability of the RT models we propose a comparison using man-made targets, topographically and optically characterised under laboratory conditions.

Three circular targets have been manufactured, each 22 cm in diameter. The first is made from aluminium, with a sanded surface. The second is also made from aluminium, but its top surface is mechanically grooved so that a matrix of 1168 cubes, each of edge length approximately 3 mm, is formed. This second target has a similar design and is made of the same material, as the one described in [4]. The third target consists of a circular baseplate and 88 cubes with a 12 mm edge length. All the components are made of standard 7075 aluminium, sanded and anodized with green pigments, measured individually, and assembled.

The intention was to measure the gonioreflectance of the targets, and compare these measurements with those predicted by the RT codes, which would use the topographic data, and the gonioreflectometric properties of the constituent surfaces, as input data.

MEASUREMENTS

The targets were measured mechanically and optically on the micro scale at MIKES. Details of these measurements are presented in [5]. Mechanical characterisation consisted of surface roughness measurements and coordinate measurements of the geometry of the targets. The radiance factors in the plane of incidence for the 12-mm green-anodised cubes were measured. Measurements were made on all 88 cubes on all five visible cube surfaces at 0°, 30º and 60° illumination angles, and 14 different viewing angles in the range -60° to 80°.

NPL performed a set of optical measurements on the macro scale using a multi-axis gonioreflectance facility (Fig. 1). The path swept out by the detector (-80° to 180°) defines the reference horizontal plane, and the incident beam is set parallel to this plane. The default position for the sample is to be vertical. The sample can then be rotated: (a) -90° to 90° about the axis co-linear with the axis of rotation of the detector, thus changing the illumination zenith angle (IZA); (b) 0° to 90° about an axis parallel to the horizontal plane, thus enabling out-of-plane measurements and changing the relative azimuth angles (RAAs); (c) -180° to 180° about the

axis defined by the normal to the sample surface, which changes illumination and reflection azimuth angles, and enables the full range of out-of-plane measurement geometries .

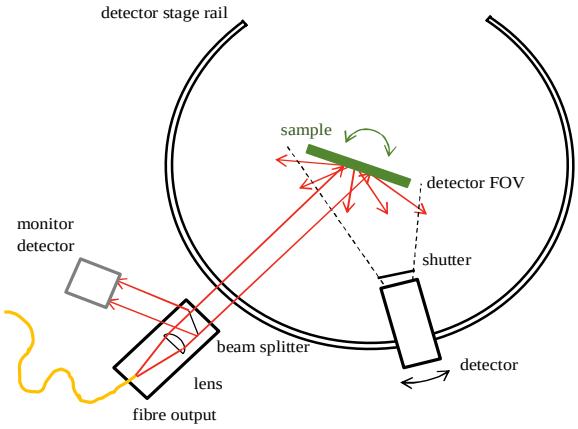

Figure 1. Current NPL BRDF measurement set-up (plan view).

The facility has been adapted to accommodate a target with a 22 cm diameter, and a detector with a large field of view (FOV) to capture the total radiant flux reflected from the sample surface. As a source of radiant flux, a 4.5 mW diode laser at 532 nm was used, coupled into a single mode fibre to obtain a well-shaped Gaussian beam. The output from the fibre was collimated, using different lenses, to give spot sizes on the target of 4 mm and 12 mm diameter. Measurement of the incident beam was done by translating the target out of the beam and rotating the detector to intercept the incident beam.

An initial set of tests was performed on a green anodized base-plate (a blank target without any assembled cubes). It was originally envisaged that the scattering properties of the baseplate would be spatially uniform over the area of the sample. However, tests demonstrated significant spatial non-uniformity in the scattered signal from the target, and the measurement approach has been adapted to provide the RT models with data which accommodates the non-homogeneity of the reference targets. The system at NPL is currently being modified to perform measurements with the illuminating beam shape as close as possible to top-hat rather than Gaussian, and varying the beam diameter from 50 mm down to 20.4 mm in order to spatially average a greater area of the target area.

RESULTS

Figure 2 presents an example of the results of the initial physical tests that were performed at NPL using a collimated laser beam of 12 mm. This is a BRDF profile of the green anodized base-plate for an Illumination Zenith Angle (IZA) of 0º. Results such as these will be used to determine the quality of current 3D Monte Carlo RT model formulations, and the suitability of current laboratory measurements of the structural, spectro-directional and illumination related characteristics for validation experiments in support of SI traceability.

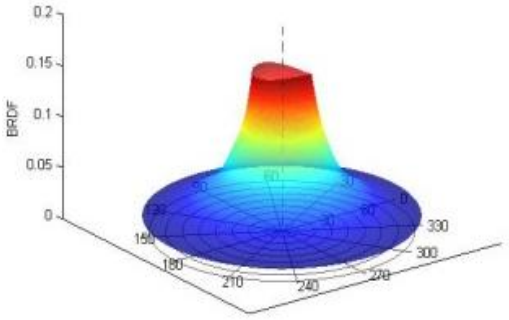

Figure 2. An example of BRDF test results for IZA=0.

REFERENCES

1. Pinty, B., et al., Radiation transfer model intercomparison (RAMI) exercise. Journal of Geophysical Research: Atmospheres, 2001. **106**(D11): p. 11937-11956.
2. Widlowski, J-L., et al., The fourth radiation transfer model intercomparison (RAMI-IV): Proficiency testing of canopy reflectance models with ISO-13528, Journal of Geophysical Research, **118**, doi:10.1002/jgrd.50497, 2013.
3. Widlowski, J.L., et al., The RAMI On-line Model Checker (ROMC): A web-based benchmarking facility for canopy reflectance models. Remote Sensing of Environment, 2008. **112**(3): p. 1144-1150.
4. Y. Govaerts, A model of light scattering in three-dimensional plant canopies: a Monte Carlo ray tracing approach. Space Applications Institute, JRC, report EUR 16394 EN, 1996.
5. P. Jaanson et al, Gonioreflectometric properties of metal surfaces, submitted to NEWRAD 2014.

ACKNOWLEDGEMENTS

This research was funded by project ENV04 MetEOC (European metrology for earth observation and climate) of the European Metrology Research Programme (EMRP). The EMRP is jointly funded by the EMRP participating countries within EURAMET and the European Union.

Size-of-Source Effect in Calibration of Large-Area Integrating-Sphere Source

Maxim Solodilov, Boris Khlevnoy, Valeriy Gavrilov, and Denis Otryaskin

All Russian Research Institute for Optical and Physical Measurements (VNIIOFI), Moscow, Russia
Corresponding e-mail address: khlevnoy-m4@vniiofi.ru

The VNIIOFI standard radiometric facility developed for calibration of Earth observation instruments includes an integrating sphere source with an output aperture of 600 mm. The source is measured in terms of spectral radiance by comparing with a blackbody with an opening of 20 mm using a spectral comparator. The size-of source effect (SSE) of the comparator has been investigated. The SSE correction for the sphere source calibration has been evaluated as -0.1 % with standard uncertainty of 0.05 %.

INTRODUCTION

The standard radiometric facility was developed at VNIIOFI in 2010 for ground-based high-accuracy calibration of Earth observation instruments with apertures up to 500 mm [1]. Several space-borne instruments were successfully calibrated on the facility since that [2]. The facility includes a large-area diffuse source based on a 2 m integrating sphere (IS) with an output aperture of 600 mm. This IS source is used as a reference spectral radiance source in the spectral range from 300 nm to 2.5 μm.

The sphere spectral radiance is measured by means of comparing with a high-temperature blackbody using a comparator based on a double-monochromator and mirror focusing system that image the sources (IS or the blackbody) to the monochromator entrance slit. The sphere and spectral comparator are shown in Fig.1. The blackbody stands next to the sphere. The comparator can move between the sphere and blackbody. The standard uncertainty of the sphere spectral radiance measurements depends on the wavelength and varies from 1.5 % (300 nm) to 0.5 % (600 nm) and again to 1.5 % (2.5 μm) [1].

It's known that imaging systems generally can suffer from so-called size-of source effect (SSE), i.e. signal of an imaging instrument increases with increasing of dimensions of radiating source area. The reason of SSE is scattering light and non-perfect optics. SSE might be especially significant when compared sources have significantly different sizes. In our case the 600 mm IS source is compared with the 20 mm blackbody source. However, up to now SSE of the system was not properly investigated, but was taken into account as an approximate estimation of an uncertainty component of 0.2 % (k=1) [1].

The objective of the present work is the proper investigation of the comparator SSE, evaluation of the SSE correction when the sphere and blackbody sources are compared, and estimation of the corresponding uncertainty.

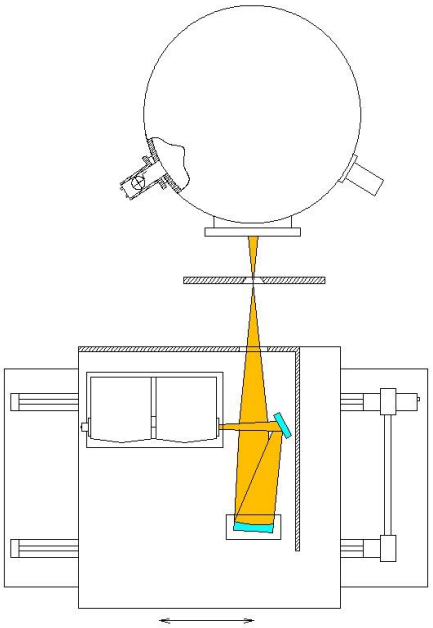

Figure 1. SSE measurement setup.

MEASUREMENT SETUP

The measurement setup diagram is shown in Fig.1. The object plane of the imaging system is located at the distance of 335 mm in front of the IS source. In this plane there is a black baffle, larger than the IS aperture, with a 100 mm circular hole centered to the system optical axis. On the baffle coaxial to the hole there is a holder for apertures. Several apertures with different diameters can be alternatively installed in the holder.

MEASUREMENT PROCEDURE

The IS source was turned on and stabilized. Then the smallest aperture with the diameter of 3.9 mm was installed in the holder. The baffle was aligned in such

a way that the aperture image as in the monochromator entrance slit is as sharp as possible and centered to the slit.

Then the apertures were alternatively changed; and for each aperture the signal of the spectral comparator was recorded at four wavelengths of 400 nm, 600 nm, 800 nm and 1000 nm. The signals were also measured for no aperture in the holder, i.e. for 100 mm hole, and for no baffle in front of the sphere. In the latter case the viewed area of the sphere was limited by the size of the window in the comparator baffle, which is always used during the system operation; for this case the diameter of the observed area was approximately estimated as 215 mm.

Therefore, the aperture diameters, used for the SSE measurement were 3.9 mm, 5.0 mm, 5.8 mm, 7.9 mm, 10 mm, 15 mm, 20 mm, 30 mm, 40 mm, 50 mm, 58 mm, 80 mm, 100 mm and 215 mm.

The measurements were carried out three times with independent alignment of the baffle/apertures. Although the usual entrance slit size during IS to blackbody comparison is 3x5 mm, the SSE measurement was done first with the slit of 1x2 mm for covering smaller aperture, and then repeated with slits of 3x3 mm and 3x5 mm to check the consistency, but with large aperture only.

RESULTS

The result of the SSE measurement is presented as a dependence of the spectral comparator signal on the diameter of the source aperture. The results of all three independent sets of measurements are shown in graph form in Fig.2 for three wavelengths and the slit of 1x2 mm.

One can see that there is no obvious spectral dependence of SSE, i.e. the measurements at three wavelengths, 600 nm, 800 nm and 1000 nm, agree to each other within the measurement repeatability. The measurements at 400 nm were much noisier than those at the other wavelengths because of low signal; so, the 400 nm results are not shown in the Fig.2. However, measurements performed with longer integration time at selected diameters confirmed the SSE obtained at other wavelengths.

Generally, the signal increases with increasing the source diameter like a logarithmic curve by about 0.2 % from 4 mm to 100 mm; at 215 mm the signal is nearly the same as that at 100 mm.

To evaluate the SSE correction corresponding to the calibration of the IS against the blackbody, we have to compare two points in the Fig.2 curve: 20 mm (it's corresponds to the blackbody) and 215 mm (the IS source). The signal increases by about 0.11% between these two points. The uncertainty of this difference is determined mainly by the combined standard deviation of nine measured signals (three sets at three wavelengths) at each point, which equals to approximately 0.02 %. However, assuming probable systematic error, we prefer to overestimate the uncertainty up to 0.05 %.

The measurement results obtained with the slits of 3x3 mm and 3x5 mm agreed with those obtained for the slit of 1x2 mm within the standard deviations.

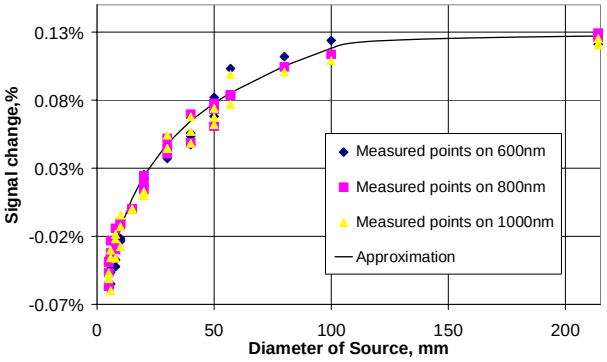

Figure 2. Dependence of the spectral comparator signal on the source diameter.

CONCLUSIONS

No spectral dependence of the SSE was detected in the spectral range from 400 nm to 1000 nm.

The correction related to the size-of-source effect has been determined for the case of measuring the 600 mm IS source against the blackbody with 20 mm opening from the VNIIOFI standard radiometric facility for calibration of Earth observation instruments. The value of the correction is -0.1 % with standard uncertainty 0.05 %.

REFERENCES

1. V. Sapritsky et al, Current activity of Russia in measurement assurance of Earth optical observations, Metrologia 49, S9–S16, 2012.
2. N. Butiaykin, V. Lin'ko, M. Luzganova, A. Li, B. Khlevnoy, M. Solodilov, V. Gavrilov, S. Ogarev, A. Panfilov, S. Arkhipov and V. Sapritsky, Hyper-Spectral Earth Observation Instrument and its Pre-flight Calibration, presented at NEWRAD 2014.

Metrology For Earth Observation and Climate 1 (MetEOC)

Nigel Fox[1], Emma Woolliams[1], Jean-Luc Widlowski[2], Jorg Hollandt[3], Mauro Rajteri[4], Jimmy Dubard[5], Antti Lassila[6], Farshid Manoocheri[7], Wolfgang Finsterle[8], Friedhelm Olschewski[9], Ralf Reulke[10], Eija Honkavaara[11], and Peter Preusse[12]

[1] *National Physical Laboratory, Teddington, UK*
[2] *Joint Research Centre, Brussels, Belgium*
[3] *Physikalisch-Technische Bundesanstalt, Brunswick, Germany*
[4] *Istituto Nazionale di Ricerca Metrologica, Torino, Italy*
[5] *Laboratoire National de Métrologie et d'Essais, Paris, France*
[6] *Mittatekniikan Keskus, Espoo, Finland*
[7] *AaltoUniversity, Espoo, Finland*
[8] *Schweizerisches Forschungsinstitut fuer Hochgebirgsklima und Medizin in Davos, Switzerland*
[9] *Bergische Universitaet Wuppertal, University of Wuppertal, Germany*
[10] *Deutsches Zentrum fuer Luft- und Raumfahrt eV, Germany*
[11] *Geodeettinen Laitos, Masala, Finland*
[12] *Forschungszentrum Juelich GmbH, Germany*
Corresponding e-mail address: nigel.fox@npl.co.uk

The Earth's climate is changing, however for governments to take concerted and significant action to mitigate and adapt requires robust unequivocal evidence on the scale and nature of its potential impact. This requires long time base global monitoring of the Earth by satellite. To be trusted these measurements must be traceable to SI units. However, achieving this at the uncertainty levels necessary is arguably one of the most critical challenges facing the metrology community to day.

INTRODUCTION

The world's Earth Observation and climate community currently require improved accuracy and SI traceability, particularly in the post-launch environment. In many cases traceability is based on unsubstantiated or debated claims, resulting in high uncertainties for climate forecasting, and weak evidence to counter the claims of climate sceptics. This delays key actions by policy makers and citizens.

The European Metrology Research Program (EMRP) funded a three year research project, started in October 2011, called Metrology for Earth Observation and Climate (MetEOC) to initiate coordinated research amongst European National Metrology Institutes (NMIs) to address these needs (http:www.emceoc.org). A follow-on project, MetEOC 2, will continue this research into 2017 and is the subject of a linked poster.

WORK PROGRAM

The objectives of MetEOC 1 were to establish new transfer standards and methodologies to enable improved accuracy and traceability (factors of 2 to 10 improvements) for:

- Laboratory based (air and vacuum) pre-flight calibration and characterisation of optical and microwave imaging cameras
- In-flight (on-board) calibration for optical imagers and atmospheric limb sounders through novel blackbodies and infra-red calibration facilities
- Surface based "test-sites" for the post-launch calibration and validation of Land and Ocean imaging radiometers
- Some models and algorithms needed to improve performance and traceability of Level 2 Land products including instrumentation to measure in-situ parameters needed for inputs such as individual leaf reflectance.
- Prototyping techniques to enable the establishment of "SI traceable benchmark measurements from space" to facilitate and

underpin the upgrade of current sensors to the performance needed to form a global climate observing system including total solar irradiance

Examples of these activities have been demonstrated by case-studies using existing or planned sensors and are contributing to scoping a long-term vision of: a European virtual centre of excellence of metrological support to EO and climate. The results of some of this work is presented in other papers submitted to this meeting.

This poster provides the overarching framework and overview of the project and its objectives.

ACKNOWLEDGMENTS

This work was funded through the European Metrology Research Programme (EMRP) Project ENV04 METEOC. The EMRP is jointly funded by the EMRP participating countries within EURAMET and the European Union.

Metrology for Earth Observation and Climate 2 (MetEOC 2)

Nigel Fox[1], Emma Woolliams[1], Priit Jaanson[2], Christian Monte[3], Wolfgang Finsterle[4], Eija Honkavaara[5], Friedhelm Olschewski[6], Peter Preusse[7], Marek Smid[8], Bernard Rougie[9], Joaquin Campos[10], David Smith[11], Jean-Luc Widlowski[12], Steven van den Berg[13], and Michael Bittner[14]

[1] *National Physical Laboratory, Teddington, United Kingdom*
[2] *Mittatekniikan Keskus, Espoo, FInland*
[3] *Physikalisch-Technische Bundesanstalt, Brunswick, Germany*
[4] *Schweizerisches Forschungsinstitut fuer Hochgebirgsklima und Medizin in Davos, Switzerland*
[5] *Geodeettinen Laitos, Masala, Finland*
[6] *Bergische Universitaet Wuppertal, Germany*
[7] *Forschungszentrum Juelich GmbH, Germany*
[8] *Cesky Metrologicky Institut Brno, Czech Republic*
[9] *Conservatoire national des arts et metiers, France*
[10] *Agencia Estatal Consejo Superior de Investigaciones Cientificas, Spain*
[11] *Science and Technology Facilities Council, Swindon, United Kingdom*
[12] *Joint Research Centre, Brussels, Belgium*
[13] *The National Metrology Institute of the Netherlands, Netherlands*
[14] *Deutsches Zentrum fuer Luft- und Raumfahrt eV, Germany*

Although not complete, the EMRP project MetEOC 1 (see other paper for this conference) has made major progress towards improving the traceability of remote sensing instrumentation and the direct physical measurands such as spectral radiance/reflectance. Whilst this is essential it is not enough to address the needs of the climate science community who are looking to monitor Essential Climate Variables (ECVs) which are in general biogeophysical parameters derived from the direct measurand through use of an additional retrieval algorithm. MetEOC 2 extends the scope of the work to address these needs.

INTRODUCTION

Warming of the climate system is unequivocal, … The atmosphere and ocean have warmed, the amounts of snow and ice have diminished, sea level has risen, and the concentrations of greenhouse gases have increased… It is extremely likely that human influence has been the dominant cause of the observed warming since the mid-20th century. Intergovernmental Panel on Climate Change IPCC) - Sept 2013 [1]

Although the IPCC has strengthened its conclusion, governments are reluctant to act, and the public remain confused. This is fuelled by the large uncertainty in climate model forecasts and arguments of sceptics. Accurate and trusted measurements of sensitive climate indicators are needed to improve our understanding of the Earth system. This will improve the climate models and understanding of the resultant impact on society; enabling policy-makers to take urgent decisions on appropriate mitigation and adaptation strategies.

MetEOC 2 will work with the climate science community to address this urgent challenge.

Remote sensing of the Earth from space is the major means of obtaining the global data needed to underpin climate change research. Essential Climate Variables, (ECVs), such as incoming radiation from the Sun or sea surface temperature, (SST), are monitored to detect small fluctuations. Such variations may reveal changes in the Earth system; indicating the effect of, climate change. In most cases detection of changes of a few tenths of a per cent per decade are required, relying on measurements with uncertainty levels currently only realisable in the National Metrology Institutes, (NMIs).

The harshness of the launch and operational environment in-space causes significant and unpredictable change in the performance of the satellite instrumentation. Re-assessment of the

accuracy of satellite instrumentation post-launch is therefore essential before the validity of data can be guaranteed. Calibration against, and traceability to, the international system of units, (SI) guarantees long-term confidence, accuracy and reliability in the satellite data and ensures consistency between satellites.

Most of the 50 ECVs established by the Global Climate Observing System (GCOS) of the United Nations are not direct measurements of a physical parameter familiar to the metrology community and are instead more complex biogeophysical parameters that have been retrieved through an algorithm for example Leaf Area Index (LAI). However, since it is these parameters that are used in practise it is essential that their uncertainty, including the retrieval algorithm is fully assessed in an SI traceable manner as far as practical.

This requires end to end (satellite to in-situ) calibration and validation and an assessment of spatial scaling, sampling strategies and a variety of different instruments and mathematical robust data harmonisation methods.

WORK PROGRAM

MetEOC 2 will establish a coordinated network of NMIs, to work with international thematic experts to progress towards establishing: *the tools, methods, and infrastructure to enable trustable confidence levels to be assigned to data used for climate change monitoring and information derived from Earth Observation for example amount of carbon stored in the forests.*
The projects outputs include:

- Transfer standards for traceability of measurements from remote sensing instrumentation pre & post launch; for land, ocean and atmosphere.
- Establishment of autonomous SI-traceable global networks of test-sites for post-launch calibration and validation of remote sensing instruments.
- Establishment of end-to-end traceable uncertainty budgets on bio-geo physical parameters typical of Essential Climate Variables, (ECVs) and long-term Climate Data Records, (CDRs),
- Prototyping of a high accuracy SI traceable satellite sensor, for making benchmark measurements to constrain climate models and calibration of other sensors.
- Improvements to instrumentation and transfer standards e.g. novel solar diffusers, carbon nanotube black coatings, surface brightness temperature measuring instruments; will increase accuracy of measurements. Tailoring mathematical methods e.g. optimised sampling, data fusion; will reduce uncertainties. Developing new transfer standards e.g. natural uniform bright targets like deserts will re-establish traceability.

The poster will describe the scope and tasks within the project which is structured into work packages.

Work Package 1 (WP) will establish a network of desert/ice/forest test-sites to calibrate satellites when in-orbit; combine and analyse data and uncertainties from multiple satellite instruments; prototype the climate satellite Traceable Radiometry Underpinning Terrestrial- and Helio- Studies, (TRUTHS).

WP2 will improve measurement of sensitive climate indicators such as emitted radiance of the mesosphere; develop in-flight standards for traceable monitoring of temperature and chemical composition in the atmosphere; determine aerosol quantities, water vapour etc. by measuring absorption/scattering losses through the atmosphere.

WP3 will establish best practice for end-to-end SI traceable uncertainty for key biophysical ECVs e.g. Leaf Area Index (LAI) and Fraction of absorbed photosynthetically active radiation (fAPAR).

WP4 will measure ECVs, impacting Radiation Balance; provide traceability for incoming Total Solar Irradiance, (TSI) and thermally-emitted radiation from the Earth's surface temperature; land and ocean.

WP5 will establish a prototype framework for a European virtual centre of excellence (European Metrology Centre for Earth Observation and Climate, EMCEOC). This will be a 'one-stop-shop' for EO and climate metrology. It will interface with all stakeholders to disseminate the project outputs and collect future requirements. It will increase public

awareness of ‘metrology and uncertainty in climate’ using the popular media and schools to deliver our message.

The high value, visibility and impact of this project are evidenced by the letters of endorsement from the major European and International organisations including:

- Global Climate Observing System, (GCOS),
- European Space Agency, (ESA),
- World Meteorological Organisation, (WMO),
- Committee on Earth Observation Satellites, (CEOS).

ACKNOWLEDGMENTS

This work was funded through the European Metrology Research Programme (EMRP) Project ENV53 METEOC2. The EMRP is jointly funded by the EMRP participating countries within EURAMET and the European Union.

A UAV goniospectrometer for the measurement of bidirectional reflectance characteristics of 3D land surfaces

Eija Honkavaara, Lauri Markelin, Teemu Hakala, and Jouni Peltoniemi

Department of Remote Sensing and Photogrammetry, Finnish Geodetic Institute
Corresponding author e-mail address: eija.honkavaara@fgi.fi

Unmanned airborne imaging technology offers new possibilities for various remote sensing applications. We present a new concept to carry out bidirectional spectral reflectance factor measurements of 3D land surfaces based on an UAV and a novel light-weight spectrometric camera. We also investigated the traceability of reflectance measurements. The results indicated high accuracy and automation level of the proposed measurement system.

INTRODUCTION

Remote sensing based on unmanned airborne vehicles (UAVs) is a rapidly developing field of technology. New UAV sensing techniques provide attractive possibilities for measuring the reflectance properties of surfaces using vertical and oblique views. Managing the uncertainties of the reflectance measurements is crucial in many UAV remote sensing applications, such as precision agriculture or water quality management.

We have developed a traceable procedure for conducting multiangular spectral reflectance measurements by UAVs. The measurement system makes use of a UAV and a spectral imager that collects area format spectral data cubes with stereoscopic and multi-view setups. An important challenge in this measurement is the anisotropy of the spectral reflectance.

The traceability chain was established from the field measurements to the Metrology Research Institute at Aalto University, which is the Finnish national standards laboratory for optical quantities. The traceable reflectance transfer include the following steps: 1) Availability of an SI-traceable reflectance standard in a national standards laboratory 2) Traceable reflectance at the FGI laboratory 3) Traceable reflectance at the measurement site 4) Traceable reflectance in the UAV output data.

The central objective of this study was to investigate the feasibility of a UAV goniospectrometer in different target areas including gravel field, agricultural crops and forest.

MEASUREMENT SYSTEM

The reflectance measurement system at Finnish Geodetic Institute is based on an eight-rotor UAV with a 1.5 kg payload (Fig. 1). The UAV was equipped with a stabilized camera mount, which allows tilting of the camera to enable desired view angles and compensates for tilts and vibrations.

The spectral reflectance measurement is based on the Fabry-Perot Interferometer-based (FPI) spectrometric camera, developed by the VTT Technology Research Center in Finland [1]. This technology provides area-format spectral data cubes, allowing for stereoscopic and multi-ray views of objects when overlapping images are used, and an even larger range of observation angles can be obtained by using oblique views. The image processing chain includes image corrections based on laboratory calibration, a determination of the orientations, digital surface model (DSM) generation, a determination of the atmospheric parameters (and radiometric model parameters), and finally, the reflectance data generation [2].

Figure 1. UAV imaging system.

EMPIRICAL STUDY AND DISCUSSION

The new measurement procedure was assessed in three different target areas in Finland: Sjökulla remote sensing test field, Vihti agricultural test field and Evo forest test field. Image blocks were collected with vertical and oblique viewing geometry.

The data processing chain was capable of automatically processing all the test data sets. The image orientations were solved (Fig. 2) and then the

digital surface model was generated (Fig. 3). Using these information, reflectance mosaics (Fig. 4) and BRF data (Fig. 5) were provided.

Figure 2. Image orientations of the Evo forest FPI spectral camera nadir-looking block.

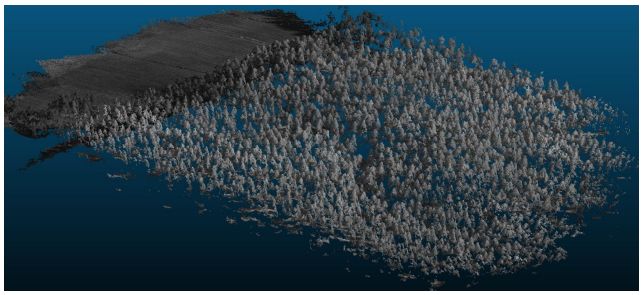

Figure 3. Digital surface model of the Evo forest test area.

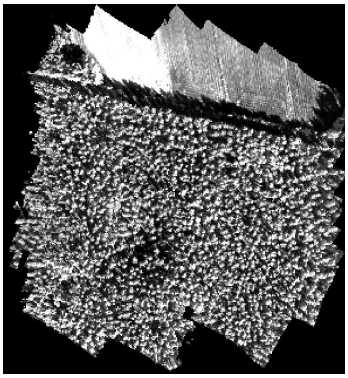

Figure 4. Reflectance image mosaic of the Evo forest test area on near infra-red channel (center wavelength 775.2; fwhm 30.495).

In this investigation, the major uncertainty components in the reflectance measurement were the uncertainty of the reflectance transformation and the image quality. The uncertainty of the output is highly dependent upon the atmospheric conditions and image quality. In particular, the quality of the radiometric calibration of the sensor is a fundamental factor influencing the uncertainty.

The overall objective for the output reflectance data quality was between 0.01 and 0.02 reflectance units; this would meet the requirements of the satellite community for global radiation budget measurements. Our theoretical results indicated that this level of accuracy could be obtained with the proposed method. Also the empirical results were promising.

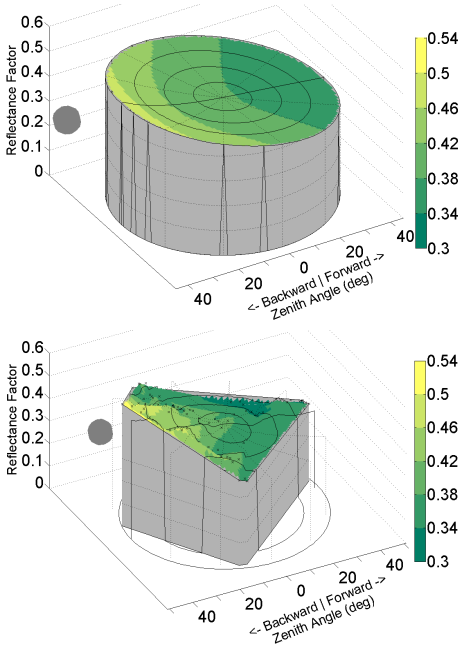

Figure 5. Example of measured BRF of white gravel. Top: reference measurement by FIGIFIGO goniospectrometer. Bottom: Measurement result by UAV. Near infra-red channel (center wavelength 775.2; fwhm 30.495).

ACKNOWLEDGMENT

We are grateful to the European Metrology Research Program (EMRP) for funding the project. The EMRP is jointly funded by the EMRP participating countries that are part of the European Association of National Metrology Institutes and the European Union. This project is part of a Researcher Excellence Grant project, which in turn falls under the EMRP project “Metrology for Earth Observation and Climate”. We acknowledge the Metrology Research Institute at Aalto University for their support in providing reflectance standard for our investigation.

REFERENCES

1. H. Saari, I. Pölönen, H. Salo, E. Honkavaara, T. Hakala, C. Holmlund, J. Mäkynen, R. Mannila, T. Antila and A. Akujärvi, Miniaturized hyperspectral imager calibration and UAV flight campaigns, Proc. SPIE 8889, Sensors, Systems, and Next-Generation Satellites XVII, October 24, 2013.
2. E. Honkavaara, L. Markelin, T. Hakala, J. Peltoniemi, The metrology of directional, spectral reflectance factor measurements based on area format imaging by UAVs, Photogrammetrie – Fernerkundung – Geoinformation 3/2014, in press.

Calibration of UV Index Measurement Device

Hsueh-Ling Yu[1], Chin-Chai Hsiao[1], Hsin-Feng Chen[1], Wen-Chi Lin [1], and Jui-Yuan Yeh[2]

[1]*Center for Measurement Standards, Hsinchu, Taiwan, R.O.C.,* [2] *Central Weather Bureau, Taipei, Taiwan, R.O.C.*
Corresponding e-mail address: hsuehling.yu@gmail.com

Two calibration methods, source-based and detector-based, for UV index (UVI) measurement device are presented in this article. For accurate measurement, spectrum mismatch correction is necessary for the source-based method. To avoid the inconvenience of adopting spectrum mismatch correction, a detector-based method is developed in this article which through measuring the spectral irradiance responsivity of the UVI meter can retain the accuracy of outdoor measurment.

INTRODUCTION

UVI is used to describe the level of UV radiation damage and is an important vehicle to alert people about the need to use sun protection. UVI is calculated from the UV irradiance weighted by the erythema reference action spectrum. For a good UVI measurement device, its spectral responsivity shall be as close to the erythema reference action spectrum as possible. Applying solar simulator for UVI meter calibration is a widely used source-based method. However the spectrum mismatch between the solar simulator and real solar light may induce measurement error for outdoor UVI measurement. This paper presents a detector-based method for UVI meter calibration which measures the absolute spectral irradiance responsivity of the UVI meter to reduce the influence of spectrum mismatch from the solar simulator.

METHOD 1: SOURCE-BASED

Figure 1 depicts the schematic diagram and measurement procedures of source-based method. First, use the standard lamp and monochromator to calibrate the spectral irradiance $S_{Xe}(\lambda)$ of the Xe lamp and calculate its erythemal weighted irradiance at distance d. Next, place the UVI meter at the same distance d to measure the irradiance of the Xe lamp. Assume its output signal is V_{Xe}, the calibration factor F_{Xe} of the UVI meter can then be expressed as:

$$F_{Xe} = \frac{\sum E(\lambda) S_{Xe}(\lambda) \Delta\lambda}{V_{Xe}} \qquad (1)$$

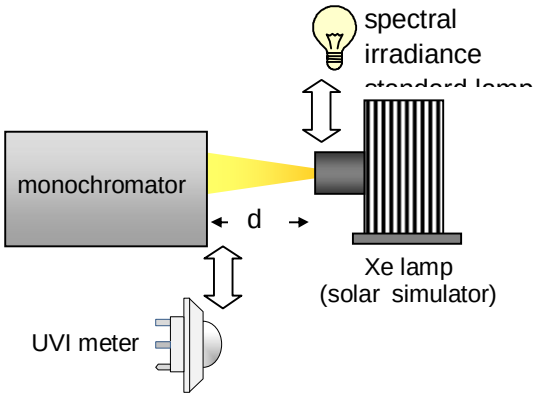

Figure 1. Schematic diagram of Method 1.

Where $E(\lambda)$ is the erythema reference action spectrum and the numerator on the right hand side of equation (1) is the erythemal weighted irradiance of the Xe lamp. Using this calibrated UVI meter to measure outdoor solar light, the measurement result of the erythemal weighted irradiance of solar light I_m will be equal to $V_{sun} \times F_{xe}$, where V_{sun} is the original reading of the UVI meter. I_m can be expanded as equation (2).

$$I_m = k\sum R_r(\lambda) S_{sun}(\lambda) \Delta\lambda \times \frac{\sum E(\lambda) S_{Xe}(\lambda) \Delta\lambda}{k\sum R_r(\lambda) S_{Xe}(\lambda) \Delta\lambda} \qquad (2)$$

$R_r(\lambda)$ is the relative spectral responsivity of the UVI meter, $S_{sun}(\lambda)$ is the spectrum of solar light, and $kR_r(\lambda)$ means the absolute spectral responsivity of the UVI meter. However the real erythemal weighted irradiance of solar light I_{sun} is equal to $\sum E(\lambda) S_{sun}(\lambda) \Delta\lambda$. According to equation (2), I_m is equal to I_{sun} only if the relative spectrums of the Xe lamp and solar light are the same and/or $R_r(\lambda) = E(\lambda)$. Otherwise, similar to the problem of photometer calibration [1], I_m shall be multiplied by a further factor F_{ccf} for spectrum mismatch correction to make $I_m \times F_{ccf}$ equal to I_{sun}. F_{ccf} is expressed as follows where $S_{Xe,r}(\lambda)$ and $S_{sun,r}(\lambda)$ represent the relative spectrums of the Xe lamp and solar light, respectively.

$$F_{ccf} = \frac{\sum R_r(\lambda) S_{Xe,r}(\lambda) \Delta\lambda}{\sum E(\lambda) S_{Xe,r}(\lambda) \Delta\lambda} \times \frac{\sum E(\lambda) S_{sun,r}(\lambda) \Delta\lambda}{\sum R_r(\lambda) S_{sun,r}(\lambda) \Delta\lambda}$$

To avoid the inconvenience of adopting the factor F_{ccf} for spectrum mismatch correction, a detector-based method is developed.

METHOD 2: DETECTOR-BASED

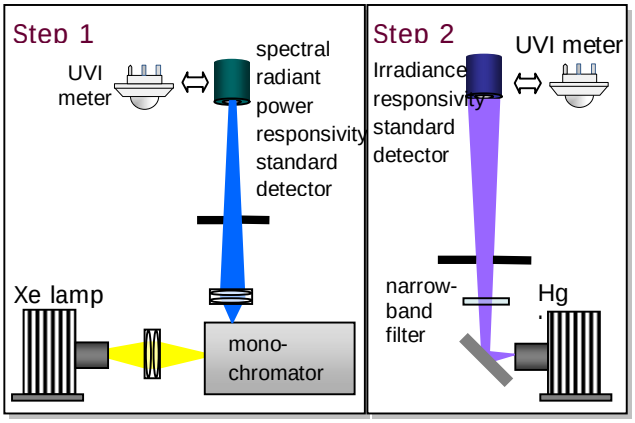

Figure 2. Schematic diagram of Method 2. Step 1: relative spectral radiant power responsivity measurement (280 nm ~ 400 nm). Step 2: absolute irradiance responsivity measurement (365 nm).

The idea of Method 2 is to obtain the absolute spectral irradiance responsivity $kR_r(\lambda)$ of the UVI meter. Knowing $kR_r(\lambda)$, the calibration factor F_{sun} of the UVI meter under solar light illumination can be expressed as equation (3).

$$F_{sun} = \frac{\sum E(\lambda) S_{sun}(\lambda) \Delta\lambda}{k \sum R_r(\lambda) S_{sun}(\lambda) \Delta\lambda} \quad (3)$$

The method of spectral irradiance responsivity measurement is similar to the DSR method [2] for photovoltaic cell which is shown in Figure 2. First, measure the relative spectral radiant power responsivity $R_r(\lambda)$ of the UVI meter from 280 nm to 400 nm. Then measure the absolute irradiance responsivity at 365 nm to obtain the absolute spectral irradiance responsivity $kR_r(\lambda)$ of the UVI meter for

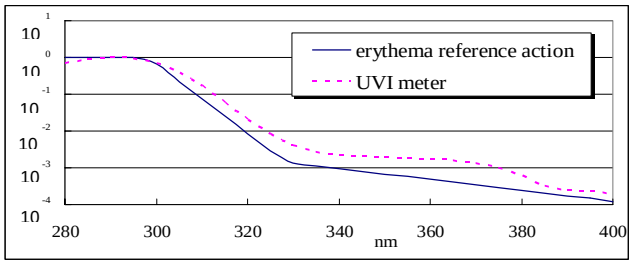

Figure 3. Spectral responsivity of the UVI meter and the spectrum of erythema reference action.

the whole wavelength rage from 280 nm to 400 nm.

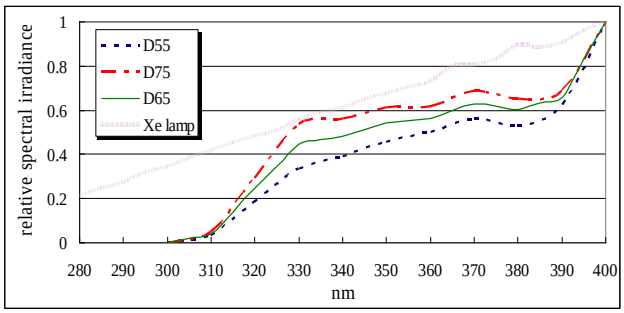

Figure 4. Spectrums of the Xe lamp (solar simulator), D55, D65, and D75 solar light.

The simulation of Method 1 and Method 2 for outdoor measurement is shown as follows.

SIMULATION RESULTS

Figure 3 shows the relative spectral responsivity of the UVI meter and the erythema reference action spectrum. For comparing the accuracy, calibrate this UVI meter with Method 1 by using the Xe lamp and Method 2 by using the D65 [3] solar light. Then calculate the deviation of this UVI meter while measuring other D55 and D75 solar light to see which calibration method can obtain closer results to the erythemal weighted irradiance of D55 and D75. The relative spectrums of the Xe lamp, D65, D55, and D75 solar light are shown in Figure 4 and the simulation results are summarized in Table 1. From Table 1, the deviation of Method 1 can be as high as 65 % without adopting the spectrum mismatch correction. Applying Method 2 for UVI meter calibration can obtain much more accurate results for outdoor UVI measurement.

Table 1. Deviation of the measurement results for the source-based and detector-based calibration methods from the erythemal weighted irradiance of solar light.

Method / Solar light	Source-based	Detector-based
D55	64.6 %	3.6 %
D75	65.6 %	4.3 %

CONCLUSIONS

Two calibration methods for UVI measurement device are presented in this article, one is source-based and the other is detector-based. Due to the spectrum mismatch between the solar simulator and real solar light as well as the mismatch between the spectral responsivity of the UVI meter and erythema reference action spectrum, the UVI meter which is calibrated with the source-based method may have extremely large deviation while measuring the

outdoor UVI without applying the mismatch correction. To avoid the inconvenience of mismatch correction, the detector-based method is developed in this article. The simulation results show that the detector-based method can obtain much more accurate outdoor UVI measurement compared with the source-based method.

REFERENCES

1. Yoshishiro Ohno, NIST measurement services: photometric calibrations, NIST spec. publication 250-37.
2. J Metzdorf, S Winter and T Wittchen, Radiometry in photovoltaics: calibration of reference solar cells and evaluation of reference values, Metrologia, 37, 573-578, 2000.
3. CIE 204, Methods for Re-defining CIE D Illuminants.

Calibration of a Fourier Transform Spectroradiometer for Surface Spectral Solar UV Irradiance Measurements

Peter Meindl, Christian Monte, and Martin Wähmer

Physikalisch-Technische Bundesanstalt (PTB), Berlin, Germany
Corresponding e-mail address: Peter.Meindl@ptb.de

The feasibility of using a commercially available Fourier transform spectrometer (FTS) as a reference spectroradiometer for solar UV irradiance measurements has been examined. For that purpose, a Bruker FTS VERTEX 80v has been adapted for measurements in the ultraviolet spectral range from 280 nm to 500 nm by applying different types of UV detectors. The spectral irradiance responsivity of the FTS equipped with a global entrance optic has been calibrated against a high-temperature blackbody radiator, and the usability of the spectroradiometer for solar UV irradiance measurements has been investigated.

INTRODUCTION

Up to now, scanning spectroradiometers are in use as reference instruments for the dissemination of radiometric units to remote measuring sites that are used for solar irradiance measurements (QASUME [1]). This type of radiometer has a couple of disadvantages. For example, the solar spectrum is scanned sequentially which needs several minutes of time for each spectrum and limits the temporal resolution of the radiometer. Because of the low throughput of these instruments, photomultipliers have to be used whose spectral responsivity has to be recalibrated each day before use. The standard uncertainty of these instruments for solar irradiance measurements is around 2.3% to 4.4% depending on wavelength and solar zenith angle [1].

It is the goal of the European Metrology Research Project ENV03 to enhance the reliability of spectral solar UV radiation measurements at the Earth's surface by developing new techniques and devices that enable a traceability of solar UV irradiance measurements of better than 2%. For this reason, wavelength accuracies of better than 50 pm are required to reach nominal uncertainties of 1% to 2% due to the steep decrease of solar UV irradiance below 330 nm over many orders of magnitude. Furthermore, the rapid temporal variation of solar UV radiation due to varying atmospheric conditions (e.g. moving clouds) requires fast spectroradiometers.

Considering these demands, the usage of FT spectroradiometers may improve the dissemination of absolute irradiance scales due to the specific advantages of these instruments [2, 3]:

- Fourier transform spectrometers have a high throughput (Jacquinot advantage).
- There are no diffraction losses to higher-order spectra as it is the case in grating spectrometers. This also enhances the signal-to-noise ratio.
- The whole spectrum is measured simultaneously which allows fast measurements.
- FT spectrometers cover broad spectral ranges with high resolution and high wavenumber accuracy.
- Modern FTS often use integrated HeNe lasers for the measurement of the position of the moveable mirror of the FTS interferometer. This laser can be used for the wavenumber calibration of the FTS [4]. In this way, the wavenumber scale of the FTS is inherently traced to the SI with low uncertainties in contrast to scanning spectroradiometers whose wavelength scale has to be recalibrated on-site periodically against spectral lamps [1].
- Instrumental distortions are often calculable and correctable.

It was considered to use semiconductor detectors instead of a photomultiplier tube because of the higher throughput of an FTS compared to scanning instruments. This type of detectors could simplify the dissemination of the irradiance scale because usually the spectral responsivity of semiconductor detectors is sufficient stable in contrast to the responsivity of photomultiplier tubes. Within this investigation two types of semiconductor detectors (Si and GaP) have been used. It is additionally planned to use a photomultiplier tube to be able to compare the FTS directly with the scanning instrument QASUME.

CALIBRATION OF SPECTRAL RESPONSIVITY

A global entrance optic has been fitted to the FTS to perform solar UV irradiance measurements. The

spectral irradiance responsivity of this Fourier transform spectroradiometer has then been calibrated in the wavelength range from 280 nm to 500 nm. This calibration has been carried out by using a blackbody radiator HTBB pg3200 as a calculable source of irradiance and additionally by using a secondary irradiance standard (halogen lamp) which was calibrated against the national irradiance standard of the PTB [5, 6, 7]. The spectral irradiance responsivity of the FTS for different semiconductor detectors is shown in Fig. 1. The largest responsivity has been found with a GaP detector which has a maximum responsivity around 450 nm.

It was intended to use the FTS in the ultraviolet range down to 280 nm to be able to measure the steep decrease of solar irradiance in this wavelength range. However, it was found that the calibration of the FTS was only reasonable down to about 360 nm where a SNR of 1 was reached because of a rather low throughput of the entrance optic. So, as a result, it is possible to use semiconductor detectors in the FTS - which is not effective in scanning instruments - but not below 360 nm if an absolute calibration is needed. As a consequence, it is planned to apply a photomultiplier tube as it is the case in the scanning

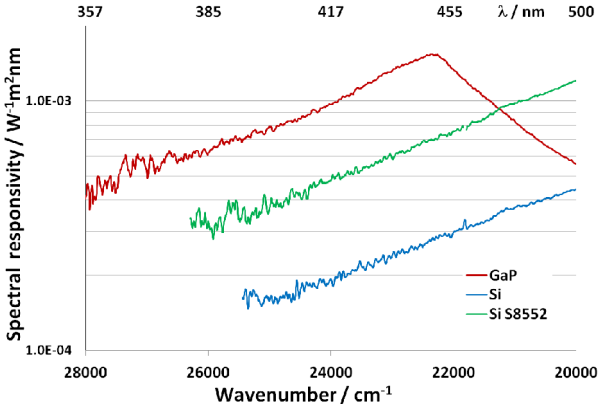

Figure 1. Spectral irradiance responsivity of the FTS with global entrance optic for different types of semiconductor detectors. Calibration against HTBB at T = 2795 K.

spectroradiometer QASUME.

As mentioned above, the statistical uncertainty is the limiting source of uncertainty when using semiconductor detectors below 500 nm. Beside the statistical uncertainty a number of systematic uncertainties contribute to the uncertainty of the calibration measurement. The largest contributions are caused by the uncertainty of the temperature of the blackbody radiator followed by the uncertainty of the distance of the entrance optic to the blackbody radiator because the position of the reference plane of the entrance optic has a comparatively large uncertainty of 1 mm [8].

RESULTS

The usage of FT spectroradiometers may improve the dissemination of absolute irradiance scales due to the specific advantages of these instruments. The investigated FTS has a comparatively small wavelength uncertainty of less than 6 pm in the wavelength range from 250 nm to 500 nm. This is well below the 50 pm which are demanded to obtain an uncertainty of irradiance measurements of less than 2%. However, the detectivity of semiconductor detectors is not large enough to enable calibrated solar irradiance measurements below 360 nm with sufficient low uncertainties because of the low throughput of the used entrance optic. The application of a photomultiplier will therefore be investigated, but in this case the advantage of a stable spectral responsivity will be lost.

ACKNOWLEDGEMENT

This report was compiled within the EMRP ENV03 Project “Traceability for surface spectral solar ultraviolet radiation”. The EMRP is jointly funded by the EMRP participating countries within EURAMET and the European Union.

The authors thank K. Anhalt, S. Schiller and P. Sperfeld for providing the sources of irradiance.

REFERENCES

1. J. Gröbner, et al.: “Traveling reference spectroradiometer for routine quality assurance of spectral solar ultraviolet irradiance measurements”, Appl. Opt., 44, 5321-5331, 2005.
2. S.P. Davis, M.C. Abrams, J.W. Brault: "Fourier Transform Spectrometry", Academic Press, 2001.
3. W. Herres, J. Gronholz: "Understanding FT-IR Data Processing, Part 1 - 3". Comp. Appl. Lab., 2, 216, 1984.
4. P. Meindl, C. Monte, and M. Wähmer: "Adaptation of a Fourier transform spectrometer as a reference instrument for solar UV irradiance measurements", AIP Conf. Proc. 1531, 829, 2013.
5. J. Hollandt, R. Friedrich, B. Gutschwager, R.D. Taubert, J. Hartmann: “High-accuracy radiation thermometry at the Nat. Metr. Inst. of Germany, the PTB”, High Temperatures - High Pressures 35/36, 379-415, 2003/2004.
6. J. Hartmann, K. Anhalt, R.D. Taubert, J. Hollandt: “Absolute Radiometry for the MeP-K: The Irradiance Measurement Method”, Int. J. Thermophys. 32, 1707-1718, 2011.
7. J. Gröbner, P. Sperfeld: “Direct traceability of the portable QASUME irradiance scale to the primary irradiance standard of the PTB”, Metrologia 42, 134–139, 2005.
8. J. Gröbner, M. Blumthaler: "Experimental determination of the reference plane of shaped diffusers by solar ultraviolet measurements", Opt. Lett. 32, 80-82, 2007.

Realization of Improved Solar UV Diffusers

Tomi Pulli[1], Petri Kärhä[1,2], Josef Schreder[3], Joop Mes[4], Allard Partosoebroto[4], and Erkki Ikonen[1,2]

[1]*Metrology Research Institute, Aalto University, Espoo, Finland,*
[2]*Centre for Metrology and Accreditation (MIKES), Espoo, Finland,*
[3]*CMS - Ing. Dr. Schreder GmbH, Kirchbichl, Austria,*
[4]*Kipp & Zonen, Delft, The Netherlands*
Corresponding e-mail address: tomi.pulli@aalto.fi

Global solar ultraviolet (UV) irradiance measurements require entrance optics whose angular response is proportional to the cosine of the zenith angle of radiation. The cosine response is typically achieved using a diffuser assembly. We have realized such devices with the aid of a Monte Carlo based method for simulating light transport in the diffuser. The method can be used to optimize the dimensions of the diffuser element itself as well as those of the diffuser housing and the protective weather dome. Two prototype solar UV diffuser assemblies were realized that have integrated cosine errors of f_2 = 2.3 % and 1.4 %. The simulation results for the latter prototype agree well with the measured angular responses.

INTRODUCTION

Solar ultraviolet (UV) radiation has various harmful health effects, including photokeratitis, erythema, and different forms of skin cancer. Therefore, accurate monitoring of solar UV irradiance is of great importance. As UV radiation scatters strongly in the atmosphere, an instrument that measures global UV irradiance needs to collect radiation from the entire hemisphere. The angular response of such an instrument should be proportional to the cosine of the zenith angle of radiation and independent of the azimuth angle of radiation. Non-ideal angular response of the instrument is one of the most significant sources of uncertainty in solar UV irradiance measurements [1]. While the measurement data can be corrected to some extent based on the known angular distribution of UV radiance at the time of the measurement, this approach has a limited accuracy only. Therefore, the quality of the entrance optics remains of utmost importance.

Shaped diffusers are commonly used at the entrances of global irradiance measuring instruments to reach near-ideal angular responses. As optimizing the dimensions of the diffuser assembly through trial-and-error prototyping can be very time-consuming and expensive, we have developed a Monte Carlo based method for simulating radiation transport inside the diffuser [2]. The method can be used to optimize different types of diffuser assemblies.

SIMULATION ALGORITHM

The diffuser assembly (Fig. 1) used in the simulations consists of a diffuser element, a protective weather dome, a shadow ring to block radiation at high incident angles, and mechanics for holding the optical elements together. The transmitted photons are collected using a detector – e.g. a photodiode or an optical fiber – behind the diffuser element.

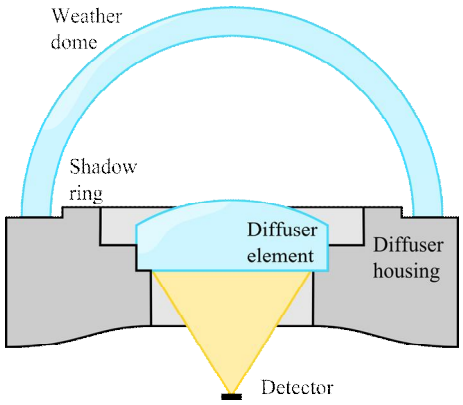

Figure 1. Schematic structure of the diffuser assembly used in the simulations.

The diffuser simulation algorithm is based on Monte Carlo ray tracing. For simulation efficiency reasons, packets of rays, here referred to as ‘particles’, are traced from the detector towards the sky. The particles that enter the diffuser element scatter multiple times before transmitting through the diffuser-air interface. The propagation-absorption-scattering cycle inside the diffuser element is implemented as detailed in refs. [2] and [3].

At the material interface, the particle is split into transmitted and reflected components according to Snell’s law and Fresnel equations. The reflected particle continues to propagate inside the diffuser. The transmitted particle contributes to the angular response of the device provided that it does not hit

the mechanics of the diffuser assembly. The effects of the weather dome on the weight and the propagation direction of the transmitted particle are accounted for in the simulation algorithm.

The ray tracing process is repeated for several particles to obtain the angular response of the diffuser assembly. A typical simulation of 10^9 particles takes approximately 10 – 15 min to complete on a modern quad core processor.

The simulation algorithm was validated by comparing the measured and the simulated angular responses at different detector geometries. Detailed description of the measurement procedure for determining the material parameters and for validating the algorithm can be found in ref. [2].

DIFFUSER PROTOTYPES

Two diffuser prototypes were constructed – one with a fiber connector and the other to be used with the Brewer spectroradiometer. In both cases, the diffuser element was a planar disc made of synthetic quartz material where gas pockets acted as scattering centers for radiation [4]. The diameters of the diffuser elements were 11 mm and 22 mm for the fiber and Brewer devices, respectively. A protective weather dome was incorporated in both structures.

Figure 2 shows the measured (circles) and the simulated (line) cosine errors of the first prototype of the new diffuser assembly for the Brewer spectroradiometer. The relatively large difference between the measured and the simulated cosine errors suggests that the spatial uniformity of the responsivity of the spectroradiometer along the diffuser area should be investigated more carefully. The effect of the exact shape and position of the weather dome on the results will also be further studied. The measured integrated cosine error of the diffuser was f_2 = 2.3 %.

Figure 3 shows the measured (red circles) and the simulated (red solid line) cosine errors of the second prototype of the diffuser assembly with the fiber connector. For comparison the cosine errors of the same device without the weather dome are also presented (blue squares, dashed line). The simulation parameters were the same as the actual dimensions of the diffuser assembly, with an exception of the diameter of the area of the diffuser that is visible to the detector, which was decreased by 1.3 mm. The difference in the diameters of the visible area of the diffuser between the simulations and the actual device is most likely explained by the angular response of the fiber head of the detector. The measured integrated cosine error of the prototype diffuser was f_2 = 1.4 %.

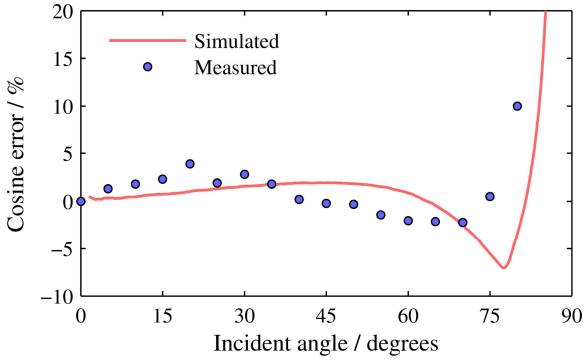

Figure 2. Measured and simulated cosine errors of the new diffuser for Brewer spectroradiometer.

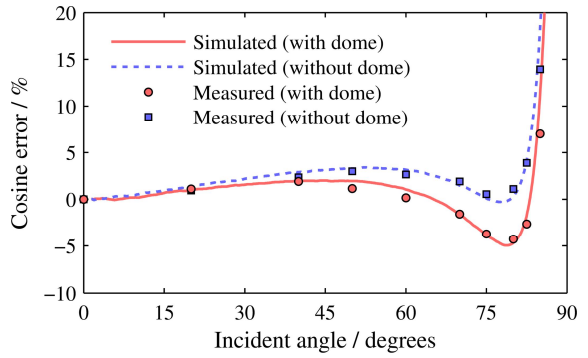

Figure 3. Measured and simulated cosine errors of the diffuser with the fiber connector with and without the protective weather dome.

ACKNOWLEDGMENTS

The work leading to this study was partly funded by the European Metrology Research Programme (EMRP) ENV03 Project “Traceability for surface spectral solar ultraviolet radiation”. The EMRP is jointly funded by the EMRP participating countries within EURAMET and the European Union.

REFERENCES

1. G. Bernhard, and G. Seckmeyer, Uncertainty of measurements of spectral solar UV irradiance, J. Geophys. Res., 104, 14321-14345, 1999.
2. T. Pulli, P. Kärhä, and E. Ikonen, A method for optimizing the cosine response of solar UV diffusers, J. Geophys. Res. Atmos., 118, 7897-7904, 2013.
3. L. Wang, S. L. Jacques, and L. Zheng, MCML — Monte Carlo modeling of light transport in multi-layered tissues, Comput. Meth. Programs. Biomed., 47, 131–146, 1995.
4. B. Barton, P. Sperfeld, S. Nowy, A. Towara, A. Höpe, S. Teichert, G. Hopfenmüller, M. Baer, and T. Kreuzberger, Characterization of new optical diffusers used in high irradiance UV radiometers, Poster presented at NEWRAD 2011, Maui, Hawaii, September 19–23, 2011.

Calibrating a Telescope for NIST Stars – SI Traceable Measurements of Stellar Spectral Flux

John T. Woodward[1], Claire E. Cramer[1], Peter Zimmer[2], John T. McGraw[2], and Keith R. Lykke[1]

[1]*National Institute of Standards and Technology, Gaithersburg, Maryland, USA,*
[2]*Univeristy of New Mexico, Albuquerque, New Mexico, USA*
Corresponding e-mail address: john.woodward@nist.gov

We have undertaken a campaign to calibrate the top-of-the-atmosphere absolute spectral flux for a catalogue of standard stars using a terrestrial telescope. Our approach involves calibrating a telescope-spectrometer system by imaging a terrestrial, spectrally calibrated source, then measuring the spectral flux from the target star. These measurements must be corrected for the atmospheric attenuation of the light along the respective paths. We will describe our overall approach to this challenging calibration problem and present preliminary results for the telescope-spectrograph calibration and measurement of the horizontal atmospheric transmission.

INTRODUCTION

Absolute stellar spectroradiometry is based on measurements in the 1970s of α Lyr (Vega) calibrated against a terrestrial blackbody source.[1] More recent observations have indicated that Vega may not be a suitable star for a radiometric standard. It is believed to be a pole-on, rapidly rotating star and contains a debris disk, both of which greatly complicate the modelling required to extend the calibration beyond the measured wavelengths.[2;3]

In the intervening decades, there have been significant advances in both radiometry and in measuring and modelling the effect of the atmosphere on light during its path to the telescope. A well calibrated (<1% uncertainty) catalogue of standard stars would have benefits for fundamental astronomy research, as well as potential applications in other scientific and commercial fields. We have previously reported the development of the Telescope Calibration Facility (TCF) at NIST for the calibration and testing of instrumentation for a field campaign.[4]

EXPERIMENTAL APPROACH

Our fundamental experimental approach to stellar radiometric calibration adheres closely to the 1970s measurements and is being performed at the same location, the F. L. Whipple Observatory at Mt. Hopkins, AZ. A calibrated light source is placed on the summit of Mt. Hopkins and observed with a telescope located on the Mt. Hopkins Ridge. The telescope then observes the target stars for calibration. Measurements of the atmospheric transmission along the light path from the summit to the telescope (horizontal transmission) and the telescope to the star (vertical transmission) are then used to correct the calibration for the atmospheric transmission.

Our observation telescope is a 25 cm Dall-Kirkham style telescope with a custom built spectrometer with ~ 1 nm resolution. This telescope can point at the Mt Hopkins summit, allowing observation of the calibration source during each night's observations.

The calibration source on the summit consists of an integrating sphere illuminated by a small tungsten halogen lamp. The output is designed to approximate the flux of a bright star when observed from the ridge, 846 meters away. A commercial spectrometer with an irradiance head calibrated to a NIST standard FEL lamp is used to calibrate the output of the source before and after it is observed by the telescope. The stability of the source is measured by a spectrometer fiber-coupled to the sphere.

To correct for the horizontal atmospheric transmission we directly measure the radiance from a large integrating sphere located near the telescope at the ridge. A small telescope with a spectrometer measures the radiance a few meters from the sphere at the ridge and then is moved to the summit to repeat the measurement while the observation telescope is measuring the calibration source. The ratio of the radiance measurement from the summit to the one at the ridge yields the atmospheric transmission which is used to correct the calibration of the observation telescope.

The correction for the vertical atmospheric transmission will be done with a combination of LIDAR measurements and atmospheric modelling. A portable system based on the University of New

Mexico's Atmospheric LIDAR for Extinction (ALE)[5] is under development and scheduled to be deployed at Mt. Hopkins later this year.

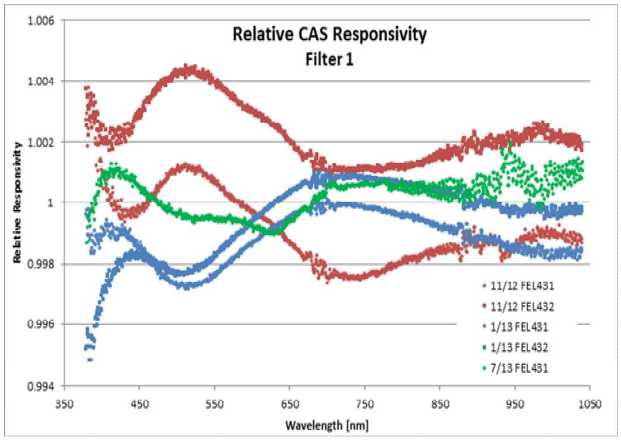

Figure 1. The relative responsivity of the calibration transfer spectrometer over multiple deployments spanning eight months.

RESULTS

Figure 1 shows the stability of the transfer spectrometer used to calibrate the summit source in the field. The reproducibility of the spectrometer responsivity calibration in the lab across multiple deployments gives us a high degree of confidence in the field calibrations.

Figure 2 shows a time series of the atmospheric transmission at 5 wavelengths over 3 hours on the morning of June 26, 2013. The transmittance is relatively stable until predawn light contaminates the measurement after 5:00 am. The lower transmittance for shorter wavelengths is primarily due to Raleigh scattering.

By measuring the atmospheric transmission simultaneously with telescope observations of the calibrated source we achieve absolute calibration of the observing telescope/spectrometer from 400 nm to 1000 nm. We are currently meeting the 0.5% uncertainty requirement assigned to the telescope calibration over the range 550 nm to 850 nm with the uncertainty dominated by the atmospheric transmission measurement.

With the addition of LIDAR measurements to characterize the light path through the atmosphere during stellar observations we are on target to make spectral irradiance measurements of standard stars at the 1% uncertainty level.

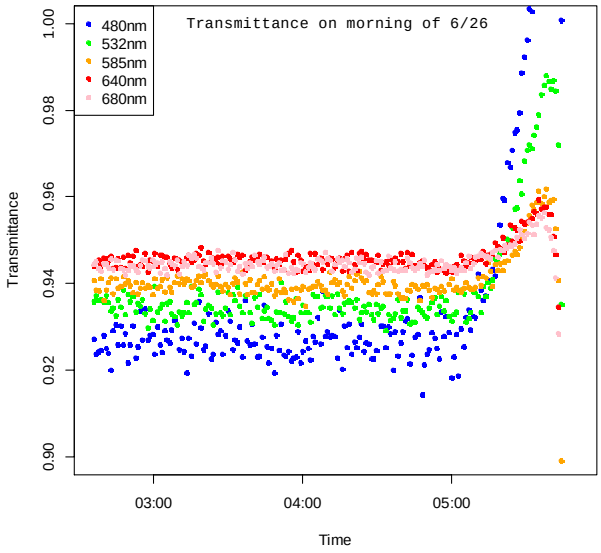

Figure 2. A plot of the atmospheric transmission between the summit calibration source and the observation telescope (846 meter path) at 5 different wavelengths as a function of time on the morning of June 26, 2013. Sunrise was shortly after 5:00 am local time.

REFERENCES

1. D.S. Hayes, Measurements of the Monochromatic Flux From Vega in the Near-Infrared, Astrophysical Journal, 197, 587-592, 1975.
2. D.M. Peterson, Vega Is a Rapidly Rotating Star, Nature, 440, 896-899, 2006.
3. C. Mégessier, Accuracy of the Astrophysical Absolute Flux Calibrations: Visible and Near-Infrared, Astronomy and Astrophysics, 296, 771-778, 1995.
4. A.W. Smith, Absolute Flux Calibration of Stars: Calibration of the Reference Telescope, Metrologia, 46, S219-S223, 2009.
5. P.C. Zimmer, Space-Based Photometric Precision From Ground-Based Telescopes, 2010.

Measurements of window transmittance for a Cryogenic Solar Absolute Radiometer

Benjamin Walter[1], Wolfgang Finsterle[1], André Fehlmann[2], and Werner Schmutz[1]

[1]*Physikalisch Meteorologisches Observatorium Davos (PMOD) and World Radiation Center (WRC), Dorfstrasse 33, 7260 Davos Dorf, Switzerland,* [2]*Institute for Astronomy, University of Hawaii, 34 'Ōhi'a Kū Street, Pukalani, USA*
Corresponding e-mail address: benjamin.walter@pmodwrc.ch

The Cryogenic Solar Absolute Radiometer (CSAR) aims to increase the accuracy of terrestrial Total Solar Irradiance (TSI) measurements [1]. Because TSI entering a cryogenic radiometer is partly reflected and absorbed by the entrance window, the integral transmittance of the broad-band solar irradiance needs to be determined in parallel to correct the power reading of the CSAR instrument. Therefore, the "Monitor to measure the Integral TRAnsmittance of windows" (MITRA) aims to measure the integral transmittance of windows with an accuracy of less than 100 ppm. Recent design improvements to the MITRA instrument resulted in an accuracy of 150 ppm for laboratory conditions. We report on the progress which was made to reduce the uncertainty of the MITRA.

INTRODUCTION

The goal of the joint project between the NPL and the Swiss National Metrology Institute (METAS) launched in 2007 is to build a cryogenic radiometer (CSAR) for TSI measurements [1]. Operating a radiometer at cryogenic temperatures in a vacuum significantly improves the equivalence of optical and electrical heating, allowing for more accurate radiant power measurements than obtained with ambient temperature radiometers as currently used for the World Radiometric Reference (WRR). The goal is to measure ground-based TSI with an accuracy of better than 0.01%, which improves the current accuracy of the WRR of 0.3% by a factor 30.

Because the entrance window of the CSAR instrument has a certain wavelength dependent transmissivity, a correction factor for the attenuation of the solar irradiance needs to be determined. As the solar spectrum significantly changes on diurnal, daily and monthly time scales because of a changing air mass and optical depth, such a correction factor needs to be determined simultaneously to the CSAR measurements. The MITRA instrument (Fig. 1) allows for simultaneously measuring the integral transmittance of the CSAR entrance window with high accuracy.

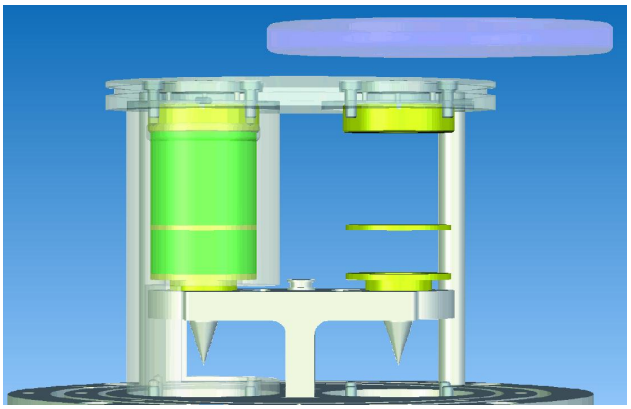

Figure 1. The MITRA instrument. The right cavity (upwards facing cone) is obstructed by the window.

METHODS

The MITRA instrument has two absorbing cavities for measuring the temperature rise against a common heat sink (Fig. 1). One of the two cavities is periodically covered by a window from the same production batch as the one used for the CSAR. The ratio of the two detectors temperature rise is used to eliminate drifts in the detector signals. The ratio of the obstructed and the unobstructed detector ratios defines the integral transmittance t_{int} of the window.

Recent design improvements to the MITRA instrument were tested by means of "dark measurements", showing an increase in the average measurement accuracy from 400 ppm down to less than 30 ppm (k =1). The improvements include the electrical separation and shielding of the motor driving the window guiding rail and the implementation of a high accuracy current measurement device. This result shows that the instruments temperature sensing and readout electronics performs well and meet the intended accuracy goal of σ = 100 ppm.

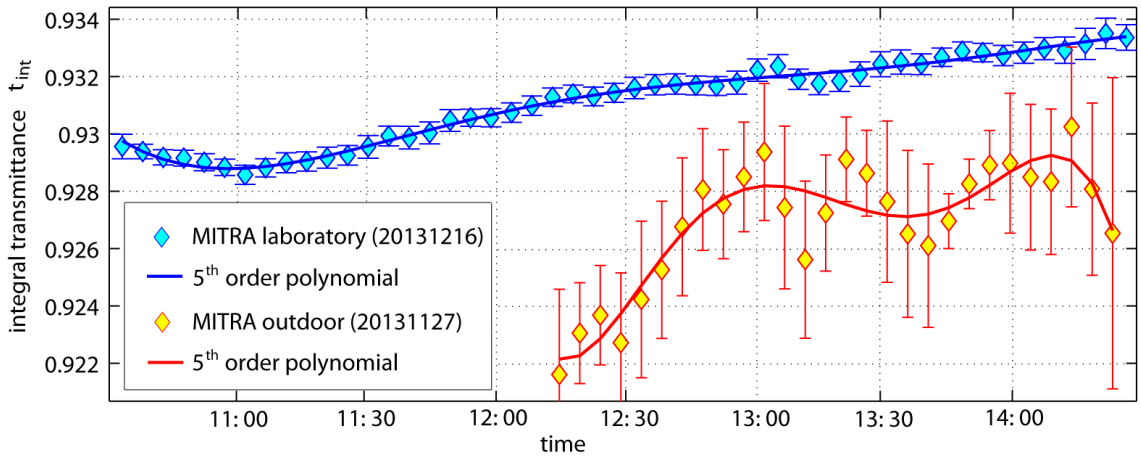

Figure 2. Integral transmittance measurements under laboratory and outdoor conditions.

RESULTS AND DISCUSSION

First measurements of the integral transmittance of a quartz window under laboratory conditions show that the improved design of the MITRA instrument allows now for detecting diurnal variations of t_{int} (Fig. 2). The accuracy of the de-trended variations after fitting and subtracting a 5th order polynomial function is σ_{lab} = 150 ppm. For the experiments, the solar radiation is guided via two mirrors of a newly installed heliostat at the PMOD into the laboratory. According to the simulations performed by Fehlmann [2], the integral transmittance should increase from 0.9268 in the morning to 0.9271 during noon and afterwards decrease again, depending on the zenith angle of the sun and thus the air mass in a standard atmosphere. Our measurements detect a diurnal trend, although at a slightly higher absolute transmittance value which indicates that the atmospheric conditions differ from those used in the simulations. Additional deviations may result from spectral variations induced by the heliostat. Because of varying incidence angles of the solar radiation on the first mirror, the spectra might be slightly altered by polarization effects. Furthermore, an increasing ambient air temperature together with the solar irradiance on the mirrors results in an increase of the temperature of the heliostat mirrors and thus its infrared emission towards the MITRA instrument.

The so far best outdoor measurement on the sun tracking platform of the WRR in Davos shows a significantly lower average integral transmittance t_{int} compared to the laboratory measurement (Fig. 2). The average level of the outdoor measurement agrees well with the values of $0.9268 < t_{int} < 0.9271$ predicted by the simulations of Fehlmann [2]. However, the t_{int} values show stronger diurnal variations and scatter than the laboratory measurements. The accuracy of the de-trended t_{int} -variations is σ_{out} = 900 ppm in this case. These stronger variations are mainly a result of unstable environmental conditions, such as wind. As the entire MITRA instrument gets heated by the ambient air and the solar irradiance during the course of a day, it was found that temperature drifts larger than ±2 °C h^{-1} result in a significant decreased of the measurement accuracy. Generally, successful t_{int} measurements with the intended high accuracy of 100 ppm can only be performed at perfect atmospheric and environmental conditions, meaning no wind, a clear sky and small air temperature changes. To increase the outdoor measurement accuracy from 900 ppm down to the intended 100 ppm, future work on this project will focus on the elimination of strong temperature drifts, wind influences, and a non-uniform heating of the MITRA instrument.

ACKNOWLEDGMENTS

We would like to thank the European Research Council (ERC) for the financial funding of this work which is part of the Joint Research Project ENV04-MetEOC. Furthermore we would like to thank Ricco Soder, Daniel Pfiffner and Nathan Mingard for their technical support.

REFERENCES

1. R. Winkler, Cryogenic Solar Absolute Radiometer – a potential replacement for the World Radiometric Reference, PhD thesis, University College London, 2011.
2. A. Fehlmann, Metrology of Solar Irradiance, PhD thesis, University of Zürich, 2011.

Sourcemeter Method for Accurate Measurement of Differential Spectral Responsivity for Large Size Solar Cell

Xuebo Huang[1], Chi Yung Siew[2], and Patrick Ng[1]

[1]*National Metrology Centre, Agency of Science, Technology, and Research, Singapore,*
[2]*Department of Mechanical Engineering, National University of Singapore, Singapore,*
Corresponding e-mail address: huang_xuebo@nmc.a-star.edu.sg

The differential spectral responsivity (DSR) measurement is one of primary calibration methods for measuring the short circuit current of a reference solar cell under standard testing conditions. The problem in DSR measurement of a large size (156 mm x 156 mm) solar cell is how to detect a weak AC photocurrent (~10 μA) produced by the cell under a modulated monochromatic light from a big DC photocurrent (> 8 A) background produced by the cell under a sun-like bias light. The sourcemeter method has been developed, with which the big DC current can be removed and weak DSR AC signal can be measured accurately.

INTRODUCTION

The differential spectral responsivity method, which has been described in detail in previously published papers [1] and IEC60904 [2] , has long been established as one of primary calibration methods for reference solar cell. While small cells are nowadays calibrated using the DSR method on a regular basis, additional problems exist for solar cells with large size (156 mm x 156 mm).

The DSR method involves the generation of a DC current by applying a bias light source together with a probe beam is used to generate an alternating current (AC) signal, which is used to determine the differential spectral responsivity of the solar cell. During the measurement, the DC current should be removed so as to prevent the pre-amplifier being saturated. For a small cell such as a WPVS reference cell, no further action is usually required as the pre-amplifier is able to remove the small DC current (<0.2 A) without intervention as shown in Fig. 1. However, for a large cell, the DC current generated might be significantly large (> 8A) enough that it cannot be passed directly to the pre-amplifer without resulting in saturation of the amplifier. Hence, for accurate measurement of large solar cells, the additional efforts would be needed for the DSR measurement.

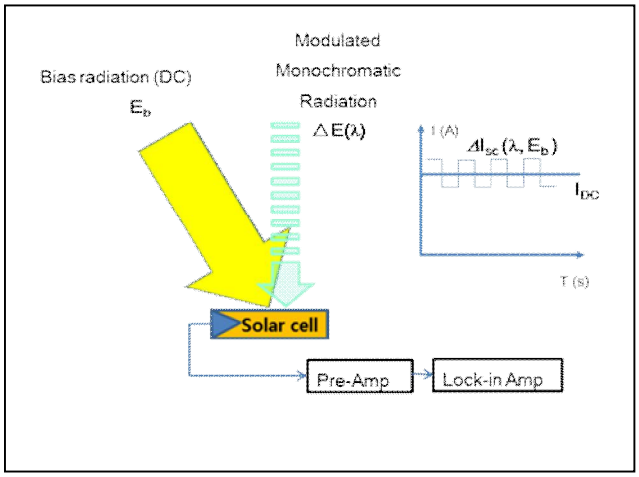

Figure 1. DSR measurement of solar cell under dual beam radiation.

MEASUREMENT METHOD

There are a variety of proposed methods in dealing with the large DC current generated during DSR measurement such as using a band pass filter or a variable resistor but unsuccessful. This paper will focus on the sourcemeter method, which has been developed and currently being employed at the National Metrology Centre, Singapore.

The sourcemeter method essentially involves the use of an external sourcemeter to provide a DC current with a same value of the short circuit current generated by the cell under the bias light. According to I –V characterisation of a solar cell, when DC photocurrent reaches to short circuit current of the cell, DC voltage across the cell will be zero while the AC signal can be detected by a pre-amplifier and a lock-in amplifier without saturation. As the DC photocurrent will be changing with bias light, the DC voltage of the cell will be changing accordingly. In order to keep zero DC voltage of the cell, the amount of DC current provided by source meter would then be adjusted accordingly. This closed loop control

process was established using LabView programme as shown in Figure 2.

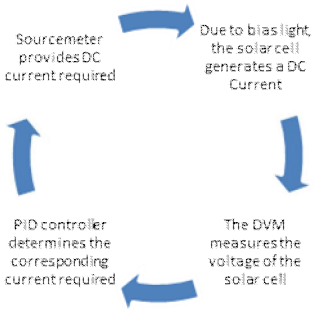

Figure 2. Closed loop control process for DC current adjustment.

MEASUREMENT RESULTS

The DSR measurement of poly-crystalline silicon solar cell (156 mm x 156 mm) was carried out under bias radiation of 370 W/m^2 on the full area of the cell and its result is shown in Figure 3.

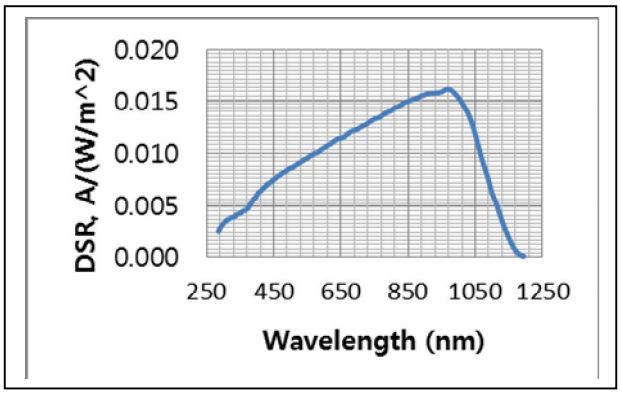

Figure 3. Differential spectral responsivity of a poly-crystalline silicon solar cell (156 mm x 156 mm).

UNCERTAINTY EVALUATION

The DSR is measured by comparison of the outputs at each wavelength from the test solar cell and reference photodiode, which was performed through two rounds of automatic wavelength scans by the monochromator. In order to correct for probe beam fluctuation during each scan, the monitor signal is recorded simultaneously with the reference photodiode or test cell signal at each wavelength and the DSR is calculated using the following formula:

$$DSR(\lambda) = s_R(\lambda)\frac{I_T / I_{MT}}{I_R / I_{MR}} \quad (1)$$

where $s(\lambda)$ is spectral responsivity of reference photodiode, I_T and I_{MT} are photocurrents of test cell and monitor respectively, I_R and I_{MR} are photocurrents of reference photodiode and monitor respectively.

The measurement uncertainty of DSR of the test cell includes the following components:

1) Uncertainty of reference photodiode calibration;
2) Uncertainty due to monochromator wavelength error and bandwidth setting;
3) Repeatability of photocurrent measurements;
4) Uncertainty due to normalisation process;
5) Non-linearity of preamplifier;
6) Non-linearity of lock-in amplifier;
7) Spatial non-uniformity of probe beam;
8) Spatial non-uniformity of bias beam;
9) Positioning and alignment error of reference photodiode and test cell;
10) Uncertainty due to temperature deviation from 25 °C;
11) Uncertainty due to bus-bar probe shading effect.

CONCLUSION

The source meter method has been developed for accurate measurement of differential spectral responsivity of large size solar cell. The weak AC signal produced by the test cell under modulated monochromatic radiation was detected from big DC current background produced by the cell under strong bias radiation using this method. LabView programme has been developed for closed loop control of short circuit current to remove the big DC current so that the measurement can be carried out automatically. The measurement uncertainty was evaluated and discussed in this paper.

REFERENCES

1. J. Metzdorf, “Calibration of Solar Cells 1: The differential spectral responsivity method”, Appl. Opt., vol 26, no. 9, 1987.
2. Standard IEC 60904-4, Photovoltaic devices Part 4: Reference Solar devices - Procedures forestablishing calibration traceability, International Electrotechnical Commission, Geneva, Switzerland.

Calibration facilities for space missions at the Metrology Light Source

R. Klein, R. Fliegauf, A. Gottwald, M. Kolbe, W. Paustian, T. Reichel,
M. Richter, R. Thornagel, and G. Ulm

Physikalisch-Technische Bundesanstalt (PTB), Berlin, Germany
Corresponding e-mail address: roman.klein@ptb.de

PTB has a long tradition in the calibration of space-based instruments using synchrotron radiation to cover the UV, VUV and X-ray spectral range. New instrumentation at the electron storage ring Metrology Light Source (MLS) has been put into operation that opens up extended calibration possibility within this framework. In particular, the set-up of a large vacuum vessel that can accommodate entire space instruments opens up new prospects. Moreover, a new facility for the calibration of radiation transfer sources with a considerably extended spectral range as been put into operation.

INTRODUCTION

Space observations in the UV, VUV and X-ray spectral range are often essential for a deeper understanding of astrophysical phenomena. Particularly, the observation of solar VUV radiation is of increasing importance for various scientific questions, such as solar and atmospheric research, e.g., for space weather forecasts. These investigations often require the absolute measurement of radiometric quantities. Based on synchrotron radiation (SR), PTB can perform these absolute measurements traceable to primary national standards, either in a detector-based (DB) calibration scheme or in a source-based (SB) scheme [1-3]. Over the past decades, PTB has performed calibrations in the frame of scientific co-operations for numerous space-missions (see Table 1 in ref. [4] or Fig. 16 in ref. [3]) and has developed into an important partner for activities related in this field [5]. With the new setups at the MLS [6, 7], PTB substantially extends its capability.

NEW VACUUM VESSEL FOR SPACE INSTRUMENTS

A new vacuum vessel that can accommodate instrumentation of up to 1.2 m in lengths, 0.6 m in width and height, and 100 kg in weight is available now at the MLS. The vacuum tank can be connected to an ISO 5 certified clean room facility for the handling and loading of delicate instruments. This clean room facility consists of three separate compartments for unpacking, assembling, and loading of the instrument. After loading, the vacuum vessel can be moved to several beamlines inside the laboratory for measurements. The front plate, facing the incoming SR, has different flanges that also allow asymmetric mounting to the beamline. By means of computer controlled stepper motors, the instrument inside the tank can be precisely positioned within a range of 140 mm horizontally and 120 mm vertically and an angular range of 6°. The tank itself can be moved by an additional 220 mm in the horizontal as well as the vertical direction. The step-width is 0.5 µm and 0.7'' for the spatial and angular movement, respectively. Moreover, the mounting structure inside the tank holding the instrument under test, is designed in such a way that the instrument can be rotated by 90° in orientation along the optical axis. This is important to take account of the polarization properties of the SR, if an instrument with a polarization dependent response is calibrated.

SOURCE-BASED CALIBRATIONS

In the UV, VUV and X-ray spectral range, electron storage rings, the spectral radiant intensity of which can by calculated by classical electrodynamics [8], are used as primary sources. At PTB, these are BESSY II [9] and the MLS [6]. In this paper, we focus on the latter one. SB calibrations can then be done either by direct calibration of the instrument under test with radiation of the primary source standard or by means of a transfer source, that itself had been calibrated traceably to the primary source standard. In the past, only the latter scheme was incorporated due to the lack of instrumentation for the handling of large space instruments in the PTB laboratory. Prominent examples for such calibrations are the calibration of transfer sources that have been used for the calibration of the CDS and SUMER spectrographs of the SOHO mission [10, 11]. For the calibration of transfer sources, a new facility has been set-up at the MLS that covers the spectral range from 7 nm to 400 nm [12].

The new large vacuum vessel now also allows the handling of complete space instruments, so opening up the way for calibration of space instruments directly to the primary source standard MLS. Since SR has a continuous spectrum, the direct calibration with the calculable, undispersed radiation is in most cases only applicable to wavelength- or energy-dispersive instruments. The direct calibration has some potential advantages as compared to the detour using transfer sources: since white radiation is used, all wavelengths are available and a spectrometer can, in principle, be calibrated by a one shot illumination over the entire spectral range. Secondly, avoiding the use of transfer sources should allow reducing the measurement uncertainties of the calibration. Moreover, large opening apertures of the instrument can be illuminated, avoiding the mapping of the instrument acceptance with a pencil beam. Furthermore, the radiant intensity of the SR can be varied over many decades by adjustment of the electron beam current, thus enabling the investigation of the linearity in response of the instrument under test.

However, the direct, white light calibration has some disadvantages that have to be traded off against the advantages: one has to avoid second order diffraction contributions and has to cope with the high degree of polarization of the SR radiation. The first one can be mitigated by a proper choice of the electron energy [13], the latter one by a calibration under two orientations with respect to the incident polarization vector of the radiation. Moreover, one has to consider, that, even if the SR radiation source point is at a large distance to the instrument under test, it is not located at infinity as many space instrument expect it to be. If, e.g., the space instrument images the source point onto an entrance slit, the focal point during SR calibration will be located slightly behind the position at which it would be located for collimated light from a point at infinity. So, care has to be taken to avoid vignetting of radiation during calibration. A direct calibration with calculable SR is planned for the calibration of the SPICE (Spectral Imaging of Coronal Environment) spectrometer onboard of the Solar Orbiter Mission [14].

Furthermore, another new perspective is opened up by having the vacuum vessel as well as the transfer source calibration facility in-house: for a calibration of instruments by means of a transfer source, this transfer source can be rather easily recalibrated at short notice and without being transported outside the laboratory. This also should enable us to reduce the relative uncertainty in the calibration in this scheme. E.g., using a hollow cathode transfer source, a dominant contribution to the relative uncertainty in the calibration is given by the reproducibility after anode replacement. This contribution to the uncertainty budget can be eliminated by near-term in-house recalibration.

DETECTOR-BASED CALIBRATIONS

DB calibrations are conducted traceable to a cryogenic electrical substitution radiometer [15] as a primary detector standard at one of the beamlines using monochromatized SR [4]. These calibrations comprise the calibration of complete instruments as, e.g., the LYRA (LYman-alpha RAdiometer) or SOL-ACES (SOLar Auto-Calibrating EUV/UV Spectrophotometers) spectrometers or the calibration of single components as detectors, e.g., for the BOLD (blind to optical light detectors) project [16]. Moreover, by reflectometry, various other components, such as reflective mirrors, gratings or filters can be characterized.

The new vacuum vessel, when operated at a beamline with monochromatized radiation, also allows the DB calibration of complete large space instruments. In the near future, the EUI (Extreme Ultraviolet Imager) spectrometer [17] onboard of the Solar Orbiter mission is planned to be calibrated that way.

REFERENCES

1. Ulm G 2003 *Metrologia* **40**, S101.
2. Hollandt et al. in: Optical Radiometry', ed. by A. Parr, R. Datla, J. Garner, Vol. 41 of Experimental Methods in the Physical Sciences, Elsevier, p. 213.
3. Beckhoff B et al. 2009 *Phys. Status Solidi* **B 246**, 1415.
4. Klein R et al. 2013 *AIP Conf. Proc.* **1531**, 879.
5. Richter M et al. 2006 *Advances in Space Research* **37**, 265.
6. Klein R et al. 2008 *Phys. Rev. Special Topics - Accelerators and Beams (PRST-AB)* **11**, 110701.
7. Klein R et al. 2009 *Metrologia* **46**, S266.
8. Schwinger J 1949 *Phys. Rev.* **75**, 1912.
9. Thornagel R et al. 2001 *Metrologia* **38**, 385.
10. Hollandt J et al. 1993 *Metrologia* **30**, 381.
11. Wilhelm K et al. 1997 *Appl. Opt.* **36**, 6416 (1997).
12. Thornagel R et al. these proceedings.
13. Didkovsky L et al. 2012 *Solar Phys* **275** 179.
14. Fludra A et al. 2013 *Proc. SPIE* **8862**, Solar Physics and Space Weather Instrumentation V, 88620F.
15. Gottwald A et al. 2010 *Meas. Sci. Technol.* **21**, 125101
16. BenMoussa A et al. *2006 Meas. Sci. Technol.* **17,** 913.
17. Halain J-P 2012 *Proc. SPIE* **8443**, Space Telescopes and Instrumentation: Ultraviolet to Gamma Ray, 844307.

Characterisation of nonlinearities of array spectroradiometers in use for measurements of the terrestrial solar UV irradiance

Saulius Nevas[1], Peter Blattner[2], Omar El Gawhary[3], Tomi Pulli[4], Petri Kärhä[4], Luca Egli[5], and Julian Gröbner[5]

[1] *Physikalisch-Technische Bundesanstalt (PTB), Braunschweig and Berlin, Germany,*
[2] *Federal Institute of Metrology (METAS), Bern-Wabern, Switzerland,*
[3] *VSL Dutch Metrology Institute, Delft, Netherlands,*
[4] *Aalto University, Espoo, Finland*
[5] *Physikalisch-Meteorologisches Observatorium Davos, World Radiation Center, Davos Dorf, Switzerland*
Corresponding e-mail address: saulius.nevas@ptb.de

Characterisation of nonlinearities of array spectroradiometers used for measurements of the terrestrial solar UV irradiance over 5 to 6 orders of magnitude is required by the application. It is also one of the tasks within the EMRP ENV03 project. Within this framework, different setups at Aalto, METAS, PTB and VSL have been applied to the characterisations. This paper will present the technical realisations of the setups and results of comparison measurements, which are meant for the validation of the methods.

INTRODUCTION

Terrestrial solar UV irradiance varies within the relatively narrow spectral range, 280 nm to 400 nm, over a large dynamic range, i.e. 5 to 6 orders of magnitude. Hence, a linear dependence between the measured solar UV irradiance values over the whole dynamic range and the respective signals of a spectroradiometer that is used for the measurements is required, i.e the linearity of the instrument must be known. Residual deviations from the linear regime will yield errors both in absolute values as well as in relative spectral distribution of the measured solar UV irradiance. In the case of compact array spectroradiometers, the linearity of the CCD instruments is typically characterised by exposing the instrument to the radiation of a stable source and varying the integration time of the detector. This is a simple but by far not complete characterisation method. In fact, it accounts for the linearity of the signal processing electronics only. In principle, the linearity of such devices should be tested by varying the spectral irradiance level over the whole dynamic range. For the radiometric characterisation of the linearity of the spectroradiometers, the technical challenge consists in providing a radiation source the spectral irradiance of which can be dynamically tuned over 5 to 6 orders of magnitude. In the case of, e.g. halogen lamps, used for the calibration of the instruments, this is difficult.

Within the framework of an EMRP ENV03 project "Traceability for surface spectral solar ultraviolet radiation", an approach to the linearity characterisation of array spectroradiometers used for the solar UV radiation measurements has been chosen based on monochromatic sources with different setups at Aalto, METAS, PTB and VSL. This paper presents technical realisations of the setups. A comparison of the linearity measurements using the setups of the NMIs will be carried out in early spring 2014. The results will be presented at the conference. As an outcome of these activities, a mobile and validated device will be available for the linearity characterisation of array spectroradiometers of participants taking part in a UV intercomparison at PMOD/WRC, Davos, Switzerland in July 2014.

MEASUREMENT SETUPS

At PTB, a wavelength tuneable laser facility is available and can be used for the purpose of the linearity characterisations of array spectroradiometers. Within the EMRP project, the TULIP facility was extended into the solar UV spectral range based on a frequency doubling and tripling of a mode-locked Ti:Sa fs-laser [1]. A beam conditioning unit was developed providing a stable, depolarised, spectrally narrow and spatially uniform irradiance field. A specially designed fibre bundle used within the beam conditioning unit acts as a pulse-to-cw converter. A continuous wave (cw) nature of the radiation is important for the linearity characterisation of the instruments. Spectral irradiance level of up to 1 Wm^{-2} nm^{-1} can be set and attenuated by a variable filter.

A similar setup, a frequency doubled and tripled Ti:Sa ps-laser with 80 MHz repetition rate, is used at METAS. The quasi cw ps-radiation is stabilized with a liquid-crystal modulator (LCM) and a monitor detector. The beam is directly applied to the entrance optics of the spectroradiometers. The power level is changed by adjusting the working point of the LCM and adding attenuation filters.

Aalto has built a setup based on a single monochromator with two light sources. A 500-W Xe-lamp provides a smooth spectrum to carry out measurements over the UV region. A 1-kW Hg-lamp is used to provide higher intensities. The light exiting the monochromator is collimated and attenuated with interchangeable neutral-density filters in two consequent filter wheels. The light beam then continues to the device to be characterized through a beam splitter taking a fraction of the beam to a photodiode serving as the linearity reference. Intensity levels have been set so that the photocurrent of the S1337 photodiode keeps in its linear region [2].

VSL has developed a portable system, for in-situ characterisation of spectroradiometers. The device combines two linear polarisers, whose reciprocal transmission axes can be set to any angle by a rotation mount, a 2-inch averaging sphere and a reference Si detector, positioned at one of the output ports of the sphere, acting as a linearity reference. The linearity response of a device under test can be monitored by accessing the signal exiting the sphere at one of the other available sphere's output ports. The system is currently powered by a UV laser at 372 nm, but in principle other sources can be also used.

FIRST RESULTS AND OUTLOOK

First linearity characterisations of an array spectroradiometer of PMOD/WRC have already been carried out at METAS. Fig.1 and Fig. 2 show exemplary results obtained for different laser irradiance at the wavelength of 370 nm. Since the signal from each pixel within the bandpass of the spectrometer is different, the slopes of the curves in Fig. 2 are different accordingly. The curve with the highest slope in Fig. 2 (369.6 nm) corresponds to the signal of the pixel at the peak of the curves seen in Fig. 1. The measured data points deviate from the linear fit by about 1% to -1.5%. The first results obtained revealed that the method was strongly dependent on the wavelength stability of the laser.

In spring 2014, a series of measurements on several array spectroradiometers is planned at Aalto, PTB and VSL. While the measurements at Aalto and PTB are carried out using stationary facilities, the device of VSL was developed to be mobile and suitable for applications in the field. This mobile device validated in the comparison of linearity measurements among the NMIs will be used during the UV intercomparison campaign at PMOD/WRC in July 2014 to characterise array spectroradiometers used in the European solar UV measurement network.

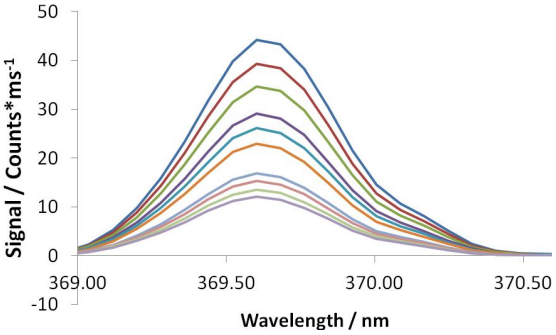

Figure 1. Signals of array spectroradiometer at different laser power setting.

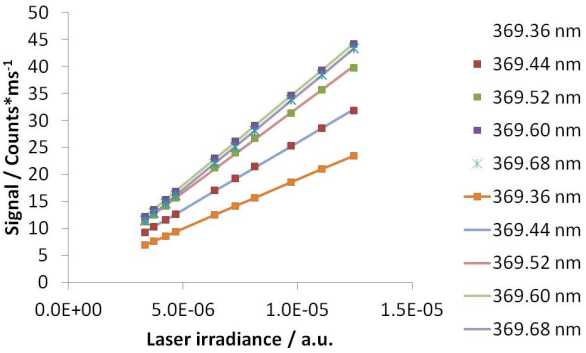

Figure 2. Signals of several detector pixels as a function of laser irradiance and linear fits to the data.

ACKNOWLEDGEMENT

Part of this work has been supported by the European Metrology Research Programme (EMRP) within the joint research project "Traceability for surface spectral solar ultraviolet radiation" (solarUV). The EMRP is jointly funded by the EMRP participating countries within EURAMET and the European Union.

REFERENCES

1. S. Nevas, Calibration of the reference spectro-radiometer for the quality assurance of the terrestrial solar spectral ultraviolet radiation measurements in Europe, in Proceedings of NEWRAD 2014.
2. T. Kübarsepp, A. Happalinna, P. Kärhä, and E. Ikonen, Nonlinearity measurements of silicon photodiodes, Appl. Opt., 13, 2716-2722, 1998.

Superposition Method for Correction of Error Caused by Bus-Bar Probe Shading Effect on Characterisation of Large Size Solar Cell

Xuebo Huang and Patrick Ng
National Metrology Centre, Agency for Science, Technology and Research, Singapore
Corresponding e-mail address: huang_xuebo@nmc.a-star.edu.sg

The bus-bar probes are used in characterisation of large size silicon solar cell. There are numbers (2 - 5) of bus-bar probe on the front surface of the cell to collect electric current produced by the cell during the measurement. As there are a few millimetres thickness of a bus-bars probe, its shading on the cell under light radiation will affect on the measurement accuracy of solar cell. In order to make a correction for the error caused, a superposition method has been developed with which the measurement error can be corrected by 3.8 % for a large size (156 mm x 156 mm) silicon poly-crystalline solar cell with three bus-bars.

INTRODUCTION

The bus-bar probes are used in characterisation of large size (e.g. 156 mm x 156 mm) silicon solar cell either in primary calibration method (e.g. Differential spectral responsivity measurement) or secondary calibration method (e.g. Indoor solar simulator based I – V characterisation). Figure 1 shows the photos of typical large size silicon solar cell and bus-bar probe.

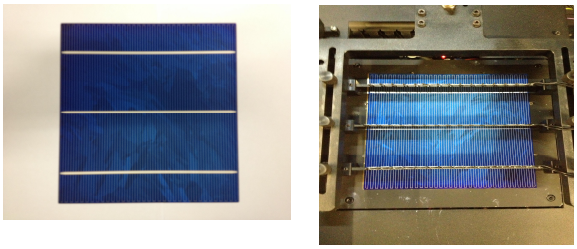

Figure 1. Photos of a solar cell with 3 bus-bars (left) and a solar cell under 3 bus-bar –probes (right)

The probes are electrical connectors which contact the cathode of solar cell and collect electrical current from the cell. There are two (or up to five) bus-bar probes in front surface of the cell during the measurement. As there are a few millimetres thickness of a bus-bars probe, its shading on the cell under light radiation will affect on the measurement accuracy as shown in Figure 2. The error caused by the bus-bar probe shading is dependent on number of the probe. The more the number of the probe is, the bigger the error of short circuit current is.

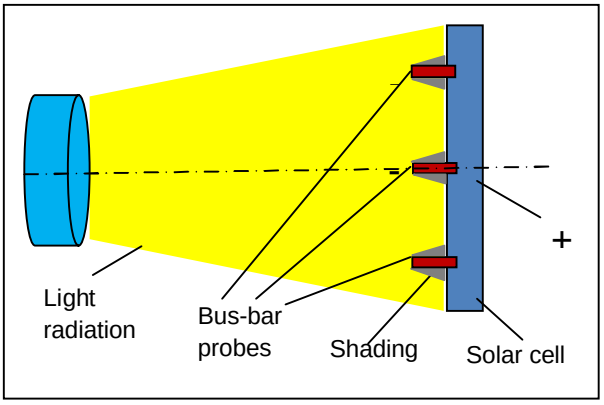

Figure 2. Bus-bar probes shading effect on solar cell

SUPERPOSITION METHOD

In order to make a correction for the error caused by bus-bar probes shading effect on solar cell, a superposition method has been developed at NMC.

Take measurement of a three bus-bars solar cell as an example. The short circuit current (SCC) of the cell was measured by three bus-bar probes when the cell was irradiated under light radiation recorded as $I_{sc\text{-}0}$. After removing bus-bar probe 1, the SCC of the cell was measured by other two bus-bar probes under same light radiation as recorded as $I_{sc\text{-}1}$.

In the same way, with removal of bus-bar probe 2 or 3, the SCC of the cell was measured and recorded as $I_{sc\text{-}2}$ or $I_{sc\text{-}3}$ respectively.

For removing the bus-bar probe 1, the correction for the SCC of the cell, ΔI_1, is calculated as shown in Eq. (1):

$$\Delta I_1 = I_{sc-1} - I_{sc-o} \qquad (1)$$

For the cell with n pieces of bus-bar probe, the SCC correction, ΔI, can be calculated as shown in Eq. (2):

$$\Delta I = \sum_{x=1}^{n} (I_{sc-x} - I_{sc-0}) \qquad (2)$$

After correction, the corrected SCC of the cell under the light radiation can be calculated as shown in Eq. (3):

$$I_{sc} = I_{sc-o} + \Delta I \qquad (3)$$

MEASUREMENT RESULTS

The measurement of poly-crystalline silicon solar cell (156 mm x 156 mm) with three bus-bars was carried out in a super solar simulator based current vis voltage characterisation tester and the correction for error caused by bus-bar shading effect was made. The measurement results are shown in the table 1 below.

Table 1. Measurement results for three bus-bar silicon solar cell with size (156 mm x 156 mm)

Removed Bus-bar probe no. (x)	*SCC of solar cell, I_{sc-x} (A)*	*Deviation of SCC after removal of bus-bar probe, ΔI_x (A)*
0	8.154	0
1	8.268	0.114
2	8.264	0.110
3	8.255	0.101
	Total (ΔI)	0.325
	$I_{sc}=I_{sc-0}+\Delta I$	8.479
	Error= $(\Delta I/ I_{sc})$	3.8%

UNCERTAIN EVALUATION

Through partial differential of Eq. (2), we obtain:

$$d(\Delta I) = \sum [\partial(I_{sc-x}) - \partial(I_{sc-0})] \quad (4)$$

Hence, measurement uncertainty of error of the SCC can be expressed as follows, assuming all components are not correlated:

$$u^2(\Delta I) = \sum [u^2(I_{sc-x}) + u^2(I_{sc-0})] \quad (5)$$

where $u(I_{sc-x})$ and $u(I_{sc-0})$ are measurement uncertainties of the SCC of the cell with removal of bus-bar probe x and without removal of bus-bar probe respectively.

The measurement uncertainty of the SCC of the cell under test with or without removal of bus-bar probes in I – V characterisation includes the following components:

1) Calibration uncertainty of SCC of the reference solar cell used in the measurement;
2) Drift of calibration value of SCC of the reference solar cell;
3) Accuracy of the current meter for measurement of SCC of the reference solar cell and the cell under test;
4) Drift of the current meter for measurement of SCC;
5) Repeatability of SCC measurements of the reference solar cell and the cell under test;
6) Accuracy of the voltage meter for voltage measurement of monitor detector for correction of light instability;
7) Drift of the voltage meter for voltage measurement of the monitor detector;
8) Repeatability of the voltage measurements;
9) Residue uncertainty after spatial non-uniformity correction of light beam;
10) Uncertainties due to temperature effect on the SCC measurements of the reference solar cell and the cell under test.

The total measurement uncertainty, $u(\Delta I)$, can be calculated according to equation (5).

CONCLUSION

A superposition method has been developed for correction of error caused by bus-bar probe shading effect on the SCC measurement of large size solar cell. With this method, the SCC measurement error of a large size silicon poly-crystalline solar cell with three bus-bars is corrected by 3.8 %. The measurement uncertainty of the SCC of the cell under test is evaluated in the paper.

REFERENCES

1. J. Metzdorf, Calibration of Solar Cells – the differential spectral responsivity method, Applied Physics, 26, 1701-1708, 1987.
2. S. Winter, T. Wittchen and J. Metzdorf, Primary Reference Cell Calibration at the PTB based on Improved DSR Facility, 16th European Photovoltaic Solar Energy Conference, Glasgow, 2000.
3. G. Xu and X. Huang, A Differential Spectral Responsivity Measuring System for Solar Cell Calibration, in Proceedings of 11th International Conference on New Developments and Applications in Optical Radiometry, edited by Seongchong Park and Erkki Ikonen, 59 - 60, 2011.
4. G. Xu and X. Huang, Primary Calibration of Solar Photovoltaic Cells at the National Metrology Centre of Singapore, Energy Procedia 25,70 – 75, 2012.

Detection Efficiency Calibration of Silicon Single-Photon Avalanche Diodes Traceable to a National Standard

S. Kück, H. Hofer, S. Peters, and M. Lopez

Physikalisch-Technische Bundesanstalt (PTB), Braunschweig, Germany
Corresponding e-mail address: stefan.kueck@ptb.de

The aim of the work presented here is the determination of the detection efficiency of Silicon Single-Photon Detectors (Si-SPAD). This determination is carried out with a newly developed measurement facility established at the Physikalisch-Technische Bundesanstalt (PTB), the German national metrology institute. The detection efficiency is determined from a measurement of the photon count rate at the Si-SPAD and its comparison with the radiation power impinging on the Si-SPAD. The latter is measured with a calibrated Si-photodiode and calibrated attenuators. The measurements are traceable to the national standard for optical radiation power via an unbroken calibration chain. A detailed measurement uncertainty analysis will be presented, giving currently an expanded (k = 2) uncertainty < 1 %.

INTRODUCTION

Silicon single-photon avalanche diodes (Si-SPADs) are commercially available since several years and gain importance in a variety of scientific research fields, like experimental quantum optics, quantum cryptography and quantum computing, but also in applications like medicine, biology and astrophysics. Still, the most important parameter for their characterization is the detection efficiency. However, thus far customers have to rely on the values given by the manufacturers or they have to measure the values themselves. The calibration of free space Si-SPADs by means of synchrotron radiation was reported recently [1]. In this paper we will report on a tabletop easy-to-handle measurement setup and technique for the detection efficiency determination of Si-SPADs. Furthermore, the influence of photon statistics on the measured detection efficiency will be analyzed and presented.

CALIBRATION SETUP AND PROCEDURE

The calibration chain for the Si-SPAD detector is shown in Figure 1. The thermopile detector is used for broadening the wavelength range, in which the calibration can be performed. The most difficult step is the comparison between the Si-diode and the Si-SPAD, because here about 10 orders of magnitude of photon rate have to be bridged.

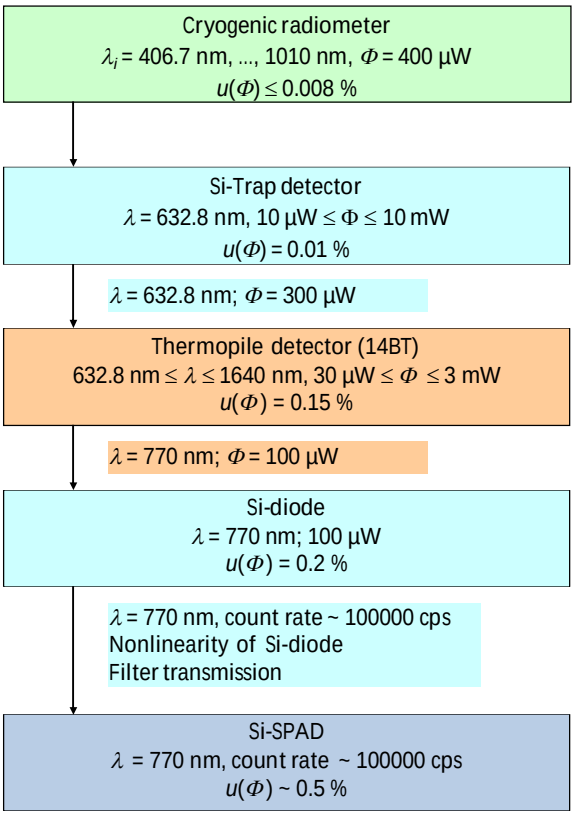

Figure 1. Calibration chain for the Si-SPAD detector.

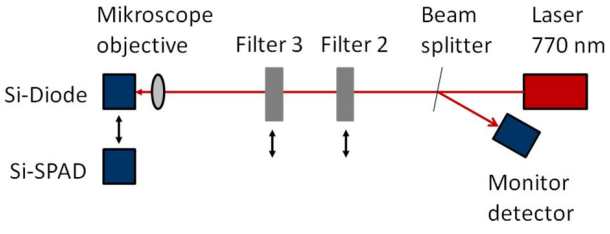

Figure 2. Scheme of the calibration setup for Si-SPADs.

This is performed as follows, as can be seen schematically in figure 2. First the radiant power Φ_1 of a diode laser operating at 770 nm is measured with the Si-diode. Then, the filter 2 (filter 3) is moved into the beam and the transmitted radiant power Φ_2 (Φ_3) is measured. Hence, the filter attenuations are

determined in-situ. This subsequent determination of the overall attenuation is necessary, because it is not possible to measure the overall attenuation in one step due to the low photon flux. Finally, the Si-SPAD and both filters are moved into the beam and the count rate is measured. Thus, the following signals V_1 to V_4 are measured:

$$\left.\begin{aligned} V_1 &= A_1 \cdot s_{\mathrm{Si}} \cdot \Phi_1 \\ V_2 &= A_2 \cdot s_{\mathrm{Si}} \cdot \Phi_2 = A_2 \cdot s_{\mathrm{Si}} \cdot T_{\mathrm{F2}} \cdot \Phi_1 \\ V_3 &= A_3 \cdot s_{\mathrm{Si}} \cdot \Phi_3 = A_3 \cdot s_{\mathrm{Si}} \cdot T_{\mathrm{F3}} \cdot \Phi_1 \\ V_4 &= CR = \eta \cdot \frac{\Phi_4}{hc/\lambda} = \eta \cdot \frac{T_{\mathrm{F2}} \cdot T_{\mathrm{F3}} \cdot \Phi_1}{hc/\lambda} \end{aligned}\right\} \qquad (1)$$

$$\Rightarrow \eta = hc/\lambda \cdot \frac{A_2 \cdot A_3 \cdot}{A_1 \cdot} \cdot \frac{CR \cdot V_1}{V_2 \cdot V_3} \cdot s_{Si}$$

With η: detection efficiency, V_i: signals, s_{Si}: spectral responsivity of the Si-diode, A_i: amplification factors, Φ_i: radiant powers, T_{F2}, T_{F3}: filter transmissions, CR: count rate of the Si-SPAD, h: Planck constant, c: speed of light and λ: wavelength.

It should be noted, that equation (1) holds only, if (i) the laser power is kept constant during the measurements, (ii) the responsivity of the Si-diode is known for all powers and (iii) for the overall filter transmission $T_{F2,\,F3} = T_{F2} \times T_{F3}$ holds. Prerequisite (i) is taken into account by using the monitor principle. The linearity (ii) of the Si-diode was determined by the flux addition method, the results will be shown in detail in the presentation. Condition (iii) was determined from independent measurements with filters of smaller attenuation and taken into account in the measurement uncertainty analysis.

The standard measurement uncertainty is determined to be < 0.5 %. Main contributions are the filter transmission and the responsivity of the reference detector.

Furthermore, the dependence of the measured detection efficiency from the photon rate impinging on the detector was investigated. Earlier studies [2] predict a clear dependence, due to the digital character of the Si-SPAD detector and the Poissonian photon statistics of the radiation used in the experiments. Figure 3 shows clearly that after a constant value for η for small count rates, the detection efficiency decreases drastically. This can be easily explained with a simple model [3], which takes into account the photon statistics and the dead time of the detector. The detection efficiency and the count rate at the Si-SPAD can be described by:

$$\eta = \frac{1 - \exp\left(-\eta_0 \langle n \rangle\right)}{\langle n \rangle} \qquad (2)$$

$$CR = \frac{1 - \exp\left(-\eta_0 \langle n \rangle\right)}{t_{\mathrm{dead}}} \qquad (3)$$

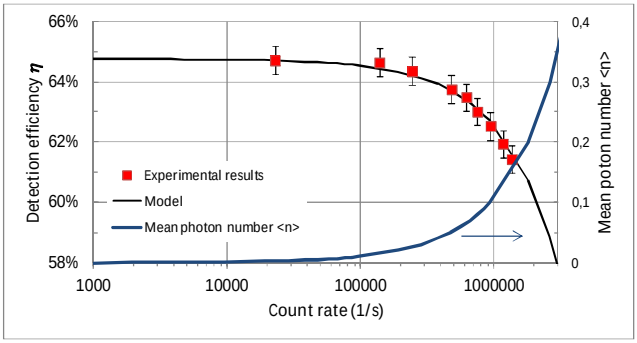

Figure 3. Count rate dependence of the detection efficiency (red squares) and corresponding model (black solid line). Also shown is the mean photon number (blue line).

This work was funded by the project SIQUTE (contract EXL02) of the European Metrology Research Programme (EMRP). The EMRP is jointly funded by the EMRP participating countries within EURAMET and the European Union.

REFERENCES

1. I. Müller, R. M. Klein, J. Hollandt, G. Ulm, L. Werner, “Traceable calibration of Si avalanche photodiodes using synchrotron radiation”, Metrologia, 49, S152 (2012).
2. W. Schmunk, M. Rodenberger, S. Peters, H. Hofer, S. Kück, “Radiometric Calibration of Single Photon Detectors by a Single Photon Source based on NV-centers in diamond”, Journal of Modern Optics, 58, 1252 (2011).
3. S. Kück, H. Hofer, S. Peters, "Detection Efficiency Determination of Si-SPAD Detectors", Single Photon Workshop 2013, Oak Ridge National Laboratory, Oak Ridge, Tennessee, USA, 15-18, October, 2013.

The SIQUTE-project – first results towards single-photon sources for quantum technologies

S. Kück[1], G.Porrovecchio[2], G. Brida[3], A. Pokatilov[4], A. Manninen[5], C. Chunnilall[6], S. Polyakov[7], J. Claudon[8], N. Gregersen[9], S. Götzinger[10], C. Becher[11], and J. Mørk[9]

[1]*Physikalisch-Technische Bundesanstalt (PTB), Braunschweig, Germany*
[2]*Cesky Metrologicky Institut (CMI), Praha, Czech Republic*
[3]*Istituto Nazionale di Ricerca Metrologica (INRIM), Torino, Italy*
[4]*AS Metrosert (Metrosert), Tallinn, Estonia*
[5]*Mittatekniikan Keskus (MIKES), Espoo, Finland*
[6]*National Physics laboratory Limited (NPL), Teddington, U.K.*
[7]*The University System of Maryland Foundation (USMF), College Park, MD, USA*
[8]*Commissariat à l'énergie atomique et aux énergies alternatives (CEA), INAC, Grenoble, France*
[9]*Danmarks Tekniske Universitet (DTU), Lyngby, Denmark*
[10]*Friedrich-Alexander-Universität Erlangen – Nürnberg (FAU), Erlangen, Germany*
[11]*Universität des Saarlandes, Fachrichtung 7.2, Germany*
Corresponding e-mail address: stefan.kueck@ptb.de

In this presentation, the first results of the EURAMET joint research project "Single-Photon Sources for Quantum Technologies" (SIQUTE) [1] will be presented and an outlook towards the realization of highly efficient single photon sources for applications in quantum technologies and radiometry will be given.

INTRODUCTION

The aim of the EURAMET joint research project "Single-photon sources for quantum technologies" (SIQUTE) is the development of highly efficient and predictable single-photon sources for a variety of application, as e.g. quantum communication, quantum computation and quantum metrology, but also for radiometry on the low photon flux level. The vision is the develop a single-photon source, which would be a new standard for the above mentioned fields of research and application. Achieved shall this goal by the common effort of the leading European metrology institutes in the field of radiometry and quantum metrology and universities in the field of theoretical modeling and technological implementation of such sources.

RESULTS

The work within the first year of the project dealt mainly with the development and formulations of designs and concepts for the single-photon sources. This included the design of optimized antenna structures for efficient single-photon collection, the design of a photonic trumpet for high mode matching (Figure 1) and the construction of an initial eigenmode solver based on the Fourier modal method. These results are prerequisites for the further development of highly efficient single-photon sources based on defect centers in diamond and on quantum dots in semiconductor structures.

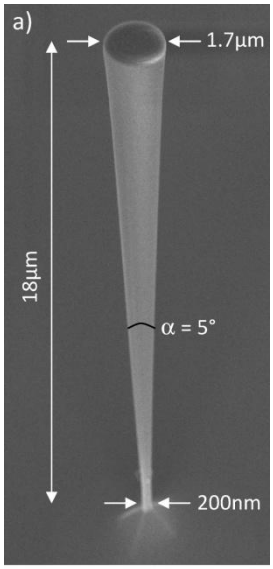

Figure 1. Tilted SEM view of a trumpet-like taper.

NV- and SiV-center doped nanodiamonds are currently under production and will be sent to PTB for further characterization. These nanodiamonds will be produced on tailored substrates with an array of markers, which allows for registering individual nanodiamonds and identification in repeated experiments.

Furthermore, an optically pumped nanowire single-photon source was prepared and is currently

under investigation at PTB for its characterisation in terms of g^2-value, spectral distribution and photon rate. The results of these measurements will be presented at the conference.

The requirements for the successful performance of low-photon-flux measurements were prepared. This includes the design of the detector-based transfer standards for very low photon fluxes (Figure 2), the sub-ns pulse diode laser driving electronics and a tunnel-type multi-element trap detector as beam attenuator (Figure 3).

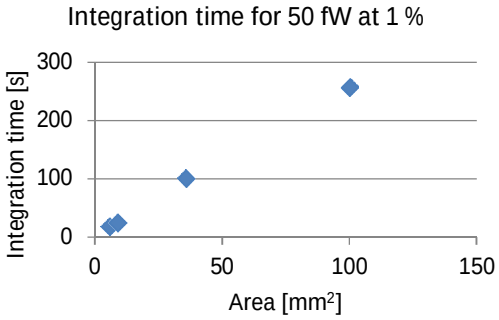

Figure 2. Estimate of integration time for low optical power (50 fW) to achieve targeted measurement accuracy 1%.

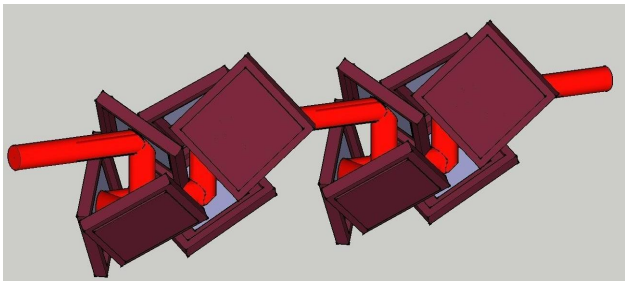

Figure 3. Illustration of the 12-element attenuator for six decades beam attenuation.

SUMMARY

The first results, obtained within the first year of this three-year joint research project will be presented as well as an outlook for the further activities will be given.

ACKNOWLEDGEMENT

This work was funded by the project SIQUTE (contract EXL02) of the European Metrology Research Programme (EMRP). The EMRP is jointly funded by the EMRP participating countries within EURAMET and the European Union.

REFERENCES

1. http://www.ptb.de/emrp/siqute.html

Accurate characterization of superconducting nanowire single photon detector

Qiang Wang[1], J. J. Renema[1], G. Frucci[2], Z. Zhou[2], A. Gaggero[3], F. Mattioli[3], R. Leoni[3], A. Fiore[2], M. P. van Exter[1], and M. J. A. de Dood [1]

[1]*Leiden Institute of Physics, Leiden, The Netherlands*
[2]*COBRA Research Institute, Eindhoven University of Technology, Eindhoven, The Netherlands*
[3]*Istituto di Fotonica e Nanotecnologie (IFN), CNR, Roma, Italy*
Corresponding e-mail address: wang@physics.leidenuniv.nl

The optical response of superconducting nanowire single photon detectors (SNSPDs) cannot be easily expressed by a single photon detection efficiency and the known properties of the quantum state of light. Instead, detector tomography is needed to separate the response to different photon numbers. We perform a detailed experimental investigation of this detector tomography process and identify laser intensity fluctuations as the limiting factor. Although these fluctuations slow down convergence, they do not affect the final accuracy of the result.

INTRODUCTION

Superconducting nanowire single photon detectors (SNSPDs) are interesting from a technological perspective as they can demonstrate high detection efficiency, high speed, low dark count rate and low jitter at telecommunication wavelengths. The response of SNSPDs to multiple photons is more complex than that of avalanche photodiodes (APDs) and cannot be captured with a single detection efficiency. Instead, detector tomography is needed to completely characterize these detectors and to capture the rich response that is intrinsic to these detectors.

We have applied detector tomography [1] to study multi-photon detection events in nanofabricated constrictions in an NbN wire [2, 3]. To obtain such results the accuracy of the tomography should be sufficient. Obviously, longer measurement times make the estimation process more accurate. However, without further knowledge it is impossible to know how long one should measure to achieve a certain level of accuracy. Similarly, it is a priori unclear which factors limit the accuracy and whether they affect the estimation itself by introducing bias. With this in mind we conducted a series of experiments to investigate the tomographic method.

EXPERIMENT

The SNSPD in this study is made out of a 4 nm thick NbN film deposited on a silicon substrate. The film is fabricated into a 100 nm wide meandering wire with 100 nm pitch. The total active area is 10 × 10 μm^2 and a 245 nm thick oxidized silicon cavity optimized for 1300 nm wavelength is made beneath the NbN film to further enhance light collecting efficiency.

The detectors are mounted in a pulse-tube cryostat with free-space optical access and are cooled to a base temperature of 3.1 K. A bias current is applied and detection events are registered when the detector becomes normal using a bias-T and a cascade of high-frequency amplifiers to produce measurable voltage pulses.

We record the count rate of the SNSPD that is illuminated by laser pulses from a spectrally filtered supercontinuum source with a repetition rate of 20 MHz. At every wavelength we vary the bias current through the detector as well the mean photon number incident on the detector using two polarizers and a rotating waveplate to tune the laser power. For a wavelength of 1200 nm, the count rate in a 0.1 sec interval is measured 1000 times at each setting.

DETECTOR TOMOGRAPHY

We distinguish between a linear optical detection probability η of the detector and intrinsic electronic probabilities $\{p_i\}$ that record the click probability for i absorbed photons. The detector click probability can be expressed by

$$R_{click} = 1 - e^{-\eta N} \sum_{n=0}^{\infty} (1 - p_n) \frac{(\eta N)^n}{n!} \qquad (1)$$

Although this model has been tested for nanofabricated constrictions that show a exceedingly low absorption efficiency η it is not clear if this effective photon number tomography will work for a meander-like SNSPD, especially if a strongly wavelength dependent cavity is used.

RESULTS

For each bias current we fit the measured click probability as a function of the mean photon number to equation (1). In the fit procedure we limit the number of free parameters by using only a finite set of $\{p_i\}$. We select the model that minimizes a least

squares with the smallest number of fit parameters. For the meander studied here, we typically use 3 fit parameters: η, p_1 and p_2.Based on the fit results we find that the nonlinear $\{p_i\}$ and linear efficiency η can be clearly separated also for high efficiency cavity- based SNSPDs. By comparing excitations at different wavelength and different photon number we find that the response of SNSPD depends only on the total energy of the absorbed photons, not on the wavelength of the individual photons [3].

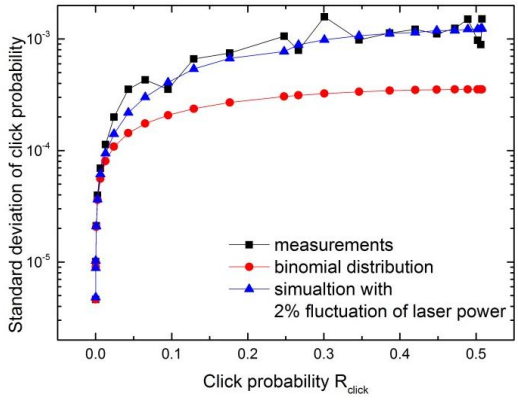

Figure 1. Standard deviation σ in a 0.1 sec time interval of the intrinsic probability p1 as a function of click probability. The standard deviation of fluctuation of the laser power is set to 2% in the simulation.

From the repeated measurements at each setting we directly calculate the standard deviation σ of the click probability R_{click} and compare this to the expected fluctuations based on the binomial distribution for the known number of absorbed photons (shot noise limit). This comparison is shown in Fig. 1 and reveals that the measured σ exceeds the prediction by more than a factor 5. Additional experiments exclude temperature stability, bias current fluctuations and counting electronics as limiting factors, leaving intensity fluctuations of the laser as a potential source of the fluctuations.

To investigate this hypothesis, we simulate the click probability by taking into account both shot noise and a Gaussian distribution of fluctuations in the laser power. We find that small intensity fluctuations with standard deviation of 2% only suffice to explain the rather large discrepancy in the standard deviation. A direct comparison between measured and simulated data is shown in Figure 1.

Based on the same simulation, we produce the p_1 with error bar as a function of measured rounds N as shown in Figure 2 (a), which can be comparable to the measured data shown in Figure 2 (b).

From both experiment and simulation it is clear that p_1 converge to the true value with a bias less than 1% after 100 measurements. (this conclusion also holds for p_2, not shown here)

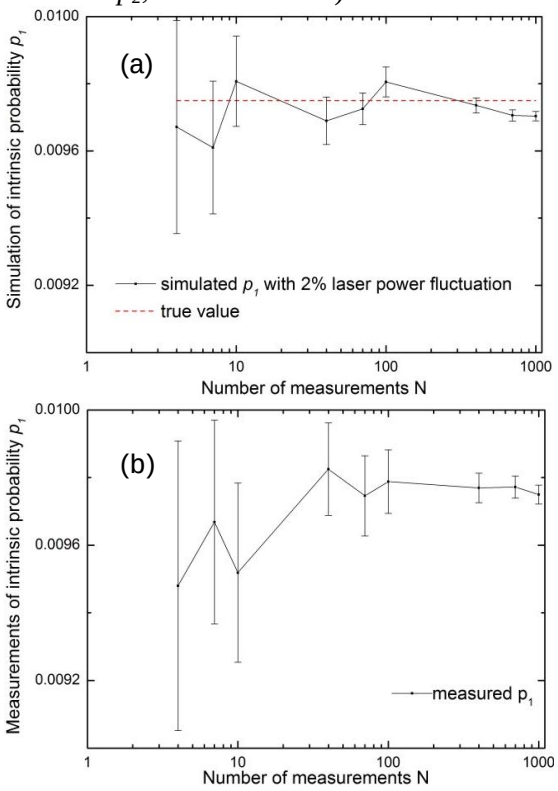

Figure 2. Standard deviation σ of the intrinsic probability p1 as a function of the number of measurements using simulated data (a) and experimental data (b).

CONCLUSIONS

We successfully characterize a cavity-based SNSPD with modified detector tomography based on an effective photon model. This results shows that the linear absorption process and the nonlinear intrinsic detection probabilities can be separated. Laser power fluctuations limit the accuracy of tomography and influence the standard deviation of the click probability. These fluctuations do not affect the correct estimation of the probabilities $\{p_i\}$ and 100 measurements per point (10 sec. measurement time) is sufficient to retrieve p_1 with 1% accuracy.

REFERENCES

1. J.J. Renema, et al., Modified detector tomography technique applied to a superconducting multiphoton nanodetector, Optics Express 20, 2806-2813, 2012.
2. D. Bitauld, et al., Nanoscale optical detector with single-photon and multiphoton sensitivity, Nano Letters 10, 2977-2981, 2010.
3. J.J. Renema, et al., Universal response curve for nanowire superconducting single-photon detectors, Physical Review B 87, 174526-174532, 2013.

The MIQC-project – Metrology for Industrial Quantum Communications

M L Rastello[1], A G Sinclair[2], I P Degiovanni[1], S Kück[3], C J Chunnilall[2], G Porrovecchio[4], F Manoocheri[5], E Ikonen[6], T Kubarsepp[7], D Stucki[8], K S Hong[9], A Tosi[10], A Al Natsheh[11], J Y Cheung[2], I Muller[3], L Werner[3], M Smid[4], and A Vaigu[5]

[1]*Istituto Nazionale di Ricerca Metrologica (INRIM), Torino, Italy*
[2]*National Physical Laboratory (NPL), Teddington, U.K.*
[3]*Physikalisch-Technische Bundesanstalt (PTB), Braunschweig, Germany*
[4]*Cesky Metrologicky Institut (CMI), Praha, Czech Republic*
[5]*Mittatekniikan Keskus (MIKES), Espoo, Finland*
[6]*AaltoUniversity, Espoo, Finland*
[7]*AS Metrosert (Metrosert), Tallinn, Estonia*
[8]*ID Quantique SA, Genève, Switzerland*
[9]*Korea Research Institute of Standards and Science (KRISS), Daejon, Republic of Korea*
[10]*Politechnico di Milano, Milano, Italy*
[11]*University of Oulu, Oulu, Finland*
Corresponding e-mail address: m.rastello@inrim.it

The objective of EURAMET joint research project "Metrology for Industrial Quantum Communication Technologies" (MIQC) [1] is to develop metrological techniques and standards to help accelerate the introduction of new industrial quantum communication technologies based on single photons. It is focussed on the requirements of quantum key distribution (QKD) via optical fibre, the most commercially advanced application. This talk presents an overview of the project, and its outcomes to date.

INTRODUCTION

The project focusses on the optical components of 'faint pulse' quantum key distribution (QKD) operated over optical fibre, the most commercially advanced quantum communication technology. The security of QKD relies upon encoding each bit of information sent between the parties seeking to establish a common secret key onto a single photon. If a hacker intercepts these photons, (s)he will disturb their encoding in a way that can be detected. These systems generically comprise a photon transmitter ('Alice') and single photon receiver ('Bob') modules that operate over optical fibre in the 1550 nm telecom band. Attenuated laser pulses are used to approximate single photons, and information is encoded on the phase of the photons [2]. Random number generators (RNGs) are also essential components of QKD systems.

QKD systems will meet a known need for improved data security in, for example, banking, commerce and the transmission of personal data. Thus far, the only initiative for the standardisation of QKD in the world is the Industry Specification Group on QKD within the European Telecommunications Standards Institute (ETSI ISG-QKD) [3]. JRP members INRIM, NPL, and PTB participate in the work of the ISG-QKD, which helped the JRP to identify the requirements for validating the optical performance of QKD systems, and the ISG to develop standards that specify appropriate and practical methods for traceably validating the performance of these systems.

The JRP has refined state-of-the-art measurement techniques and adapted them to the requirements of fibre-coupled QKD devices operating in the telecom band, as well as developing new techniques that advance single photon metrology.

QKD MEASUREMENT REQUIREMENTS

QKD is based on a physical process, and characterising the optical components of a QKD system can establish whether they satisfy the assumptions and requirements of security proofs [2,4], their expected secure bit-rate and range, and their immunity from known hacking attacks.

The following properties of the photons emitted by a QKD transmitter were considered the most important: probability distribution, mean photon number(s), temporal jitter and duration, wavelength, spectral bandwidth and indistinguishability. It is essential to the security of a QKD system that phase

encoding imparts no distinguishing information onto the photons (e.g. on their spectral properties) which an eavesdropper can probe.

The photon detection probability, dark count probability, after-pulse probability, dead-time, and recovery time of the photon receivers impact directly on the achievable range and quantum bit error rate (QBER). Photon counters in the 1550 nm region are normally gated to reduce their dark count rate.

Methods are therefore required not only for fibre-coupled devices operating in the single photon regime, but also require synchronization with up to GHz repetition rate optical pulses and detector gates.

STATE-OF-THE-ART TECHNIQUES

Measurement of mean photon number has been established by calibrating a photon counting detector using a fibre-optic power meter whose traceability can be linked back to cryogenic radiometry [5]. Wavelength can be established using standard techniques traceable to $^{13}C_2H_2$ [6]. Characterisation of receiver properties has been established by using a pulsed laser source calibrated against a traceably calibrated fibre-optic power meter.

ADVANCES IN SINGLE-PHOTON METROLOGY

The measurement of probability distribution has been addressed via the development of a photon-number resolving (PNR) detector composed of a tree arrangement of non-PNR detectors [7].

A tunable Fabry-Perot cavity spectrometer has been constructed to measure the spectral bandwidth and indistinguishability of differently phase encoded photons. It has an operating range from 1270 nm to 1630 nm, a free spectral range of 119 GHz, a linewidth of ~ 600 MHz, and is coupled to a photon counting detector to operate at single photon level.

A method which links power measurement at the level at which a photodiode can be calibrated with a cryogenic radiometer to that required for a photon counting detector using the calculable scaling of the power with current in a synchrotron beam [8] has now been applied to fibre-coupled superconducting nanowire single photon detectors.

A fibre-coupled two-element trap detector for the telecom regime which has an attenuation of 50dB and can measure input powers in the tens of picowatt regime has been developed. This simplifies measurements in the photon counting regime.

An open-system quantum random number generator has been constructed, which is being used to establish a model to link the performance of its optical components with the quality and rate of the random numbers generated.

SUMMARY

This JRP lays the *foundations* for a European measurement infrastructure able to validate the performance of QKD systems, and technologies that use and manipulate single photons. Specifications based on the outputs of this JRP will enable systems to be evaluated and standard measures to be defined, thus helping to shape a validation and certification process for wider implementation of this technology. Engagement with manufacturers and ETSI has highlighted the importance of characterising the physical performance of QKD systems in order to assure both suppliers and customers that the devices are operating as intended. The MIQC results will also enable the development of new hardware for manipulating single and few photons, required for next-generation communication systems and quantum networks.

REFERENCES

1. http://projects.npl.co.uk/MIQC/
2. N. Gisin et al., Quantum cryptography, Rev. Mod. Phys. 74(1), 145-195, 2002.
3. http://www.etsi.org/technologies-clusters/technologies/quantum-key-distribution
4. V. Scarani et al., The security of practical quantum key distribution, Rev. Mod. Phys. 81(3), 1301-1350, 2009.
5. J. E. Martin et al., A cryogenic radiometer for absolute radiometric measurements, Metrologia, **21**(3), 147-155 1985.
6. C.S. Edwards et al., High-accuracy frequency atlas of $^{13}C_2H_2$ in the 1.5 μm region, Appl. Phys. B 80, 977-983, 2005.
7. E. A. Goldschmidt et al., Mode reconstruction of alight field by multi-photon statistics, Phys. Rev. A 88, 013822, 2013.
8. I. Müller et al., Traceable calibration of Si avalanche photodiodes using synchrotron radiation, Metrologia, 49, 152–155, 2012.

ACKNOWLEDGEMENT

This work was funded by the project MIQC (contract IND02) of the European Metrology Research Programme (EMRP). The EMRP is jointly funded by the EMRP participating countries within EURAMET and the European Union.

Reconstruction of the mode structure of multimode optical fields through photon number resolution

I.P. Degiovanni[1], E.A. Goldschmidt[2,3], F. Piacentini[1], S.V. Polyakov[2], I. Ruo Berchera[1], S. Kück[4], G. Brida[1], A. Migdall[2,3], and M. Genovese[1]

[1]*Istituto Nazionale di Ricerca Metrologica, Torino, Italy;*
[2]*National Institute of Standard and Technology, Gaithersburg (MD), USA;*
[3]*Joint Quantum Institute, Gaithersburg (MD), USA;*
[4]*Physikalisch-Technische Bundesanstalt, Braunschweig, Germany.*
Corresponding e-mail address: i.degiovanni@inrim.it

Achieving a proper knowledge of the number and structure of occupied modes of a light field is fundamental in several research fields, e.g. quantum information.
Here we present a new method for the reconstruction of the mode structure of multimode fields exploiting photon number resolution, showing excellent reconstruction up to three modes and great robustness in several experimental regimes.

INTRODUCTION

Engineering and detecting single photons is of paramount importance from foundational tests of nature [1] to precision measurement. Anyway, most of real light sources contain more than just one mode, thus the mode structure of a source can give information about the physical properties of a source, since different kinds of modes generate light with different statistics.

First- and second-order photon number statistics are commonly used to study several optical systems [2-13]. In any case, low-order number statistics is often not sufficient to describe non-ideal multimode sources.

A method able to discriminate between different modes of an optical field by means of higher-order photon number statistics, on the contrary can help understanding the physical processes contributing to the light field generation.

Here we present our reconstruction method [14], applied to mixed states composed of up to one Poissonian mode, one or more pseudo-thermal modes and up to one attenuated single-photon mode: our experimental results show successful discrimination of up to three total modes, also giving proof of the robustness of our method in many experimental regimes.

THEORETICAL METHOD

The photon number distribution of a multi-mode field can be expressed through the photon fractions μ_i of the modes composing the field: for thermal and poissonian statistics $\mu_i = \langle n \rangle$ is the mean photon number of the relative mode, while and for attenuated single-photon statistics μ_i indicates the probability of finding a single photon. For each different mode, the corresponding photon number statistics can be described by a probability generating function $G(s)$:

$$G_{\text{thermal}}(s) = [1 + \mu\,(1 - s)]^{-1}$$
$$G_{\text{single-photon}}(s) = [1 - \mu\,(1 - s)]$$
$$G_{\text{poissonian}}(s) = e^{-\mu(1-s)}$$

For a multi-mode state, the global generating function $G(s)$ is given by the product of the generating functions for all the underlying modes. It is convenient to translate this formalism into a set of relations between the μ_i and the intensity auto-correlation functions $g^{(k)} = \langle :n^k: \rangle / \langle n \rangle^k$ by taking $g^{(k)} = (G^{(k)}|_{s=1})/(\mu_{total}{}^k)$, being $G^{(k)}|_{s=1}$ the k-th derivative of $G(s)$ evaluated at $s = 1$. Being by definition $g^{(1)}=1$, we replace the first order expression with $\langle n \rangle = \Sigma \mu_i$.
It is straightforward to demonstrate that for a state composed of N modes, N orders of correlation functions are required to fully characterize its mode structure. For fields with only a few photons, measuring $g^{(k)}$ requires photon number resolution up to k photons.

For $\mu_{total} << k$, photon number resolution up to k photons is required to accurately measure $g^{(k)}$. We stress that, by overdetermining the system by using $M>N$ correlation functions to reconstruct N modes, one can improve the accuracy of reconstruction.

THE EXPERIMENT

The experimental setup used to test this reconstruction method is reported in Fig. 1.

For the experimental demonstration of this technique, we used as sources a pulsed laser, a

simulated pseudo-thermal state (a pulsed laser sent through the rotating ground glass, always with $g^{(2)}>1.9$), and a heralded single-photon state characterized by a $g^{(2)} < 0.05$ [15].

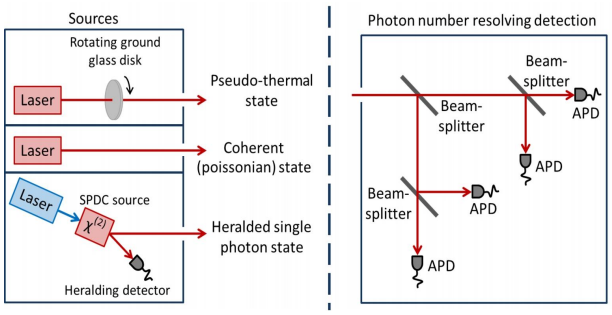

Figure 1. Experimental setup. SPDC: Spontaneous Parametric Down-Conversion. APD: Avalanche Photo-Diode.

We generate a "controlled" multi-mode state by combining up to three modes from our sources, so that we can independently verify the mode structure. Because our pseudo-thermal sources are derived from the same laser, we insert short time delays between the fields to avoid interference.

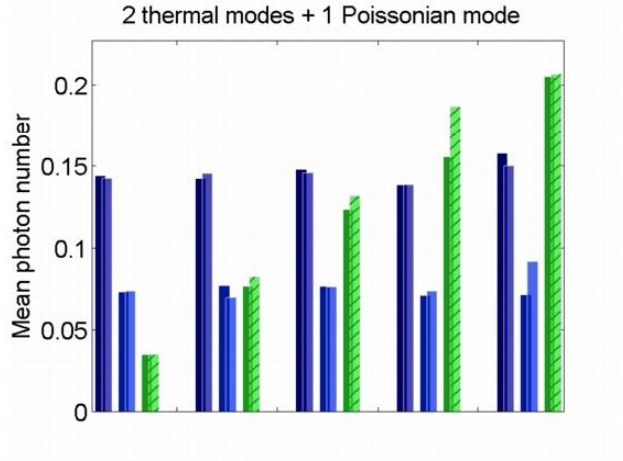

Figure 2. Reconstructions of a state composed of two pseudo-thermal modes and a poissonian mode, in several different regimes. The background bars are the measured photon numbers, while the superimposed cross-hatched ones are the reconstruction results. All these reconstructions show fidelities above 99%.

To resolve photon-number statistics up to $g^{(3)}$, we employ a detector 4 non-photon-number-resolving detectors tree configuration. Given the high non-linearity of the detection device, we perform post-processing of the data taking into account the Positive Operator-Value Measure (POVM) of our detection system [16].

For each of the optical fields generated, we find excellent agreement for a wide range of input powers (see e.g. Fig. 2), with our reconstruction method being able to identify the correct number and type of modes belonging to the analysed field (up to three modes, being this the limit given by the photon number resolution of our setup): all the reconstructions performed show a fidelity above 99% with the expectations, demonstrating the great robustness and reliability of our method.

REFERENCES

1. M. Genovese, Phys. Rep. 413, 319, 2005.
2. C. Kurtsiefer, S. Mayer, P. Zarda, and H. Weinfurte, Phys. Rev. Lett., 85, 290–293, 2000.
3. D. Press et al., Phys. Rev. Lett. 98, 117402, 2007.
4. W. Schmunk et al., Metrologia 49(2), S156, 2012.
5. E.A. Goldschmidt, M.D. Eisaman, J. Fan, S.V. Polyakov, and A. Migdall, Phys. Rev. A 78, 013844, 2008.
6. A. Kuzmich et al., Nature 453, 731-734, 2003.
7. M. Aßmann, F. Veit, M. Bayer, M. van der Poel, and J. M. Hvam, Science 325, 297-300, 2009.
8. M. Hennrich, A. Kuhn, and G. Rempe, Phys. Rev. Lett. 94, 053604, 2005.
9. D. Elvira et al., Phys. Rev. A 84, 061802, 2011.
10. M. Aßmann et al., Phys. Rev. B 81, 165314, 2010.
11. A. Allevi et al., JOSA B 30, 2621, 2013.
12. T. Iskhakov et al., Opt. Lett. 37(11), 1919, 2012.
13. I.B. Bobrov, S.S. Straupe, E.V. Kovlakov, and S.P. Kulik, New J. Phys. 15, 073016, 2013.
14. E.A. Goldschmidt et al., Phys. Rev. A 88, 013822, 2013.
15. G. Brida et al., Opt. Expr. 19(2), 1484–1492, 2011.
16. G. Brida et al., Phys. Rev. Lett. 108, 253601, 2012.

ACKNOWLEDGEMENT

This work was funded by the project MIQC (contract IND02) of the European Metrology Research Programme (EMRP). The EMRP is jointly funded by the EMRP participating countries within EURAMET and the European Union.

Traceable calibration of a fibre-coupled superconducting nano-wire single photon detector using characterised synchrotron radiation

Ingmar Müller, Roman M. Klein, and Lutz Werner

Physikalisch-Technische Bundesanstalt, Berlin, Germany
Corresponding e-mail address: ingmar.mueller@ptb.de

Radiometric calibrations of fibre-coupled single photon detectors are seeing growing demand, especially at the telecommunication wavelengths. In this paper the radiometric calibration of a fibre-coupled superconducting nano-wire single photon detector by means of well-characterised synchrotron radiation is described. At the telecom wavelengths the achievable calibration uncertainties are limited by the single photon detector characteristics, which are inferior to those of single photon detectors, designed for operation at visible wavelengths. The first radiometric calibration of a fibre-coupled single photon detector traceable to a cryogenic radiometer by means of synchrotron radiation is presented and a preliminary uncertainty budget of the calibration is given.

INTRODUCTION

The unique properties of synchrotron radiation (SR) are used at the Physikalisch-Technische Bundesanstalt (PTB) for many years to calibrate detectors in the NIR, visible, UV, VUV and soft X-ray spectral region. For this purpose PTB operates laboratories at BESSY II and owns and operates a dedicated electron storage ring, the Metrology Light Source (MLS) [1]. The huge dynamic range in terms of spectral radiant power available at BESSY II and the MLS (11 orders of magnitude at the MLS) has been used for many years to calibrate photon-counting detectors in the UV and X-ray regime [1, 2]. The calibration of a single photon avalanche photodiode in the visible, traceable to a cryogenic radiometer of PTB has been shown recently [3]. Here, this SR based calibration method is extended to fibre-coupled detectors suitable for the operation in the NIR.

CALIBRATION METHOD

This calibration method is based on the strict proportionality of emitted radiant intensity and the number of stored electrons of an electron storage ring. For the calibration of fibre-coupled single photon detectors, the influence of the photon statistics has to be known and has, thus, been measured as described in [4]. The measurement principle for fibre-coupled detectors is similar to the principle for the free space detectors [3]. A schematic of the setup is shown in Figure 1. The detection efficiency of the SNSPD is polarization dependent. Hence, a fibre-coupled polarizer was used for this calibration and the polarization had been adjusted to reach the maximum count rate of the SNSPD.

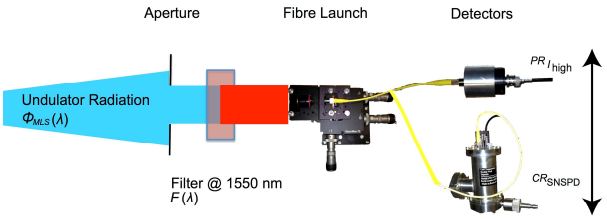

Figure 1. Calibration set-up for the radiometric calibration of an SNSPD traceable to a cryogenic radiometer by means of synchrotron radiation.

Additionally, the vertical source size of the synchrotron radiation becomes a critical parameter and limits the maximum ring current for this application to values of approximately 1 mA. At higher ring currents the coupling between the electrons in the circulating electron bunches is current dependent and, thus, changes the vertical source size. Hence, the coupling efficiency of the synchrotron radiation into the fibre is ring current dependent for ring currents above 1 mA. To perform the calibration of the SNSPD, the synchrotron radiation was monochromatized by a filter with a central wavelength of 1551.97 nm and fed into a single mode optical fibre (SMF-28) for a wavelength of 1550 nm. The fibre-coupled synchrotron radiation was then connected to the reference detector, a calibrated InGaAs photodiode, and the SNSPD sequentially (see schematic of the setup in Figure 1). The SNSPD was current biased to 90% of the critical bias current. The absolute photon rate, PR_{high} that was coupled into the

fibre at a ring current I_{high} of about 1 mA was determined using the InGaAs photodiode that was calibrated traceable to a cryogenic radiometer of PTB. At this level, the ring current could be measured with a relative standard uncertainty of $5 \cdot 10^{-3}$ by cooled photodiodes with aluminum filters. The ring current was then reduced to approximately 5 nA. At this ring current I_{low}, corresponding to about five thousand stored electrons, the count rate CR_{SNSPD} of the SNSPD was measured.

The uncorrected detection efficiency DE^* of the SNSPD is determined from:

$$DE^* = \left(CR_{SNSPD} / I_{low}\right) / \left(PR_{high} / I_{high}\right) \quad . \qquad (1)$$

RESULTS

The measured dark count rate and measured detection efficiency of the SNSPD are shown in Figure 2. The detection efficiency increases with increasing bias current and reaches a maximum value of about 17% before the detector enters the resistive state at a normalized bias current of 0.946 and, thus, becomes insensitive for single photons.

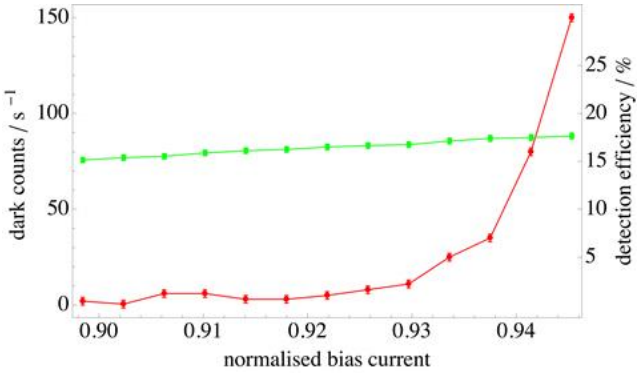

Figure 2. Measured detection efficiency (green squares) and dark count rate (red circles) of the SNSPD plotted over the bias current normalised to the critical bias current.

For typical bias currents of the SNSPD the dark count rate is below 10 s^{-1}. However, the dark count rate shows, for normalized bias currents higher than 0.92, a much stronger increase with increasing bias current than the quantum efficiency (see Figure 2). Hence, the noise equivalent power increases steeply for normalized bias currents above 0.92. The preliminary uncertainty budget is shown in Table 1. For the simplification of the presentation the contributions to the uncertainty budget are grouped in three categories: fibre, calibration method and detector. The biggest source of uncertainty that occurred during the calibration of the SNSPD was the control of the polarization state incident on the SNSPD which introduced a relative standard uncertainty of 1.4 %.

Table 1. Preliminary uncertainty budget for the radiometric calibration of an SNSPD traceable to a cryogenic radiometer of PTB**.**

Uncertainty source group	**combined relative standard uncertainty**
Fibre (e.g. fibre connection)	0.65 %
Calibration method (e.g. electron beam current measurement)	0.75 %
Detector (e.g. polarization dependence of the quantum efficiency)	1.6 %
Combined relative standard uncertainty of DE_{SNSPD}	**1.9 %**

The combined relative standard uncertainty associated with the employment of optical fibres is dominated by the uncertainty of coupling efficiency of the synchrotron radiation into the fibre which introduced a relative standard uncertainty of 0.38 %. The uncertainties related to the calibration method itself were dominated by the electron beam current measurements at about 1 mA which introduced a relative standard uncertainty of 0.75 %. Finally, the detection efficiency of the SNSPD could be measured with a small relative standard uncertainty of 1.9 %.

ACKNOWLEDGEMENT

The research leading to these results has received funding from the European Union, through the EMRP project IND06-MIQC, under Grant Agreement No 912/2009/EC. The EMRP is jointly funded by the EMRP participating countries within EURAMET and the European Union.

REFERENCES

1. Beckhoff B. et al., A quarter-century of metrology using synchrotron radiation by PTB in Berlin. physica status solidi (b), 246(7), 1415–1434, 2009.
2. Richter M. et al., Calibration of space instrumentation with synchrotron radiation. Advances In Space Research, 37(2), 265–272, 2006.
3. Müller I. et al., Traceable calibration of Si avalanche photodiodes using synchrotron radiation. Metrologia, 49(NEWRAD), S152–S155, 2012.
4. Müller I. and Klein R., Calculation and experimental validation of the photon statistics of the Undulator U180 of the Metrology Light Source in the visible and NIR, these proceedings.

Photon-counting optical time-domain reflectometry at 1550 nm

A. Meda[1], F. Piacentini[1], P. Traina[1], H. Kee Suk[2], I.P. Degiovanni[1], G. Brida[1], M. Gramegna[1], I. Ruo Berchera[1], M. Genovese[1], and M. L. Rastello[1]

[1]*INRIM, Torino, Italy,*

[2]*Division of Physical Metrology, Korea Research Institute of Standards and Science (KRISS), Korea,*

Corresponding e-mail address: g.brida@inrim.it

In this presentation the main results achieved with photon-counting OTDR at telecom wavelength will be described with an outlook towards improvements and possible applications.

INTRODUCTION

Standard Optical Time Domain Reflectometry (OTDR) is a popular and . indispensable diagnostic technique for measuring long-distance fibre-optic communication links. Measurement of fibre attenuation, connector loss, and the detection of fibre breaks can be determined by access to only one end of the link. The key specifications, sensitivity and spatial resolution, of a direct detection OTDR are related to the bandwidth of the optical receiver.

By using photon-counting technique the sensitivity is greatly improved; the noise floor is set by the background dark counts and the quantum efficiency of the photon-counting detector. The spatial resolution is set by the jitter of the photon counting detector. Although high sensitivity and good spatial resolution were achieved since the earlier test at 850 nm with Silicon Single Photon Avalanche Detector (SPAD) operated in Geiger mode [1,2], the extension of photon-counting OTDR, with comparable performances, into the second (1300 nm) and third windows (1500 nm) was delayed since the improvements of the InGaAs/InP technology [3,4,5].

EXPERIMENTAL SET-UP

In this presentation we describe two configurations of photon-counting OTDR operating at 1550 nm based on commercially available equipment. The layout of the photon-counting OTDR set-up is depicted in Fig. 1. The first configuration is based on a gated avalanche photodetector (ID201 Id Quantique), while the second configuration is based on a recently developed free-running avalanche photodetector (ID220, Id Quantique). In this set-up both detectors are operated simultaneously, in parallel, sharing the same source.

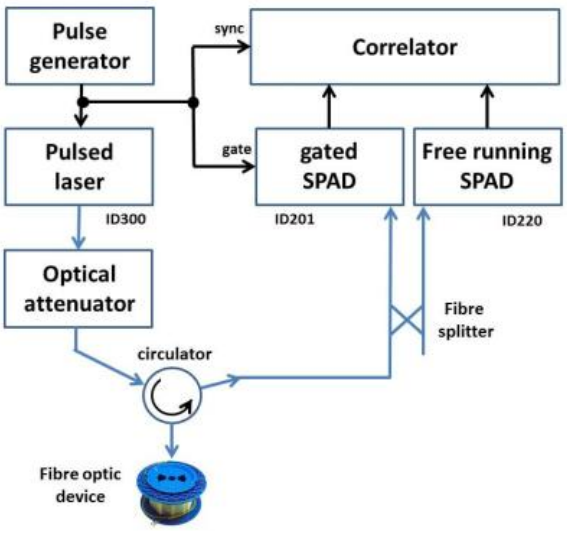

Figure 1. Set-up of the photon-counting OTDR,

The source is a commercial 1550 nm pulsed diode laser (ID300, Id Quantique) with pulse width shorter than 300 ps and energy per pulse lower than 1 fJ; repetition rate of the pulses is set with an external pulse generator according to the length of the fibre under test. The pulse generator provides also triggering signals for the gated detector and the correlator. The laser output is attenuated with a 60 dB variable optical attenuator and by 20 dB with a single-mode fused fibre optic splitter with 99:1 coupling ratio.

The fibre-optic circulator is a non-reciprocating device that transports an optical signal from one port to the next port, but only in one direction (i.e. with low losses, about 0,6 dB) and not vice versa (i.e. with high isolation or directivity, over 50 dB typically). The optical signal back scattered from the fibre-optic device under test, the fibre spool in Fig. 1, is splitted and sent simultaneous to both avalanche photodetectors

The output pulse from the SPAD detectors are sent to a commercial correlator (HydraHarp 400, PicoQuant) together with the laser trigger signal. The output of the correlator is an histogram which represents the probability of a reflected photon as a

function of time delay which is proportional to optical reflectivity versus distance.

MEASUREMENTS

The first objective of this work was to highlight the capability of a free running SPAD to measure directly backscattered photons from long-haul fibre links while in the case of the gated SPAD, because of the limited maximum gate width of 100 ns, we measure backscattered from a small portion of the fibre; scanning the delay between trigger of the laser and opening of the gate window it is possible to reconstruct reflectivity behaviour versus distance, even with a gated detector, increasing the complexity of the measurement set-up.

The second objective was to compare the specifications, sensitivity and spatial resolution, of the two configurations measuring backscattered signal on short fibre links. Comparison with traditional direct detection OTDR has been also performed.

Finally the high sensitivity of the photon-counting OTDR opened the way to measure back-flash light produced by the avalanche in a SPAD, at the detection of a photon. This is a critical point for security in Quantum Key Distribution systems.

The results obtained in these measurements will be reported at the conference with perspectives of improvements and other possible applications.

ACKNOWLEDGEMENT

This work is funded by the project MIQC (contract IND06) of the European Metrology Research Programme (EMRP). The EMRP is jointly funded by the EMRP participating countries within EURAMET and the European Union.

REFERENCES

1. P. Healey, P. Hensel, Optical Time _Domain Reflectometry by Photon Counting, Electronics Letters, Vol. 16, Issue 16, p. 631-633 (1980).
2. C. G. Bethea, B. F. Levine, S. Cova, and G. Ripamonti, High-resolution and high-sensitivity optical-time-domain reflectometer, Optics Letters, Vol. 13, Issue 3, p. 233-235 (1988).
3. A. L. Lacaita, P. A. Francese, S. D. Cova, G. Ripamonti, Single-photon optical-time-domain reflectometer at 1.3 μm with 5 cm resolution and high sensitivity, Optics Letters, Vol. 18, Issue 13, pp. 1110-1112 (1993).
4. R.E. Warburton, M.A. Itzler, G.S. Bulle, Free-running, room temperature operation of an InGaAs/InP single-photon avalanche diode, Appl. Phys. Lett. 94, 071116 (2009).
5. R.E. Warburton, M.A. Itzler, G.S. Bulle, Improved free-running InGaAs/InP single-photon avalanche diode detectors operating at room temperature, Electronics Letters, Vol. 45, Issue 19 (2009).
6. P. Eraerds, M. Legré, J. Zhang, H. Zbinden and N. Gisin, Photon-counting OTDR: Advantages and Limitations, J. of Lightwave Technology, Vol. 28, Issue 6, pp.952-964 (2010).

Traceable metrology for characterising quantum optical communication devices

C J Chunnilall[1], G Lepert[1], D Stucki[2], and A G Sinclair[1]

[1]*National Physical Laboratory (NPL), Teddington U.K.,* [2]*ID Quantique SA, Genève, Switzerland*
Corresponding e-mail address: christopher.chunnilall@npl.co.uk

Industrial technologies based on the production, manipulation, and detection of single and entangled photons are emerging. Quantum key distribution (QKD) and quantum random number generators (QRNGs) are two of the most commercially advanced technologies, and among the first to directly harness the peculiar laws of quantum physics. In order to accelerate the development and commercial uptake of this quantum industry, the National Physical Laboratory (NPL) is using traditional, and quantum, approaches to develop traceable performance metrology for the quantum devices used in these technologies. We report on the instrumentation we have developed to characterise such systems, and the results we have obtained.

INTRODUCTION

A focus of current work at NPL is to develop a measurement infrastructure for characterising the quantum optical components of emerging quantum technologies, such as QKD and QRNGs [1-6]. This is based around measurements for traceably characterising single and entangled photons, and photon-counting detectors, which underpin emerging quantum optical technologies. This ranges from 'traditional' measures such as photon number, and detection efficiency, to others such as indistinguishability that determine device utility.

QKD is underpinned by a physical, as opposed to algorithmic, process. Its security relies upon encoding each bit of information sent between the parties seeking to establish a common secret key onto a single photon. If a hacker intercepts these photons, (s)he will disturb their encoding in a way that can be detected. QKD does not prevent hacking, but reveals whether a hacker has been able to compromise the key.

Current algorithmic key distribution is vulnerable to advances in classical computing power and quantum computing, as well as new mathematical insights. The laws of physics prove the future-proof security of QKD, *if faithfully implemented*. Therefore, the security of a QKD system depends on its physical performance at the time of key creation. NPL has developed a test-bed to measure the performance of constituent components of optical fibre QKD systems. This work will enable QKD systems to be evaluated and standard measures to be defined, thus helping to shape a validation and certification process for the technology.

Random number generators (RNGs) are also essential components of QKD systems. Optical true quantum RNGs operate at the single photon level, and depend on the performance of their constituent single-photon sources and detectors [6].

QKD THROUGH OPTICAL FIBRE

NPL has enhanced its measurement infrastructure to enable it to characterise the photon transmitter ('Alice') and single photon receiver ('Bob') modules of faint-pulse QKD systems operating over optical fibre in the 1550 nm telecom band at clock rates up to 1 GHz. Attenuated laser pulses are used to approximate single photons, hence some pulses will contain more than one photon. Information is encoded on the phase of the photons [2].

Characterising the optical components of a QKD system can establish: (i) whether they satisfy the assumptions and requirements of the security proofs [3,4]; (ii) the performance of the system in terms of expected secure bit-rate and range; (iii) immunity from known side-channel attacks; (iv) whether component performance has changed, either from natural ageing, or from hacking [3].

The most important properties of the photons are their mean photon number(s) and timing jitter. Furthermore, phase encoding should impart no discriminating information onto the photons (e.g. on their spectral properties) which an eavesdropper can probe. Solid-state photon counters for the 1550 nm region are normally gated to reduce their dark count rate. The photon detection, dark count and after-pulse probabilities, dead-time, and recovery time of the photon receivers impact directly on the achievable range and quantum bit error rate (QBER) of the QKD system. Their spectral and temporal

distinguishability are also important, as is monitoring the loss of the optical channel.

MEASUREMENTS WHICH ARE KEY TO QKD SECURITY AND PERFORMANCE

In order to characterize the 'Alice' and 'Bob' modules, the measurement instrumentation has to be synchronized with the pulse emission, or detector gate, respectively. The NPL facility is able to synchronise the instrumentation, with low jitter (< 10 ps r.m.s.), to either 'Alice' or 'Bob' as required.

Protocols have been developed to reduce the power of photon-number-splitting (PNS) attacks on multi-photon pulses [3]. In the decoy-state protocol, the mean photon number, μ, of each pulse is randomly switched between two or three values which, if set incorrectly, opens a route to undetectable eavesdropping. A photon counter (Princeton Lightwave PGA-602) operating at 4 MHz gate frequency, was traceably calibrated to the NPL cryogenic radiometer. The photon counter can be synchronised, with low jitter, with pulses from a QKD transmitter operating at up to 1 GHz. Electronic signals from the transmitter can be used to identify the nominal μ values of the pulses, either in real time using bespoke fast logic circuitry, or by post-processing saved events. An uncertainty of ~ 2% for measured μ values can be achieved.

When the laser in a QKD source is driven to emit short optical pulses, typically < 100 ps in duration, the spectral width of the source ($\Delta\lambda_{source}$) ~ 0.1 nm, i.e. $\Delta\nu_{source}$ ~ 12 GHz. A tunable Fabry-Perot cavity spectrometer has been constructed to characterise the spectra of differently phase-encoded photons. It has an operating range from 1270 nm to 1630 nm, a free spectral range of 119 GHz and a linewidth of ~ 570 MHz. These parameters enable a unique scan range of adequate resolution for QKD sources. The device is coupled to a photon counting detector to operate at single photon level.

It is usual to have at least two detectors in a QKD receiver. The characteristics of both detectors should ideally be identical, including their spectral and temporal behaviour. Attenuated laser pulses of known mean photon number, traceable to the NPL cryogenic radiometer, can be used to characterise detectors, which operate at gate rates up to 1 GHz, with an uncertainty of ~ 2%.

QRNGs

Two open-system QRNGs have been constructed: one comprises a photon source, a beam-splitter and two single photon detectors; the second uses a matrix of single photon detectors. In the first, the randomness is restricted by the beam-splitter to two possible outcomes, for the second it is based on the fact that it cannot be predicted where a photon will collapse on the matrix of detectors. An accurate characterisation of the optical components has been carried out in order to test models for linking the performance of the QRNG optical components with the entropy and rate of the generated bit sequence.

DISCUSSION

We will discuss the importance of certain properties of the optical components for the security and performance of QKD systems. We will describe the infrastructure that has been developed at NPL for traceably characterising the quantum optical components of emerging quantum technologies, such as QKD and QRNGs, and present and discuss measurements obtained with these facilities.

REFERENCES

1. The age of the qubit, Iop Publishing 2011, http://www.iop.org/publications/iop/2011/page_52065.html
2. N. Gisin et al., Quantum cryptography, Reviews of Modern Physics 74(1), 145-195, 2002.
3. V. Scarani et al., The security of practical quantum key distribution, Rev. Mod. Phys. 81(3), 1301, 2009.
4. http://tech.fortune.cnn.com/2013/10/14/quantum-key/
5. K. Patel et al., Coexistence of high-bit-rate quantum key distribution and data on optical fiber, Physical Review X 2(4), 041010, 2012.
6. Stucki et al., Towards a high-speed quantum random number generator, Proc. SPIE, 8899, 8890R, 2013.

ACKNOWLEDGEMENTS

This work was funded by: the National Measurement Office of the UK Department of Business, Innovation and Skills; UK Technology Strategy Board Trusted Services Project TP 1913-19252; project MIQC (contract IND06) of the European Metrology Research Programme (EMRP). The EMRP is jointly funded by the EMRP participating countries within EURAMET and the European Union.

TRACEABILITY AT THE SINGLE PHOTON LEVEL FOR QUANTUM COMMUNICATION

A. Vaigu[1,3], T. Kübarsepp[2] F. Manoocheri[1,3], M. Merimaa[3], and E. Ikonen[1,3]

[1]*Aalto University, Metrology Research Institute, Espoo, Finland,* [2]*Metrosert AS, Tallinn, Estonia*
[3]*Centre for Metrology and Accreditation (MIKES), Espoo, Finland*
Corresponding e-mail address: aigar.vaigu@aalto.fi

We have developed a predictable light source for a traceable calibration method of single photon detectors for quantum key distribution. The developed device takes advantage of the known properties of a polarisation insensitive transmission trap detector with predictable attenuation and active fibre coupling system. The attenuator is based on two 10-mm diameter InGaAs photodiodes. An attenuation of 6.3×10^{-5} was observed by direct measuremant at the wavelength of 1550 nm. Furthermore, the attenuation was measured to be independent of incident power levels between 1mW and 1µW.

MOTIVATION

Quantum key distribution systems rely on accurate knowledge of the performance of the optical components within the system. In particular, inefficiencies of the components can be exploited by an eavesdropper. In this work instrumentation for traceable calibration of photon detectors for quantum key distribution systems is developed [1].

METHOD

The calibration method is based on transferring the traceability of conventional optical power measurements to the single photon level using a well-characterized actively fibre coupled attenuator and variable power levels at the source (see Fig. 1).

Transmission trap detectors [2-4] can be viewed as optical attenuators. The incident beam is attenuated by several orders of magnitude depending on the photodiode material, geometrical arrangement and the number of reflections. Attenuators based on transmission trap detectors can be polarisation insensitive. Their further advantage as compared to other types of free space optical attenuators (i.e. filters) is that they have no back reflection.

The attenuator is characterized at 1mW input power level and below to determine the attenuation and the dependence of the attenuation on incident power. The attenuation is obtained from a direct comparison of input and output power levels. The dependence of attenuation on the incident power is studied using the ratio of photocurrents from the photodiodes mounted inside the detector. The coupling efficiency to the fibre is assumed to be independent on the power.

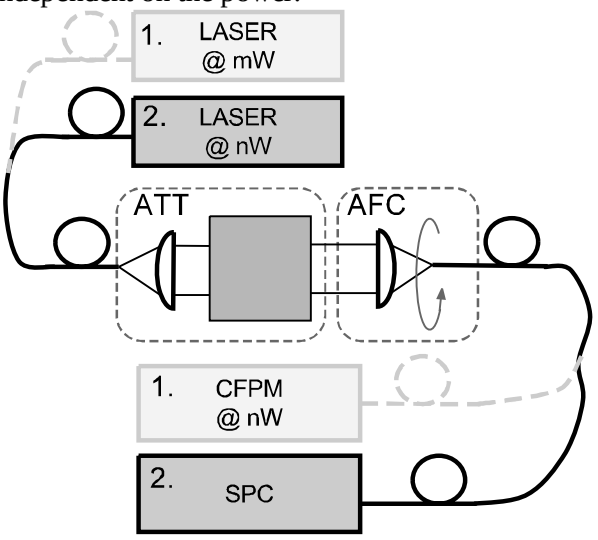

Figure 1. The principle of calibration of single photon detectors. 1. Characterization of the attenuator ATT and active fibre coupling AFC with conventional fiber optic power meter CFPM. 2. Calibration of the single photon counter SPC.

After characterization at high (mW) power levels, the system is used to attenuate the low power (nW) of Fig. 1 down to power levels suitable for single photon counters.

THE APPARATUS

The apparatus for achieving predictable attenuation is made of two main devices: the transmission trap detector providing a predictable attenuation and an actively controlled fibre coupling to achieve unchanged coupling efficiency. The simplest polarization insensitive mechanical design of the attenuator uses only two photodiodes. That design was used to minimize the potential risk of misalignment of the photodiodes.

The body of the attenuator is machined of aluminium and anodized black (Fig. 2). In addition to photodiodes a temperature sensor was placed into the main body part to monitor temperature inside the detector. Windowless InGaAs photodiodes [5] were used, because photodiodes with protective surfaces cannot be used in trap detectors [6]. The two 10-mm diameter photodiodes were mounted into the trap detector in such a way that reflection from photodiode surfaces takes place at the angle of incidence of 17°. The planes of incidence of the photodiodes are perpendicular to each other ensuring polarization insensitivity of the total reflection and attenuation. The reflected, non-absorbed fraction of incoming beam exits from the output aperture of the attenuator at the angle of 34° relative to the direction of the incoming beam as shown in Fig. 2.

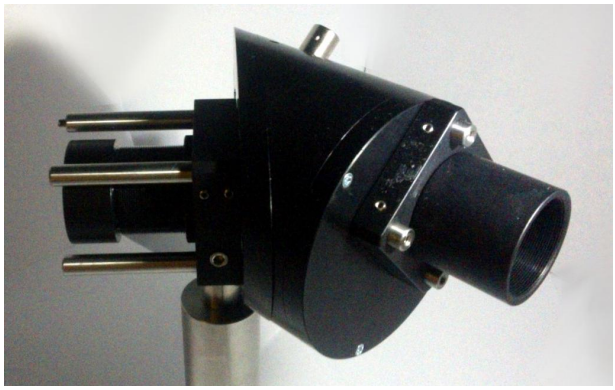

Figure 2. Body of the transmission trap detector. Light enters from the leftmost and exits from the rightmost part of the detector.

Using a two-dimensional modulation of the fibre end position, the coupling efficiency is kept constant at the output of the transmission trap detector. The feedback needed for maintaining the coupling efficiency comes directly from the detector that is under calibration in the setup.

CHARACTERISATION

The attenuation measurements were carried out by direct measurement of the photocurrents from reference detectors. The attenuator provides an attenuation of 6.3×10^{-5} at the wavelength of 1550nm in the range of 1µW up to 1mW incident power (Fig. 3). The attenuation is independent of incident power over that range. The power range was determined by limitations of detectors used in the measurements.

The comparison of photocurrents from the two photodiodes mounted inside the attenuator is shown in Fig 3. The results confirm that the loss mechanisms of the photodiodes are not dependent on the incident power.

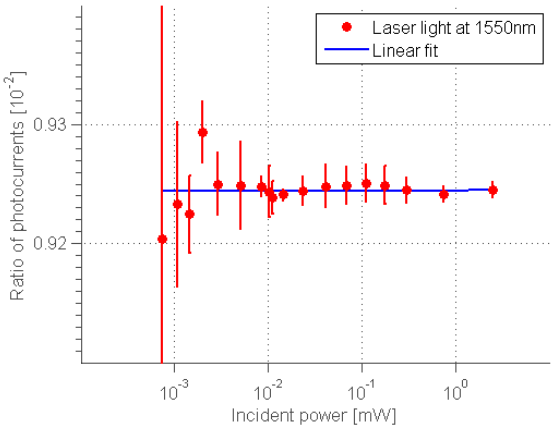

Figure 3. The ratio of photocurrents from the photodiodes inside the attenuator. The variation of the attenuation is much less than 1% in the measured range.

CONCLUSION

The active fibre-coupled attenuation system with predicted attenuation can be used for traceable calibration of the responsivity of photon counters at telecom wavelengths. The calibration results will be presented at the NEWRAD 2014 conference.

ACKNOWLEDGMENT

The work leading to this study was partly funded by the European Metrology Research Programme (EMRP) Project “Metrology for Industrial Quantum Communication.” The EMRP is jointly funded by the EMRP participating countries within EURAMET and the European Union.

REFERENCES

1. Metrology for Industrial Quantum Communications. www.miqc.org
2. Gardner J.L, Transmission trap detectors, Appl. Opt. 33, 5914-5918, 1994.
3. Kübarsepp T, Kärhä P, Ikonen E, Characterization of a polarization-independent transmission trap detector, Appl. Opt. 36, 2807-2812, 1997.
4. Kübarsepp T, White M, Ten-element photodetector for optical power and attenuation measurements, Appl. Opt. 49, 3774-3779, 2010 .
5. Hamamatsu Photonics large active area InGaAs PIN-type photodiode G8370-10.
6. Noorma M et al, Characterization of GaAsP trap detector for radiometric measurements in ultraviolet wavelength region, Rev.Sci.Instrum 76, 033110, 2005.

Detection efficiency measurement for single photon detectors based on correlated photon pairs and superconducting photon detectors

Daiji Fukuda, Takayuki Numata, Akio Yoshizawa, and Hidemi Tsuchida

National Institute of Advanced Industrial Science and Technology(AIST), Tsukuba, Japan
Corresponding e-mail address: d.fukuda@aist.go.jp

Quantum-correlated photon pairs generated by four-wave mixing in dispersion-shifted fiber were utilized to determine detection efficiency for superconducting transition edge single photon detectors. High detection efficiency of the detectors enables a high coincident count rate of 3 kHz at 76 μW pump laser power. Deduced detection efficiency in this method was well consistent with the value obtained with conventional method. This method has high flexibility to optical fiber-based devices used at telecommunication wavelength.

INTRODUCTION

The use of extremely low level optical power with a few photons is widely spreading in many research fields, such as environmental or space measurements, bio-photonics, and quantum telecommunications. For these applications, single photon detectors are now becoming essential tools to detect very weak lights or to reveal the nature of photon emission performances in non-classical light sources [1]. For these purposes, precise determination of the detection efficiency (DE) is a very important task. So far, conventional calibrations for the DE determination were performed by comparison to a reference standard. This method, however, is very complex and difficult, and results in a large measurement uncertainty. On the other hand, quantum-correlated photon pairs can be used to realize an absolute DE measurement without any reference standards. Klyshko [2] first proposed this method, and many experiments have been performed by several groups.

In this paper, we will demonstrate highly efficient calibration system for the DE of single photon detectors aiming at less measurement uncertainty. Spontaneous four-wave mixing (SFWM) in a dispersion-shifted fiber (DSF) is used to generate photon pairs, which is suitable to optical fiber-based telecommunication devices at 1550-nm wavelength. Instead of using conventional InGaAs-APD single photon detectors, high DE superconducting TES detectors are employed to improve the coincident count rates.

THEORY

The correlated photon pairs are generated by launching a pulsed pump laser into a DSF. Among the generated photon pair, one photon (we call this an idler photon) is detected with a trigger single photon detector, and the other photon (a signal photon) is introduced to the single photon detector that is a device under test (DUT). Then, we can deduce the DE of the DUT η_{DUT} by measuring a two-photon coincident count rate of both detectors C_{c}, and a single count rate of the trigger detector N_{iF} and by using the following formula,

$$\eta_{DUT} = \frac{C_c}{\xi_s N_{iF} \eta_{ts}}, \qquad (1)$$

where ξ_{s} and η_{ts} are the collection efficiency of the photon pairs and the transmission efficiency in the signal channel, respectively [3].

Figure 1. Experimental setup for DE measurement based on spontaneous four-wave mixing in DSF.

EXPERIEMNT

Figure 1 shows an experimental setup for the DE measurement. The DSF with 300-m length is pumped with a femto-second pulsed laser, whose center wavelength is set to the zero-dispersion wavelength of the DSF. The spectral bandwidth of the pump laser is narrowed to 0.3 nm with a band pass filter. The DSF is cooled down to liquid nitrogen temperature to reduce noise photons originated from Raman scattering. The $\chi^{(3)}$ non-linear effects of the DSF were investigated by stimulated four-wave mixing with two tunable laser sources (not shown in the figure). As a result, the dispersion wavelength of the DSF is found to be 1559 nm at room temperature; however it

is slightly shifted to 1555 nm at liquid nitrogen temperature. The non-linear coefficient is γ=2.5 W^{-1} km^{-1} without any temperature dependences. The generated photons are separated with an arrayed waveguide grating (AWG), and are further filtered with band pass filters with 0.6 nm bandwidth to reduce pump photons (the extinction ratio > 100 dB). The center wavelengths of signal and idler photons are set to +5 nm and -5 nm to that of the pump laser, respectively. The signal and idler photons are detected with two single photon detectors, which are based on superconducting transition edge sensors (TESs) [4]. The typical DE of the optical TES is over 80 %. This high DE is very effective to enhance the coincident count probability of the signal and idler photons, because the probability is proportional to the square of DE. This high DE in this setup also allows low-pump-power operation to the DSF, which is effective to avoid unwanted non-linear effect, such as noise photons generated through self-phase modulation (SPM) in the DSF.

RESULTS

The DSF is pumped with the 76-μW power. Around this power level, no spectral change or distortion is observed at the DSF output. With this pump power, we observed the coincident count at about 3 kHz with two TES photon detectors. Figure 2 shows an example of a temporal profile of the coincident count obtained with a time to amplitude converter (TAC). We successfully observed a peak of the coincident counts at the delay of 480 ns. The solid line in the figure is the results of the Gaussian fitting with the data. From these results, we obtained the total counts in the peak area. The observed peak width is currently broad, but narrower peak will be expected by optimizing jitter performances of the TES detectors.

As for the trigger count rate N_{iF}, we deduced idler photon counts by subtracting Raman scattered photons from the total counts. This can be done by utilizing the incident power P dependences of the Raman scattered photons ($\sim P^1$) and FWM generated photons ($\sim P^2$). The collection efficiency of the photon pairs is theoretically estimated to ξ_s=0.63 taking account of the spectral function of correlated photon pairs. The transmission efficiency in the signal channel is measured to be 0.12. From these results, we finally deduced the DE to be η=0.84, which is consistent with the value of η=0.83 obtained with the conventional method [4].

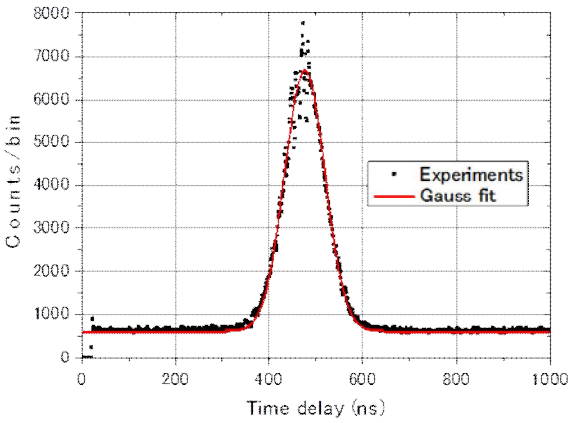

Figure 2. Example of time profile of the coincident counts obtained by two TES photon detectors.

CONCLUSION

The correlated photon pairs were generated through four-wave mixing in the dispersion-shifted fiber, and applied to the determination of the detection efficiency of high performance superconducting TES single photon detectors. We have shown that the obtained results were well consistent with the conventional method.

One of the advantages of the DE measurement method based on the correlated photon pairs is the needlessness of reference standards. We believe this method will become a powerful and essential tool for low-level power measurements with low uncertainty, and for few-photon metrology.

REFERENCES

1. D. N. Klyshko, Use of two-photon light for absolute calibration of photoelectric detectors, Sov. J. Quantum Electron., 10, 1112-1116, 1980.
2. M. D. Eisaman, J. Fan, A. Migdall, and S. V. Polyakov, Invited Review Article: Single-photon sources and detectors, Rev. Sci. Instrum., 82, 071101, 2010.
3. Xiaoying Li, Xiaoxin Ma, Limei Quan, Lei Yang, Liang Cui, and Xueshi Guo, Quantum effiency measurement of single-photon detectors using photon pairs generated in optical fibers, J. Opt. Soc. Am. B, 27, 1857-1865, 2010.
4. D. Fukuda, Go, Fujii, T. Numata, K. Amemiya, A. Yoshizawa, H. Tsuchida, H. Fujino, H. Ishii, T. Itatani, S. Inoue and T. Zama, Titanium-based transition-edge photon number resolving detector with 98 % detection efficiency with index-matched small-gap fiber coupling, Optics Express, 19, pp. 870-875, 2011.

Broadband visible source for spectral response measurement of single photon detectors

Hee Jung Lee[1], Heonoh Kim[1], Myoungsik Cha[1], Dong-Hoon Lee[2,†], and Han Seb Moon[1,*]

[1]*Pusan National University, Busan, Republic of Korea,*

[2]*Division of Physical Metrology, Korea Research Institute of Standards and Science, Daejeon, Republic of Korea*

*Corresponding e-mail address: *hsmoon@pusan.ac.kr; †dhlee@kriss.re.kr*

In this paper, we propose a broadband visible source for relative spectral response measurement of a single photon detector using the fluorescence generated from a 405 nm laser diode. The spectrum of the fluorescence spread from 560 nm to 720 nm. The photon counting stability of the fluorescence was estimated to be ± 1.48% for 5500 s. After the fluorescence was coupled by a single-mode fiber, the total output power of the fluorescence was measured to be 4.2 nW.

INTRODUCTION

For absolute radiometry at the quantum level, on-demand single-photon sources or calibrated photon detectors are needed. Quantum optics techniques have been used for a single-photon detector (SPD) calibration in the photon counting regime [1-2]. However, spectral response measurement of SPD is also important problem of photometry. Broadband sources based on lamps have been used for spectral response measurement of a detector in the visible region.

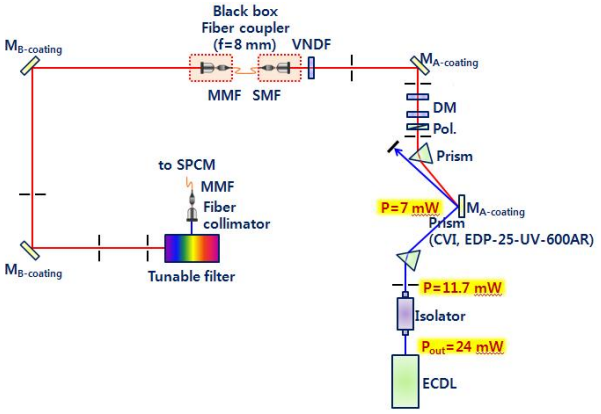

Figure 1. Experimental setup.

There are researches on the fluorescence from gallium nitride (GaN) laser diode (LD), which has also broadband spectra in the visible region [3-4]. The fluorescence from LD has several advantages as a broadband visible source. First, we can make simple and compact source system, because the source is generated from 405 nm LD. Second, directionality of the fluorescence is same as the pump laser (collinear condition), resulting in easy collecting by a fiber coupler. Lastly, the price of the LD is much cheaper than other broadband sources. In this paper, we propose a method for generating broadband visible source from a LD, and the source could be useful for calibration of detectors.

EXPERIMENTAL SETUP

Figure 1 shows a schematic of our experimental setup. The pump laser we used is a 405 nm blue LD. To find only the effect of the fluorescence, we use two prisms. After passing through the first prism, the incident light spreads into a spectrum which consists of a 405 nm line and the fluorescence continuum. Then we collect the fluorescence only by using the second prism. The collecting light is coupled into the single mode fiber. The fiber output propagates into a tunable filter (LLTF VIS-2, Photon etc.) to investigate the fluorescence spectrum, and then output of the tunable filter was connected to a single photon detector.

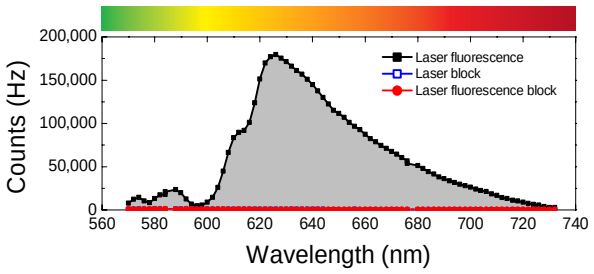

Figure 2. The fluorescence spectrum.

EXPERIMENTAL RESULTS

A. Fluorescence Spectrum

We measure the fluorescence spectrum with the tunable filter at the collinear condition. Figure 2 shows the fluorescence spectrum after single mode fiber coupling. The spectrum of the fluorescence spread from 560 nm to 720 nm The bandwidth in the visible region is about 80 nm.

B. Digital camera image

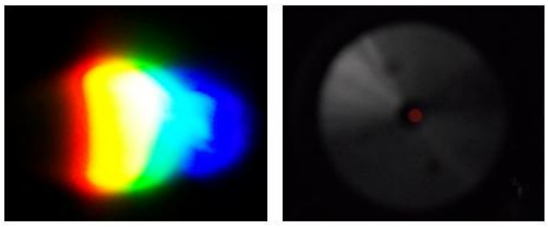

(a) (b)

Figure 3. Digital image (a) free space and (b) after single mode fiber coupling.

We take photos of the fluorescence after the second prism as shown in Fig.3. Figure 3 (a) is an image taken in the free space. Through the image we find the fluorescence consists of broadband spectra. Figure 3 (b) shows an image after single mode fiber coupling, where the total output power is 4.2 nW. The red color is dominant because we use a single mode fiber for 780nm.

C. Photon counting stability

Finally, we measure the photon counting stability of total fluorescence and at three wavelengths (570 nm, 655 nm, and 700 nm). The photon counting stability of total fluorescence is estimated to be ±1.48 % for time duration of 5500 s (Fig.4).

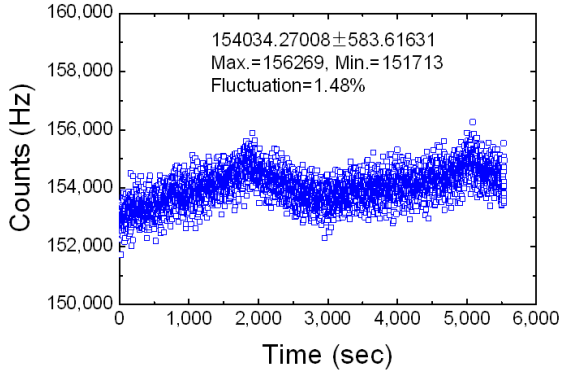

Figure 4. The photon counting stability for total fluorescence.

We also select representative wavelengths and measure the stability, as show in Fig. 5. The stability for 570 nm, and 655 nm, 700 nm is estimated to be ± 9 %, ± 4 %, and ± 3 %, respectively.

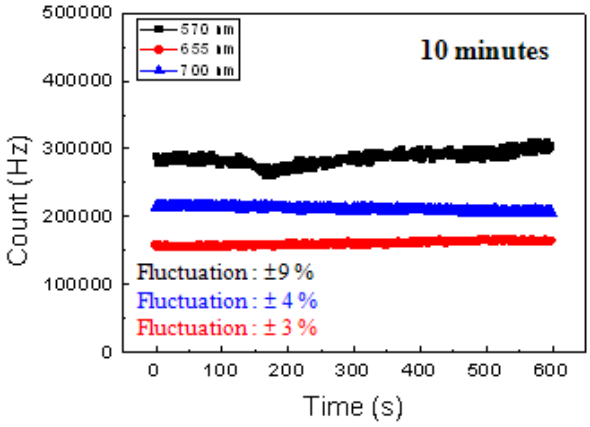

Figure 5. The photon counting stability for three wavelengths (570 nm, 655 nm, and 700 nm)

CONCLUSION

We investigated the properties of LD fluorescence such as the spectrum, total output power, digital camera image, and photon counting stability. From these experimental results, we checked the possibility of using LD as a broadband visible source for calibration of detectors. We plan to characterize the performance of broadband visible source.

REFERENCES

1. J. C. Zwinkels, E. Ikonen, N. P. Fox, G. Ulm, and M. L. Rastello, Photometry, radiometry and 'the candela': evolution in the classical and quantum world, Metrologia **47,** R15–R32, 2010.
2. S. V. Polyakov and A. L. Migdall, High accuracy verification of a correlated photon-based method for determining photon-counting detection efficiency, Opt. Express **15**, 1390-1407, 2007.
3. T. Ogino and M. Aoki, Mechanism of Yellow Luminescence in GaN, Jpn. J. Appl. Phys. **19**, 2395-2405, 1980.
4. S. J. Chua, S. Tripahy, P. Chen, E. Takasuka, and M. Ueno, Near-field optical characterization of GaN and $In_xGa_{1-x}N$/GaN heterostructures grown on freestanding GaN substrates, Physica E **25**, 356-365, 2005.

High-attenuation tunnel-type detector for calibration of single-photon devices

T. Kübarsepp[1,2], A. Pokatilov[1,2], V. Vabson[1], K. Dhoska[2], G. Porrovecchio[3], S. Götzinger[4], A. Manninen[5], andS. Kück[6]

[1]*AS Metrosert, Tallinn, Estonia*
[2]*Tallinn University of Technology, Tallinn Estonia*
[3]*Czech Metrology Institute, Prague, Czech Republic*
[4]*Friedrich-Alexander-Universität, Erlangen, Germany*
[5]*MIKES, Espoo, Finland*
[6]*Physikalisch-Technische Bundesanstalt (PTB), Braunschweig, Germany*
Corresponding e-mail address: tkubarsepp@metrosert.ee

The tunnel type twelve-photodiode detector with high attenuation of transmitted beam has been designed for use in calibration of very low photon rates in the wavelength range 400 nm – 950 nm. The attenuation is based on predictable reflectance of Si-based photodiodes in the detector. The estimated attenuation of a beam is from ~$5\cdot10^4$ to ~$3\cdot10^6$. The geometrical properties and spectral characteristics of the attenuator are briefly presented.

DESIGN

The design of the tunnel-type attenuator is based on two transmission trap detectors in which six photodiodes have been assembled in the device [1] to provide coaxial input and outgoing beams. The photodiodes are arranged in such a configuration that the photodiode active areas face the incidence light beam close to angle 45°. The mounting of the photodiodes in the device provides polarization-independent attenuation of incidence beam.

In our transmission-type trap detector, the number of photodiodes is extended to twelve. This is done to achieve sufficient attenuation of a laser beam used in high-accuracy comparison measurements of single photon detectors or single photon sources against conventional transfer standards [2].

The windowless silicon photodiodes (S1337 11, Hamamatsu) are used in our device. Photodiodes are electrically connected in parallel to measure the photosignal generated by incoming light.

ATTENUATION

The transmittance of the attenuator (ie transmission trap detector) can be calculated based on optical constants for SiO_2 and Si and using multiple reflection modelling in the device [3]. The transmittance $T(\lambda)$ and the attenuation $\gamma(\lambda)$ of the 12-photodiode attenuator can be calculated as:

$$T(\lambda) = \left[\rho_s(\lambda) \times \rho_p(\lambda)\right]^6 \quad (1),$$

$$\gamma(\lambda) = 1/T(\lambda) \quad (2).$$

where $\rho_s(\lambda)$ is the reflectance of a single photodiode in the *s*-polarization plane and $\rho_p(\lambda)$ is the reflectance of a single photodiode in the *p*-polarization plane, both at a 45° angle of incidence.

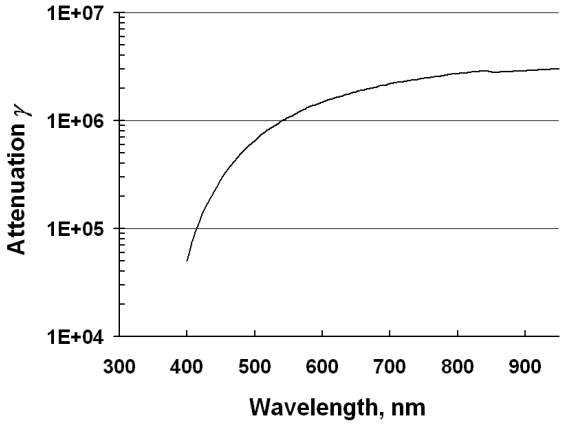

Figure 1. Calculated attenuation of the 12-photodiode transmission trap detector in the wavelength range from 400 nm to 950 nm.

The calculated attenuation of the 12-photodiode transmission trap detector, having 30 nm thick antireflection SiO_2 coating, is depicted in Figure 1.

This work was funded by the project SIQUTE (contract EXL02) of the European Metrology Research Programme (EMRP). The EMRP is jointly funded by the EMRP participating countries within EURAMET and the European Union.

REFERENCES

1. T.Kübarsepp, P. Kärhä, and E. Ikonen, "Characterization of a polarization-independent transmission trap detector," Appl. Opt. **36**, 2807-2812 (1997).

2. S. Kück et al, “The SIQUTE-project – first results towards single-photon sources for quantum technologies”, submitted to NEWRAD 2014, Espoo, Finland.
3. A. Haapalinna, P. Kärhä, and E. Ikonen, “Spectral reflectance of silicon photodiodes,” Appl. Opt. **37**, 729-732 (1998).

Calculation and experimental validation of the photon statistics of the Undulator U180 of the Metrology Light Source in the visible and NIR

Ingmar Müller and Roman M. Klein

Physikalisch-Technische Bundesanstalt, Berlin, Germany
Corresponding e-mail address: ingmar.mueller@ptb.de

The strict proportionality of emitted radiant intensity and the number of stored electrons of an electron storage ring provides a unique possibility to bridge the radiometric gap between radiant power measurement and photon counting by means of synchrotron radiation. The emitted synchrotron radiation can be classically described and, thus, does not have single photon source characterisitics. If synchrotron radiation is used to calibrate non-photon number resolving single photon detectors, the photon statistics of the radiation has to be known. In this paper the measurement of the photon statistics of the Undulator U180 of the Metrology Light Source by means of a coincidence technique at a wavelength of 1.55 µm is described. Furthermore, the photon statistics of the U180 radiation is calculated for different radiation bandwidths in the wavelength range from 1 nm to 2000 nm.

INTRODUCTION

The primary source standard Metrology Light Source (MLS) [1] of the Physikalisch-Technische Bundesanstalt (PTB) has the necessary equipment installed to obtain a dynamic range of the emitted spectral radiant power of 11 orders of magnitude. PTB also operates primary detector standards for spectral radiant power based on cryogenic radiometers (CR) (see for instance [2]). With these two tools, a calibration chain for single photon detectors (SPDs) traceable to the CR can be established [3,4]. However, the single photon detectors calibrated in [3,4] are non-photon number resolving detectors, i.e., since the Metrology Light Source is no single photon source the measured count rate of the SPDs has to be corrected for detected events that contained two or more photons [5,6]. As shown in Figure 1, the photon statistics correction $[p(2)+p(3)]p(1)^{-1}$, with $p(i)$ the probability that synchrotron radiation pulse contains i photons, can heavily influence the calibration result. For rates above 500000 photons/s, it would become the dominant uncertainty contribution for this calibration

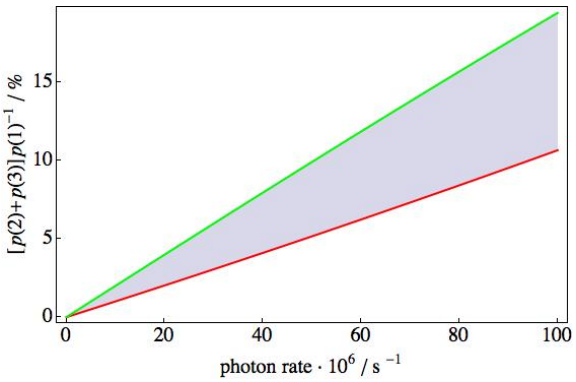

Figure 1. Photon statistic correction plotted over the photon rate of the Metrology Light Source for the assumptions, thermal radiation (green line) and coherent radiation (red line).

method if the photon statistics is unknown. The photon statistics of a radiation source can be determined from the measurement of the intensity correlation function, the so-called $g^{(2)}(\tau=0)$ function [7]. The measured value of $g^{(2)}(\tau=0)$ of a classical radiation source can have values between 2 and 1 indicating a thermal photon distribution ($g^{(2)}(0)=2$), a Poissonian distribution ($g^{(2)}(0)=1$) or mixtures of both distributions ($2>g^{(2)}(0)>1$). To correct for the photon statistics of the Metrology Light Source, a thermal statistics is assumed [8]. However, in reality the thermal behaviour of the emitted radiation is weakened because the pulse width of the synchrotron radiation is longer than the longitudinal coherence length and the cross section of the beam is larger than the transverse coherence length. Taking these effects into account, the estimated value of $g^{(2)}(\tau=0)$ is given by [8]:

$$g^{(2)}_e(0) = 1 + F(\pi^{½} d_x/l_x)F(\pi^{½} d_y/l_y)\tau_c/\tau_p \qquad (1)$$

with l_x and l_y the transverse coherence widths in vertical and horizontal direction, $d_{x,y}$ the dimensions of the entrance optics, $\sigma_{x,y}$ the standard deviation of the Gaussian source size, τ_c the coherence time of the beam, τ_p the pulse width of the synchrotron radiation with $\tau_c << \tau_p$. A detailed description of $F(b)$ can be found in [9]. The value of $g^{(2)}(\tau=0)$ of the Undulator U180 of the MLS was measured using fibre-coupled superconducting nano-wire single

photon detectors (SNSPDs) and $g^{(2)}_e(0)$ was calculated for different radiation bandwidths.

MEASUREMENT

The measurement of the photon statistics was performed at a wavelength of 1.55 µm. To measure $g^{(2)}(0)$ the synchrotron radiation was monochromatised with an interference filter with a central wavelength of 1551.97 nm and a spectral width $\Delta\lambda$ of (10±2) nm and was coupled into an optical fibre. A fibre-coupled beam splitter with a splitting ratio of 50/50 was used to irradiate two SNSPDs with the synchrotron radiation. The two SNSPDs were connected with the start and stop input of a coincidence counter (*Picoharp 300, Picoquant*), respectively. This setup was used to measure the coincidences in a certain time window. To correct for the systematical temporal evolution due to the bunched structure, that contributes to a large amount of trivial correlation [10] in the measurement of $g^{(2)}(0)$, the coincidences were normalised by using a synchrotron radiation pulse from the same electron bunch to trigger the initial coincidence measurement and the normalisation coincidence measurement using an additional coincidence counter (*Picoharp 300, Picoquant*) delayed by one revolution of the ring [8]. The measured value with normalisation of $g^{(2)}(0)$ yields 1.0051 ± 0.0008 and, thus, a quasi-poissonian photon statistics.

CALCULATION

The value of $g^{(2)}_e(0)$ was calculated for the condition at the U180 of the MLS for different spectral widths $\Delta\lambda$ (see Figure 2). The calculation of $g^{(2)}_e(0)$ for the measurement condition described above yields a value of 1.0064. The simulations show that the photon statistics of the synchrotron radiation strongly depends on $\Delta\lambda$, and, hence, on the coherence time τ_c. The decrease of the thermal behaviour of the synchrotron radiation with decreasing wavelengths can be explained by the size of the emitting coherence cells in the radiation source. The size of the coherence cells is directly connected to wavelength. A reduction of the wavelength reduces the overlap of the coherence cells and, thus, the rate of excess photons.

CONCLUSION

The calculated value of $g^{(2)}_e(0)$ and the measured value of $g^{(2)}(0)$ for a wavelength of 1551.97 nm show a good agreement. The difference in the measured and calculated value is most probably caused by the spectral shape of the used interference filter. However, the measurement proved that the calculation of $g^{(2)}_e(0)$ can be used to determine the appropriate correction factor for high accuracy calibrations of SPDs by means of synchrotron radiation as described in [3,4].

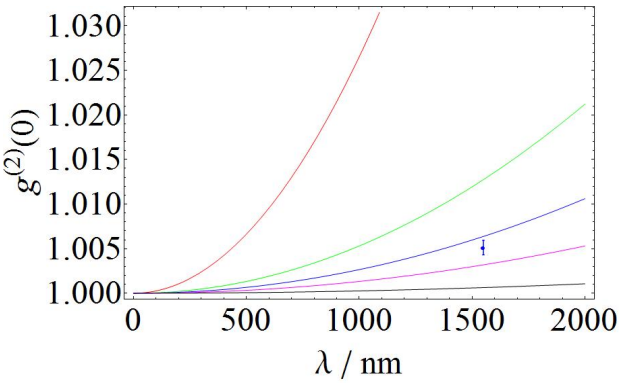

Figure 2. Calculated $g(2)_e(0)$ for the U180 of the MLS for spectral widths $\Delta\lambda$ of 1 nm (red line), 5 nm (green line), 10 nm (blue line), 20 nm (magenta line), 100 nm (black line) and the measured value of g(2)10nm(0) (blue circle).

REFERENCES

1. Burkhard B., et al., A quarter-century of metrology using synchrotron radiation by PTB in Berlin., physica status solidi (b), 246(7), 1415–1434, 2009.
2. Hartmann J., et al., Traceable radiometric calibration of semiconductor detectors and their application for thermodynamic temperature measurement, Mapan, 25(1), 2010.
3. Müller I., Klein R.M., Hollandt J., Ulm G., and Werner L., Traceable calibration of Si avalanche photodiodes using synchrotron radiation. Metrologia, 49(NEWRAD), S152–S155, 2012.
4. Müller I., Klein R.M., Traceable calibration of a fibre-coupled superconducting nano-wire single photon detector, these proceedings.
5. Schmunk W., Rodenberger M, Peters S., Hofer H., Kück S., Radiometric Calibration of Single Photon Detectors by a Single Photon Source based on NV-centers in diamond, Journal of Modern Optics 58, 1252, 2011.
6. Kück S., Hofer H., Peters S., Detection Efficiency Determination of Si-SPAD Detectors, Single Photon Workshop 2013, Oak Ridge National Laboratory, Oak Ridge, Tennessee, USA, 15-18, October, 2013, http://web.ornl.gov/sci/qis/SPW2013_Program.pdf, p. 95.
7. Glauber R., The Quantum Theory of Optical Coherence, Physical Review, 130(6), 2529–2539, 1963.
8. Kunimune Y. et al., Two-photon correlations in X-rays from a synchrotron radiation source, Journal of Synchrotron Radiation, 4, 199–203, 1997.

9. Ikonen E. and Rüffer R., Correlated gamma rays in synchrotron radiation, Hyperfine Interactions, 92, 1089-1094, 1994.
10. Miyahara T., From First-Order Coherence to Higher-Order Coherence of Synchrotron Radiation, Journal of Synchrotron Radiation, 5, 305–308, 1998.

Visible Zone Spectral Radiance Flux Measurement in NIM china

Zhao Weiqiang[1], Liu Hui[1], Liu Jian[2], and Zhao Haisu[1]

[1] *National Institute of Metrology, Beijing, P.R.China;* [2]*Beijing Normal University, Beijing, P.R.China*
Corresponding e-mail address:zhaowq@nim.ac.cn

An array-based goniospectroradiometer for visible zone spectral radiance flux measurement in National Institute of Metrology China (NIM) is established. The facility is used to calibrate total spectral radiance flux standard lamp, which is highly demand for those integrating sphere equipment. A group of four lamps is tested to investigate the repeatability and consistency. The total luminous flux results are good coincided with NIM standards. The deviation of the spectral radiance flux for each lamps is small than 0.3% (400 nm -780 nm). The goniospectroradiometer is calibrated in-situ, and all the results are traceable.

PROBLEM

Nowadays, the LED factories are always using integrating sphere to measure the total luminous flux and colour quality. The integrating sphere is connecting to a spectroradiometer. To calibrate such a spherical system, visible zone spectral radiance flux standard lamps are needed. In National Institute of Metrology China (NIM), we have setup an array-based goniospectroradiometer to calibrate those standard lamps. [1-2]

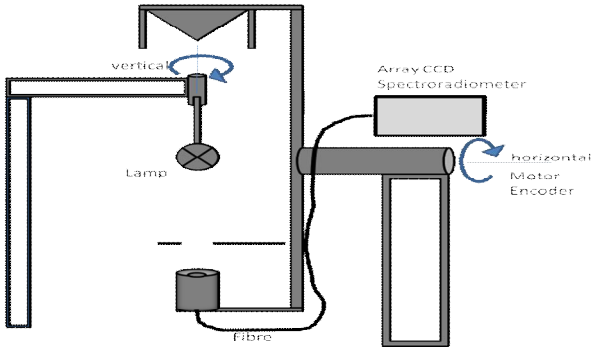

Figure 1. Structure of the goniospectroradiometer.

METHODS

The structure of the array-based gonio-spectroradiometer is shown in figure 1. The direction of the rotation axes are guaranteed by a water level. The intervals of the vertical and horizontal rotation are 15°and 5° respectively, controlled by a computer. The distance from the lamp center to collecting surface of the fibre is 0.8250 m, measured by a tubular type inside micrometers. The spectroradiometer is calibrated in-situ by a spectral radiant standard lamp (spectral) and an illuminance meter (absolute value).

RESULTS

A group of four halogen lamps are measured to investigate the repeatability and consistency of this facility. The total luminous flux (TLF) and the visible zone (380 nm - 780 nm) spectral radiance flux are tested. Table 1 is the result of measured total luminous flux, showing the difference between this facility and the NIM's standard spherical photometer, about 0.3%.

Table 1. The result of measured total luminous flux.

Lamps	TLF by this facility (lm)	TLF by NIM's standard (lm)
24V50W #4	788.2	790.8
24V50W #7	797.7	800.0
24V100W #11-10	1399	1403
24V100W #131	1403	1407

We use an integrating sphere with a spectro-radiometer to test the consistency of these four lamps. The visible zone spectral radiance flux is $\Phi_i(\lambda)$. The reading of the spectroradiometer is $R_i(\lambda)$. The Relative deviation from average value is defined as

$$\eta_i(\lambda)= \frac{\frac{\Phi i}{Ri}}{\left(\frac{\Phi i}{Ri}\right)}, \quad i=1...4 \qquad (1)$$

The results are shown in figure 2. The relative deviations are smaller than 0.3% when the wavelength is larger than 400 nm. We believe higher deviation in 380 nm is due to the weak signal in our array CCD, which will be improved when a broadband array CCD is used.

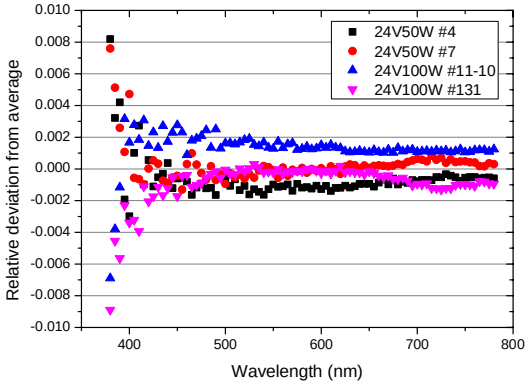

Figure 2. Relative deviation from average (380 nm – 780 nm, per 5 nm)

CONCLUSION

NIM has setup a facility, an array-based gonio-spectroradiometer, for visible zone spectral radiance flux measurement. The equipped spectroradiometer is calibrated in-situ by a spectral radiant standard lamp (spectral) and an illuminance meter (absolute value). A group of four lamps is tested to investigate the repeatability and consistency. The total luminous flux results are good coincided with NIM standard, about 0.3%. The deviation of the spectral radiance flux for each lamps is small than 0.3% (400 nm - 780 nm). All the results are traceable.

REFERENCES

1. Yoshi Ohno and Yuqin Zong, NIST Facilityfor Total Spectral Radiant Flux Calibration, Simposiode Metrología, 25 al 27 de Octubre, 2004.
2. Michael Shaw* and Teresa Goodman, Array-based goniospectroradiometer for measurement of spectral radiant intensity and spectral total flux of light sources, Applied Optics, 47(14), 2637-2647.

Spectral Irradiance Measurement and Actinic Radiometer Calibration for UV Water Disinfection

Peter Sperfeld[1], Bettina Barton[1], Sven Pape[1], Anna-Lena Towara[1], Jutta Eggers[2], and Gabriel Hopfenmüller[3]

[1]Physikalisch-Technische Bundesanstalt, Braunschweig & Berlin, Germany,
[2]DVGW-Technologiezentrum Wasser, Karlsruhe, Germany ,[3]sglux SolGel Technologies GmbH, Berlin, Germany
Corresponding e-mail address: Peter.Sperfeld@ptb.de

In a joint project, sglux and PTB investigated and developed methods and equipment to measure the spectral and weighted irradiance of high-efficiency UV-C emitters used in water disinfection plants.

A calibration facility was set-up to calibrate the microbicidal irradiance responsivity of actinic radiometers with respect to the weighted spectral irradiance of specially selected Hg low-pressure and medium-pressure UV radiators.

To verify the calibration and to perform on-site tests, spectral measurements have been carried out directly at water disinfection plants in operation. The weighted microbicidal irradiance of the plants was calculated and compared to the measurements of various actinic radiometers.

INTRODUCTION

More and more water disinfection systems are equipped with high-efficiency UV emitters which have to fulfil special requirements for their spectral irradiance. A high irradiance should be achieved in the spectral range covering the microbicidal action spectrum between 240 nm and 290 nm, whereas below 240 nm, the irradiance should be low, in order to avoid any possible photochemical processes leading to by-product formation.

Actinic radiometers [1] monitor UV radiators, but they cannot provide any information on the spectral distribution of the radiators in the plants.

The radiometer response has to represent the weighted microbicidal irradiance of the UV emitters. However, the spectral responsivity does not exactly match the microbicidal action spectrum and the readout of the radiometer has to be corrected by its spectral mismatch. The direct spectral responsivity calibration of such actinic radiometers is very limited due to the high spectral power needed for such measurements. Thus, a calibration facility has been constructed, where actinic radiometers are calibrated with respect to the spectral irradiance of typical high-power UV sources.

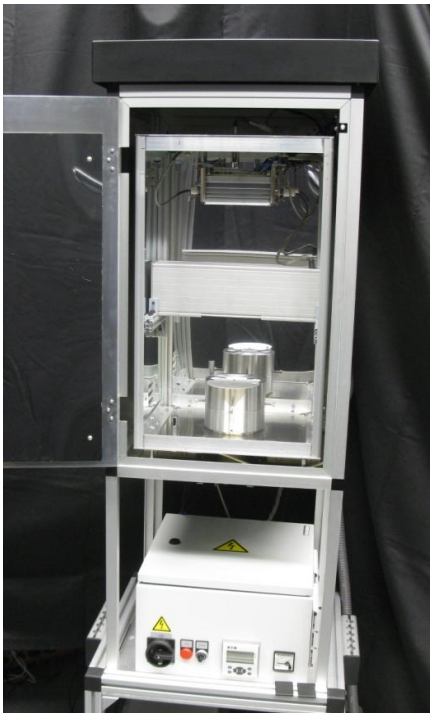

Figure 1. The transfer standard for high-power UV irradiance.

THE CALIBRATION FACILITY

Commercially available UV radiators designed specifically for UV disinfection have been characterized, and their suitability as a calibration standard has been investigated [2]. To calibrate sensors for UV water disinfection plants based on Hg medium-pressure emitters as well as on Hg low-pressure sources, a 1000 W medium-pressure lamp and a 40 W low-pressure lamp were selected.

The Hg medium-pressure lamp is mounted on top of a ventilated cabinet and the Hg low-pressure can be mounted underneath (Fig. 1). A UV sensor mounted at the bottom of the cabinet can hold actinic radiometers to be calibrated as well as specially designed entrance optics of spectroradiometers. The spectral irradiance $E_S(\lambda)$ of the UV sources is measured using an array spectroradiometer as well as a fast scanning double monochromator system.

The measured spectra are shown in Fig. 2 compared to the spectral irradiance distribution of typical standard lamps.

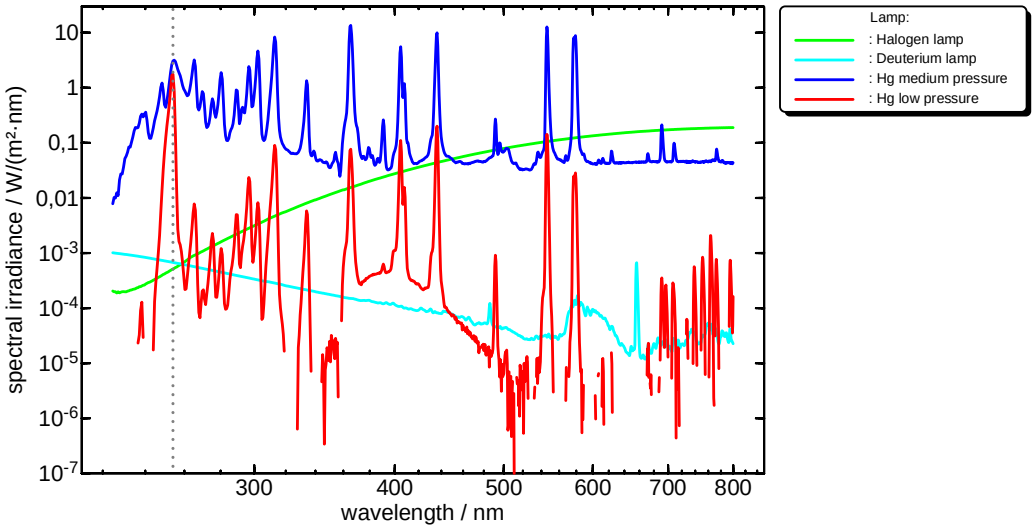

Figure 2. Spectral irradiance of classical standard lamps compared to the high-power UV transfer standard lamps.

Weighted with the microbicidal action spectrum $a_{\mathrm{mic}}(\lambda)$, the microbicidal irradiance $E_{\mathrm{mic,S}}$ of the Source *S* can be calculated and actinic radiometers are calibrated with respect to the weighted irradiance

$$E_{micS} = \int a_{mic}(\lambda) \cdot E_S(\lambda) d\lambda \qquad (1)$$

ON-SITE SPECTRAL MEASUREMENTS

Traceable spectral measurements of high-power UV sources are rather challenging. The spectral irradiance of such radiators is higher by several orders of magnitude than the spectral irradiance of typical transfer standard lamps. Therefore, two spectroradiometers have been adapted to measure high irradiances.

The entrance optics of the fibre-coupled instruments have been constructed similarly to that of the actinic radiometers [4]. Density filters inside the spectroradiometers allow the attenuation of the incoming radiant power by up to three orders of magnitude. Combined with the high dynamics of the spectroradiometers they were calibrated using deuterium lamps and quartz halogen lamps.

For the first time, spectral measurements directly on UV disinfection plants in operation were carried out. Water disinfection systems using both types of UV emitters were measured at the DVGW test centre in St. Augustin, Germany [3]. The resulting calculated microbicidal irradiances agreed well with the measurements of the reference radiometers used at the test centre.

Additional measurements of different reference radiometers at the new calibration facility confirmed the source-based calibration method.

CONCLUSION

Direct spectral measurements allow the examination of new water disinfection systems and radiator types. Combined with new UV transfer standard sources it is possible to calibrate broadband actinic UV radiometers in terms of microbicidal irradiance responsivity.

ACKNOWLEDGMENTS

This work was supported in part by the Federal Ministry for Economy and Technology based on a decision of the German Parliament under Grant No KF2303704RR9.

REFERENCES

1. G. Hopfenmüller, T. Weiss, B. Barton, P. Sperfeld, S. Nowy et al., PTB traceable calibrated reference UV radiometer for measurements at high irradiance medium pressure mercury discharge lamps, Proceedings of 2013 EMEA Regional Conference, Karlsruhe.
2. B. Barton, P. Sperfeld, A. Towara, G Hopfenmüller et al., Developing and setting up a calibration facility for UV sensors at high irradiance rates, Proceedings of 2013 EMEA Regional Conference, Karlsruhe.
3. P. Sperfeld, B. Barton, S. Pape, J. Eggers, G. Hopfenmüller,. Traceable measurements of the spectral irradiance of UV water disinfection plants, Proceedings of 2013 EMEA Regional Conference, Karlsruhe.
4. B. Barton, P. Sperfeld, S. Nowy, G. Hopfenmüller et. al, Characterization of new optical diffusers used in high irradiance UV radiometers, NEWRAD 2011.

New Pyrolytic-Graphite Blackbody for Spectral Irradiance

Boris Khlevnoy, Denis Otryaskin, Maxim Solodilov, Andrey Puzanov, Irina Grigoryeva, Svetlana Kolesnikova, Valeriy Gavrilov, and Sergey Ogarev

All-Russian Research Institute for Optical and Physical Measurements (VNIIOFI), Moscow, Russia
Corresponding e-mail address: khlevnoy-m4@vniiofi.ru

A new blackbody suitable for spectral irradiance measurements has been developed. The blackbody, BB-PyroG/3000/20 has a pyrolytic graphite radiator and similar design to the blackbody BB3500M that widely used for spectral irradiance, but much smaller, less power consuming and, thus, accessible for to a wider range of users. The new blackbody has a cylindrical cavity with diameter of 20 mm and an opening of 15 mm that large enough for spectral irradiance in combination with an outer aperture of about 6 mm. A comparison of spectral irradiance measurements in the range from 250 nm to 1600 nm were performed using BB-PyroG/3000/20 and BB3500M. The comparison shows the agreement of two blackbodies within measurements uncertainties.

INTRODUCTION

Spectral Irradiance is one of the main radiometric quantities, selected by the CCPR as a "key comparison" quantity. In the wavelength range from 250 nm to 2500 nm the spectral irradiance scale is usually realized using a high-temperature blackbody (HTBB). One type of HTBB, namely BB3500M [1] (previous modifications are also known as BB3200pg and BB3500) with a cavity consisting of a set of pyrolytic graphite rings, has become the most popular for the last two decades. Pyrolytic graphite (PG) allows using a cavity at the temperature level of 3000 K to 3100 K (the most convenient temperature for spectral irradiance) for hundreds of hours and achieving the maximum temperature of 3500 K. Its other advantages are high emissivity, large cavity and opening, good uniformity and stability. All this allows realizing spectral radiance and irradiance with the highest accuracy [2-4]. BB3500M is also used for such important application as high-temperature fixed points (HTFP) [5].

The BB3500-type HTBB is well investigated and is used at many NMIs [6]. However, relatively high price of pyrolytic graphite in a market and power consumption limit a potential usage of this blackbody at some other laboratories.

A few years ago VNIIOFI developed a smaller version of the pyrolytic-graphite HTBB [7]. That smaller blackbody, BB3300-PyroG, was designed mostly for spectral radiance and temperature measurements, and hardly can be applied for spectral irradiance because of its relatively small cavity. Therefore, a new modification of BB-PyroG with increased cavity, suitable for spectral irradiance, was developed. To confirm the reliability of the new blackbody, comparative spectral irradiance measurements were performed with two blackbodies: the new one BB-PyroG/3000/20 and with BB3500M.

BLACKBODY DESIGN

The design of BB-PyroG/3000/20 is similar to that of BB3500M, but all dimensions are smaller. The cross-section of BB-PyroG/3000/20 is shown in Fig.1.

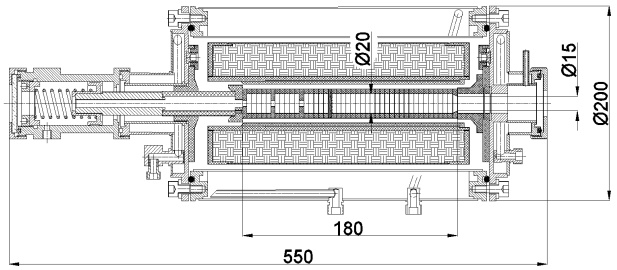

Figure 1. Cross-section of BB-PyroG/3000/20.

The blackbody is assembled in water-cooled housing, containing a cylindrical set of PG rings, which is surrounded by a thermoshield. The ring set is compressed in between the front flange and a rear movable graphite electrode, which is pushed by a spring and has an electrical contact with the rear flange. The rings are heated up by electrical current going through the rings. Electrical ports are located on the housing flanges. The Table 1 presents the main dimensions of the BB-PyroG/3000/20 in comparison with those of BB3500M. Ring outer diameter is 30 mm, the length of the ring set is 180 mm; therefore, the volume of pyrographite used is 5 times less than that used in BB3500M. The rings contain a

cylindrical radiating cavity with a diameter of 20 mm and depth of 120 mm.

Table 1. Main dimensions of BB-PyroG and BB3500M.

Parameter	BB-PyroG	BB3500M
Housing diameter/length, mm	200 / 550	360 / 800
Ring outer diameter / length, mm	30 / 180	54 / 290
Volume of PG, cm^3	127	664
Cavity diameter, mm	20	38
Cavity length / opening, mm	120 / 15	185 / 24
Max. temperature, K	3200	3500
Max. current, A	300	750
Max. voltage, V	22.5	26
Power consumption, W	7	19.5
Emissivity	0.9992 ±0.0007	0.9995 ±0.0005

TEMPERATURE AND SUPPLY POWER

The rings are annealed at the temperature of 3000 ºC and the maximum working temperature of the blackbody is 3200 K. It is good enough for spectral irradiance, because the ideal temperature for FEL lamp calibration is about 3050 K.

Electrical supply current and voltage as functions on temperature are shown in Fig.2. One can see that the maximum current and voltage are 300 A and 22.5 V, respectively. The electrical parameters of two blackbodies are compared in Table 1. The power consumption of BB-PyroG/3000/20 is within 7 kW while BB3500M needs about 19.5 kW. Lower consumption makes a power supply smaller, lighter and cheaper.

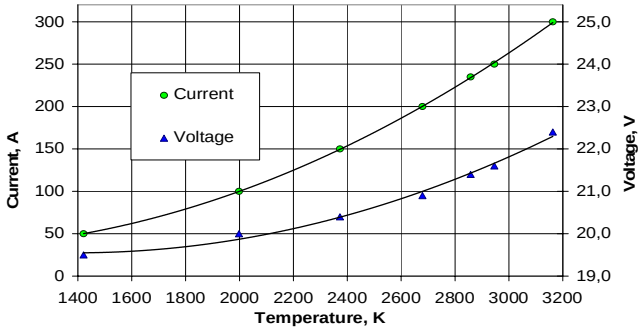

Figure 2. Electrical parameters of BB-PyroG.

EMISSIVITY

The ration of a cavity length to opening of BB-PyroG and BB3500M is nearly same; therefore the "isothermal" emissivities for both blackbodies are similar. However, due to smaller cavity diameter the bottom non-uniformity of BB-PyroG could be higher. The stronger temperature gradient and higher uncertainty of the gradient leads to lower emissivity with higher uncertainty. The emissivity of BB-PyroG estimated with Monte-Carlo method is 0.9992±0.0007, while the emissivity of BB3500M is 0.9995±0.0005.

SPECTRAL IRRADIANCE COMPARISON

To validate BB-PyroG as a standard planckian source for spectral irradiance measurements it was compared with BB3500M. First, a 1000W FEL lamp as calibrated against BB3500M in the spectral range 2500 nm to 1600 nm. Then, the same lamp was calibrated against BB-PyroG/3000/20. Both blackbodies were operated at the temperature of about 3020 K; the temperature was measured by the same radiation thermometer. The only difference in measurement schemas was diameter of a precise aperture: 8 mm and 6 mm apertures were used with BB3500M and BB-PyroG, respectively.

The results of calibration carried out with two blackbodies agreed within measurement uncertainties.

REFERENCES

1. B. Khlevnoi, Metrological Investigation of Pyrographite High-Temperature Blackbodies, Measurement Techniques vol 44 No 12 (2001) 1211-1218
2. E. Woolliams, N. Fox, M. Cox, P. Harris, N. Harrison, Final report on CCPR K1-a: Spectral irradiance from 250 nm to 2500 nm, Metrologia 43 (2006).
3. B. Khlevnoy, V. Sapritsky, B. Rougie, C. Gibson, H. Yoon, A. Gaertner, D. Taubert, J. Hartmann, CCPR-S1 Supplementary comparison for spectral radiance in the range of 220 nm to 2500 nm, Metrologia 46 (2009) S174-S180.
4. D-J. Shin, C-W. Park, S. Kolesnikova B. Khlevnoy, Final report on bilateral comparison APMP.PR-K1.a.1-2008 between KRISS (Korea) and VNIIOFI (Russia): Spectral irradiance from 250 nm to 2500 nm, Metrologia, 47 (2010), Tech. Suppl., 02005.
5. B. Khlevnoy, M. Sakharov, S. Ogarev, V. Sapritsky, Y. Yamada and K. Anhalt, Investigation of Furnace Uniformity and its Effect on High-Temperature Fixed-Point Performance, Int J Thermophys 29 (2008) 271-284.
6. P. Sperfeld, J. Metzdorf, N. Harrison, N. Fox, B. Khlevnoy, V. Khromchenko, S. Mekhontsev, V. Shapoval, M. Zelener, V. Sapristky, Investigation of high-temperature black body BB3200, Metrologia 35 (1998) 419-422.
7. B. Khlevnoy, M. Samoylov, I. Grigoryeva, N. Ibragimov, V. Shapoval, A.Puzanov, S. Ogarev, Development of High-Temperature Blackbodies and Furnaces for Radiation Thermometry, Int J Thermophys 32 (2011) 1686–1696.

Decade-long Stability of the NIST Detector-based Spectral Irradiance Scale

Howard W. Yoon, Charles E. Gibson, and Vladimir B. Khromchenko

[1]*Sensor Science Division, National Institute of Standards and Technology, Gaithersburg, USA*
Corresponding e-mail address: hyoon@nist.gov

The long-term stability of the NIST spectral irradiance scale as maintained on FEL lamps was validated in 2013 using the spectral irradiances from a high-temperature blackbody. The process of the 2013 scale realization will be described. The new 2013 scale is compared to the previous scale of 2000 that was utilized by NIST to issue customer lamps from 2000 to 2013. The comparison is performed with a set of check-standard lamps. The measurements show that a set of FEL lamps can be stable to better than ± 0.5 % (k=2) over a decade time period. A revised uncertainty budget will be described.

INTRODUCTION

Spectral irradiance standard lamps are used in many areas of spectroradiometry and photometry. For example, these lamps are used to calibrate spectroradiometers which measure the down-welling solar spectral irradiance to determine the atmospheric ozone levels [1]. These lamps can be used to calibrate remote sensing satellites whose data products are used for weather predictions and climate-change monitoring. They can also be used in photometry to determine the color temperatures of various sources. During the last 13 years, NIST calibrated 281 lamps for customers all over the world.

Due to the expense and the effort needed to routinely operate the high-temperature blackbody (HTBB), the NIST spectral irradiance scale is maintained on a set of 1000 W FEL check-standard lamps (CSL) and working-standard lamps (WSL). The process of calibrating all the NIST standard lamps with the HTBB is called the scale realization. The scale realization is performed when the assigned spectral irradiances of all the WSL are found to be deviating outside their assigned uncertainties as determined by the comparison to the CSL. The previous realizations were performed in 2000 and in 2003 just prior to the Consultative Committee for Photometry and Radiometry K1.a key comparison.

In this work, we describe the 2013 NIST spectral irradiance scale realization. A set of three, broad-band filter radiometers were calibrated for spectral irradiance responsivity. These filter radiometers were then used to determine the temperature of the HTBB using a spectroradiometric flux transfer equation. Then in the Facility for Automated Spectroradiometric Calibrations 2 (FASCAL 2), a set of CSL and WSL were calibrated using the spectral irradiances from the HTBB. The comparison of the 2000 scale to the 2013 scale shows that, over the last 13 years, the spectral irradiances of the issued NIST lamps at the time of their calibration have been within their stated uncertainties.

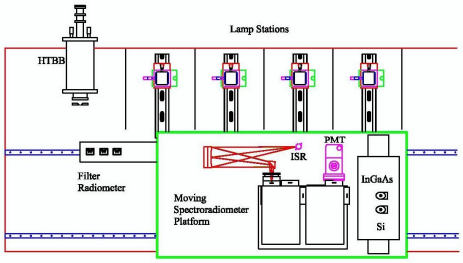

Figure 1. The schematic of the FASCAL2 setup.

EXPERIMENTAL SETUP

The schematic of the laboratory setup [2] used for these measurements is shown in Fig. 1. Briefly, the moving platform holds a double monochromator which can be used for measurements from 250 nm to 2400 nm with a combination of two gratings and three different detectors. A spherical mirror and a folding mirror are used to image the output of the integrating sphere receiver onto the entrance slits of the monochromator. The FEL lamps are placed on multi-axis adjustable mounts in four stations. The HTBB is placed at the left-most station and is fitted with a precision water-cooled aperture. The temperature of the HTBB is determined from the use of the filter radiometers which are shown attached to the left side of the stage.

FILTER RADIOMETER CALIBRATIONS

A set of three filter radiometers were used for the temperature determinations. Both the filters and the diodes were temperature stabilized at room

temperature. As shown in Fig. 2, the spectral power responsivities of the filter radiometers were calibrated using the quasi- monochromatic output from a prism-grating monochromator and a calibrated Si diode [3].

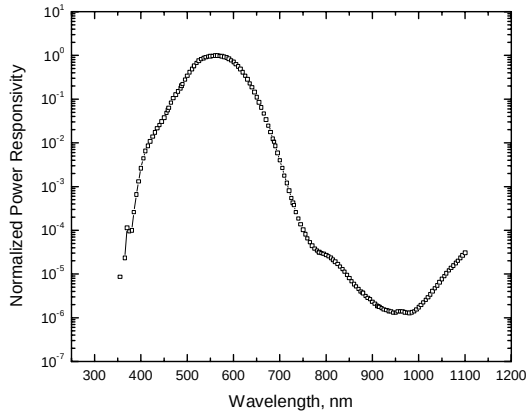

Figure 2. Normalized power responsivity of one of the filter radiometers.

The out-of-band responsivity was determined using a larger opening of the entrance and exit slits of the monochromator to obtain greater signals. This technique demonstrates that the noise floor of the measurements can be reduced to optical density (OD) 8 or greater.. The measurement of the power responsivity was performed with the precision apertures removed from the filter radiometers, and the irradiance responsivity was calculated using the knowledge of the areas of the precision apertures [4].

The preamplifiers used with these filter radiometers were separately calibrated using the NIST preamplifier calibration setup [5].

FEL MEASUREMENTS

The HTBB was operated at temperatures just below 3000 K to reduce the amount of carbon sublimation which can lead to absorption features in the ultraviolet wavelength region [6]. The comparisons were performed over a month's period using slightly different blackbody temperatures for each run. The percent differences of the check standard FEL lamps between the 2000 spectral irradiance assignment and the 2013 spectral irradiance assignment are shown in Fig. 3. The check standard lamps are only used to validate the spectral irradiances of the working standard lamps and thus were not frequently operated during the last decade. The scatter in the ultraviolet region is due to the lack of signal in this spectral region, but the set of lamps have remained quite stable since the 2000 scale realization

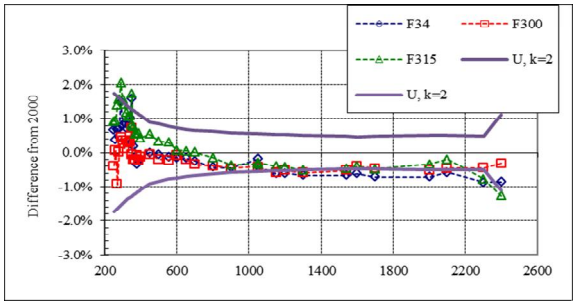

Figure 3. The percent differences of the 2000 spectral irradiance assignment to the 2013 spectral irradiance assignments. The differences are within the assigned expanded uncertainties.

CONCLUSION

The comparison of 2000 scale with the 2013 spectral irradiance scale using the check standard lamps validates that the spectral irradiances of the FEL lamps issued by NIST during this time period were remaining within their assigned uncertainties.

REFERENCES

1. The U.S. Interagency UV-Monitoring Network Plan, United States Global Change Research Program, 1995, USGCRP-95-01.
2. H. W. Yoon and C. E. Gibson, Spectral Irradiance Calibrations, NIST Special Publication 250-89, NIST, Gaithersburg, 2011.
3. T. C. Larason and J. M. Houston, Spectroradiometric Detector Measurements: Ultraviolet, Visible, and Near-Infrared Detectors for Spectral Power, NIST Special Publication 250-41, NIST, Washington, 2008.
4. J. Fowler and M Litorja, Geometric area measurements of circular apertures for radiometry at NIST, Metrologia 40, S9-S12, 2003.
5. G. Eppeldauer, H. W. Yoon, D. G. Jarrett and T. C. Larason, Development of in-situ calibration method for current-to-voltage converters for high-accuracy SI-traceable low-DC-current measurements," Metrologia 50 509 2013.
6. P. Sperfeld, S. Galal-Yousef, J. Metzdorf, B. Nawo, and W. Moller, The use of self-consistent calibrations to recover absorption bands in the black-body spectrum, Metrologia 37, 373-376, 2000.

Evaluation of Commercially Available Spectral Irradiance Scales in Japan

Shu Takeshita
Research Institute of Science & Technology, Tokai University, Hiratsuka, Japan
Corresponding e-mail address: stake@keyaki.cc.u-tokai.ac.jp

Calibration constant of solar UV-B irradiance meters were different between the National Metrology Institute of Japan (NMIJ) scale and the National Institute of Standards & Technology, USA (NIST) scale. And the spectral irradiance scale which provided by the NMIJ was changed in April, 2012. However, these numeric adjustment data of each wavelength are not provided. For evaluating commercially avairable spectral irradiance scale in Japan, an intercomparison was conducted. It become clear that the scale which the NIST manages differs from the scale which the NMIJ manages. And the scale adjustment value of previous NMIJ scale is about +2 % less from 300 nm to 800 nm in the wavelength.

INTRODUCTION

Solar ultraviolet-B irradiance (UV-B: 280 nm – 315 nm) on the earth's surface has been measured with solar UV-B irradiance meters[1] at 4 monitoring stations in Japan since 1990 for evaluating a long-term trend of solar UV-B irradiance on the earth's surface[2][3]. To make an accurate evaluation, UV-B irradiance meters which are using these monitoring stations are calibrated against spectral irradiance standard lamps which are traceable with the National Metrology Institute of Japan (NMIJ) combined with spectral miss match correction[4] every once a year or more. Calibration constants of UV-B irradiance meters were different between the result obtained by NMIJ scale and obtained by NIST scale. And the spectral irradiance scale which provided by the NMIJ was changed in April, 2012. For evaluating long-term trend of the UV-B irradiance, all UV-B irradiance data measured have to be corrected. However, numeric adjustment data of each wavelength are not provided by the NMIJ. From these reasons, commercially available spectral irradiance scales in Japan were evaluated.

EXPERIMENTAL METHODS

Two spectral irradiance standard lamps (JPD100V-500WCS, Ushio) which were traceable with previous NMIJ scale, one lamp (JPD100V-500WCS, Ushio) which was traceable with current NMIJ scale and two FEL lamps which were traceable with the National Institute of Standards & Technology, USA (NIST) were evaluated. Previous NMIJ scale lamps and current NMIJ scale lamp were calibrated by a registered company A in the Japan Calibration Service System (JCSS). Two NIST scale lamps were calibrated by company D. Two spectral radiometers with fibre optics input system (Radiometer 1, company B and Radiometer 2, company C) were used for this research. The Radiometer 1 was calibrated against previous NMIJ scale lamp by a company B which was a registered company in the JCSS. The Radiometer 2 was calibrated against the NIST scale lamp by company C. Spectral irradiance scale from (250 nm or 300 nm) to 800 nm in the wavelength was evaluated. Spectral irradiance lamps were operated at calibrated current and voltage. Uncertainty caused by setting of a distance between lamp and spectral radiometer was in +/-0.4 %.

RESULTS AND DISCUSSIONS

Spectral irradiance standard lamps having previous NMIJ scale calibrated by company A is recalibrated against the Radiometer 1. Previous NMIJ scale of company A gives close agreement with that of company B (less than about 1.2 %). This result shows the previous NMIJ scale having both companies is the same. And the JCSS is affective for control the spectral irradiance scale which traceable with the NMIJ.

Two FEL lamps having NIST scale are recalibrated against the Radiometer 1. The NMIJ scale in the wavelength less than 500 nm is about +4 % more than NIST scale (Fig. 1). And difference of the scale among two FEL lamps is about 8 % from 250 nm to 800 nm in the wavelength. Furthermore, spectral irradiance standard lamp having previous NMIJ scale is recalibrated against the Radiometer 2. The previous NMIJ scale is about 5 % more than the NIST scale (Fig. 2). After applying correction factors of spectral irradiance

provided by these results, calibration constant of UV-B irradiance meters calibrated against NIST scale lamps gives close agreement with the value calibrated against NMIJ scale lamps. From these results, spectral irradiance scale commercially available in Japan is different between NMIJ manages and NIST manages.

Spectral irradiance standard lamps having previous and current NMIJ scale are calibrated against the Radiometer 2 (NIST scale). The scale adjustment value is about -2 % less than the previous scale from 300 nm to 800 nm except around 420 nm in the wavelength (Fig. 3).

CONCLUSIONS

To evaluate the spectral irradiance scale commercially available in Japan, the intercomparison is conducted.

Results shows spectral irradiance scale of the NMIJ manages is difference from that of the NIST manages in Japan clearly. And the JCSS is affective to control the NMIJ spectral irradiance scale in Japan. Current NMIJ scale is about -2 % less than previous NMIJ scale from 300 nm to 800 nm except around 420 nm in the wavelength.

This research is supported by three companies. I am thankful to three companies which cooperated in this research.

REFERENCES

1. S. Takeshita, T. Sakata and M. Sasaki, Development and evaluation of a solar ultraviolet-B radiometer, J. Light & Visual Environment, **20** (1), 51-59 1996.
2. S. Takeshita and M. Sasaki, Solar radiation monitoring network of Tokai University, Japan, Proc. SPIE, **5156**, 303-310, 2003.
3. M. Sasaki, S. Takeshita, T. Oyanagi, Y. Miyake and T. Sakata, Increasing trend of biologically active solar ultraviolet-B irradiance in mid-latitude Japan in the 1990s, Optical Engineering, **41**(12), 3062-3069, 2002.
4. S. Takeshita, Calibration of Solar UV-B and UV-A Radiometer, Proc. East-Asia Regional UV Symposium on Monitoring and Health Study, 2008.

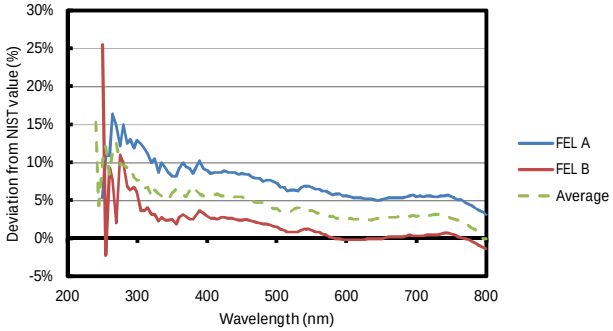

Figure 1. Deviation between the NIST scale and NMIJ scale (Two FEL lamps are recalibrated against the Radiometer 1).

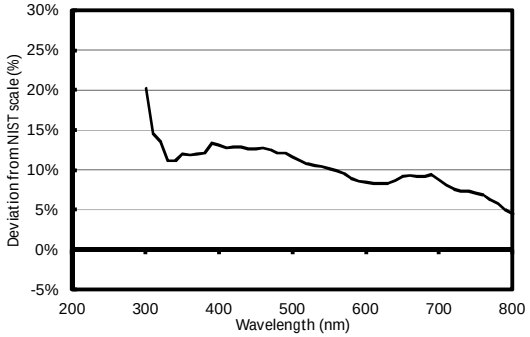

Figure 2. Deviation between the NIST scale and NMIJ scale (One previous NMIJ scale lamp is recalibrated against the Radiometer 2).

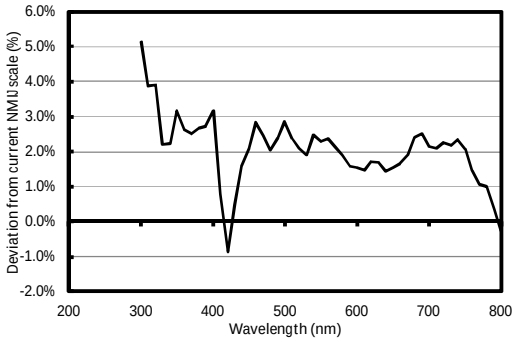

Figure 3. Comparison between current NMIJ scale and previous NMIJ scale evaluated with the Radiometer 2.

Intensity stabilized monochromatic radiance source for thermodynamic temperature determinations

Maija Ojanen[1,3], Stéphan Briaudeau[2], Mohamed Sadli[2], Bernard Rougié[2], and Frédéric Bourson[2]

[1]Centre for Metrology and Accreditation (MIKES), Espoo, Finland, [2]Laboratoire Commun de Metrologié – Conservatoire National des Arts et Metiers (LNE-CNAM), La Plaine – Saint Denis, France, [3]Post-Doc position at LNE-CNAM during the project

Corresponding e-mail address: maija.ojanen@mikes.fi

We present a power stabilization system for a monochromatic radiance source used as a reference in thermodynamic temperature determination. The radiance source consists of a Ti:Sapphire laser injected in an integrating sphere. The power stabilization system is based on two feedback loops. The first loop is based on a rotating half wave plate. The second loop is based on an acousto-optic modulator (AOM) in double-pass mode. We demonstrate that with the two feedback loops, the value of the radiance source can be stabilized in such a way that the signals measured inside and at the output port of the sphere are stable in the level of $\pm 10^{-5}$ and $\pm 2 \cdot 10^{-4}$, respectively, for several tens of minutes.

INTRODUCTION

For thermodynamic temperature determination of the new high-temperature fixed points, LNE-CNAM has developed a measurement setup [1,2] based on the radiance method [3]. For this setup, an intensity stabilized reference source is required as a reference. To meet this requirement, we have set up a monochromatic radiance source around 800 nm. The radiance source consists of a wavelength tuneable Ti:Sapphire laser injected in an integrating sphere. The output radiance of the sphere is measured with a trap detector traceable to the cryogenic radiometer in well-defined measurement geometry. The comparison of the reference radiance and the unknown blackbody radiance allows the determination of the blackbody temperature via Planck's radiation law.

The measurements are carried out in the wavelength range 780 nm – 820 nm. The peak power of the laser is about 800 mW at the wavelength of 800 nm. The high power level is incompatible with the commercially available power stabilisation systems. For this reason, we built a setup for the sphere signal stabilization. The setup is based on two feedback loops. The first feedback loop is based on a rotating half wave plate. The second loop is based on an acousto-optic modulator (AOM) in double-pass mode. With the setup presented, the sphere signal can be stabilized to 10^{-5} level for several tens of minutes. The stability of the sphere output signal measured with a Si trap detector is within $2 \cdot 10^{-4}$.

SETUP

The laser stabilization setup is presented in Figure 1. The first, slower feedback loop is based on a rotating half wave plate equipped with a stepper motor. The half wave plate is used to change the polarization of the laser beam. Tuning the wavelength from 780 nm to 820 nm affects the level of the power by a proportion of 20 %. The loop keeps the laser beam power stabilized within 1 % during one day, and over the 780 nm – 820 nm range of the scan of the laser wavelength. The error signal for the loop is taken with a beam splitter as presented in Figure 1. It is measured with a commercial Si photodetector. The time constant of this feedback loop is about 1 s.

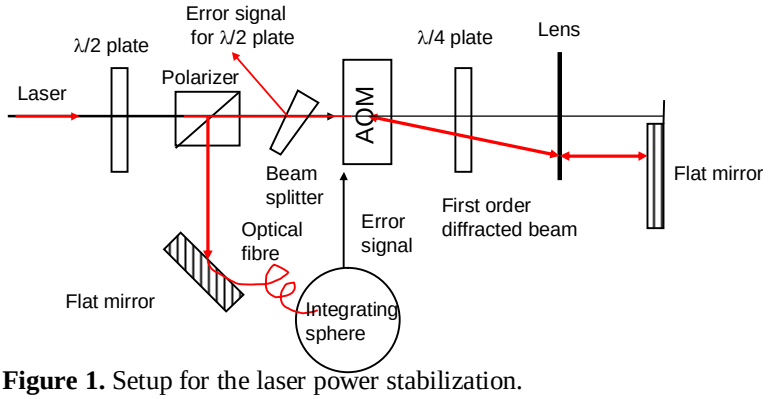

Figure 1. Setup for the laser power stabilization.

The second loop is based on an AOM used in double-pass mode. First, the laser beam is polarized with a Glan-Thompson polarizer with an extinction ratio of 10^{-5}. Then, the beam enters to AOM. The first order diffracted beam is then retro-reflected by a mirror on which it is focused, using the cat eye configuration [4]. The cat-eye compensates the deviation of the diffracted beam while scanning the wavelength. The beam is then diffracted second

time by the AOM exactly in the opposite and fixed direction of the incident laser beam, whatever the laser wavelength within 40 nm. A quarter wave plate inserted between the lens and the mirror makes the laser polarization rotate by 90°. Finally, the beam exits through the exit port of the polarizer and can be injected into the sphere using an optical fibre. The signal measured with a 1 mm^2 Si photodetector inside the sphere is used as the error signal for the AOM.

The bandwidth of the second feedback loop is 100 kHz. The AOM is driven by a radio frequency generator at 100 MHz. The optimum working point for the feedback loop is at 50 % of diffraction efficiency. The maximum diffraction efficiency for the AOM in double-pass mode is 65 %.

RESULTS AND CONCLUSIONS

Figure 2 presents the relative stability of the signal measured inside the sphere for 30 minutes. As can be seen in the figure, the relative stability is well within $\pm 10^{-5}$ for the duration of the measurement.

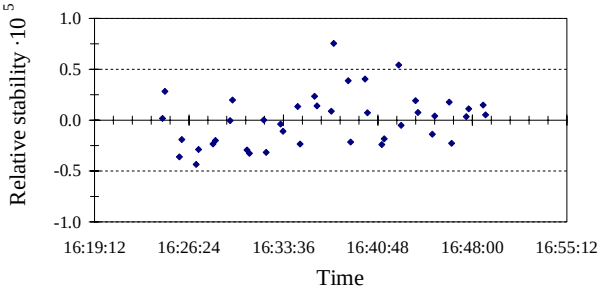

Figure 2. Relative stability of the sphere signal during a 30-min measurement.

In Figure 3, the sphere output radiance is measured with a Si trap detector. The relative stability of the measured signal is $\pm 2 \cdot 10^{-4}$.

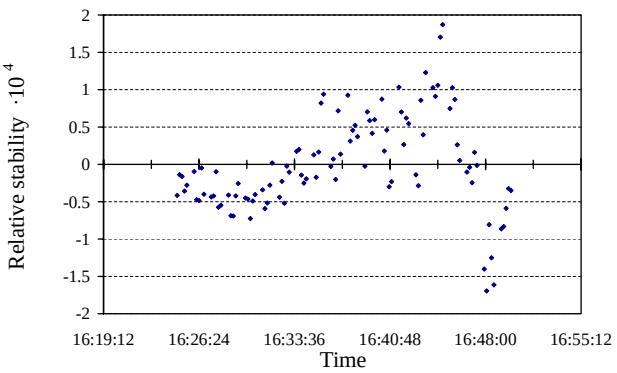

Figure 3. Relative stability of the output signal of the sphere measured with a trap detector.

The set-up presented is not sensitive to polarisation effects and very slightly sensitive to wavelength in the range 780 nm - 820 nm. The uncertainties related to the sphere radiance measurement correspond to standard uncertainty of 63 mK in the thermodynamic temperature of the Cu fixed point [5].

ACKNOWLEDGEMENTS

This work is performed in close collaboration with the partners of the European metrology joint research projects (InK and NOTED) and the concerted high-temperature fixed-points research programme led by the working group “radiation thermometry” of the CCT.

REFERENCES

1. S. Briaudeau, M. Sadli, F. Bourson, B. Rougié, A. Rihan, J.-J. Zondy, Primary radiometry for the mis-en-pratique: The laser-based radiance method applied to a pyrometer, Int. J. Thermophys. 32, 2183-2196, 2011.
2. S. Briaudeau, b. Rougié, M. Fanjeaux, M. Sadli, G. Bonnier, A. Richard, J.M. Coutin, J. Bastie, Thermodynamic temperature determination in high temperature range at BNM-INM, in TEMPMEKO 2004, 9th International Symposium on Temperature and Thermal Measurements in Industry and Science, p.119-125, ed. D. Zvizdic, June 22-25, Cavtat-Dubrovnik, Croatia.
3. G. Machin, p. Bloembergen, K. Anhalt. J. Hartmann, M. Sadli, P. Saunders, E. Woolliams, Y. Yamada, H. Yoon, Practical Implementation of the Mise en Pratique for the Definition of the Kelvin Above the Silver Point, Int. J. Thermophys. 31, 1779-1788, 2010.
4. E. A. Donley, T. P. Heavner, F. Levi, M. O. Tataw, S. R. Jefferts, Double-pass acousto-optic modulator system, Rev. Sci. Instrum., 76, 063112-1-6, 2005.
5. S. Briaudeau, M. Ojanen, F. Bourson, M. Sadli, B. Rougié, Thermodynamic temperature of the copper fixed point: Experimental validation of the uncertainty budget, submitted to Int. J. Thermophys.

Luminous Efficacy Measurement of OLEDs Using an Integrating Sphere

Minna Santaholma[1], Tuomas Poikonen[2], Janne Askola[1], Tomi Pulli[1], and Erkki Ikonen[1,2]

[1]*Metrology Research Institute, Aalto University, Espoo, Finland*
[2]*Centre for Metrology and Accreditation (MIKES), Espoo, Finland*
Corresponding e-mail address: minna.santaholma@aalto.fi

A 2-axis holder was designed and constructed for characterization of organic light-emitting diodes (OLEDs) using a 1.65-m integrating sphere. The sphere has been earlier used for measurements of luminous flux standard lamps and other E27-base lamps [1]. The developed holder allows OLEDs of different sizes to be measured in arbitrary geometrical alignments. The construction of the holder was designed to minimize the absorption of the edge emission and backward emission. The luminous efficacy and edge emission of three OLEDs were characterized to investigate the performance of the new generation light sources. The expanded uncertainty of the luminous efficacy test measurements is 1.0 % (k = 2).

INTRODUCTION

New generation solid-state light sources, such as OLEDs, are rapidly coming into market, and are already widely utilized in Asia for illumination of public places. Traceable measurement methods are needed for these devices, as they have high potential to be used as reference calibration sources of the future [2]. Luminous flux of light sources is often measured using integrating spheres with E27-lamp base [1,3,4]. Sources with different types of connectors often require modifications to the equipment. Due to the challenging optical properties of solid-state light sources, special attention is needed to avoid measurement errors due to the near-field absorption caused by the holder. Light-emitting diodes (LEDs) can be measured with an E27-base system using an adapter that reduces the effect of the near-field absorption [5]. Measurement of partial LED-flux or larger LED-modules may still require a dedicated system designed for measurements of LEDs [6]. OLEDs cannot be directly attached to the E27-base either, but the size of E27-base sphere systems is often suitable for OLED measurements [7].

INTEGRATING SPHERE SETUP

Our measurement setup consists of a 1.65-m integrating sphere with ports for the detector, auxiliary lamp, and the external reference luminous flux [1]. A 3D-model of the sphere was created for optimizing the holder dimensions. The port and baffle configuration was left intact to maintain the original functionality of the sphere. Because OLEDs are often used in complex installations with varying operating orientations, the new holder was designed to allow characterization of panels in arbitrary geometrical alignments (Fig. 1). Panels up to 20x20 cm^2 can be attached for measurement. Most of the holder parts were machined of aluminium, and painted with $BaSO_4$ having 97-% reflectance. Parts that need to be adjusted during measurements were made of Polytetrafluoroethylene (PTFE). The OLED is held in place with two narrow PTFE arms that can slide and rotate to adjust the angle of elevation. The horizontal angle is adjusted by rotating the construction at the lower end of the holder arm.

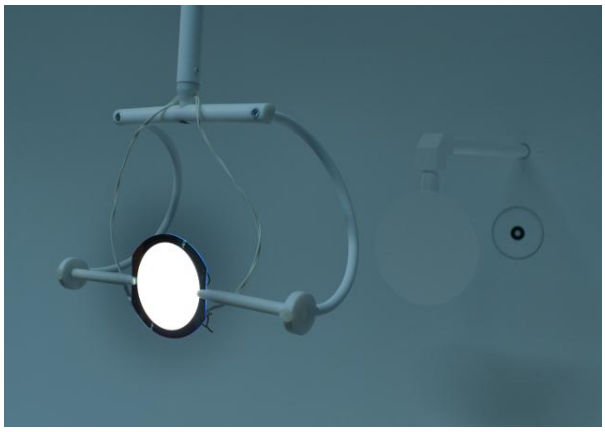

Figure 1. Photograph of the new 2-axis OLED holder. Panel 1 was attached for efficacy measurement.

The dimensions of the holder structure were chosen in such a way that the detector port baffle blocks the direct view of the OLED and the surrounding holder structure from the detector in all operating positions. The thicknesses of the parts were chosen as thin as possible, while maintaining rigidity. The shape of the holder was optimized to leave enough room around the OLED so that the light can propagate with only small influence by the holder. Curved side arms and off-centric positioning of the panel with respect to the vertical axis of the holder

were used for minimizing the absorption of the edge-emission. The holder is equipped with two built-in temperature sensors for monitoring the stability of the system. During the measurement, the OLED is connected to a DC-source using a 4-wire connection.

TEST MEASUREMENTS

Luminous efficacy test measurements were carried out for three forward-emitting OLEDs from different manufacturers. Panel 1 had a circular mirror surface with a diameter of 7 cm. Panels 2 and 3 had rectangular diffusing surfaces with the size of 9x9 cm^2. The panels were measured in both vertical and horizontal positions, and were driven with 150 mA DC-current using a Keithley sourcemeter model 2420. The luminous flux of all panels stabilized within 12 minutes. The relative spectral radiant flux of the panels was measured using a spectroradiometer in the detector port of the sphere. The results of the measurements are shown in Table 1. The self-absorption and spectral mismatch corrections were in the range of 1.03 – 1.05 and 1.002 –1.004, respectively. The spatial nonuniformity corrections were 1.004 –1.006. The highest corrections were analyzed for the horizontal position, where the OLED illuminates the bottom of the sphere.

Table 1. Results of luminous efficacy test measurements. CCT is the correlated color temperature.

Panel	Power [W]	Luminous efficacy [lm/W]		CCT [K]
		Vertical	Horizontal	
P1	1.07	15.08 ± 0.15	15.10 ± 0.15	3350 ± 30
P2	0.88	55.03 ± 0.55	54.95 ± 0.55	3590 ± 30
P3	1.20	40.78 ± 0.41	40.69 ± 0.41	3020 ± 30

The influence of the edge emission on the measured luminous efficacy was investigated by scanning the luminance and spectral radiance of the OLED panels, as well as their edges in the vertical position using an XY-translator and a Konica Minolta CS2000A spectral radiance meter. The order of magnitude of the edge emission in the efficacy measurements was calculated by multiplying the measured luminance values of the face emission and the edge emission by the areas of the emitting surfaces (or edges), and comparing their ratio. According to this simple analysis, the effect of the edge emission to the results of the luminous efficacy test measurements is only 0.01 – 0.05 %. The averages of the spectral radiances measured for the face and edge emissions, weighted by the emitting areas, are presented in Fig. 2.

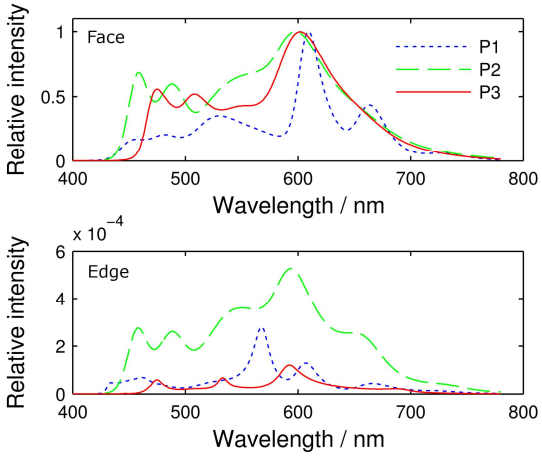

Figure 2. Weighted spectral radiance of the face emission and the edge emission of the three OLEDs studied.

CONCLUSIONS

The developed 2-axis OLED holder and spatial nonuniformity correction method allow panels of different sizes to be measured in arbitrary geometrical alignments. The luminous efficacies measured for three different OLED panels were 15.1 – 55.0 lm/W. The differences in the measured luminous efficacies between the vertical and horizontal operating positions were less than 0.22 %. Preliminary tests indicate that the effect of edge emission to the value of luminous efficacy in the case of the three panels measured is small. The expanded uncertainty of the luminous efficacy test measurements is 1.0 % (k = 2).

REFERENCES

1. T. Poikonen, T. Pulli, A. Vaskuri, H. Baumgartner, P. Kärhä, E. Ikonen, Luminous efficacy measurement of solid-state lamps, Metrologia, 49, 135-140, 2012.
2. T. Gerloff, M. Meyer, M. Taddeo, A. Sperling, Measurements on OLEDs: Optical Properties, Reference Standards, Stability, Light Eng., 20, 12-16, 2012.
3. CIE 84-1989, The measurement of luminous flux, 1st Edition, Commission international d'éclairage, Wien, Austria, 1989.
4. Y. Ohno, Detector-based luminous-flux calibration using the Absolute Integrating-Sphere Method, Metrologia, 35, 473-478, 1998.
5. C.C. Miller and Y. Ohno, Luminous Flux Calibration of LEDs at NIST, in Proceedings of the Second CIE Expert Symposium on LED Measurement, p. 45, CIE, Gaithersburg, 2001.
6. T. Poikonen, P. Manninen, P. Kärhä, and E. Ikonen, Multifunctional integrating sphere setup for luminous flux measurement of light emitting diodes, Rev. Sci. Instrum., 81, 023102, 2010.
7. T. Kawabata, Y. Ohno, Optical measurements of OLED panels for lighting applications, J. Mod. Optic., 60, 1176-1186, 2013.

Total Luminous Flux Measurement for 2π LED

Hsueh-Ling Yu, Hsin-Feng Chen, Kuei-Neng Wu, and Wen-Chun Liu

Center for Measurement Standards, Hsinchu, Taiwan, R.O.C.
Corresponding e-mail address: hsuehling.yu@gmail.com

Applying the integrating sphere with side-mounted accessories for 2π LED luminous flux mesurement is a widely used method in the present day. However it is inconvenient to design the side-mounted port for each different shape of the test lighting. This article develops a new type of reference lamp for the traditional center-mounted method which can greatly reduce the measurement error comparing with adopting the 4π reference lamp for 2π lighting measurement.

INTRODUCTION

LED lighting is more and more popular recently. Unlike traditional lighting, the distribution of LED lighting has a strong angular dependence. A 4π reference lamp like a naked tungsten lamp may not be suitable for 2π style LED lighting while adopting the center-mounted integrating sphere for total luminous flux measurement unless the spatial responsivity of the integrating sphere is homogenous, otherwise spatial correction is necessary. Side-mounted method [1] was developed in response to the 4π and 2π spatial mismatch between the reference lamp and test LEDs. However it is inconvenient to design different side-mounted ports to fit various shapes of the 2π test lighting. By comparison, it is easier to mount the 2π lighting at the center of the sphere. To reduce the effect caused by spatial mismatch between 4π reference source and 2π test lighting, a 2π reference source is designed in this article. Choosing the surface mount device (SMD) LED as the test sample, the comparison of total luminous flux measurement for the SMD LED by using the goniophotometer and integrating sphere is presented in this article.

DESIGN OF THE 2π REFERENCE SOURCE

As shown in Figure 1(a), similar to the idea of total luminous flux measurement for flexible surface sources [2], the reference source is designed by covering a tungsten lamp with a small box and leaving only one surface for light emitting to make this covered tungsten lamp have similar spatial distribution as the 2π lighting. Figure 1(b) presents

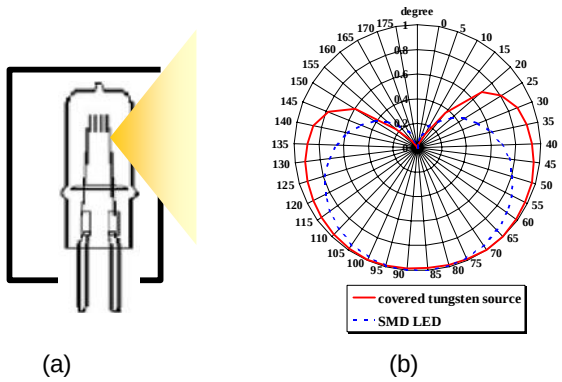

Figure 1. (a) Schematic diagram of the new type reference lamp. (b) spatial distributions of the covered tungsten source and the test SMD LED.

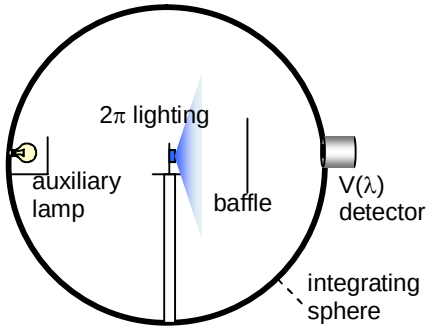

Figure 2. Centre-mounted method for 2π LED luminous flux measurement.

the spatial distributions of the covered tungsten source and the test SMD LED. The schematic diagram of the center-mounted integrating sphere is shown in Figure 2. The sphere is 1.5 m in diameter and coated with $BaSO_4$ on the internal wall. Not knowing the spatial uniformity of the integrating sphere, according to reference [2], the effect of orientation shall be checked before applying this covered tungsten source as the reference source for 2π lighting total luminous flux measurement while adopting the center-mounted method. The results are presented in Table 1 where the SMD LED and the reference source are aligned for four different orientations. In Table 1, the orientations I ~ IV mean both the reference source and SMD LED are facing the baffle, the auxiliary lamp, the left side, and the right side, respectively. I_{std} and I_{LED} are the signals of the V(λ) detector while measuring the

reference source and SMD LED. Both I_{std} and I_{LED} have been corrected by the factors of spectrum mismatch and self-absorption. The deviation between the maximum and minimum values for different orientations is within 0.11 %. It means this type of reference source is quite suitable for the SMD LEDs.

To verify the applicability of applying the covered tungsten source as the reference source for 2π LED total luminous flux measurement, using the SMD LED as the test sample and measuring it total luminous flux with centre-mounted integrating sphere to see if the result is consistent with that measured by the goniophotometer. The experimental results are shown as follows.

Table 1. The effect of orientation for the centre-mounted method.

orientation / ratio	I	II	III	IV	max-min / max+min
I_{LED}/I_{std}	0.044506	0.044590	0.044494	0.044511	**0.11 %**

EXPERIMENTS

First, measure the total luminous flux of the test SMD LED with the centre-mounted integrating sphere as shown in Figure 2. The total luminous flux of the covered tungsten source is measured by a 1.5 m goniophotometer in advance and it is 172.8 lm. Applying this covered tungsten source as the reference source and measuring the total luminous flux of the test SMD LED with the integrating sphere, the result of the SMD LED is 7.70 lm.

Next, measure the total luminous flux of the test SMD LED with the goniophotometer. Figure 3 shows the small goniophotometer used in CMS/ITRI for 2π LED total luminous flux measurement. The LED sample is mounted on a 5-axis robot. Through rotating and spinning the LED, the total luminous flux of the SMD LED is obtained as 7.55 lm.

Comparing the results measured by the integrating sphere and goniophotometer, the difference is 2.0 % which is within the uncertainty range. It can say that the results are consistent and the covered tungsten source is applicable to be the reference source for 2π LEDs.

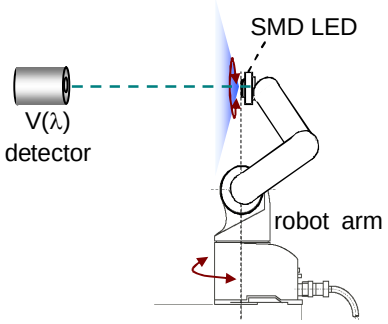

Figure 3. Small goniophotometer for 2π LED luminous flux measurement.

CONCLUSIONS

The covered tungsten source is designed as the reference source for 2π LED total luminous flux measurement while employing the center-mounted integrating sphere method. The effect due to the spatial non-uniformity of the sphere can be greatly reduce to around 0.11 % if the covered tungsten source and the test 2π LED have the same orientation. To verify the applicability of applying the covered tungsten source as the reference source for 2π LED, the total luminous flux of a test SMD LED is measured with both the center-mounted integrating sphere method and the goniophotometer to check if the results are consistent. The experimental results show that the difference between these two methods is 2.0 % which is within the uncertainty range. It means this covered tungsten source is applicable to be the reference source for the SMD LEDs.

In particular, the effect of orientation likes the data shown in Table 1 shall be checked in advance while measuring other types of the 2π LED lighting.

REFERENCES

1. Measurement of LEDs, CIE 127:2007.
2. H.-L. Yu and W.-C. Liu, Total Luminous Flux Measurement for Flexible Surface Sources with Integrating Sphere Photometer, Meas. Sci. Technol., 25, 1, 015012, 2014.

Characterization of an ammonia heatpipe blackbody source

Maija Ojanen[1], Antti Lakka[1], Davor Stjelja[1,2], and Martti Heinonen[1]

[1]*Centre for Metrology and Accreditation (MIKES), Espoo, Finland*
[2]*University of Zagreb,Croatia*
Corresponding e-mail address: maija.ojanen@mikes.fi

An ammonia heat pipe blackbody is characterized in the temperature range -40 °C to +50 °C in this work. We study the spatial temperature variation in the blackbody cavity and across the cavity back wall by measurements with platinum resistance thermometers and a radiation thermometer. The effect of thermal convection is studied by numerical modelling. According to our analysis the expanded uncertainty of the blackbody is between 0.26 °C and 0.62 °C.

INTRODUCTION

At the Centre for Metrology and Accreditation (MIKES), an ammonia heat pipe variable temperature blackbody is used as a calibration source for radiation thermometers in the temperature range from -40 °C to +50 °C. In this work, we characterize the blackbody: First we measure the spatial temperature variation in the closed blackbody cavity. Then, we construct a numerical model to study the thermal convection in the cavity. The thermal homogeneity of the back wall of the cavity is studied by scanning it with a radiation thermometer. Finally, we conclude the characterization in an uncertainty budget, which is drawn up according to [1].

DETERMINATION OF THE BLACKBODY TEMPERATURE

To obtain traceability to the ITS-90 [2], the reference temperature of the blackbody is measured with a calibrated platinum resistance thermometer (PRT). In the blackbody, the PRT is in a thermometer well located in the back side of the cavity along the axis of the cylindrical heat pipe. The blackbody temperature is obtained as

$$t_{\mathrm{BB}}=t_{\mathrm{Meas}}+\delta t_{\mathrm{rG}}+\delta t_{\mathrm{eG}}+\delta t_{\mathrm{eR}}+\delta t_{\mathrm{Conv,}} \quad (1)$$

where δt_{rG} is the correction due to inhomogeneous cavity bottom temperature, δt_{eG} is the emissivity correction due to non-isothermal cavity, δt_{eR} is the correction due to reflection of ambient radiation, and δt_{Conv} is the correction due to thermal convection, including the radiant heat exchange through the back wall [1]. The correction terms $\delta t_{rG,}$ $\delta t_{eG,}$ δt_{eR} and δt_{Conv} are assumed to be zero with non-zero uncertainties.

The term t_{Meas} includes the following components: indication of the reference thermometer, calibration correction of the reference thermometer, correction due to drift of the reference thermometer since the last calibration, and correction due to the non-ideal resolution of the reference thermometer. Magnitudes of these corrections and related uncertainty components are based on the calibration and stability monitoring of the PRT.

The uncertainty for the measured temperature is obtained as

$$u^2(t_{\mathrm{BB}})=u^2(t_{\mathrm{Meas}})+u^2(\delta t_{\mathrm{rG}})+u^2(\delta t_{\mathrm{eG}}) +u^2(\delta t_{\mathrm{eR}})+u^2(\delta t_{\mathrm{Conv}}), \quad (2)$$

where $u(x)$ is the standard uncertainty of the component x.

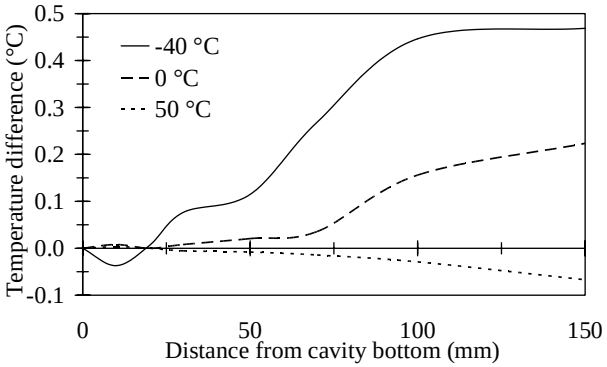

Figure 1. Temperature difference as a function of distance from the cavity bottom.

CHARACTERIZATION OF THE BLACKBODY SOURCE

In order to evaluate the uncertainty of the emissivity due to non-isothermal blackbody cavity, we measured the spatial temperature variation in the cavity closed with an insulation block. The measurements were performed at different distances from the cavity bottom with a PRT inserted through a small hole on the insulation block. The stability of the cavity temperature was monitored with another PRT in the thermometer well.

Figure 1. presents the measured temperature differences up to 150 mm from the cavity bottom. The corresponding uncertainty in the cavity emissivity estimated according to [1] is given in Table 1.

Especially in the calibrations with large-aperture blackbodies below the ambient temperature, thermal convection can be an important source of uncertainty [1]. At MIKES, the blackbody is typically cooled down with its cavity closed with an insulation block. The block is opened for the duration of the measurement, which is of the order of a few minutes. No purging gas is used. Keeping the cavity closed helps to reach the thermal equilibrium and prevents the condensation of water in the cavity, but the effect of opening the cavity on the spatial temperature distribution and emissivity needs to be studied.

The effect of convection after opening the cavity was studied by COMSOL modelling. We constructed an axisymmetrical model with the following cavity parameters: the length was is 300 mm and the diameter of the cylindrical part was 75 mm. The angle of the back wall cone was 120 º. The emissivity of the cavity was 0.999. We studied the behaviour of the cavity temperature five minutes after opening the cavity. The temperature outside the cavity was assumed to be constant.

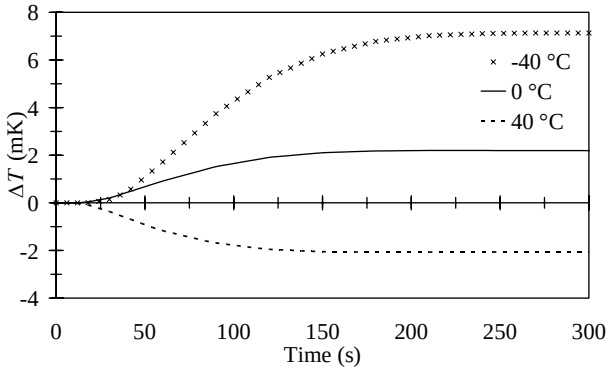

Figure 2. Modelled temperature changes at 150-mm distance from the cavity bottom after opening the cavity.

Figure 2. shows the modelled temperature changes during 300 seconds following the cavity opening, at the central axis and at 150-mm distance from the cavity bottom. For the uncertainty budget, the maximum deviation in temperature was estimated to be twice the modelled temperature at 150-mm distance. The uncertainty distribution was assumed rectangular.

The thermal homogeneity of the cavity bottom was studied by scanning the cavity bottom with a radiation thermometer. The uncertainty component was calculated from the maximum deviation, assuming a rectangular uncertainty distribution.

UNCERTAINTY BUDGET

As a summary, an uncertainty budget for the blackbody source is given in Table 1. for the temperature range -40 °C to 50 °C. When estimating the overall uncertainty of a calibration with the blackbody, components related to the radiation thermometer under calibration must be added to the analysis. These include the size-of-source effect, repeatability of the instrument readings, non-ideal resolution, effects of ambient temperature and alignment, including atmospheric absorption. These are not discussed in this abstract.

Table 1. Uncertainty budget for NH3 heatpipe blackbody calibration. Uncertainties related to the radiation thermometer are not included.

Uncertainty component	Temperature, °C		
	-40	0	50
t_{Meas}	0.12	0.12	0.12
δt_{rG}	0.17	0.06	0.03
δt_{eG}	0.05	0.02	0.01
δt_{eR}	0.08	0.06	0.03
δt_{conv}	0.21	0.06	0.06
Combined standard uncertainty	0.31	0.15	0.13
Expanded uncertainty (k = 2)	0.62	0.30	0.26

CONCLUSIONS

We have characterized an ammonia heat pipe blackbody source used as a calibration reference at MIKES. The study included measurements of spatial temperature uniformity in the blackbody cavity and on the back wall, and numerical modelling of the thermal convection. As a conclusion of the work, we presented the uncertainty budget for the temperature range from -40 °C to +50 °C.

REFERENCES

1. J. Fischer et al, Uncertainty budgets for calibration of radiation thermometers below silver point, version 1.71, CCT-WG5 April 2008.
2. H. Preston-Thomas, The International Temperature Scale of 1990 (ITS-90), Metrologia 27, 3-10 (1990).

Spectral radiance and irradiance UV reference based on a high temperature blackbody

Bernard Rougié[1], Mai Huong Valin[1], and Annick Razet[1]

[1]Laboratoire Commun de Métrologie, Cnam, Conservatoire National des Arts et Métiers, LNE-Cnam /LCM-Paris, France
Corresponding e-mail address: bernard.rougie@cnam.fr

This paper shows the works and the means that the "Laboratoire Commun de Métrologie" (LNE-Cnam/LCM) has implemented to obtain a new reference of radiance and irradiance at the 1 % level in the ultraviolet (200 nm).
A black body exceeding the 3000 K temperature is used as a standard source whose irradiance, then temperature, is measured with a calibrated filter radiometer. The corrections associated to the homogeneity and the emissivity of the black body are exactly determined.

INTRODUCTION

To address the need to make high-precision measurements in the ultraviolet for industry, health, climate change, earth observation, ... the LNE-Cnam/LCM has the objective of developing a standard source of spectral radiance and irradiance with high performance in terms of uncertainty (lower than 1% at 200 nm) and spectral coverage especially in the ultraviolet but can go into the infrared to 2500 nm .

Now in LCM , these references are based on the use of a black body but the spectral range does not reach the ultraviolet down to 200 nm [1]. The traceability of these measurements to the primary reference are linked to the reference of temperature.

LCM has chosen to base his reference on a black body at a higher temperature by improving an existing high temperature source (3000 K) and expanding the means of measurement based on the skills and systems already developed in both radiometry and radiation thermometry. This method looks like other setups previously developed in some other National Measurement Institutes [2]. The method, the traceability scheme and the first results of characterisation are presented.

DESCRIPTION OF THE METHOD

A black body heated up to 3000 K provides sufficient ultraviolet radiation above 200 nm and can be used in the 200 nm to 2500 nm range. Its temperature will be measured by using a filter radiometer calibrated against the cryogenic radiometer, our national flux reference, and against our dimensional references. Using Planck's radiation law and assessing precisely corrections due to the characteristics of the instruments such as the homogeneity and the emissivity of the black body, it is possible to calculate the irradiance, then the radiance produced by this source. The knowledge of the emissivity allows to calculate the radiance and the irradiance of this source over a large range, from UV, our first aim, to infrared

DESCRIPTION OF THE INSTRUMENTS

The output of the furnace is equipped with a precise aperture and a large aperture which could be changed during the running time, allowing to act as an irradiance or radiance source at a same time.

The blackbody is a 25 mm diameter, 180 mm long graphite cylinder maintained in the centre of the heater which is constituted by 6 graphite strips 500 mm long placed in a cage arrangement, connected to annular electrodes. A cavity at the backside is used for the temperature servo control.
All is carefully insulated and placed in a cooled housing. An argon gas flow prevents the air to enter the furnace.

This furnace has been previously used as a source for high temperature calibrations. It has been operated up to 3000 °C. The heater of this device was too much fragile. It broke two times without having been used for a long time. A new device [Fig 1] has been designed and installed. Its characterisation will be presented.

A pyrometer has been adapted for having a small aperture number. A mechanical system allows the scanning of the radiance in vertical and horizontal directions in order to make non uniformity corrections. The axis of the pyrometer can be tilted so that it can measure the radiance along the wall of the blackbody. This third measurement gives essential

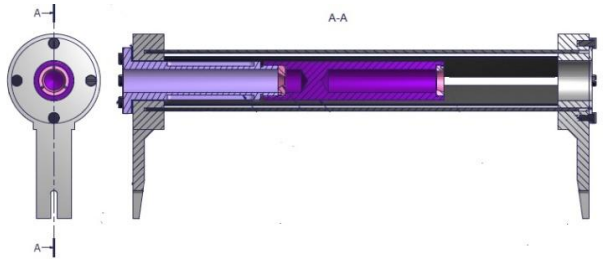

Figure 1. Blackbody cavity in its furnace.

parameters for the computation of emissivity with numerical models.

Our radiometer is constituted with a trap detector, a colour glass filter and a sharp edge precise aperture. This assembly is enclosed in a temperature stabilized housing.

CHARACTERIZATION OF THE INSTRUMENTS

We had characterized the transverse radiance variations of the initial blackbody. The horizontal scan showed a 0.5% radiance variation over 20 mm which would be good enough for our purpose although such a variation has to be accurately characterized and the irradiance corrected according these measurements.

The measurement of the new furnace characterization are now in progress and will be presented.

The elements of the radiometer have been already calibrated separately. The two filters whose mean wavelengths are 500 nm and 575 nm, have already been used in a previous radiometer. They show a good stability with time, in the 10^{-3}, over 3 years. But their temperature sensitivity requires a 0.3°C stability to reach the 10^{-3} stability in irradiance measurement.

The trap detector is calibrated against the cryogenic radiometer at laser line wavelengths between 453 nm up to 633 nm. An interpolation allows the computation of the integral responsivity over all the spectral range of the filters.

The area of the circular aperture has also been measured on our setup constituted by a two axis micrometric table on which the aperture is placed. The edge of the aperture is centred by the operator on the reticule crossing of a microscope for 36 regularly spaced positions, then the centre position and the diameter are computed with a least square method [3]. We can use a 8 mm or a 10 mm diameter aperture.

The distance of between the diaphragms of the blackbody and the radiometer is accurately measured with length standards rods.

CONCLUSION

The aim of this project is to obtain a relative uncertainty lower than 1% at 200 nm. The actual uncertainty issued from our traceability chain is about 0.2% at the working 500 nm of the radiometer. The differences between a perfect blackbody, uniform and with emissivity equal to unity, and a real source, give rise to corrections and their additional uncertainty components whose good determination is the key of a low uncertainty in the ultraviolet range. First results obtained with the newly installed blackbody will give information on the uncertainty budget

REFERENCES

1. Boris Khlevnoy, Victor Sapritsky, Bernard Rougie, Charles Gibson, Howard Yoon, Arnold Gaertner, Dieter Taubert, Juergen Hartmann “CCPR-S1 Supplementary comparison for spectral radiance in the range of 220 nm to 2500 nm”,. Metrologia, 46 (2009), S174–S180.
2 W. Moller, P. Sperfeld, B. Nawo, K. Hube and J. Metzdorf, Realization of the spectral irradiance scale in the air-ultraviolet using thermal radiators, Metrologia, 35, (1998), 261-265.
3. A. Razet, J. Bastie, “Uncertainty evaluation in non-contact aperture area measurements”, Metrologia, 43, 2006, 361-366.

Broad-band UV measurement standard

G. P. Eppeldauer, R. E. Vest, H. W. Yoon, and T. C. Larason

National Institute of Standards and Technology, Gaithersburg, Maryland, USA
Corresponding e-mail address: george.eppeldauer@nist.gov

The spectral distribution of UV sources is not standardized and the CIE standardized rectangular-shape UV response functions can be realized only with large spectral mismatch errors. As a consequence, the readings of different UV meter models, even if they measure the same UV source, can be different. In order to avoid large measurement errors, standardization of both the UV source and the broadband UV measurement procedure is needed. Implementation of the LED based UV source standard and the standardized measurement procedure using both new and existing UV meters are discussed.

INTRODUCTION

In the broadband UV measurement shown as an example here, irradiance from UV sources that peak at 365 nm is used for non-destructive testing of metal parts. The UV meters showed 22 % irradiance differences when the irradiance from the same 365-nm source was measured. The large measurement errors were obtained because no proper standards are available for broad-band UV measurements. The CIE standardized rectangular-shape UV-A response function (for the 320 nm to 400 nm range) has a square-shape that cannot be realized with detector-filter combinations. Even the best realizations show large spectral mismatch errors [1]. Also, the UV excitation sources have not been standardized which is a must if the realized spectral responsivity function of the UV meter is different from the standard responsivity function. Standardization of the detector spectral response function (like in photometry) will not give a solution here because small spectral mismatch errors cannot be achieved in the UV. The number of the available spectral response correction filters that can be used in the UV is limited. Also, the traditionally used Hg sources, because of safety reasons, should not be used anymore.

The first step to solve the above problems is to substitute mercury sources with LED sources. The LED sources can be standardized. In the second step, instead of standardizing the spectral response function of the UV meters, a standard measurement procedure was worked out [2] where the spectral product of the source distribution the UV meter response is standardized to obtain output signals within the expected measurement uncertainty. In the standardized procedure, reasonable spectral limits are given for the broadband measurement. In order to verify the new standard procedure, LED based UV excitation sources were developed. These sources were measured with the newly developed UV meters and also with existing commercially available UV-A meters to validate that the standard procedure gives uniform measurement results with low uncertainties.

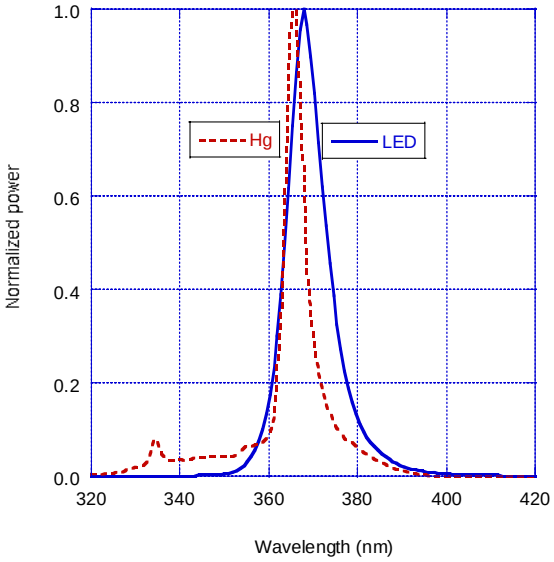

Figure 1. Normalized spectral power distribution of a traditional Hg lamp and a new LED source.

LED-BASED UV IRRADIANCE SOURCE STANDARD

High-power UV LED sources were applied to produce a uniform irradiance of higher than 1 mW/cm^2 within a diameter of 7.5 cm at a distance of 40 cm from the excitation source. The LEDs were selected with a peak of close to 365 nm. As shown in Fig. 1, the normalized spectral power distribution (SPD) of the LED source is compared to the normalized SPD of a Hg source. The Hg source has a continuum radiation and the 334 nm neighbouring line could not be attenuated enough. The LED source does not have the continuum radiation.

The LEDs were temperature controlled and the exiting radiation was imaged with an objective lens positioned after a hexagonal-shape homogenizer. The irradiance sources were characterized and calibrated. A stray-light corrected spectrograph was used for the LED-based UV irradiance-source measurement which is calibrated against an FEL lamp standard. The spectral band-limits and peak tolerances for the 365-nm LEDs were established. The suggestion is to use LEDs with 365 nm +/- 5 nm peaks and a maximum spectrum-half-width (FWHM) of less than 15 nm to keep the spectral mismatch errors and the uncertainties of the spectral products (signals) at a reasonably low level even if different meters and/or sources are used.

The UV source can be used as a separate standard and it also can be utilized in the standardized broadband measurement procedure.

SPECTRAL RESPONSE OF UV METERS

After standardizing the UV source, the spectral response of the UV meters was determined. The wavelength coverage of the response functions must be significantly wider than the spectral power distribution of the measured sources. The response function is wide enough only if the spectral product of the source-distribution and the meter responsivity function will produce a (measured) signal error of less than the required measurement-uncertainty when different UV meters (types) measure different 365-nm sources. The standardization of the broadband UV measurements makes sense only if more than one UV meter and/or more than one 365-nm sources are used.

It is discussed what spectral responsivity functions are needed for new and existing UV irradiance meters to perform low-uncertainty broadband (with ~365 nm peak) measurements.

The suggested source standard and the standardized broadband UV measurement procedure have been implemented at NIST for non-destructive testing of metal parts. Traditionally used Hg sources have been phased out from future applications.

The newly realized spectral response function that satisfies the requirements of the above standardized broadband UV measurement procedure is shown in Fig. 2. The bandpass around 365 nm is significantly higher than the spectral distribution of the 365-nm standard source.

Existing UV-A meters with a broad enough spectral response function and a peak response close to the source-peak can satisfy the requirements of the standard procedure. Care should be taken with UV-A meters where the response-peak is significantly different than the peak of the measured source and/or the bandpass is not broad enough. With these meters, the requirements of the standard procedure may not be satisfied and large measurement errors can be obtained. These meters are not suggested to use for broadband measurements if uniform measurement results are needed.

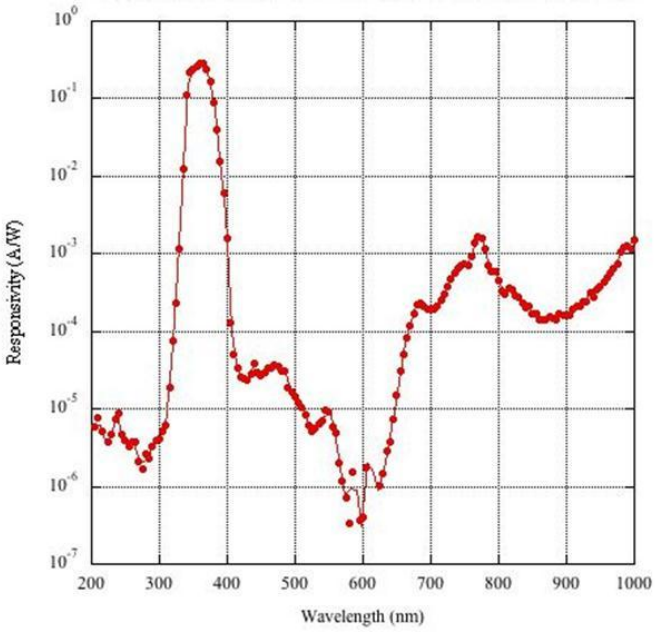

Figure 2. Spectral power responsivity of a UV-A meter that satisfies the requirements in the standard broadband (365 nm peak) measurement procedure.

The here discussed standardization for the UV source and the broadband UV measurement procedure can be extended to other UV ranges like measurement of 254 nm sources.

REFERENCES

1. T. C. Larason and C. L. Cromer, Sources of error in UV radiation measurements, J. Res. NIST, Vol. 106, No. 4, p. 649-656, 2001.
2. G. P. Eppeldauer, Standardization of broadband UV measurements, UVNews 9, Newsletter of the Thematic Network for Ultraviolet Measurements of the European Metrology Research Program of EURAMET, Issue 9, January 2013, Published by Aalto University, Helsinki, Finland.

Measurement of relative spectra of LEDs

Hans Baumgartner[1], Anna Vaskuri[1], Tuomas Poikonen[2], Timo Dönsberg[1], Tomi Pulli[1], Johannes Oksanen[1], Petri Kärhä[1,2], and Erkki Ikonen[1,2]

[1]*Metrology Research Institute, Aalto University, Espoo, Finland*
[2]*Centre for Metrology and Accreditation, (MIKES), Espoo, Finland,*
Corresponding e-mail address: hans.baumgartner@aalto.fi

Relative emission spectra are often needed when characterizing LEDs and using them in applications. A straightforward measure of the reliability of the relative spectra can be obtained by measuring the same LED with different calibrated spectroradiometers. Such a test provided confidence on the intensity scales of two instruments used at the standard uncertainty level of 0.002. For the wavelength scale verification of an instrument, a new method was developed, with an uncertainty better than 0.1 nm, using the LED spectra at different junction temperatures.

INTRODUCTION

Spectral irradiance key comparison K1.a of incandescent lamps has demonstrated relative deviations smaller than 0.5% in the visible wavelength region between participants declaring the lowest uncertainties [1]. The relative standard uncertainty of MIKES (then HUT) in this comparison was 0.4%. The corresponding uncertainty budget indicated components correlating with various parameters, such as the wavelength. Analysing the uncertainty components suggests that the standard uncertainty is 0.002 when measuring relative emission spectra of narrow-band LEDs using spectroradiometers calibrated directly against the spectral irradiance scale used in the comparison. Validation of the above estimate is of high interest for research of LEDs.

The spectra of incandescent lamps are not very sensitive to wavelength in the visible range, but LEDs have sharp spectral features that enhance the significance of wavelength. Thus, methods are needed to help in the validation of the wavelength scales of spectroradiometers used for measurements of LED spectra.

This work presents approaches for both of the above topics.

INTENSITY SCALE

The relative intensity scales of two spectroradiometers, Konica Minolta CS2000A and Bentham DTMc300, were studied by measuring the spectrum of a blue LED at a distance of 85 cm. The operation principles of the spectroradiometers are quite different, because the former uses a detector array and the latter is a wavelength scanning instrument. The bandwidths of the spectroradiometers were 5 nm and 1 nm, respectively. Both instruments were calibrated against a spectral irradiance standard lamp similar to those in [1].

The spectra were corrected for the bandwidth difference using the slit function of the Konica Minolta spectroradiometer measured with a spectral line of a mercury lamp. **Figure** shows the measured spectra and their difference after the bandwidth correction. The intensity difference between the two relative spectra is less than 0.005 and the standard deviation from the average difference is 0.0023 in the interval 440 – 500 nm.

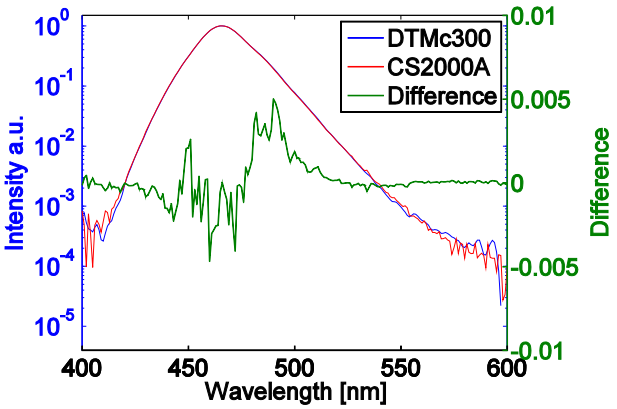

Figure 1. Bandwidth corrected relative spectra of a blue LED measured with two spectroradiometers and their difference.

The obtained difference in relative spectra is small taking into account the different operation principles of the spectroradiometers. The difference is compatible with the estimated standard uncertainty of 0.002.

WAVELENGTH SCALE

The usual way of checking the wavelength scale of a spectroradiometer is to measure the spectrum of a line source with known emission wavelengths, such

as a mercury lamp or a laser. Here, we describe a new method of checking the wavelength scales with LED light sources. The method can provide high resolution even for broad emission spectra of LEDs.

The emission intensity of an LED as a function of energy is proportional to

$$I(E) \propto \sqrt{E - [E_g(0) - aT]}\, e^{-\frac{E}{k_B T}}, \qquad (1)$$

where I is the emission intensity, E is the photon energy, $E_g(0)$ is the bandgap energy at $T = 0$ K, a is a constant, k_B is the Boltzmann constant, and T is the junction temperature [2].

From Eq. (1), we can conclude that at the photon energy corresponding to the bandgap energy $E_g(0)$, the relative intensity does not depend on temperature T, thus

$$\frac{I(E_g(0))}{I(E_{max})} = \sqrt{\frac{2 \cdot e \cdot a}{k_B}}\, e^{-\frac{a}{k_B}} \qquad (2)$$

where $E_{max} = k_B T/2 + E_g(0) - aT$ is the photon energy at the maximum intensity.

In Eq. (1), the bandgap energy $E_g(0)$ and the constant a vary with different LED types and specimens, leading to spectral variations between LEDs. By measuring the spectra of an LED at different junction temperatures, it is possible to find values for constants $E_g(0)$ and a for the specific LED.

The spectra of the studied LEDs were measured at different junction temperatures. Before the spectral measurements, the current-voltage-characteristics of the LEDs as a function of junction temperature were characterized as described in [3]. The LEDs were attached to a temperature controlled heat sink, and the junction temperature was varied by changing the temperature of the heat sink.

The spectral measurements were carried out using the Konica Minolta CS2000A array spectroradiometer. **Figure** 2 shows the spectra of a blue LED measured at six different junction temperatures.

The common intersection point in **Figure** 2 is at the energy $E_g(0)$ [wavelength = $hc/E_g(0)$] according to Eq. (2). **Figure** 3 shows a close-up of the red square area in **Figure** 2. The intersection point at 443.03 nm varies less than 0.1 nm with temperature.

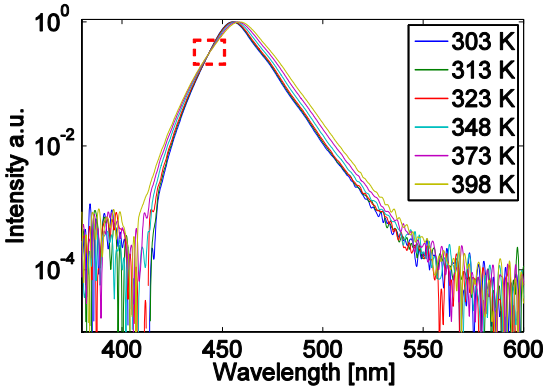

Figure 2. Normalized spectra of a blue LED measured at six different junction temperatures.

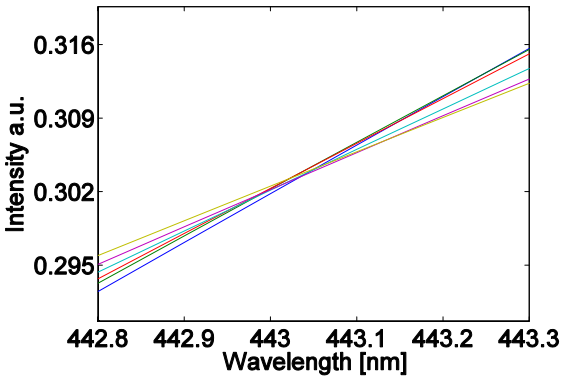

Figure 3. Close-up of the spectra in Figure 2.

The intersection wavelength can be utilized in calibrations by varying the LED temperature and measuring the spectra at two or more different temperatures. Similar intersection wavelengths were also found in the spectra of phosphor based white LEDs and red LEDs.

CONCLUSIONS

A good agreement between the shapes of relative LED spectra was achieved in measurements with two spectroradiometers operating according to different principles. For the wavelength scale, an intersection point, independent on the junction temperature was found in LED spectra. This point can be used to verify and correct wavelength scales of spectroradiometers without using line sources.

REFERENCES

1. E. Woolliams *et al*, Final report on CCPR K1-a: Spectral irradiance from 250 nm to 2500 nm, Metrologia, 43, 02003, 2006.
2. E.F. Schubert, Light-Emitting Diodes, second ed., Cambridge University Press, Cambridge UK, 2006.
3. Y. Xi *et al*, Junction and carrier temperature measurements in deep-ultraviolet light-emitting diodes using three different methods, Appl. Phys. Lett., 86, 031907, 2005.

New source and detector technology for the realization of photometric units

T.Dönsberg[1,2], M.Sildoja[1], F.Manoocheri[1,2], T.Pulli[1], T.Poikonen[2], H.Baumgartner[1], P.Kärhä[2], and E.Ikonen[1,2]

[1]*Metrology Research Institute, Aalto University, Espoo, Finland,*
[2]*Centre for Metrology and Accreditation (MIKES), Espoo, Finland*
Corresponding e-mail address: timo.donsberg@aalto.fi

Temporally stable light emitting diodes (LEDs) are potential candidates to replace incandescent lamps as photometric source standards. When the spectra of LEDs are limited to the visible wavelength range, new silicon detector technology can be advantageously exploited. We present a novel method – based on the recently introduced Predictable Quantum Efficient Detector (PQED) – for the realization of photometric units which completely eliminates the need to use $V(\lambda)$ filters. The illuminance values of a blue LED determined using the new method and a conventional reference photometer deviated only by 0.25% from each other. The PQED-based value has lower standard uncertainty (0.41%) than the value based on the reference photometer (0.51%).

INTRODUCTION

The production of incandescent light bulbs is bound to end, as incandescent lighting is being phased out globally in favour of more energy-efficient and sustainable solutions. Therefore, new photometric source standards are also needed to replace the traditional incandescent lamps. Light emitting diodes (LEDs) are promising candidates as new reference standards, because certain types of LEDs have been shown to be temporally stable within 0.2% in luminous flux over a time period of 20,000 hours of operation [1].

Photometric quantities are obtained from corresponding radiometric quantities by weighting the radiation with the spectral luminous efficiency function $V(\lambda)$ which represents the relative spectral responsivity of the human eye under daylight illumination levels. In practice, this is realized by using a filter, the transmittance of which closely follows the $V(\lambda)$ curve [2]. The deviation between the $V(\lambda)$ and the relative spectral responsivity of the photometer, $s_{rel}(\lambda)$, is corrected by using the so-called spectral mismatch correction factor

$$F = \frac{\int \Phi_e(\lambda) V(\lambda) d\lambda}{\int \Phi_e(\lambda) s_{rel}(\lambda) d\lambda}, \quad (1)$$

where $\Phi_e(\lambda)$ is the incident spectral radiant flux. For example, illuminance E_v is obtained from the measured photocurrent i using the equation

$$E_v = \frac{K_m F i}{A s(555)}, \quad (2)$$

where constant K_m = 683 lm/W is the maximum luminous efficacy, A is the area of the limiting aperture and $s(555)$ is the absolute responsivity of the photometer at the $V(\lambda)$ peak wavelength of 555 nm.

The uncertainties of the measurement methods based on $V(\lambda)$ filtered detectors may increase when measuring LEDs instead of incandescent lamps. This is due to the narrow and complicated spectra of LEDs. The situation is most problematic in the blue region of the visible spectrum where the uncertainty of the $V(\lambda)$ weighted spectral responsivity is the highest [3].

We present a novel method for basic realization of photometric units based on new detector technology which completely eliminates the need to use $V(\lambda)$ filters. The new method is applicable for LED light sources, but not for incandescent lamps, since they have too broad emission spectra.

METHOD

The new method utilizes the PQED operated at room temperature [4-6]. It has been experimentally confirmed that the spectral responsivity of the PQED can be predicted with a relative standard uncertainty of around 0.007 % in the visible wavelength range [4,5]. Such a low uncertainty is achieved by the use of induced-junction photodiodes with almost unity internal quantum efficiency. The photodiodes are mounted in a wedged trap configuration for the elimination of specular reflectance losses (see Fig. 1). The detector is operated without a window using a nitrogen flow to prevent dust contamination of the photodiodes [6]. An aperture is placed in front of the

PQED to limit the field of view. No filter is used. This is possible when measuring LEDs that have no signal outside the silicon detector spectral range.

The reflectance loss of the PQED is affected by the state of polarization of the incident light. However, when the spectral distribution of the light source is known, the ratio of the photocurrents of the two photodiodes can be used to determine the polarization distribution of the incident light and, further, the reflectance correction of the PQED [7].

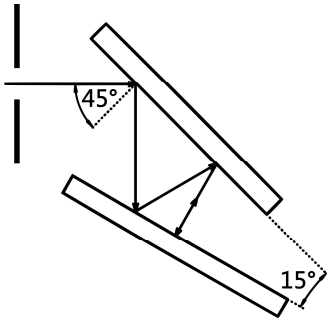

Figure 1. Schematic structure of the PQED with seven reflections between two 11 x 22 mm^2 silicon photodiodes.

In conventional photometry, $s_{rel}(\lambda)$ resembles the $V(\lambda)$ in Eq. (1) and the uncertainty of F due to the incident spectral flux $\Phi_e(\lambda)$ is small. In the new method, the $V(\lambda)$ filter is not used, so the relative spectral responsivity is simply that of the quantum flat PQED, and the absolute responsivity $s(555)$ in Eq. (2) is accurately known. The main uncertainty component with PQED is due to $\Phi_e(\lambda)$ affecting via F.

MEASUREMENT RESULTS

The illuminance produced by a blue LED with a peak wavelength of 466 nm and bandwidth of 24 nm was measured at the same position with the reference photometer and with the PQED as described above. The measurement distance and the aperture diameter were 850 mm and 3 mm in both measurements.

The relative spectral flux $\Phi_e(\lambda)$ of the LED was measured with a scanning spectroradiometer with 1 nm bandwidth. The reliability of the measurement was estimated by comparing results obtained with two spectroradiometers [8]. The determined spectral mismatch correction factors were 0.1243 for the PQED and 0.9357 for the reference photometer.

The measured photocurrent values were 192.7 nA and 13.44 nA for the PQED and the reference photometer, respectively. These correspond to illuminance values of (5.046 ± 0.041) lx and (5.033 ± 0.052) lx by Eq. (2). The uncertainties are given at 95 % confidence level. The main uncertainty components of both measurements are listed in Table 1. The uncertainty due to the spectral mismatch correction factor is dominated by the transmittance of the $V(\lambda)$ filter when the reference photometer is used, and by the measurement of the LED relative spectrum $\Phi_e(\lambda)$ when the PQED is used.

Table 1. Main uncertainty components of illuminance measurements using the reference photometer and PQED.

Source of uncertainty	Relative standard uncertainty / %	
	Photometer	PQED
Absolute responsivity of the detector	0.10	0.01
Aperture area, A	0.07	0.07
Spectral mismatch correction factor, F	0.50	0.40
Photocurrent measurement, i	0.01	0.01
Combined standard uncertainty	0.51	0.41

CONCLUSIONS AND OUTLOOK

The congruent measurement results between the PQED-based method and the reference photometer demonstrate that the new method is suitable for characterization of narrow-band LED sources, such as separately measured colours of RGB lamps. A phosphor based white LED lamp was found to be a good candidate as a photometric reference source in [1]. A preliminary uncertainty analysis shows that also this type of lamps can be accurately calibrated with the PQED: the uncertainty of their relative emission spectra can be estimated to be the same as the uncertainty of the irradiance standard used for the calibration of the spectroradiometer. With a standard uncertainty of 0.4% for the latter, the uncertainty of F for the white LEDs would be smaller than the value listed for the narrow-band LEDs in Table 1.

In conclusion, realizing the illuminance and luminous intensity units without a $V(\lambda)$ filter using the PQED potentially gives lower uncertainty and a simpler method than measurement of LEDs with $V(\lambda)$ weighted photometers.

REFERENCES

1. P. Kärhä *et al*, Natural and Accelerated Ageing of Solid State Lamps, submitted to NEWRAD 2014.
2. P. Toivanen *et al*, Realization of the unit of luminous intensity at the HUT, Metrologia, 37, 131-140, 2000.

3. T. Poikonen *et al*, Uncertainty analysis of photometer quality factor f_1', Metrologia, 40, 75-80, 2009.
4. M. Sildoja *et al*, Predictable quantum efficient detector: I. Photodiodes and predicted responsivity, Metrologia, 50, 385–394, 2013.
5 I. Müller *et al*, Predictable quantum efficient detector: II. Characterization and confirmed responsivity, Metrologia, 50, 395–401, 2013.
6. T. Dönsberg *et al*, A primary standard of optical power based on induced-junction silicon photodiodes operated at room temperature, Metrologia (in press).
7. M. Sildoja *et al*, Use of the predictable quantum efficient detector with light sources of uncontrolled state of polarization, Meas. Sci. and Technol,, 25, 015203, 2014.
8. H. Baumgartner *et al*, Measurement of relative spectra of LEDs, submitted to NEWRAD 2014.

Pre-burning test of standard lamps at KRISS

Chul-Woung Park, Bong-Hak Kim, Dong-Joo Shin, Dong-Hoon Lee,
Seung-Nam Park, and Seongchong Park

Division of Physical Metrology, Korea Research Institute of Standards and Science
Corresponding e-mail address: spark@kriss.re.kr

We present the preparation of radiometric and photometric standard lamps based on a long-term pre-burning test at KRISS. The facility is capable of continuously monitoring the change of optical output of multiple DC-operated incandescent lamps of two different types: an 1 kW FEL type with CCT of 3100 K and an 150 W E11-based type with CCT of 2700 K. The pre-burning sequence consists of a 24-hour maximum-rate burning and a 48-hour working-rate burning. In addition, a periodic off-time of 2-hour duration is realized every 10 hours in oder to test the on-off reproducibility. After the pre-burning of more than 60 hours, the drift rate is reduced to less than 0.02 %/h for both types of standard lamps.

INTRODUCTION

To disseminate the photometric and radiometric scales, quartz tungsten-halogen (QTH) incandescent lamps are mostly used as transfer standard artefacts. However, they are known to considerably drift in terms of their optical and electrical characteristics at the initial phase of burning. For this reason, the candidate lamps need to be pre-burned or seasoned for at least 5 % of the rated life time of those lamps before they are certified as standard lamps [1]. In addition, screening is also required to find the lamps that show excessive drift rate after the pre-burning. For example, NIST employs one of the screening criteria related to the post-seasoning drift rate of less than 0.02 %/h in photometric output [1].

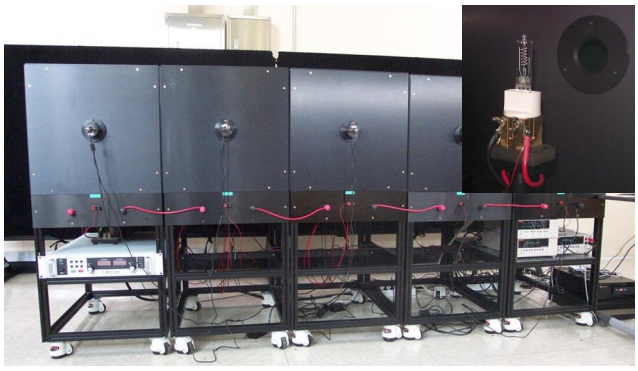

Figure 1. The pre-burning facility for 1 kW FEL-type lamps consisting of 5 partitions for 5 individual lamps.

In this work, we present the preparation of standard lamps at KRISS through a pre-burning procedure. The sequence of pre-burning is designed to effectively monitor the drift characteristics by mixing the maximum-rate, working-rate, and the periodic on-off operations for more than 80 hours. Two facilities are used for two different types of standard lamps: one for 1 kW FEL-type lamps for luminous intensity or spectral irradiance and the other for 150 W E11-based lamps for total luminous flux or total spectral radiant flux.

PRE-BURNING FACILITIES

Figure 1 shows the facility for 1 kW bi-pin FEL-type QTH lamps (Model: Ushio FEL 120V 1000 W [2]), while Figure 2 the facility for 150 W E11-based QTH lamps (Model: IWASAKI JD 110V 150W GSN [2]).

Each of the facilities consists of 5 partitions for 5 individual lamps, and is separately operated by two constant-current power supplies (Model: Magna XR 800V-10A, Magna XR 800V-2.5A [2]). Lamps are connected in series with a current sensing 0.1 Ω shunt (Model: Guildline 9230A-30 [2]) to provide a constant current. The lamp current and voltage of the individual lamp are monitored with a combination of a home-made voltage multiplexer and a digital voltmeter. On each partition of both facilities, a temperature-controlled photometer (Model: Inphora IPR-PDET012/A [2]) is mounted to monitor the

Figure 2. The pre-burning facility for 150 W E11-based lamps consisting of 5 partitions for 5 individual lamps. The inner surface is white-painted to monitor the spatially averaged photometric output imitating an integrating sphere. A baffle is placed in-between a photometer and a lamp.

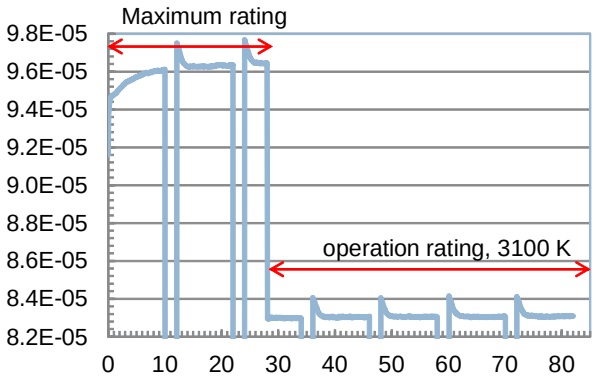

Figure 3. Pre-burning characteristics of an 1 kW FEL QTH lamp. The x-axis and the y-axis are in the unit of hour (h) and the current (A), respectively.

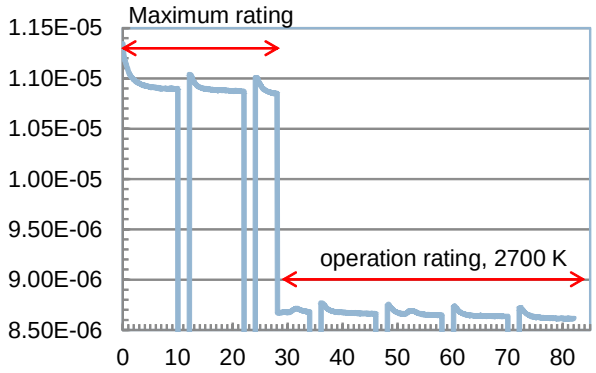

Figure 4. Pre-burning characteristics of an 150 W E11-based QTH lamp. The x-axis and the y-axis are in the unit of hour (h) and the current (A), respectively.

photometric output of the individual lamp, whose readout is measured with a combination of a current multiplexer and a picoammeter (Model: Keithley 6485 [2]). Each facility is capable of operating five lamps simultaneously via a PC control.

PRE-BURNING SEQUENCE AND RESULTS

Figure 3 and 4 show the measured pre-burning characteristics of a 1 kW and 100 W lamps, respectively. In these figures, the sequence of pre-burning is clearly visible. The sequence consists of two phases similar to the realization at NIST [1]. First, the lamps are burned at the maximum rating for 24 hours of cumulative burning time to accelerate the initial ageing. After this phase, the lamps are operated at the nominal rating for 48 hours of cumulative burning time to monitor the residual drift. For such a continuous pre-burning, however, the effects when the lamps are repetitively turned on and off during their application are not simulated. Therefore, we added a periodic off-time of 2 hours with an interval of 10 hours during the burning.

Figure 3 shows the representative pre-burning result of an 1 kW FEL lamp. For the first phase, the lamp is burned at the maximum-rate current of 8.23 A, and then the lamp is burned at the nominal operating-rate current of 8.0 A, which corresponds to a CCT of 3100 K. During the initial ageing phase, the photometric output shows a positive drift with a relatively high slope, but the drift rate is 0.004 %/h after more than 60 hours of burning time.

In the case of a 150 W lamp in Fig. 4, the maximum-rate current was 1.30 A, and the nominal operating-rate current 1.25 A, which corresponds to a CCT of 2700 K. The initial ageing phase shows a negative drift in this case. We noticed that the direction of the drift in the initial ageing phase is related to the operating CCT [1]

For the both lamp types, the abnormal “peaks” of photometric output are observed at each on-off cycle. We assigned these peaks to a temperature effect of the monitor photometers. Although the photometers are temperature-stabilized at about 35 °C, the chamber temperature of the facility increases to higher than 50 °C in the case of the 1 kW lamps. Therefore, there is a considerable temperature difference between the 2-hour off-time and the following burning time, which causes a discontinuity of the photometric output at each on-off cycle. Note that the peaks are smaller for the 150 W lamps due to the smaller thermal load compared to the 1 kW lamps. We propose to minimize this temperature effect by improving the temperature control of the photometers. Besides these peaks, the drift rate is 0.01 %/h after more than 60 hours of burning time.

ACKNOWLEDGEMENTS

This work was partly supported by the Korean Ministry of Knowledge and Economy under the project of Development of performance evaluation, certification, quality control techniques for LED luminaires, grant KI002202.

REFERENCES

1. Y. Ohno, “Photometric standards,” in Handbook of Applied Photometry, C. DeCusatis, ed. (Springer-Verlag, 1998), pp. 65–70.
2. All the manufacturer and model names appeared in this paper were specified only for describing our work and experiences in detail, thus we do not claim any kinds of considerations or preferences in performance on those products.

Facility for Studying Gallium Cells in a Space-Based Blackbody Model

S.P. Morozova[1], A.S. Panfilov[1], V.I. Sapritsky[1], B.E. Lisyansky[1], A.A. Katysheva[1], M.N. Pavlovich[1], N.A. Parfentyev[1], D.M. Karpunin[2], and E.V. Makolkin[2]

[1] All-Russian Research Institute for Optical and Physical Measurements (VNIIOFI), Moscow, Russia, [2]Central Research Institute of Machine Building (TSNIIMASH), Moscow, Russia

Corresponding e-mail address: morozova-m4@vniiofi.ru

The gallium phase transition blackbody model is a promising reference source for the in-flight calibration of space-based equipment. This paper describes a facility designed by VNIIOFI that allows us to conduct experimental studies of the phase transition temperature plateau duration and pattern with varying cell parameters. The facility consist of a gallium transition blackbody model with changeable cells, an optical system made as a vacuum chamber, and a precision pyrometer. Analysis results allows us assess compliance of the blackbody model gallium cell structural dimensions with the preset pattern and time parameters of the phase transition temperature plateau.

A blackbody model based on the pure metal phase transition is very popular as a reference source in radiometric calibration of IR-range optoelectronic equipment [1, 2, 3, 4]. The gallium phase transition blackbody model is a promising reference source for the in-flight calibration of space-based equipment. No weight or size limitations are imposed upon an IR-range radiation source when the pre-flight calibration of space-based optoelectronic equipment is conducted. Gallium may weigh up to 2.7 kg in a cell that is used, and phase transition temperature plateau duration under certain thermal conditions of the cell may be more than a week. When the Earth is studied from space, certain requirements are imposed upon reference sources. On the one hand, the phase transition time may be limited to the communication session duration between the calibration equipment and the radiometer being calibrated. On the other hand, it is imperative to minimize the source weight and power consumption. A facility described in this paper was built to optimize the design of a gallium phase transition space-based reference source. The facility is shown schematically in Figure 1.

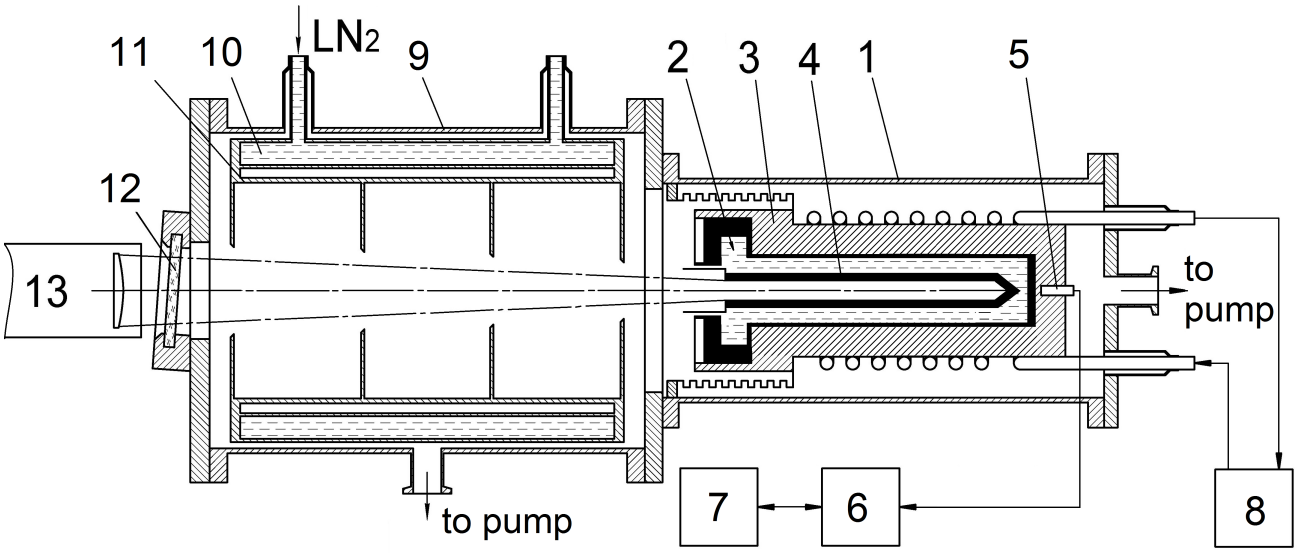

Figure 1. Facility for Studying Space-Based Blackbody Model Gallium Cells. 1 - Blackbody model at gallium m.p., 2 - changeable Teflon cell filled with gallium, 3- heat exchanger with a removable liner, 4 - emitting copper cavity 5 - platinum resistance thermometer, 6 - digital multimeter , 7 computer, 8 - liquid thermostat, 9 - vacuum chamber, 10 - liquid nitrogen vessel, 11 - radiation shields, 12 - input window, 13 - precision pyrometer.

The main components of the facility are: a gallium transition blackbody model with changeable cells, an optical system made as a vacuum chamber having a cylindrical liquid nitrogen-filled vessel, and a precision pyrometer for measuring the temperature in the cavity. The exit aperture of the blackbody model is located in the analysis plane of the pyrometer. The blackbody model radiation is incident upon the pyrometer input via the vacuum chamber, which imitates the on-board conditions.

The blackbody model is a sealed enclosure in which a heat exchanger is supported by means of heat-insulating posts and bellows. The heat exchanger is a copper cylinder, which is externally provided with a copper tube coil, with coolant from the external liquid thermostat being pumped through the coil. The enclosure interior space is evacuated using a primary vacuum pumping system to insulate the heat exchanger from the ambient environment. The heat exchanger temperature is measured using a system having a platinum thermometer, multimeter, and computer. The heat exchanger copper block has a 74-millimeter diameter 176 millimeters long cylindrical cavity, which receives removable copper liners containing gallium cells. The cell is made as a cylindrical Teflon casing having an inner passage, with gallium being placed between the casing and the passage. The casing and the inner passage of the cell are sealingly connected to each other. The emitting cavity, which is made as a copper cylinder with a conical bottom, is tight-fitted in the internal passage of the gallium cell. The emitting cavity is internally coated with a black dull paint. A flange installed in the front part of the casing is used to attach the blackbody model to the vacuum chamber flange. This facility allows us to conduct experimental studies of the phase transition temperature plateau duration and pattern with varying cell parameters.

The relationship between the phase transition temperature plateau duration and pattern and a fixed temperature difference, ΔT, between the cell outer wall temperature and the phase transition temperature for a given blackbody model design was calculated for preliminarily sizing the gallium cell. The bidimensional gallium cell radius-to-height temperature profile for a real-size blackbody was computed during the entire phase-transition period. The computation was performed using the finite element method in which a temperature-dependent term was used in the gallium heat capacity equation to describe the phase transition. This term was described by a Gaussian curve, and the integral of the above temperature dependence was limited by the phase transition energy. As a result, a family of curves was obtained for the relationship between the average temperature at the emitting cavity bottom of a real-life blackbody model and time for different half-width values of the Gaussian curve. Processing these curves allows us to determine the size and position of an area where the average temperature is as close as possible to the known gallium phase transition temperature. When the analysis results are reviewed, we can assess compliance of the blackbody model gallium cell structural dimensions with the preset pattern and time parameters of the phase transition temperature plateau.

REFERENCES

1. S.P. Morozova, V.I. Sapritsky, V.S. Ivanov, B.E. Lisiansky, U.A. Melenevsky, Liang Yan Xi, Liang Pei, “Facility for blackbody calibration”, TEMPMEKO’99 Proceedings, 587-591, 1999.
2. V.S. Ivanov, B.E. Lisiansky, S.P. Morozova, V.I. Sapritsky, U.A. Melenevsky, Liang Yan Xi, and Liang Pei, “Medium-Background radiometric facility for calibration of sources or sensors”, Metrologia 37, 599-602, 2000.
3. C. Monte, B. Gutschwager, S.P. Morozova and J. Hollandt, “Radiation Thermometry and Emissivity Measurements under Vacuum at the PTB,” *International Journal of Thermophysics,* Vol. 30, 203-219 (2009).
4. E. Theocharous, N.P. Fox, V.I. Sapritsky, S.N. Mekhontsev and S.P. Morozova, “ Absolute measurements of black-body emitted radiance”, Metrologia 35, 549-554, 1998.

Improving cell for black body sources of aluminum fixed point

Iu. A. Sild and E.V. Vizulaynen

D.I. Mendeleyev Institute for Metrology (VNIIM), Saint-Petersburg, Russian Federation
Corresponding e-mail address: y.a.sild@vniim.ru

A new cell for black body sources of aluminum fixed point temperature **was developed. Experience has shown that the cell design must be performed on the basis of a floating finger - the cylinder with the special channel. The cell was made of graphite and held her filling high purity aluminum. On the state primary standard of total radiance carried out research of black body sources with a new cell. Preliminary results are showed that black body sources of aluminum** fixed point **with a new cell design meets the requirements for this type of black body sources.**

INTRODUCTION

In the structure of the state primary standard of total radiance are included black body sources based on the phase transitions of pure substances – black bodies based on: the triple point of water, gallium melting, freeze of zinc, tin, aluminum and copper. Black bodies allow to reproduce the total radiance values from 100 to $61 \cdot 10^3$ W/sr·m^2 [1].

A fundamental element of any black body sources is the cell filled corresponding pure substance. Construction the cell must enforce mandatory requirements for the external dimensions of the cell, thickness the wall and emissivity parameters of cavity. It's no exception for the cell from the black body sources of aluminum fixed point.

DESCRIPTION OF THE CELLS

The black body sources with the previously developed cell, allow to provide necessary characteristics and being the task. However, it requires extremely scrupulous compliance with implementation technology for realization freeze plate of aluminum. In addition, there was a gradual burnout graphite, which will soon require replacement cell in black body.

Experience has shown that peculiarities of used high-purity metal are advisable to apply a new design of the cell, the so-called «tube with floating finger». Accordingly, the new cell designs for black body of aluminum fixed point temperature include the following components (figure 1): the housing with the cavity (1), finger (2), emphasis (3), cover (4). The construction is shown in Figure 1. Changes in the structure of a cell reference points emitter must be performed in compliance with the external dimensions, the required parameters emissivity cavity and measuring channel.

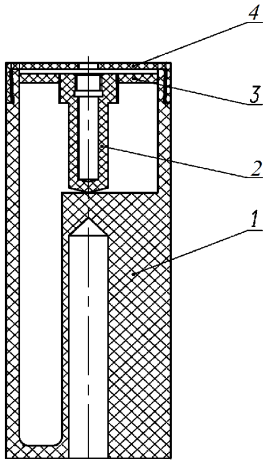

Figure 1. Components of the cell.

Details of the cell were made from purified graphite trademark DE-24, and before the assembly was thermally processed. Subsequently, the cell was filled with high-purity aluminum (Puratronic®, 99,999+ %, production Alfa Aesar).

The special device is used when filling for fixing the housing relative to the housing. After filling, damping ring was placed between the emphasis and the cover.

The cell was placed in the case, which was placed in the center of the heating three zone resistive furnace.

In what follows held a number of registration sites solidification of aluminum. A calculation based on the Stefan-Boltzmann law reproducible value of total radiance and evaluation of the components of the uncertainty of measurement results.

The expanded uncertainty value does not exceed 1.5% for k = 2.

CONCLUSIONS

Black body sources of aluminum fixed point temperature using a new cell design meets the requirements for this type of black body and developed cell potential should provide a longer service life.

The research of black body sources will be continued to establish its long-term stability.

REFERENCES

1. I. I. Dolgikh, A. I. Pokhodun, O. V. Rybolovleva, V. V. Smirnova, State Primary Standard of the Unit of Infrared Radiance, Measurement Techniques, October 2001, Volume 44, Issue 10, pp 965-971.

Realization of Total Spectral Radiant Flux Scale at NMIJ

Kenji Godo , Kazuki Niwa, Kenichi Kinosita, Yoshiro Ichino, and Tatsuya Zama

NMIJ, AIST, 1-1-1 Umezono, Tsukuba, Ibaraki, JAPAN
Corresponding e-mail address: kenji-goudo@aist.go.jp

The total spectral radiant flux (TSRF) scale has been realized at the National Metrology Institute of Japan (NMIJ). Our realization method is a relative gonio-spectroradiometric method with both the NMIJ spectral irradiance scale and the NMIJ total luminous flux scale. We have also investigated quarts halogen lamps from domestic manufacturers and decided a standard lamp for TSRF. We found that the standard lamp for TSRF could have appropriate stability properties after 100 h seasoning processing.

INTRODUCTION

With remarkable improvement of a luminous efficiency of Solid State Lighting (SSL), importance of a total luminous flux measurement of SSL is increasing. For measuring the luminous flux of SSL accurately by a conventional sphere-photometer system, a colour correction factor, which is calculated by using a relative spectral responsivity of the sphere-photometer and a spectral distribution of SSL, is indispensable. For SSL industry, however, it is difficult to evaluate the relative spectral responsivity of the sphere-photometer, such colour correction is not practical. Thus, the conventional sphere-photometer systems have been replaced by sphere-spectroradiometer systems. The spectral responsivity of the sphere-spectroradiometer system needs to be calibrated against a total spectral radiant flux (TSRF) standard. Recently, National Institute of Standards and Technology (NIST) realized the TSRF scale in visible region using a relative gonio-spectroradiometric method, and the TSRF standard comes to be used widely in photometric measurements of SSL in USA [1]. In Japan, development of TSRF standard at NMIJ started in 2010 to address the strong demands for TSRF standard by domestic lighting manufacture.

In this study, we have realized TSRF scale in the visible range (360 nm – 830 nm), where candidate standard lamps for TSRF were investigated.

REALIZATION METHOD

Our realization method is similar to the NIST realization method, where we also used the relative gonio-spectroradiometric method [1].

Firstly, we measure a luminous intensity distribution of a quartz halogen (QH) lamp (test lamp) by using a gonio-photometer to determine a total luminous flux (Φ_v) of the test lamp. The measurement method of Φ_v follows the realization procedure for the total luminous flux scale at NMIJ. After the measurement of Φ_v, the photometer is replaced with an array spectroradiometer, and a relative spectral radiant intensity distribution ($I_{rel}(\lambda, \theta, \phi)$) of the test lamp is measured over 4π solid angle. Then, a relative spectral responsivity of the array spectroradiometer is calibrated against NMIJ spectral irradiance standard lamps. Thus, the TSRF ($\Phi_e(\lambda)$) of the test lamp is given by

$$\Phi_e(\lambda) = k_{scale} \int_{\phi=0}^{2\pi} \int_{\theta=0}^{\pi} I_{rel}(\lambda,\theta,\phi) \sin\theta \cdot d\theta \cdot d\phi \quad (1)$$

and,

$$k_{scale} = \frac{\Phi_v}{K_m \int_{\lambda=360}^{830} V(\lambda) \int_{\theta=0}^{\pi} \int_{\phi=0}^{2\pi} I_{rel}(\lambda,\theta,\phi) \sin\theta \cdot d\theta \cdot d\phi \cdot d\lambda} \quad (2)$$

where, K_m is the maximum spectral luminous efficacy being 683 lm/W, $V(\lambda)$ is the spectral luminous efficiency, and θ and ϕ are polar coordinates of the gonio-photometer.

REALIZATION FACILITY

Figure 1 shows the NMIJ gonio-photometer/ spectroradiometer system. The system has been used for the realization of total luminous flux scale. The system is equipped with a photometer, three aperture screens, two laser diodes for alignment, lamp supports etc. The photometer is detachable and easily mounted onto the photometric bench. An illuminance responsivity of the photometer is calibrated against luminous intensity standard lamps on the photometric bench. The NMIJ gonio-photometer system is a moving photometer type which has two rotation axes (θ, ϕ) and compensatory axes (θ'). A rotating arm, which the photometer and the test lamp are attached

to in each ends, rotates around the θ axis on the stop-and-go mode, while the pole of the test lamp keeps vertically upward during the measurement by rotating the θ'axis. When the $I_{rel}(\lambda,\theta,\phi)$ of the test lamp is measured, an array spectroradiometer, an irradiance head and an optical fiber are mounted to the NMIJ gonio-photometer system. The relative spectral responsivity of the array spectroradiometer is calibrated against the spectral irradiance standard lamps which are directly mounted on the rotating arm.

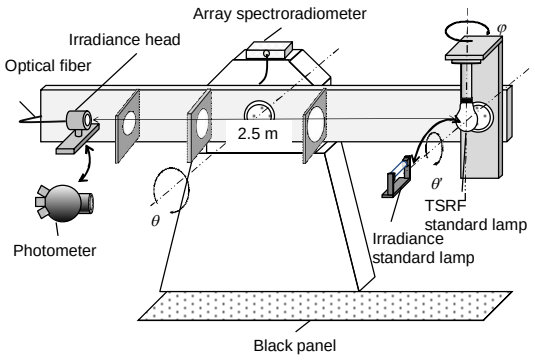

Figure 1. The NMIJ gonio-photometer/spectroradiometer system.

STANDARD LAMP FOT TSRF

We have traditionally used tungsten lamps commercially available as luminous flux standard lamps as transfer standards for the total luminous flux. Their distribution temperature is typically approximately 2790 K. Their optical power at near UV region (360 nm-450 nm) is not sufficient for a TSRF transfer standard. Therefore, we have examined output stability and reproducibility for twelve types of QH lamps for deciding a suitable standard lamp for TSRF. We decided a 24V-150W QH lamp from a domestic manufacturer (Phoenix Electric Inc.) as the standard lamp. Their CCT is approximately 3000 K-3100 K at a rated voltage. The QH lamp has a small screw base (E11), thus a special adapter socket (E11-E26) was designed to fit to our facility.

The standard lamps for TSRF are selected according to the output stability after 100 h seasoning processing. Figure 2 shows ageing properties of the standard lamp after the 100 h seasoning processing. The ageing rate was below 0.5 % in 20 h of operation, indicating that these lamps have extremely good ageing properties as the standard lamps for TSRF.

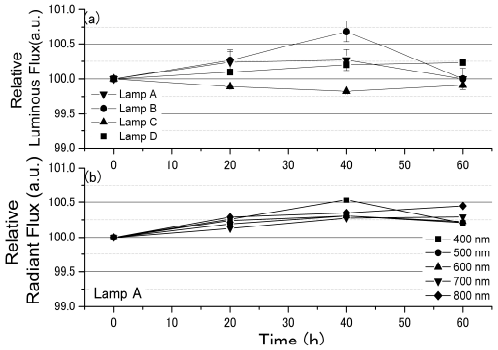

Figure 2. Ageing curves of the standard lamp for TSRF at approximately 3000 K-3100 K CCT after the 100 h seasoning processing. (a) luminous flux for 4 lamps with the same type, (b) TSRF of lamp A. Each curve is normalized as 100 with its value at 0 h.

CALIBRATION FACILITY

A TSRF calibration service is performed with the NMIJ 1.65 m sphere-spectroradiometer system. The standard lamps, whose TSRF scale is realized by the NMIJ gonio-photometer/spectroradiometer system, is used as reference standards. The spectroradiometer is equipped with both a high-sensitivity charge-coupled device (CCD) array detector and a photomultiplier tube (PMT) as photo detectors. Usually, the CCD array detector is used to calibrate a customer's lamp in short measurement time. A photometer and a silicon photodiodes (Si-PD) are used as monitor detectors to check optical power stability during the TSRF calibration. An uncertainty due to spatial response distribution of an integrating sphere was estimated experimentally by using the 4π beam scanner [2].

CONCLUSIONS

The total spectral radiant flux (TSRF) scale has been realized in visible spectral range with NMIJ gonio-photometer/spectroradiometer system. The standard lamps for the TSRF scale were carefully selected with respect to high CCT and output optical power stability.

REFERENCES

1. Y Zong.Y Ohno, Realization of total spectral radiant flux scale and calibration service at NIST, Proc. the 26th Session of the CIE, 2-182, 2007.

2. K Niwa. K Godo. etc., Measurement of angular nonuniformity of an integrating sphere for total spectral radiant flux measurement, Proc. CIE 2012 Lighting Quality and Energy Efficiency, 659-662, 2012.

The spectrally tuneable absolute irradiance and radiance source (STAIRS)

Andrew Levick, Claire Greenwell, Jane Ireland, Emma Woolliams, and Teresa Goodman

National Physical Laboratory, Teddington, United Kingdom
Corresponding e-mail address: emma.woolliams@npl.co.uk

A new spectrally tuneable source has been developed for calibrating radiometric detectors in radiance, irradiance or power mode. It is termed the Spectrally Tuneable Absolute Irradiance and Radiance Source (STAIRS) and consists of a supercontinuum laser, wavelength tuneable bandpass filter, power stabilisation feedback control and output coupling optics. It is relatively portable, and provides a tuneable monochromatic alternative to lamps, blackbodies or lasers.

INTRODUCTION

This paper presents a reasonably portable, monochromatic tuneable source that can be configured as a laser beam (as a source of optical power), or as an irradiance or radiance source. In this way it can replace tuneable lasers or monochromator-based sources in many radiometry applications. We have also designed the source for use within a vacuum chamber, providing a convenient source for Earth Observation instrument calibration.

The source is based on a supercontinuum laser (wavelength range 400 nm – 2500 nm) commercially available from Fianium. Such sources, combined with a monochromator, are increasingly being used for radiometric measurements e.g. [1]. In STAIRS, the supercontinuum laser is coupled into a filter, which provides spectral tuneability in a convenient fibre-coupled manner. The laser power is also actively controlled using a feedback photodiode, and a software-emulated PID controller fed into the internal optical amplifier of the supercontinuum laser.

The supercontinuum laser is fully fibre coupled and can provide a laser beam from the fibre. For irradiance mode operation, the laser is fed into a small integrating sphere and for radiance mode operation we are developing, with Polymer Optics (a commercial partner) a flat panel source that is also suitable for operation in a vacuum chamber.

Traceability for the power, radiance and irradiance mode operation is provided by viewing the STAIRS output using a calibrated silicon trap detector with zero, one or two apertures to define the appropriate geometry, for each of these illumination modes.

STABILISING THE SOURCE

Without active stabilisation, the output power of the supercontinuum laser drifts by ~1 % per hour due to the alignment- and temperature-sensitive optical instrumentation and complex physics of the supercontinuum laser generation. With active stabilisation, there is no apparent drift, and the signal fluctuations are due to white noise (**Figure** 1). For averaging times greater than 100 s, the uncertainty associated with the laser power, due to this noise, is <0.01 %.

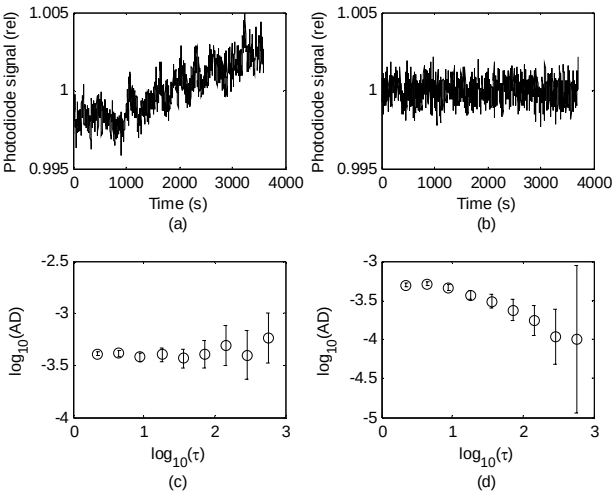

Figure 1. Measurement with a photodiode that is independent of the feedback system, of the stability of the STAIRS laser, a) when not stabilised, b) when actively stabilised. c) and d) are the corresponding Allan Deviation plots. The gradient in (c) indicates drift, while that in (d) indicates white noise.

WAVELENGTH TUNEABLE FILTER

The large wavelength range of the supercontinuum laser means that if a wavelength band of only a few nm is required, over 99 % of the radiation must be removed by a filter of some sort. The filter must have a very good rejection of 'out-of-band' light, especially if radiometric traceability is provided with a broadband detector, such as a silicon photodiode, that is sensitive to light in many of the out-of-band

spectral regions. For example, to achieve a total out-of-band contribution to the uncertainty budget of less than 0.1 % requires better than six orders of magnitude suppression of the out-of-band radiation.

Several different types of filter were considered during the development of STAIRS, including acousto-optic, grating monochromators, prisms and volume Bragg gratings. The final choice was to use the Laser Line Tuneable Filter (LLTF) [2] based on Volume Bragg Grating technology. The advantage of the LLTF is a low out-of-band transmission; its main disadvantage is the high cost of the filter, and therefore at present we have only obtained one for the 400 nm – 1000 nm spectral region.

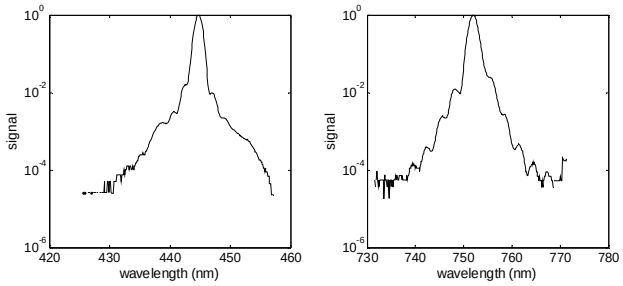

Figure 2. LLTF bandpass function, as measured by an Optical Spectrum Analyser at two wavelengths.

The LLTF has a bandwidth of 1 nm – 2 nm, with the shape and full width half maximum of the bandpass function changing with wavelength. There are also some minor side peaks (**Figure** 2)

The LLTF is based on diffraction grating technology and there is some transmission due to second orders. To remove second-order radiation, a glass blocking filter (RG695) is inserted for LLTF filter wavelength settings longer than 790 nm.

Beyond the local spectral profile, as shown in **Figure** , the out-of-band blocking is better than 10^{-6}. The out-of-band radiation was tested by setting STAIRS to a wavelength of 633 nm and measuring the output with a double monochromator (Figure 3). Further tests with an RG695 long-pass blocking filter testing the integrated output at longer wavelengths. These tests show that when STAIRS is set to blue or green wavelengths, the contribution to the signal on a silicon photodiode due to out-of-band wavelengths is <0.01 %.

OUTPUT COUPLING OPTICS

The STAIRS source has already been used to calibrate the irradiance responsivity of ocean colour radiometers, to test the stray light responsivity of an array spectrometer and as a source for reflectance measurements. For these measurements the STAIRS radiation was used either directly from the fibre, or coupled into a small integrating sphere, with additional mirrors or lenses. We are currently also developing a flat-panel source with our commercial partner, Polymer Optics. This will create a tuneable monochromatic source, in a box 30 mm deep and ~200 mm by ~220 mm, with an illuminated surface 170 mm by 170 mm. The system has an inbuilt feedback photodiode and is anticipated to be uniform to 1 % across the illuminated surface. The source is intended for use within, for example, vacuum chambers.

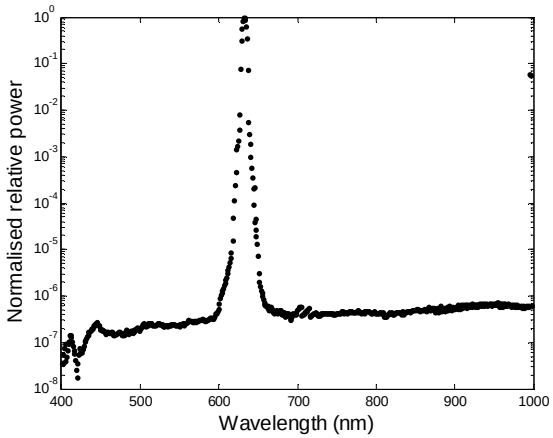

Figure 3. Out-of-band radiation from STAIRS measured with a double monochromator.

CONCLUSIONS

NPL has developed an optical source based on a supercontinuum laser and a Volume Bragg Grating. The source can be used in power, irradiance or radiance mode and is actively stabilised and can be tuned, at present from 400 nm to 1000 nm. It operates at power levels of 0.5 mW – 5 mW. Extension to longer wavelengths is planned.

REFERENCES

1. J. T. Woodward, A. W. Smith, C. A. Jenkins, C. S. Lin, S. W. Brown and K. R. Lykke, Supercontinuum sources for metrology, Metrologia, 46, S277-S282, 2009.
2. S. Blais-Ouellette, E. H. Wishnow, P. L. Shopbell, W. van Breugel, K. Taylor and R. Smith, Double Bragg grating tunable filter, Spie-Int Soc Optical Engineering, 2004.

Calibration of UV and VUV radiation sources at the Metrology Light Source

R. Thornagel, R. Fliegauf, R. Klein, S. Kroth, W. Paustian, and M. Richter

Physikalisch-Technische Bundesanstalt, Berlin, Germany
Corresponding e-mail address: reiner.thornagel@ptb.de

PTB has a long tradition in the calibration of radiation sources using synchrotron radiation to cover the UV and VUV spectral range. New instrumentation in the PTB laboratory at the Metrology Light Source (MLS) has been put into operation that opens up extended calibration possibilities. A new measuring station for radiation source calibration has been set up in the spectral range from 7 nm to 400 nm using a combined normal incidence - grazing incidence monochromator.

SOURCE-BASED CALIBRATION

In the UV and VUV spectral range, electron storage rings, the spectral radiant intensity of which can be calculated by classical electrodynamics [1], may be used as primary radiation sources [2,3]. In case of PTB these are BESSY II [4] and the MLS [5,6]. The radiation source under test will be compared with a spectrally resolving measuring station against the primary radiation source, the storage ring. Now, a new facility has been set-up at the MLS that covers the spectral range from 7 nm to 400 nm.

THE NEW MEASURING STATION

The core of this new radiation source calibration facility is a monochromator with three gratings under normal incidence and three gratings under grazing incidence geometry which are exchangeable under vacuum. The radiation from the source is imaged into the monochromator by an elliptical mirror under 10 ° grazing incidence. For taking into account the polarization efficiency of the transfer device and the very high degree of polarization of the synchrotron radiation, the entire mirror monochromator unit can be rotated around the incoming radiation beam. The transfer device can be moved to either be illuminated by the primary source or the source under test, in such a way, that either source has the same distance to the transfer station. This assures that the optical path on the mirror and inside the monochromator is identical for both sources. Fig. 1 shows a drawing of the whole measuring station.

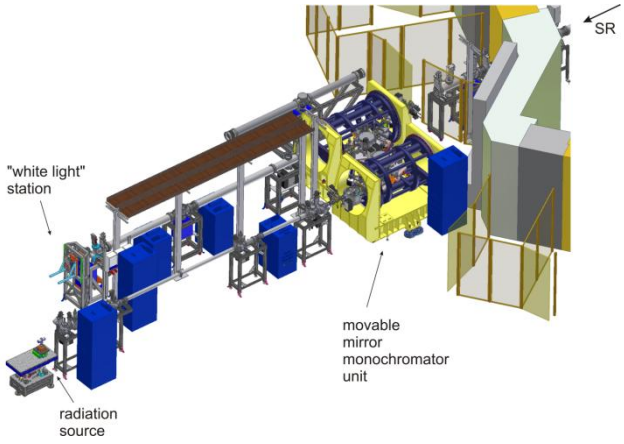

Figure 1. Drawing of the source calibration facility. The transfer device (yellow) can be either placed to face the synchrotron radiation or the radiation source under test (both positions shown in sketch).

For reducing the higher order effects, the station is equipped with different solid filters. For the spectral range below 115 nm in the normal incidence part, the monochromator can be flooded with rare gas, differentially pumped towards the beamline, acting as a gas filter.

COMMISSIONING OF THE FACILITY

Commissioning of the measuring station started with the normal incidence spectral range. Measurements were performed with a hollow cathode lamp for verifying the wavelength calibration and for investigating higher order behaviour. Deuterium lamps were used for aligning, stability, and reproducibility measurements.

Then, the device was rotated to the storage ring and measurements with synchrotron radiation were performed. Because the electron multiplier detectors are very sensitive, adapted to the faint sources to calibrate, the synchrotron radiation from the MLS in normal operation mode would be much too bright. Therefore, the storage ring has to be operated in a special operation mode with 10,000 times smaller ring current than usual (15 µA instead of 150 mA). Due to the high horizontal polarization of the synchrotron radiation, all measurements were performed with the monochromator in horizontal and in vertical rotated position.

VALIDATION

With these measurements against the calculable synchrotron radiation, we got a first absolute calibration of the measuring station. Now further lamp measurements were performed with Deuterium lamps, which were carefully calibrated at the normal incidence measuring station in the PTB laboratory at BESSY II as secondary spectral radiant intensity radiation source standards.

The results of the new calibration against the MLS agree very well with the calibration at BESSY II within the calibration uncertainty level.

REFERENCES

1. Schwinger J 1949 *Phys. Rev.* **75**, 1912.
2. Ulm G 2003 *Metrologia* **40**, S101.
3. Holland J et al. in :Optical Radiometry', ed. by A. Parr, R. Datla, J. Garner, Vol. 41 of Experimental Methods in the Physical Sciences, Elsevier, p. 213.
4. Thornagel R et al. 2001 *Metrologia* **38**, 385.
5. Klein R et al. G 2008 Phys. Rev. Special Topics - Accelerators and Beams (PRST-AB) 11, 110701.
6. Klein R et al. 2009 *Metrologia* **46**, S266.

Traceable terahertz radiometry with a high absorbance coating

Yuqiang Deng, Qing Sun, Jing Yu, and Yandong Lin

Optics Division, National Institute of Metrology, Beijing 100013, China
Corresponding e-mail address: yqdeng@nim.ac.cn

We develop a high-absorbance coating in the terahertz region. This coating has an absorbance of more than 99% both in 0.1 THz~2.5 THz region and in laser wavelengths range, which allows for an absolute measurement of terahertz radiometry and traceability to the International System of Units. We introduce a terahertz radiometer, which is made with this high-absorbance coating as an absorber. A traceable measurement to Chinese National Laser Prime Standard and its uncertainty for measurement of THz sources are discussed.

1. INTRODUCTION

Terahertz (THz) radiation is sandwiched between the microwave and the infrared, bridging the gap between electronics and optics. In the electromagnetic spectrum, both electronic metrology and optical radiometry and photometry are well developed; however, there are no THz standards available at all for a long time. THz detectors have only a relative "reading", but no traceably absolute value. Recently, the national metrology institutes have notified the importance of THz radiometry. In 2009, Physikalisch-Technische Bundesanstalt (PTB) made a traceable measurement of THz detectors against cryogenic radiometer (CR) [1]. And In 2011, National Institute of Standards and Technology (NIST) used a 1.5 mm long carbon nanotube array (VANTA) as an absorber for THz radiometry [2].

We report a high-absorbance coating with a broad bandwidth for terahertz radiometry. A THz radiometer is fabricated with this coating, which allows for the traceability of THz radiometry to the International System of Units (SI).

2. THZ ABSORPTIVE COATINGS

We developed a mixture coating with silicon carbide (SiC) particles and 3M Velvet-coating paint [3]. We use a homemade THz spectrometer in reflection geometry to measure the reflectance of the coating. The measured spectral reflectance of this coating is shown in Fig. 1.

Figure 1 shows that the mixture coating has an extremely low reflectance in the THz region. The low reflectance is down to 50 GHz. For the radiation frequency higher than 50 GHz, the reflectance goes down dramatically. The measured result shows that the reflectance decreases with the increase of frequency below 1.0 THz. The measured reflectance is 1% at 0.1 THz, and it goes down to 0.1% at 0.5 THz. The increase of reflectance from the frequency larger than 1.0 THz is not an actual increase of the reflectance, because the measured reflectance is nearly the same with noise.

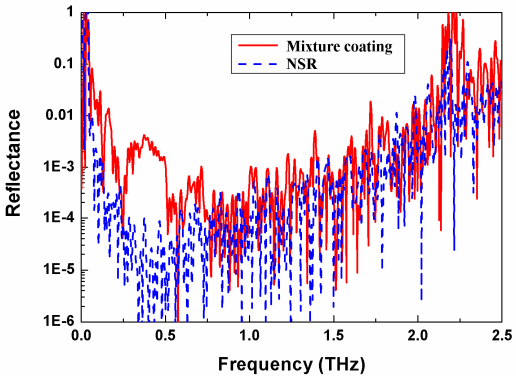

Figure 1. Measured spectral reflectances of the mixture coating and signal to noise ratio (NSR) in semilogarithmic scale.

3. DESIGN OF THE THZ RADIOMETER

With the mixture coating as an absorber, we fabricate a THz radiometer. The particle scale of the mixed coating is 300 μm and the thickness of the coating is 1.2 mm. From Fig. 1, the measurement frequency range can reach down to 50 GHz. The structure of the THz radiometer is shown in Fig. 2.

We applied a high density thermopile as a sensor, and sprayed the coating on the heat surface of the thermopile. The other surface of the thermo sensor is pasted on a heat sink. The heat sink is a solid block of aluminium (Al). We attached a reflective dome on the front side of the absorber. A hemisphere cavity is formed between the inner surface of the dome and the front suface of the heat sink. The residual reflection from the absorber can be reflected once again from the inner surface of the

dome, and goes back to the absorber. Thus the absorbance is improved by re-absorption. We wrapped up the radiometer with a Teflon housing to keep the radiometer insulated from the surrounding so that the radiometer became insensitive to the change of the suronding tempurature.

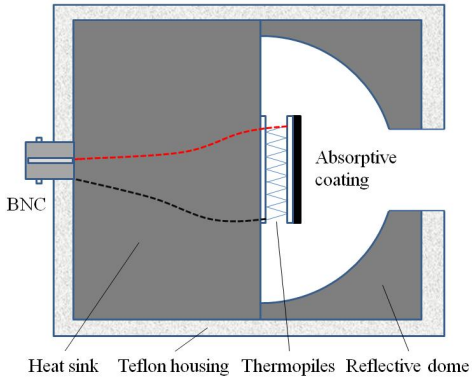

Figure 2. Schematic of the section profile of the THz radiometer.

4. TRACEABILITY TO LASER POWER STANDARD

The mixture coating consist of SiC particles and 3M Velvet-coating paint. 3M Velvet-coating paint also has excellent performance of absorbance in the visible and NIR spectral range; therefore, it should be possible to link THz radiometry to laser radiometry with this mixture coating. To investigate the performance of the THz radiometer at laser wavelengths, we measured the absorbance of the mixture coating at 632.8 nm wavelength with an integrating sphere [4]. The measurement setup is shown in Fig. 3. With this setup, the measured reflectance of this mixture coating at 632.8 nm wavelength is 0.979%; therefore, the absorbance is 99.021%.

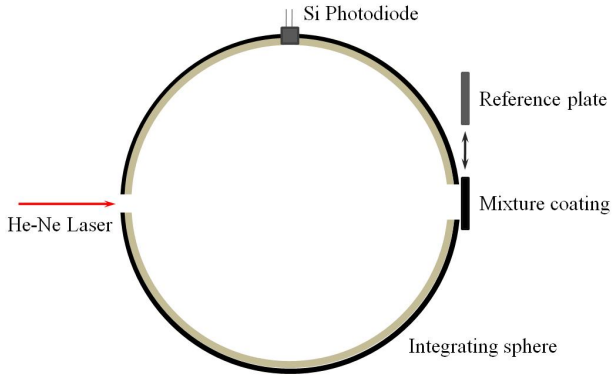

Figure 3. Reflectance measurement of the mixed coating with an interating sphere.

With the measured absorbance, we performed a traceable measurement of the power responsivity to Chinese National Laser Prime Standard with a He-Ne laser operating at 632.8 nm wavelength. This traceable measurement results in a power responsivity of 317.67 μV/mW.

5. UNCERTAINTY BUDGET AND DISCUSSIONS

We measured the THz radiation emitted from a backward wave oscillator (BWO) source. The source was operated at 0.775 THz (corresponding wavelength of 387 μm), and we applied a 10 mm diameter aperture to limit the beam size. The outlet voltage was read via a nanovoltage meter. An uncertainty budget is summarized in Table. 1. At last, an uncertainty of 1.13% (k=1) is obtained.

Table 1. Uncertainty budget of THz radiometry.

Source	uncertainty
National Laser Standard (room temperature radiometer)	0.3%
Absorbance at He-Ne laser wavelength	0.49%
Repeatability of the radiometer	0.65%
Absorbance at THz wavelength (0.775 THz)	0.1%
Stability of THz source	0.5%
Humidity and temperature	0.5%
Combined uncertainty	1.13% (k=1)

6. CONCLUSION

We introduce a high-absorbance coating with a broad bandwidth in the terahertz frequency range for THz radiometry. A THz radiometer is fabricated with this coating and its power responsivity is traceable to Chinese National Laser Prime Standard. This coating and the radiometer provide a probability of absolute measurement and traceability to SI of terahertz radiations.

REFERENCES

1. L. Werner, H-W Hübers, P. Meindl, R. Müller, H. Richter, and A. Steiger, “Towards traceable radiometry in the terahertz region,” **Metrologia 46**, S160–S164, 2009.

2. J. H. Lehman, B. Lee, and E. N. Grossman, “Far infrared thermal detectors for laser radiometry using a carbon nanotube array,” Appl. Opt. **50**, 4099-4104, 2011.
3. Y. Deng, Q. Sun, J. Yu, Y. Lin, and J. Wang, “Broadband high-absorbance coating for terahertz radiometry,” Optics Express **21**(5), 5737-5742, 2013.
4. M. López, H. Hofer, and S. Kück, “Measurement of the absorptance of a cryogenic radiometer cavity in the visible and near infrared,” Metrologia **42**, 400-405, 2005.

Non-linearity of silicon photodiodes with a dependence on wavelength and incidence geometry

Dong-Joo Shin, Seongchong Park, Ki-Lyong Jeong, Seung-Nam Park, and Dong-Hoon Lee

Division of Physical Metrology, Korea Research Institute of Standards and Science (KRISS), Daejeon, Korea
Corresponding e-mail address: djshin@kriss.re.kr

We report the non-linearity measurement of Si photodiodes at different wavelengths and incidence geometries by using a high-accuracy flux addition instrument based on LEDs. The tested Si photodiode (S1337-1010BQ) shows a supralinearity of up to 0.2 % at a photocurrent level of 10^{-4} A at a wavelength of 750 nm, while this is not observed at 390 nm. At the same output photocurrent, we observed that the supralinearity becomes larger as the active area becomes smaller or as the field of view of the incidence beam becomes smaller. The observed behaviour can be explained based on minority charge carriers generated behind the pn-junction.

INTRODUCTION

Spectral responsivity of optical detectors is a key measurand for the detector-based realization of the photometric and radiometric scales. Especially, the Si photodiode is widely used in realizing, disseminating, and comparing the spectral responsivity scale at many national metrology institutes [1]. For accurate measurement of spectral responsivity, the non-linearity of responsivity, i.e. the dependence of responsivity on the input flux level, should be tested at various conditions.

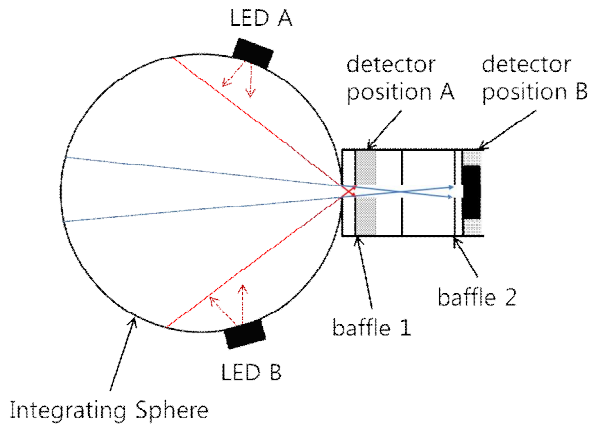

Figure 1. Schematic diagram of the linearity measurement setup.

Recently, we have developed a high-accuracy linearity tester based on flux addition of LEDs in an integrating sphere [2]. With this instrument, the correction factor of spectral responsivity can be measured with an uncertainty as low as 2×10^{-5} ($k = 1$) for photocurrent ranges from 10^{-8} A to 10^{-3} A at different wavelengths. We also reported that the Si photodiode of type S1337-1010BQ (Hamamatsu, Japan) show a wavelength-dependent supralinearity when measured at a field of view (FOV) of almost 180° at the wall of the integrating sphere [2].

In this work, we report the measurement results of the nonlinearity of the Si photodiodes of type S1337-1010BQ at different geometric conditions. The instrument is modified so that the test detector is measured at two different FOV conditions. Moreover, the active area of the test detectors is varied by using various apertures in front of the detectors. Such a variation of the incidence geometry can provide valuable information not only to estimate the related error and uncertainty of spectral responsivity but also to explain the origin of the observed supralinearity.

EXPERIMENTAL SETUP

Figure 1 schematically shows the experimental setup of the linearity tester with variable incidence geometry. The main modification from the setup described in Ref. [2] is the cylindrical detector mount with two baffles attached at the detector port. The distance between the two baffles is 40 mm, and the diameters of the baffles are selected to be slightly larger than that of the active area of the test detector. The active area of the test detector is varied by attaching an aperture with different diameter of 3 mm, 5 mm, and 8 mm on the rectangular photodiode with a dimension of 10 mm × 10 mm.

When the test detector is placed at the position A in Fig. 1, its FOV is approximately 90° regardless of the aperture size. At the position B, the FOV are calculated to be 5.7°, 8.6°, and 14.3° for the aperture diameter of 3 mm, 5 mm, and 8 mm, respectively. For simplicity, we refer here the detector position A and position B as “large FOV” and “small FOV,” respectively.

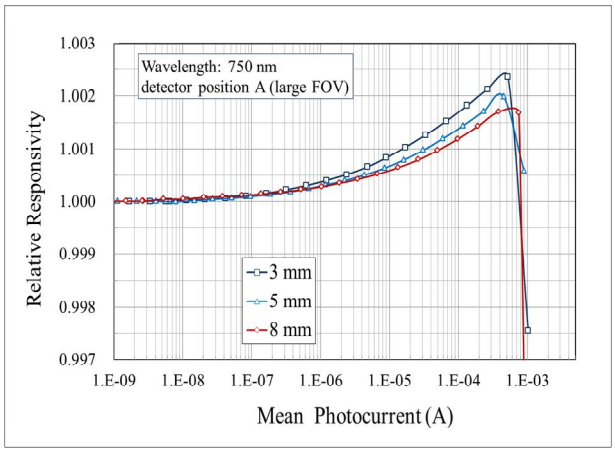

Figure 2. Nonlinearity correction factors measured by using LEDs at 750 nm for the large FOV condition and different diameters of active areas.

The measurement and calculation procedures of the nonlinearity correction factor, i.e. the relative change of responsivity, as a function of the mean output photocurrent is described in details in Ref. [2].

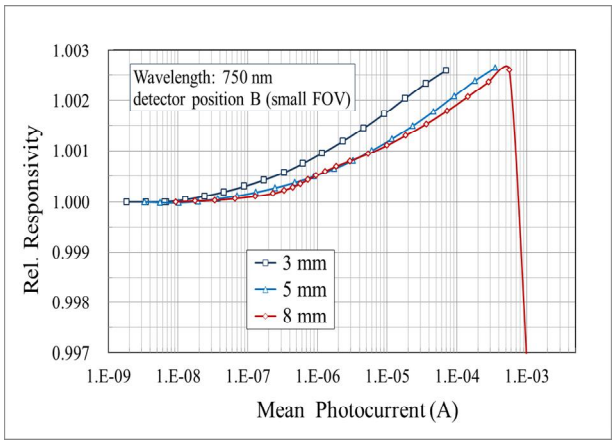

Figure 3. Nonlinearity correction factors measured by using LEDs at 750 nm for the small FOV condition and different diameters of active areas.

EXPERIMENTAL RESULTS

The results of the nonlinearity correction factors as a function of output photocurrent measured by using LEDs emitting at 790 nm are shown in Fig. 2 and Fig. 3 for the large FOV and small FOV conditions, respectively. The supralinearity of up to 0.2 % is clearly observed in both the cases at a photocurrent level of 10^{-4} A. At a fixed value of photocurrent, the supralinearity becomes larger as the active area decreases. Moreover, the supralinearity is stronger in the small FOV than in the large FOV condition. Uncertainty of the nonlinearity correction factor is evaluated to be in the order of 10^{-5} as a relative standard uncertainty (k = 1).

Figure 4 shows the results measured by using LEDs emitting at 390 nm. In contrast to the results at 790 nm, the supralinearity is almost disappeared as the wavelength changes from infrared to ultraviolet. This confirms our previous report on the wavelength dependence in Ref. [2].

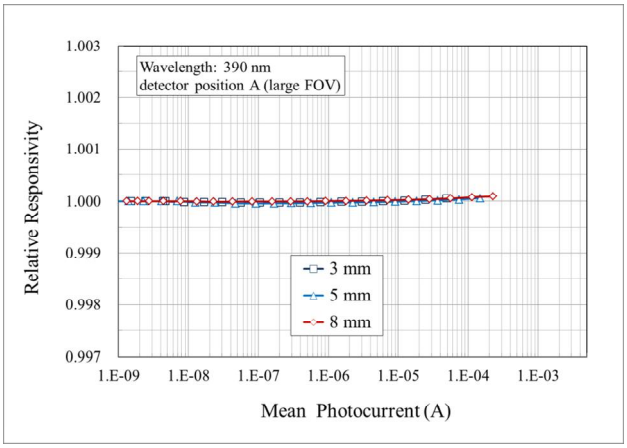

Figure 4. Nonlinearity correction factors measured by using LEDs at 390 nm for the large FOV condition and different diameters of active areas.

DISCUSSION

The supralinearity of Si photodiodes in the long-wavelength range is reported and discussed in Ref. [3-4]. As the mechanism of this, the generation of the minority charge carries in the bulk region beyond the pn-junction and their dynamic contribution to the photocurrent are modelled [3]. The strong supralinearity in the infrared is explained by the decreasing absorption in the pn-junction and the related increasing penetration into the bulk region as the wavelength increases beyond the red region.

Our observation of the dependence on the incidence geometry in this work qualitatively confirms this model. The absorption in the pn-junction becomes weaker as the incidence angle approaches to normal or the active area becomes smaller, which means that the penetration beyond the pn-junction increases as the FOV or the beam size becomes smaller at the same photocurrent.

Finally, we note that the nonlinearity of 0.2 % is of significant magnitude when the photodiode should be used as a transfer standard for the spectral responsivity scale [1].

REFERENCES

1. R. Goebel and M. Stock, Report on the comparison CCPR-K2.b of spectral responsivity measurements in

the range 300 nm to 1000 nm, Metrologia, 41, 02004 (2004).
2. D. J. Shin *et al*, High-accuracy measurement of linearity of optical detectors based on flux addition of LEDs in an integrating sphere, Metrologia 51, 25 (2014).
3. A. R. Schaefer *et al*., Silicon detector nonlinearity and related effects, Applied Optics, 22, 1232 (1983).
4. K. D. Stock, Si-photodiode spectral nonlinearity in the infrared, Applied Optics, 25, 830 (1986).

Determining the uncertainty associated with an integrated quantity calculated from partially correlated spectral data

Emma R Woolliams

[1]*National Physical Laboratory, Teddington, United Kingdom*
Corresponding e-mail address: emma.woolliams@npl.co.uk

Photometric, colorimetric and other similar quantities can be determined from spectrally-evaluated radiometric quantities by integration. This paper describes the uncertainty associated with a calculated value of an integral due to random and systematic experimental effects. It builds an error model and shows how to apply this, both with the 'normal' law of propagation of uncertainties and using a covariance matrix.

INTRODUCTION

It is increasingly common to make spectral measurements using, for example, an array spectrometer, and then calculate other quantities through integration. For example, illuminance will be determined from spectral irradiance. The integral itself is usually straightforwardly calculated with a trapezium rule. The challenge is determining the associated uncertainty. This paper reviews numerical approaches to determine a value for the integral and its associated uncertainty. The methods presented are an application of the GUM [1] and have previously been developed by Gardner [2]. The ideas are more fully developed in [3] and [4].

The determination of a photometric quantity from the analogous spectroradiometric quantity involves integration of the product of an *experimentally determined* spectral quantity, which has an associated uncertainty at each wavelength, and a *defined* spectral quantity, with no associated uncertainty. We shall call these 'defined-product integrals', I_{dp}, which take the form

$$I_{\mathrm{dp}} = \int E(\lambda)V(\lambda)\mathrm{d}\lambda, \qquad (1)$$

where $E(\lambda)$ represents the experimentally determined quantity (e.g. irradiance) and $V(\lambda)$ the defined quantity. Although the $V(\lambda)$ function is used here, the same analysis approach applies equally to other quantities calculated using defined functions.

NUMERICAL INTEGRATION

The standard method for evaluating integrals in this field is to use the trapezium rule. This treats the integrand as varying linearly between adjacent measurement points. Thus, the integral in (1) becomes

$$\hat{I}_{\mathrm{dp}} = \sum_{i=1}^{i=n} c_i E(\lambda_i)V(\lambda_i), \qquad (2)$$

where $\lambda_1,\ldots,\lambda_n$ are the ordered wavelength values at which E is measured or $V(\lambda)$ is defined and is related to the wavelength step. If the data are evenly spaced, such that $\lambda_{i+1}-\lambda_i = \delta\lambda$ for all wavelength steps, then, for the trapezium rule

$$c_i = \begin{cases} \delta\lambda/2 & i = 1, n \\ \delta\lambda & i = 2,\ldots,n-1. \end{cases} \qquad (3)$$

There are some occasions when the trapezium rule is insufficient, in those cases, see [5].

RANDOM AND SYSTEMATIC EFFECTS

When an integral is calculated from the spectral data, it is necessary to go beyond a wavelength-by-wavelength uncertainty analysis and determine the covariance associated with measured values at different wavelengths. Such correlations are introduced whenever there is something in common between the measured values at one wavelength and those at a different wavelength.

One of the simplest ways to deal with correlation is to create an *error model* that explicitly distinguishes systematic and random effects. Consider Eq. (2). The only terms with associated uncertainties are the $E(\lambda_i)$. With random and systematic effects separated, we can write an error model where the measured irradiance $E(\lambda)$ at wavelength λ_i is defined in terms of the true irradiance $E_{\mathrm{T}}(\lambda_i)$, a systematic error S (which is the same at all wavelengths) and random errors R_i (which change from wavelength to wavelength)

$$E(\lambda_i) = E_{\mathrm{T}}(\lambda_i)(1+S)(1+R_i). \qquad (4)$$

S has an expected value of zero, assuming a correction has been made if necessary, and an uncertainty equal to the relative uncertainty associated with systematic effects, and the R_i all have an expected value of zero and uncertainties equal to the relative uncertainty associated with

random effects for the *i*th measured value. (Note the distinction between the *errors* S and R_i and the *uncertainties* associated with them). If we insert (4) into (2) we obtain

$$\hat{I}_{\mathrm{dp}} = (1+S)\sum_{i=1}^{i=n} c_i E_{\mathrm{T}}(\lambda_i) V(\lambda_i)(1+R_i). \qquad (5)$$

Applying the law of propagation of uncertainty [1], the relative standard uncertainty $u(\hat{I}_{\mathrm{dp}})/\hat{I}_{\mathrm{dp}}$ associated with the calculated value of the integral is given by

$$\left[\frac{u(\hat{I}_{\mathrm{dp}})}{\hat{I}_{\mathrm{dp}}}\right]^2 = u^2(S) + \frac{1}{\hat{I}_{\mathrm{dp}}^2}\sum_{i=1}^{i=n}\left[c_i E(\lambda_i) V(\lambda_i) u(R_i)\right]^2. \qquad (6)$$

The first term is the relative variance associated with systematic effects, which are unchanged by the integration. The second term is the sum of the squares of the absolute standard uncertainties associated with random effects, divided by the square of the calculated value of the integral. Thus the relative standard uncertainties associated with random effects are scaled in proportion to the fractions of the calculated value of the integral and then added in quadrature across all wavelengths.

To apply this method of analysis, the uncertainty budget must be separated into random and systematic effects. All uncertainties associated with random effects are added in quadrature and then separately all uncertainties associated with systematic effects are added in quadrature. With a single 'systematic' and 'random' effect uncertainty, Equation (6) can be used directly to determine the relative standard uncertainty associated with the integral.

The error model can also be extended to account, for example for wavelength effects, or for systematic effects with a different sensitivity coefficient at different wavelengths. This is discussed further in [3].

COVARIANCE MATRICES

The error model can also be used to create a covariance matrix. For data that will subsequently be integrated spectrally, the covariance matrix we need to develop is that showing the covariance associated with, e.g. spectral irradiance values determined at different wavelengths. Each row of the covariance matrix represents a different measurement wavelength. The diagonal terms give the variance $u^2(E_i)$ and the off-diagonals the covariance $u(E_i, E_j)$ between the irradiance at the row wavelength and the irradiance at the column wavelength. For the error model in (4), the variances (diagonal terms) are given by

$$u^2(E(\lambda_i)) = \left[u^2(S) + u^2(R_i)\right] \times E^2(\lambda_i). \qquad (7)$$

The off-diagonal terms, written $u(E_i, E_j)$, give the covariance between the spectral irradiance value determined at λ_i and that determined at λ_j. This covariance will arise only from those effects that are common to both measured values: the systematic effects. Thus for the error model in (4), only the term $u(S)$ is included. The off-diagonal covariance values for this error model are

$$u(E(\lambda_i), E(\lambda_j)) = u^2(S) \times E(\lambda_i) \times E(\lambda_j). \qquad (8)$$

The uncertainty associated with the defined-product integral calculated in (2), is calculated as

$$u^2(I_{\mathrm{dp}}) = \boldsymbol{c}^{\cdot}\left(\boldsymbol{V}\boldsymbol{U}_E\boldsymbol{V}^{\cdot}\right)\boldsymbol{c} \qquad (9)$$

where $\boldsymbol{V}$ is a vector containing the $V(\lambda)$ values at the different wavelengths, $\boldsymbol{U}_E$ is the covariance matrix for the irradiance values and $\boldsymbol{c}$ is a vector containing the values of Eq. (3).

CONCLUSIONS

This short abstract has introduced some of the main ideas behind uncertainty analysis for integrated quantities. It is important to distinguish between uncertainties associated with random effects and those associated with systematic effects. If that distinction is properly made, then 'the rest is just algebra'.

REFERENCES

1. JCGM, JCGM 100:2008 Evaluation of measurement data – Guide to the expression of uncertainty in measurement, Report, 2008.
2. J. L. Gardner, Uncertainties in source distribution temperature and correlated colour temperature, Metrologia, 43, 403-408, 2006.
3. E. R. Woolliams, Determining the uncertainty associated with integrals of spectral quantities, Report: EMRP-ENG05-1.3.1, http://tinyurl.com/NPLIntegrals, 2013.
4. E. R. Woolliams, Uncertainty analysis for filter radiometry based on the uncertainty associated with integrated quantities, submitted to International Journal of Thermophysics, 2014.
5. M. G. Cox, The area under a curve specified by measured values, Metrologia, 44, 365-378, 2007.

Predicting wavelength dependent responsivity-drift in silicon

Ian Littler, Errol Atkinson, and Peter Manson

National Measurement Institute, Sydney, Australia
Corresponding e-mail address: ian.littler@measurement.gov.au

The shape of the relative spectral responsivity of silicon photo-detectors has long been known to change with time, independent of many externalities. Maintaining the calibration of such photo-detectors to within measurement uncertainty across the whole spectrum would require frequent re-measurement. To investigate the required re-calibration frequency, a drift-model has been developed which allows the wavelength dependent responsivity to be predicted into the future many years after spectral calibration.

INTRODUCTION

The advent of cryogenic radiometry allowed the accurate measurement of absolute responsivities at selected wavelengths over time. In 2005 Nield *et al.* [1] published responsivity drift rates across two institutes using different types of detectors, showing that the drift was essentially independent of type and environment, but did vary with wavelength. Indeed, the average drift-rate was −0.03 % p.a. at 476 nm and up to −0.3 % at 351 nm. Yet one critical aspect shown was that the drift-rate decreased markedly with increasing wavelength, becoming essentially zero at the red end of the spectrum.

Given these demonstrated drift rates in the blue and near UV, a model was developed to predict the future value of responsivity for any silicon photo-diode, whilst increasing the uncertainty appropriately.

METHODOLOGY

Since cryogenic radiometry only yields drift rates at discrete wavelengths, to provide more wavelength data for the model the relative spectral responsivity was used from an ensemble of detectors constructed using Hamamatsu S1337 photo-diodes. This data was collected over a period of 17 years using reference bolometers which have been shown to be spectrally stable [2]. The drift in absolute responsivity as a function of wavelength is ascertained by normalising the relative responsivity to its value in the red part of the spectrum, where absolute drift data confirms that the responsivity is constant with time, then differencing responsivity spectra from different times.

In Fig. 1, the average value of the wavelength dependent responsivity is shown for an ensemble of 4 detectors (3 difference spectra from different time periods for each). The wavelength dependent standard deviation is also given.

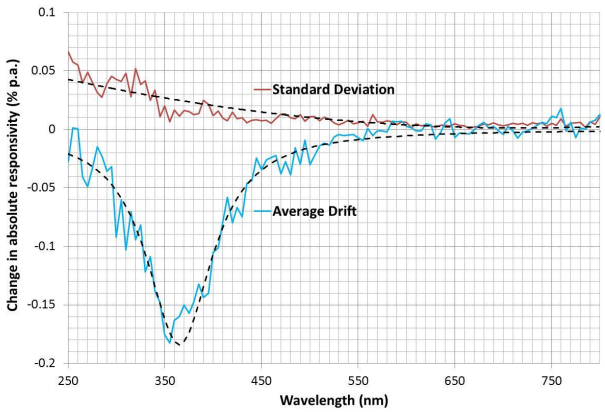

Figure 1. Spectrally resolved drift-rate for the ensemble, together with the standard deviation of the values.

Remarkably, the shape of this drift-rate was essentially the same across all detectors considered. Limited data available for other types of detectors was consistent with this conclusion. The standard deviation of the data is also less than the drift rate, meaning that these rates could be used to predict future responsivities without overly increasing the combined uncertainty over the first few years.

To assist in making future predictions, an analytic inverted Lorentzian curve (eq. 1) was found to fit the data well, where λ is in units of nm.

$$Drift(\lambda_{nm}) = \frac{-0.184}{1+\frac{(\lambda_{nm}-365)^2}{1691}}\% \qquad (1)$$

The wavelength dependent standard deviation of the drift-rate $\sigma(\lambda)$ can be well approximated by a simple 2nd order polynomial (eq. 2), where λ is in units of nm. For wavelengths longer than the turning point at 716.9 nm, the very small constant minimum value is used.

$$\sigma(\lambda_{nm}) = 1.89\times10^{-7}\,\lambda_{nm}{}^{2} - 2.71\times10^{-4}\,\lambda_{nm} + 0.0987\%;\ \lambda_{nm} < 716.9 \text{ nm}$$

$$\sigma(\lambda_{nm}) = 0.00156\%;\ \lambda_{nm} > 716.9 \text{ nm} \quad (2)$$

The model has been built using just 4 photo-diodes, with an assumed function fitted. The assigned value for the degrees of freedom is 3. As the drift component will often be of the same order as the measurement uncertainty, this does not overly increase the combined coverage factor.

COMPARISON WITH NIELD *ET AL.* DATA

The current model predicts a drift rate of (−0.022 ± 0.040) % p.a. with k = 3.18 at 476 nm. This is in agreement with the Nield *et al.* value of (−0.03 ± 0.01) % p.a. at 476 nm. At 351 nm, the model predicts a peak drift of (−0.18 ± 0.09) % p.a. with k = 3.18. This is consistent with the Nield *et al.* value of −0.3 % p.a.

APPLYING THE MODEL

How far into the future can the model be used before the predictive uncertainty becomes too large? As an example, table 1 shows the typical absolute responsivity measurement uncertainties at wavelengths used at NMIA, together with the additional uncertainty introduced by the predictive model each year. The final column shows the time period over which the additional uncertainty from the prediction would lead to an increase in the combined uncertainty of a factor of √2.

Table 1. Additional uncertainty contribution.

λ (nm)	Measure-ment U95% (%)	Prediction contribution U_i p.a. (%)	√2 increased uncertainty (years)
375.650	0.11	0.024	2.3
476.486	0.05	0.012	2.0
487.986	0.05	0.011	2.2
496.508	0.05	0.011	2.3
514.531	0.05	0.009	2.7
632.817	0.05	0.0029	8.6
656.143	0.05	0.0023	11
807.655	0.05	0.0016	16
912.430	0.05	0.0016	16

PREDICTIVE POWER DEMONSTRATED USING HISTORICAL DATA

Whilst in the future, the predictive power of the model will be checked by comparison with the cryogenic radiometer, some historical absolute responsivity data exists. This absolute data may be used to cross-check the efficacy of the model, which has been derived using relative spectral data and a knowledge that drift rates are negligible in the red part of the spectrum. In Fig. 2a and 2b, the measured absolute responsivity of a single element S1337 photo-diode is given at two wavelengths in 1994 and again in 2010 (and 2012), together with the predicted value and the expanded uncertainty. The predicted value is in excellent agreement with the actual measured absolute responsivity 16 years later. The same is found for the other photo-detectors in the ensemble.

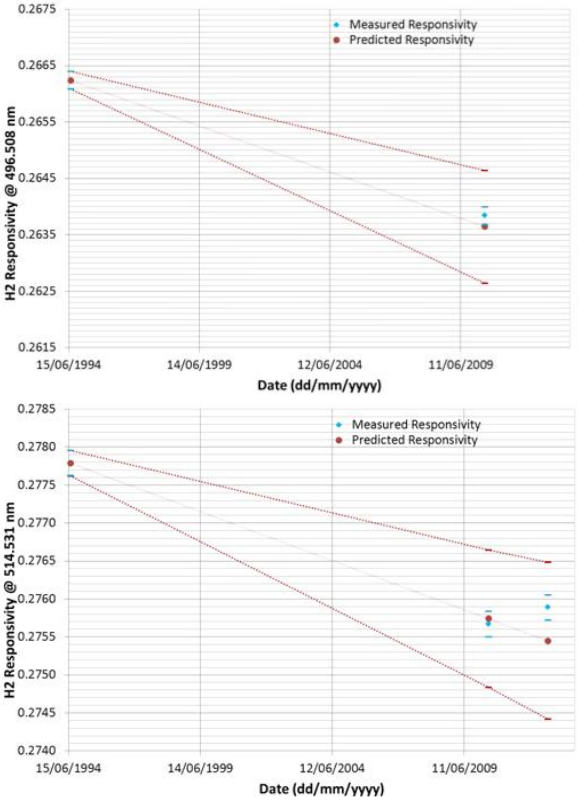

Figure 2a & 2b. At 497 nm & 515 nm, the predicted values and actual measured values at the

CONCLUSION

A simple model has been introduced which predicts responsivity drift in silicon at an arbitrary wavelength. This allows the frequency of spectral recalibrations to be decreased, especially in the blue to ultra-violet.

REFERENCES

1. Nield, K. M., Lukins, P. B., Bittar, A., Hamlin, J. D., 2005, Drift in the absolute responsivities of solid-state

photodetectors at two NMIs, NEWRAD ’05, Davos, Switzerland.
2. Atkinson E. G., Littler I. C. M., 2011, Long-term Stability of Gold Black Bolometers, NEWRAD ’11 Hawaii, USA.

ACKNOWLEDGEMENT

The early measurements of Frank Wilkinson, Duncan Butler and Jim Gardner are gratefully acknowledged.

Aperture area measurement by laser occlusion: 3-way comparison with contact-probe and relative flux methods

Ian Littler, Errol Atkinson, Erik Thorvaldson, Peter Manson, Andrew Baker, Peter Cox, and Mark Ballico

National Measurement Institute, Sydney, Australia
Corresponding e-mail address: ian.littler@measurement.gov.au

Aperture area measurement is central to the realisation of radiometric units and thermodynamic temperature. NMIA's new non-contact area measurement system uses occlusion of a laser beam. It is fast (~40 minutes) and has a typical uncertainty of 0.034% for a 6 mm diameter aperture. To validate the system, measurements of a number of apertures were compared with those made with a contact-probe and also with relative light flux measurements. The agreement is excellent across all three methods.

THE LASER OCCLUSION INSTRUMENT

The experimental set-up is shown in Fig. 1. A laser beam λ=405 nm is focussed to a tight waist ~2 μm full width half maximum (FWHM). The aperture is mounted on a calibrated X-Y stage which allows the edge of the aperture to be traversed radially through the laser beam. Photo-diodes detect the transmitted, reflected and edge-scattered light, but the edge position along the circumference is determined using the transmitted light whilst the other detectors serve as monitors [1].

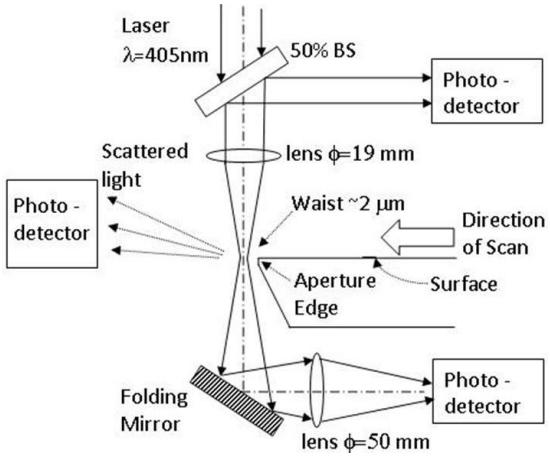

Figure 1. Set-up for area measurement by laser beam occlusion.

In Fig. 2, the signal is shown as the X-Y stage steps the edge across the laser beam. The curve is differentiated since a Gaussian may be more easily fitted than the raw spatially integrated laser beam signal.

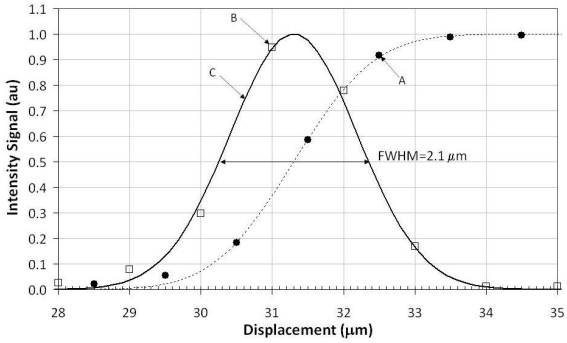

Figure 2. Laser signal (solid circles) with its derivative (open squares) and fitted Gaussian (solid curve).

WHY TRANSMISSION?

The photo in Fig. 3 shows an electron micro-graph of a portion of the edge of a typical aperture. Rather than being a step function, the edge transitions irregularly from the land of the disc to the open aperture over ~8 μm. If the reflected signal were to be used to determine the geometric edge of the aperture, a large error would result because the reflected signal would be scattered from the irregularities near the edge before the actual edge were reached.

Scatter (laser speckle) from the imperfect disc surface would also lead to a lower signal to noise ratio than may be achieved with a transmitted signal.

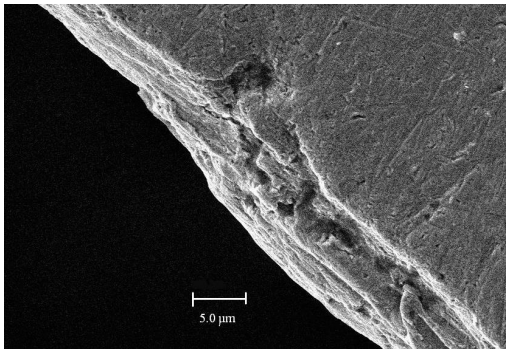

Figure 3. Electron micrograph of a typical NMIA 10 μm aperture edge.

UNCERTAINTY ANALYSIS

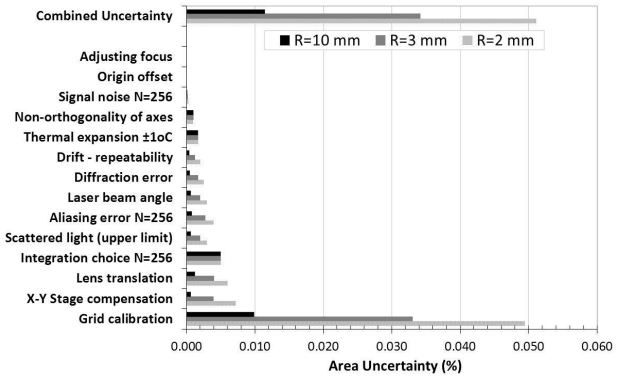

Figure 4. Relative uncertainty contributions for aperture radius R= 2 mm, 3 mm and 10 mm.

Fourteen contributions to the uncertainty were identified and analysed, including: X-Y stage calibration, edge diffraction, sample aliasing, integration choice, drift, thermal expansion, axes non-orthogonality and laser beam related terms. The relative size of each contribution is found in Fig. 4.

In Fig. 5, the stage is moved to 36 random positions, on a 24 mm × 24 mm grid from random directions. With the error enlarged by 500× for clarity, the solid circles show the target positions and the open squares show the actual positions reached relative to a reference line grid. The standard deviation is 180 nm. The dominant term is not the error in the commanded position but rather the X-Y reference line grid calibration. There is scope for improving that accuracy by 70%.

Diffraction, whilst introducing a small shift in the edge position, is small as long as the capture angle is large enough. For a diffracted light capture angle of 32°, the apparent shift is 0.05 µm. For a 6 mm diameter aperture this is an error of 0.0033%.

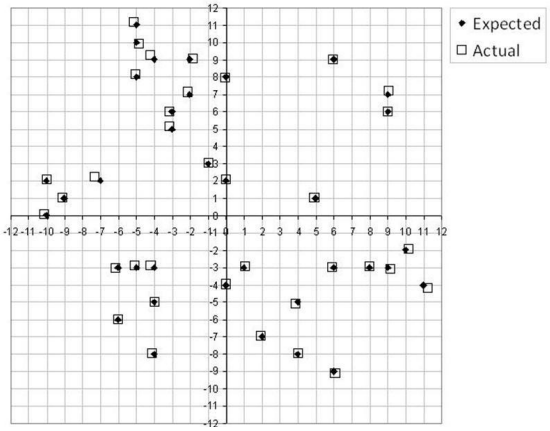

Figure 5. Testing the X-Y stage compensation on a 24 mm × 24 mm grid. For the error; 1 mm = 2 µm.

A simple relationship has been found between area error and the number of circumferential samples, thus allowing prediction of the area uncertainty due to aliasing for a given aperture material and number of sample points. Here, 256 points are sufficient.

Axes non-orthogonality is found to be a cosine error and is therefore negligible. A misalignment of as much as 7 mrad leads to only 0.005% area error.

VALIDATION: COMPARISON WITH OTHER AREA MEASUREMENT METHODS

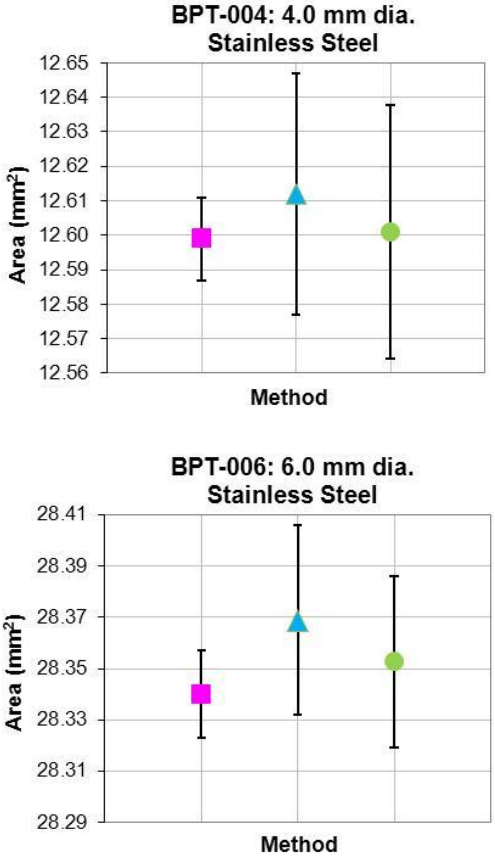

Figure 6. Area measurement; R=2 mm & 3 mm.
■ Non-contact laser occlusion, ▲ Contact probe,
● Relative flux; with 95% confidence intervals.

The area of a number of apertures has also been measured using both a contact probe method and relative light-flux methods (see Fig. 6 for two stainless steel aperture examples). In the contact probe method, the diameter was measured using a contact probe and interferometer (Renishaw ML10) which was then combined with a surface contact radial profile to compute the area. For the relative flux measurement, the light flux through the apertures

was measured in a uniform light field generated by a 2 m integration sphere. A 25 mm diameter aperture served as the absolute reference. The agreement is excellent amongst the three methods.

REFERENCES

1. C. M. Littler, E. G. Atkinson and P. J. Manson, “Non-contact aperture area measurement by occlusion of a laser beam,” Metrologia 50, 596-611 (2013).

The NEWSTAR project: NEW primary STAndards and traceability for Radiometry

M. L. Rastello[1], J. Gran[2], I. Müller[3], M. Smid[4], G. Brida[1], T. Dönsberg[5,6], M. Tamre[7], E. Monakhov[8], and M. Juntunen[6]

[1] *Istituto Nazionale di Ricerca Metrologica (INRIM), Torino, Italy*
[2] *JV, Justervesenet, Kjeller, Norway*
[3] *Physikalisch-Technische Bundesanstalt (PTB), Berlin, Germany*
[4] *Cesky Metrologicky Institut (CMI), Praha, Czech Republic*
[5] *Centre for Metrology and Accreditation (MIKES), Espoo, Finland*
[6] *Aalto University, Espoo, Finland*
[7] *TUT, Tallinn University of Technology, Tallinn, Estonia*
[8] *UiO, University of Oslo, Norway*
Corresponding e-mail address: m.rastello@inrim.it

In this presentation the framework of the new EURAMET joint research project "New primary standards and traceability for radiometry" will be described with an outlook towards the expected results and its potential impact on the end-users.

INTRODUCTION

The EURAMET joint research project "NEW primary STAndards and traceability for Radiometry" (NEWSTAR) [1] both complements and builds on some excellent results of the recent iMERA-Plus Joint Research Project T1.J2.3 qu-Candela "Candela: Towards quantum based photon standards"[2], where the feasibility of a new radiometric standard based on photoelectric effect in Silicon semiconductor, working at liquid nitrogen temperature, called Predictable Quantum Efficient Detector (PQED) [3,4,5] has been demonstrated. The responsivity of the PQED was predicted on the basis of fundamental constants and material parameters. [4,6]

At liquid nitrogen temperature, 77 K, the standard uncertainty of the predicted responsivity of the PQED was shown to be less than 10 ppm [4,6]. This uncertainty of spectral responsivity is by a factor of 5 smaller than obtained earlier with any other method. The outstanding performance of the PQED at 77 K offers the opportunity to push fundamental physics. Comparing results obtained by high accuracy standards based, from one side, on thermodynamics (i.e. cryogenic radiometers) and electromagnetisms (PQED) on the other will play a significant role in searching for consistency between the two fields. Fundamental limitations can be tackled by basic research on the interaction between light and matter, on novel materials, and on new structures with revolutionary photonic properties. This requires work in materials science, quantum optics, thermodynamics and solid-state physics.

Experimental tests also indicated that, at room temperature, the external quantum efficiency agreed with the predicted value within an uncertainty of 100 ppm over the visible wavelength range. This result has been obtained by measuring the responsivity of the PQED with the aid of the best presently available optical power standard, i.e., the absolute cryogenic radiometer [5]. The operation of the cryogenic radiometer at 4 K temperature is considerably more complicated than the operation of the equally accurate PQED operating at room temperature. This outcome set a favorable starting point to develop new applications and improved traceability based on the PQED at room temperature.

PROJECT OUTLINE

The main goal of the project is an improved silicon detector primary standard for radiometry having approximately the same cost and functionality as present transfer standard detectors enabling the primary standard to be built into different applications taking full advantage of properties of Predictable Quantum Efficient Detectors (PQEDs) developed in an earlier EMRP project (Fig. 1)

The first work-package of the project will develop primary standards for absolute radiometry at 1 ppm uncertainty in the visible wavelength range by realising a cryogenic temperature (CT) PQED, while at room temperature (RT) the PQED responsivity will be calculated within 100 ppm uncertainty. This will be achieved through thorough characterisations,

advanced modelling and an improved PQED layout, described in [7].

The second work-package will validate the claimed ultra-low uncertainty of CT-PQEDs by best possible measurements (10 ppm nominally) with the improved existing primary standard, the cryogenic radiometer based on the electrical substitution principle, and by direct comparison of several PQEDs. The direct comparison is sensitive at the ppm level to deviations of the PQEDs with each other [8]. Eventually, a radiometric measurement of the ratio of the fundamental constants e and h (e/h) will be obtained.

The third work-package will implement RT-PQEDs for applications at 100 ppm uncertainty as spectral responsivity standards. Positive outcome will lead to the realization of a primary standard for radiometry operating at room temperature and having approximately the same cost and functionality as present transfer standard detectors.

The applicability of RT-PQEDs as primary radiometric standard for the determination of the luminous responsivity of a reference photometer, as a primary radiometric standard for the direct, one-step determination of the spectral irradiance responsivity of filter radiometers, and, as a primary radiometric standard for fibre optic power meter, for 850 nm wavelength, will be investigated in the fourth work-package.

Finally, the suitability of RT-PQEDs as travelling artefacts for comparisons, in terms of robustness and stability over time will be verified in work-package 5. Direct comparison of these RT-PQEDs has shown that their responsivities are consistent within 13 ppm peak-to-peak [9].

SUMMARY

The outline and the preliminary results obtained within this joint research project will be presented as well as an outlook for the expected results and the potential impact on the end-users.

ACKNOWLEDGEMENT

This work is funded by the project NEWSTAR (contract SIB57) of the European Metrology Research Programme (EMRP). The EMRP is jointly funded by the EMRP participating countries within EURAMET and the European Union.

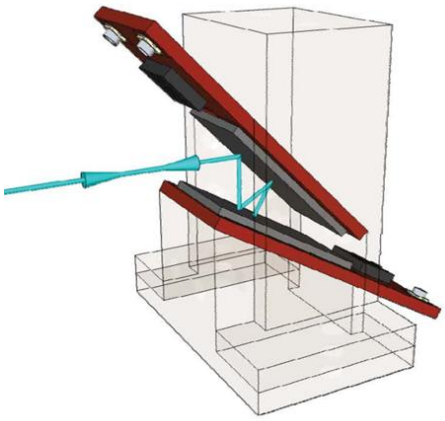

Figure 1. PQED layout with seven internal reflections.

REFERENCES

1. http://www.inrim.it/Newstar
2. http://www.quantumcandela.org/
3. M. Sildoja, F. Manoocheri, and E. Ikonen, Reflectance Calculations for a Predictable Quantum Efficient Detector, Metrologia 46, S151-S154 (2009).
4. M. Sildoja, F. Manoocheri, M. Merimaa, E. Ikonen, I. Müller, L. Werner, J. Gran, T. Kübarsepp, M. Smîd and M. L. Rastello, Predictable quantum efficient detector: I. Photodiodes and predicted responsivity Metrologia 50, 385 (2013).
5. I. Müller, U. Johannsen, U. Linke, L. Socaciu-Siebert, M. Smîd, G. Porrovecchio, M. Sildoja, F. Manoocheri, E. Ikonen, J. Gran, T. Kübarsepp, G. Brida and L. Werner, Predictable quantum efficient detector: II. Characterization and confirmed responsivity Metrologia 50, 395 (2013).
6. J. Gran, T. Kübarsepp, M. Sildoja, F. Manoocheri, E. Ikonen and I. Müller Simulations of a predictable quantum efficient detector with PC1D Metrologia 49, S130 (2012).
7. M. Sildoja, T. Dönsberg, H. Mäntynen, M. Merimaa, F. Manoocheri and E. Ikonen, Use of the predictable quantum efficient detector with light sources of uncontrolled state of polarization Meas. Sci. Technol. 25, 015203 (2014).
8. I. Müller, C.K. Tang, J. Gran, and L. Werner, Experimental validation of the predictability of a Predictable Quantum Efficient Detector by a direct intercomparison, these proceedings.
9. T. Dönsberg, M. Sildoja, F. Manoocheri, M. Merimaa, and E. Ikonen, A compact primary standard of optical power operated at room temperature, these proceedings.

A compact primary standard of optical power operated at room temperature

Timo Dönsberg[1,2], Farshid Manoocheri[1,2], Meelis Sildoja[1], Mikko Merimaa[2], and Erkki Ikonen[1,2]

[1]*Metrology Research Institute, Aalto University, Espoo, Finland,*
[2]*Centre for Metrology and Accreditation (MIKES), Espoo, Finland*
Corresponding e-mail address: farshid.manoocheri@aalto.fi

We present the design and characterization of a new room temperature Predictable Quantum Efficient Detector (PQED). The compact detector consists of two induced junction photodiodes mounted in a trap configuration. Measurements of individual detectors at the wavelength of 488 nm indicate that the spectral responsivity is consistent within 13 ppm peak-to-peak variation and agrees with the predicted value. The internal quantum efficiency of the photodiodes is shown to be spatially uniform within 50 ppm. These results together with the predictable responsivity indicate that the room temperature PQED can potentially be used as a primary standard of optical power in the visible wavelength range.

INTRODUCTION

The Predictable Quantum Efficient Detector (PQED) [1,2] consists of two custom-made induced junction silicon photodiodes mounted in a wedged trap configuration. At room temperature, the spectral responsivity of the PQED can be predicted with a relative standard uncertainty of around 70 ppm in the visible wavelength range [3] and comparisons with cryogenic radiometers confirm the predicted responsivity [2]. As the uncertainty of the room temperature PQED is comparable with that of the cryogenic radiometer, the PQED is a promising candidate to be used as a primary standard of optical power in the visible wavelength range.

Requirements for a primary standard detector, such as predictable and spatially uniform responsivity, and congruent responsivity and reflectance between individual detectors are validated in this research.

DESIGN OF THE DETECTOR

The detector contains similar induced junction photodiodes as described and characterized in [1] and [2]. In these photodiodes the pn-junction is produced by light p-type doping of the substrate and by the positive surface charge in the SiO_2 layer covering the substrate. The photodiodes are mounted in a wedged light-trapping configuration where seven reflections of the incident beam take place and a fraction of around tens of ppm is then reflected back.

The photodiodes are encased in a cylindrical body that has a maximum aperture of 10 mm in diameter. The air-tight assembly, shown in Figure 1, has a length of 215 mm and an outer diameter of 75 mm. The window in front of the detector is aligned in Brewster angle for high transmission of *p* polarized light. The design is such that the plane of incidence is the same for the Brewster window and the photodiodes.

Unlike cryogenic detectors, the room temperature PQED can also be operated without the window in front of the photodiodes. This eliminates the need for window transmittance correction, which is a major contribution to the uncertainty. We have developed a nitrogen flow system which protects the photodiodes from contamination when the window is removed [4].

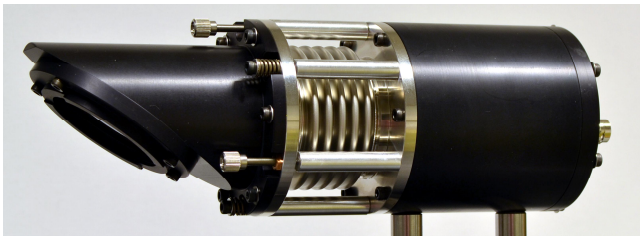

Figure 1. Photo of the room temperature PQED showing (from left to right) the Brewster window, adjustment screws, flexible bellows and the photodiode chamber.

CHARACTERIZATION

Several PQEDs were assembled and characterized for spatial uniformity of responsivity, photocurrent ratio, specular reflectance, and relative and absolute responsivity. All measurements were conducted at room temperature using an intensity stabilized argon ion laser operated at the wavelength of 488 nm. The optical power was approximately 200 μW and the incident light was *p* polarized in all the measurements. A description of the measurement setups and the uncertainty budgets of the measured values are given in [4].

A set of three PQEDs were measured for spectral responsivity against a conventional three

element reflection trap detector. The relative responsivities deviate from the average value by 8 ppm, -5 ppm and -3 ppm. The standard uncertainty of the results is 39 ppm. The average absolute responsivity of the three detectors deviates from the ideal spectral responsivity of a quantum detector by (103 ± 340) ppm (k = 1).

Specular reflectance measurements were conducted with the PQED entrance window inclined at Brewster's angle. Measured specular reflectances of 15 PQEDs are shown in Figure 2. The values are in agreement with the calculated value of 27.5 ppm with the standard uncertainty of 4.6 ppm [1].

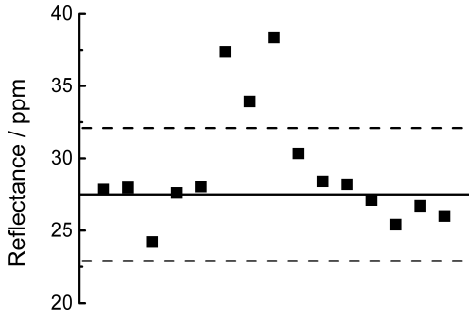

Figure 2. Measured reflectances of 15 PQEDs (squares) and the calculated value (solid line) at the wavelength of 488 nm. The uncertainties of the measured values are within the symbol height. The dashed lines indicate the standard uncertainty in the calculated value due to uncertainties in the detector and photodiode parameters [1].

A measurement result of spatial uniformity of responsivity is presented in Figure 3. The data indicate that with a $1/e^2$ laser beam diameter of around 1.2 mm, the responsivity changed only 50 ppm within a diameter of 4 mm. Thus, the non-uniformity of the PQED is about ten times lower than the non-uniformity of single induced junction photodiodes over similar area, as measured in [2].

The ratio of the photocurrents of the two photodiodes can provide additional information about the detector reflectance losses without direct measurement of the reflectance [5]. The spatial variation of the photocurrent ratio, on the other hand, can be used to approximate the uniformity in the thickness of the silicon dioxide layer [4]. The spatial uniformity measurements revealed peak-to-peak variations of about 1 % in the photocurrent ratios. These variations are not seen in spatial uniformity of responsivity, obtained from the same measurement, indicating high sensitivity of the photocurrent ratio method to determine the variation in oxide thicknesses. Consequently, the internal quantum efficiency of the photodiodes is concluded to be spatially uniform within 50 ppm.

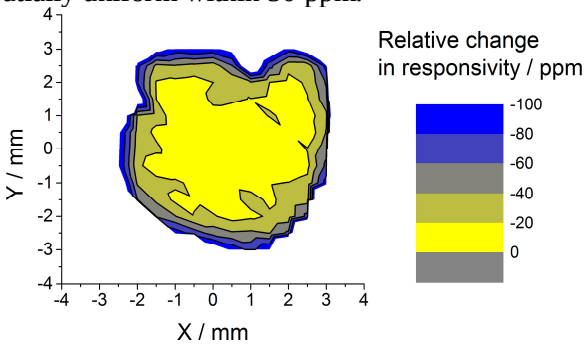

Figure 3. Spatial uniformity of responsivity measured without the Brewster window of the PQED [4]. Values are given as a relative deviation from the measured peak value.

CONCLUSIONS

The room temperature PQED detectors are intended to serve as primary standards of optical power in the visible wavelength range. Measurements of selected detectors at the wavelength of 488 nm indicate that the responsivity is spatially uniform within at least 50 ppm in the central area of 4 mm in diameter. The spatial non-uniformity is thus an order of magnitude lower than that of single photodiodes. The consistency of reflectance and responsivity between detectors provide data to support the earlier reported standard uncertainty of 70 ppm [1-3] of the room temperature PQED responsivity in the visible wavelength range and indicate that the room temperature PQED meet the expectations for a high quality primary standard.

ACKNOWLEDGEMENTS

This work was funded by the project NEWSTAR (contract SIB57) of the European Metrology Research Programme (EMRP). The EMRP is jointly funded by the EMRP participating countries within EURAMET and the European Union.

REFERENCES

1. M. Sildoja et al "Predictable quantum efficient detector: I. Photodiodes and predicted responsivity," Metrologia, 50, 385–394, 2013.
2. I. Müller et al, "Predictable quantum efficient detector: II. Characterization and confirmed responsivity," Metrologia, 50, 395–401, 2013.
3. J. Gran et al, "Simulations of a predictable quantum efficient detector with PC1D," Metrologia, 49, S130–S134, 2012.
4. T. Dönsberg et al, "A primary standard of optical power based on induced-junction silicon photodiodes operated at room temperature" Metrologia (in press)
5. M. Sildoja et al, "Use of the predictable quantum efficient detector with light sources of uncontrolled state of polarization," Measurement Science and Technology, 25, 015203, 2014.

The CCPR K2.c key comparison of spectral responsivity from 200 nm to 400 nm

Lutz Werner

Physikalisch-Technische Bundesanstalt, Berlin, Germany
Corresponding e-mail address: lutz.werner@ptb.de

The CCPR K2.c key comparison of spectral responsivity from 200 nm to 400 nm was carried out in the framework of the CIPM Mutual Recognition Arrangement by 14 participating national metrology institutes. The key comparison was piloted by the Physikalisch-Technische Bundesanstalt (PTB). The comparison principle, measurements, analysis and results including a procedure to deal with the issue of inconsistent data are described.

INTRODUCTION

The Mutual Recognition Arrangement (MRA) for national measurement standards and for calibration and measurement certificates issued by the national metrology institutes (NMIs) was signed in 1999. The objectives of the MRA were to establish the degree of equivalence of national measurement standards maintained by NMIs and to provide for the mutual recognition of calibration and measurement certificates issued by NMIs. Under the MRA the metrological equivalence of national measurement standards is determined by a set of key comparisons chosen and organized by the Consultative Committees of the CIPM working closely with the Regional Metrology Organizations (RMOs). At its meeting in March 1997, the Consultative Committee for Photometry and Radiometry (CCPR) identified several key comparisons in the field of optical radiation metrology. One of these was the CCPR K2.c key comparison of spectral responsivity in the spectral range from 200 nm to 400 nm.

The Physikalisch-Technische Bundesanstalt (PTB), the NMI of Germany, was asked to be the pilot of this key comparison. The technical protocol of the key comparison was drawn up by a small working group comprising PTB (convenor), BIPM, MSL, NPL, NIST, and NRC.

Laboratories from 14 NMIs including the pilot laboratory took part in this comparison. These were LNE-Cnam (France), NMIA (Australia), MIKES (Finland), IO-CSIC (Spain), MSL (New Zealand), NIM (China), NIST (United States of America), NMIJ AIST (Japan), VSL (Netherlands), NPL (United Kingdom), NRC (Canada), PTB (Germany) - Pilot, NMC-A*STAR (Singapore), and VNIIOFI (Russian Federation).

COMPARISON ARTEFACTS AND PRINCIPLE OF THE COMPARISON

Three types of transfer detectors based on two types of photodiodes were used as comparison artefacts: (i) single element photodiode detectors based on windowless SUV100 PtSi/n-Si Schottky photodiodes manufactured by the Swiss Federal Institute of Technology (ETH) in Zurich, Switzerland, (ii) single element photodiode detectors and (iii) three element reflection trap detectors, both based on windowless Hamamatsu S5227 1010 Si pn junction photodiodes.

The comparison was organized in a star form, carried out in three phases with three groups of participants and using sets of transfer detectors each consisting of three PtSi photodiodes, three Si photodiodes and one Si-photodiode-based trap detector. The Si-photodiode-based detectors were intended to be used only in the wavelength region 250 nm to 400 nm because their responsivity can alter due to exposure in the short-wavelength ultraviolet spectral range. Each detector was equipped with a Pt100 temperature sensor to monitor the detector temperature during the measurements. Because of the large temperature coefficient of the PtSi photodiodes and the possibility of large differences in laboratory temperature between the participants and the Pilot, these photodiodes were mounted on a brass block which could be warmed or cooled by water. Thus, the temperature of the PtSi photodiodes could be set independently of the laboratory temperature.

MEASUREMENTS

The participating NMIs determined the spectral responsivity of their transfer detectors in order to perform the comparison on the spectral responsivity. The transfer detectors were compared with reference detectors of the Pilot at each wavelength before they were sent to the participants and after their return to check their stability. For this, the ratios of the photocurrent of the Pilot's reference detectors and the photocurrent of each transfer detector when irradiated

by the same source at the same wavelength were measured. These photocurrent ratios are equal to the ratios of the spectral responsivity of the corresponding detectors and were used to calculate for each participant the spectral responsivity of the reference detector as derived from his results on the responsivity of his set of transfer detectors. Thus, *N* values of the spectral responsivity of the reference detector, derived from the *N* participants' results, could be obtained and be used to calculate a reference value. A separate reference value was calculated for each wavelength.

Because of the large differences between PtSi photodiodes and Si photodiodes, different reference detectors were used: a PtSi photodiode as reference detector for PtSi-photodiode-based transfer detectors and a Si-photodiode-based trap detector as reference detector for Si-photodiode-based transfer detectors. The reference detectors were compared against a group of secondary detector standards of PTB in each phase of the comparison to check their stability. It turned out that the detectors were not stable. The time dependent spectral responsivity of the Si-photodiode-based reference could be well fitted using a linear drift model with a wavelength dependent annual drift rate between -0.24 % and -0.07 %. The temporal change of the spectral responsivity of the PtSi photodiode reference was less regular and was described by the more common approach of a stepwise drift.

ANALYSIS

The calculation of the degrees of equivalence (DoE) and the key comparison reference value (KCRV) were performed in agreement with the guidelines of the CCPR [1]. The drifting spectral responsivity of the Si-photodiode-based reference trap detector was determined using a linear drift model. The two unknown quantities of this model, the drift rate and the value at a certain time of the spectral responsivity of the reference, and their uncertainties were determined by fitting the model to the data, that are the *N* values of the spectral responsivity of the reference, derived from the *N* participants' results, and the result of the Pilot on the drift rate of the reference. The best fit was obtained by least square fit, which means, the best fit minimizes the sum of squared weighted differences between data and model. The weights were chosen proportional to the squared reciprocal uncertainties after applying a cut-off for the uncertainties reported by the participants according to the guidelines of the CCPR [1]. The drifting spectral responsivity of the PtSi photodiode reference was determined accordingly using a stepwise drift model. For comparison only, the KCRVs and the DoEs were in addition calculated by the weighted mean with cut-off.

The use of the above models requires the consistency of the set of data which was checked using the chi-squared test. The chi-squared test failed at a considerable number of wavelengths. Therefore, a procedure to achieve consistency and to exclude outlying results was developed by the pilot and discussed and agreed on by all participants. Although this procedure was acceptable within this comparison, it is obvious that a widely accepted and well reasoned model that includes outlying results and does not require consistent data is urgently needed.

Because of the poorer results of the PtSi photodiodes in comparison with those of the Si-photodiode-based detectors, only the Si-photodiode-based detectors were used to calculate the KCRVs and the DoEs in the wavelength range from 250 nm to 400 nm. In the wavelength range from 200 nm to 240 nm the KCRVs and the DoEs are based on the PtSi photodiodes.

RESULTS

The results of the key comparison are still confidential at the time of submission of the abstract. It is expected that they will be approved in time and can be reported at the NEWRAD conference.

ACKNOWLEDGEMENT

The author would like to thank Dr. Clemens Elster and Alfred Link for their helpful short lectures and discussions on statistics and the introduction to Bayesian model averaging, Alfred Link for the data analysis based on the fixed effects bias model and the Bayesian model averaging technique which served as a check for the results on the exclusion of outliers, Peter Meindl for encouraging and helpful discussions, and Katrin Vogel, Peter Meindl, Josef Breuer, Marianne Fleischer-Bartsch, and Sylvia Ludwig for performing the large number of measurements PTB had to perform as the Pilot of this comparison.

The author would like to thank all participants for their cooperation and their patience.

REFERENCES

1. Guidelines for CCPR Comparison Report Preparation, http://www.bipm.org/utils/common/pdf/Guidelines_for_CCPR_KC_Reports.pdf.

Use of Photocurrent Ratio for Reflectance Determination of the Predictable Quantum Efficient Detector

Meelis Sildoja[1], Timo Dönsberg[1,2], Henrik Mäntynen[1], Mikko Merimaa[2], Farshid Manoocheri[1,2], and Erkki Ikonen[1,2]

[1]*Metrology Research Institute, Aalto University, Espoo, Finland*
[2]*Centre for Metrology and Accreditation, Espoo, Finland*
Corresponding e-mail address: meelis.sildoja@aalto.fi

We present a simple method to determine the reflectance losses for Predictable Quantum Efficient Detector (PQED) without direct measurement of the reflectance. The ratio of photocurrents produced by the two photodiodes inside the PQED is used to determine the fractions of the s- and p- polarized components of the incident light. The reflectance of the PQED with either seven or nine internal reflections can be calculated based on the obtained polarization information for the light sources of any polarization. For the 7-reflection PQED the method allows reflectance losses to be determined with uncertainty mostly below 100 ppm (part per million) and for the 9-reflection PQED below 20 ppm in the wavelength range from 400 nm to 900 nm.

INTRODUCTION

Predictable Quantum Efficient Detector (PQED) [1,2] is a silicon photodiode based photodetector that can theoretically measure optical radiation with relative standard uncertainty below 1 ppm when operated at low temperatures [3]. At room temperature the predicted and experimentally validated relative standard uncertainty of spectral responsivity is about 70 ppm [1-3]. Such a low uncertainty requires reliable determination of the reflectance losses of the PQED.

Presently the reflectance losses of the PQED are estimated and measured for p-polarized light due to the design of the PQED and due to low reflectance of p-polarized light [1]. Any other polarization type increases the reflectance losses and their estimation uncertainty. On the other hand, the knowledge of reflectance losses using arbitrarily polarized light is required for example with light sources based on integrating spheres.

PQED REFLECTANCE BASED ON PHOTOCURRENT RATIO MEASUREMENT

The PQED consists of two photodiodes arranged in a wedge-like structure [1,4]. Figure 1 indicates that the reflectance of such structure depends strongly on the polarization state of incident light.

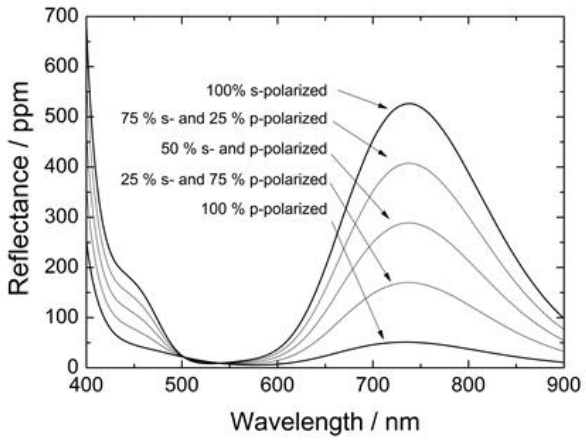

Figure 1. Reflectance of the 7-reflection PQED in the case of incident light with different combinations of normalized *s*- and *p*-polarized components. For 9-reflection PQED the spectral reflectance is reduced by a factor of ten.

Calculations show that the distribution of photocurrents between two photodiodes contains information about the polarization properties of the incident light. By measuring the photocurrents individually from the PQED photodiodes and calculating the ratio of those two signals, one can determine the fractions of normalized s- and p-polarized components (Figure 2) and through that calculate the associated reflectance [5]. Sildoja et al have determined the largest uncertainty components of the calculated reflectance for the 7-reflection PQED [1] (see Table 1). Similar components affect the uncertainty of the calculated photocurrent ratio and estimated fractions of the s- and p-polarized components in the incident light.

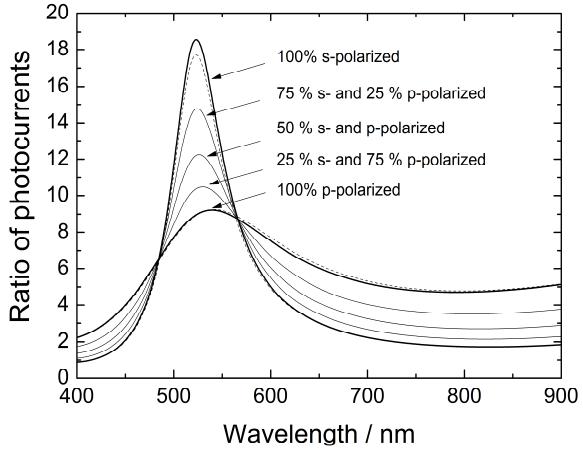

Figure 2. Ratio of photocurrents of the 7- and 9-reflection PQED in the case of incident light with different combinations of s- and p-polarized components. The thin dashed lines show photocurrent ratios of the 7-reflection PQED in the case of s- and p-polarized light. The differences in photocurrent ratios for 7- and 9-reflection PQED are within the standard uncertainties of the predicted photocurrent ratios.

Table 1. Main uncertainty components affecting the reflectance and photocurrent ratio values of the PQED, calculated on the basis of detector geometry and material parameters.

Uncertainty component	Standard
Angle between the photodiodes	0.4°
Oxide thickness of the 1st diode	2 nm
Oxide thickness of the 2nd diode	2 nm
SiO_2 index of refraction	0.2 %
Si index of refraction	0.5 %
Si extinction coefficient	5 %
Optical thickness of Si/SiO_2 interface layer	8 nm
PQED rotation around horizontal axis	0.5°

Figure 3 shows how the photocurrent ratio measurement at the wavelengths of 400 nm and 760 nm can be used to determine the PQED reflectance and its uncertainty for the 7-reflection detector. Similar figure can be plotted for the 9-reflection PQED. In the latter case, the reflectance is reduced by a factor of ten and the uncertainty of reflectance is reduced by about a factor of eight. Calculated photocurrent ratios and their uncertainties for the 9-reflection PQED are similar to those with the 7-reflection PQED, differing notably only at 760 nm in the case of p-polarized light. Then the ratio shown in Figure 3 is reduced about 2%. The biggest components affecting the uncertainty of the photocurrent ratio are the angle between the photodiodes and the uncertainty of the oxide thickness of the first photodiode.

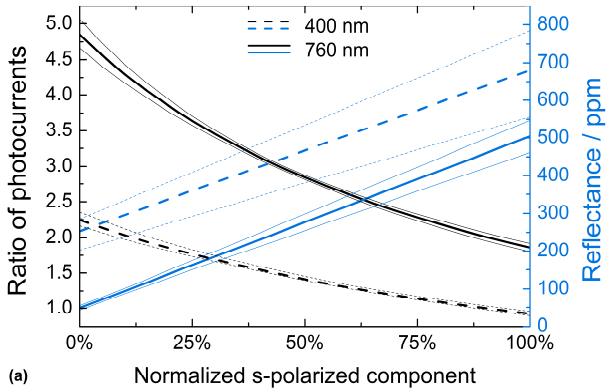

Figure 3. Ratio of photocurrents and corresponding reflectances of the 7-reflection PQED as a function of light polarization. Thinner lines indicate the standard uncertainty corridors due to detector and photodiode parameters of Table 1.

CONCLUSIONS

The ratio of photocurrents produced by the two photodiodes inside the PQED provides information about the fractions of s- and p-polarized components in the incident light. This knowledge allows us to calculate the reflectance of the PQED. The reflectance can be determined with an uncertainty mostly below 100 ppm for the 7-reflection PQED and with an uncertainty below 20 ppm for the 9-reflection PQED in the wavelength range from 400 nm to 900 nm. The design of the 9-reflection PQED reduces the absolute reflectance by about a factor of ten as compared with the 7-reflection PQED. These achievements allow the wedged trap design of the PQED to be used with monochromator based and other light sources where the polarization properties of the beam are unknown and still maintain the low uncertainty previously available only for fully s- or p-polarized light.

REFERENCES

1. M. Sildoja et al, “Predictable quantum efficient detector: I. Photodiodes and predicted responsivity,” Metrologia, 50, 385–394, 2013.
2. I. Müller et al, “Predictable quantum efficient detector: II. Characterization and confirmed responsivity,” Metrologia, 50, 395–401, 2013.
3. J. Gran et al, “Simulations of a predictable quantum efficient detector with PC1D,” Metrologia, 49, S130–S134, 2012.
4. T. Dönsberg et al, “New source and detector technology for the realization of photometric units”, these porceedings.
5. M. Sildoja et al, “Use of the predictable quantum efficient detector with light sources of uncontrolled state of polarization,” Measurement Science and Technology, 25, 015203, 2014.

Use of a Laser-Driven Plasma Source in the Ultraviolet Spectral Comparator Facility

Uwe Arp and Rob Vest

National Institute of Standards and Technology NIST, Gaithersburg, MD, U.S.A.
Corresponding e-mail address: uwe.arp@nist.gov

The National Institute of Standards and Technology operates the Ultraviolet Spectral Comparator Facility to provide detector calibrations in the ultraviolet spectral range. Recently, the illumination source used in the Ultraviolet Spectral Comparator Facility has been changed from an argon mini-arc source to a laser-driven plasma light source. This new source has higher brightness, a smaller source size, better temporal stability, and much better conversion efficiency than the previous source.

INTRODUCTION

The National Institute of Standards and Technology (NIST) provides radiometric detector and source calibration services, which span the optical portion of the electromagnetic spectrum. The Ultraviolet Spectral Comparator Facility, called UV SCF [1,2], covers the spectral range from 200 nm to 500 nm. In the UV SCF the spectral radiant power responsivity of photodetectors is determined. The absolute spectral power responsivity scale is established using absolute cryogenic radiometers (ACR) [3,4] and transfer standards.

ULTRAVIOLET SPECTRAL COMPARATOR FACILITY

Fig. 1 depicts the UV SCF optical system. The calibrations are performed using the substitution method with monitor that minimizes uncertainties caused by light source fluctuations. Historically, the light source in the UV SCF was an argon mini-arc source (AMAS) [5,6]. The AMAS was recently replaced by a commercially available laser-driven light source (LDLS) [7,8]. This LDLS is based on a bulb-contained plasma discharge, which is sustained by a continuous near-infrared laser operating at 20 W.

LASER-DRIVEN LIGHT SOURCE VERSUS ARGON MINI-ARC

In the top panel of Fig. 2 the optical power in the detector plane of the UV SCF for both the argon mini-arc P_{AMAS} and the laser-driven light source P_{LDLS} are shown. Also displayed in the top panel of Fig. 2 is the ratio of the optical power for both sources P_{LDLS}/P_{AMAS}. The use of the LDLS in the UV SCF increases the available optical power considerably, especially at wavelengths shorter than 250 nm. The largest optical power increase is at 200 nm, where 12 times more power is available with the LDLS. At wavelengths longer than 250 nm the available power increased by a factor of about 4.

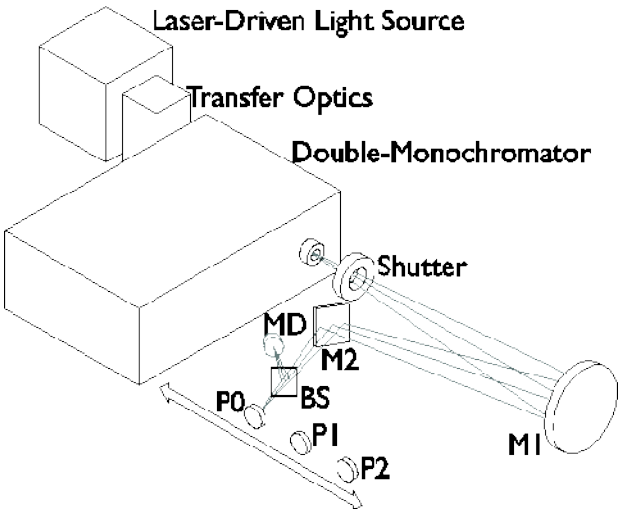

Figure 1. Schematic layout of the Ultraviolet Spectral Comparator Facility (UV SCF). The light generated in the Laser Driven Light Source is imaged onto the entrance slit of the double monochromator using transfer optics. The exit slit of the monochromator is imaged onto the detector under test (**P0**) or one of two working standard detectors 1 (**P1**) and 2 (**P2**), using the spherical mirror **M1** and flat mirror **M2**. Source fluctuations are monitored with a beamsplitter (**BS**) and monitor detector (**MD**). The shutter allows measurement of the background signal of the data acquisition system.

In the future, we hope to capitalize on this increase in optical power by shortening the calibration chain. Instead of using detectors calibrated in the SIRCUS [9] facility to calibrate working standard detectors in the UV SCF, we are planning to calibrate working standard detectors in the UV SCF directly, using an absolute cryogenic radiometer.

This will reduce the uncertainties, especially in the short wavelength range below 250 nm. The ultraviolet lasers used in the SIRCUS facility cannot be tuned to wavelengths shorter than 210 nm.

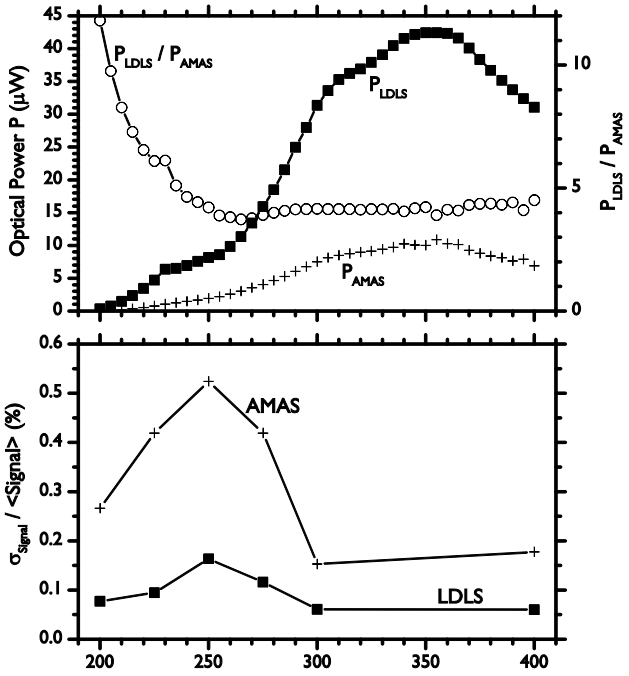

Figure 2. TOP: Comparison of the optical power at the detector position of the UV SCF: Laser driven light source (LDLS) P_{LDLS} ■, argon mini-arc source (AMAS) P_{AMAS} +. The ratio P_{LDLS}/P_{AMAS} is indicated by the open circles ○. **BOTTOM:** Relative standard deviation σ_{Signal} / <*Signal*> of the detector. Decreased stability caused by ozone generation is clearly visible around *250* nm.

Therefore the calibration of the transfer standard between 200 nm and 210 nm is based on an extrapolation, which models the data at longer wavelengths. Between 200 nm and 210 nm, direct calibration of working standard detectors will greatly reduce the uncertainties. Additionally, calibration of the working standards at SIRCUS often requires interpolation of data at the laser lines. This interpolation can increase the calibration uncertainty, especially in highly curved regions of the detector responsively function. In the bottom panel of Fig. 2 the temporal stability of the two sources is displayed. The relative standard deviation of the mean signal accumulated over about 2 minutes is shown. The LDLS exhibits better temporal stability by a factor of 2−5. The output of both sources exhibits less stability in the range of the ozone absorption, which peaks around 250 nm [6]. Ozone is produced by both sources through photodissociation of molecular oxygen at wavelengths shorter than about 200 nm [7]. To avoid ozone production in the LDLS the lamp housing is purged with dry nitrogen.

CONCLUSION AND OUTLOOK

Replacement of the argon mini-arc source in the UV SCF by a laser-driven light source significantly increased the available optical power in the detector plane. The boosted optical power will make it possible to shorten the calibration chain and in the future, working standard detectors will be calibrated directly against an absolute cryogenic radiometer in the UV SCF, thus eliminating all uncertainties resulting from the use of transfer standards, which were calibrated in a separate system with a different light source and optics. Any uncertainty caused by differences in bandpass, out-off-band radiation, spectral purity, collimation, or data extrapolation will be removed. This will reduce the uncertainties of the calibrations done using the UV SCF, especially in the short wavelength range below 220 nm.

The laser-driven light source is temporally stabler than the argon mini-arc, which reduces the uncertainties in the data acquisition through improved data acquisition statistics.

REFERENCES

1. T. C. Larason and J. M. Houston, *Tech. Rep.* **SP250-41**, NIST (2008).
2. T. Larason, S. Bruce, and C. Cromer, *J. Res. Natl. Inst. Stand. Technol.* **101**, 133–140 (1996).
3. C. R. Yokley, (SPIE, Bellingham, WA, 1983), vol. **416**, pp. 2–8.
4. T. J. Quinn and J. E. Martin, *Philos. Trans. Roy. Soc. London* **A 316**, 85–189 (1985).
5. J. M. Bridges and W. R. Ott, *Appl. Opt.* **16**, 367-76 (1977).
6. J. L. Lean, H. J. Kostkowski, R. D. Saunders, and L. R. Hughey, *Appl. Opt.* **28**, 3246-3253 (1989).
7. S. Horne, D. Smith, M. Besen, M. Partlow, D. Stolyarov, H. Zhu, and W. Holber, (SPIE, Bellingham, WA, 2010), vol. **7680**, 76800L.
8. J. Feng, J. Nasiatka, J. Wong, X. Chen, S. E. Hidalgo, T. Vecchione, H. Zhu, F. Javier Palomares, and H. A. Padmore, *Rev. Sci. Inst.* **84**, 085114 (2013).
9. S. W. Brown, G. P. Eppeldauer, and K. R. Lykke, *Appl. Opt.* **45**, 8218–37 (2006).
10. E. C. Y. Inn and Y. Tanaka, *J. Opt. Soc. America* **43**, 870 (1953).
11. T. Matsui, A. S.-C. Cheung, K. W.-S. Leung, K. Yoshino, W. H. Parkinson, A. P. Thorne, J. E. Murray, K. Ito, and T. Imajo, *J. Molec. Spectrosc.* **219**, 45–57 (2003).

Optimizing the carbon nanotube radiometer for operation at helium temperatures

Nathan Tomlin[1], Malcolm White[1], Solomon Woods[2], and John Lehman[1]

[1] *National Institute of Standards and Technology, Boulder, Colorado, USA*

[2] *National Institute of Standards and Technology, Gaithersburg, Maryland, USA,*

Corresponding e-mail address: nathan.tomlin@nist.gov

The recently developed carbon nanotube radiometer (CNTR) is quite different from conventional cryogenic radiometers in terms of absorber design, size, speed, and thermistor. We have designed a version of the CNTR for operation at 2 K, with sensitivity better than 1 pW and time constant less than 1 ms. We describe in detail the device components, design parameters used to optimize performance, and the limitations of the CNTR.

INTRODUCTION

Conventional electrical-substitution cryogenic radiometers (CRs) are the primary standards for optical power measurements [1] and sensitive radiometers typically have time constants on the order of seconds to minutes due to the large heat capacity of the absorber cavity. By using an absorber of vertically-aligned carbon nanotubes (VACNT), which can have near unity absorption over a broad range of wavelengths [2], we are able to use a planar design, resulting in a much smaller carbon nanotube radiometer (CNTR) with a time constant less than 1 ms.

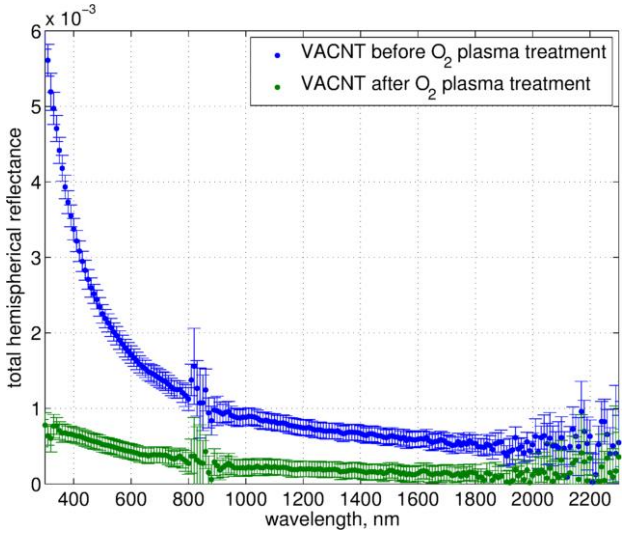

Figure 1. Measured total hemispherical reflectance of VACNT sample before and after oxygen plasma treatment.

DEVICE COMPONENTS

ABSORBER

The absorber for incident optical power is composed of VACNT. Many factors affect the absorbing properties of the VACNT, including growth method (CVD or PECVD), underlayer (SiO_2, Mo, or Nb), catalyst, and height. Post treatment with oxygen plasma has also been shown to decrease reflectance (Fig. 1) [3]. The size of the absorber is limited only by the required absorber size and lithographic resolution.

THERMISTOR

Thin film Mo pads make electrical connection to a small patch of VACNT for the thermistor. VACNT have been shown to have a negative temperature coefficient, with sensitivities below 10 K comparable to commonly used thermistors [4]. Density and height of the VACNT influence the temperature sensitivity.

The geometry of the Mo pads determines the absolute resistance value at the temperature of interest.

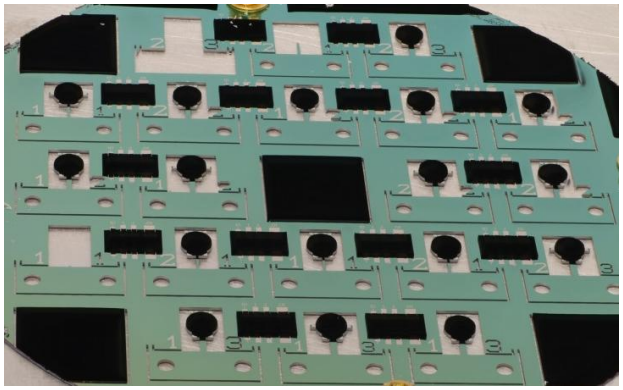

Figure 2. Image of 76.2 mm (3 inch) diameter silicon wafer fabricated for 20 CNTR including 8 different variations.

HEATER

Thin film Mo is used for the electrical substitution heater. The geometry and thickness determine the heater resistance.

WEAK THERMAL LINK

The dimensions of a single micro-machined silicon leg determine the thermal conductance (*G*) of the weak thermal link. By varying the thickness and length of the leg, we have measured thermal conductances at 4 K from 300 µW/K to 2800 µW/K, and values as low as 3 µW/K are possible. Even lower thermal conductances could be attained by using a silicon nitride membrane weak link.

FABRICATION

All components are lithographically defined on a 76.2 mm (3 inch) diameter silicon wafer. Due to the flexibility of the lithographic process and small size of each device, it is possible to fabricate multiple designs on a single wafer (Fig. 2).

DESIGN PARAMETERS

HEAT CAPACITY & TIME CONSTANT

The heat capacity is dominated by the volume of silicon. The main difference from conventional CRs is the extremely small size of the CNTR. For the design shown in Fig. 3, the silicon area is only slightly larger than the absorber area (3 mm diameter). With a thermal conductance of 750 µW/K at 4 K, the device in the figure has a time constant of ~700 µs.

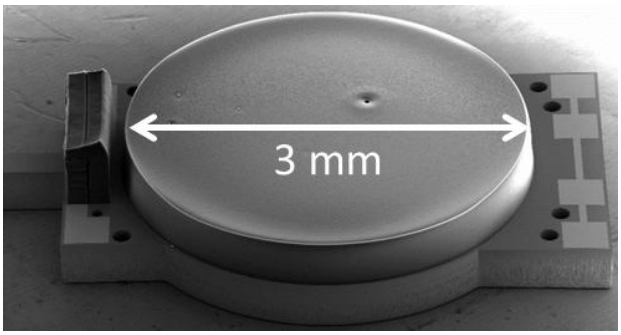

Figure 3. Scanning electron microscope image of CNTR. From left to right, the components are weak thermal link, VACNT thermistor with Mo leads, VACNT absorber, and Mo heater.

THERMAL MODEL & EQUIVALENCE

Assuming we can neglect radiation loss and heat conduction along the aluminium wirebonds, the thermal model is shown in Fig. 4. We will discuss measurements of equivalence between electrical and optical heating.

ILLUMINATION

We typically illuminate the CNTR using standard telecommunications optical fiber, aligned to the center of the absorber at normal incidence. However, the device shown in Fig. 3 was designed to be illuminated by a free space beam in the Low Background Infrared (LBIR) facility at NIST Gaithersburg [5].

We have also used piezoelectric nanopositioners to map out the spatial uniformity of the VACNT absorber.

CONCLUSION

The CNTR is similar in function and use to a conventional CR, but radically different in size, time constant, and specifics of each component. Due to the lithographic nature of the fabrication, many characteristics can be modified accurately and easily, including absorber size, thermistor resistance, heater resistance, thermal conductance, and time constant.

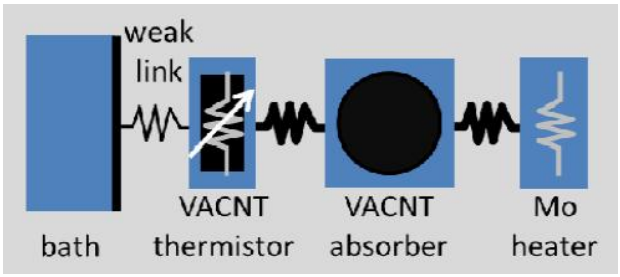

Figure 4. Thermal model of CNTR.

ACKNOWLEDGMENTS

Scanning electron microscopy was performed by Aric Sanders in the Precision Imaging Facility at NIST Boulder.

REFERENCES

1. J. Martin, N. Fox, P. Key, A cryogenic radiometer for absolute radiometric measurements, Metrologia, 21, 147-155, 1985.
2. Z. Yang, L. Ci, J. Bur, S. Lin, P. Ajayan, Experimental observation of an extremely dark material made by a low-density nanotube array, Nano Letters, 8, 446-451, 2008.
3. N. Tomlin, A. Curtin, M. White, J. Lehman, Decrease in reflectance of vertically-aligned carbon nanotubes after oxygen plasma treatment, Carbon, in press, 2014, doi: 10.1016/j.carbon.2014.03.040.
4. N. Tomlin, J. Lehman, Carbon nanotube electrical-substitution cryogenic radiometer: initial results, Optics Letters, 38, 175-177, 2013.
5. A. Carter, R. Datla, S. Woods, T. Jung, Infrared absolute calibrations down to 10 fW in low-temperature environments at NIST, Proc. SPIE, 7021, 70210S, 2008.

Traceable Wavelength Calibration of a Monochromator Using a Fourier Transform Spectro*radio*meter

Stefan Winter, Thomas Fey, Ingo Kröger, and Fabian Plag

Physikalisch-Technische Bundesanstalt, Braunschweig, Germany
Corresponding e-mail address: Stefan.Winter@PTB.de

The calibration of detectors with a spectral responsivity that differs from that of the reference detector requires an accurate traceable wavelength calibration of the monochromator system. For such detectors the wavelength uncertainty may even be the largest uncertainty component. Typically the wavelength calibration is performed with cw lasers or mercury pencil lamps. Its result though depends on the exact position of the optical image of the sources on the entrance slit. However, for this application the radiation that *exits* the monochromator is essential. We solve this challenge by using a radiometrically calibrated Fourier Transform Spectrometer (FTS) and, with this approach, reduce the wavelength uncertainty from 0.3 nm to 0.03 nm.

INTRODUCTION

An accurate traceable wavelength calibration of the monochromator system used for spectral responsivity measurements is important for the calibration of detectors with a spectral responsivity that differs from the reference detector, e.g. the calibration of photometers, UV detectors, or filter radiometers against silicon trap detectors. In these cases the wavelength uncertainty may be the largest uncertainty component. With a detailed uncertainty analysis it was shown that the wavelength uncertainty contributes more than 90 % to the combined uncertainty of relative quantities like the spectral mismatch index or the general $V(\lambda)$ mismatch index f_1' of photometers [1].

TRADITIONAL METHOD

Typically, the wavelength calibration of monochromators is performed with lasers or mercury pencil lamps. For these measurements the slits are reduced to a minimum width to ensure that the laser beam or the optical image of the pencil lamp enters the monochromator in the centre of the entrance slit and also to get a high resolution. While spectroradiometers have entrance optics with diffusers or integrating spheres and therefore do not show an important dependence of the centre wavelength on the uniformity of the irradiation, monochromators are optimized for high throughput and are very sensitive to a horizontal non-uniformity at their entrance. For the application of the monochromator a quartz halogen or a xenon lamp is imaged onto the entrance slit. It is thus not illuminated uniformly. In an extreme case this may lead to any centre wavelength within the range of the adjusted bandwidth (Full Width Half Maximum, FWHM). Especially if the application needs a high optical power, the slits must be opened wide and this leads to a large wavelength error. At the DSR facility of the authors a misalignment of the xenon lamp of 1 mm results in a wavelength offset at the exit of the monochromator of more than 0.6 nm.

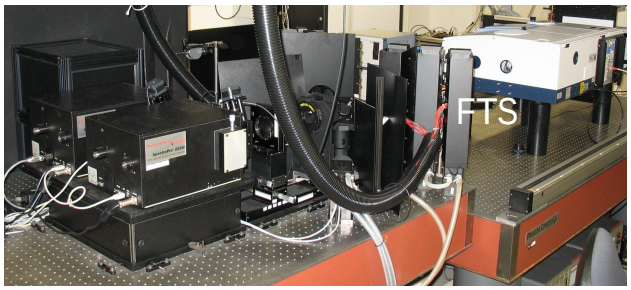

Figure 1. Setup with the monochromator system on the left. Its monochromatic and parallel beam enters the FTS that stands on the right optical table at the place where usually the detectors (e.g. solar cells) were mounted.

A further problem of the calibration with pencil lamps is the limited number of usable spectral lines for the calibration and the need to interpolate between these lines. Typical monochromators are built up with a worm gear that rotates a gearwheel with the grating on its top. With very precise measurements as presented at the end of this paper, the periodical wavelength errors due to the mechanical errors of the worm gear may be made visible (Fig. 5).

A third issue is the influence of the spectral irradiance of the source on the centre wavelength of the radiation because the spectrum of the outgoing radiation is the product of the spectral irradiance of the source, the slit function of the monochromator

and the reflectance of the components within the monochromator. Thus a peak of a xenon lamp influences the centre wavelength of wavelength settings of the monochromator close to the peak (Figs. 3+4).

To summarize, it can be concluded that it is not sufficient to calibrate a monochromator system with incoming radiation of a known wavelength. It is much more important to characterize the wavelength of the outgoing radiation at every wavelength and slit setting used individually.

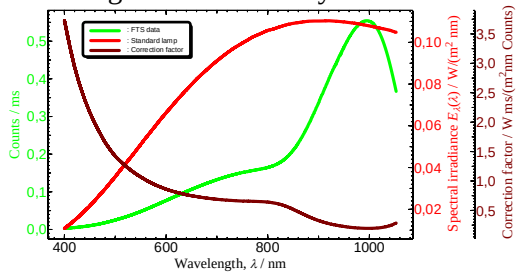

Figure 2. Result of the radiometric calibration of the FTS.

APPLYING AN FTS AS A FOURIER TRANSFORM SPECTRO*RADIO*METER

The solution to the above-mentioned issues is the spectral measurement of the radiation that comes out of the monochromator. One possibility would be to use an array spectroradiometer, but its wavelength uncertainty is too high and its wavelength must be first calibrated. Another idea could be to use wavemeters. They state the wavelength with a very high resolution and accuracy, but only for very narrow band sources such as cw-lasers. Thus we chose a system that is suitable for broad band light sources:

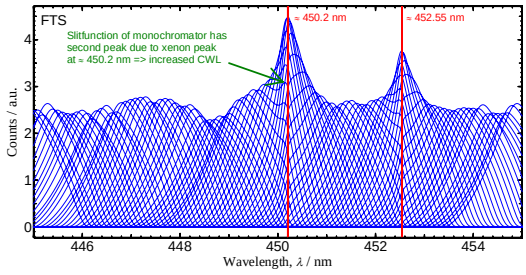

Figure 3. Spectral irradiance measured every 0.1 nm.

A Fourier Transform Spectrometer that can measure down to 200 nm was implemented (Fig. 1). At least an external HeNe laser that is coupled in from outside into the FTS on the same path as the radiation from the monochromator, must be used as a wavelength reference in air. This enables a wavelength uncertainty of the FTS smaller than 0.01 nm. The obtained values however are only valid for the peak wavelength at this step. After a radiometric calibration of the FTS against a standard lamp (Fig. 2), the radiometric centre wavelength can be determined. To estimate the uncertainty, the influence of a wrong distribution temperature was calculated. It was shown that a wrong distribution temperature of 3020 K instead of 3000 K would lead to an error in the centre wavelength of only 0.006 nm (parameters: radiation at 300 nm with an FWHM of 10 nm).

With this setup the spectral irradiance of the radiation behind the monochromator and its centre wavelength is determined with high wavelength accuracy (Fig. 3 - 5) and thus it can be corrected.

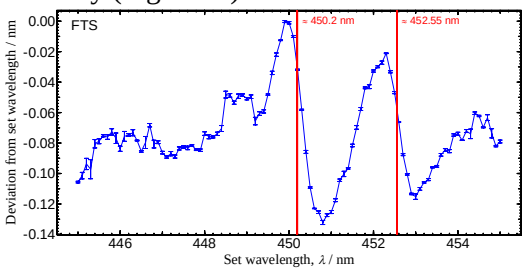

Figure 4. Deviation from the set wavelength. The xenon peaks lead to deviations of 0.14 nm (peak-to-peak).This is about 10 % of the FWHM of the monochromator output!

SUMMARY

With the integration of a radiometric calibrated FTS in the monochromator setup the uncertainty of the centre wavelength of the outgoing radiation could be reduced from 0.3 nm to 0.03 nm.

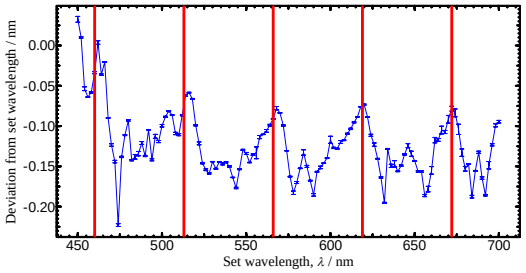

Figure 5. Deviation from the set wavelength. The red lines indicate the periodically identical position of the worm gear in the monochromator. The main wavelength deviations show the same periodicity, despite the superposition of other smaller effects (e.g. at 450 nm, see Fig. 4).

A further advantage of this method is that the unstabilized HeNe wavelength value (in vacuum) is recommended by the CIPM as a realization of the definition of the metre with a relative standard uncertainty of $1.5 \cdot 10^{-6}$ [2], while mercury lines are not recommended for this purpose by the CIPM.

REFERENCES

1. S. Winter, A. Sperling: “Uncertainty Analysis of a Photometer Calibration at the DSR Setup of the PTB” in “Proc. 2nd Expert Symposium on Measurement Uncertainty” (Braunschweig 2006), pp. 139-142, CIE x029:2006, ISBN 3-9810021-4-8
2. http://www.bipm.org/utils/common/pdf/mep/M-e-P_unstab-HeNe_633.pdf

The standard of average power, attenuation and wavelength of optical radiation for fiber-optic communication systems

V.A. Dlugunovich[1], A.I. Glazov[2], A.V. Isaevich[1], M.L. Kozachenko[2], S.V. Nikanenka[1], S.V. Tikhomirov[2], and A.V. Holenkov[1]

[1]*B. I. Stepanov Institute of Physics National Academy of Sciences of Belarus, Minsk, Belarus,*
[2]*All-Russian Research Institute for Optical and Physical Measurements, Moscow, Russia*
Corresponding e-mail address: s.nikonenko@ifanbel.bas-net.by

Results of research of metrological characteristics of the created standard of average power, attenuation and wavelength of optical radiation for fiber-optical communication systems are given. The standard provides storage, reproduction and transfer in a spectral range from 0.6 to 1.7 μm of the unit of average power from 0.1 to 5 mW with the relative expanded uncertainty less than 0.2 %, attenuation from 0.05 to 60.00 dB with the expanded uncertainty less than 0.2 dB and wavelength of optical radiation with the relative expanded uncertainty no more than 10^{-6} %.

The standard of average power, attenuation and wavelength of optical radiation for fiber-optical communication systems is developed and constructed in the Institute of Physics National Academy of Sciences of Belarus together with All-Russian Research Institute for Optical and Physical Measurements. It is used for storage, reproduction and the transfer of specified above units, and also for verification and calibration of the secondary and working standards applied in fiber-optic communication systems.

The standard consists of a complex of the stabilised sources of optical radiation with the fiber-optical connectors, standard calorimetric system (SCS) for reproduction and transfer of the unit of average power of optical radiation in fiber-optical communication systems, a complex of measuring instruments (MI) for reproduction and transfer of the unit of attenuation in fiber-optic communication systems, a complex of MI for reproduction and transfer of the unit of wavelength of optical radiation in fiber-optic communication systems and auxiliary equipment for maintenance of functioning of the standard and information processing.

As radiation sources are used single-mode and multi-mode stabilised lasers with wavelength 655, 850, 1310, 1490, 1550 and 1625 nanometers. Stabilisation of laser radiation characteristics is carried by maintaining of constant temperature of lasers by thermoelectric coolers and use of special schemes of stabilisation.

Functionally SCS consists of the calorimetric converter, systems of registration and electric calibration of the calorimetric converter, meteometer for measurements of temperature, pressure and humidity of environment and the personal computer (PC) for operating SCS and processing of results of measurements (figure 1).

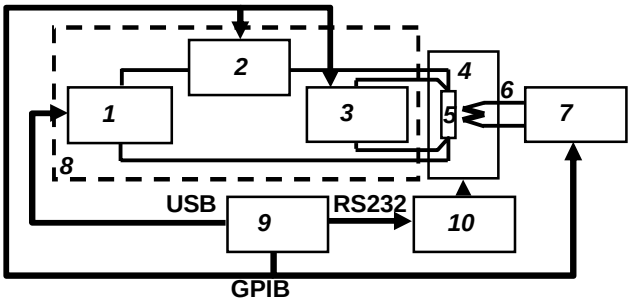

1 – calibrator; *2* – digital multimeter 3458A for current measurement; *3* – digital multimeter 3458A for voltage measurement; *4* – PSM.PM; *5* – electric heater of PSM.PM; *6* – thermo battery of PSM.PM; *7* – nanovoltmeter 34420A; *8* – system of calibration; *9* – PC; *10* – meteometer

Figure 1. Scheme of SCS.

Standard basis is the reference primary calorimetric converter for measuring of average power of optical radiation for fiber-optic communication systems – PSM.PM. SCS works on a replacement method, i.e. necessary accuracy of optical power measurements is reached by replacement of optical power by electric power, that could be measured with high accuracy at calibration of SCS. The system of calibration *8* includes the stabilised source of an electric current – the calibrator *1*, the ampermeter *2* for measurements of a current *I* and the voltmeter *3* for measurements of calibration voltage *U*.

At electric calibration in the calorimetric converter PSM.PM *4* there is a consecutive transformation of electrical power P_s in a thermal power, and then, in its thermobattery, in the analogue electric signal *V* proportional to formed average

thermal power. This signal is measure by nanovoltmeter *7* and define conversion ratio of average power of electric current K_s:

$$K_s = V_e / P_s = V_e / (U_K \times I_K) \quad (1)$$

Having disconnected an electric current source, submit in SCS *4* optical radiation. In a sensor of the calorimeter this radiation is absorbed and will be transformed to the thermal power proportional to average power of radiation. As a result of it, as well as at electric influence, thermo battery PSM.PM *6* reacts to thermal influence and provides occurrence of the electric signal V_O proportional to power of this influence, and, hence, and average power of optical radiation P_O. It allows to made by means of SCS indirect measurements of average power of optical radiation in fiber-optic communication systems and to reproduce this unit:

$$P_O = V_O/(K_s \times K_e \times K_T) \quad (2)$$

where K_e – estimated coefficient of equivalence, K_T – sensitivity coefficient of the calorimeter to changing of environment temperature on 1°C.

All components of SCS can work independently and under control of the personal computer *9*. The program of work SCS provides several algorithms of work with various optical systems.

Reproduction and transfer of the unit of attenuation to secondary and working standards is spent by normalization of its calibration characteristics, and to attenuation measures (optical attenuators) – by method of direct measurements with use of a photo-electric wattmeter with a wide dynamic range and known calibration characteristic. Normalization of calibration characteristic is made by a method of «light addition method».

The complex of MI for reproduction of the unit of attenuation in fiber-optic communication systems consists of variable single mode attenuators FVA-3150-B-EI-EUI-89, variable multimode attenuators FVA-3150-C-EI-EUI-89, photo-electric watt meters with wide dynamic range OET-2 and measurement unit for measurement of calibration characteristic nonlinearity of optical radiation detectors.

Reproduction and transfer of the unit of wavelength is made by measurement wavelength of single-frequency lasers of the standard by comparison of their interferograms, received by a set of Fizeau - interferometers with various bases, with interferogram of the frequency-stabilised laser with known wavelength.

The complex of MI for reproduction of the unit of laser radiation wavelength in fiber-optic communication systems includes wavelength meter WS-U (Angstrom company) on the basis of four vacuumed Fizeau interferometers, calibrated by means of single-frequency laser Clarity-NLL-1541-HP, and spectrum analyzer model 721B (Bristol company).

In the research process of metrological characteristics of the standard the estimation of accuracy of reproduced values of optical radiation average power, conversion ratio of average power of an electric current, coefficient of equivalence, and also influence on reproduction accuracy of the unit of optical radiation average power of such factors, as power level, environmental conditions, power and spectral stability of lasers, an error of used measuring instruments was carried out.

The average value of conversion ratio of average power of an electric current K_s received as a research result is in limits 273±2 mkV/mW, value of coefficient of equivalence K_e does not exceed 1.00009, and value of sensitivity coefficient of the calorimeter to changing of environment temperature on 1°C K_T in limits 0.00025±0.00002. The relative root-mean-square error of reproduction by the standard of the unit of optical radiation average power does not exceed 0.05 %, the relative systematic error in limits ±0.08 %.

The metrological tests shows, that standard provides storage, reproduction and transfer in a spectral range from 0.6 to 1.7 μm of the unit of average power from 0.1 to 5 mW with the relative expanded uncertainty less than 0.2 %, attenuation from 0.05 to 60.00 dB with the expanded uncertainty less than 0.2 dB and wavelength of optical radiation with the relative expanded uncertainty no more than 10^{-6} %.

Bilateral Comparison of Cryogenic Radiometers using Transfer Detectors

Thiago Menegotto[1,*], Thiago Ferreira da Silva[1], Allan Smith[2], Ping-Shine Shaw[2], and Howard W. Yoon[2]

[1]*Optical Metrology Division, National Institute of Metrology, Quality and Technology, Duque de Caxias, Brazil*
[2]*Sensor Science Division, National Institute of Standards and Technology, Gaithersburg, USA*
*Corresponding e-mail address: *tmenegotto@inmetro.gov.br*

A comparison of cryogenic radiometers between NIST and Inmetro using trap detectors is described. The comparison was performed with NIST as the pilot lab so that Inmetro could link to the CCPR intercomparison of cryogenic radiometers. The measurements were performed at three laser wavelengths. The differences are found to be within the combined uncertainties of the intercomparison.

INTRODUCTION

The measurement of optical power, traceable to the International System of Units (SI) is essential for wide ranging applications in basic metrology, such as the realization of the SI base unit of luminous intensity, the candela, to remote sensing, as in climate change studies [1]

At many National Metrology Institutes (NMI), the optical power is measured with an electrical substitution cryogenic radiometer (ESCR), where the optical power is determined by comparison to the electrical watt. A critical step in the validation of the realization of the optical watt is the comparison to other NMIs which have participated in international key comparisons.

The present work describes the preliminary results of a bilateral comparison of ESCR's based on reflection trap as transfer detectors between National Institute of Metrology, Quality and Technology (Inmetro) and the National Institute of Standards and Technology (NIST) (pilot). The purpose of this comparison is to determine the degree of equivalence of Inmetro in the measurement of optical power to the results of the Consultative Committee for Photometry and Radiometry (CCPR).S3 key comparison.

BILATERAL COMPARISON PROTOCOL

For the bilateral comparison, four, 3-element-reflection-trap detectors were measured, two from each participant. The detectors were measured first at NIST, and once at Inmetro, and then at NIST in that sequence in a time duration of one year.

EXPERIMENTAL SETUP: INMETRO

The experimental setup at Inmetro consisted of HeNe and an Ar^+ laser sources, operated at 632.8 nm, 458 nm and 514.5 nm, respectively. The linearly polarized laser beam is spatially filtered and actively stabilized in power at around 100 μW. The ESCR (Cryorad II, Cambridge Research Instruments)* absorbing cavity and the trap detector are positioned at the same distances from the source. The diameter of the gaussian beam at the detection plane is typically 2 mm full-width at half-maximum (FWHM). The Brewster-angled ESCR's window was carefully aligned at each wavelength.

EXPERIMENTAL SETUP: NIST

The measurements at NIST were performed using the Primary Optical Watt Radiometer (POWR) with the same laser sources as at Inmetro. A more detailed description of POWR can be found here [2].

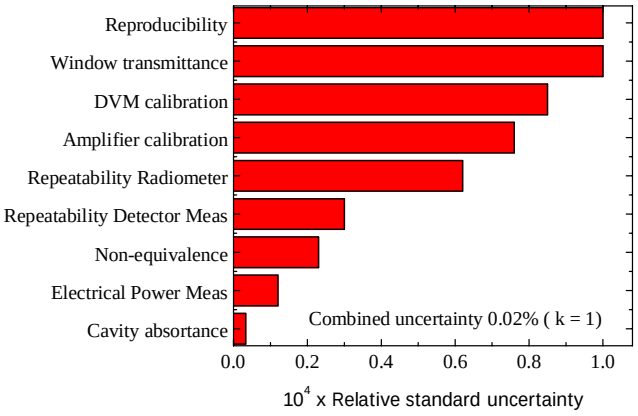

Figure 1. Components of the measurement uncertainty of the responsivity of the transfer detectors measured at Inmetro.

RESULTS AND DISCUSSION

Figure 1 presents the uncertainty components for the measurement of the transfer detectors at Inmetro.

The main contributions to the combined uncertainty are due to the reproducibility and the characterization of the transmittance of the window of the ESCR. The uncertainties at NIST are substantially the same as at Inmetro. The

uncertainties of the comparison results must take into account the long-term stability of the transfer detectors and the repeatability of the NIST measurements.

Figure 2 shows the results of the spectral responsivity for the transfer detectors used in the comparison. The error bars indicate the expanded uncertainty (k=2).

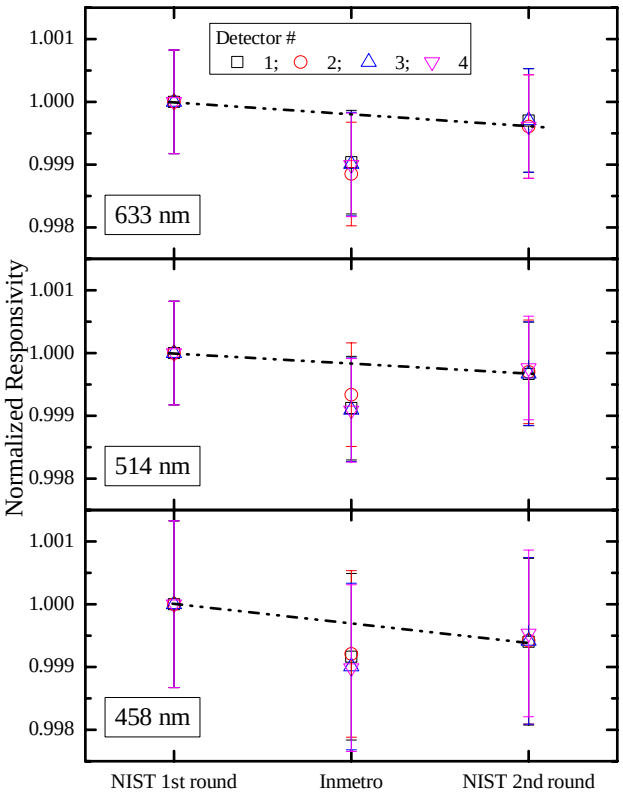

Figure 2. Spectral responsivity of the detectors measured at nominal wavelengths of (a) 633 nm, (b) 514 nm and (c) 458 nm. The results were normalized by the first measurement at each wavelength.

The results of the measurements at both institutes agree under the normalized error criterion for all wavelengths.

All detectors exhibit a considerable drift from the first to the second round of measurements at NIST. This drift, which was considered in the measurement uncertainty, is more pronounced for the 458 nm wavelength. This kind of ageing behaviour was also an issue for the CCPR S3 comparison [3] and might indicate that these types of trap detectors are not well suitable as transfer detectors for this kind of comparison.

Figure 3 depicts the spectral responsivity at nominal wavelengths of 458 nm, 514 nm and 633 nm for a trap detector which was held at Inmetro, hereafter named *reference detector*.

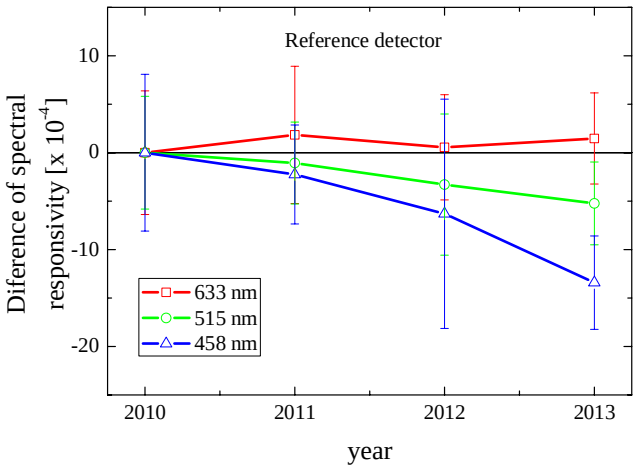

Figure 3. Variation of spectral responsivity of the reference detector at nominal wavelengths of 633 nm, 514 nm and 458 nm as measured at Inmetro over the course of three years.

The results clearly show a spectrally-dependent temporal behaviour of the responsivity. Again, the shorter the wavelength in the range, the bigger the drift. The maximum variation is about 0.06% at 458 nm, then reduces to 0.02% at 515 nm, and becomes 0.01% at 633 nm.

CONCLUSION

A bilateral comparison of ESCR's was performed between the NIST (pilot) and the Inmetro. Four trap detectors were used as transfer standards. The devices were measured at both institutes in a one-year time span. The results for both institutes agree under the normalized error criterion, in spite of the systematic off-set of Inmetro's results.

REFERENCES

1. A. C. Parr, "A National Measurement System for Radiometry, Photometry and Pyrometry Base Upon Absolute Detectors." NIST TN 1421, Washington DC, 1996.
2. J. M. Houston and J. P. Rice, "NIST reference cryogenic radiometer designed for versatile performance," Metrologia, 43, S31-S35, 2006.
3. R. Goebel, M. Stock and R. Koehler, "Report on the International Comparison of Cryogenic Radiometers based on transfer detectors," BIPM-2000/9, 2000.

*Certain commercial equipment, instruments, or materials are identified in this paper to foster understanding. Such identification does not imply recommendation or endorsement by the National Institute of Standards and Technology, nor does it imply that the material or equipment are necessarily the best available for the purpose.

SI-traceable calibrations and nonlinearity measurements of current-to-voltage convertors

T. C. Larason, G. P. Eppeldauer, H.W. Yoon, and D. G. Jarrett

National Institute of Standards and Technology, Gaithersburg, Maryland, USA
Corresponding e-mail address: thomas.larason@nist.gov

Current-to-voltage convertors are used in many photometric and radiometric applications. The calibration of current-to-voltage convertors at one or a few input currents is not always sufficient. The linearity of the device is of equal, or in some applications, greater concern than the gain calibration. The National Institute of Standards and Technology has developed a system to calibrate the gain and nonlinearity of current-to-voltage convertors. Measurements of several current-to-voltage convertors have shown a larger than expected nonlinearity such that the nonlinear component of the gain uncertainty dominates the budget. In some cases the nonlinearity varies greatly with input current in a pattern that is not easily described and may limit the realistically achievable uncertainty. The equipment used for the calibration is described and the results and uncertainties are discussed.

INTRODUCTION

Current-to-voltage convertors are key elements in photocurrent measurement and are used in many photometric and radiometric applications. The reductions in the uncertainties of other components have made the amplifier calibration uncertainty a large contributing factor to the overall uncertainty budget. Advances have also been made in reducing the uncertainty in the calibration of current-to-voltage convertors [1].

The National Institute of Standards and Technology (NIST) has developed a calibration system with low, current-measurement uncertainty which is capable of < 20 $x10^{-6}$ expanded uncertainties in the current determinations to calibrate the gain current-to-voltage convertors [2]. A current source was programmed to output currents with defined steps so that the preamplifier gains can be calibrated over the entire output range. This system was used to measure three commercially available amplifiers. The larger than expected nonlinearities observed with some amplifiers may limit the realistically achievable uncertainty for typical photometric or radiometric applications.

SETUP AND MEASUREMENTS

The NIST amplifier calibration system consists of a precision current source and digital voltmeter [3]. The current source is calibrated using the NIST transfer-standard current-to-voltage convertor to < 20 $x10^{-6}$ expanded uncertainties in the current determinations [2]. The current-to-voltage conversion (gain) of the test amplifiers were measured over their output voltage range, ± 10 V or ± 5 V, in 0.5 V steps so that the gains over the entire range can be calibrated to the uncertainties of the current determinations. A least-square linear fit was applied to the output voltages and the residuals were calculated to determine the deviations from a linear fit. This was repeated for each amplifier gain range from 10^4 [V/A] to 10^9 [V/A]. A settling time of 5 s was used at each current setting and the amplifier (zero current) offset voltage was measured once for each gain range and subtracted from all the measurements for that range.

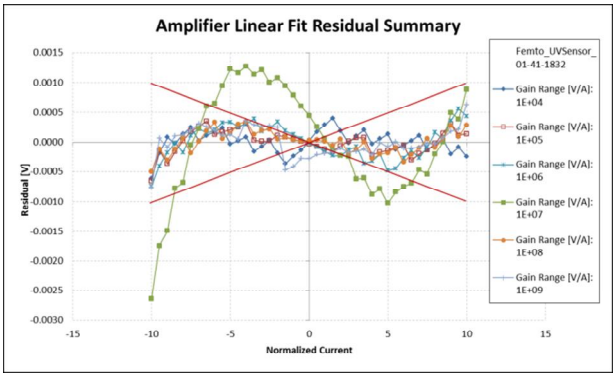

Figure 1. Graph of Amplifier #1 linear fit residuals for each gain range. The straight lines indicate 100$x10^{-6}$ uncertainties.

RESULTS AND DISCUSSION

The amplifier nonlinearity is shown for each amplifier in Fig. 1, 2, and 3. Fig. 1 shows the linear fit residuals for Amplifier #1. The 100$x10^{-6}$ (100 ppm) uncertainties are shown as straight lines. Most of the ranges are linear to within these uncertainties.

The residuals at 10^7 gain are significantly larger than the other ranges. This is repeatable. In Fig. 2, Amplifier #2 shows an unexpected saw-tooth pattern which is repeatable for each range. The cause of the larger deviations near zero current for gain 10^7 and 10^9 is unknown. The residuals are well within the 100 ppm lines shown in Fig. 2

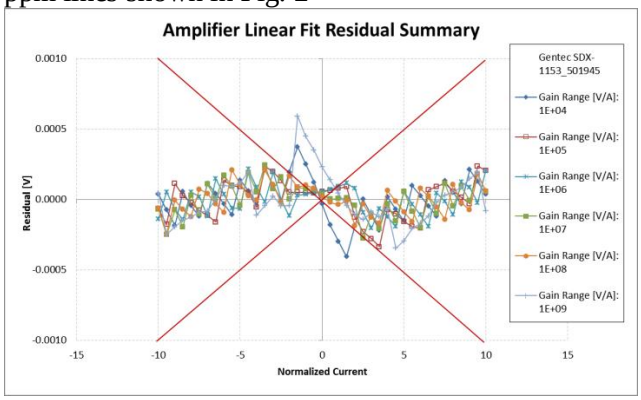

Figure 2. Graph of Amplifier #2 linear fit residuals for each gain range. The saw-tooth pattern is repeatable for each range. The cause of the larger deviations near zero current for gain 10^7 and 10^9 is unknown. The straight lines indicate 100 ppm uncertainties.

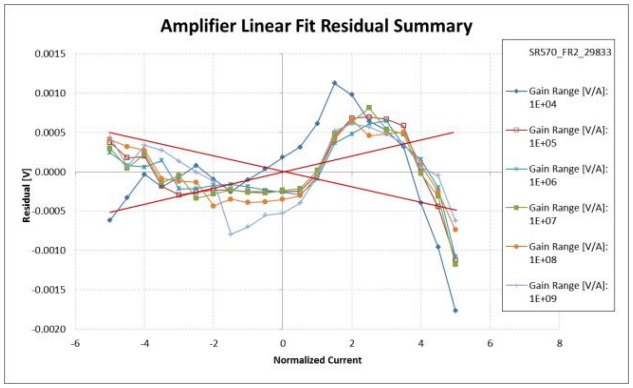

Figure 3. Graph of Amplifier #3 linear fit residuals for each gain range. The curvature in the residuals for positive current values in unknown. The straight lines indicate 100 ppm uncertainties.

Fig. 3 shows a curvature in the residuals for positive current values. The cause of this curvature is unknown and problematic for assigning calibration values and uncertainties.

The question arises whether to include in a calibration the analysis to quantify the various patterns seen in the output voltages or just include the variation as an uncertainty component. If the deviations are substantially outside the 100 ppm values, then a polynomial fit can be performed to reduce the residuals.

REPEATABILITY

To test the repeatability of the calibrations, all the amplifiers were measured at least 5 times. The measurements repeat well. In Fig. 4, the mean and the standard deviations of the 5 measurements of Amplifier #3 at a representative gain of 10^7 are shown. This clearly shows that a single slope of the V/A cannot be used to set the gain.

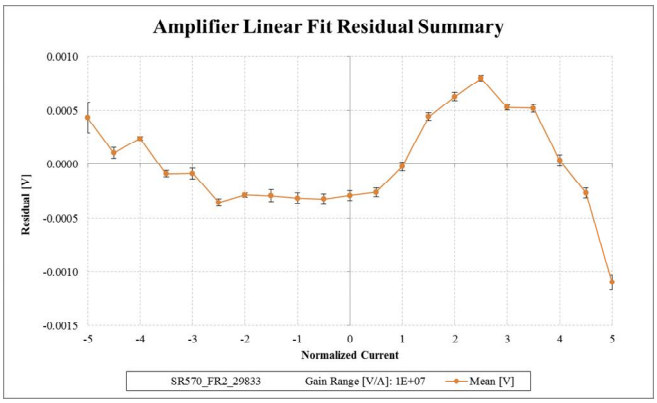

Figure 4. The mean and the standard deviation of 5 measurements at gain 10^7 of Amplifier #3.

CONCLUSIONS

Current-to-voltage preamplifiers have been measured over the output voltages of interest at each gain setting. Difference preamplifiers have been found to deviate from linear behaviour substantially outside the achievable uncertainties. The low uncertainties of preamplifier gains can only be realized by measuring over the entire gain range of interest.

REFERENCES

1. P. Sipila, et al, Calibration of current-to-voltage converters for radiometric applications at picoampere level, in Proceedings of NEWRAD (Davos, Switzerland), edited by J. Grober, pp 17–19, 2005.
2. G. P. Eppeldauer, et al, Development of an in situ calibration method for current-to-voltage converters for high-accuracy SI-traceable low dc current measurements, IOP Publishing, Metrologia, Vol. 50, p. 509-517, 2013.
3. G. P. Eppeldauer, Traceability of photocurrent measurements to electrical standards, Natl. Inst. Stand. Technol., Tech. Note 1621, 2009.

Establishment of Pulsed Laser Energy Measurement Scale

Özcan BAZKIR

National Metrology Institute (UME),TURKEY

A method linking pulse energy scale to continuous-wave (CW) power scale is described. CW power scale is realized with Electrical Substitution Cryogenic Radiometer and transferred to working standards via photodiode based trap detectors and Electrically Calibrated Pyroelectric Radiometer. The reference and working standards intended to be used for the pulse laser measurement are calorimeter and pryroelectric based laser energy meter. The connection between CW power and pulse energy is established by generating a train of pulses from CW beam, and correlating the CW signal measured by radiometer and pulsed-signal measured by calorimeter. In this connection CW laser source from which pulses are generated is Nd:YAG laser and the lengths of pulses adjusted are at the order of milliseconds. The realized energy scale is transferred from calorimeter to laser energy meters through using pulsed Nd:YAG laser having one fundamental (at 1064 nm) and two harmonics (at 532 nm and at 365 nm) with nano-second level pulse length . These pulsed laser sources with its harmonics are also used for the optical characterization of calorimeter and laser energy meters.

Key Words: Calorimeter, Radiometer, Pulse Laser

Detector-based terahertz radiometry: scale realization with reduced uncertainty

Andreas Steiger and Ralf Müller

Physikalisch-Technische Bundesanstalt, Berlin, Germany
Corresponding e-mail address: Andreas.Steiger@ptb.de

As part of its official services PTB offers the calibration of terahertz detectors from 1 THz to 5 THz. A detector-based calibration facility is operated with a far-infrared molecular gas laser and a novel THz detector standard. The radiation absorber of a commercial thermopile detector was exchanged to a NG1 neutral filter glass with optically polished surfaces and a gold coating on its back side. Thus, a precise calibration of this detector by means of a HeNe laser yields a THz power responsivity scale traced back to SI with a standard uncertainty as low as 1.2 %.

INTRODUCTION

The terahertz spectrum is the last spectral range of optical radiation where radiometry was not well established. PTB is the first national metrology institute which offers the calibration of THz detectors as part of its radiometric services. In order to determine the spectral responsivity with respect to radiant power traceable to the International System of Units SI in the THz spectral range, PTB operates a THz detector calibration facility [1].

THZ CALBRATION FACILITY

Its design (Fig. 1) is based on a pilot experiment of measuring the power of a quantum cascade laser at 2.52 THz and the very first calibration of a THz detector against a cryogenic substitution radiometer of PTB [2].

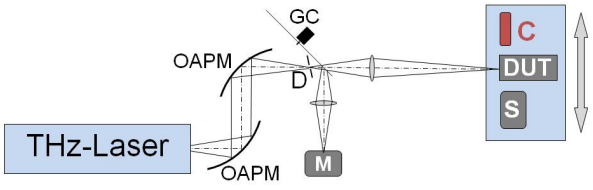

Figure 1. Sketch of the THz calibration facility.

Now the THz laser source for detector-based radiometry is a far-infrared molecular gas laser. It is running at 2.52 THz but can also be operated at a variety of discrete molecular lines of different gases at laser frequencies spanning from 1 THz and 5 THz. Pumped by a frequency stabilized CO_2 laser, this continuous wave laser delivers monochromatic THz radiation power of several milliwatts. A nearly Gaussian like beam profile is achieved by focusing the divergent laser output by two off-axis parabolic mirrors (OAPM) to an iris aperture (D). It acts as spatial filter by adjusting its position and diameter. A chopper with a gold-plated blade (GC) of 200 mm diameter and two slots symmetrically modulates the power and splits it into two beams. The reflected part is focused with a Tsurupica lens on a monitor detector (M) which is used to correct for any changes of the output power of the laser during the measurement. The transmitted beam is also focused by another lens on the detector under test (DUT).

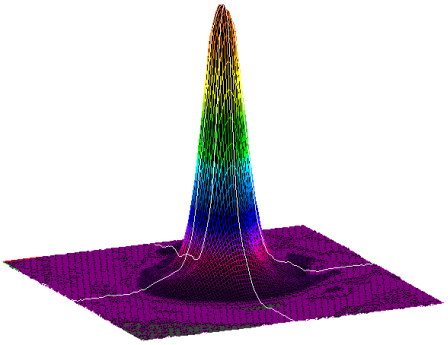

Figure 2. 3D-plot of a typical focal beam profile of the molecular gas laser at 1.4 THz. The sensitive area of the THz camera is 12 mm x 12 mm

The calibration procedure consists of three steps: First the focal beam profile is recorded by a THz camera (C), cf. Fig. 2. Then the THz radiant power is determined by a standard detector (S) with known responsivity. Finally, the DUT is moved into the focus of the THz beam at exact the same position as the standard detector. Special care is taken to assure that the THz radiation impinges totally the absorbing surface of the detectors without any clipping losses.

NOVEL THZ STANDARD DETECTOR

The power responsivity of the novel standard detector is well known, i.e. traced back to the International System of Units (SI). This is achieved by its special designed radiation absorber which renders possible the application of a simple physical model which

accounts for the frequency dependence of its radiation losses. As a consequence a calibration at a single frequency that may or may not be within THz range is sufficient to calculate the spectral variation of its responsivity because both parameters of the model, the surface reflection and the transmission of the absorber, were measured before [3].

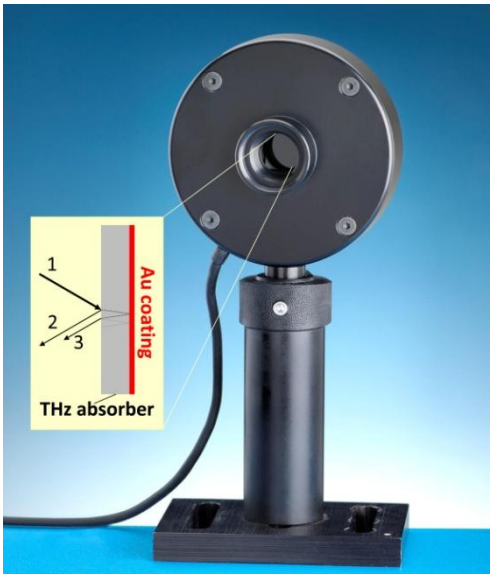

Figure 3. Photo of the new THz detector standard. The cutaway view exhibits a schematic cross-section of the THz radiation absorber with a gold (Au) coating on its back side.

Shown in Fig.3, the new THz standard detector is a modified commercial thermopile detector, model 3A-P from Ophir Optronics Ltd. It uses a thin disk made of NG1 neutral density filter glass from Schott AG as radiation absorber. This is exchanged by a new NG1 disk of same dimensions but with optically polished surfaces on both sides and its back side is coated with a thin gold layer (Au) acting as a mirror for the residual transmitted radiation (Fig. 3). Thus, a second absorption process takes place on the way back to the surface. Sufficient absorption of THz radiation (1) by the doubled absorption path is indicated by the absence of interference (3) on the beam reflected (2) from the front surface of the NG1 disk. The reflected part $R(v)$ is measured as ratio of reflected and incident radiation at any laser frequency v. Then the absorbance $A(v)$ of the NG1 disk is given by the model: $A(v) = 1 - R(v)$ and the power responsivity $s(v)$ is simply proportional to $A(v)$.

NEW THZ POWER RESPONSIVITY SCALE

As NG1 absorbs in the visible spectral range as well the reflection loss could be accurately measured with a HeNe laser $R_{HeNe} = 4.38\,\%$. The model results in $s(v) = s_{HeNe}/0.9562 * [1 - R(v)]$. The power responsivity s_{HeNe} is calibrated with 0.2% standard uncertainty at the optical laser radiometry lab of PTB.

The combined standard uncertainty of the new THz power responsivity scale of the modified thermopile as THz standard detector in the spectral range from 1 THz to 5 THz is reduced to $1.2\,\%$ which is more than a factor of six lower than before [3]. The reduced uncertainty results from the absence of any black paint as THz radiation absorber because all optical black coatings become more and more transparent when the optical wavelength is increased to the long wavelengths of THz radiation. Namely, the main uncertainty of the previous traceability is caused by the limited absorbance of the black paint inside the radiation absorbing cavity of the cryogenic substitution radiometer which is known as most accurate primary detector for visible radiation.

By the innovation of tracing back the power responsivity of the THz standard detector by means of visible laser radiation the THz detector calibration facility is now in operation in order to calibrate customer´s detectors with an uncertainty as low as 1.7 % in the frequency range from 1 THz to 5 THz. A prerequisite to achieve this low uncertainty for a DUT is its sufficiently uniform spatial responsivity. In addition special care has to be taken to avoid standing waves caused by interference of the incoming THz radiation with any non absorbed residual radiation e.g. reflected from the surface of the DUT.

ACKNOWLEDGMENT

Part of this work is supported by the ongoing joint research project “THz Security” with the number NEW07 within the European Metrology Research Program (EMRP). The EMRP is jointly funded by the EMRP participating countries within EURAMET and the European Union.

REFERENCES

1. A. Steiger, B. Gutschwager, M. Kehrt, C. Monte, R. Müller, J. Hollandt, “Optical methods for power measurement of terahertz radiation,” *Optics Express* **18**, 21804-21814, 2010
2. L. Werner, H-W. Hübers, P. Meindl, R. Müller, H Richter, A. Steiger, “Towards traceable radiometry in the terahertz region,” *Metrologia* **46**, S160–164, 2009
3. A. Steiger, M. Kehrt, C. Monte, R. Müller, “Traceable terahertz power measurement from 1 THz to 5 THz,” Optics Express **21**, 14466-14473, 2013

Experimental validation of the predictability of a Predictable Quantum Efficient Detector by a direct intercomparsion

Ingmar Müller[1], Chi Kwong Tang[2], Jarle Gran[2], and Lutz Werner[1]

[1]*Physikalisch-Technische Bundesanstalt, Berlin, Germany*

[2]*Justervesenet, Kjeller, Norway*

Corresponding e-mail address: ingmar.mueller@ptb.de

The Predictable Quantum Efficient Detector is a potential radiometric primary detector standard for the wavelength range from 400 nm to 900 nm. It is based on custom made photodiodes with a surface-charge-induced p-n-junction. The experimental validation of Predictable Quantum Efficient Detectors by comparison with cryogenic radiometers showed an agreement of the measured and calculated spectral responsivity within the combined uncertainties of the measurements and the calculations. For the validation of the expected reduction of the uncertainties associated with the prediction of the spectral responsivity by means of advanced software models, the uncertainties achievable with cryogenics radiometers are not sufficient. Here the experimental validation of detectors with predictable quantum efficiency based on a direct comparison of these detectors is described. The uncertainties of this comparison are expected to be considerably smaller than those achievable with cryogenic radiometers.

INTRODUCTION

The Predictable Quantum Efficient Detector (PQED) [1,2] is a potential photodiode based radiometric primary detector standard with a special "wedge" design. The photodiodes applied in this novel type of detector are, so-called, induced junction photodiodes [3]. The prediction of the responsivity of the PQED is, up to now, based on the one-dimensional modelling of the internal quantum deficiency of the photodiodes [4] and the calculated [5] and measured reflectance [1]. However, the comparison of the measured and predicted internal quantum deficiencies of the PQED [2] indicated a systematically underestimation of the predicted internal quantum deficiency [1]. To overcome this issue, enhanced three-dimensional software models are used at Justervesenet to reduce the uncertainties of the predicted internal quantum deficiency. To test the validity of the prediction made by three-dimensional modelling with the lowest uncertainties a direct comparison of PQEDs is necessary to meet the required level of uncertainty. The PQEDs to be compared are made of either identical photodiodes or of photodiodes with different critical parameters as bulk doping concentration, induced surface charges and backside doping of the photodiode. Thus, a check of the predicted responsivity on the parameters mentioned above can be made with very low uncertainties. In addition, the comparison of allegedly identical PQEDs allows checking the uniformity of the critical parameters over the batch of produced photodiodes. The use of an UHV environment for all the measurements assures that the possible influence of adsorbates at the photodiode surface on the measured responsivity can be minimized. The results of these measurements will be used to validate and enhance the software models to predict the responsivity of PQEDs used within EMRP JRP SIB57 NEWSTAR.

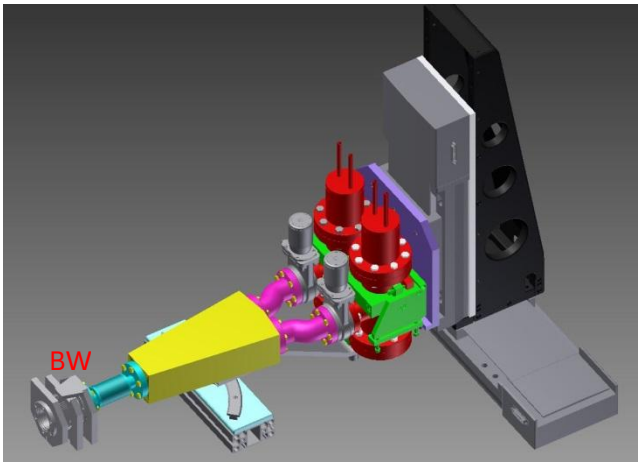

Figure 1. Setup for the UHV comparison of PQEDs. The PQED-cryostats are red colored. The detectors are are mounted on an x-y-stage and connected to the Brewster-window (BW) via flexible bellows.

EXPERIMENTAL SETUP

The setup for the direct comparison of PQEDs, shown in Fig. 1, has been designed to meet the following requirements: UHV compatibility, use of a

shared Brewster-window, operation at room temperature and the temperature of liquid nitrogen, use of intensity stabilized p-polarized laser radiation, measurement of the photocurrent of each detector at an identical position relative to the laser beam. The cryostats (see Fig. 2) are equipped with a mechanism that allows tilting and rotation of the cryostats in order to align the PQEDs to the laser beam. The angle between the photodiodes can be set to values of 9°, 11.25°, and 15° yielding 11, 9 or 7 internal reflections, respectively. The angle between the laser radiation and the lower photodiode (hit first by radiation) is 45°.

UNCERTAINTIES

A comparison of the uncertainties achieved in [2] during the experimental validation of the PQED and the expected uncertainties occurring in the direct comparison of PQEDs is shown Table 1. Because the photo and dark currents of the two compared PQEDs are expected to be almost identical and will be measured with the same equipment, the uncertainty of the photocurrent measurement can be drastically reduced. Furthermore, all uncertainty contributions associated with the cryogenic radiometer can be omitted. Additionally, the influence of the stray light can be reduced assuming that the apertures in front of the PQEDs are almost identical in diameter. Due to the reduced measurement times with semiconductor based detectors of seconds (several minutes with cryogenic radiometer) the influence of the laser stability can be reduced as well.

Hence, the predictions on the responsivity dependence on critical parameters made by the three-dimensional software modelling can be tested and validated with uncertainties well below the 10 ppm level.

Table 1. Comparison of the expected relative standard uncertainties occuring for the experimental validation of a PQED against a cryogenic radiometer (CR) and directly against another PQED. The uncertainties for the comparison CR-PQED are taken from [2].

Source of uncertainty	**Comparison CR-PQED**	**Comparison PQED-PQED**
Photocurrent PQED	10 ppm	1 ppm
Cavity absorptance CR	13 ppm	0 ppm
Stray Light	20 ppm	5 ppm
Heater power CR	10 ppm	0 ppm
Typical laser stability	4 ppm	2 ppm
Wavelength	2 ppm	1 ppm
Non-equivalence CR	7 ppm	0 ppm
Measured reflectance PQED [1]	< 1 ppm	< 1ppm
Combined relative standard uncertainty	**29 ppm**	**6 ppm**

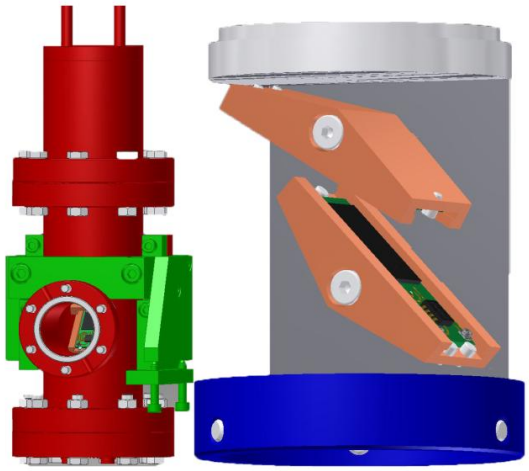

Figure 2. Left Side: Drawing of the UHV-cryostat, designed to incorporate the PQED (red) and holding and alignment mechanism (green). Right side: Inset of the cryostat (not in scale). The two photodiodes are mounted on adjustable holders (copper). The angle between the photodiodes can be set to 9°, 11.25°, and 15°.

ACKNOWLEDGEMENT

This work was funded by the project NEWSTAR (contract SIB57) of the European Metrology Research Programme (EMRP). The EMRP is jointly funded by the EMRP participating countries within EURAMET and the European Union.

REFERENCES

1. Sildoja M., et al., Predictable quantum efficient detector: I. Photodiodes and predicted responsivity. *Metrologia*, *50*(4), 385–394, 2013.
2. Müller I., et al., Predictable quantum efficient detector: II. Characterization and confirmed responsivity. *Metrologia*, *50*(4), 395–401, 2013.
3. Hansen T. E., Silicon UV-Photodiodes Using Natural Inversion Layers. *Physica Scripta*, *18*, 471–475, 2013.
4. Gran J., et al., Simulations of a predictable quantum efficient detector with PC1D. *Metrologia*, *49*(NEWRAD), S130–S134, 2012.
5. Sildoja M., et al., Reflectance calculations for a predictable quantum efficient detector. *Metrologia*, *45*(1), 151–154, 2007.

Measurement of Spectral Irradiance Responsivity of Filter Radiometers

Denis Otryaskin, Boris Khlevnoy, Valeriy Gavrilov, and Maxim Solodilov

All Russian Research Institute for Optical and Physical Measurements (VNIIOFI), Moscow, Russia
Corresponding e-mail address otryaskin@vniiofi.ru

VNIIOFI participates in the Consultative Committee for Thermometry working group 5 "Radiation Thermometry" (CCT-WG5) international project on investigation of high temperature fixed points (HTFPs) [1]. Piloted by the National Physical Laboratory Workpackage 5 (EMRP Project: SIB01 InK Workpackage 1) of the project [2] is dedicated to the measurements that will result in definitive thermodynamic temperatures being assigned to a set of high temperature fixed points of Co-C, Pt-C and Re-C. For determining the HTFPs thermodynamic temperatures a radiance-mode radiation thermometer is used. The thermometer is calibrated against an irradiance-mode filter radiometer (FR) with known spectral irradiance responsivity via a variable-high temperature blackbody. This paper is devoted to VNIIOFI's measurements of spectral irradiance responsivity of the FR.

DESIGN OF FILTER RADIOMETER

Three identical FRs were involved to measurements. Each FR is a combination of a silicon photodiode Hamamatsu S1337BQ, two glass filters (blue-green and green) and a black coated thin metal aperture with a diameter of about 5 mm. The glass filters are tilted at the angle 1,5º from the aperture plane (Fig. 1).

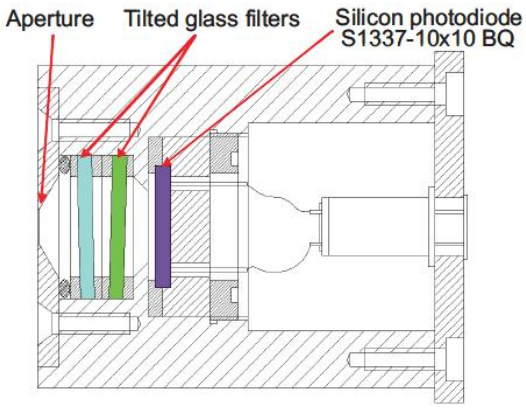

Figure 1. Design of the filter radiometer.

The relative spectral responsivity of the photodiode S1337BQ and spectral transmission curves of the filters are shown in Fig. 2.

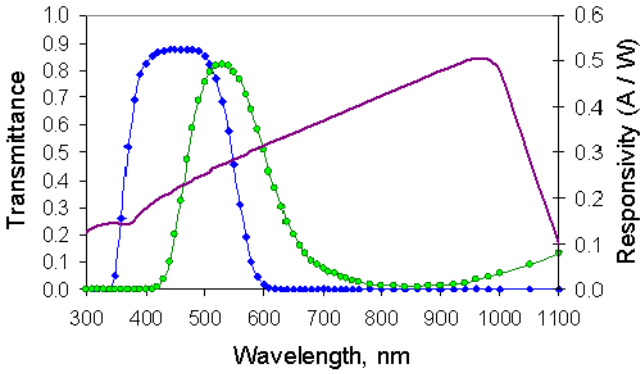

Figure 2. Relative spectral responsivity of the photodiode and the spectral transmission curves of the blue-green and green filters.

SPECTRAL COMPARATOR

The FRs were compared against three different trap detectors (TDs) by use of the spectral comparator facility. Each TD was preliminarily calibrated in terms of spectral power responsivity against a cryogenic radiometer with expanded uncertainty of 0.025 %. During the comparing each TD was equipped with a precise aperture with a diameter *d* of about 5 mm measured with standard uncertainty of 0.02 %.

The spectral comparator facility is based on a 1 m double grating monochromator with an extremely low scattering light (10^{-14}), high wavelength repeatability (≤ 0.01 nm) and bandpass of about 1 nm. In front of the entrance slit of the monochromator (4) (Fig. 3) there are a filter wheel (7) and a shutter (8). The entrance slit was eliminated by a halogen lamp source (5). The mirrors (6) mounted behind the exit slit form a quasi-parallel beam that overfills the detector apertures. The FR (1) and the TD (2) were installed on a translation stage (3). The detectors and the exit slit of the monochromator was covered with a light-tight box (9). The FRs and the TDs were equipped with a water jacket. Temperature of the detectors was maintained within 20±0.2 ºC. The same amplifier and digital

voltmeter were used for measuring signals of both the TD and the FR.

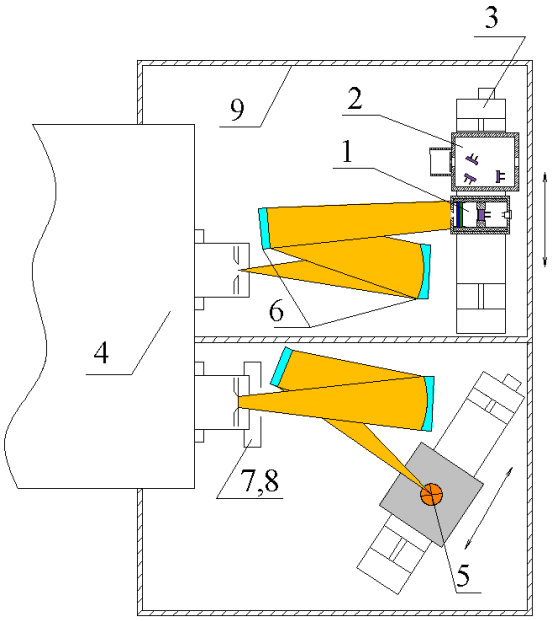

Figure 3. Facility for comparing the filter radiometer and the trap detector.

MEASUREMENT OF FILTER RADIOMETER SPECTRAL IRRADIANCE RESPONSIVITY

At first it was found the spatial domain of the most uniform irradiance by translating the FR inside the illuminating beam. Signals of the detectors were measured within the spectral range from 405 nm to 600 nm with a step of 1.5 nm in the following order: TD-FR-TD. The last was aimed to reduce effect of the lamp drift.

The spectral irradiance responsivity of the FR was calculated as

$$S_{FR}(\lambda) = R_{FR/TD}(\lambda) \cdot s_{TD}(\lambda) \cdot \pi \cdot d^2 / 4 \quad (1)$$

where $R_{FR/TD}(\lambda)$ is the ratio of the measured signals, $s_{TD}(\lambda)$ is the spectral power responsivity of the TD and d is the diameter of the TD aperture.

The wings of the FR spectral responsivity curve were measured separately by use of the more powerful source (xenon lamp) up to the level of 10^{-6} with respect to the maximal value and farther were estimated. Finally the resulting spectral irradiance responsivity curve was determined for each FR in the range from 351 nm to 705 nm. The typical curve is shown in Fig. 4.

UNCERTAINTY BUDGET

The sources of uncertainty in measurement of the FR spectral irradiance responsivity and their contributions to the resulting thermodynamic temperature of the Re-C fixed point (≈2748 K) are summarised in Table 1 [3].

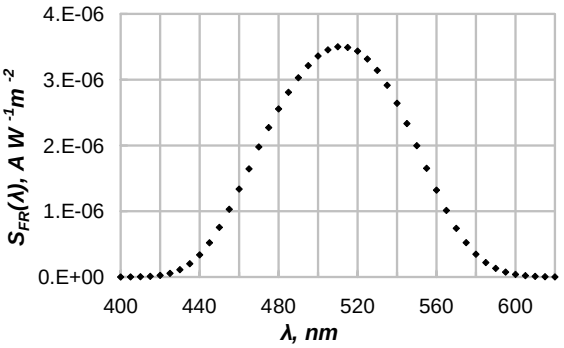

Figure 4. Spectral irradiance responsivity of the filter radiometer.

Table 1. Uncertainty budget in measurement of the filter radiometer spectral irradiance responsivity.

Uncertainty component	Type	Standard uncertainty, K
TD spectral responsivity	B	0.03
Diameter of TD aperture *d*	B	0.03
Monochromator wavelength setting	B	0.07
Reproducibility of FR spectral responsivity	A	0.05
Nonequivalence of measuring flux	B	0.1
Discrepancy between TDs	B	0.1

The relative combined standard uncertainty of the FR spectral irradiance responsivity is 0.08% at the maximum wavelength (λ≈510 nm).

Discrepancy between three FRs contributes an additional component of 0.08 K to the standard uncertainty of the Re-C fixed point thermodynamic temperature.

REFERENCES

1. G. Machin, P. Bloembergen, J. Hartmann, M. Sadli, Y. Yamada, A concerted international project to establish high temperature fixed-points for primary thermometry, Int. J. Thermophys., 28, 1976-1982, 2007.
2. E. R. Woolliams, P. Bloembergen, G. Machin, Proposed process for estimating definitive temperatures of high temperature fixed-points, Int. J. Thermophys., 2014, to be published.
3. V. R. Gavrilov, B. B. Khlevnoy, D. A. Otryaskin, I. A. Grigorieva, M. L. Samoylov and V.I. Sapritsky, Measurement of thermodynamic temperature of high temperature fixed points, in proceedings AIP Conference Proceedings 1552, edited by AIP Publishing LLC, 329-334, New York, 2013.

Devices for characterizing the wavelength scale of UV spectrometers

Peter Blattner[1], Stella M. Foaleng[1], Steven van den Berg[2], Omar El Gawhary[2], M. Blumthaler[3], Julian Gröbner[4], and Luca Egli[4]

1Federal Institute of Metrology, Bern-Wabern, Switzerland, 2VSL, Delft, The Netherlands,3Innsbruck Medical University, Biomedical Physics, Innsbruck, Austria, 4Physikalisch-Meteorologisches Observatorium Davos, World Radiation Center (PMOD/WRC), Davos Dorf, Switzerland

Corresponding e-mail address: peter.blattner@metas.ch

Accurate wavelength calibration is a key parameter for solar spectral measurements. Typically, spectroradiometers are calibrated with spectral emission lines. However, for small spectral ranges only few lines are typically available. Within the framework of an EMRP ENV03 Project solarUV, different devices were realized

INTRODUCTION

For the measurement of solar UV radiation that reaches the earth, there is a need for improved accuracy of the wavelength scale. Due to absorption by ozone for wavelengths below 330 nm, a large dynamic range is required for measuring spectral irradiance throughout the solar UV wavelength range (280-400 nm). This also puts stringent requirements on the accuracy of the wavelength scale, since a small difference in wavelength implies a large difference in spectral irradiance, when measuring close to the edge of the ozone absorption. For this reason a wavelength accuracy of 50 pm is needed. In order to compare and to calibrate the wavelength scale of UV spectroradiometers, different type of devices were designed, realized, characterized and compared.

METAS realized devices based on different Fabry-Perot etalons. VSL developed a wavelength ruler that is based on a one-stage Lyot filter.

FABRY PEROT ETALON DEVICES

Initial work on Fabry Perot etalon has been presented by Balmer and Heuberger [1] using an Fabry-Perot etalon based on Mica. Unfortunately Mica has a high absorptance in the UV region. In the frame work of the EMRP-project ENV03 "Traceability for surface spectral solar ultraviolet radiation"different Fabry-Perot etalons were realized and characterized with respect to temperature, uniformity and angular dependences. The Fabry-Perot is based on a thin layer of fused silica coated on both sides by semi transparent mirrors. For this purpose a 525 μm thick SiO2 (silica) substrate was used as support. A first mirror was created by sputtering a 10 nm thick Al layer on one side of the substrate. At the next step a 3 μm to 9 μm thick fused silica layer was created using a Low Pressure Chemical Vapor Deposition at Low Temperature Oxide (LPCVD-LTO) process. A second Al mirror was deposited with a thickness of 10 nm using sputtering process. Figure 1 shows the transmittance

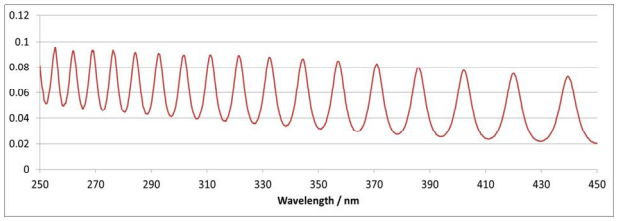

Figure 1. Spectral transmittance of the FP devices

ONE-STAGE LYOT FILTER

VSL has designed and developed a one stage Lyot filter consists of two linear polarizers with transmission axes aligned to each other. Between the polarizers a birefringent quartz plate is inserted with its crystal axes (slow and fast axis) aligned at 45° with respect to the polarization axis. The quartz plate has a nominal thickness of 0.7 mm and is thermally stabilized within 0.1 °C. Due to the birefringence of the material, a polarization rotation is induced. The polarization state after the quartz plate depends on thickness, refractive index and wavelength of the light. As a result, the amount of light that is transmitted by the second polarizer is wavelength dependent (see Fig2)

COMPARISON OF THE DEVICES

To validate the different methods a direct comparison of the devices took place in January 2013 in Davos. Three different spectrometers were characterized with both devices. Furthermore two fixed laser

wavelengths have been measured as additional references. The results of both approaches are very promising and may allow decreasing the uncertainty of wavelength calibration in UV spectrometers to below the 0.05 nm level.

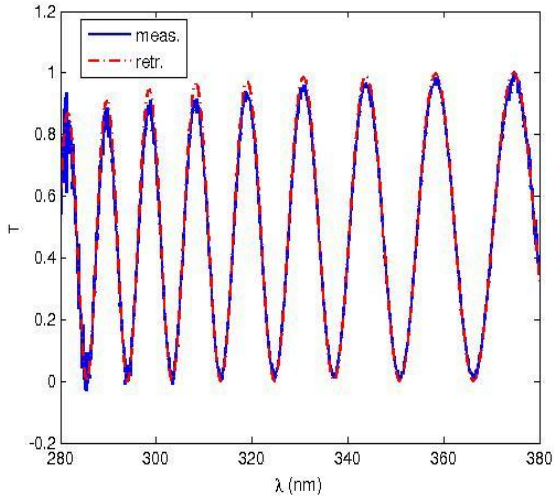

Figure 2. Measured and retrieved (simulated) spectral transmittance of the birefringence-based wavelength ruler.

REFERENCES

1. Perret, E., Balmer, T., & Heuberger, M., Self-consistent algorithm for calibrating spectrometers to picometer accuracy over the entire wavelength range. Appl Spectrosc. , 2010, Vol 64(10), p 1139-44.

Comparison of WC-C peritectic fixed point cells between VNIIOFI, NIM and NMIJ

Naohiko Sasajima[1], Boris Khlevnoy[2], Irina Grigoryeva[2], Wei Dong[3], Tiejun Wang[3], and Yoshiro Yamada[1]

[1]*National Metrology Institute of Japan (NMIJ), AIST, Tsukuba, Japan,*
[2]*All-Russian Research Institute for Optical and Physical Measurements (VNIIOFI), Moscow, Russia,*
[3]*National Institute of Metrology (NIM), Beijing, China*
Corresponding e-mail address: n.sasajima@aist.go.jp

Three WC-C peritectic fixed-point cells of VNIIOFI, NIM, and NMIJ, constructed from different sources of tungsten and with different design of graphite crucibles, were compared to evaluate the melting temperature reproducibility for the first time. The VNIIOFI and NMIJ cells agreed within 0.05 K at 3021 K, while the melting temperature of the NIM cell was 0.4 K lower than that of VNIIOFI cell. The result confirms that good quality WC-C cells agree within 0.05 K, which proves the potential reliability of the WC-C cell as temperature reference above 3000 K.

INTRODUCTION

High-temperature fixed points (HTFPs) are very important for optical radiometry, especially for blackbody-based radiometry. HTFPs of metal-carbon (M-C) eutectics are currently the subject of an extensive international investigation within the joint CCT/CCPR project "HTFP research plan". To supplement these projects by undertaking what is not covered but has significant impact in high-temperature thermometry and radiometry, inter-NMI comparisons of two fixed points, the WC-C peritectic point (3021 K) and the Ru-C eutectic point (2227 K), were conducted in the APMP TC Initiative project "Extending the frontier of HTFPs".

The WC-C peritectic point is of interest for its outstanding performance: its plateau has better quality in terms of shape and repeatability [1-3], and its temperature is comparable with quartz halogen lamp widely used in radiometry that makes WC-C as very convenient reference source for spectral radiance and irradiance. The long-term stability [4] allows checking drift of optical sources and detectors. At VNIIOFI the WC-C cell is already used as a part of facilities for spectral irradiance and for large-area spectral radiance sources involved in the calibration of the Earth observation instruments.

Bilateral comparison of ITS-90 realization with three WC-C cells constructed from different sources of tungsten as transfer standards was conducted between NIM and NMIJ [3]. NIM and NPL also performed a similar comparison with two WC-C cells both constructed from the same tungsten powders [4]. These results showed that WC-C cell has high potential to be used for the scale comparison at high temperature above 3000 K. However, inter-NMI comparison of WC-C point reproducibility among cells had not been conducted so far. In this paper, we report the first comparison of the WC-C peritectic cells constructed from different sources of tungsten powder at VNIIOFI, NIM, and NMIJ.

EXPERIMENTAL

WC-C peritectic cells were constructed at individual NMIs from different sources of tungsten powder and with different design of graphite crucible. These cells were transported to NMIJ to compare their melting temperatures. The details of the cells are given in Table 1.

The crucible of the VNIIOFI WC-C7 cell was made of graphite with a nominal purity of 99.999 % supplied by SGL Group. The cell has a hybrid structure, i.e. the ingot is protected by a graphite sleeve wrapped by C/C sheet. High purity tungsten powder with a nominal purity of 99.999 % (supplier: Alfa Aesar) and graphite powder with a nominal purity of 99.9999 % (supplier: JSC 'CARBOTEC') were used. The new 'drop + piston' method was applied for filling with the carbon fraction of 5.0 %.

The NIM-WC-4# cell was constructed at NIM. The graphite crucible was manufactured at Beijing Sanye Carbon Co., Ltd. with a nominal purity of 99.9998 %. The cell is of hybrid type as well, but with graphite foil instead of C/C sheet. Tungsten powder (supplier: ZKI) and graphite powder (Alfa Aesar) with nominal purities of 99.998 % and 99.9999 %, respectively, were mixed to fill the cell with the final carbon fraction of the 5.0 %.

The 6SSC-7 cell was manufactured at NMIJ. The crucible with a nominal purity of 99.9995 % was

machined by SGL Group. The cell contains graphite sleeve. Tungsten powder with a nominal purity of 99.99 % (supplier: Kojundo Chemical Laboratories Co., Ltd.) was mixed with the graphite powder with a nominal purity of 99.9999 % (Alfa Aesar) at the carbon fraction of 6.0 % to fabricate the cell.

Table 1. Main parameters of the WC-C cells. Dimensions of the cells are in mm.

Cell ID	WC-C7	NIM-WC-4#	WC-C-6SSC-7
Institute	VNIIOFI	NIM	NMIJ
Crucible dia./ length	24 / 44.5	24 / 43	24 / 45
Cavity dia./ opening/ length	5 / 3 / 34.5	3 / 3 / 32	3 / 3 / 34
Emissivity	0.9997	0.9997	0.9997
Cell type	hybrid	hybrid	sleeve
W purity	99.999 %	99.998 %	99.99 %
Graphite purity	99.9999 %	99.9999 %	99.9999 %
Ingot mass	48.7 g	50.9 g	38.7 g

Two Nagano furnaces, whose heater elements and insulators were modified to achieve 2800 °C, were used to realize WC-C peritectic fixed point. An LP5 radiation thermometer (manufactured by KE) with an operating wavelength of 650 nm was employed to measure melting and freezing plateaux.

RESULT AND CONCLUSION

The inflection point of the melting plateau was taken as the melting temperature, and the slope at the inflection point multiplied by the plateau duration was taken as the melting range. The melting and freezing plateaux were realized with furnace temperature settings of ΔT = ±20 K and ΔT = ±30 K with respect to the peritectic transition temperature.

Table 2. Melting temperatures of three WC-C cells.

VNIIOFI	NIM	NMIJ
3020.55 K	3020.14 K	3020.50 K

Two cells were set in the two furnaces, and three melt/freeze plateaux were realized for each cell in a day. All cells were measured in both furnaces to eliminate any furnace effect. Typical melting plateaux, realized by the furnace temperature setting of ΔT = +20 K, are shown in Fig. 1. The VNIIOFI cell shows flat and long melting plateau with the highest melting temperature. The averaged melting temperatures of the three WC-C peritectic cells are given in Table 2.

One can see that the VNIIOFI and NMIJ cells agree within 0.05 K: agreement of 0.05 K is hard to achieve even with other established HTFPs of lower temperatures. Although the melting temperature of the NIM cell was 0.4 K lower than that of the VNIIOFI cell, this cell has been known to show melting temperature 0.4 K lower than the NPL-WC-1 cell [6]. Thus, we can conclude that properly built WC-C cells have high agreement at the level of 0.05 K, corresponding to spectral radiance/irradiance of 0.03 % and 0.01 % at 250 nm and 600 nm, respectively. Even in the agreement of 0.4 K, which corresponds to 0.25 % and 0.11 % at the same wavelengths, it is smaller than standard uncertainties of spectral radiometric quantities realization. The result also demonstrates the capability of the WC-C peritectic as a reliable, highest-temperature reference point.

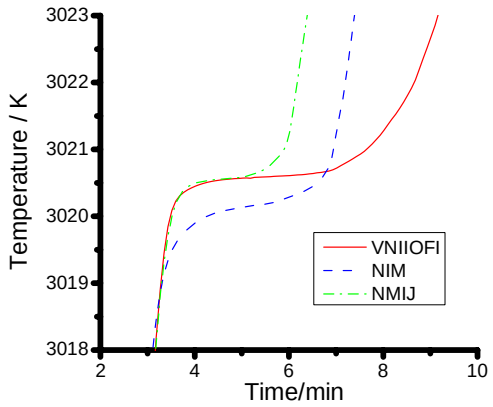

Figure 1. Typical melting plateaux of the WC-C cells realized with the furnace temperature of ΔT = +20 K.

REFERENCES

1. Y. Yamada, Y. Wang, N. Sasajima, Metal carbide- carbon peritectic systems as high-temperature fixed points in thermometry, Metrologia 43 (2006) L23–L27.
2. N. Sasajima, Y. Yamada, Investigation of TiC-C Eutectic and WC-C Peritectic High-Temperature Fixed Points, Int J Thermophys 29 (2008) 944–957.
3. B. Khlevnoy, I. Grigoryeva, D. Otryaskin, Development and investigation of WC–C fixed-point cells, Metrologia 49, S59–S67, 2012.
4. B. Khlevnoy, I. Grigoryeva Long-term stability of WC-C peritectic fixed point, Int J Thermophys (submitted).
5. T. Wang, N. Sasajima, Y. Yamada, C. Bai, Z. Yuan, W. Dong, C. Ara, X. Lu, Realization of the WC-C peritectic fixed point at NIM and NMIJ, Temperature: Its Measurement and Control in Science and Industry, vol. 8, AIP Conf. Proc. 1552 (2013) 791-796.
6. W. Dong, D. H. Lowe, X. Lu, G. Machin, Z. Yuan, T. Wang, P. Bloembergen, C. Xiao, Bilateral ITS-90 Comparison at WC-C Peritectic Fixed Point Between NIM and NPL, Temperature: Its Measurement and Control in Science and Industry, vol. 8, AIP Conf. Proc. 1552 (2013) 786-790.

Experimental prediction of Predictable Quantum Efficient Detector responsivity

Jarle Gran

Justervesenet, Kjeller, Norway,
Corresponding e-mail address: jag@justervesenet.no

A relative measurement of a Predictable Quantum Efficient Detector (PQED) to a spectrally invariant pyroelectric detector is used to experimentally predict the single photodiode PQED responsivity. The negligibly small internal quantum deficiency at visual wavelengths enables determination of the reflection losses of a single photodiode and ensures correct scaling through a two parameter fit to the relative measurement. The proposed method is a user friendly alternative to simulation software to predict with moderate uncertainty the responsivity of a PQED single photodiode.

INTRODUCTION

With the introduction of the recently developed Predictable Quantum Efficient Detector (PQED) [1-3] the radiometric community has a promising alternative to the Cryogenic Radiometer (CR) as a primary standard. The PQED has a simple design, a high and predictable internal quantum efficiency over a wide spectral range [3-5].

The predictability of the PQED has limitations and require detailed knowledge about the experimental setup and the internal structure of the diode such as bulk doping concentration, charge carrier lifetime, surface recombination velocity, density of fixed oxide charge, absorption coefficient as a function of wavelength and irradiance. These characterisations combined with 3D software are necessary to get a good understanding of the device and a reliable prediction at the lowest level of uncertainty as is planned in the ongoing NewStar project [6].

Though one-dimensional software is available free of charge, the owner of a PQED would benefit of having an independent experimental technique that could predict its responsivity with moderate accuracy in the order 0.1 %. As a consequence, the experimental procedure would take into account the individuality of each of the PQEDs the owner would possess.

A previously developed technique by Gran et. al. [7] has demonstrated that the responsivity of a trap detector consisting of Hamamatsu photodiodes could be determined. Here the measured response of a trap detector relative to a pyroelectric detector from 400 to 900 nm was made. Reflectance was measured separately. A five parameter model of the internal quantum deficiency was fitted to the relative response after having quantified the reflection losses. The models built-in constraints ensured correct estimation of the trap responsivity. Fortunately, the PQED is more suited for this technique than a standard trap detector, because of its negligible IQD over a wide spectral range from 400 nm and upwards. As shown in the following a two parameter fit to a relative measurement of a single PQED diode is all that is needed to predict its responsivity.

EXPERIMENTAL PROCEDURE

A relative measurement of a 10 V biased single PQED photodiode against a pyroelectric detector [8] from 400 to 1000 nm was performed in a monochromator set-up. Though noisy, the wavelength independent properties of the pyroelectric detectors makes it well suited as a reference to determine the spectral shape of the PQED single photodiode. The average results of multiple series are shown in Fig. 1.

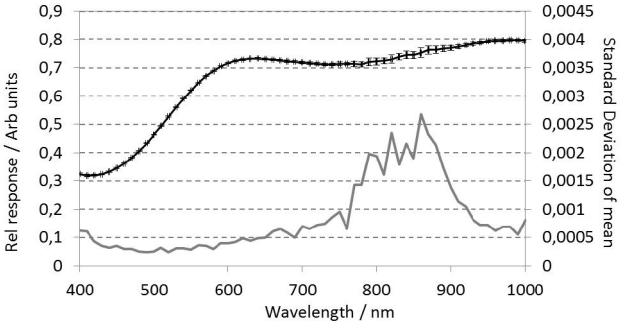

Figure 1. Measured relative response (black) and its standard deviation of mean value (grey) between a single PQED photodiode and a pyroelectric detector.

The relative response curve can be modelled as

$$F(\lambda, d, k) = {}^{e\lambda}/_{hc}\left(1 - \rho(\lambda, d)\right)/k \qquad (1)$$

where *e*, *h* and *c* are the fundamental constants elementary charge, Planck's constant and speed of

light in vacuum respectively. ρ is the reflectance depending on the vacuum wavelength λ and is accurately modelled by varying the oxide thickness *d* [9]. *k* is a scaling constant representing the responsivity of the pyroelectric detector.

The model in (1) represents our relative measurement of the PQED and is fitted to the measured data given in Fig. 1 through a generalised least square fit [10] by varying the two parameters *d* and *k*. Only the data in the spectral range between 400 and 680 nm were used in the fit, because we over this range expect to have reflection losses only without significant internal losses. It is required that the internal losses are negligible in order to make the correct scaling of the curve. The results from the fit gave an oxide thickness of 303,40 nm and a scaling constant of 0,61394. The covariance of the two parameters in the fit is shown in Table 1.

Table 1. The covariance of the fitted values are shown.

	d	*k*
d	$1{,}97 \cdot 10^{-3}$	$-1{,}38 \cdot 10^{-6}$
k	$-1{,}38 \cdot 10^{-6}$	$1{,}14 \cdot 10^{-8}$

When adjusting the relative measurement in Fig. 1 with the scaling constant the absolute responsivity of the PQED photodiode is found as shown in Fig. 2.

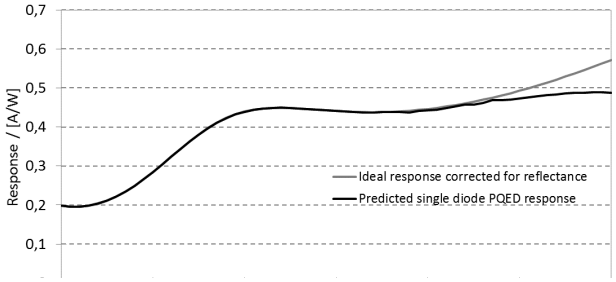

Figure 2. The predicted responsivity of the PQED⁰ photodiode (black) compared to the reflection corrected ideal model of the PQED (grey).

A good fit is observed and the difference between the curves shown in Fig. 2 is a measure of the internal quantum deficiency.

If measuring a PQED trap detector by this method the reflectance can be neglected to [11] and the reflection term can be omitted from (1). In that scenario even oxide thickness is irrelevant and the data is fitted only by a scaling constant.

ERROR SOURCES AND IMPROVEMENTS

Any spectral deviations in the pyroelectric detector or nonlinearities in its responsivity will appear as a poor fit of the model (1) to the measured data. The same applies for unaccounted deviations in the specular reflectance. The photodiode has to be clean, because diffuse reflectance is not accounted for. However, there is suggested a method in [7] based on a uniformity measurement that could quantify the diffuse reflectance. The uniformity measurement is recommended as it will reveal dysfunctional diode as well.

As shown in [7], the uncertainty can be calculated from the observed variance in the relative measurement between the PQED photodiode and the pyroelectric detector and could be propagated through the calculations for the 400 to 680 nm range used in the fit. For longer wavelengths the observed standard deviation of the mean plus the uncertainty in the scaling constant should be used.

The systematic error one makes by this method is the unaccounted internal losses in the short wavelength range of the visual spectrum which is known to be small (< 50 ppm) for a well functioning diode.

Improved spectrally invariant detectors, signal processing and measurement techniques will fit the development of PQEDs and the proposed method very well.

REFERENCES

1. http://www.quantumcandela.org/
2. M. Sildoja et al., Predictable quantum efficient detector: I. Photodiodes and predicted responsivity. Metrologia, 50, 385–394, 2013.
3. I. Müller et al., Predictable quantum efficient detector: II. Characterization and confirmed responsivity. Metrologia, 50, 395–401, 2013.
4. J. Gran et al., Simulations of a predictable quantum efficient detector with PC1D. Metrologia, 49, S130–S134, 2012.
5. C. K. Tang et al., Two-dimensional simulation of an induced-junction detector with Genius device simulator towards a predictable quantum efficient detector, these proceedings.
6. http://www.inrim.it/Newstar.html
7. J. Gran et al., Absolute calibration of silicon photodiodes by purely relative measurements, Metrologia, 41, 204-212, 2004.
8. E. Theocharous et al., Assembly and evaluation of pyroelectric detector bonded to vertically aligned multiwalled carbon nanotubes over thin silicon, Applied Optics, 52, No. 33, 8054-8059, 2013.
9. A. Haapalinna et al., Spectral reflectance of silicon photodiodes, Applied Optics., 37 No. 4, 729-732, 1998.
10. I. Lira, Curve adjustment by the least-squares method Metrologia, 37, 677-681, 2000.
11. M. Sildoja et al., Use of the predictable quantum efficient detector with light sources of uncontrolled state of polarization, Meas. Sci. Technol., 25015203, 7 pp, 2014.

.

Reducing the uncertainties of detector calibrations against cryogenic electrical substitution radiometers

Lutz Werner, Uwe Johannsen, Ulrike Linke, Peter Meindl, Ingmar Müller, and Jürgen Schirren

Physikalisch-Technische Bundesanstalt, Berlin, Germany
Corresponding e-mail address: lutz.werner@ptb.de

A new calibration facility based on a cryogenic electrical substitution radiometer and power-stabilized laser radiation in the spectral range from 400 nm to 1000 nm has been set up at PTB with the aim of achieving lowest possible uncertainties for the spectral responsivity calibration of semiconductor detectors. The new calibration facility has successfully been used to measure the spectral responsivity of trap detectors with a relative standard uncertainty of 30 ppm and replaces PTB's former cryogenic radiometer facility RTCR.

INTRODUCTION

A new calibration facility based on a cryogenic electrical substitution radiometer (CR) and power-stabilized laser radiation in the spectral range from 400 nm to 1000 nm has been set up at PTB. It has replaced the laser-based Radiation Thermometry Cryogenic Radiometer (RTCR) [1] that has been operated at PTB since 1990. The aim of the new facility is to achieve lowest possible uncertainties for the spectral responsivity calibration of semiconductor detectors by avoiding and reducing main uncertainty contributions such as, e.g., those caused by stray light and the determination of the transmittance of the Brewster window. This new calibration facility will be used within the EMRP project SIB57 to examine the suitability of a Predictable Quantum Efficient Detector (PQED) as a potential new primary detector standard in the visible spectral range with a target relative standard uncertainty in the 10 ppm range [2, 3].

SETUP OF THE CRYOGENIC RADIOMETER CALIBRATION FACILITY

The design of the calibration facility is shown in Figure 1. The laser radiation enters the setup through the fixed Brewster window (BW). The cryogenic radiometer (CR) - a modified CryoRad II of L-1 Standards and Technology, Inc. - and the detectors under calibration (DUC) (DetC, O) are mounted on a swivelling table with the vertical swivel axis (A) to move either the cryogenic radiometer or a DUC into the laser beam. The spectral responsivity is determined by the ratio of the photocurrent of the DUC and the radiant power measured by the cryogenic radiometer. The power of the laser radiation is stabilised and, in addition, monitored with a silicon photodiode based three-element trap detector to correct for any temporal change during the measurement.

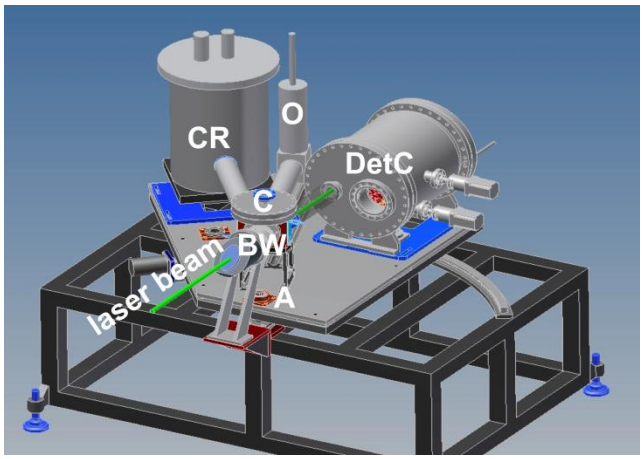

Figure 1. Design of the cryogenic radiometer calibration facility. The picture shows the Brewster window (BW), the cryogenic radiometer (CR), the detector chamber containing the detectors to be calibrated (DetC), an optional detector operated in vacuum (O), the distribution chamber (C) and the vertical swivel axis (A).

The detector chamber contains a wheel with up to six DUC. The detector chamber, the optional detector operated in vacuum and the cryogenic radiometer are connected with the distribution chamber via valves and vacuum tubes allowing the DUCs being calibrated in vacuum, air or any suitable gas. All detectors, i.e. the cryogenic radiometer and the DUCs, are positioned on the swivelling table in that way that the distances of their apertures to the swivel axis are almost identical. As a consequence, they are at a nearly identical position behind the fixed Brewster window when they are moved into the beam. Thus, a window-correction-free and distant-error-free setup is realised that was proposed in a similar design already 20 years ago [4]. To further reduce the effect of stray light, the DUCs are

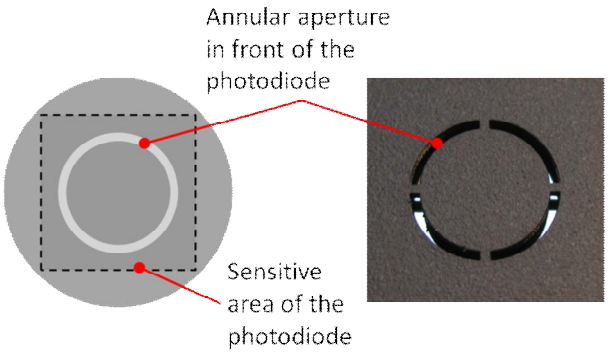

Figure 2. Schematic view (left) and photo (right) of the stray light detector.

equipped with apertures having the same diameter as the aperture in front of the absorber cavity of the cryogenic radiometer. The remaining effect of stray light on the calibration result depends now on the small difference between the aperture areas and the stray light level in the vicinity of the edges of the circular apertures and can be corrected. To measure the latter quantity a special stray light detector consisting of a large area Si photodiode behind an annular aperture (see Figure 2) is positioned concentrically to the laser beam and in the same distance to the Brewster window as the detectors. The measured stray light in the vicinity of the edges is used to determine the correction and uncertainty contribution arising from the stray light.

Table 1. Main contributions to the uncertainty budget of the spectral responsivity calibration. Relative standard uncertainties are stated. ([a] including the uncertainty contribution arising from the detector position and the difference of the aperture sizes.)

Source of uncertainty	**Uncertainty / ppm**
Cavity absorptance (cryogenic radiometer)	13
Wavelength	2
Stray light correction[a] (DUC)	20
Non-equivalence between optical and electrical heating (cryogenic radiometer)	7
Heating power (cryogenic radiometer)	10
Typical laser stability	4
Photocurrent (DUC)	10
Combined relative standard uncertainty	**29**

MEASUREMENT UNCERTAINTIES

The main contributions to the uncertainty budget of the spectral responsivity calibration of a trap detector are given in Table 1. As mentioned above, the effect of stray light was minimised and corrected. However, the residual stray light causes the largest uncertainty contribution even after a careful beam preparation. The second largest uncertainty is caused by the determination of the absorptance of the cryogenic radiometer cavity followed by uncertainties of electrical measurements. The dominating uncertainty contributions are intended to be further reduced.

It becomes apparent that at the achieved level of uncertainty each source of uncertainty becomes relevant and has to be thoroughly considered.

FIRST DETECTOR CALIBRATION RESULTS

The new calibration facility has successfully been used within the iMERA-Plus project “qu-Candela” to measure the spectral responsivity of a new type of detector whose responsivity is supposed to be predictable (Predictable Quantum Efficient Detector [3]) with a relative standard uncertainty of 30 ppm. The first recalibration of PTB's secondary detector standards with this new facility has shown a good agreement to the results obtained with the former cryogenic radiometer RTCR [1].

ACKNOWLEDGEMENT

We would like to thank Liana D. Socaciu-Siebert for her contributions to the initial setup and testing of the facility.

REFERENCES

1. L. Werner, J. Fischer, U. Johannsen and J. Hartmann, Accurate determination of the spectral responsivity of silicon trap detectors between 238 nm and 1015 nm using a laser-based cryogenic radiometer, *Metrologia*, *37*(4), 279–284, 2000.
2. M. Sildoja, F. Manoocheri, M. Merimaa, E. Ikonen, I. Müller, L. Werner, J. Gran, T. Kübarsepp, M. Smîd and M. L. Rastello, Predictable quantum efficient detector: I. Photodiodes and predicted responsivity, *Metrologia*, *50*(4), 385–394, 2013
3. I. Müller, U. Johannsen, U. Linke, L. Socaciu-Siebert, M. Smîd, G. Porrovecchio, M. Sildoja, F. Manoocheri, E. Ikonen, J. Gran, T. Kübarsepp, G. Brida and L. Werner, Predictable quantum efficient detector: II. Characterization and confirmed responsivity, *Metrologia*, *50*(4), 395–401, 2013.
4. K. Stock, H. Hofer, Present state of the PTB primary standard for radiant power based on cryogenic radiometry, *Metrologia, 30*, 291-296, 1993.

Measurement of the absorptance of the new cryogenic radiometer cavity from the ultraviolet to the near infrared range

Jeanne-Marie COUTIN and Bernard ROUGIE

LCM – Laboratoire Commun de Métrologie LNE-Cnam, La Plaine - Saint-Denis, France
jeanne-marie.coutin@cnam.fr; bernard.rougie@cnam.fr

This paper describes the study of a new cryogenic radiometer cavity, at the French National Measurement Laboratory. The absorption of the cavity has been improved and the absorptance factor is given to be higher than 0,999 98 at 632,8 nm. We tried to verify the absorption of the cavité at several laser wavelengths from 266 nm to 1525 nm. The measurements results confirmed the value given by the manufactor and showed that the change in the absorptance with wavelengths is now negligible.

INTRODUCTION

The French National Measurement Laboratory, the LNE-Cnam, uses a cryogenic radiometer as the basis for its optical radiation measurement scales. Three years ago, we replaced our first cryogenic radiometer (LaseRad, manufactured by Cambridge Research & Instrumentation (CRI)) by a new one, the CryoRad-II supplied by L-1 Standards and Technology.

The cryogenic radiometer is an absolute radiometer operating at 4.2 K. It uses the electrical substitution method, that is, it gives absolute measurement of the radiant power by comparing it with an electrical power. However, the radiometric power calculated by the cryogenic radiometer needs several corrections, which must be determined with a high accuracy level.

The basis element of the cryogenic radiometer is a highly absorptive cavity which heats up when irradiated. Therefore, one of the main corrections depends on its absorptance which is a non-ideal.

For the new cryogenic radiometer we now used, the absorption of the cavity has been improved and the manufactor reports an absorption coefficient of 0,999 982 ± 0,000 001 at 632,8 nm, instead of 0,999 89 ± 0.000 02 for the first generation cryogenic radiometers [1], [2]. However, to achieve lower measurements uncertainties it is necessary to know the exact spectral response of tne radiometer. Hence we measured the absorption coefficient of the new cavity at several wavelengths between 266 nm to 1525 nm.

MEASUREMENT METHOD

In order to facilitate this study, the new cryogenic radiometer was purchased with an additional cavity, identical to this mounted in the radiometer.

The cavity is built from 50 microns thick copper and the inside is blackened with a highly specular reflective paint whose reflectance is lower than 20 ppm. The external diameter of the cavity is 19 mm and the entrance aperture is 7 mm.

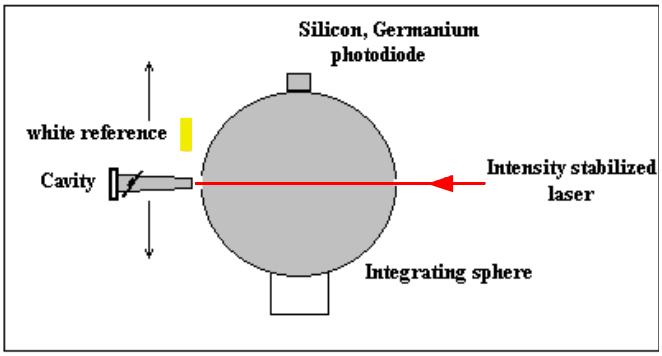

Characteristics of the set-up:

Ø sphere : 50 mm

Ø exit port : 7 mm

Ø entrance cavity : 7 mm

Figure 1. Cavity reflectance measurement method.

The absorption coefficient α at the cavity is determined from the measurement of the reflective factor from the cavity ρ using the simple formula $\alpha = 1 - \rho$.

An integrating sphere is used to measure the diffuse flux reflected from the cavity when illuminated with a laser beam. It is a modular integrating sphere of diameter 50 mm with Spectralon reflectance coating. It contains three ports : an entrance port for the laser beam, a diametrically opposite sample port to put alternately the cavity or a white standard, and an exit port in an orthogonal direction where is placed a photodetector. The detector converts the reflected flux into a photo-current. The entrance port has a diameter of 5 mm, the detector port 3 mm, and the diameter of the sample port was adapted to 7 mm with appropriate port to be the same as the entrance diameter of the cavity. The measurement method consists of a relative comparison between the diffuse reflectances of the white standards and the cavity. The reflectance factor of the cavity, ρ_c, can be calculated, as a first approximation, from the equation schown in the the figure 1, where S_C and S_E are respectively the signals generated by the photodetector when the cavity and the white standard are placed alternately on the sample port. Both signals S_C and S_E have to be corrected by the signal S_0 in order to eliminate the scattered light : S_0 is measured when the cavity is away from the sample port. And ρ_E is the reflectance of the diffuse standard.

MEASUREMENT SETUP

The measurements of the diffuse reflectance of the cavity have been carried out on the set-up used to compare trap detectors to the cryogenic radiometer[3]. Several lasers are used to cover the spectral range from the ultraviolet to the infrared. In the visible wavelength range, three helium-neon lasers at the wavelengths of 543nm, 611 nm and 633 nm are used with a tunable argon-laser with wavelengths from 454 nm to 514 nm. For the ultraviolet, a helium cadmium laser at the wavelength of 325 nm and 442 nm is used, and a solid-state, diode-pumped, continuous-wave laser at 266 nm. For the near infrared, a Ti:Sa laser is used for wavelengths around 800 nm, and two helium-neon lasers at the wavelengths of 1150 nm and 1523 nm are used. The power stabilization is better than $4x10^{-5}$ over an hour and the laser beam is spatially filtered and focused to a beam spot diameter in the order of 1 mm.

The measurement system was characterized to optimize the measurements : the localization of the optimal distance of the cavity from the sample port sphere was studied, the position of the cavity on the sample port was verified, the beam scatter light and stray light have been analyzed.

MEASUREMENT RESULTS

The results are reported in table 1 with the standard deviation on the measurements (measures to 1523 nm are in progress and the results not yet available).

The comparison of the measurement at 633 nm with those carried out by the manufactor exhibits a good agreement.

Table 1. Major results of the measurements of the absorptance of the cryogenic radiomete cavity

Wavelength (nm)	Standard deviation	Absorptance factor
800	0,82 ppm	0,999 986
633	0,57 ppm	0,999 983
612	0,37 ppm	0,999 982
543	0,39 ppm	0,999 985
514	0,99 ppm	0.999 977
442	0,78 ppm	0,999 987
325	0,48 ppm	0,999 989

These measurements are difficult to achieve because the value of the reflectance factor is in fact of the same order of the uncertaintie, which is estimated for now to 1 to 2 parts in 10^5. But the interest of this study is to make sure that the absorptance of the new cavity is negligible on the overall spectral range used.

REFERENCES

1. Touayar O., Rougié B. Coutin J.-M. and Bastie J. - Measurement of the reflectance of the INM cryogenic radiometer cavity at several wavelengths - Metrologia 35, 387-391 (1998).
2. López M., Hofer H., Kück S.[CENAM, PTB], Measurement of the absorptance of a cryogenic radiometer cavity in the visible and near infrared , Metrologia, 2005, 42, n°5, 400-405.
3. Coutin J-M., Touayar O., Bastie J. - The using conditions of the BNM-INM cryogenic radiometer as the basis of for the French optical radiation scales - Proceedings of the 24th session of the CIE , CIE-133, 22 (1999).

Near-infrared detector spectral response scale – short wavelength comparison between MSL and CMI

François Shindo[1], Kathryn Nield[1], Marek Šmíd[2], and Petr Kliment[2]

[1]*Measurements Laboratory of New Zealand, Callaghan Innovation, Lower Hutt, New Zealand,*
[2]*Czech Metrology Institute, Praha, Czech Republic.*
Corresponding e-mail address: francois.shindo@callaghaninnovation.govt.nz

MSL has started the extension of its radiometric scale to the near infrared (NIR) by the transfer of the absolute responsivity of a 5-element trap detector, based on Hamamatsu photodiodes S1337, onto single element InGaAs detectors. This scale transfer has been compared with the scale held on InGaAs detectors at CMI showing agreement to within 0.5 %. The scales realized in the two laboratories are based on different methodologies. The motivation for this comparison was to give confidence in these methodologies.

INTRODUCTION

Work to develop a scale for the responsivity of photodetectors in the NIR has commenced at MSL. The initial part of this work was to transfer the near infrared portion of the detector scale held on a set of MSL built 5-element silicon photodiode trap detectors, specifically over the wavelength range 850 nm to 1020 nm. An informal comparison took place with CMI over the wavelength range 900 nm to 1010 nm.

SCALE REALIZATION AT MSL

Currently at MSL the NIR detector spectral responsivity (DSR) scale from 900 nm to 1030 nm is held on 5-element silicon trap detectors. At these wavelengths the DSR is determined using the model for spectral responsivity of silicon detectors [1, 2]. This model is underpinned by the calibration of the trap detectors at 8 laser wavelengths from 406.7 nm to 650.1 nm against the MSL cryogenic radiometer (CR) [3, 4]. The model is also supported with measurements of the relative shape of the trap detectors with a pyroelectric detector in the region (900 nm - 1010 nm) where the shape of the spectral responsivity becomes non-linear. This relative measurement aids the fitting of the diode thickness and diode substrate back reflectance, the two parameters in the responsivity model which influence the near-infrared region.

SCALE REALIZATION AT CMI

The CMI DSR scale in the NIR is realized by extrapolation of the visible DSR scale, which is traceable to calibrations of 3-element silicon trap detectors calibrated against the CMI mechanically cooled CR at 7 laser lines from 406.7 nm to 799.3 nm [5]. This scale is then transferred to single element InGaAs detectors by the absolutely calibrated pyroelectric detector method [6]. This method utilizes the absolute calibration of a hemispherical pyroelectric detector [7] against the CMI visible scale.

MEASUREMENTS

MSL InGaAs detector systems have been built using GPD-GAP5000 chips with a 5 mm diameter active surface. The detectors are temperature-stabilized using a heat-pipe system [8] developed at MSL. The detectors have been assessed for linearity of response at 950 nm using the MSL-developed combinatorial linearity tester [9].

The InGaAs detectors were calibrated for DSR against one of our 5-element silicon trap detectors via the Detector Responsivity System (DRS) developed at MSL [10]. The transfer was realized between 800 nm to 1010 nm with at an increment of 10 nm using a bandwidth of 2 nm. The beam exiting from the DRS double monochromator spectrometer was carefully constrained to fall within the field of view of the 5-element trap and to describe a 2 mm spot centred on the InGaAs detector. Due to the high temperature sensitivity of the detectors in the wavelength domain under investigation, the detectors were stabilized at a temperature of 20.0 °C with stability of ±0.01 °C. The repeatability of these measurements was better than 0.04 % at the level $k = 1$.

At CMI the two MSL InGaAs detectors were calibrated against the CMI reference detectors within the CMI DSR system. Like the MSL DRS system, the CMI system is based upon the McPherson 2035 double monochromator, the main difference being

that the CMI monochromators are configured in subtractive mode as opposed to additive, as is the case at MSL.

The CMI scale was transferred onto the MSL detectors from 900 nm to 1650 nm at an interval of 10 nm with a bandwidth of 5 nm. A circular aperture and associated optics at the exit of the double monochromator focussed the beam to a 3 mm spot. The CMI reference detector was temperature-stabilized using a CMI-built unit which uses an on-chip Peltier device, which was attached immediately behind the reference detector. The reference detector temperature was set to 31 °C with stability better than ±0.1 °C. The MSL detectors were stabilized at 20.0 °C as previously described. The repeatability of the measurements was better than 0.02 % at the level $k = 1$.

CMI AND MSL NIR SCALE COMPARISON

The comparison between the two scales in the spectral range from 900 nm to 1010 nm showed an agreement between MSL and CMI to within 0.5 % for wavelengths shorter than 970 nm (figure 1).

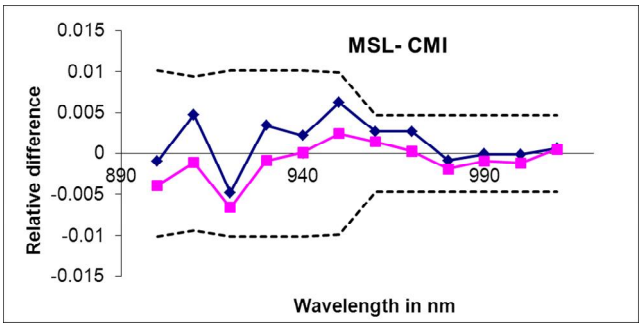

Figure 1. Comparison of MSL and CMI infrared scales. Coloured lines represent the relative difference of the CMI and MSL scales on the two MSL InGaAs detectors. The black dotted lines correspond to CMI uncertainties at $k = 2$.

In this short NIR region the responsivity of both the InGaAs and Si detectors have strong non-linear shape with wavelength and significant temperature sensitivity (figure 2). Beyond 970 nm the two scales agree to better than 0.2 %.

CONCLUSION

The NIR detector spectral responsivity scales realized at MSL and CMI agree to better than 0.5 % over the wavelength range 900 nm to 1010 nm. It is clear there is some systematic residual in the comparison from 900 nm to 970 nm. This residual could arise from the either the response shape held on the MSL 5-element trap detectors or due to the temperature sensitivity of response of the InGaAs detectors, as the CMI InGaAs detectors were not temperature stabilized during the original CMI scale realization.

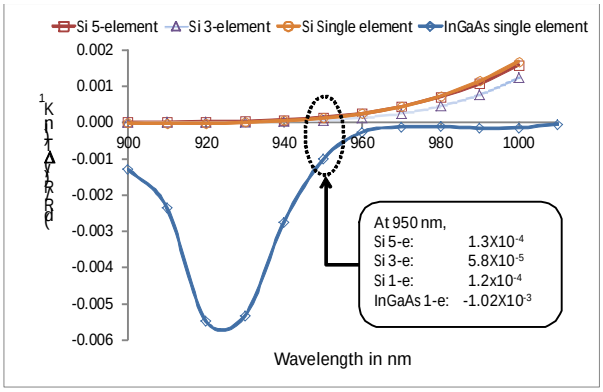

Figure 2. Temperature coefficients measured for MSL Si trap detectors and for CMI InGaAs detector.

REFERENCES

1. L. Werner *et al.*, "Accurate determination of the spectral responsivity of silicon trap detectors between 238 nm and 1015 nm using a laser-based cryogenic radiometer", Metrologia, 37, 279-284, 2000.
2. T. R. Gentile, J. M. Houston, C. L. Cromer, "Realization of a Scale of Absolute Spectral Response Using the National Institute of Standards and Technology High-Accuracy Cryogenic Radiometer.", Applied Optics, 35, 4392–4403, 1996.
3. K. M. Nield *et al.*, "Calibration of a Trap Detector against a Cryogenic Radiometer.", Metrologia, 35, 581, 1998.
4. R. Goebel, M. Stock, R. Köhler, "Report on The International Comparison of Cryogenic Radiometers Based on Transfer Detector", Rapport BIPM-00/09, BIPM Publications, 2000
5. M. G White, M. Šmíd, "Final Report on the Bilateral Supplementary Comparison of Cryogenic Radiometers CCPR-S3: NPL-CMI", Metrologia, 47,Tech. Suppl., 02006, 2010.
6. E. Theocharous, M. Šmíd, T. Ward, N. Fox, "The establishment of an absolute infrared scale using cavity pyroelectric detectors", in preparation.
7. J. Lehman, E. Theocharous, " Gold-Black coatings for freestanding pyroelectric detectors", Measurement Science and Technology, 14, 916-922, 2003
8. R. Mason *et al.*, "Heat-Pipe temperature Stabilisation System for Detectors and other Calibration Artefacts", Proceedings of the 11th NEWRAD Conference, 2011.
9. P. Saunders, D. R. White, H. Edgar, "A Compact Combinatorial Device for Measurement of Non-Linearity of Radiation Thermometers", submitted to the International Journal of Themophysics, Special Issues, TEMPMEKO 2013.
10. K. M. Nield, J. D. Hamlin, A. Bittar, "Comparison of two methods for spectral irradiance scale transfer", Proceedings of the 9th NEWRAD Conference, 267, 2005.

Practical metrology aspects of the determination of spectral responsivity for optical radiation detectors

Scums D.V.[1], Tarasova O.B.[1], and Nikanenka S.V.[2]

[1]*National Metrological Institute of the Republic of Belarus (BelGIM), Minsk, Belarus,*
[2]*B. I. Stepanov Institute of Physics National Academy of Sciences of Belarus, Minsk, Belarus*
Corresponding e-mail address: optic@belgim.by

In article presents some results of works on research of the National standard of unit of spectral responsivity. Substantiated physical schema of a standard. Features of the basic functional units are described. Presented basic metrological characteristics of the standard.
Key words: metrology, spectral responsivity, trap-detectors.

1. INTRODUCTION

Sometimes in usual metrological practice there is a necessity to report on total uncertainty of concrete spectral ranges. In article, definition of spectral responsivity in three spectral subrange on an example of research of the National standard of unit of spectral responsivity of the optical radiation detectors of Republic of Belarus is considered.

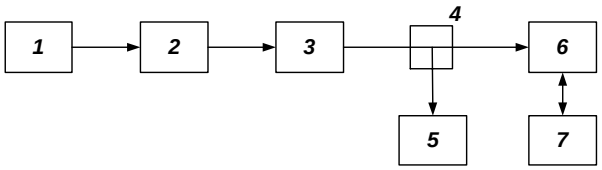

Figure 1. Scheme of measurement of the spectral responsivity with use of the monitor-detector [1].

2. THE MEASURMENT METHOD

The main method of measuring of the spectral responsivity of optical radiation detectors (ORD) is the method of substitution, i.e. alternately compares the output signals of the test and reference detectors when they are illuminated by the same light source. In the general case, the output signal Y_x from the test detector (TORD) or systems with a linear response can be written as

$$Y_x = s_x X_{x,} \tag{1}$$

where s_x – TORD spectral responsivity, X_x – input signal. Respectively we can present responsivity Y_s of standard detector (SORD)

$$Y_\text{s} = s_\text{s} X_\text{s} \tag{2}$$

where s_S - SORD spectral responsivity, X_S - input signal. If input signal for TORD and SORD are constant during measurement, TORD spectral responsivity can be presented as

$$s_X = \frac{Y_X}{Y_\text{s}} s_\text{s} \tag{3}$$

It is assumes that the radiation source is stable over time but that is false in general. To eliminate the effect of fluctuations of the sources radiation power we use the beam splitter and monitor-detector (MD) (see Fig. 1).

In general TORD spectral responsivity can be presented as [1]

$$s_x = \frac{R_x}{R_s} \cdot s_\text{s} = \frac{\dfrac{Y_x - Y_{\text{d},x}}{Y_\text{m} - Y_{\text{d,m}}}}{\dfrac{Y_\text{s} - Y_{\text{d,s}}}{Y_\text{m} - Y_{\text{d,m}}}} \cdot s_\text{s} \tag{4}$$

where $Y_{\text{d},x}$, $Y_{\text{d,m}}$ and $Y_{\text{d,s}}$ are “dark signals” of TORD, SORD and MD respectively; R_x and R_s .ratio of the signals of TORD and SORD to MD respectively.

The National standard of unit of spectral responsivity of the optical radiation detectors of Republic of Belarus in spectral range from 350 to 1100 nm, is based on this method.

3. EVALUATION OF MEASURMENT UNCERTAINTIES

Based on Bartlett criterion, it was found that when estimating the measurement uncertainty of the spectral responsivity of the ORD can examine the results of measurements on the groups: in the range of 350 to 400 nm, 400 nm to 750 nm from 750 to 1100 nm. Evaluation of measurement uncertainty for “clear” signal ΔY_x for TORD based on next mathematic model

$$\Delta Y_x = Y_x - Y_{\text{d}x} \tag{5}$$

Since signals Y_x and $Y_{\text{d}x}$ are measured by the same multimeter standard uncertainty $u(\Delta Y_x)$ is characterized by the standard deviation of the mean

signal. Sensitivity coefficients are takes the value as C1 = C2 = 1. The combined standard uncertainty $u_{\Sigma}(\Delta Y_x)$ is calculated as

$$u_{\Sigma}(\Delta Y_x) =$$

$$= \sqrt{\mathrm{C1}[u(Y_x)]^2 + \mathrm{C1}[u(R)]^2 + \mathrm{C2}[u(Y_{\mathrm{dx}})]^2 + \mathrm{C2}[u(R)]^2} \quad (6)$$

where expanded uncertainty $U_{\Delta Y_x}$ calculated as

$$U_{\Delta Y_x} = k \cdot u_{\Sigma}(\Delta Y_x) \quad (7)$$

where k – coverage ratio at the selected confidence level of P = 1.65 at a confidence level P = 0.95.

In a similar way uncertainties for SORD are evaluated.

The combined standard uncertainty $u_{\Sigma}(s_x)$ of the measurement of spectral responsivity ORD calculated as

$$u_{\Sigma}(s_x) =$$

$$\sqrt{(u'(\Delta Y_x))^2 + (u'(\Delta Y_s))^2 + (u'(\Delta Y_{rs}))^2 + (u'(\Delta Y_{rx}))^2 + (u'(P_s))^2 + (u'(P_x))^2 + (u'(c_a \Delta T))^2} +$$

$$\sqrt{(u'(w_s(\varepsilon)))^2 + (u'(w_x(\varepsilon)))^2 + (u'(\Delta l_{s(X-X)}))^2 + (u'(\Delta l_{x(X-X)}))^2 + (u'(\Delta l_{s(Y-Y)}))^2 + (u'(\Delta l_{x(Y-Y)}))^2} +$$

$$\sqrt{(u'(\Delta l_{s(Z-Z)}))^2 + (u'(\Delta l_{x(Z-Z)}))^2 + (u'(S_s))^2} \quad . \quad (8)$$

4. STUDY OF METROLOGICAL CHARACTERISTICS OF A STANDARD

In the investigation of the standard, following studies were conducted, the results of which were taken into account in determination of its main metrological characteristics: estimation of influence of adjustment of TORD on measurement results; estimation of influence of intensity of radiation source on measurement results; estimation of influence of integration time and time of delay on measurement results; estimation of influence of fluctuations of electronic noises in a standard on measurement results; estimation of the spectral range of the measurements; determination of the power of monochromatic radiation; estimation of the error of the wavelength scale of the monochromator; estimation of the temperature depends of the measurement results; definition of a limits of nonexclusion systematic error, standard deviation of amount of non-excluded systematic errors, standard deviation of amount of non-excluded systematic and random errors and confidence limits of error.

5. CONCLUSION

The carried out researches have allowed to establish, that:

the combined standard uncertainty $u_{\Sigma}(s_x)$ of the measurement of spectral responsivity ORD is for spectral range from 350 to 400 nm $u_{\Sigma}(s_x)$ = 0,585 %, for spectral range from 400 to 750 nm $u_{\Sigma}(s_x)$ = 0,207 %, for spectral range from 750 to 1100 nm $u_{\Sigma}(s_x)$ = 0,226 %;

the expanded uncertainty $U_{s(\lambda)}$ of the measurement of spectral responsivity ORD is (expanded uncertainty values are given for k = 1,65, P = 0,95) for spectral range from 350 to 400 nm $U_{s(\lambda)}$ = 0,965 %, for spectral range from 400 to 750 nm $U_{s(\lambda)}$ = 0,342 %, for spectral range from 750 to 1100 nm $U_{s(\lambda)}$ = 0,373.

REFERENCES

1. NlST measurement services: Spectroradiometric Detector Measurements: Part I-Ultraviolet Detectors and Part II-Visible to Near-Infrared Detectors. / Larason T.C., Bruce S. S., Parr A.C. NlST Special Publication 250-41. U.S. government printing office Washington. 1998.

Towards the implementation of spectral irradiance scale based on a filter radiometer in Brazil

Maurício S. de Lima[1], Thiago Menegotto[1], Thiago F. da Silva[1], Iasmim Duarte[1], Hakima Belaidi[1], Luciana C. Alves[1], Muriel A. de Souza[1], Giovanna Borghi[1], Renato N. Teixeira[2], and Iakyra B. Couceiro[1]

[1]*Optical Metrology Division,* [2]*Thermal Metrology Division,*
National Institute of Metrology, Quality and Technology, Duque de Caxias – Xerém, Brazil
Corresponding e-mail address: mslima-cnpq@inmetro.gov.br

This paper describes the main steps in the implementation of the spectral irradiance scale based on a filter radiometer constructed and characterized at the Photometry and Radiometry Laboratory (LARAF) of the Optical Metrology Division of INMETRO, Brazil. This description includes the ageing and evaluation of stability of FEL lamps, the determination of the areas of the apertures, the spectral transmittance of the interference filters and the evaluation of the spectral responsivity of the trap detectors selected to be used in the filter radiometer.

INTRODUCTION

The realization of the spectral irradiance scale at INMETRO is based on a filter radiometer [1, 2]. This device is composed, at least, by an aperture, interference filters and a trap detector. All these components have to be characterized to get a traceability chain in spectral irradiance measurements. The spectral responsivity of the trap detector is linked to a cryogenic radiometer [3]. The aperture areas were measured at the Mechanical Metrology Division and the quality of these apertures were investigated using a Scanning Electron Microscope (SEM). The interference filters were analysed and calibrated and their temperatures has been fixed at approximately 25 ^{o}C by using a Peltier module and monitored with a multimeter.

A FEL lamp was used as a radiation source and its stability in the time was analysed [4]. All these analyses and results are presented in this paper.

METHODOLOGY AND RESULTS

Measurements of all the main parts for the experimental set up have been realized and preliminary results are presented and discussed in the following sections.

Lamp ageing

The experimental set-up is presented in Figure (1a). Four FEL tungsten-halogen lamps were aged using a constant voltage of 120 V for 4 hours and after that a fixed current of 8.2 A for 48 hours. The most stable FEL lamp would be used in the system as a future standard source of irradiance. It is possible to see in Figure (1b) the typical temporal stability of such standard lamp. The stability criterion is less than 0.5 % over 24 h at 655 nm.

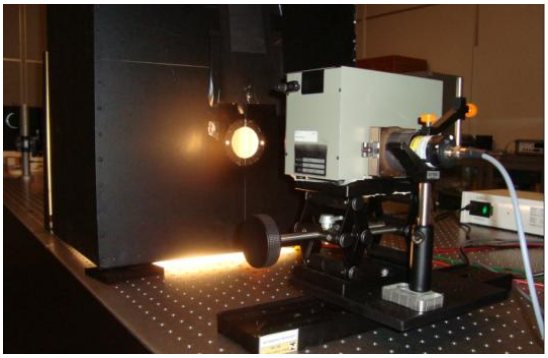

(1a)

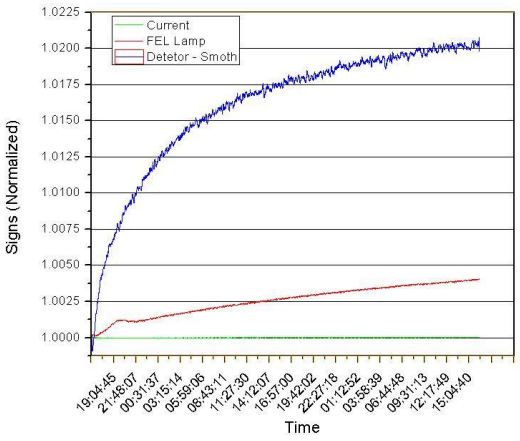

(1b)

Figure 1. (1a) Part of the experimental set up. (1b) Temporal stability of the FEL lamp power.

Aperture area determination

The nominal diameter of circular apertures used in the filter radiometers is 3 mm. They have been machined from aluminium and anodized black. For example, one of the selected apertures has a measured area of 7.074 mm^2 with an associated uncertainty of 0.1 %. The Figure 2 shows the image of a part of the circular aperture, obtained by SEM. Apertures with sharp edges and good finishing are

fundamental to avoid stray light and diffraction in the filter radiometer.

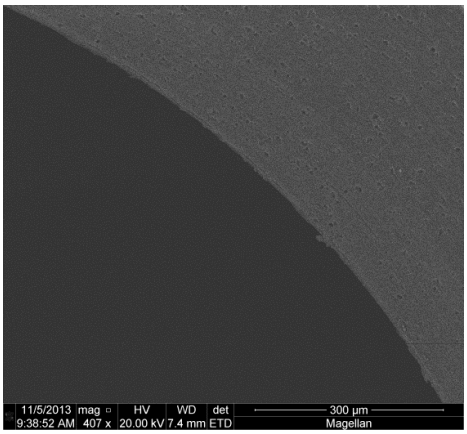

Figure 2. SEM image of a circular aperture.

Filter transmittance measurements

Transmittance of twelve interference filters was measured by mean of a characterized commercial spectrophotometer, in the range of 340 nm to 940 nm. The filters are from Edmunds and have a passband of 10 nm. The filter temperature was controlled around 25 ^{o}C with a Peltier module, and monitored by HP multimeter. Figure 3 shows the results of the transmittance measurements.

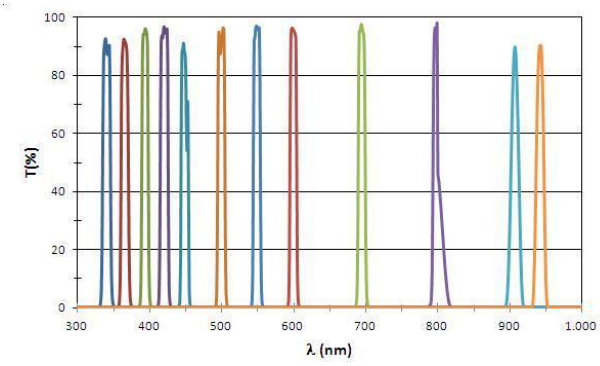

Figure 3. Spectral transmittance of the filters.

Spectral responsivity

The spectral responsivity of the trap detectors was measured against the cryogenic radiometer of INMETRO on the lines of HeNe lasers (632.8 nm) and Ar ion (457.9 nm - 514.5 nm). Table 1 shows the spectral responsivity, the external quantum efficiency (EQE) and the expanded uncertainty of the spectral responsivity (k=2) for one detector used in the filter radiometer. Figure 4 presents the spectral responsivity curve for the visible region.

CONCLUSION

Preliminary tests and measurements have been performed for the implementation of a detector-based absolute spectral irradiance scale. FEL lamps were aged and some of them selected as future standard radiation sources. The area apertures were measured and analysed, and can be used in the filter radiometer. The transmittance interference filters were measured. Spectral responsivity of a trap detector was determined by comparison to a cryogenic radiometer. Uncertainty analysis for the irradiance scale is ongoing. Such promising results give a good basis to follow up this work in the LARAF laboratory.

Table 1. Spectral responsivity, external quantum efficiency (EQE) and expanded uncertainty (k=2) for a TRAP detector.

(nm)	457.9	472.7	488.0	501.7	514.5	632.8
S (A/W)	0.3631	0.3759	0.3888	0.4003	0.4110	0.5077
EQE	0.9833	0.9860	0.9879	0.9893	0.9904	0.9947
U (A/W)	0.0002	0.0001	0.0001	0.0001	0.0002	0.0002

ACKNOWLEDGMENTS

The authors acknowledge the support of the National Council for Research and Development (CNPq /PROMETRO), and Pedro Costa of the LAMED - Mechanical Metrology Division – INMETRO.

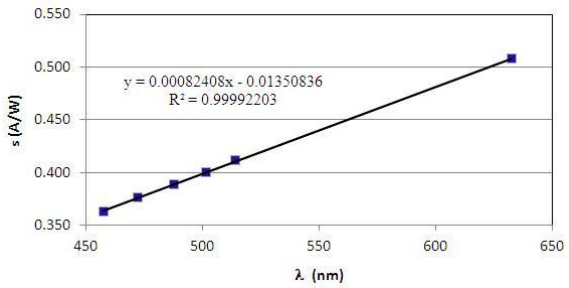

Figure 4. Spectral responsivity curve of trap detector.

REFERENCES

1. P. Kärhä, P. Toivanen, F. Manoocheri, and E. Ikonen, Development of a detector-based absolute spectral irradiance scale in the 380-900 nm spectral range, Appl. Opt., vol. 36, no. 34, 1997.
2. P. Kärhä, P. Toivanen, F. Manoocheri, and E. Ikonen, Spectral irradiance measurements of tungsten lamps with filter radiometer in the spectral range 290 nm to 900 nm, Metrologia, 37, 305-312, 2000.
3. S. Maurício, P. Augusto, G. Hans and C. Iakyra, Cryogenic Radiometer: Performance and Characterization as a Primary Standard at INMETRO, Imeko TC02, Prague - CZ, 2008.
4. Howard W. Yoon and Charles E. Gibson, NIST measurement service: spectral irradiance calibration, NIST special publication, 250-89, 2011.

Verification of the detector-based radiometry scale against ITS-90 via a filter radiometer calibrated by using the pulsed laser-based uniform source at KRISS

Yong Shim Yoo, Kee Suk Hong, Bong-Hak Kim, Seongchong Park, and Dong-Hoon Lee

Division of Physical Metrology, Korea Research Institute of Standards and Science (KRISS), Daejeon, Korea
Corresponding e-mail address: ysyoo@kriss.re.kr

A filter radiometer is constructed and its spectral irradiance responsivity is calibrated by using the pulsed laser-based uniform source (PLUS) of KRISS. The calibrated filter radiometer is used to measure the thermodynamic temperature of a high-temperature blackbody, which is then compared with the international temperature scale ITS-90. The preliminary results show an offset of 0.35 % (1.4 K) between the detector-based radiometry scale and the ITS-90 in a temperature range from 1080 °C to 2500 °C, both realized at KRISS.

INTRODUCTION

The detector-based scale realization in photometry and radiometry can be compared with the international temperature scale ITS-90 based on the freezing points of Ag, Au, or Cu by using a filter radiometer [1-2]. High-accuracy measurement of the spectral irradiance or radiance responsivity of the filter radiometer with high dynamic range and high spectral resolution is of essential importance for this purpose.

To calibrate a filter radiometer, a uniform source based on an integrating sphere combined with a tunable continuous-wave (cw) or quasi-cw laser has been used [3-4]. Recently, a uniform source based on a nano-second pulsed laser source is reported at KRISS [5] and at NIST [6], which provides a cost-effective solution to cover a wide wavelength range.

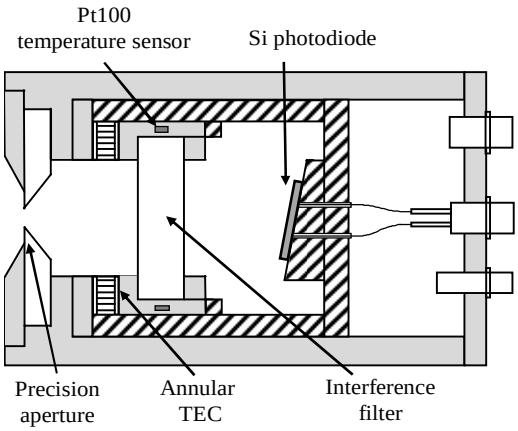

Figure 1. Schematic diagram of the filter radiometer used for the scale comparison.

In this work, we present the current status of the scale comparison by using a filter radiometer, whose spectral irradiance responsivity is calibrated by using the pulsed laser-based uniform source (PLUS) setup at KRISS. The calibration result is used to measure the thermodynamic temperature of a variable-temperature blackbody. By comparing with a radiation thermometer calibrated against a Cu point, the difference between the detector-based radiometry scale and the ITS-90 is evaluated, which are both realized at KRISS.

FILTER RADIOMETER DESIGN

Figure 1 shows the schematic design of the filter radiometer constructed for the scale comparison. It consists of a precision aperture (diameter 5 mm), an interference filter, and a windowless Si photodiode (Hamamatsu S1337 with a dimension of 10 mm x 10 mm). The centre wavelength and the spectral bandwidth of the interference filter are 650 nm and 10 nm (FWHM), respectively. The Si photodiode is tilted with respect to the interference filter to avoid the inter-reflection. The filter radiometer is temperature-stabilized by an annular thermoelectric cooler (TEC) and a water-cooled housing. The interference filter is thermally isolated from the housing, and its temperature is separately and more precisely controlled by using two Pt100-sensors attached to the filter mount.

CALIBRATION

The calibration of the spectral irradiance responsivity of the filter radiometer is performed in two ways. First, the spectral power responsivity is measured by using a conventional lamp-monochromator-based comparator setup in the under-filled geometry with a Si trap detector as the reference. The spectral bandwidth and the scan interval of this measurement were 1 nm and 0.6 nm, respectively. The spectral irradiance responsivity is then calculated by multiplying the size of the precision aperture to the measured spectral power responsivity. This way provides the data with a small interval in a wide wavelength range.

The second way is to measure the absolute values of spectral irradiance responsivity directly by using the PLUS setup in the overfilled geometry. A Si trap detector with a precision aperture attached is used as the reference. The PLUS is based on an integrating sphere with a diameter of 25.4 mm irradiated by a nano-second optical parametric oscillator (OPO) with a repetition rate of 1 kHz (EKSPLA, NT242). A monitor detector is used to correct the fluctuation of the pulse energy during the comparison [5]. This way provides a higher spectral resolution and higher dynamic range than the other way. Figure 2 shows the results of the spectral irradiance responsivity measurement in both the ways, which are in coincidence within their uncertainties.

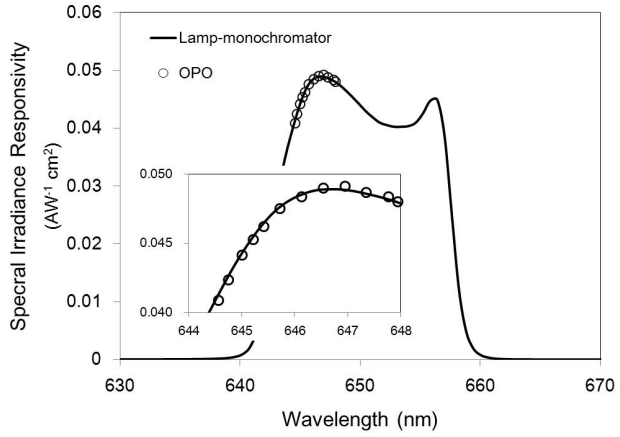

Figure 2. Calibrated spectral irradiance responsivity of the filter radiometer.

SCALE COMPARISON

The thermodynamic temperature of a high-temperature variable blackbody (VINIIOFI BB3500MP) is measured by using the calibrated filter radiometer. The blackbody cavity has a diameter of 58 mm, a length of 280 mm, and an opening diameter of 35 mm, and an estimated emissivity of 0.9997. In order to define the source-size, a temperature-controlled aperture with a diameter of 7 mm is installed in front of the blackbody opening. The distance between the aperture and the reference plane of the filter radiometer is set to be 1 m.

For scale comparison, the temperature of the same blackbody is also measured by using a radiation thermometer (KE LP4) that is calibrated against the Cu fixed point [7]. Figure 3 shows the difference between the thermodynamic temperature measured by using the filter radiometer and the ITS-90 temperature in a temperature range from 1080 °C to 2500 °C. The maximum difference is 1.4 K at 2500 °C, which corresponds to a relative signal difference of 0.35 % for the filter radiometer.

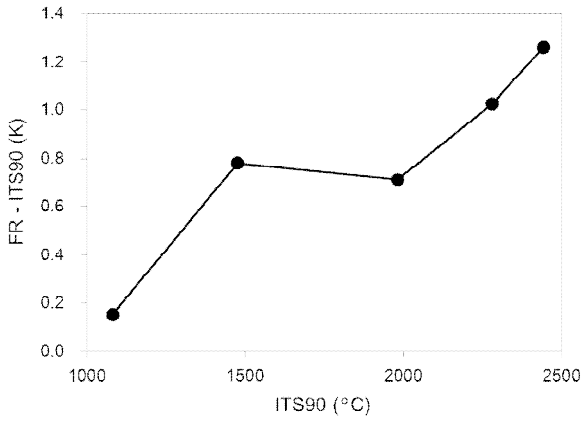

Figure 3. Difference between the thermodynamic temperature measured by using the filter radiometer (FR) and the ITS-90 temperature by using a radiation thermometer.

The presented preliminary results shows an offset of 0.35 % of the detector-based radiometry scale from the ITS-90, both realized at KRISS. We note that such an offset is also verified through the international key comparisons in photometry and radiometry which KRISS has participated. Detailed uncertainty and error analysis of the scale comparison is in progress, which should help us to improve the accuracy of the scale realization.

REFERENCES

1. R. L. Rusby *et al.*, Thermodynamic basis of the ITS-90, Metrologia, **28**, 9-18 (1991).
2. M. Stock *et al.*, Measurement of T-T90 in the range from 660 to 962 by absolute spectral radiometry employing a cryogenic radiometer and a double heatpipe blackbody, Proceedings of TEMPMEKO'96, 19-24 (1996).
3. S. W. Brown *et al.*, Facility for spectral irradiance and radiance responsivity calibrations using uniform sources, Applied Optics, **45**, 8218-8237 (2006)
4. N. Noorma *et al.*, Characterization of filter radiometers with a wavelength-tunable laser source, Metrologia, **40**, S220-S223 (2003).
5. D.-H. Lee *et al*, The KRISS PLUS for measurement of spectral radiance responsivity, Proceedings of XX IMEKO World Congress, 1018 (2012)
6. Y. Zong *et al*, A new method for spectral irradiance and radiance responsivity calibrations using kilohertz pulsed tunable optical parametric oscillators, Metrologia, **49**, S124-S129 (2012).
7. Y. S. Yoo *et al*, High dynamic range measurement of spectral responsivity and linearity of a radiation thermometer using a super-continuum laser and LEDs, Temperature: Its Measurement and Control in Science and Industry, **1552**, 698-703 (2013).

Realization of the scale of illuminance in the range from 0.001 to 1 lux at BelGIM

N.V. Bakovec[1], V.A. Dlugunovich[2], O.B. Tarasova[1], and S.V. Nikanenka[2]

[1]*National Metrological Institute of the Republic of Belarus (BelGIM), Minsk, Belarus,*
[2]*B. I. Stepanov Institute of Physics National Academy of Sciences of Belarus, Minsk, Belarus*
Corresponding e-mail address: optic@belgim.by

The scale of illuminance in the range from 0.001 to 1 lux at BelGIM is presented. The approach of the scale realization is described. The main characteristics of setup for photometers calibration in the range of low illuminance levels are presented.

1. INTRODICTION

For the last years, the assortment of optic-electronical products (devices of night vision; systems of video surveillance, etc.) has considerably increased. Their calibration and working capacity check are made at low levels of illuminance.

In this paper we describe a realization of the scale of illuminance in the range from 0.001 to 1 lux at the National Metrological Institute of the Republic of Belarus (BelGIM). The main characteristics of a setup for photometers calibration in the range of low illuminance levels are presented.

2. PRINCIPLE OF THE SCALE REALIZATION APPROACH

To carry out the calibration of photometers at illuminance low levels, it is necessary to have a precise scale of illuminance. Traditionally such an illuminance scale by is created means of the increase distance between a standard lamp and a photometer. It will be noted, that in this case a lengthy optical table is required.

At realization of the illuminance scale in the range from 0,001 to 1 lux on the National standard of unities of luminous intensity and illuminance of the Republic of Belarus (NSLII) the approach, which is based on precisely known of the luminance factor of plate, is offered. Fig.1 shows the optical scheme of this approach.

The diffusely-reflected plate of opal glass or polytetrafluoroethylene is uniformly illuminated by a standard lamp with a color temperature T_c = 2856 K.

The illuminance E_1 on the plate surface can be defined as

$$E_1 = \frac{I_v}{l^2}, \qquad (1)$$

where l_1 is the distance between the plane of filament lamp and a diffusely-reflected plate, m; I_v is a luminous intensity of standard lamp, cd.

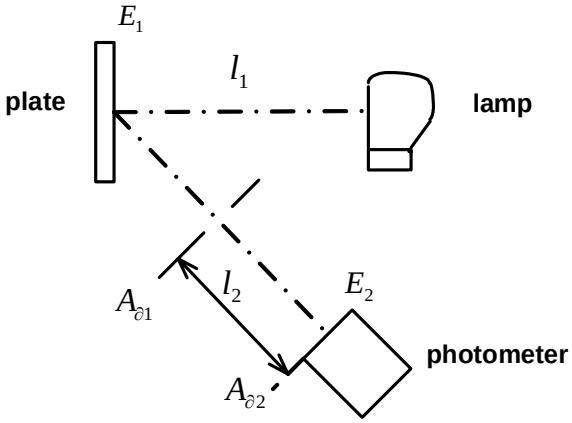

Figure 1. Optical scheme of the approach of illuminance scale

In fact, the diffusely-reflecting plate (that reflects radiation at an angle of 45 °), is a radiation source with the luminance

$$L_v = \frac{kE_1\rho}{\pi}, \qquad (2)$$

where ρ is a luminance factor of diffusely-reflected plate; k is a correction factor, which is defined by [1]

$$k \cong 1 + \left(\frac{r_{\partial 1}}{l_2}\right)^2 + \left(\frac{r_{\partial 2}}{l_2}\right)^2, \qquad (3)$$

where l_2 is a distance between the calibrated aperture and the aperture of the tested photometer, m; $r_{\partial 1}$ and $r_{\partial 2}$ is the radiuses of the calibrated aperture and the aperture of the tested photometer, m.

The calibrated aperture area $A_{\partial 1}$ can be calculated as

$$A_{\partial 1} = \frac{\pi d_1^2}{4} \qquad (4)$$

where d_1 is a calibrated aperture diameter, m.

The result is that the test photometer can measure the illuminance E_2

$$E_2 = \frac{L_v A_{\partial 1}}{l_2^2} = \frac{I_v k \rho d_1^2}{4 l_1^2 l_2^2} \qquad (5)$$

The numerical simulation and analysis of the published data reveal that, for the realization of illuminance scale in the range from $1 \cdot 10^{-3}$ to 1 lux, the measurement setup must have the following key parameters: the luminous intensity of standard lamp should be from 1 to 10 cd; the diffusely-reflected plate must possess the luminance factor not less than 0.8; the distance between the plane of filament lamp and the diffusely-reflected plate should be from 50 to 700 mm; the distance between the calibrated aperture and aperture of the investigated photometer should be from 10 to 500 mm; the calibrated apertures should have the following nominal diameters: 2, 5, 10, 20 and 30 mm.

3. CONCLUSION

The approach described was the basis for creation of the setup for photometers calibration [2], which is included as a part of the NSLII. At selection of this approach, we have took account, that the calibration of standard lamp by the luminous intensity, the calibration of the diffusely-reflected plate by the luminance factor and the calibration of apertures by diameter can be performed on the standards which are available in BelGIM.

The setup for photometers calibration has the following main characteristics: the reproduction of illuminance in the range from $1 \cdot 10^{-3}$ to 1 lux; the bounds of non-excluded systematic error of luminance transfer is ± 1.6 %; the root-mean-square deviation of luminance observation is 0.001 dimensionless units.

REFERENCES

1. Ohno, Y. NlST measurement services: Photometric Calibrations. NlST Special Publication 250-37. U.S. government printing office Washington, 1997.
2. Patent RU 95398U1.

The new reference set-up for regular spectral transmittance and reflectance at PTB

Alfred Schirmacher, Steven Hesse, and Eva Velke

PTB Braunschweig, Braunschweig, Germany
Corresponding e-mail address: Alfred.Schirmacher@PTB.de

The national reference set-up for regular transmittance and reflectance (NaNoTrans and NaNoRef) was rebuilt after the removal of the old system ([1],[2]). With this improved apparatus optical filters and mirrors can be calibrated in the wavelength range between 200 nm and 20 µm. Due to its flexible design the investigation of various experimental problems is possible. In the following the main features of the set-up are discussed and examples of possible measurements are shown.

DESCRIPTION OF THE APPARATUS,

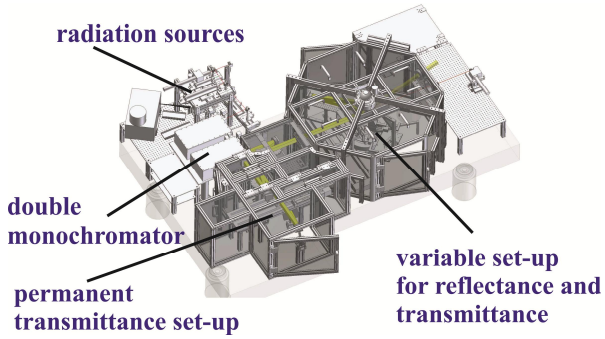

Figure 1. Sketch of the reference apparatus, dimensions are approx. 3.6 m x 2.4 m.

MEASUREMENT EXAMPLES

In Fig. 1 a sketch of the set-up exhibits the main components. The optical radiation prepared by a double monochromator (f = 0.5 m) can be fed into two different measurement sides of the set-up. Radiation sources for both parts are conventional radiators (D_2-, halogen lamp, heat emitters) as well as super continuum sources, laser driven light sources, lasers or infrared diodes. Coupling-in is performed by mirror set-ups allowing also the use of optical fibres.

The permanent transmittance set-up uses an optical path which projects the exit slit of the double monochromator onto the sample by a 1.5 magnification in a slightly convergent beam. Primarily cuvette type filters are examined. However, the size of the samples or structures under investigation can be up to 90 mm x 110 mm. Sample positioning can be performed with a minimum spatial resolution of 5 µm. Detectors are photomultipliers and various diodes (Si, InGaAs) in the wavelength range between 200 nm to 2.5 µm. In Fig. 2 a result of the measurement of a metal on quartz filter is given showing a distinctive transmittance gradient in the visible spectral range. The filter of nominal 1% transmittance exhibits a local variation of about 0.2%.

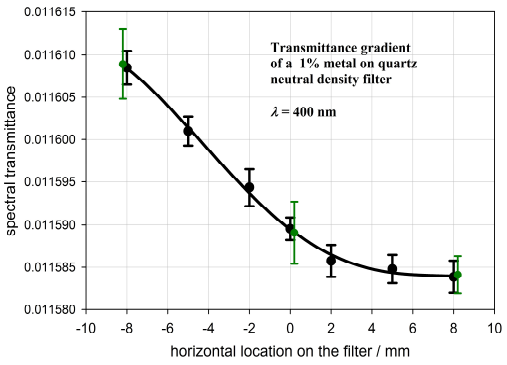

Figure 2. Local variation of transmittance; green: re-measurement after 6 months; standard deviation plotted.

In the octagon-shaped sample chamber (d = 1.5 m) of Fig. 1 diverse optical set-ups can be realised for transmittance or reflectance measurements (NaNoRef). When using the double monochromator, beam forming is performed in most cases by z-shaped mirror combinations placed in an upstream chamber. But it is also possible to use the radiation distribution of lamps, e.g. in luminous reflectance measurements, or laser beams by coupling-in through two back-end ports (0° and 15°). The central part of this chamber is a goniometer (Fig. 3), which consists of two rotation devices (detector arm and sample rotation) and an x-y-z displacement unit with an optional cradle for out of plane measurements. All units use absolute position decoding and can be applied in high resolution mode. A series of detectors for the envisaged spectral range can be either mounted directly on the detector arm or can be positioned on top of the chamber if a reflection optic is used. Conventional calibrations of reflectance standards are performed at angles of incidence between approximately 6° and 85° with a size of the measurement beam of typically 10 mm x 35 mm. Apart from this a multitude of different

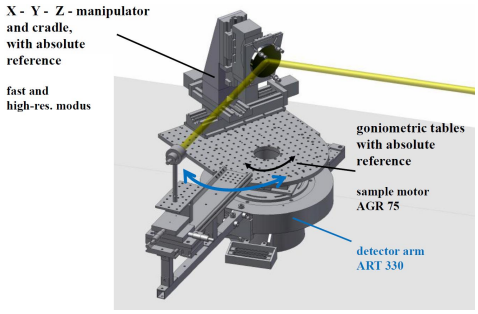

Figure 3. Central goniometric unit for reflectance measurements.

measurements is feasible. As an example in Fig. 4 the relative scattering distribution as measured for a Zerodur sample is given. The measurement was performed using the polarised radiation of a diode laser and a Si detector equipped with a polarisation analyser moving around the scattering sample. The resulting distribution can be evaluated fairly well by a Raleigh-Debye-Gans model curve giving the mean size of the scattering centres.

When calibrating a holographic diffuser for its

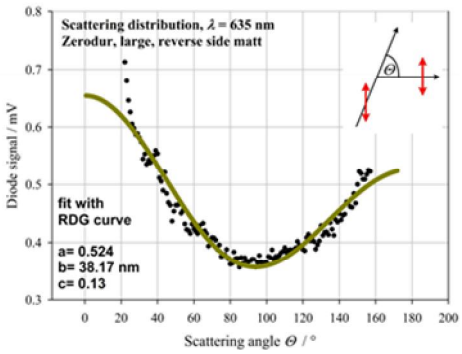

Figure 4. Scattering distribution of a Zerodur sample.

half width of the scatter function, the distribution outside the plane of incidence is detectable by measuring also the azimuthal dependence. The observed curves are globally fitted well by a Gaussian distribution. However, especially in the range of small scattering angles, reproducible structures are observed (Fig. 5) which can most probably be attributed to regularly ordered sub-ranges on the sample.

Fig. 6 gives the experimental results for a 45° optical beam splitter. In this measurement regular transmittance and reflectance were determined both in one process by sweeping the detector arm to the head-on (with and without sample in the beam) and to the 90° position, respectively. The angle of incidence

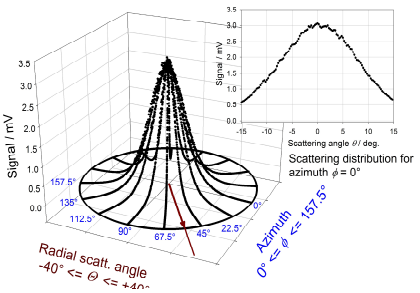

Figure 5. Scattering distribution of a holographic diffuser; insert: profile for the azimuthal angle $\Phi = 0°$.

and the radiation cone angle were defined by the experimental set-up. The results are close to the design parameters with respect to effectivity and curve steepness.

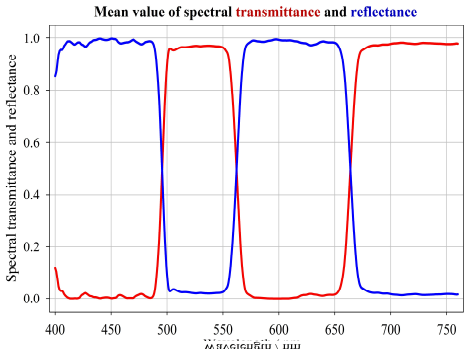

Figure 6. Calibration of a dichroitic beam splitter.

SUMMARY

The newly developed reference set-up at PTB is ready for traceable calibrations of regular spectral transmittance and reflectance. It is currently being used in the CCPR-K6 Key Comparison on regular transmittance. During the course of these measurements the transmittance of a set of standards is determined in both parts of the apparatus, using a slightly divergent and the standard parallel beam set-up as defined in [3], respectively. In addition, because of the flexible design of the set-up, a variety of measurement tasks can be dealt with resulting in precise calibrations of different optical components.

REFERENCES

1. J.F. Verill, Intercomparison of spectrophotometric measurements of regular transmittance (metal on quartz filters), Revised summary report, NPL COEM 16 (1998)
2. G. Obein, J. Bastie, Report on the CCPR Key Comparison K6 Spectral regular transmittance, LNE-INM – Sept 2008
3. CCPR-K6:2010 Key Comparison, Spectral Regular Transmittance, Technical Protocol, February 2013

Method for the characterization of an optical imaging system using the MLS synchrotron radiation primary source standard

S. Anevsky[1], Y. Akimov[1], V. Krutikov[1], R. Minaev[1], O. Minaeva[1],
D. Senin[1], R. Klein[2], D. Taubert[2], G. Ulm[2]

[1]*All-Russian Institute for Optical and Physical Measurements (VNIIOFI), Moscow, Russia*
[2]*Physikalisch-Technische Bundesanstalt (PTB), Berlin, Germany*
Corresponding e-mail address: anevsky@vniiofi.ru

An imaging system consisting of a commercial astronomical telescope and a CCD camera will be characterized with calculable synchrotron radiation at the Metrology Light Source (MLS), the primary synchrotron radiation source standard of PTB. The radiant intensity of the synchrotron radiation is calculated from the storage ring parameters. The white, undispersed synchrotron radiation source point is imaged on to the CCD camera. The response of the system can so be characterized in terms of radiance. Also other properties as the linearity of the system or the CCD homogeneity can be investigated.

INTRODUCTION

Electron storage rings with calculable bending magnet radiation according to the Schwinger theory [1] are used as primary source standards for radiometry at several national metrology institutes [2, 3]. PTB uses the BESSY II [4] electron storage ring in the soft X-ray spectral region and the MLS [5, 6] in the NIR, visible, UV and VUV spectral region for this purpose.

The spectral radiant intensity

$$I_\lambda(\lambda) = I_\lambda(\lambda; I_e, W, B, \Sigma y)$$

of synchrotron radiation (SR) from electron storage rings can be calculated from basic electrodynamic relations (Schwinger equation) from the measured storage ring parameters, i.e. the electron beam energy W, the magnetic induction at the radiation source point B, the stored electron beam current I_e and the effective vertical source size Σ_y. The spectral radiant intensity is directly proportional to the stored electron beam current $I_e = N\, e\, \nu$ given by the number of stored electrons N, the electron charge e and the electron revolution frequency in the storage ring ν. With the necessary equipment installed to measure and control the electron beam current over a wide dynamic range, the radiant intensity of the SR can so be adjusted accordingly without changing the spectrum [7].

SCHEME OF THE MEASUREMENT

The imaging system consists of a telescope, having a focal length of 1250 mm and an opening diameter of 90 mm, a V_λ filter for limiting the observed spectral band-pass and a CCD camera of 3326 x 2504 pixels. The pixel size is 5.4 x 5.4 μm^2. The telescope-CCD system will be mounted at the MLS white light beamline [8] at a distance of approximately 22 m from the radiation source point behind a characterized vacuum view port.

The large distance to the radiation source point ensures a rather homogeneous illumination of the telescope entrance. The radiant intensity of SR shows a homogeneous angular distribution in the horizontal direction and a directed distribution in the vertical, the opening angle of which is wavelength dependent [6], but is rather wide and flat for wavelengths in the visible (Fig. 1).

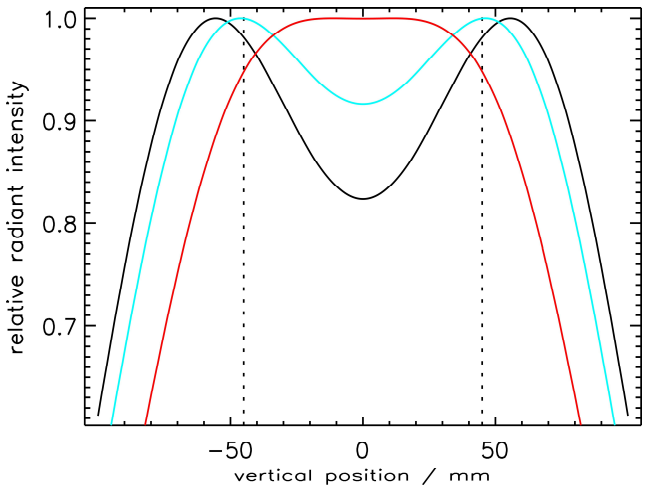

Figure 1. Vertical spatial distribution of MLS bending magnet radiation in at a distance of 22 m and a wavelength of 555 nm for 630 MeV (black curve), 250 MeV (blue curve) and 150 MeV (red curve) electron beam energy. The dashed vertical lines mark the opening diameter of the telescope.

The device can be moved by means of computer controlled stepper motors in the horizontal and

vertical direction, the latter is important for centring the SR onto the telescope. Provision will also be taken to be able to control the vertical and horizontal angle in order to align the optical axis of the telescope to the direction of the SR.

The SR source point is imaged with a demagnification of approximately 0.06 onto the CCD camera. The exact de-magnification factor can be determined during the measurements by shifting the entire system in the horizontal direction by a well defined amount and observing the shift on the CCD image.

PTB operates two systems with similar design and functionality that are permanently installed at the MLS facility for the measurement of the horizontal and vertical source size [9]. One of these systems looks into a section of the storage ring which has – due to the symmetry of the storage ring lattice functions -equivalent beam optical functions as the section where the white light beamline is installed and thus allows a direct comparison of the measured electron beam sizes. This system works for a wide range of electron beam currents, from maximum stored current (up to 200 mA) to minimum stored current (1 pA), which is generated by a single stored electron.

CHARACTERIZATION OF THE SYSTEM

The electron beam ideally has a 2D Gaussian shape with rms size of σ_x and σ_y in the horizontal and vertical direction, respectively. A rms beamsize of typically 500 μm will be de-magnified to 30 μm in the CCD plane, corresponding to roughly six pixels.

Electron storage rings are primary standards in term of radiant intensity I_λ. Nevertheless, for the purpose of this characterization a radiance L_λ^{SR} of the SR source point can be defined, e.g., as

$$L_\lambda^{SR} := I_\lambda \frac{1}{2\pi \sigma_x \sigma_y} e^{-\left(\frac{(x-x_0)^2}{2\sigma_x^2} + \frac{(y-y_0)^2}{2\sigma_y^2}\right)}$$

for a source point that is symmetrically with respect to the orbital plane. This SR-radiance can be calculated from the known radiant intensity of the SR-radiation. The source point is then imaged onto the CCD, the response of which can so be characterized in terms radiance. By an angular tilt, the spot can be moved across the CCD ship area to determine the chip homogeneity. Moreover, by variation of the stored electron beam current, the linearity in the response of the system can be investigated.

SUMMARY

The response of the imaging system can be characterized in terms of radiance using calculable SR. Moreover, the flexibility in operation the storage ring at various electron beam currents allows characterizing the linearity of the system. The high temporal stability of the radiant intensity normalized to the electron beam current enable the investigation of spatial homogeneity of the CCD responsivity. The imaging system has previously been investigated using an absolutely calibrated, large aperture (40 cm Ø), variable radiance integrating sphere. The results obtained with this set-up can be compared to the ones obtained from the SR primary source measurements.

REFERENCES

1. Schwinger J 1949 On the classical radiation of accelerated electrons *Phys. Rev.* **75**, 1912.
2. Ulm G 2003 Radiometry with synchrotron radiation *Metrologia* **40**, S101.
3. Hollandt J, Friedrich R, Gutschwager B, Taubert D, Hartmann J 2003/2004 High Temperatures – High Pressures **35/36**, 379.
4. Thornagel R, Klein R, and Ulm G 2001 The electron storage ring BESSY II as a primary source standard from the visible to the X-ray range *Metrologia* **38**, 385.
5. Klein R, Brandt G, Fliegauf R, Hoehl A, Müller R, Thornagel R, Ulm G, Abo-Bakr M, Feikes J, v. Hartrott M, Holldack K and Wüstefeld G 2008 Operation of the Metrology Light Source as a primary radiation source Standard Phys. Rev. Special Topics - Accelerators and Beams (PRST-AB) 11, 110701.
6. Klein R, Brandt G, Fliegauf R, Hoehl A, Müller R, Thornagel R, and Ulm G 2009 The Metrology Light Source operated as a primary source standard *Metrologia* **46**, S266.
7. Klein R, Thornagel R, and Ulm G 2010 From single photons to milliwatt radiant power – electron storage rings as radiation sources with a high dynamic range *Metrologia* **47**, R33.
8. Klein R, Gottwald A, Kolbe M, Richter M, Scholze F, Thornagel R and Ulm G 2013 UV and VUV calibration capabilities at the Metrology Light Source for solar and atmospheric AIP Conf. Proc. 1531, 879.
9. Koschitzki C, Hoehl A, Klein R, Thornagel R, Feikes J, Hartrott M, Wüstefeld G 2010 Highly sensitive beam size monitor for pA currents at the MLS electron Proc. IPAC10, 894-896.

Detector-based Absolute Calibration of a 1.6 µm Radiation Thermometer for Validation of Source-based ITS-90 Temperature Scale

T. Keawprasert, P. Wongnut, and U. Norranim

National Institute of Metrology (Thailand), Klong Luang, Pathum Thani, Thailand
Corresponding e-mail address: thada@nimt.or.th

The new experimental setup has been assembled at the National Institute of Metrology Thailand (NIMT) for the detector-based absolute spectral responsivity measurement of a 1.6 µm radiation thermometer. The concept of this setup is to measure the relative spectral responsivity of the radiation thermometer for a whole range using a monochromator facility also used for the ITS-90 realization above the Ag point. Subsequently the absolute spectral responsivity is derived from a Ag fixed-point blackbody measurement. Thereafter a detector-based radiance temperature scale is realized between 157 °C and 1100 °C and finally used to validate a ITS-90 fixed-point radiance temperature scale. Comparison results of the two different calibration approaches are presented.

INTRODUCTION

Recently a spectral responsivity measurement facility has been established at the NIMT in order to calibrate radiation thermometers according the ITS-90. In combination with the Cu point measurement and a non-linearity measurement, the ITS-90 temperature scale can be realized on a 0.65- and 0.9 µm radiation thermometer up to 2,500 °C. However, below the Cu point, the multiple fixed-point method is used to calibrate a 0.9- and 1.6 µm radiation thermometer for realization of source-based radiance temperature scale down to the freezing point of Zn (419.527 °C) and the freezing point of indium (156.5985 °C) respectively.

Based on the first calibration method, a detector-based radiance temperature scale can be also realized down to the Zn freezing point for the 0.9 µm radiation thermometer and already compared to the fixed-point radiance temperature scale [1]. Presently differences in temperature between the two calibration methods are in good agreement within 0.1 °C for the 0.9 µm radiation thermometer.

In the same way, these two calibration methods are performed for the 1.6 µm radiation thermometer in to compare the detector-based radiance temperature scale with the source-based radiance temperature scale in the temperature range from the In freezing point to the the Cu freezing point. Therefore, this paper will describe the measurement facility and measurement results of the two methods. Comparison results of obtaining radiance temperature scales will be shown and its future work will be discussed.

SPECTRAL RESPONSIVITY CALIBRATION

In this work, a 0.25 m Czerny-Turner double-grating monochromator is used to calibrate the 1.6 µm radiation thermometer, covering the spectral range from 1000 nm to 2200 nm by using a diffraction grating with 300 lines/mm [2]. A low pressure mercury lamp is used to calibrate the wavelength of the monochromator. Its accuracy in the wavelength scale is better than 0.4 nm in the wavelength region. For a measurement, a Quartz-halogen lamp is used as radiation sources for the monochromator. At the exit port of the monochromator, the output radiation is divided into two parts by a half mirror. One part is collimated into a InGaAs reference detector, and another part is focused to a thermopile used as standard detector or projected into an optics of the radiation thermometer behind the thermopile with matching f-number as shown in Fig.1.

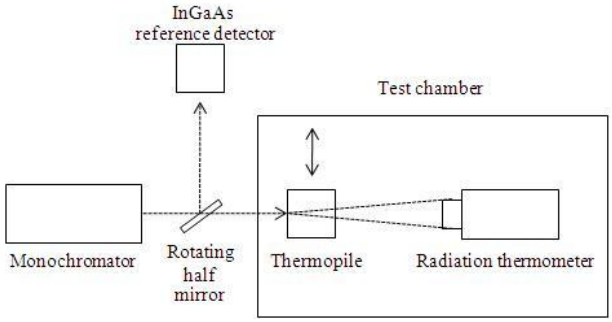

Figure 1. Schematic of the experimental setup.

That is the test radiation thermometer is indirectly compared via the reference detector against the thermopile, whose spectral responsivity is assumed to be flat in the desired wavelength range. Finally the relative spectral responsivity of the radiation thermometer can be calculated by this equation

$$R(\lambda) = \frac{V_{RT}(\lambda)}{V_{REF,2}(\lambda)} \cdot \frac{V_{REF,1}(\lambda)}{V_{TP}(\lambda)} \qquad (1),$$

where $R(\lambda)$ is the relative spectral responsivity, $V_{REF,1}$, $V_{REF,2}$ is the voltage obtained from the reference detector while measuring the thermopile and while measuring the radiation thermometer, V_{TP} is the voltage obtained from the thermopile and V_{RT} is the voltage from the radiation thermometer.

Firstly the thermopile was compared against the reference detector in the wavelength range of 1000 nm to 2200 nm with the spectral bandwidth of 10 nm and the test thermometer was then measured against the reference detector with the same arrangement. After that, a measurement with the spectral bandwidth of 1.0 nm was performed to cover the bandpass region of the test thermometer (1400 nm to 1800 nm). Finally the fine structure was investigated around the flat responsivity of the test thermometer (1500 nm to 1700 nm) with the spectral bandwidth of 0.2 nm. Even with this bandwidth, the signal to noise ratio is higher than 3 x 10^{-4}. Measured spectral responsivity of the test thermometer is shown in Fig. 2.

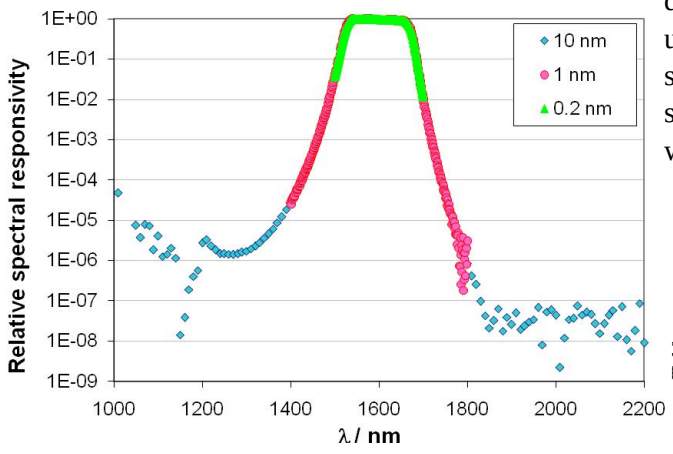

Figure 2. Relative spectral radiance responsivity of the 1.6 µm test radiation thermometer.

The out-of-band responsivity of the thermometer is lower than 10^{-5} and down to 10^{-7} in the wavelength range above 1800 nm. From the investigations in the fine structure, any interference effects are not found with the spectral bandwidth of 0.2 nm. According to Ref. 3, the total relative uncertainty is estimated to 0.5%, yielding the temperature uncertainty of 100 mK at the In freezing temperature.

ITS-90 FIXED-POINT MEASUREMNT

The test radiation thermometer is also calibrated at the ITS-90 fixed-point blackbodies from In (419.527 °C) to Cu (1084.62 °C). The combined uncertainty (k = 1) due to the fixed-point blackbodies excluding drift is estimated to 25 mK at the In point to 100 mK at the Cu point. The ITS-90 radiance temperature scale is realized between these fixed-point by interpolating with the Planck's version of Sakuma-Hattori equation. According to Ref. 4, the uncertainty (k=1) in realized temperature scale varies between 50 mK to 200 mK in the temperature range between 157 °C and 1100 °C.

From the measurement at Ag point, a detector-based radiance temperature scale can be realized by integrating the spectral responsivity $R(\lambda)$ multiplied by the Planck function $L(\lambda, T)$,

$$V(T) = a\int L(\lambda,T)R(\lambda)d\lambda \qquad (2),$$

where the coefficient a was determined from signal at the Ag freezing point.

Finally the two radiance temperature scales are compared. For the test radiation thermometer, the differences in radiance temperature with combined uncertainty between the detector-based scale and the source-based scale at the fixed-point temperatures are shown in Fig.3. The maximum difference is 0.14 °C, within the combined uncertainty of 0.2 °C.

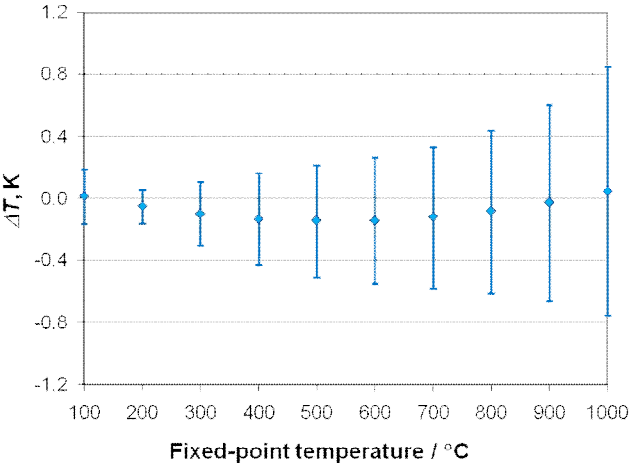

Figure 3. Temperature differences between the two calibration approaches and their combined uncertainty.

CONCLUSION

The double monochromator is set up to perform the spectral responsivity calibration from 1000 nm to 2200 nm for a 1.6 µm radiation thermometer. The same radiation thermometer is also calibrated with fixed-points of In, Sn, Zn, Al, Ag and Cu to perform

its ITS-90 radiance temperature scale. Two radiance temperature scales are compared. The differences of both temperature scales are in agreement within <0.15 ºC over the whole temperature range.

FUTURE WORK

The detector-based absolute spectral radiance responsivity calibration of a radiation thermometer will be developed based on a tuneable fibre laser and an 50 mm diameter integrating sphere in the wavelength range from 1550 nm to 1650 nm.

REFERENCES

1. T. Keawprasert, P. Wongnut and U. Norranim, in Proceeding of NEWRAD 2010, edited by Dong-Hoon Lee, 287-288, Kriss, Daejong, 2008.
2. F. Sakuma and L. Ma, in Proceeding of SICE-ICASE 06, 3336-3341, 2006
3. J. Fischer et al., Temperature: Its Measurement and Control in Sceience and Industry, 7, 631-638, AIP, New York, 2003.
4. P. Saunders et al. Int. J. Thermophys, 29, 1066, 2008.

How to ensure the highest quality of LED measurements using the halogen reference light source for the calibration of measuring instruments?

Jan Lalek

GLOPTIC, Puszczykowo, Poland
Corresponding e-mail address: j.lalek@lafot.com

The wide range and significant changeability of the up-to-date light sources available on the market, in particular of the LED type, brings about the necessity of the accurate measurement of the parameters of these light sources.

Due to different properties of spectrum of the new sources, a significant number of devices currently used do not provide the sufficient measurement accuracy. In a large number of cases, it is caused by the improper calibration of the mentioned devices.

To obtain an accurate calibration, it is indispensible to use the new reference light sources, which will make it possible to eliminate inaccuracy caused by the commonly used existing reference sources. This paper discusses the problems encountered in the widely used reference light sources and presents an innovative solution to the reference light source in which these defects have been eliminated.

Practical limitations of near-field goniophotometer measurements imposed by a dynamic range mismatch

Jan Audenaert, Peter Hanselaer, and Frédéric B. Leloup

Light&Lighting Laboratory, Dept. ESAT, KU Leuven, Gent, Belgium
Corresponding e-mail address: jan.audenaert@kuleuven.be

To accurately describe the spatial and angular light distribution of a light source, near-field goniophotometry relies on the data captured by both an imaging luminance measurement device and a photometer. Since both detectors exhibit a difference in dynamic range, the resulting ray file and luminous intensity distribution (LID) may be incorrect. In result, significant deviations may be encountered between LIDs generated from near-field and from far-field measurements. In this paper, a practical example of this dynamic range mismatch induced error is discussed. A method to check for this error is proposed and applied to a practical example.

INTRODUCTION

Near-field goniophotometry [1-4] allows the generation of an LID and a ray file of a light source through the combined use of an imaging luminance measurement device (digital camera) and a photometer. These detectors are used to quantify the relative luminance distribution and the illuminance, respectively, during a scanning process on a virtual spherical surface around the device under test (DUT). Afterwards, the relative luminance distributions measured at each position are weighted with the total luminous flux.

Within a specified sensing scale, determined from the direction of maximum flux in order to avoid saturation during the scanning process, the photometer has a dynamic range of 18 bits (S/N ratio of 108 dB). On the contrary, the charge-coupled device of the digital camera only has a dynamic range of 12 bits (S/N ratio of 72 dB) for a specified integration time.

Two different issues may result from this restricted dynamic range of the camera. First, it is possible that in specific directions, the camera does not capture a luminance distribution because of a too low signal, while the photometer still records an emitted flux. Second, luminance values below the detection limit of the camera may not be incorporated within a relative luminance distribution image.

In result, when generating an LID or ray file from both the data obtained by the camera and the photometer, each pixel of each relative luminance image will be attributed an incorrect luminous flux. Subsequently, the generated LID and ray file will also be erroneous.

It was already coined by Ashdown [1] that this dynamic range mismatch issue might arise when a light source exhibits large variations in luminance within a single image, or between images captured from different directions. However, no experimental results have confirmed this.

PRACTICAL EXAMPLE

A luminaire consisting of a ceramic reflector placed around a light emitting diode (LED), as shown in Fig. 1, was chosen to illustrate the problem.

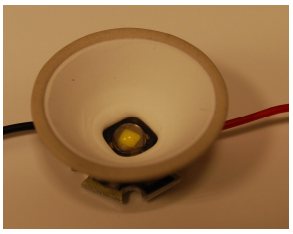

Figure 1. Luminaire under investigation consisting of an LED and ceramic reflector.

First, a measurement of the LID of the luminaire was performed in a near-field goniophotometer (NFG) using both the camera and photometer detector of the device, revolving about the DUT at a distance of 28 cm. Next, the LID of the luminaire was measured in another goniophotometer, using only the photometer detector. Since in this second device, the distance from the DUT, aligned in the centre of the goniometer, to the photometer equals 147 cm while the diameter of the DUT only equals 2.7 cm, the photometer can be considered to be positioned in the far-field [5].

The LIDs within the C0 half-plane, both generated from the near-field measurement and measured under far-field conditions, are compared in Fig. 2. An important difference between both

distributions can be observed. The maximum intensity at $\gamma = 0°$ measured in far-field conditions equals 0.93 cd, being 1.03 cd when generated from the near-field measurement.

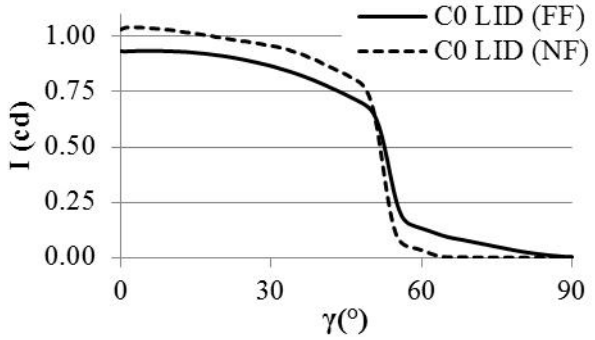

Figure 2. Comparison between the LID in the C0 half-plane, generated from a near-field measurement and measured under far-field conditions, respectively denoted as 'C0 LID (NF)' and 'C0 LID (FF)'.

The percentage error between both LIDs (PE_{LID}) is plotted as a function of γ in Fig. 3. PE_{LID} is around 10.5% between $\gamma = 0°$ and $\gamma = 50°$, to increase dramatically for larger angles of γ.

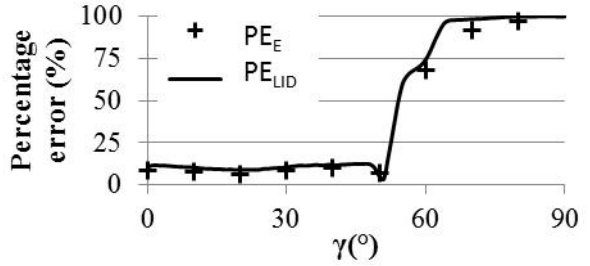

Figure 3. Percentage error between the LIDs (PE_{LID}) and between the illuminance values (PE_E) in the C0 half-plane, generated from the near-field and far-field measurement.

Note that both LIDs, when integrated, yield the same luminous flux, as this is solely determined by integration of the illuminance values registered by the photometer.

DYNAMIC RANGE INDUCED ERROR CHECKING METHOD

At this moment, no standard way to check for these dynamic mismatch induced errors in both the LID and the ray file is implemented in the commercial proprietary software steering the measurement process of the NFG [6]. However, a so-called sanity check could be incorporated to detect such erroneous results [1]. Basically, the sanity check consist of comparing an illuminance value measured with a photometer in a certain position, to an illuminance value simulated from the generated ray file. The simulated illuminance value can be calculated by performing a ray intersection algorithm with a surface which has the same size, position and orientation as the photometer. A significant difference between the measured and simulated illuminance would indicate a dynamic range mismatch induced error.

This procedure was applied to the DUT. In Fig. 3, the percentage error between simulated and measured illuminance values (PE_E), at a distance of 147 cm is shown for several angles γ. As expected, a satisfactory correspondence with the percentage error values found for the LID comparison PE_{LID} is obtained.

CONCLUSIONS AND FUTURE WORK

It was shown that the effect of the dynamic range mismatch between the camera and photometer of a NFG can have a significant impact on the LID and ray file generated from near-field measurement data. A method to check whether such an error occurred was discussed.

In order to eliminate these errors several solutions could be proposed. For example, multiple scans could be made with different integration times set to the camera system. By analysing each set of relative luminance images captured in a single direction, saturated pixels could be detected and swapped with non-saturated pixels corrected with a factor to take into account the different integration times. This would however result in a prolonged measurement time.

Another option, not affecting measurement time, is to combine the signal of several pixels into one, i.e., an effective increase of the dynamic range of the camera. This binning method has been discussed in the literature [1], but the influence on the angular and spatial resolution still needs to be investigated.

REFERENCES

1. I. Ashdown, "Near-field photometry in practice," IESNA Annual Conference Technical Papers, pp. 413-425, 1993.
2. I. Ashdown, "Near-field photometry: a new approach," Journal of the Illuminating Engineering Society, 22(1), pp. 163-180, 1993.
3. M. López, K. Bredemeier, N. Rohrbeck, C. Véron, F. Schmidt, and A. Sperling, "LED near-field goniophotometer at PTB," Metrologia, 49(2), S141 2012.
4. TC-2–62, "Imaging-photometer-based near-field goniophotometer," CIE Draft No. 1, 2010.
5. Commission Internationale de L'éclairage Technical Report 121:1996, "The photometry and goniophotometry of luminaires," CIE, 1996.
6. K. Bredemeier, R. Poschmann, and F. Schmidt, "Development of luminous objects with measured ray data," Laser+Photonik, 2, pp. 20–24, 2007.

Two-dimensional simulation of an induced-junction detector with Genius device simulator towards a predictable quantum efficient detector

Chi Kwong Tang and Jarle Gran

Justervesenet, Kjeller, Norway
Corresponding e-mail address: ckt@justervesenet.no

Internal quantum deficiency (IQD) is investigated under various conditions for an induced-junction detector using Genius device simulator, with the focus on a predictable quantum efficient detector. The 2D simulation results of IQD are compared with reported 1D simulations and experimental values. Good agreements in the trends are observed. Quantitative agreements are seen for wavelengths of 476 and 760nm at 77K. In addition, the results suggest improvements for the detector to further decrease the IQD.

INTRODUCTION

Photodiodes deviate from their ideal response through internal and external loses. These losses and their uncertainties are important to determine under various conditions in order for photodiodes to become a primary standard for optical power measurement [1]. Müller *et al.* have investigated these losses using induced-junction diodes mounted as a predictable quantum efficient detector (PQED) [2]. The measured amount of losses are observed to be larger than the prediction from 1D simulation by Gran *et al.*[3], which could be due to dimensional limitation in the software.

In this work, the internal quantum deficiency (IQD) is investigated in a 2D structure of a real size induced-junction diode described in [2]. In addition, structural variations are investigated to further reduce the IQD.

SIMULATION STRUCTURE AND PARAMETERS

The structure of a single detector of a PQED is given in [1] and the 2D simulation structure is built accordingly, shown in Fig.1. In short, the 2D structure has the dimension of 6000µm x 500µm where only half of the width of the real detector is implemented due to symmetry. The front-side of the structure is located at bottom of the figures, where the three electrodes and the uniform illumination are indicated from the colour representation in Fig.1a) and Fig.1b), respectively. It should be mentioned

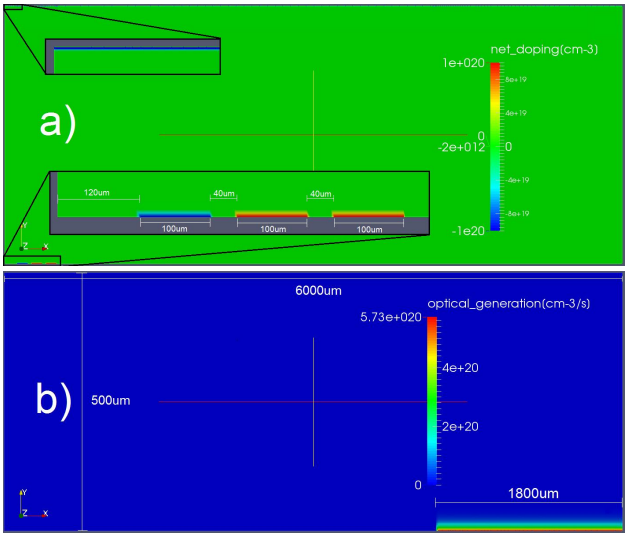

Figure 1. Simulation structure with colour representation of doping concentration in a) and optical generation in b). The two left corners in a) are enlarged and shown in the insets. The depth is increased by a factor of 10 for clarity.

that 2D simulation in Genius device simulator is in reality a quasi-3D simulation where a third axis is added with 1µm [4]. This simplifies the conversion between optical power and intensity.

Table 1 shows the simulations parameters used. Some values are extracted from [3]. The IQD is extracted from the ratio of between total recombination and optical generation of electron-hole pair. Different variations in structure and conditions are also investigated. The optical coefficients of Si at different temperatures are extracted with the power law equation from [4].

RESULTS AND DISCUSSIONS

Fig. 2 shows the IQD as a function of substrate doping concentration under various conditions. It can be observed that the IQD curves have a minimum and that it moves towards lower doping concentration for lower absorption coefficient. This behaviour is consistent with the 1D simulation results reported in [3] and the position of the IQD minima agree remarkably well with thepresent work. Further investigations have shown that the increase

Table 1. Simulation parameters.

Simulation parameters	
Substrate doping	$2x10^{12}$ cm^{-3}
Oxide charge	$6.2x10^{11}$ cm^{-2}
Carrier lifetime	400 µs
Surface recombination velocity	35 cm/s
Illumination intensity	100 µW/cm^2
Illumination diameter	1800 µm

in IQD from its minimum is caused by increased recombination of electron-hole pairs in the bulk and at the interface of Si-SiO_2 for increased and decreased doping concentration, respectively.

Fig. 3 shows the IQD as a function of illumination intensity under various conditions. Depending on the wavelength of the illumination, it can be seen that above a threshold intensity the IQD increases by several orders of magnitude. This threshold intensity can be significantly shifted by changing the applied reverse bias voltage over the detector. Furthermore, a significant shift of the threshold intensity can also be obtained depending on the treatment of the rear-side of the detector. Fig. 3c) shows the case of no rear-side p^+-doping and the threshold intensity is decreased by more than a factor 4 compared to a structure with rear-side p^+-doping. Thus, the IQD is highly dependent on the detector structure and the illumination intensity applied during measurement.

Experimental values of external quantum deficiency are extracted from [2] and correspondingly added in Fig. 3. Considering that the illumination intensity is modified for a single detector in a mounted PQED, the absolute value of the IQD is in a good agreement in the case of 760nm at 77K. Furthermore, the simulated IQD shows the same trend when varying the temperature.

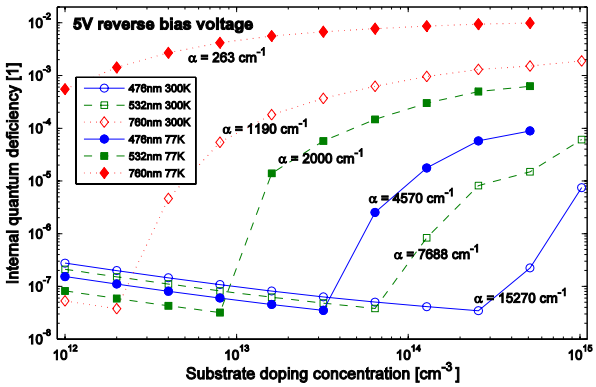

Figure 2. Internal quantum deficiency as a function of substrate doping at 77 and 300K for illumination at different wavelengths and with a reverse bias of 5V.

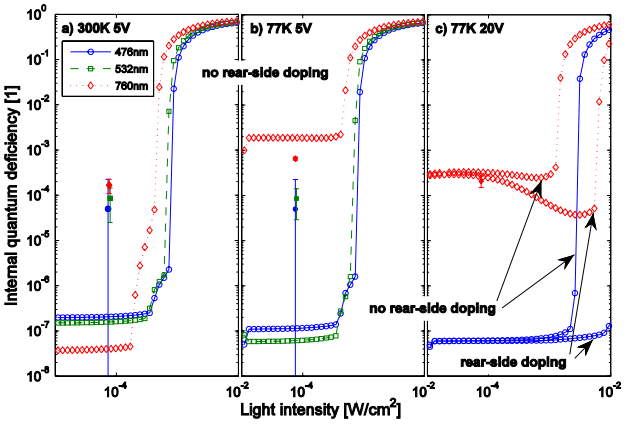

Figure 3. Internal quantum deficiency as a function of illumination intensity at 77 and 300K for illumination at different wavelengths and with a reverse bias of 5V or 20V. Experimental values from [2] are added in correspondingly. Furthermore, the added values are slightly shifted relative to other wavelengths for clarity.

SUMMARY

Two dimensional simulation of a single detector in a PQED is investigated with the focus on the IQD under various conditions. In certain cases, both qualitative and quantitative agreements are observed compared to reported theoretical and experimental data.

ACKNOWLEDGEMENT

The research leading to this work has received funding from the EMRP JRP SIB57 NEWSTAR. The EMRP is jointly funded by the EMRP participating countries within EURAMET and the European Union.

REFERENCES

1. M. Sildoja et al., *Predictable quantum efficient detector: I. Photodiodes and predicted responsivity*, Metrologia, Vol. 50, 385-394, 2013.
2. I. Müller et al., *Predictable quantum efficient detector: II. Characterization and confirmed responsivity*, Metrologia, Vol. 50, 395-401, 2013
3. J. Gran et al., *Simulations of a predictable quantum efficient detector with PC1D*, Metrologia, Vol. 49 S130-S134, 2012.
4. Genius semiconductor device simulator V1.7.4 manual, http://www.cogenda.com/downloads/docs/genius_ug_en.pdf
5. M. A. Green, *Self-consistent optical parameters of intrinsic silicon at 300K including temperature coefficients*, *Sol. Energ. Mat. Sol. C.*, Vol. 92, 1305-1310, 2008.

Diode Array UV Solar Spectroradiometer Implementing a Digital Micromirror Device

A. Feldman[1,5], T. Burnitt[2], G. Porrovecchio[1] , M. Smid[1], L. Egli[3] , J. Gröbner[3], and K. M. Nield[4]

[1] *Cesky Metrologicky Institut, Prague, Czech Republic*

[2] *Principal Optics , Reading, UK*

[3] *Physikalisch-Meteorologisches Observatorium Davos, World Radiation Center, Davos Dorf, Switzerland*

[4] *Measurement Standards Laboratory of New Zealand, Callaghan Innovation, Lower Hutt, New Zealand*

[5] *National Institute of Standards and Technology, Boulder, Co, United States of America*

Corresponding e-mail address: ari.feldman@nist.gov

The solar ultraviolet spectrum captured by commercially available diode-array spectroradiometers is dominated by stray light from longer wavelengths with higher intensity. The implementation of a digital micromirror device in an array spectroradiometer enables the precise selection of desired wavelengths as well as the ability to reduce spectral intensity via selective mirror modulation, both reducing long wavelength stray light. A prototype consisting of off-the-shelf components has been assembled to verify the validity of the base concept and initial measurements have been performed to confirm the throughput and image qualities such as spectral resolution and astigmatism.

INTRODUCTION

Diode-array spectroradiometers provide a low-cost and effective alternative to expensive scanning double monochromators, yet their dynamic range is insufficient to accurately measure ultraviolet (UV) radiation. While diode-array spectroradiometers can complete the acquisition of the entire UV solar spectrum in few seconds, the portion of the spectrum below 300 nm is dominated by the stray light signal. The stray light originates from radiation with high intensities at longer wavelengths, which affects the signal at the detector pixels for wavelength regions with low irradiance levels. The high dynamic range of atmospheric solar UV radiation (approx. 6 orders of magnitude depending on atmospheric conditions between 290 nm – 440 nm) results in considerable bias of the low intensity at around 290 -320 nm measurements with conventional array spectroradiometers[1].

In a previous study[2], it was demonstrated via libRadtran [3] modeling that there is a 4 order of magnitude stray light contribution from wavelengths above the UV range of interest (290nm to 440nm) that would interfere with an accurate UV spectral intensity measurement. Furthermore, implementing a digital micromirror device (DMD) could significantly reduce the impact of stray light using two techniques. The first includes levelling the dynamic range of the incoming radiation by selective wavelength modulation[2], [4]. The undesired wavelengths are modulated at high frequency creating an effective repetition rate, reducing their intensity and stray light contribution. The second method is to select a precise range of wavelengths using the DMD as an effective bandpass filter[2].

While the use of DMD's in spectroradioometer applications has been previously explored for visible light[5]–[7] and infrared applications[8], in this study a novel micromirror diode array spectroradiometer (µ-MUV) is assembled from off-the-shelf components to demonstrate the validity of the modelled stray light reduction concepts in the ultraviolet range. Device specific attributes such as spectral resolution, bandwidth, and slit function were measured. To assess reduced stray light, initial DMD modulation techniques, spectral selection techniques, spectral filters, and physical baffling attempts were measured.

EXPERIMENTAL SETUP

Initial modeling of a prototype using Zemax was used as the basis for the experimental design[9]. The optical design was carried out with the main aim to preserve throughput of the optical system and to optimize its spectral resolution. The key elements of the model and subsequent prototype consist of a plain ruled 600 G/mm diffraction grating, a 1024x720 pixel XGA DLP micromirror chip, a back-lit 2048x250 pixel CCD detector, and four spherical mirrors. The astigmatism generated by the use of off-axis spherics is exploited by binning the CCD camera's vertical pixels, effectively using it as a 1-dimensional array.

EXPERIMENTAL RESULTS

Using the whole DMD as just a mirror in the "on" position we are able to determine device specific parameters such as spectral resolution, bandwidth, and the slit function. Using a 407 nm laser the full width half maximum (FWHM) of the slit function of the spectroradiometer was determined to be 2.5 nm. This could be improved with reduced fiber width, effectively reducing the slit function. The spectral resolution was determined to be 0.2 nm based on the incident wavelength range and number of pixels illuminated.

Basic light modulation techniques were implemented for initial stray light reduction, where 50% of the DMD was modulated at various frequencies. The portion with longer wavelengths was chosen to flatten the dynamic range and reduce stray light in the shorter wavelength region. Duty cycles ranging from 5% to 100% are shown in Fig. 1.

As the duty cycle decreases, the range in the "on" portion from 290 nm-350 nm subsequently decreases by a fraction of a percent. It is interesting to note that while the contribution in this range does demonstrate some stray light reduction, the reduction in amplitude of the background signal is more pronounced.

Additional data were taken where spectral cut-off filters were placed directly in front of the detector identifying stray light contribution from wavelengths above 550 nm. Spectral range selection was demonstrated by scanning the DMD then reconstructing the full spectrum. Lastly, physical baffling was implemented to further reduce stray light contribution.

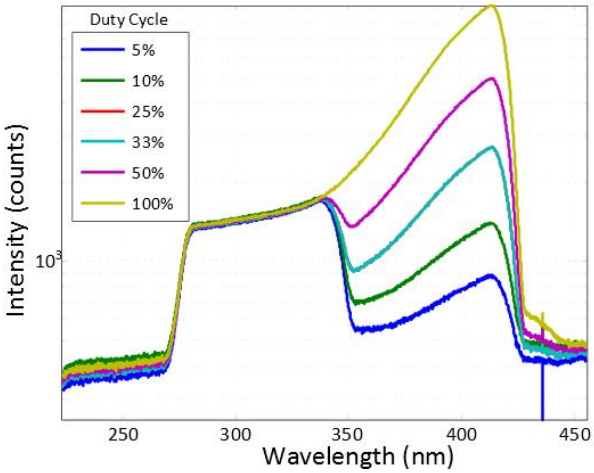

Figure 1. Longer wavelength light modulated via DMD to demonstrate dynamic range leveling and stray light reduction.

CONCLUSIONS AND FUTURE WORK

A prototype solar UV spectroradiometer implementing a DMD was constructed from off-the-shelf components and basic device parameters were measured. In comparison to commercially available spectroradiometers, the µ-MUV prototype has a wider slit function and poorer spectral resolution but is capable of reducing stray light via modulation techniques as predicted. Future work includes construction of a light-tight enclosure and wavelength specific modulation to further explore dynamic range levelling.

REFERENCES

1. G. Seckmeyer, A. Bais, G. Bernhard, M. Blumthaler, S. Drüke, P. Kiedron, K. Lantz, R. L. McKenzie, and S. Riechelmann, "GAW Report No . 191 Instruments to Measure Solar Ultraviolet Radiation Part 4: Array Spectroradiometers," 2010.
2. L. Egli, J. Gröbner, M. Smid, G. Porrovecchio, T. Burnitt, K. M. Nield, S. Gibson, J. Dubard, S. Nevas, and M. Tormen, "New technologies to reduce stray light for measuring solar UV with array spectroradiometers," in *AIP Conference Proceedings*, 2013, vol. 825, pp. 825–828.
3. B. Mayer and A. Kylling, "Technical note: The libRadtran software package for radiative transfer calculations-description and examples of use," *Atmos. Chem. Phys.*, vol. 5, pp. 1855–1877, 2005.
4. J. Rice and J. Neira, "DMD diffraction measurements to support design of projectors for test and evaluation of multispectral and hyperspectral imaging sensors," *Proc. SPIE*, vol. 7210, 2009.
5. R. D. Meyer, K. J. Kearney, Z. Ninkov, C. T. Cotton, P. Hammond, and B. D. Statt, "RITMOS: a micromirror-based multi-object spectrometer," *Proc. SPIE*, vol. 5492, pp. 200–219, Sep. 2004.
6. T. M. Spudich, C. K. Utz, J. M. Kuntz, R. a Deverse, R. M. Hammaker, and D. L. McCurdy, "Potential for using a digital micromirror device as a signal multiplexer in visible spectroscopy.," *Appl. Spectrosc.*, vol. 57, no. 7, pp. 733–6, Jul. 2003.
7. E. Wagner and B. Smith, "Construction and evaluation of a visible spectrometer using digital micromirror spatial light modulation," *Appl. Spectrosc.*, vol. 49, no. 11, pp. 1715–1719, 1995.
8. D. Beasley and M. Bender, "Dynamic IR scene projector based upon the digital micromirror device," *Proc. SPIE*, vol. 4366, pp. 96–102, 2001.
9. T. Burnitt, "Optical Layout for Prototype DLP Spectrometer," 2012.

This work was funded in part through the EMRP Traceability for surface spectral solar unltraviolet radiation.

Spectral non-linear responsivity of silicon photodiodes

Minoru Tanabe, Kuniaki Amemiya, Takayuki Numata, Daiji Fukuda, and Tatsuya Zama

National Metrology Institute of Japan, Tsukuba, Japan
Corresponding e-mail address: tanabe-m@aist.go.jp

The non-linear responsivity for commercial silicon photodiodes was investigated at a number of wavelengths in the range from visible to near-infrared using the flux addition method. Wavelength-dependence of nonlinear responsivity, particularly suprarresponsivity, is experimentally determined, and compared with a theoretical model to describe internal quantum efficiency of photodiode. Reasonable agreements between the measurements and the models for the photodiode were observed in the near-infrared wavelength region.

INTORODUCTION

Photodetectors constructed of silicon photodiodes are widely used for accurate radiometric measurements in region from visible to infrared. Of various optical measurements, linear response with respect to optical power for the photodiodes is demanded to cover the wide dynamic range. It is therefore vitally important to measure precisely the nonlinearity for the photodiodes.

The non-linearity of a silicon photodiode is dependant on several parameters, which is the characteristics of the incident beam, the different manner for the photodiode, and surrounding condition during the test. Several experimental and theoretical studies on non-linearity response of the photodiodes were reported [1-5], and it is well known to depend on the incident wavelength strongly. This paper describes the wavelength-dependence of linearity test for any silicon photodiodes in range of visible to near-infrared. We present results of the non-linearity behaviour, and compare with the theoretical model.

MEASUMENT SET-UP

The method chosen for testing the non-linearity of silicon photodetectors is the flux addition method. The measurement set-up used is shown in Figure 1. This system is based on the non-interferential addition of two optical fluxes.

The various laser diodes and the external cavity laser diodes from visible to near-infrared wavelength ranges were used. The temperature of the laser diodes are controlled with a Peltier cooler, and their intensity fluctuations were observed to be smaller than 0.01 %. Each beam was adjusted with a collimating lens and some optical lenses, which allow us to create near-Gaussian shape of 1.0 mm in diameter. Beam spots smaller than the detection area illuminated the photodiodes.

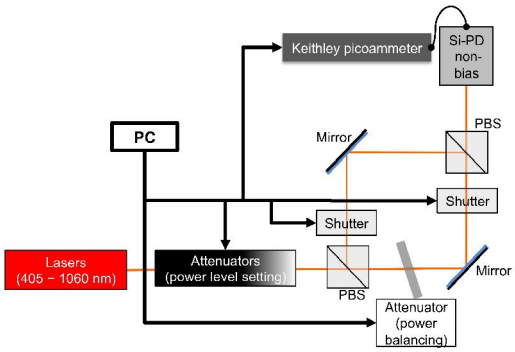

Figure 1. Measurement set-up of the non-linearity.

The laser beam was divided into two parts (A and B) by applying a polarization beam-splitting cube. Power balance between each beam was adjusted with an attenuator. Two beams were aligned with same spot by adjusting the plane mirrors, as shown in figure 1, and checking with a C-MOS camera. Blocking one each time and superimposing them on the photodiode using the mechanical shutters, photocurrents I_A, I_B, and I_{A+B} were measured with a Keithley picoammeter. In the measurements, a few attenuators were used to provide wide and suitable range of power levels. The linearity factor for any power levels is obtained by $LF = I_{A+B} / (I_A+I_B)$, and the non-linearity $NL(n)$ to be applied at the current I_n is given as following:

$$NL(n) = \prod_{k=1}^{n} LF(k) - 1$$

All components of this system are kept in a box in order to ensure temperature stability, and the system is controlled a computer program. In this system, the measurement uncertainty was attained less than 0.1%.

RESULTS AND DISCUSSION

The spectral non-linearity behaviour at nine different wavelengths is shown in figures 2 (a)-(c) for silicon

photodiodes made by manufacture A-C. These results are normalized at the photocurrent level of 1 nA. These photodiodes show saturation and good linear behaviour in the visible (up to 760 nm), but large deviations from linearity in the near-infrared and small deviations in 405 nm for the photodiode by manufacture B and C.

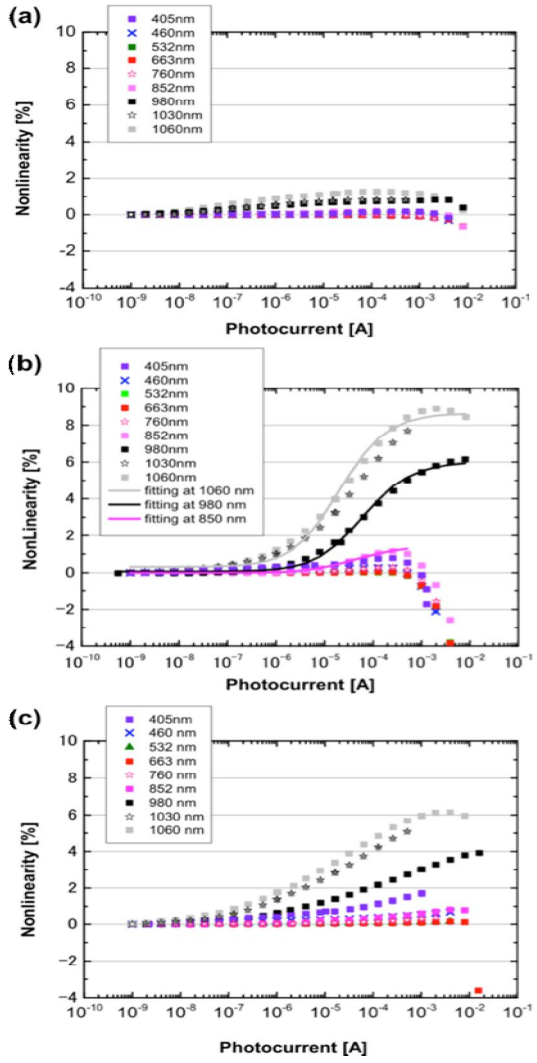

Figure 2. Spectral non-linearity of silicon photodiodes made by (a) manufacture A, (b) manufacture B, and (c) manufacture C.

Their non-linear behaviours are known as suprarespons ivity [1,2], which is explained as a decrease of the recombination losses in the silicon-bulk region. At the low incident flux, recombination losses are constant, however, at the higher incident flux, the recombination losses decrease as recombination centers are filled by more electron-hole pairs generated in the bulk. As a result, photocurrent increases. And then, longer wavelength shows larger suprarespons ivity as absorption length is long in the bulk. Ferrero *et al.* proposed a new model using Shockely-Read-Hall recombination model, including suprarespons ivity quantitatively, as following:

$$R(I) = r(\infty) - \frac{a}{I}\ln\left(\frac{1+bI}{1+cI}\right) - \frac{a'}{I}\ln\left(\frac{1+b'I}{1+c'I}\right)$$

where I is the generated photocurrent and $r(\infty)$ represents the response at infinite incident power, i.e. the ideal response without any recombination losses. The parameters, a, b, c, and a', b', c', are determined by the absorption length of silicon, the incident laser condition, the spectral responsivity, the photodiode structure, and the recombination center character, which contains a function of wavelength. Therefore, the suprarespons ivity is strongly dependent on the wavelength. The solid lines in Fig.2 (b) show the best fitting plots calculated by the model for wavelengths of 850 nm, 980 nm, and 1060 nm. These are supported by the fact the Ferrero model explains the present experimental data for near-infrared region well. The observed non-linearity behavior for this photodiode can be explained and modeled.

CONCLUSIONS

The spectral suprarespons ivity of the commercial silicon photodiodes was measured by using the flux addition method. The suprarespons ivity was compared with the theoretical model in the near-infrared region. A possible prediction of the spectral suprarespons ivity for the photodiode is proposed by using the model.

ACKNOWLEFGMENTS

This work was supported by JSPS KAKENHI Grant Number 25790077.

REFERENCES

1. K. D. Stock, Si-photodiode spectral nonlinearity in the infrared, App. Opt. 25, 830-832, 1986.
2. L. O. Boivin, Automated Absolute and Relative Spectral Linearity Measurements on Photovoltaic Detectors, Metrologia 39, 355-360, 1993.
3. T. Kübarsepp, A. Haapalinna, P. Kärhä , and E. Ikonen, Nonlinearity measurements of silicon photodetectors, App. Opt. 37, 2716-2722, 1998.
4. A. Ferrero, J. Campos, A. Pons, and A. Corrons, New model for the internal quantum efficiency of photodiodes based on photocurrent analysis, App. Opt. 44, 208-216, 2005.
5. K. Amemiya, S. Mukai, D. Fukuda, T. Zama, Wavelength dependence of no-linearity of optical fibre power meters, IET Optoelectronics, 5, 62-67, 2011.

Predictable Photodiode Cryogenic Radiometer; Two primary radiometric standards combined in one artefact

Jarle Gran[1], Malcolm White[2], and Nathan Tomlin[2]

[1]*Justervesenet, Kjeller, Norway,* [2]*NIST, Boulder, USA*

Corresponding e-mail address: jag@justervesenet.no

We present the Predictable Photodiode Cryogenic Radiometer (PPCR), the first dual-mode primary standard detector for comparison of electrically calibrated and quantum based primary standard. The dual-mode detector is realised as a predictable Quantum Efficient Detector (PQED) photodiode with a temperature sensor mounted on its back side. Electrical heating is implemented by forward biasing the PQED. Non-equivalence between the two modes of operation is minimised, as the same absorber and measurement equipment are used in both modes, enabling unprecedented accuracy in the comparison between the two modes at an ideal operating temperature around 25 K.

INTRODUCTION

Optical power measurement and traceability is currently realised by two inherently different primary standards; the cryogenic radiometer (CR) [1] and the PQED [2-4]. The CR usually operates at temperatures in the range 4 – 15 K, where optical heating of an absorber is matched to electrical heating of the same absorber. Though accurate, limitations in the transfer from the CR to working standards do apply, principally due to the optical window of the CR and absorber differences.

The basic idea with predicting the responsivity of photodiodes, is that the photodiode's ideal responsivity is determined from fundamental constants and the wavelength of the radiation only. The deviation from ideal performance of the diodes, due to reflection and internal losses, is estimated or eliminated by independent techniques. In this way the photodiode technique is basically a quantum technique, where each absorbed photon generates on electron hole pair (EHP). Realisation of the PQED [2] technique was performed through the common European project qu-Candela [5]. The results by Gran [4] suggest that sub-ppm accuracy can be achieved in the measurement of optical power using optimised PQEDs.

We present here the first realisation of a dual mode primary standard for ultimate comparison of the two fundamentally different primary standards within radiometry; the CR and the PQED. This is done by modifying a PQED photodiode to work as both a quantum detector and thermal detector, which is accomplished by attaching a thermistor to the back of the photodiode and adding a weak thermal link. In this way, many of the uncertainties in calibration of transfer standards or even primary standard comparisons can be eliminated as it is the same artefact that absorbs the photons in both cases, generating either heat or photocurrent, depending on the mode of operation.

SILICON CRYOGENIC RADIOMETER

The following characteristics are important for a CR:

- The absorber needs to absorb all radiation.
- The thermal diffusivity of the cavity should be high to avoid non-equivalence between electrical and optical heating.
- The thermal conductance of the heat link must be low enough to give a sufficient temperature rise.

While the single photodiode is not a perfect absorber, the comparison between photodiode and CR mode is unaffected by the absorbance of the silicon because it is physically the same device with the same absorption that generates the signal in both measurement modes. The thermal conductivity of silicon [6] is quite high, even exceeding copper in the temperature range 30 K to 150 K, so we expect the electrical and optical non-equivalence to be low. The heat link can be easily engineered to give a sufficient temperature rise for the thermistor and optical powers required.

PREDICTABLE QUANTUM EFFICIENT DETECTOR

The PQED is designed to be operated with reverse bias and has proven to work well as a predictable absolute standard in the comparison to CR at 77 K [3] with an internal quantum deficiency (IQD) of about 50 ppm. Measurement of the photocurrent from the

PQED with temperatures from 300 K to 4 K, revealed that the PQED works perfectly until its responsivity rapidly drops to zero around 20 K. This shows the promising result that our PPCR dual-mode detector should work optimally somewhere between 20 K and 30 K.

EXPERIMENTAL REALISATION OF DUAL MODE PRIMARY STANDARD

The first realisation of a PPCR dual-mode primary standard detector was made by gluing a cernox temperature sensor on the back side of a PQED photodiode. The 11 by 11 mm^2 PQED photodiode was glued on a FR-4 printed circuit board (PCB) working as a photodiode carrier and a heat link for the CR mode. To operate as a dual-mode detector there are in principle three measurements necessary to perform a comparison between the two primary standards realised on the same artefact:

I. Negative bias is applied to the photodiode while illuminated with a constant optical power source, while measuring the photocurrent from the photodiode. In other words, normal PQED photodiode operation mode. Absorbed photons generate EHPs which are separated by the electrical field generated by the sum of the built-in and applied bias voltage. For a perfect photodiode, the measured rate of electrons is exactly the same as the rate of photons.

II. The bias voltage is switched off and the circuit is opened, preventing any current to flow in the external circuit. The temperature change when optical power is switched on is recorded. The photodiode is still illuminated with the same constant optical power as in I. The energy of all photons absorbed is now transformed into heat as the steady state of generation and recombination rate of EHP are the same after a very short settling time.

III. The optical power is switched off and a positive bias is applied to the photodiode in the forward direction. In this way the applied voltage and the series resistance of the photodiode heats it. The bias voltage is controlled so that the temperature change is comparable to II and thereby establishes a link between optical and electrical heating. The voltage over and current through the photodiode is measured to quantify the electrical heating. By using forward bias as electrical heating we are dissipating the heat inside the silicon device as is done by the optical heating. Non-equivalence is limited by the high thermal diffusivity of silicon.

Fig. 1 shows a sketch of the experimental setup for the PPCR dual-mode primary detector. An accurate dual polarity power supply is connected in series to the PQED and an ampere meter. The voltage drop across the photodiode is measured with a volt meter to quantify the power dissipated in the photodiode when forward biased. A temperature sensor measures the temperature difference between the PQED and the heat sink. The same ampere meter is used to both measure the forward biased current and the photocurrent of the PQED. In this way, we are exploiting the effect of relative measurements made by the same instrument in the two different realisations. The set-up has the further advantage that the absorber is exactly the same device in both CR and PQED modes, ensuring absorption equivalence in both modes.

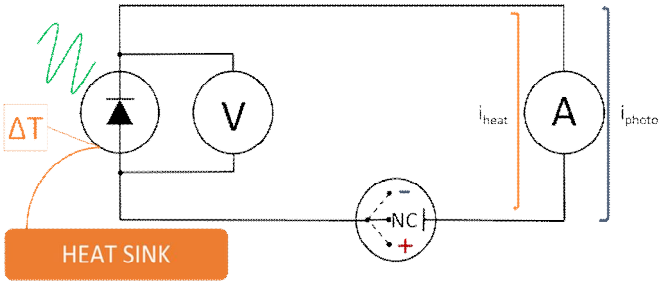

Figure 1. Operation of the dual-mode primary standard.

REFERENCES

1. Martin J. E. et al.: A Cryogenic Radiometer for absolute Radiometric Measurements, Metrologia, 21 (1985), 147-155.
2. Sildoja M. et. al.: Predictable Quantum Efficient Detector I: Photodiodes and Predicted responsivity, Metrologia, 50 (2013), 385-394.
3. Muller I. et. al.: Predictable Quantum Efficient Detector II: Characterization and confirmed responsivity, Metrologia, 50 (2013), 395-401.
4. Gran et. al.: Simulations of a predictable quantum efficient detector with PC1D, Metrologia, 49 (2012), S130-S134.
5. http://www.quantumcandela.net/
6. http://www.efunda.com/

High sensitivity radiance and luminance meters

G. P. Eppeldauer and V. B. Podobedov

National Institute of Standards and Technology, Gaithersburg, Maryland, USA
Corresponding e-mail address: george.eppeldauer@nist.gov

High sensitivity radiance and luminance meters were developed at the National Institute of Standards and Technology (NIST) for the calibration of night vision goggles (NVG). The computer controlled transfer standard radiometers (TR) are equipped with radiometric and photometric filters to transfer either radiance responsivity or luminance responsivity to NVG test instruments. The errors in the transfer of the integrated (broadband) responsivity scales are modelled. Spectral tests have been made to perform responsivity corrections. The filter combinations are evaluated and the uncertainties in the scale transfers are estimated. The output noise of the radiometers is characterized. The new method for radiance transfer from NIST to the test-set (used for NVG gain calibration) is described.

DESIGN ISSUES

The widely used multiple-lens input imaging optics of radiance meters was replaced with a biconvex lens. This simple design improved the out-of-target rejection (blocking) by an order of magnitude at the +/- 15° radiance measurement angles. The radiometric and photopic filters could be alternately attached to the input optics.

Green and infrared LEDs are used in the test instruments for NVG calibration purposes. The measured spectral functions of the sources and detectors used in the test instruments are illustrated in Fig. 1. The photopic filter measures a green LED and the radiometric filter measures different IR LEDs. The IR LEDs emit radiation with peaks at 690 nm, 810 nm, and 820 nm. The peak wavelengths and the spectral bandwidths can change among the applied components. The wavelength of the 814.5 nm diode-laser in the NIST Transfer-Radiometer Calibration Facility is roughly in the center of the wavelength interval where the test-instrument LEDs emit radiation. As shown in Fig. 2, the spectral responsivity of the radiometer with the radiometric filter is nearly flat (similarly to the NV goggles) in the spectral correction range. The result is decreased uncertainty in the radiance transfer.

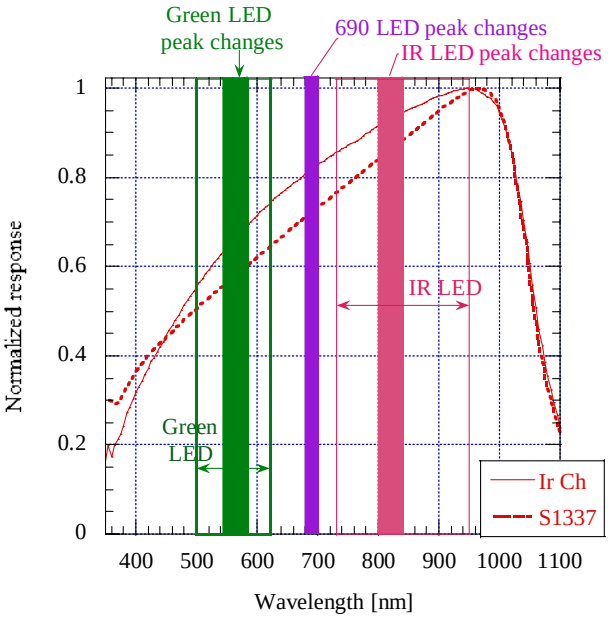

Figure 1. Spectral characteristics of components used in the scale transfers.

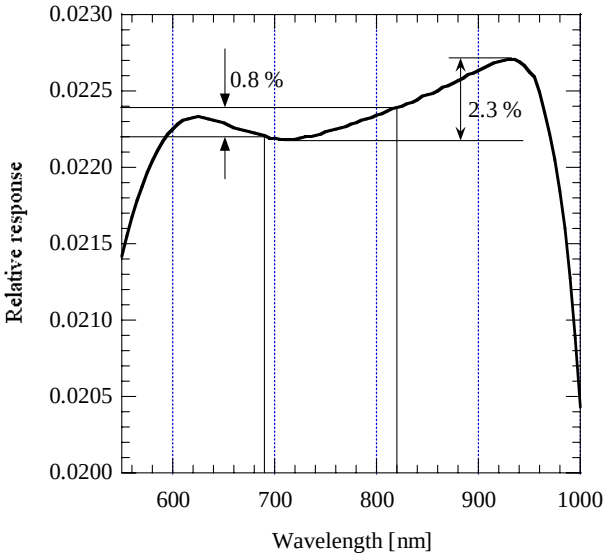

Figure 2. Filters corrected "flat" response of the transfer standard radiance meter.

The photopic filter of the TR was optimized for the spectral range of the green LED. The source spectral distribution and the spectral responsivities of

the TR (reference) and 070 test detectors were measured to apply spectral mismatch corrections in the transfer of the luminance responsivity first from the NIST standard to the TR and then from the TR to the test device.

OUTPUT NOISE AND DRIFT

The measured noise-and-drift equivalent current is 1 fA when the detector is in dark and the signal gain is 10^{10} V/A. In this case, the current meter is in high resolution mode, 1 measurement is made in 1 s, and an average is calculated from 13 data points.
The noise and drift measurement was drift dominated, and the noise component was 0.3 fA.

METHOD OF RADIANCE TRANSFER FROM NIST TO TEST-SETS USING THE TRS

The spectral radiance responsivity of the TR, $s(\lambda)=s$, is determined at the Night-Vision Radiometer Calibration Facility (NVRCF) of NIST using a diode-laser source for flux-transfer with an emission-wavelength similar to the LED-peak in the test-set(s)
Then, the output signal of the TR when plugged into a test-set is:

$$i = \int_{\lambda} L(\lambda) s(\lambda) \mathrm{d}\lambda$$

where L(λ) is the spectral radiance of the test-set to be determined.
The broad-band (integrated) test-set radiance is:

$$\bar{L} = \frac{i}{s} \quad [\mathrm{W / cm^2\ sr}]$$

where *s* is corrected to between 690 nm and 820 nm and the unit of *s* is A cm^2 sr / W at 814.5 nm and the unit of *i* is A.
The uncertainty of the TR radiance responsivity was 3 % (*k*=2) at 815 nm and the uncertainty of the luminance responsivity was 2.0 % (*k*=2).
The output radiance of the test-set measured by three TRs is shown in Fig. 3. The radiance measurements showed high nonlinearity and poor radiance stability at equivalent fL levels of 10^{-4} or lower. It is suggested to perform the NVG gain calibrations at higher levels where the radiance is linear versus the set value on the test-set (scaled by the manufacturer). In this range, the highest standard deviation of the mean was 0.6 % for a TR measured signal. At the level of 10^{-4} equivalent fL, the radiance uncertainty from the three TR measurements was 4.6 % (*k*=2). The absolute deviation of the NIST traceable calibration factor (radiance / equivalent fL) from the manufacturer used calibration factor of 2.48 x 10^{-6} W/cm^2 sr (at 1 fL) was 9 %. This result indicates the need for SI traceable radiance calibrations for the NVG test instruments.

DISCLAIMER

Certain commercial equipment, instruments, or materials are identified in this paper to foster understanding. Such identification does not imply recommendation or endorsement by the NIST, nor does imply that the equipment are necessarily the best available for the purpose.

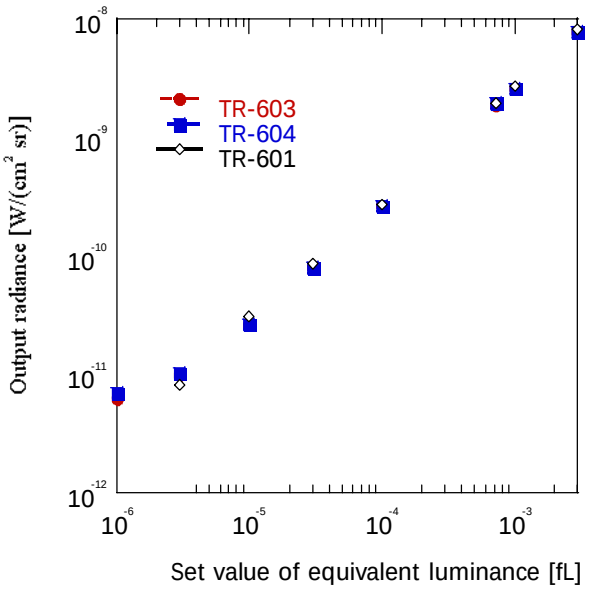

Figure 3. TRs measured radiance levels of a test-set used for NVG gain calibration.

Noise analysis in differential measurement of detector responsivity

Jae-Keun Yoo[1], Seongchong Park[2], Seung-Nam Park[1,2], and Dong-Hoon Lee[1,2]

[1]*Science of Measurement Department, University of Science and Technology (UST), Daejeon, Korea*
[2]*Division of Physical Metrology, Korea Research Institute of Standards and Science (KRISS), Daejeon, Korea*
Corresponding e-mail address: dh.lee@kriss.re.kr

We present how to analyse and improve the noise characteristics in the differential measurement of detector responsivity. By measuring the noise spectrum of the test detector signal at various conditions, the AC noise components originating from mechanical and optical disturbances such as vibration of choppers and fans could be identified and minimized. We demonstrate the noise analysis and the resulting accuracy improvement at the differential measurement instrument of spectral responsivity of photovoltaic detectors.

INTRODUCTION

Differential measurement is a useful technique to measure spectral responsivity of an optical detector at different levels of output signal [1]. For photovoltaic solar devices which should be used at very high irradiance level of higher than 1 kW/m^2, the differential measurement technique is the standard method to measure their spectral responsivity [2]. More generally, the principle of the differential measurement by superposing a DC bias signal with an AC test signal can be applied to test the nonlinear behaviour of any optical detector.

We developed a differential measurement setup of spectral responsivity for photovoltaic detectors by using a monochromator-based tunable source. This setup was regarded as a complementary instrument to the LED-based broadband setup we have reported previously [3]. During the development of the new setup, we soon realized that a systematic noise analysis is required to achieve the satisfactory signal-to-noise level of the measurement signal, as the very weak AC test signal in a 1 μA-range should be filtered out from the very strong DC in a 100 mA range. Although the lock-in detection is applied to filter within a narrow frequency band, we found that several noise sources should be carefully considered and suppressed.

In this work, we report the methodology and results of our noise analysis at the differential measurement setup for spectral responsivity of photovoltaic detectors. We measured the noise spectrum of the output signal from the test detector by using a function generator and a lock-in amplifier in a frequency range from 10 Hz to 120 Hz. From the measured noise spectrum, various AC noise source could be identified and suppressed. Note that this noise analysis method can be applied generally to other cases in the field of radiometry, in which the radiation source needs to be modulated, e.g. by using a chopper, to improve the detection sensitivity.

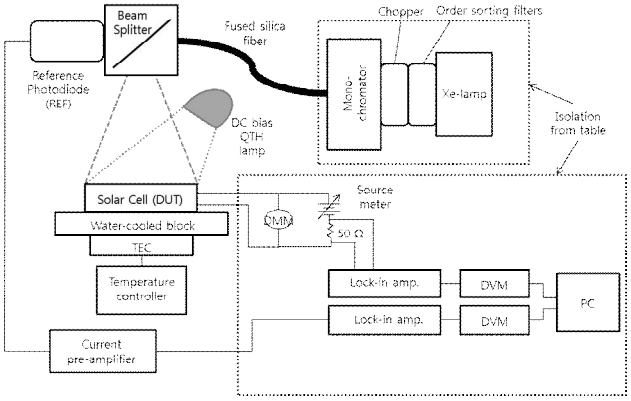

Figure 1. Schematic setup diagram of the differential spectral responsivity instrument for photovoltaic detectors at KRISS.

EXPERIMENTAL SETUP

Figure 1 shows a schematic diagram of the differential measurement setup at KRISS, which is used for measuring the spectral responsivity of photovoltaic detectors at a high irradiance level. Combination of a Xe lamp and a grating-monochromator is used as the wavelength-scanning test source, while a quartz-tungsten halogen (QTH) lamp is used as the white DC bias source. A mechanical chopper is used to realize the AC modulation of the test source. The optical output of the test source is delivered by using a fiber-bundle guide to the detector under test (DUT) mounted on a temperature-stabilized stage. A beam-splitter and a reference photodiode (REF) is used to monitor the radiant power of the test source. The DC component of the DUT photocurrent signal is compensated by an electric reverse voltage source [4] so that only the AC component is amplified and detected by using a lock-in amplifier and a digital voltmeter (DVM).

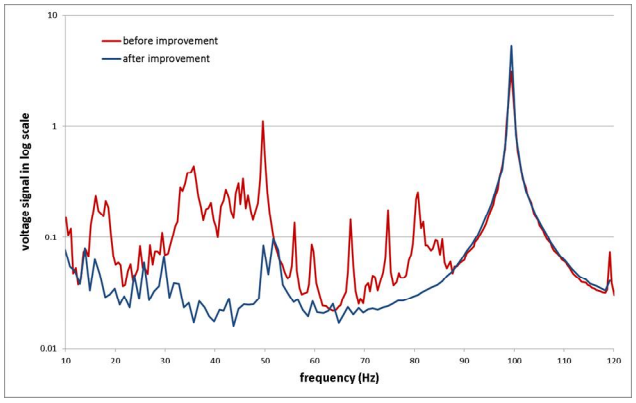

Figure 2. Noise spectra measured before (red) and after (blue) improvement of the setup for noise reduction.

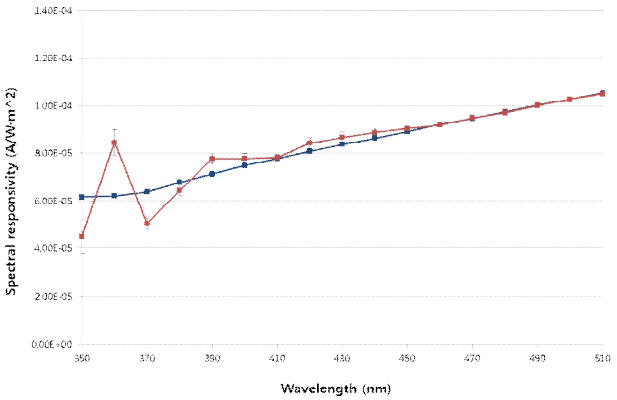

Figure 3. Measurement results of differential spectral responsivity of a solar cell before (red) and after (blue) improvement of the setup for noise reduction.

NOISE SPECTRUM MEASUREMENT

For noise analysis, the noise spectrum of the DUT output signal is measured by using a function generator, which gives a square wave of a variable frequency to the reference signal input of the lock-in amplifier. The amplified voltage output signal is recorded as a function of frequency that is scanned from 10 Hz to 120 Hz. Figure 2 show two examples of the measured noise spectra.

The red line in Fig. 2 shows the noise spectrum of the setup at the initial stage before the analysis and improvement of noise characteristics are performed. The spectrum is measured in the condition of the differential measurement at 650 nm and the maximum bias. The strong peak at 100 Hz corresponds to the output signal at the chopper frequency, which is to be recorded by synchronizing the lock-in detection with the chopper trigger signal. Beside the "signal" peak at 100 Hz, we see various other "noise" peaks at different frequencies, some of which are only factor 10 smaller than the signal peak. Although the lock-in detection filter out these noise peaks, we found that the measurement result is influenced by them due to the limited suppression of the out-of-band noise of the used lock-in amplifier.

In order to identify and minimize the noise peaks, we have repeated the noise spectrum analysis in various different conditions. For example, we measured the noise spectrum without any light input and found that the mechanical vibration of the copper and cooling fans of the lamp produces the noise peaks. Especially, the strong peak in Fig. 2 at 50 Hz that is the half frequency of the chopper is identified to be correlated with the mechanical influence of the chopper. As a result of the setup improvement to minimize the noise peaks, we finally obtained the noise spectrum as shown in Fig. 2 with the blue line. A significant improvement of the noise characteristics can be confirmed.

ACCURACY IMPROVEMENT

Figure 3 shows the effect of the improvement of the noise characteristics on the measurement results of differential spectral responsivity of a solar cell (Si reference solar cell according to the IEC standards) at a bias level of 1 sun (1 kW/m^2). The red plot and the blue plot correspond to the result before and after the noise reduction, respectively. The error bars show the repeatability uncertainty of each measurement point.

The wavelength range shown in Fig. 3 is sensitive to the noise because the power level of the AC test light is low. Comparing the two plots in Fig. 3, we confirm that the setup improvement based on the noise analysis improves the accuracy and also the sensitivity of the differential measurement through improving the signal-to-noise ratio of the lock-in detection.

REFERENCES

1. J. Metzdorf *et al.*, Principle and application of differential spectroradiometry, Metrologia, 28, 247 (1991).
2. IEC 60904-8:1998, Photovoltaic devices Part 8: Measurement of spectral response of a photovoltaic (PV) device, International Electrotechnical Commission
3. G. Zaid *et al.*, Differential spectral responsivity measurement of photovoltaic detectors with a light-emitting-diode-based integrating sphere source, Applied Optics, 49, 6772 (2010).
4. B. H. Hamadani *et al*, Versatile light-emitting-diode-based spectral response measurement system for photovoltaic device characterization, Applied Optics, 51, 4469 (2012).

Using a laser driven light source for spectral responsivity calibration of detectors between 250 nm and 400 nm

Paul R. Dekker and Omar El Gawhary

VSL, Delft, the Nehterlands

Corresponding e-mail address: pdekker@vsl.nl

In this research, a method is proposed to overcome the wavelength errors induced by misalignment of a laser driven light source (LDLS) to the entrance port of a monochromator-based facility for calibration of spectral responsivity of detectors and filter radiometers.

SOURCE ALIGNMENT

Xenon arc lamps are often used in combination with a monochromator to provide the spectrally tunable flux needed for calibration of the spectral responsivity of detectors[1,2]. However, the poor short term stability (about 0.2%) of these lamps often dominates the uncertainty budget of the spectral responsivity of such detectors, as well as those of filter radiometers calibrated though similar procedure, especially in the UV range of the electromagnetic spectrum. With the aim of reducing the said calibration uncertainty, a LDLS[3] has been used to power the monochromator-based facility in used at VSL. Spectrally tunable light sources based on an LDLS, combined with a reflection grating systems, have been studied previously[4]. However, to our knowledge, the application performances of an LDLS on monochomator-based calibration facility for detector has not yet been studied, neither the differences and the additional complications with respect to the commonly employed light sources, have been properly investigated.

As can be expected, due to the small size of the plasma spot (about 100 μm) of the LDLS, alignment to the relatively large entrance slit (2.5 mm) of the monochromator proved to be critical. Vertical and angular misalignment of the LDLS can cause asymmetry and shifts in the spectral distribution of the flux at the exit slit of the monochromator. Wavelength errors of several nanometers are easily observed when the LDLS is aligned to the entrance of the monochromator by using the common procedures typically used. To provide a good signal-to-noise ratio in the wavelength calibration of the monochromator against spectral calibration lamps and to enable a comparison with the measurements performed through the common sources, e.g. Tungsten halogen lamp and Xenon arc, the slit width of the monochromator was not reduced in size. Instead the LDLS has been further aligned based on the spectral distribution at the exit of the monochromator.

To measure the spectral distribution of the quasi-monochromatic light used to calibrate spectral responsivity of detectors, the beam exiting the output slit of the monochromator was sent into a 2-inch diameter integrating sphere and coupled into a fiber based array spectroradiometer. The wavelength scale of the spectroradiometer was independently calibrated against a wavelength ruler recently built at VSL, providing a scale in the spectral range 280 - 400 nm. The vertical alignment of the LDLS was optimized so that the effective wavelength of the spectrum measured would match the wavelength setting of the monochromator. Subsequently, the angular alignment of the LDLS to the entrance port was optimized to get a symmetrical spectral distribution. Following this procedure, the wavelength error due to misalignment of the LDLS has been reduced to 0.03%, which is well below the wavelength uncertainty of 0.2 %. Furthermore, by implementing the LDLS, the uncertainty contribution of source stability on the spectral responsivity calibration could be reduced to only 0.04%.

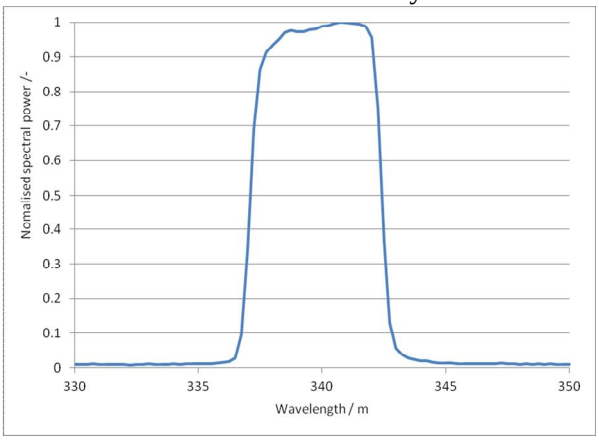

Figure 1. Normalised spectral power of monochromator-based detector calibration facility equipped with laser driven light source measured at a wavelength of 340 nm.

REFERENCES

1. Schrama, C. A., Bosma, R., Gibb, K., Reijn, H. & Bloembergen, P. Comparison of monochromator-based and laser-based cryogenic radiometry. *Metrologia* **35,** 431–435 (1998).
2. Meindl, P., Klinkmüller, A. E., Werner, L., Johannsen, U. & Grützmacher, K. New UV spectral responsivity scale of the PTB based on a cryogenic radiometer and an argon plasma arc radiation source. *Metrologia* **43,** S72–S77 (2006).
3. Horne, S. *et al.* A novel high-brightness broadband light-source technology from the VUV to the IR. in **7680,** 76800L–76800L–7 (2010).
4. Feng, J. *et al.* A stigmatic ultraviolet-visible monochromator for use with a high brightness laser driven plasma light source. *Rev. Sci. Instrum.* **84,** 085114 (2013).

IR enhanced Si reference detector for 1-step scale transfer between 300 nm and 1000 nm

G. P. Eppeldauer, T. C. Larason, and J. M. Houston

National Institute of Standards and Technology, Gaithersburg, Maryland, USA
Corresponding e-mail address: george.eppeldauer@nist.gov

IR enhanced Si photodiodes have improved performance in the NIR and can be used as responsivity standards in the wavelength range of 300 nm to 1000 nm. Their predicted uncertainty for radiant power responsivity measurements can improve the existing Si responsivity scales in the NIR wavelength range. They have several advantages over traditionally used Si trap detectors such as broader wavelength coverage, wider acceptance angle, higher sensitivity, and better performance in the NIR region. Radiometric and electronic test results are discussed here to illustrate their main characteristics. The spectral power responsivity scales can be improved using a set of the IR enhanced Si photodiodes not only to transfer the calibration from the cryogenic radiometer, but to use as the monochromator facility working standards. This improvement will reduce the length of the calibration chain and create a 1-step scale transfer between the cryogenic radiometer and the monochromator facility.

INTRODUCTION

Si trap detectors perform optimally up to 950 nm in part due to their spatial uniformity and their low temperature coefficient of responsivity. However, above 950 nm the Si trap detectors are subject to spatial nonuniformities and temperature dependent responsivities. The traps have small acceptance angles that limit their use in some monochromator applications. These trap limitations increase uncertainties for measurements at wavelengths longer than 950 nm.

The monochromator spectral responsivity scales above 950 nm, can be improved using the IR enhanced Si detector. In this work, the Hamamatsu Model S11499-01 Si photodiode was used in the described experiments. It is a 5 mm diameter single element photodiode with no temperature control required for optimal performance up to 1000 nm. It has better spatial response uniformity up to 1000 nm than InGaAs, or Ge photodiodes. This single element silicon photodiode is inexpensive and simple to use.

A set of the IR extended Si photodiodes calibrated by the cryogenic radiometer can be used directly as the everyday working standards between 300 nm through 1000 nm for the monochromator based spectral power responsivity measurements. Additionally, previous scale transfers for this wavelength range required the use of three different types of transfer standards from the cryogenic radiometer, the nitride passivated Si photodiode, the Si trap detector, and an InGaAs device. One IR enhanced Si detector can be used instead of the three types of transfer standards and the sets of Si and InGaAs working standards. This would be a 1-step transfer of the calibration instead of a multistep, multiple standard process. The IR enhanced Si photodiode characterization results presented will support the use of this device as the proposed transfer/working standard from 300 nm to 1000 nm. The SCF responsivity uncertainties for wavelengths between 950 nm and 1000 nm will be decreased significantly.

RADIOMETRIC CHARACTERISTICS

A series of measurements were made to characterize the IR enhanced Si device which included temperature dependence, spatial and spectral power responsivity. The temperature control was applied only for detector characterization purposes. The radiometric testing was performed from 350 nm to 1100 nm. Results from the complete wavelength range will be discussed.

The temperature dependent responsivity is shown in Fig. 1. The temperature coefficient of responsivity is close to zero to about 980 nm and it is 0.02 %/^{o}C at 1000 nm. The temperature coefficient at 1000 nm is a decade lower than that of the Hamamatsu 1337 Si photodiodes used in many trap detectors. It is shown that temperature control is not needed to 1000 nm.

As shown in Fig. 2, the spectral power responsivity was tested between 350 nm and 1100 nm. The peak responsivity is at 1000 nm. The 0.2

% max-to-min spatial non-uniformity at 1000 nm (as shown in Fig. 3) makes it possible to obtain a position produced uncertainty component of less than 0.1 % (k=2) when the incident beam is centered to the detector in power measurements.

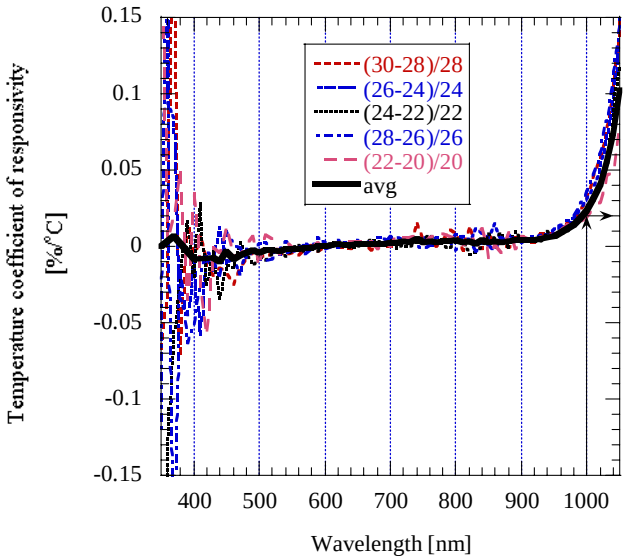

Figure 1. Temperature coefficient of responsivity of an IR-enhanced Si photodiode.

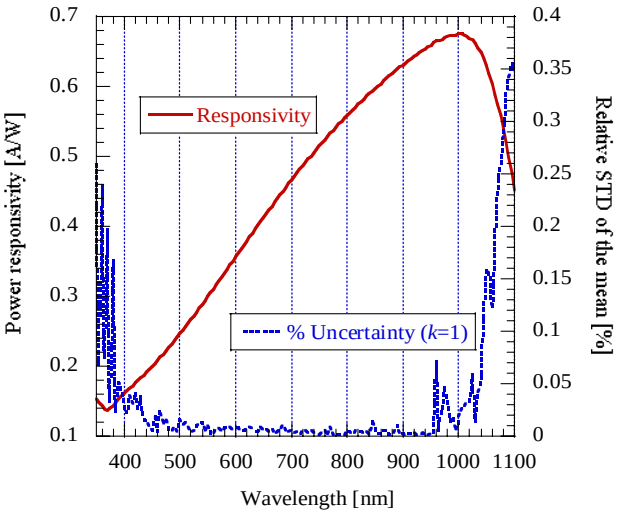

Figure 2. Spectral power responsivity of an IR enhanced Si photodiode measured at the SCF.

ELECTRICAL CHARACTERISTICS

The IR enhanced Si photodiode has a shunt resistance of 1 GΩ, thirty times higher than that of a Si tunnel trap detector. The 1 GΩ shunt resistance can result in a noise and drift equivalent photocurrent of about 3 fA at an electrical bandwidth of 0.3 Hz. This current corresponds to an NEP of about 7 fW/Hz^{½} which is more than a decade lower than the NEP=85 fW/Hz^{½} of a Si tunnel-trap transfer standard. This electrical performance improves the radiometric sensitivity of the spectral responsivity measurements over the entire wavelength range.

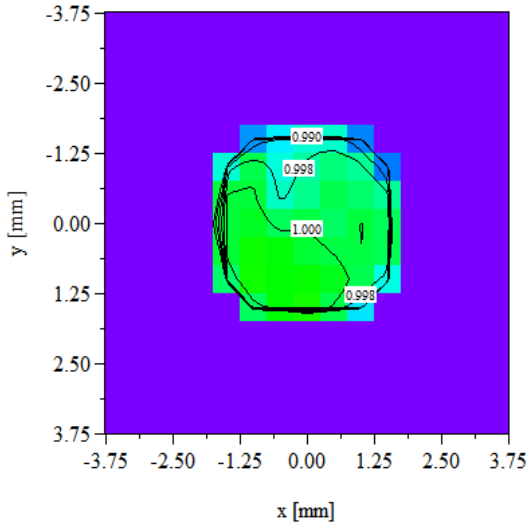

Figure 3. Spatial uniformity of responsivity of an IR enhanced Si photodiode at 1000 nm using 1.1 mm scanning beam diameter and 0.5 mm steps.

SUMMARY

The present spectral power responsivity scale transfer from the cryogenic radiometer to the monochromator facility can be improved by using the IR enhanced Si photodiode. This device can extend the lower uncertainties achieved by the Si photodiodes into the NIR. Additionally, as this device is spatially uniform and has a large acceptance angle, it can be used as the working standard in monochromator facilities. The uncertainty chain and thus the resulting uncertainties would be decreased by using the cryogenic radiometer calibrated IR enhanced Si photodiode as the monochromator facility's working standard. This improvement creates a 1-step scale transfer from the primary standard to the dissemination facility.

DISCLAIMER

Certain commercial equipment, instruments, or materials are identified in this paper to foster understanding. Such identification does not imply recommendation or endorsement by the NIST, nor does imply that the equipment are necessarily the best available for the purpose.

REFERENCES

1. P. Sipila et al, NEWRAD Proc. p. 223, 2005.
2. G. P. Eppeldauer et al, IOP Publishing, Metrologia, Vol. 50, p. 509-517, 2013.

A Transition Edge Sensor Bolometer for Fourier Transform Spectroscopy in the FIR Range – Design and Characterization

M. Kehrt, J. Beyer, C. Monte, and J. Hollandt

Physikalisch-Technische Bundesanstalt (PTB), Berlin, Germany
Mathias.Kehrt@PTB.de

A Transition Edge Sensor (TES) composite bolometer for Fourier Transform spectroscopy was designed for the spectral range from 0.1 THz to 3 THz aiming to achieve a higher dynamic range at similar detectivity as commercially available silicon composite bolometers. The design is based on a thin film metal mesh absorber, a super conducting thermistor and SiN membrane technology. A prototype was built and characterization and first application results are presented.

INTRODUCTION AND BACKGROUND

The Physikalisch-Technische Bundesanstalt (PTB), applies Fourier Transform (FT) spectroscopy in the THz frequency range for the measurement of the spectral emissivity and other optical properties of materials as well as for the calibration of spectral radiance of radiation sources.

For these applications we are developing specific liquid helium cooled composite bolometers that are based on superconducting thermistors and microstructured metal film absorbers. The bolometers are designed to replace conventional semiconductor-based bolometers in FT spectrometers operating in the frequency range from approx. 0.1 THz to 3 THz.

Special emphasis in the design was given on a high and specrally uniform absorption in this spectral range as well as on a highly linear response in order to avoid artifacts in the data processing of FT spectroscopy. The composite design allows a separate optimization of all relevant components, especially of the absorber and the thermistor.

ABSORBER AND THERMISTOR DESIGN

One approach realizing the desired spectrally flat absorption is matching the vacuum impedance. By using a continuous metal layer with a thickness smaller than the skin depth and a sheet resistance of $R_{\square} = 188\,\Omega$, a theoretical maximum absorption of 0.5 can be obtained [1]. With this approach the absorption is expected to be independent of the frequency. But at low temperatures this sheet resistance corresponds to a thickness in the order of 1 nm for a continuous film of usually used metals in the fabrication process. So technological limits are reached and a different approach is required. For our bolometers the absorbers are based on micro-structured metal meshes to match the vacuum impedance. In order to achieve a spectrally flat absorption the structural dimensions are much smaller than the relevant wavelengths. Two structures were identified as optimal absorbers. The design variants are one mesh with and one without loops but different structure sizes for the variants. Fig. 1 shows an example of such an absorbing metal mesh. The absorbers were lithographically fabricated on 1.1 µm thin SiN membranes with a thickness of about 100 nm and a sheet resistance of approx. 20 Ohm for the metal.

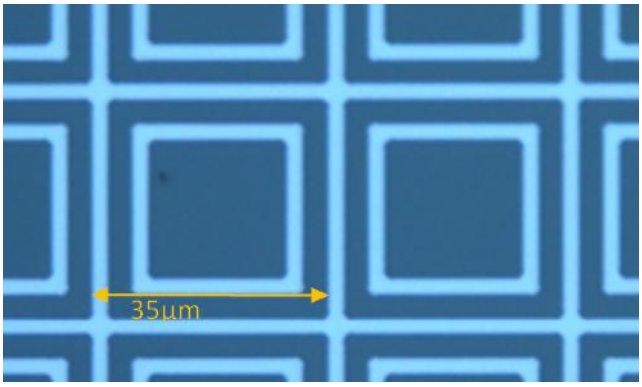

Figure 1. Microscopic image of a microstructured metal mesh absorber, optimized for a high and uniform absorption from 0.1 THz to 3 THz. The design variant with a loop inside each grid is shown.

The absorption determined for both variants is spectrally flat and near the theoretical maximum of 0.5 for this approach as is illustrated in Fig 3. The absorption was calculated from reflectance und transmittance measurements using FT spectroscopy. The background corrected determination of these optical properties is described in [2] in more detail.

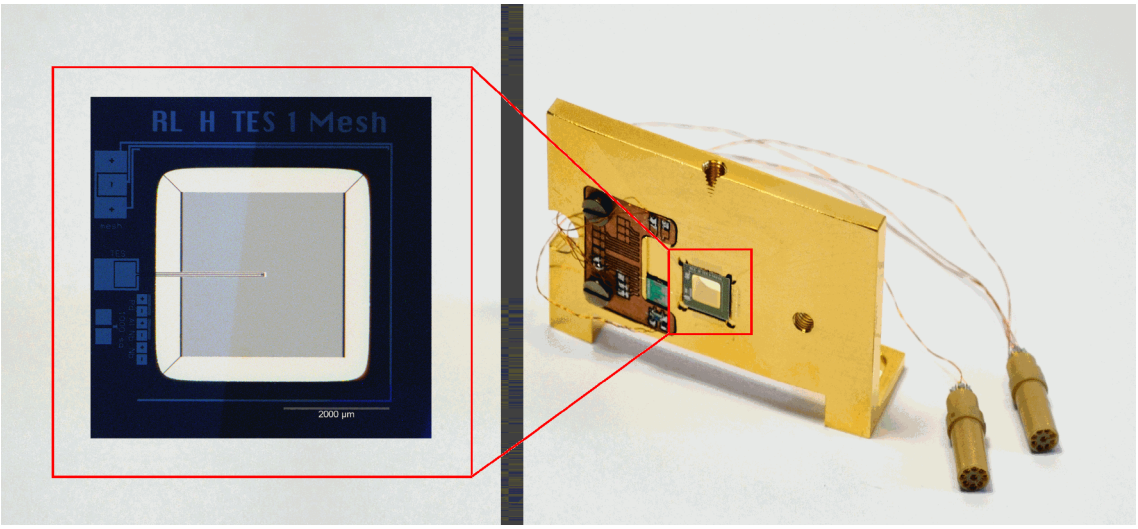

Figure 2. The TES-Bolometer and its mounting. Left: Bolometer element with a TES in the centre, surrounded by the absorber mesh on a SiN membrane. Right: Mounted bolometer with SQUID and wiring.

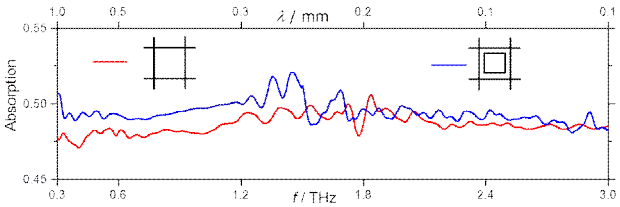

Figure 3. Spectrally flat absorption of the two selected absorber designs. Both designs are close to the theoretical absorption limit of 0.5.

A further requirement on the thermistor and its readout is a high dynamic range in combination with a highly linear response. To achieve this, the thermistor is realized as a transition edge sensor (TES) which utilizes the resistive transition of a superconductor structure [3]. Our TES thermistors are made from bilayers of Niobium and Aluminium. They show superconducting transition temperatures of $T_C \approx 8\,\mathrm{K}$ and approx. 30 mK wide resistive transitions. Operating the TES in a negative electrothermal feedback extends the dynamic range [4]. The response of the TES and the feedback circuit to a change in radiant load is an output current. This current is measured using a Superconducting Quantum Interference Device (SQUID) current sensor.

Several composite bolometers consisting of TES thermistors and both absorber variants have been fabricated in a multilayer lithographic process on SiN membranes. On the left of Fig. 2 a bolometer element with a TES in the center is shown. The thermistor is surrounded by the absorber with a physical dimension of 3.3 mm in square. The mounted bolometer with the SQUID readout and wiring is shown on the right of Fig. 2.

First characterization measurements with an electrically heated absorber are depicted in Fig. 4. They show a stable response of the detector at different operating points of the TES to a periodically heated absorber up to frequencies of several hundred Hertz. The results of its optical characterization and first applications of the bolometer will be presented.

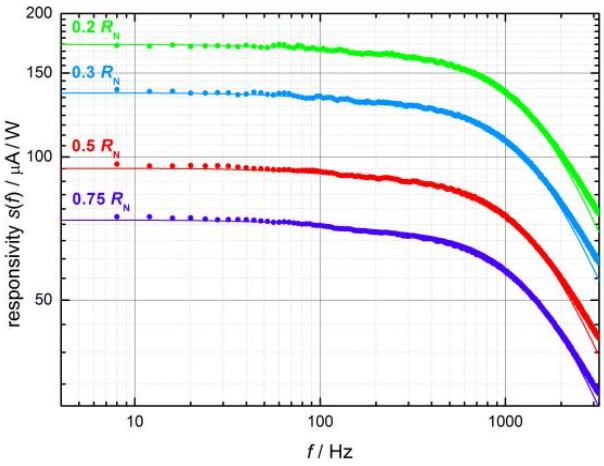

Figure 4. Responsivity of the bolometer at different operating points in the transition region referred to the resistance of the normal conduction state R_n.

REFERENCES

1. W. Woltersdorff. über die optischen konstanten dünner metallschichten im langwelligen ultrarot. *Zeitschrift für Physik*, 91(3-4):230–252, 1934.
2. M. Kehrt, R. Müller, A. Steiger, and C. Monte. Background corrected transmittance and reflectance measurements in the FIR. In *Infrared, Millimeter, and Terahertz Waves (IRMMW-THz), 2013 38th International Conference on*, pages 1–2, 2013.
3. P. L. Richards. Bolometers for infrared and millimeter waves. *Journal of Applied Physics*, 76(1):1–24, 1994
4. K. Irwin and G. Hilton. Transition-edge sensors. In C. Enss, editor, *Cryogenic Particle Detection*, volume 99 of *Topics in Applied Physics*, pages 63–150. Springer Berlin Heidelberg, 2005.

Spectral Dependence of Solar Cell Conversion Efficiency for Monochromatic Radiation

Terubumi Saito and Minato Takesawa

Tohoku Institute of Technology, Sendai, Japan
Corresponding e-mail address: terubumi.saito@tohtech.ac.jp

Solar cell conversion efficiencies for quasi-monochromatic radiation has been measured as a function of wavelength. It has been proven that the conversion efficiency is proportional to the wavelength of the input radiation as the theory predicts. Also, it has been shown that the efficiency increases as a logarithmic function of the input irradiance. In conclusion, highest conversion efficiency is realized by illuminating a solar cell by intense radiation of low energy photons close to the bandgap energy while satisfying sufficient absorption.

INTRODUCTION

In spite of great efforts to increase the energy conversion efficiency of solar cells, the efficiency of single junction cells still remains around 20 % for commercial available crystalline silicon ones, which are one of the highest quality types.

Theoretical limit of the efficiency is given by Schockley and Queisser to be 29 % for single junction crystalline silicon [1]. The limit is calculated for the case that the cell is illuminated by solar radiation. If the input radiation is monochromatic and the material of solar cell is optimized for its wavelength, the efficiency is expected to exceed the limit. Contrary to this rather known theoretical prediction, there are few detailed experimental verification [2] to the prediction. In this paper, we report on its experimental results of spectral dependence of conversion efficiency intending to provide the basis to the future applications of more efficient ways to use the solar cells.

THEORETICAL[3]

Causes of energy losses are categorized into the following: 1) Optical losses such as reflection at the surface and transmission through the substrate, 2) Carrier recombination losses at the surfaces of and in the substrate, 3) Joule heating in the series and shunt resistance, 4) Mismatch in resistance between the source and the load, and 5) Mismatch in energy between the semiconductor bandgap and the input photon energy. Continuous efforts have made it possible to steadily decrease the losses of the first 4 types and approaches its limit of nearly zero.

However, concerning the loss 5), it is, in principle, difficult to decrease due to the fact that the sun, the input radiation, has a very wide spectrum. This is because the excess energy of photo-excited electrons between the excited level and the bottom of the conduction band is finally lost to the heat.

In general, solar cell conversion efficiency, ε, is given by the following equation,

$$\varepsilon = P_e / P_r = FF\, V_{oc}\, I_{sc} / P_r, \quad (1)$$

where P_e is the output electrical power, P_r the input radiant power, FF the fill factor, V_{oc} the open circuit voltage, I_{sc} the short circuit current. The fill factor is obtained by measuring the current-voltage characteristics through the following equation,

$$FF = V_m I_m / (V_{oc} I_{sc}), \quad (2)$$

where V_m and I_m are the voltage and the current that gives the maximum power output, respectively.

If the input radiation is monochromatic with the photon energy E_p and photon flux Φ, then $P_r = \Phi E_p$. If the spectral quantum efficiency for E_p is η, then it holds that $I_{sc} = e\Phi\eta$ where e is the elementary electronic charge and η the spectral external quantum efficiency. Therefore,

$$\varepsilon = P_e / P_r = FF\, V_{oc}\, I_{sc} / (\Phi E_p) = e\eta\, FF\, V_{oc} / E_p, \quad (3)$$

If the photon energy, E_p, is expressed in eV and the open circuit voltage, V_{oc}, is expressed in V, then

$$\varepsilon = \eta\, FF\, V_{oc} / E_p. \quad (4)$$

It shows that the conversion efficiency is expected to be inversely proportional to the photon energy provided that $\eta\, FF\, V_{oc}$ is constant.

EXPERIMENTAL

For measurements of solar cell conversion efficiency, IEC60904-3 standard defines to use solar radiation with spectrum of AM1.5G at the irradiance of 1 kW/m^2 as input radiation. Here, we extend the definition by replacing the solar radiation with

(quasi-)monochromatic radiation at an arbitrary irradiance level.

We have tested two types of specimen; one is (a): poly-crystalline silicon solar cells for toy applications, OptoSupply OPL15A25101, and the other is (b): crystalline silicon photodiode, Hamamatsu S1337-1010BQ. As a source, we used two types; one is color LEDs of blue (peak wavelength of 450 nm), green (510 nm) and red (650 nm) and the other is a combination of an incandescent lamp and interference filters. We evaluated the conversion efficiencies by measuring FF, V_{oc} and I_{sc} based on Eqs. (1) and (2). Radiant power, P_r, was determined by a calibrated irradiance meter or a photodiode.

RESULTS

Irradiance dependence of conversion efficiency at some wavelengths for sample (a) and (b) are shown in Fig. 1 and 2, respectively. As theory predicts (see Eq.(3)), the efficiency increases roughly as a logarithmic function of the irradiance. Fig. 1 shows that the efficiency is larger for the shorter wavelength, contradicting to the theory, which strongly suggests that the sample thickness is not thick enough to absorb photons. Measurement results in Fig. 2 show that since the efficiency is satisfactory and the longer wavelength gives higher efficiency, the product has a higher quality.

The efficiency as a function of wavelength at the irradiance of 1 W/m^2 is shown in Fig. 3. It clearly shows that the efficiency is proportional to the wavelength as Eq.(4) predicts.

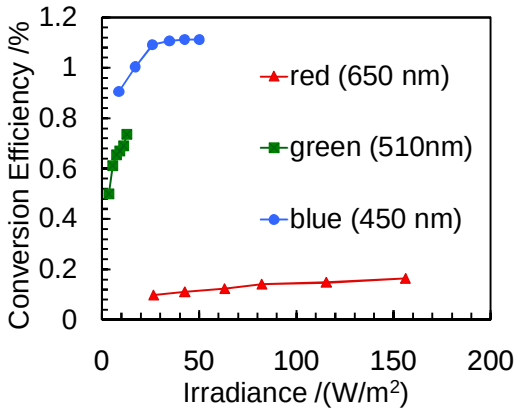

Figure 1. Conversion efficiencies of crystalline silicon solar cell for color LEDs as a function of the irradiance.

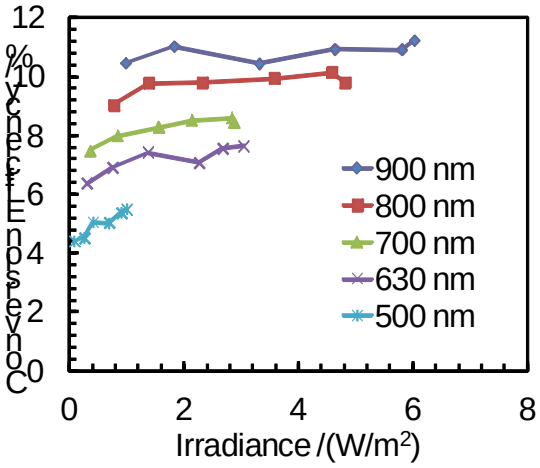

Figure 2. Conversion efficiencies of silicon photodiode (S1337-1010BQ) for color LEDs as a function of the irradiance.

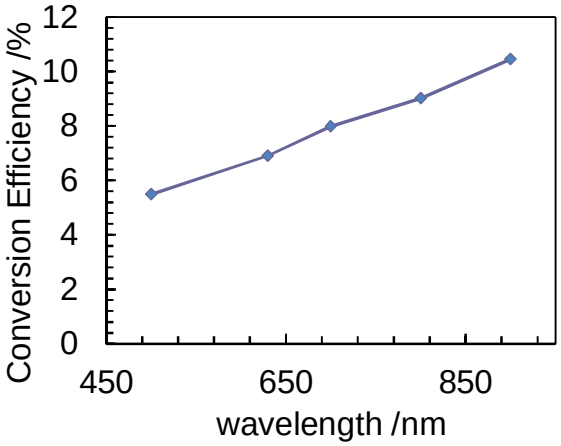

Figure 3. Conversion efficiencies of silicon photodiode (S1336-1010BQ) at 1 W/m^2 as a function of the wavelength.

CONCLUSION

Solar cell conversion efficiencies for quasi-monochromatic radiation has been measured as a function of wavelength. It has been proven that the conversion efficiency is proportional to the wavelength of the input radiation.

REFERENCES

1. W. Shockley and H. J. Queisser, “Detailed balance limit of efficiency of p-n junction solar cells”, J. Appl. Phys., 32, 510–519, 1961.
2. L. C. Olsen et al, “High efficient monochromatic GaAs solar cells”, in Conf. Record of IEEE Photovoltaic Specialists Conf. Vol. 1, 419-424, IEEE, New York, 1991.
3. T. Saito, “Spectral properties of semiconductor photodiodes”, Chapter 1 (pp. 3-24) in “Advances in photodiodes” (ISBN 978-953-307-163-3), Intech, Croatia, March 2011.

Characterization of a Predictable Photodiode Cryogenic Radiometer for measuring fundamental constants

Marit Ulset Sandsaunet, Chi Kwong Tang, and Jarle Gran

**Norwegian Metrology Service (Justervesenet), Kjeller, Norway*

Corresponding e-mail address: mas@justervesenet.no

This paper presents characterization of the first prototype of a predictable photodiode cryogenic radiometer (PPCR) at 77 K. The PPCR combines a predictable quantum efficiency detector (PQED) with a cryogenic radiometer (CR). When combining these two inherently different primary standards for measuring optical power on the same device, systematic error sources are eliminated, and the relationship between the elementary charge *e* and Planck's constant *h* can be found from the modelled responsivity of the PQED.

INTRODUCTION

The PPCR combines high accuracy standards from two sides of fundamental physics. On one side, there is the cryogenic radiometer (CR) from thermodynamics, and on the other side the predictable quantum efficiency detector (PQED) from electromagnetism. The potential of exploiting the PQED as a new radiometric standard in different applications will be explored in the European Metrology Research Programme (EMRP) through the NewStar project [1].

The idea of combining two different methods of measuring optical power to determine Planck's constant has already been explored by Razet *et al.* [2]. They used a photon-counting detector and an electric substitution radiometer to determine Planck's constant. However, the determination of the quantum efficiency of the photon-counting detector yielded a high relative uncertainty of 3.4 %.

In this work, we have substituted the photon-counting detector with a PQED [3-5], operating under near ideal response condition to minimize the uncertainty in internal quantum efficiency potentially down to 1 ppm (parts per million) [4-6]. In addition, the PQED is the light absorber in the CR operation mode, eliminating systematic errors such as reflection and absorbance differences between the two primary standard modes.

By combining the PQED primary measurement and CR to measure the optical power of a stabilized laser source, we show that the relationship between the elementary charge *e* and Planck's constant *h* can be extracted. In addition, the extraction of *e/h* tests the validity of the two independent primary standards for measuring optical power.

MEASUREMENT SETUP

The PPCR consists of a PQED with a cernox temperature sensor attached to its backside. It is operated at 77 K, and the carrier for the PPCR works as a weak heat link to the liquid nitrogen dewar of the cryostat. Another cernox temperature sensor is mounted on the heat sink, to correct for ambient temperature changes. Illumination is achieved through laser with a wavelength of 488 nm.

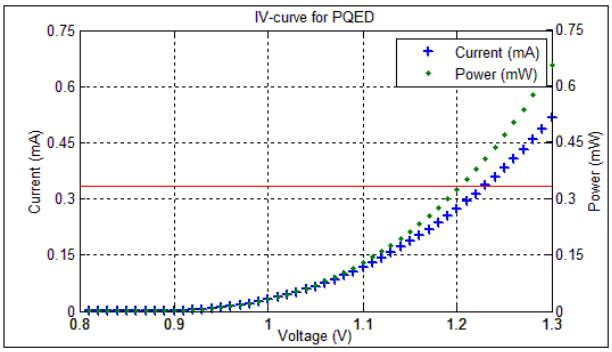

Figure 1. IV characteristics for silicon photodiode. Current and power as a function of voltage. The red horizontal line shows the optical power from the PQED measurement.

WORKING PRINCIPLE

The principle of the PPCR is to measure optical power under PQED-mode and compare it with the power measured under CR-mode. This is performed in three measurement series, denoted as PQED-, optical CR- and electrical CR-mode.

In the PQED-mode, the PQED functions as a simple photodiode where it is exposed to illumination, and the generated photo current I_{photo} is measured. While illuminated, the PQED is put under reverse bias voltage to minimize the loss of response due to recombination of the optically generated electron-hole pairs. Disregarding reflection losses, the PQED responsivity is given by

$$R(\lambda) = \frac{e\lambda}{hc}\left(1-\delta(\lambda)\right) \qquad (1)$$

Here e is the elementary charge, λ is the optical wavelength, h is Planck's constant and c is the speed of light in vacuum. $\delta(\lambda)$ is the predictable internal loss of the PQED [6,7].

In optical CR-mode, the PQED is the light absorber, converting optical energy into heat. This is realized by having an open-circuit to the power supply ensuring that no net current will flow in the absorber. The temperature rise due to the illumination is constantly monitored by the temperature sensor at the backside of the PQED. After a certain period, the temperature saturates due to an equal loss of heat to a cold reservoir. It is assumed that the optical power in this mode is negligibly different from the one in the PQED-mode.

In the electrical CR-mode, the PQED functions as a heating element where a forward bias voltage is applied over it. The applied forward bias is chosen such that the electrical power, P, matches the saturation temperature under the optical CR-mode. Fig. 1 shows the I-V characteristics of the PQED photodiodes including the calculated power. A red line is added to show the optical power as extracted from the PQED-mode. By finding the cross-section between the two power-curves, an approximated voltage is chosen to electrically heat the PQED.

RESULTS AND DISCUSSIONS

The results from two different forward bias electrical CR measurements and one optical CR measurement are shown in Fig. 2. It should be mention that the temperature sensor is monitored by its resistance value and, thus, the coordinate has a unit related to resistance. The optical power of 0.3331 mW was found from a linear interpolation between the two measurement series of the electrical CR-mode – one above and one below the approximated value. The interpolated value differed slightly from the value found in PQED-mode of 0.3333 mW.

The time constant (1/e) for both the optical and electrical CR-mode was roughly 90 seconds, while the sensitivity of the CR was found to be approximately 1.1 K/mW. Both the sensitivity and the time constants, which are closely related, can be tuned through heat link engineering.

One source of error in the measurement is the resistance in the wires. Current flowing between the PQED and the contact point where the real voltage is measured, will dissipate heat, which will be transported partly along the wires, and not be measured by the temperature sensor at the backside of the PQED. This means that the applied electrical power will not give sufficient temperature rise and will result in an overestimation of the optical power in the CR-mode. The true optical power will be lower than estimated.

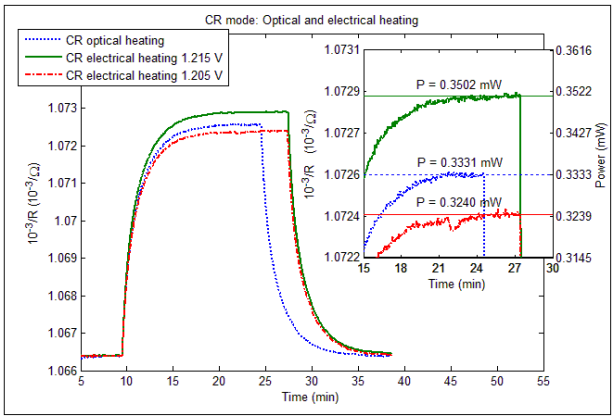

Figure 2. Electrical and optical heating of the PPCR. Inset shows values for applied electrical power and calculated optical power.

As mentioned, the PQED is assumed to have an ideal responsivity. However, if there are internal losses in the PQED, the true power will be higher than estimated from the PQED mode. The internal quantum deficiency $\delta(\lambda)$ can be estimated by simulations, see Tang et al. [7].

SUMMARY

A working prototype of a predicable photodiode cryogenic radimeter has been described and demonstrated. Some sources of error are discussed, and improvements will be performed.

REFERENCES

1. http://www.inrim.it/Newstar/
2. A. Razet, et al., A determination of Planck's constant from radiometric measurements, Metrologia 43(5): 367, 2006.
3. http://www.quantumcandela.net/
4. M. Sildoja, et al., Predictable quantum efficient detector: I. Photodiodes and predicted responsivity, Metrologia 50(4): p 385-394, 2013.
5. I. Müller, et al., Predictable quantum efficient detector: II. Characterization and confirmed responsivity, Metrologia 50(4): 395-401, 2013.
6. J. Gran et al. Simulations of a predictable quantum efficient detector with PC1D, Metrologia 49(2): S130-S134, 2012.
7. C. K. Tang et al., Two-dimensional simulation of an induced-junction detector with Genius device simulator towards a predictable quantum efficient detector, these proceedings, 2014.

Selected aspects of measurement uncertainty evaluation of chromaticity values for LED measurements including correlations

Udo Krüger[1] and Peter Blattner[2]

[1]*TechnoTeam Bildverarbeitung GmbH, Ilmenau, Germany,* [2]*METAS, Bern, Switzerland*

Corresponding e-mail address: udo.krueger@technoteam.de

Based on a model of calibration and evaluation for spectrometer measurements the calculation of the measurement uncertainty associated with the chromaticity values for LED measurements including correlations is described. Using R, G, B and white LEDs as examples, the sensitivity coefficients for the influence of the wavelength calibration, the dark signal estimation and the influence of the distribution temperature of the calibration source will be evaluated in detail. The calculation of the correlations and the explanation of their origin will be discussed in detail.

INTRODUCTION

According to the "Guide to the Expression of Uncertainty in Measurement" (GUM, [1]) and its supplements [2] and [3], the statement of the expanded measurement uncertainty for the measurement result is necessary.

This means, the measurement uncertainty is connected to the measurement result rather than to the measurement device. While calculating the measurement uncertainty not only the properties of the measurement device but also the properties of the DUT and the measurement process itself have to be taken into account.

MU FOR COLOUR MEASUREMENTS

Colour measurement have at least two outputs (e.g. the chromaticity values (x and y)) and, therefore, all information from the GUM supplement 2 [3] should be taken into account. The main problem in the evaluation of the measurement uncertainty in colorimetry is to model the correlations correctly. The chromaticity values are correlated due to the spectral overlap of the colour matching functions. This means, an uncertainty contribution from the measurement is influencing both output channels causing correlations.

For the calculation of the measurement uncertainty at least the following aspects have to be taken into account:

Measurement instrument: reproducibility, repeatability, calibration, non linearity (range calibration), spectral matching, ambient conditions (e.g. lab temperature, stray light)

Device under test (DUT): modulation, burn in, stability, temperature sensitivity, on/off behaviour

Measurement process and interaction: interaction between measurement device and DUT (stray light, reflection)

In this paper only some of the contributions from the measurement device itself and its calibration (wavelength calibration, dark signal estimation and the influence of the distribution temperature of the calibration source) will be handled in detail.

LED BASED LIGHT SOURCES

LED based light sources, represented by typical R, G, B and phosphor type white LEDs here, having a characteristic distribution of their chromaticity values. This results in specific correlation matrixes for the MU statements. The size of the distributions and therefore the MU can be described with ellipsoids in most cases. An example was shown in [4].

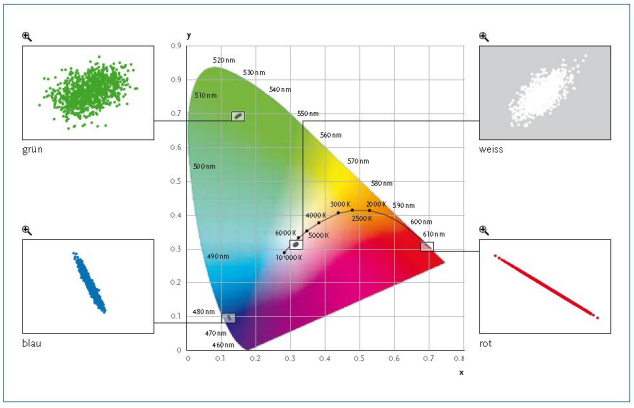

Figure 1. Typical distribution plots for chromaticity values of R, G, B and white LEDs. [4]

MODELING

The measurement process will be modelled for the measurement of the calibration source (temperature radiator) and the DUT separately. Many properties of the measurement device generates similar impact on the measurement of the calibration source and the DUT (e.g. wavelength shift). Other properties (e.g. the dark signal) will have a very different effect.

Furthermore a part of the model will describe the interaction of both properties of the measurement device and the DUT.

EXAMPLE

As an example the influence of the uncertainty of the distribution temperature of the calibration source is estimated as following: The source is modelled as a Planckian radiator and a correction term. The measurement uncertainty of the distribution temperature results in a distribution of the chromaticity values along the Planckian locus. The uncertainty of the correction term (including the usually uncorrelated given uncertainty of the calibration source from the calibration certificate) generates a distribution normal to the Planckian locus. This is shown for a measurement of the calibration source itself in the following figures.

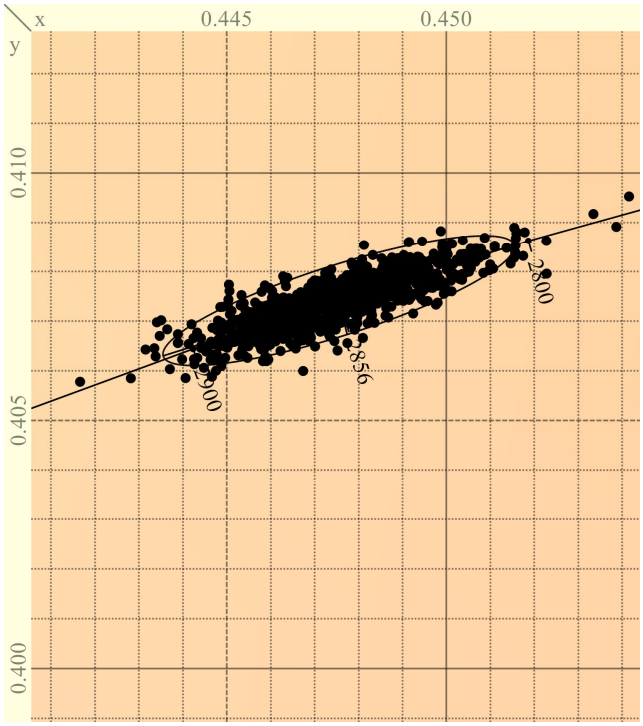

Figure 2. Chromaticity values for a calibration of a spectroradiometer using a standard illuminant A source contributing its measurement uncertainty in the colour temperature.

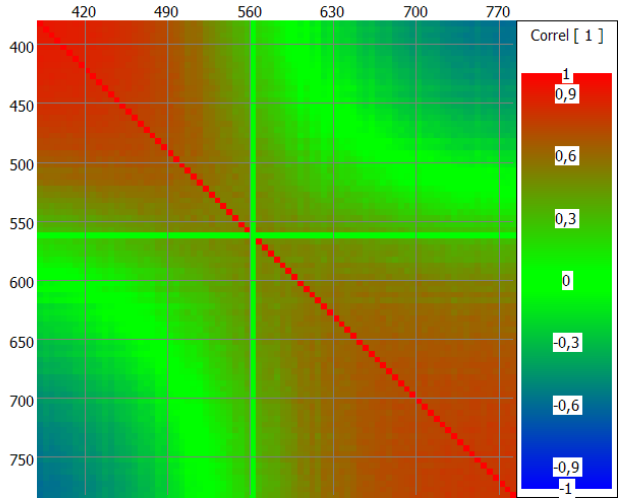

Figure 3. Correlation effect caused by the uncertainty contribution from the colour temperature of the standard illuminant A source for the spectral values.

SUMMARY

The calculation of the measurement uncertainty associated with chromaticity values based on a model of calibration and evaluation is possible using the information given in the GUM and supplements.

The correlation is caused by the spectral overlap of the color matching functions and model parameters linking different spectral information to each other (e.g. correlated wavelength shifts and uncertainty in the distribution temperature of the calibration source).

The measurement result including the expanded measurement uncertainty (Attention: k=2.45 in this case! [3]) and its correlation is an important information necessary for every conformity tests based on chromaticity values.

REFERENCES

1. Evaluation of measurement data – Guide to the expression of uncertainty in measurement. JCGM 100:2008.
2. Evaluation of measurement data – Supplement 1 to the "Guide to the expression of uncertainty in measurement" – Propagation of distributions using a Monte Carlo method JCGM 101:2008.
3. Evaluation of measurement data – Supplement 2 to the "Guide to the expression of uncertainty in measurement" – Extension to any number of output quantities JCGM 102:2011.
4. Blattner, P: Wenn weisses Licht farbig wird. METinfo, Vol. 17, No. 1, S. 12-17, 2010.

Development and Characterization of Broadband UVA and UVB Radiometers

Luciana C. Alves*, Thiago Menegotto, Thiago Ferreira da Silva,
Jaqueline S. P. M. Corrêa, and Iasmim F. Duarte

National Institute of Metrology, Quality and Technology − Inmetro, Duque de Caxias, Brazil
Corresponding e-mail address: lcalves-pronametro@inmetro.gov.br

Optical filters, UV enhanced silicon photodiodes and precision limiting apertures have been studied in order to characterize the components of broadband UV radiometers. Results of spectral power responsivity of assembled UVA and UVB radiometers based on UV photodiodes are also presented. The results indicate a spectral mismatch which must be considered in the measurement calculation.

INTRODUCTION

Most commercial UVA radiometers currently available have non-ideal spectral response, resulting in spectral mismatching of the radiometer to the ideal actinic action. The higher the spectral mismatch, the greater the measurement error when spectrally different sources of optical radiation are used [1].

This paper presents some results aiming on providing Inmetro with radiometric standards in the UVA and UVB spectral ranges. The UV photodiodes, optical filters and precision apertures, which will be used in the construction of the UV broadband radiometers, have been characterized in the available calibration and measurement facilities. Additionally, the assembled UV broadband radiometers have been preliminarily characterized in terms of their spectral power responsivity.

COMPONENTS CHARACTERIZATION

Each part of UV radiometers was characterized separately initially assuming that interreflections between filter and photodiode are negligible.

Bandpass filters:

The regular spectral transmittance of UVA and UVB optical filters (XUVA315 and XUVB280 from Asahi Spectra) was measured using a reference spectrophotometer (model Cary 5000 from Varian). The transmittances of each filter were also studied outside the passband in order to evaluate the out-of-band blocking, Figure 1 shows the spectral transmittance curves of the XUVA315 and XUVB280 optical filters. They exhibit an undesirable transmittance outside the bandpass above 750 nm and 700 nm, respectively, which can contribute to the radiometer signal, resulting in measurement errors. The spatial uniformity of regular spectral transmittance of each filter was also investigated. Considering a centered 10 × 10 mm^2 area, XUVA315 and XUVB280 filters presented a spatial non-uniformity equal to 6.7 × 10^{-3} at 365 nm and 2.5 × 10^{-3} at 313 nm, respectively, relative to the transmittance at the center of each filter.

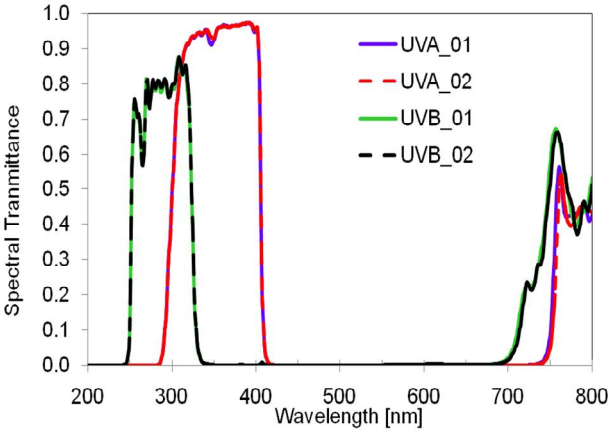

Figure 1. Measured spectral transmittance of the XUVA315 and XUVB280 optical filters.

Photodiodes:

Two UV enhanced silicon photodiodes (model UV-100L from UDT Sensors Inc. [2]) were investigated in terms of their spectral power responsivity in the UV, VIS and NIR spectral regions. These measurements were performed in an experimental set-up based on a single grating monochromator using quartz tungsten halogen (VIS and NIR) and xenon arc lamps (UV) as sources of optical radiation, hereafter referred as spectral responsivity system (SRS). In the VIS and NIR spectral range, a 3-reflection silicon trap detector with traceability to the cryogenic radiometer was used as transfer standard allowing to achieve a relative expanded uncertainty lower than 9.5 × 10^{-3} (k = 2). In the UV spectral region, the spectral power responsivity was determined by extrapolation using an electrically-calibrated pyroelectric radiometer (ECPR) (from Laser Probe Inc.). The ECPR was calibrated to a relative expanded uncertainty of 2.3 × 10^{-2} (k = 2),

traceable to the cryogenic radiometer. Additionally, the absolute spectral power responsivity of both photodiodes was determined directly against the cryogenic radiometer at HeNe laser line of 632.8 nm with good agreement. The relative expanded uncertainty was better than 3.5×10^{-4} ($k = 2$). Figure 2 presents the measured spectral responsivities of the photodiodes.

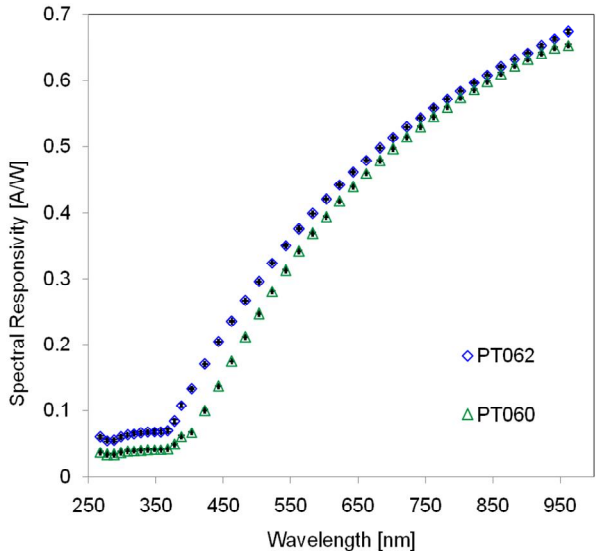

Figure 2. Spectral responsivity curves of the UV photodiodes. The expanded uncertainties are smaller than the symbols.

The spatial non-uniformity at 632.8 nm of PT060 and PT062 was measured to be 4.5 parts in 10^3 and 1.9 parts in 10^3 over the active area (10 x 10 mm^2), respectively. The obtained shunt resistance values were equal to 58.4 MΩ and 42.8 MΩ for PT060 and PT062 photodiodes, respectively.

Apertures:

Two precision apertures with cylindrical edge and nominal area of 0.5 cm^2 have been used in the UV broadband radiometers to define the area of the input flux for irradiance measurement. A non-contact technique was used for area measurement of the radiometric apertures with an expanded uncertainty of 2.8×10^{-2} mm^2 ($k = 2$). The quality of the edge of each aperture was also assessed from images obtained by scanning electron microscopy.

RADIOMETERS CHARACTERIZATION

A preliminary evaluation of the spectral responsivity of the assembled UVA and UVB radiometers was performed in the UV up to 450 nm using the ECPR in the SRS. As expected, the resulting curves from the spectral sensitivity of the photodiode combined with the spectral transmittance of the selected optical filter showed a large spectral mismatch relative to the UVA and UVB curves. The spectral matching of the UVA and UVB radiometers was estimated to be equal to 0.44 and 1.02, considering the spectral range up to 450 nm. Figure 3 shows the spectral responsivity of UVA and UVB radiometers.

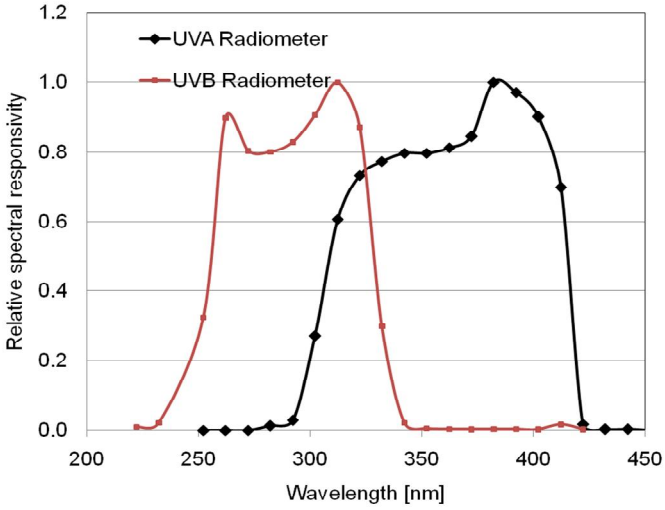

Figure 3. Spectral responsivity curves of the assembled UVA and UVB radiometers.

CONCLUSION

The increasing spectral responsivity of UV photodiodes in the VIS and NIR spectral regions, associated with the regular transmittance of the bandpass filters, confirmed the need of further blocking the influence of the radiation outside the band of interest. Spectral responsivity of UV radiometers must also be evaluated at shorter wavelengths in order to investigate the detector rejection in this range. Furthermore, different optical filters and photodiodes can be evaluated in order to reduce the spectral mismatch of the device to the ideal actinic action.

ACKNOWLEDGEMENTS

L. C. Alves acknowledges the financial support from PRONAMETRO. J. S. P. M. Corrêa and I. F. Duarte acknowledge the support from PROMETRO/CNPq.

REFERENCES

1. G. Xu e X. Huang, “Characterization and calibration of broadband ultraviolet radiometers”, *Metrologia*, vol. 37, pp. 235 –242, 2000.

2. UDT Sensors Inc. in http:\\www.udt.com.

The Establishment of a Detector-Based Transfer Standard Spectrograph for the Measurement of Broadband Sources

Ping-Shine Shaw, Yuqin Zong, John Woodward, Steven W. Brown, Howard W. Yoon, and Keith R. Lykke

National Institute of Standards and Technology, Gaithersburg, MD, USA
Corresponding e-mail address: shaw@nist.gov

Traditionally, broadband sources are generally calibrated with source-based standards such as lamps and blackbodies while monochromatic sources are calibrated with detector-based standards such as solid state detectors. Comparing source-based radiometry and detector-based radiometry typically requires filter radiometers which can measure a few wavelengths for validation. Currently, this cross-calibration is important because of lower uncertainty of detector-based radiometry compared with the uncertainty of source-based radiometry. In recent years, as CCD-based spectrographs have become more compact, stable and rugged, several projects at NIST such as the lunar irradiance and the NIST Stars projects are beginning to use spectrographs instead of filter radiometers to measure broadband sources. Here, we discuss the technique and setup of a facility using tunable lasers to calibrate spectrographs with detector-based standards. The goal is to achieve an uncertainty below 0.5%. Because spectrographs have short measurement times and cover a wide range of wavelengths, a calibrated spectrograph traceable to detector-based standards can potentially be used to bridge detector-based radiometry with source-based radiometry and reduce measurement uncertainty for broadband sources.

EXPERIMENTAL SETUP

The basic concept for this calibration work is simply to treat the spectrograph as a multichannel filter radiometer with each pixel of the spectrograph as a single filter radiometer. By mapping out the single pixel spectral responsivity for all pixels, the spectrograph is fully characterized. For the spectrograph used for this work, there are 1024 readout pixels covering a wavelength range from 380 nm to 1040 nm. The bandwidth for each pixel is about 3 nm full-width-half-max. It is a major challenge and a daunting task to calibrate so many narrow-band pixels. However, with the use of computer-controlled fine-tuning lasers, it is possible to perform the calibration over a range of wavelengths within a reasonable amount of measuring time. For this work, two tunable lasers were used; an OPO laser with nanosecond pulses and 1 kHz repetition rate and a cw Ti-sapphire laser. The wavelength step used for this calibration ranges from 0.2 nm to 0.4 nm.

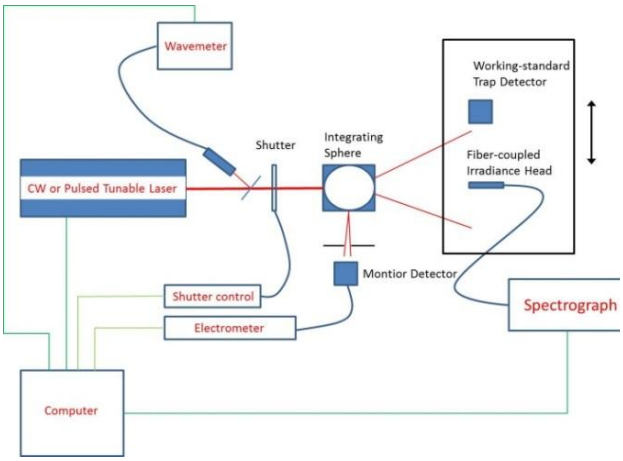

Figure 1. Experimental setup for spectrograph calibration.

Figure 1 shows the experimental setup for the spectrograph calibration. The laser beam is directed into an integrating sphere to create a uniform irradiance field at the plane of detection. A reference trap detector with calibrated irradiance responsivity is placed right next to the irradiance head of the spectrograph to transfer the scale to the spectrograph. Because of the large power fluctuations from the pulsed laser due to pulse-to-pulse variation, a charge integration scheme is employed and used for both pulsed and cw lasers. The measurement sequence for a single wavelength is as follows: First, with the shutter closed the computer resets the electrometer of the monitor detector and the spectrograph. Second, the computer initiates the accumulation of charges for both the electrometer and the spectrograph. Third, after ensuring the electrometer and the spectrograph are accumulating charges, the computer sends a command to open the shutter to let light into the integrating sphere. Fourth, after a pre-determined

time, typically 1 second, the shutter is closed. Fifth, the computer stops the charge accumulation for both the electrometer and the spectrograph and the total charge accumulated is read out.

The same procedure is used for the transfer standard detector measurement except that in this case an electrometer connected to the transfer standard is used for charge accumulation instead of the spectrograph.

RESULTS

Figure 2 shows the response of the spectrograph for a single wavelength (i.e., the line spread function) for several selected wavelengths from 570 nm to 620 nm. Because the wavelength between neighbouring pixels is about 0.6 nm, one can clearly see the effect of digitization for all the line spread functions.

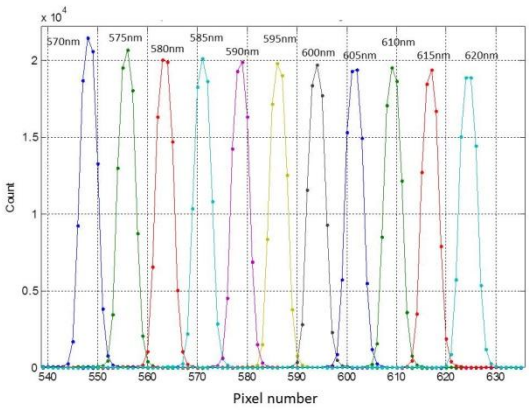

Figure 2. Line spread function of the spectrograph.

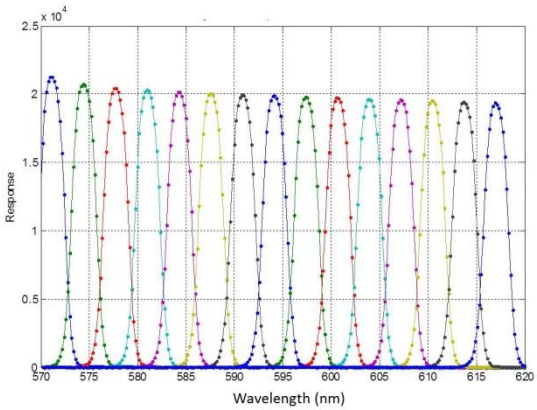

Figure 3. Single pixel response function of the spectrograph.

Figure 3 shows the spectral response of a single pixel of the spectrograph for several selected pixels. The pixel range shown covers 70 pixels and, for clarity, only one pixel out of neighbouring 5 pixels is displayed. The wavelength step is 0.2 nm in this case. Comparing figures 2 and 3, one can clearly see the benefit of small wavelength steps. One should note that the single pixel response shown in Figure 3 can be well approximated by a Gaussian. Using a Gaussian with the same band width, it can be demonstrated that a 0.2 nm wavelength step causes negligible error in calculating the integrated response of a pixel.

Lastly, Figure 4 shows the integrated pixel response of the spectrograph from 500 nm to 700 nm. The integrated responsivity can be used to establish the absolute spectral irradiance of the incident flux.

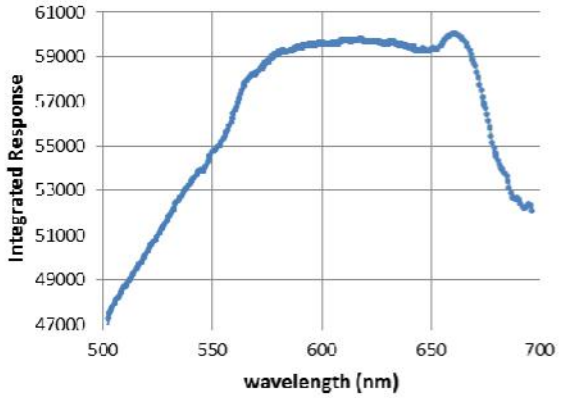

Figure 4. Integrated pixel response function of the spectrograph.

CONCLUSIONS

We have shown that a tunable-laser based system can calibrate spectrographs with a detector-based standard. We will present the final uncertainty of this calibration by including other effects such as stray-light correction and the uncertainty caused by the spectral shape of the incident light. The important validation of this calibration will be conducted by comparing the calculated spectral irradiance from a source with known irradiance such as an FEL lamp and variable high temperature blackbody source. This calibration will have an immediate impact by reducing the measurement uncertainty for lunar and NIST Stars field works and it allows calibration in the field using lasers or LEDs. Moreover, we plan to establish spectrographs as transfer standards for source-based radiometry.

Uncertainty evaluation of solar UV irradiance measurement using array spectroradiometer

J. Dubard, R. Etienne, and T. Valin

Laboratoire National de métrologie et d'essais ,TRAPPES, FRANCE
Corresponding e-mail address: jimmy.dubard@lne.fr

Array spectroradiometers are widely used to measure source spectral irradiance. Within the European Metrology Research Program EMRP-ENV03 project such spectroradiometers are used for solar UV spectral irradiance measurement including stray light correction.. We have performed spectral irradiance uncertainty evaluation using Monte Carlo technique taking into account correlation between input quantities. A software using Matlab has been developed for the uncertainty evaluation.

INTRODUCTION

Array spectroradiometers are widely used in many applications due to their characteristics: portability, fast measurement (<1s), low cost. However they suffer from drawbacks that limit the measurement accuracy. Among those drawbacks stray light effect is the more difficult to deal with. Characterisation techniques have been developed to correct the measurement data from stray light. This leads to complex correction process and uncertainty evaluation must take into account the contribution of this correction process. This is crucial when performing UV light measurement such as solar UV.

We present the work that has been done at LNE in the framework of the European Metrology Research Program EMRP-ENV03 project to evaluate the uncertainty of solar UV measurement using array spectroradiometers. Monte Carlo (MC) technique is used and correlations between input quantities are taken into account.

We described the measurement model, how the MC technique is implemented in a software developed under Matlab.

MEASUREMENT MODEL

Prior to measure the solar UV spectral irradiance the array spectroradiometer must be calibrated using a standard lamp. The measured signal $S_{Std,i}$ given by the spectroradiometer corresponding to wavelength λ_i is:

$$S_{Std,i} = \frac{\left(M_{Std,i} - M_{DStd,i}\right) C_{Lin}\, C_{\lambda}}{T_{Int,Std}} \quad (counts/s) \quad (1)$$

$M_{Std,i}$, the signal for pixel "i" corresponding to λ_i when measuring the standard lamp

$M_{DStd,i}$, the measured dark signal for pixel "i" corresponding to λ_i when measuring the standard lamp

$T_{Int,Std}$, the integrating time when measuring the standard lamp

C_{Lin} is the correction due to non-linearity response of array detector of the spectroradiometer

C_{λ} is the correction due to wavelength accuracy

Because array spectroradiometers are based on single monochromator stray light contributes to the measured signal. Stray light correction technique is applied [1] and equation (1) can be written in matrix form as:

$$S_{Std} = S_{True} + S_{True}\, D \quad (2)$$

S_{Std} is the matrix representing the measured signal

S_{True} is the matrix representing the signal corrected from stray light

D is the matrix representing the stray light distribution function SDF. It is a square 2D matrix.

S_{True} can be determined from equation (2) and the spectral responsivity of the spectroradiometer SR_i at wavelength λ_i is given by:

$$SR_i = \frac{S_{True,i}}{E_{Std,i}} \quad (3)$$

Once calibrated solar UV spectral irradiance can be measured using the same process described above to correct the measured signal. Then the sun spectral irradiance $E_{Sun,i}$ at λ_i is given by:

$$E_{Sun,i} = \frac{S_{Sun,i}}{SR_i} \quad (4)$$

UNCERTAINTY EVALUATION

According to the measurement model uncertainty evaluation of solar UV irradiance can be performed in two steps: first evaluation of the uncertainty of the spectral responsivity, second

evaluation of the uncertainty of the solar UV spectral irradiance.

When dealing with spectral measurements classic GUM uncertainty evaluation technique is tedious. We propose to use the Monte Carlo technique [2,3] to determine the uncertainty of solar UV spectral irradiance measurements.

Correlation between input quantities are taken into account. For instance uncertainty due to the stray light correction is evaluated based on equation (2) that can be written as :

$$S_{True} = (1+D)^{-1} S_{Std} \qquad (5)$$

Where "1" is the matrix unity. D contains diagonal elements set to zero and non-zero off diagonal elements that are small compare to "1". Therefore $(1+D)^{-1}$ reduces to (1-D). Therefore each element of the column matrix S_{True} is:

$$S_{True,i} = \sum_j S_{Std,j} (1-D)_{i,j} \qquad (6)$$

(j=1 to N), where N is the number of wavelengths taken into account.

The $S_{Std,j}$ elements are correlated as well as the $(1-D)_{i,j}$ elements. The multivariate Gaussian algorithm is used to evaluate the uncertainty associated to these correlated input quantities.

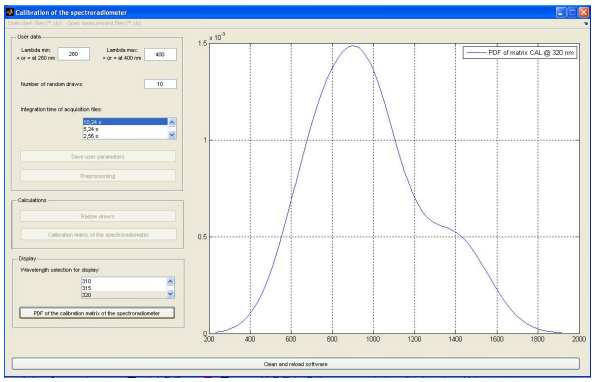

Figure 1. User software interface and PDF associated to array spectroradiometer spectral responsivity.

A software using Matlab has been developed to evaluate the uncertainty. The output is the probability distribution function (PDF) of the solar UV irradiance at selected wavelengths from which the value of the irradiance and the associated uncertainty are obtained from respectively the average and standard deviation of the PDF. Example of user interface and PDF for the array spectroradiometer spectral responsivity is shown on figure 1.

CONCLUSION

Monte Carlo technique is used to evaluate the uncertainty of solar UV spectral irradiance measurement using array spectroradiometer. Based on the measurement model that includes the stray light correction the uncertainty is evaluated taking into account correlations between input quantities. A software using Matlab is developed to evaluate the uncertainty at selected wavelengths. The software can be used also to evaluate the uncertainty of spectral irradiance measured using any type of UV-Visible-IR array spectroradiometers.

AKNOWLEDGEMENTS

The EMRP is jointly funded by the EMRP participating countries within EURAMET and the European Union**.**

REFERENCES

1. Y. Zong, S B Brown, B C Johnson, K R Lykke and Y. Ohno, "Simple spectral stray light correction method for array spectroradiometers, Applied Optics, 45, 2006.
2. ISO/IEC Guide 98-3/Suppl. 1 "*Propagation of distributions using a Monte Carlo method*", (2008).
3. A F Obaton, J Lebenberg, N Fischer, S Guimier and J. Dubard, "Two procedures for the estimation of uncertainty of spectral irradiance measurement for UV source calibration", Metrologia, 44, 2007.

Advantages of a two-channel luminance meter for photopic and scotopic measurements in determining mesopic luminance

Petri Kärhä[1,2], Maksim Shpak[1,2], and Erkki Ikonen[1,2]

[1] *Metrology Research Institute, Aalto University, Espoo, Finland,*
[2]*Centre for Metrology and Accreditation (MIKES), Espoo, Finland*
Corresponding e-mail address: petri.karha@aalto.fi

A two-channel luminance meter for simultaneous measurements of scotopic and photopic luminances has been thoroughly characterized. Photometer spectral quality factors f_1' are 3.6% and 6% for the photopic and scotopic channels, respectively. Nonlinearity of the responsivity is less than 0.3% throughout the mesopic region. Direct measurement of the scotopic luminance offers significant advantages in uncertainties as compared to calculating the mesopic luminance from a photopic measurement, combined with the S/P ratio of the source.

INTRODUCTION

Commission Internationale de l'Eclairage has recently published a recommendation on mesopic photometry [1] that describes methods for calculating the luminous efficiency function in dusk conditions, where the eye has adapted between scotopic and photopic visions. In the mesopic lighting conditions, both cone and rod cells are active, and the visual response $V_{mes}(\lambda)$ is defined as a weighted average of the photopic luminous efficiency function $V(\lambda)$ and the scotopic luminous efficiency function $V'(\lambda)$. The luminance range considered mesopic is 0.005 – 5 cd/m^2.

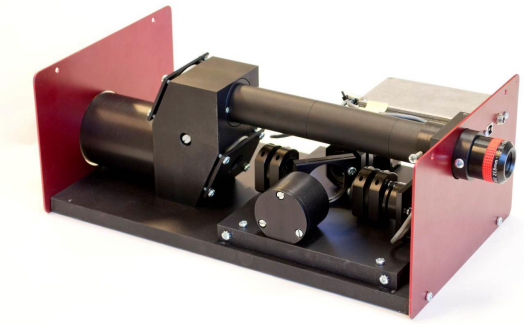

Figure 1. View of the two-channel luminance meter with its cover opened.

In practice, there are three basic ways how mesopic luminance can be measured. All of these require knowledge on the adaptation level of the eye, the measurement of which is presently undefined. If the absolute spectral radiance of the target is known, mesopic luminance can be calculated by multiplying the spectral radiance values $L(\lambda)$ with $V_{mes}(\lambda)$ and integrating over the wavelength. If the absolute photopic luminance and the relative spectrum of the light source are known, the relative spectrum can be used to calculate the S/P ratio, i.e., the ratio of the scotopic response over the photopic response. Mesopic luminance can then be derived from the photopic luminance and the S/P ratio. Finally, if we have two luminance meters with photopic and scotopic weighting functions, mesopic luminance can be calculated as a weighted average of the two luminances.

We have built and characterized a dual-channel luminance meter for simultaneous measurements of luminance with photopic and scotopic weightings [2,3]. This device measures spot luminance with two channels utilizing filtered photodiodes providing $V(\lambda)$ and $V'(\lambda)$ responsivities. We first briefly describe the properties of and the latest advances with the device. Measurement with a built-in $V'(\lambda)$ channel has advantages over methods relying on the known spectrum. These advantages are demonstrated by calculating the obtainable uncertainties.

DEVICE PROPERTIES

The instrument is a spot luminance meter with two spectrally weighted channels as can be seen in Fig. 1. The collected light is detected with silicon detectors and a computer-controlled dual-channel switched-integration amplifier [4].

The instrument has been characterized for its relative spectral responsivities (Fig. 2). Photometer spectral quality factor f_1' for the photopic channel is 3.6%. For the scotopic channel it is 6%. The deviations from ideal spectral responsivities are corrected for by applying spectral mismatch correction factors. Nonlinearity is less than ±1% over a wide luminance range of 10^{-4} – 10^3 cd/m^2. In the mesopic range, the nonlinearity is less than 0.3%.

The device has been calibrated for absolute luminance responsivity against a sphere-based

luminance standard with a standard uncertainty of 0.3% for the photopic channel and 0.6% for the scotopic channel. Additionally, the size of source effect and the polarization sensitivity were characterized. The expanded uncertainty for measurements of typical light sources is estimated to be 2.2 %.

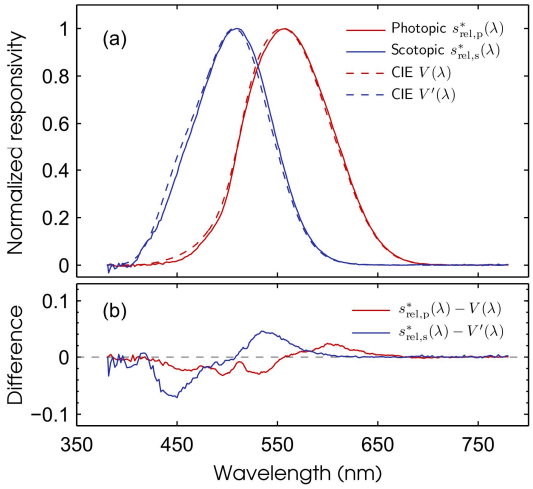

Figure 2. (a) Normalized relative spectral responsivities of the photopic [$s^*_{rel,p}(\lambda)$] and scotopic channels [$s^*_{rel,s}(\lambda)$], the corresponding CIE luminous efficiency functions, and (b) their magnified differences.

ADVANTAGES

A thorough uncertainty analysis has been carried out for the device. It appears that the largest contributions to the uncertainty come from the luminance calibration, 0.3% for the photopic and 0.6% for the scotopic channel, and the spectral shape of the source. The uncertainty in the absolute calibration would be practically similar in all measurement methods so when comparing advantages of the methods, the spectral shape contribution is the most relevant. Furthermore, with a filter-based scotopic luminance meter, higher signal-to-noise ratio can be obtained than with spectrally dispersing instruments.

In practical field measurements, such as road lighting, the shape of the source spectrum is highly uncertain. Although we might know accurately the S/P ratio or the relative spectrum of the light source used, luminance is measured through a reflecting surface, which may be, e.g., sand, snow, asphalt or grass. This unknown reflection adds uncertainty to the spectrum.

Let us assume a measurement of mesopic luminance of a surface, whose relative spectral radiance has an uncertainty of 20%. We also assume that the uncertainty is more pronounced in the blue part of the spectrum and determine the mesopic luminance close to the scotopic limit.

If we measure the photopic luminance of the surface with a photopic luminance meter and use the relative spectrum of the light source to calculate the S/P ratio, the resulting scotopic luminance will have an additional uncertainty of 6.5 % in the case of a white LED and 7.2 % in the case of a high pressure sodium (HPS) lamp, due to the reflectance.

With the two-channel luminance meter, the uncertainty contributes through the spectral mismatch correction factors that are used to account for the deviations in the spectral responsivities. If no mismatch corrections are applied at all, the additional measurement error in the scotopic luminance caused by the deviation from the $V'(\lambda)$ is 1.1% for the LED lamp and 1.8 % for the HPS lamp. Furthermore, if spectral mismatch correction factors are calculated using the nominal lamp spectra and applied in measurements, the additional uncertainties in the scotopic luminances caused by the uncertainty due to the reflectance of the surface reduces to 0.5% for the white LED and to 0.4% for the HPS.

The latter values demonstrate an order of magnitude lower uncertainty with the two-channel luminance meter than obtainable with a photopic measurement combined with the S/P ratio of the source.

ACKNOWLEDGMENTS

The authors acknowledge the Aalto Energy Efficiency Research Programme project “Light Energy – Efficient and Safe Traffic Environments” and the European Metrology Research Programme (EMRP) project ENG05 “Metrology for Solid State Lighting” for partially financing this work. The EMRP is jointly funded by the EMRP participating countries within EURAMET and the European Union.

REFERENCES

1. CIE Technical report 191, *Recommended System for Mesopic Photometry Based on Visual Performance*, Commission Internationale de l’Eclairage, Vienna, 2010.
2. M. Shpak, P. Kärhä, G. Porrovecchio, M. Smid, and E. Ikonen, Luminance meter for photopic and scotopic measurements in the mesopic range (submitted).
3. M. Shpak, P. Kärhä, G. Porrovecchio, J.-M. Hirvonen, M. Smid, and E. Ikonen, Characterized photopic-scotopic luminance meter for measurements in the mesopic range, Proc. CIE Centenary Conference “Towards a New Century of Light” (Paris), 601 – 604, 2013.
4. A. Mountford, G. Porrovecchio, M. Smid, and R. Smid, Development of a switched integrator amplifier for high-accuracy optical measurements, Appl. Opt., 47, 5821–5828, 2008.

Application of a compact array spectroradiometer for the UV spectral range

Peter Sperfeld, Saulius Nevas, and Sven Pape

Physikalisch-Technische Bundesanstalt, Braunschweig & Berlin, Germany
Corresponding e-mail address: Peter.Sperfeld@ptb.de

The characterization, calibration and application of an array spectroradiometer optimized for spectral irradiance measurements in the UV is demonstrated, allowing traceable spectral measurements down to below 250 nm.
The characterization of the system, including linearity measurements, determination of the stray light correction matrix and the out-of-range stray light influence, as required by the measurement application was carried out. The source-based calibration method for array spectroradiometers is demonstrated and major contributions to the measurement uncertainty are analyzed. The transition from the calibration with typical standard lamps to the measurement of high-power UV radiators is discussed and typical applications of the array spectroradiometer system are presented.

INTRODUCTION

Compact array spectroradiometers are intended to be more frequently used for measuring spectro-radiometric quantities. Their applicability, however, is not always thoroughly confirmed. Strictly speaking, the calibration capability of array spectroradiometers has to be investigated and confirmed for every single instrument and application. Several types of spectroradiometers have been investigated at the Physikalisch-Technische Bundesanstalt (PTB) during the last few years [1],[2].

All systems should be calibrated with respect to standard sources or reference spectroradiometers. These calibration standards are often different from the sources used in the final radiometric application. This results in even higher requirements on the transfer capabilities of investigated array spectro-radiometers.

For fast, precise and reliable measurements of high-power UV sources, a commercially available array spectroradiometer has been modified, characterized and calibrated. The Si-CCD array-based system is designed to measure spectroradiometric quantities in the spectral range from 200 nm up to 800 nm. For the majority of array spectroradiometers the spectral range below 400 nm is typically interfered by internal stray light. Its influence has to be thoroughly investigated. As the spectral range of silicon photoresponsivity exceeds the nominal spectral range of the instrument, the out-of-range stray light influence for the spectral range from 800 nm to 1100 nm had to be investigated prior to the instrument calibration.

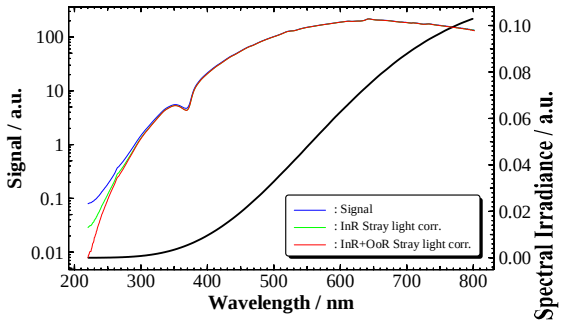

Figure 1. Signal of the array spectroradiometer (left axis) for the measurement of the spectral irradiance of a QTH lamp (right axis). What is shown are the raw (dar-corrected) signal of the instrument (blue curve), the in-range (InR) corrected stray light (green curve) and the signal corrected for both the in-range and the out-of-range (OoR) stray light (red curve).

INSTRUMENT CHARACTERIZATION

In many applications the radiant power level of the measured radiators may vary by several orders of magnitude. Thus, a wide dynamic range has to be covered by the instruments. The variation of integration times as well as the attenuation of incoming radiation are frequently used techniques to span the requested range. This results in high requirements on linearity and variability. The UV array spectroradiometer is equipped with a set of neutral density filters which have been spectrally characterized and the system was checked for linearity using both integration-time and radiant-power variation methods.

The major aspect of array spectrometer characterizations, however, is the determination and (if possible) elimination of the spectral-dependent internal stray light of the instrument. A stray light correction matrix for the instrument has been

determined using the laser-based measurement of the instrument's line spread functions [3],[4].

Similar to the stray light correction matrix, an out-of-range correction matrix was calculated using the outer band of the line spread functions for the spectral range from 800 nm to 1100 nm. The resulting out-of-range signal is strongly source-dependent and has to be subtracted from the measurement signal prior to the internal stray light correction procedure [5].

In Fig. 1 the effect of out-of-range as well as in-range stray light on the array spectroradiometer signal generated by a tungsten halogen lamp is demonstrated. In the spectral range below 300 nm the strong stray light influence is evident.

SPECTRORADIOMETER CALIBRATION

The spectral irradiance responsivity of the UV array spectroradiometer has been calibrated with respect to typical standard lamps.

This source-based substitution method is commonly used to calibrate array spectroradiometers. A system is calibrated using a radiant source *S* with known spectral irradiance $E_S(\lambda)$. The spectral irradiance responsivity $R_{i,E}$ for each pixel can be calculated from the (dark- and out-of-range stray light corrected) readout $Y_{i,S}$:

$$R_{i,E}(\lambda_i) = \frac{Y_{i,S}}{E_S(\lambda_i)} \cdot \frac{1}{\prod_{j=1}^{n} a_{S,j}(\lambda_i)} \qquad (1)$$

Several correction factors $a_{S,j}(\lambda_i)$ correct the incident spectral irradiance E_S for every pixel *i* of the array spectroradiometer. This might be the internal stray light correction as well as linearity corrections or the adaption of geometrical parameters. They strongly depend on the source *S* used for calibration and have to be recalculated whenever a different source is used for measurements.

For the measurement of unknown sources *U*, different correction factors $a_{U,j}(\lambda_i)$ have to be applied. However, if the spectral distribution of the unknown source is similar to that used during calibration, several correction factors might be eliminated. The spectral irradiance $E_U(\lambda)$ of the unknown source can then be calculated by direct substitution:

$$E_U(\lambda_i) = E_S(\lambda_i) \cdot \frac{Y_{i,U}}{Y_{i,S}} \cdot \frac{\prod_{j=1}^{n} a_{S,j}(\lambda_i)}{\prod_{j=1}^{n} a_{U,j}(\lambda_i)} \qquad (2)$$

If for example, the spectral distribution is similar for both the standard source and the unknown source, the ratio of the correction factors for the stray light and bandpass is close to one. Therefore, direct substitution should be prioritized whenever applicable. In some cases this can be achieved by using specific standard lamps similar to those of the application.

The investigated UV array spectroradiometer, however, is intended to measure high-power UV radiators, but was directly calibrated by typical standard lamps. In the spectral range from 200 nm to 350 nm, deuterium lamps, and in the spectral range from 250 nm to 800 nm, tungsten halogen lamps, were used to calibrate the array spectroradiometer. The overlap region from 250 nm to 350 nm demonstrates the feasibility of in-range and out-of-range stray light correction with two completely different radiant sources.

To illustrate the applicability of such a calibration, the system was used to measure different high-power UV sources [6]. The measurement results were in good agreement to those of a double monochromator-based spectroradimeter system. The corresponding measurement uncertainties underline the appropriateness of the array spectroradiometer.

CONCLUSION

It is demonstrated that an array spectroradiometer system which has been thoroughly characterized and calibrated, can serve for high quality spectroradiometric measurements even in demanding spectral ranges.

REFERENCES

1. S. Nevas, A. Teuber, A. Sperling and M. Lindemann, Stability of array spectroradiometers and their suitability for absolute calibrations, Metrologia, 49 (2012) S48-S52.
2. P. Sperfeld, D. Dzafic, F.Plag, F. Haas, et. al., usability of compact array spectroradiometers for the traceable classification of pulsed solar simulator, Proceedings of 27th PVSEC 2012, Frankfurt, Germany.
3. Y. Zong, S. Brown, C. Johnson, K. Lykke, Y. Ohno, Simple spectral stray light correction method for array spectroradiometers, Appl. Opt., 45 (2006) 1111-1119.
4. S. Nevas, G.Wübbeler, A. Sperling, C. Elster and A. Teuber, Simultaneous correction of bandpass and stray light effects in array spectroradiometer data, Metrologia. 49 (2012), S43–S47.
5. S. Nevas, J. Gröbner, L. Egli, , Stray light correction of array spectroradiometer data for solar UV measurements, Thematik Network for Ultraviolet Measurements, UVNews 9, January 2013, 17-19
6. P. Sperfeld, B. Barton, S. Pape, A. Towara, J. Eggers, G. Hopfenmüller, Spectral Irradiance Measurement and Actinic Radiometer Calibration for UV Water Disinfection, NEWRAD2014.

A new filter radiometer for the thermodynamic measurement of high temperature fixed points

J. M. Mantilla[1], M. J. Martin[1], M. L. Hernanz[2], A. Pons[2], J. Campos[2], and D. Del Campo[1]

[1]*Centro Español de Metrologia (CEM), Tres Cantos, Spain,*

[2]*Instituto de Óptica del Consejo Superior de Investigaciones Científicas (IO-CSIC), Madrid, Spain*

Corresponding e-mail address: mjmartinh@cem.minetur.es

The Centro Español de Metrologia (CEM) in collaboration with the Instituto de Óptica of the Consejo Superior de Investigaciones Científicas (IO-CSIC) has developed a filter radiometer to measure the thermodynamic temperature of high temperature fixed points. The design allows the filter radiometer to be calibrated with a laser based experimental setup, which will really improve the measurement uncertainty. The filter radiometer design, its characterization (linearity, size of source effect, ...) and the system used for its calibration will be described.

INTRODUCTION

CEM and IO-CSIC, in prior works, measured the thermodynamic temperature of high temperature fixed points using a commercial radiation thermometer (KE-LP2) [1]. However the uncertainty of these measurements is about that obtained with the International Temperature Scale (ITS-90) method, i. e. from 0,3 K to 1,1 K (from 1084,62 °C to 2474 °C, k = 2). The reason is because this commercial radiation thermometer has to be spectrally calibrated by using a facility based on a monochromator and a high stability lamp which results in higher uncertainties [1]. In order to reduce them, it could be used a laser based facility instead, but, when calibrating the KE-LP2, interference fringes were detected, resulting in a ripple in the spectral distribution of the radiation thermometer. This is difficult to measure (to obtain full fringe information [2]) or account for (if fewer measurements are made).

In consequence, CEM and IO-CSIC have developed a new filter radiometer whose design allows the laser based calibration. In this new design some other considerations have also been taken into account: low size of source effect, high amplifier stability, temperature control system, etc.

This paper describes the development of the CEM-IO-CSIC filter radiometer (FIRA), its characterization and the absolute spectral responsivity calibration setup.

RADIOMETER DESIGN

The scheme and a picture of the FIRA can be seen in Figures 1 and 2.

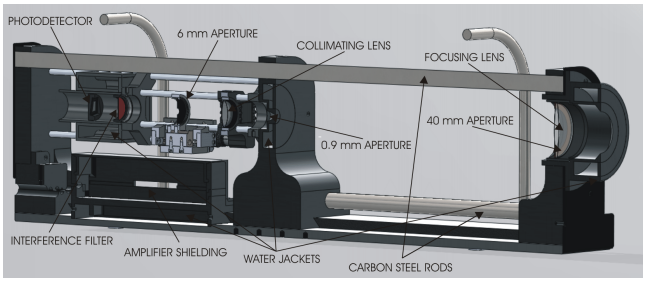

Figure 1. The FIRA scheme.

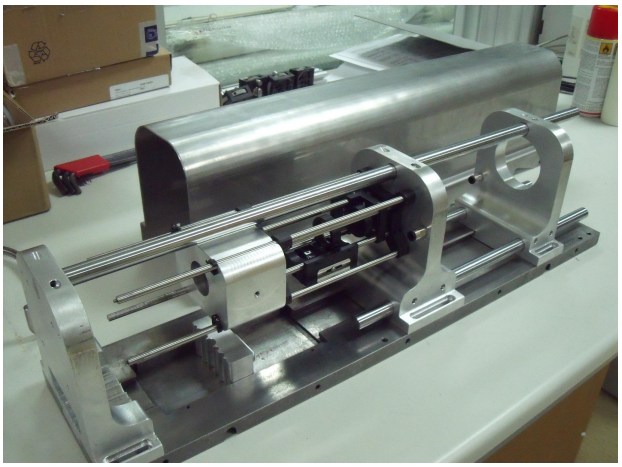

Figure 2. Picture of the FIRA. It is 65 cm long and 18 cm high. It weights 30 kg.

The main features of the FIRA are:

- It is an imaging filter radiometer with achromatic lens. Lens and field stop aperture are separated via carbon steel rods, with low thermal expansion and high stability along time.

- It has got an interference filter nominally centred at 650 nm (10 nm bandwidth)

- The Si detector is slightly tilted (10º) with respect to the interference filter, in order to avoid interference fringes during laser calibration

- Everything inside is temperature controlled by a water cooled system.

- There is a Lyot stop to reduce SSE

- The amplifier is very close to the detector and shielded to reduce the noise in the photocurrent measurement

- The alignment can be made by means of a laser inserted in the optical path

RADIOMETER CHARACTERIZATION AND CALIBRATION

The FIRA linearity is measured by using an addition method: two stable light sources and a beam splitter up to 2000 °C [3] and a double aperture system in front of the FIRA from 2000 °C to 2500 °C.

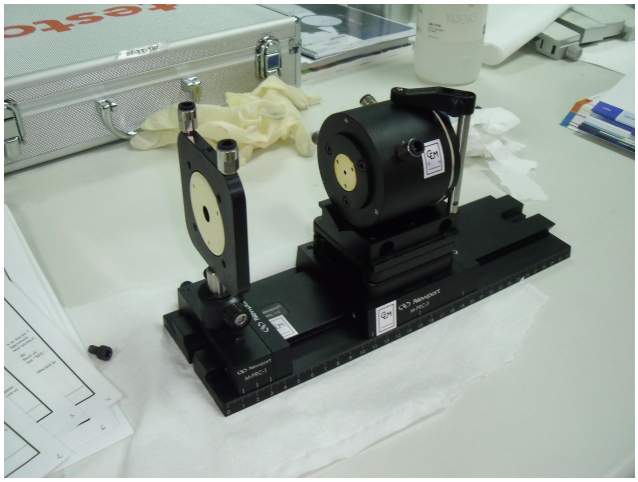

Figure 3. Radiancemeter (Si trap detector plus two precision apertures at a fixed distance) used to calibrate the FIRA in absolute spectral response.

The SSE is measured by using an integrating sphere and different diameter apertures. The differential method is used [3].

The absolute spectral responsivity of the FIRA is measured by using a setup based in a dye laser and an integrating sphere as light source. The transfer standard is a Si trap detector mounted in a track with a fixed geometry (see figure 3). It has two precision apertures of 10 mm and 3 mm of diameter in water cooled frames. The distance between the apertures is 10 cm. All the geometrical magnitudes have been calibrated at the length division of CEM. This Si trap detector has been previously calibrated with respect to the cryogenic electrical substitution radiometer of the IO-CSIC. The absolute spectral responsivity is measured at several points (about 10) along the detection band of the interference filter.

The relative spectral response is measured using a setup with a monochromator and a halogen incandescence lamp. Firstly, a spectral scan of the radiometer response was done across the range in which the detector is sensitive (300 nm to 1000 nm approximately) to check for the absence of transmission bands outside the nominal interference filter's band. Then the calibration was performed between 600 nm and 700 nm.

The expected uncertainty of the temperature measurement with the FIRA is from 0,1 K to 0,7 K (from 1084,62 °C to 2474 °C, $k = 2$). This FIRA will be used to measure the thermodynamic temperature of the selected high temperature fixed points within the project "InK" [4]

ACKNOWLEDGEMENTS

The authors wish to acknowledge the support and the advices of: G. Machin, E. Woolliams, M. Dury and D. Love (NPL) in the design of this filter radiometer; F. Raso (electricity division of CEM) in the calibration of the amplifier and A. Arce (length division of CEM) in the dimensional measurements.

This research is partially included in an EMRP Joint Research Project jointly funded by the EMRP participating countries within EURAMET and the European Union.

REFERENCES

1. J. M. Mantilla, M. L. Hernanz, J. Campos, M. J. Martin, A. Pons and D. del Campo. Int. J. Thermophys. (Tempmeko 2013 special issues) (submitted, 2013) .

2. T. Keawprasert, K. Anhalt, D. R. Taubert, A. Sperling, M. Schuster and S. Nevas. Temperature: Its measurement and control in science and industry. Volume 8. AIP Conf. Proc 1552, 682-687, 2013.

3. NPL Report ENG 2. "The examination of base parameters for ITS-90 scale realisation in radiation thermometry" EUROMET T-S1. H. C. McEvoy, 2007.

4. G. Machin, J. Engert, R. Gavioso, M. Sadli and E. Woolliams. Int. J. Thermophys. (Tempmeko 2013 special issues) (submitted, 2013) .

.

Determination of the spatial uniformity of a light source for camera calibration by principal components analysis

M. López[1], A. Ferrero[2], J. Campos[2], and A. Sperling[1]

[1]*Physikalisch-Technische Bundesanstalt (PTB), Germany,*

[2]*Instituto de Óptica, Consejo Superior de* Investigaciones Científicas (CSIC), Spain

Corresponding e-mail address: marco.lopez@ptb.de

The determination of the spatial uniformity of an extended light source developed at PTB and used for the characterization of low-uncertainty radiometric cameras is presented. The uniformity of the source is determined by using an uncalibrated CCD camera as a detector. In order to distinguish between the non-uniformity of the camera and those of the light source, a procedure based on the application of Principal Components Analysis (PCA) is used.

INTRODUCTION

Imaging systems like CCD- or CMOS-based cameras are nowadays commonly used for the measurement of the radiance of extended sources in many applications [1,2]. The advantage of such devices is the ability to spatially evaluate the radiance of the source by a single acquisition, and hence, to avoid scanning systems which are more time-consuming and less practical for many applications. However, in order to achieve reliable measurements, a calibration which includes the spatial response characterization of the camera is required. A radiometric characterization of a camera means to relate the response of every pixel of the camera to the respective radiance emitted by a light source. For that purpose a directional and spatial, i.e. with respect to uniformity and lambertianity of the emission, well- characterized light source is required. In principle, the characterization of the non-uniformity of the source can be accomplished by a camera calibrated with respect to a more uniform source. However, sometimes this is not possible. An approach which would not require a calibrated camera ought to be more practicable. Here, the main task to be solved is to distinguish between the non-uniformity of the source and the non-uniformity of the image due to the non perfect camera itself. In this paper we report on the determination of the non-uniformity of an extended source by relative measurements of a camera and by means of Principal Components Analysis (PCA) [3].

EXPERIMENTAL SETUP AND PROCEDURE

The extended source developed at PTB [4] consists of an integrating hemisphere of 50 cm of diameter, coated with barium sulphate with a reflectance factor higher than 98 %. The front of the hemisphere is covered by a double-sided opal glass serving as the radiant face. In the interior of the hemisphere, seven tungsten halogen lamps, shielded by an opal glass itself, are arranged to obtain a uniform irradiation on the front surface (see Figure 1).

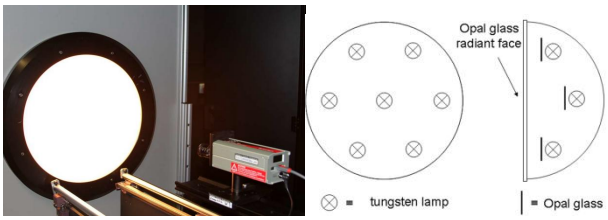

Figure 1. (*Left*) Picture of the PTB hemisphere light source and CCD Camera. (*Right*) Arrangement of the seven tungsten halogen lamps within the hemisphere.

The luminance of the hemisphere is adjusted by controlling the seven lamp-currents individually. This allows to reach the best uniformity possible by means of an automatic iterative optimization process, where the relative standard deviation of the pixel´s values of an image of the radiant face corresponding to the central region of the source is minimized. After the uniformity of the source has been optimized by that image taking camera, a set of measurements of the virtual source are taken at different distances using the same integration time and refocusing the source plane at every distance (see Figure 2, where d is the focus setting number in the objective lens; the higher it is, the longer the distance).

In the PCA procedure to determine the effective non-uniformity of the source the key element is the definition of a multidimensional random variable $F = \{F_1, F_2, \ldots, F_N\}$, having M realizations of it. For a camera, this variable is formed as a concatenation of N images, F_i. The collection of the data is arranged in a matrix having N columns and M rows. The first step is to calculate the covariance matrix of the images. This covariance matrix is typically non-diagonal showing the inner correlations between images.

The PCA method diagonalizes this covariance matrix and produces three types of elements: N

eigenvalues λ_j, N eigenvectors e_{ij}, and N eigenimages A_j. The eigenimages A_j describe uncorrelated data that provide spatial insight about the location within the bidimensional CCD arrangement of the different contributions. By using the eigenvector it is possible to change from the image coordinate system $\{F_1, F_2, \ldots, F_N\}$ to the eigenimage coordinate system $\{A_1, A_2, \ldots, A_N\}$, and vice-versa. That is, $\bar{F}_i = \sum_{i=1}^{N} e_{i,j} A_j$, where $\bar{F}_i$ is obtained from the original image F_i by subtracting the mean of the image ($\bar{F}_i = F_i - \langle F_i \rangle$). From this previous equation it is possible to obtain filtered versions of images and to remove or select a given collection of contributions characterized by their associated eigenimages.

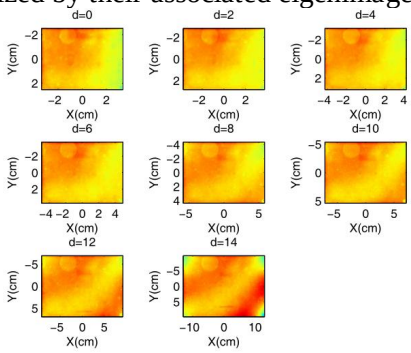

Figure 2. Images at different distances from the source after canceling out the dependence on the pixel´s viewing projected angle.

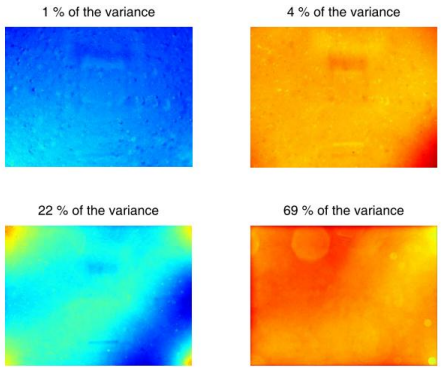

Figure 3. Eigenimages obtained from PCA.

The eigenimages obtained from PCA and their associated variance is shown in Figure 3. Comparing these eigenimages with those from Figure 2, it is observed that the eigenimage corresponding to 69 % of the total variance has a very similar pattern. This means that this eigenimage is determined by the Photo-Response Non Uniformity (PRNU) of the CCD camera. The other eigenimages are related to random noise and to specific spatial radiance distributions.

Thus, if the principal component corresponding to the PRNU (69%-eigenimage) is filtered in the images shown in Figure 2, the resultant image represents the non-uniformity of the source. Figure 4 shows the filtered images for the different distances. Finally, the effective non-uniformity of the source is determined by means of the standard deviation calculated for each image (see Figure 5). Thus, the estimated effective non-uniformity of the observed (virtual) source lies between 0.15 % and 0.3 % at intermediate distances.

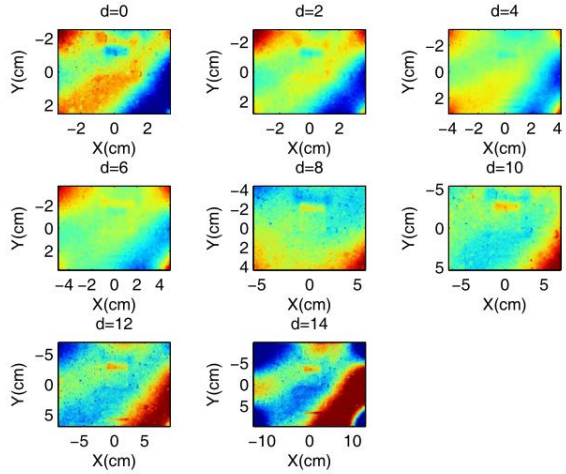

Figure 4. PCA-filtered images.

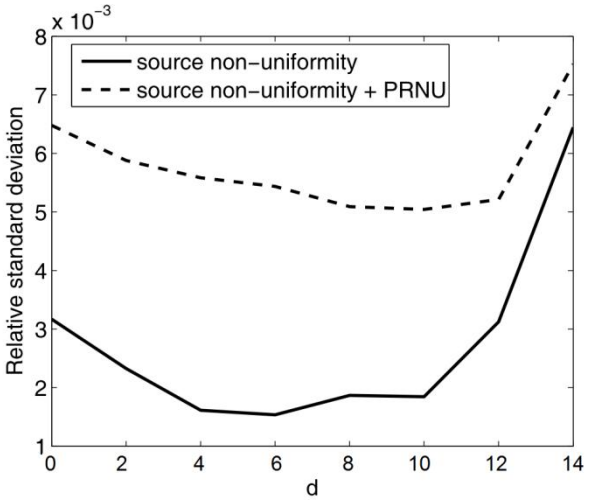

Figure 5. Effective non-uniformity of the observed virtu al source before and after PCA-filtering.

REFERENCES

1. M. López, K. Bredemeier, N. Rohrbeck, C. Véron, F. Schmidt, A. Sperling, "LED near-field goniophotometer at PTB", Metrologia **49**, S141--S145 (2012).
2. Krüger, U., Anhalt, K., Taubert, D., Schmidt, F. and Hartmann, J., "CCD-CAMERA FOR MEASURING TEMPERATURE AND SPECTRAL RADIANCE", CIE 2010 Tutorial and Expert Symposium on Spectral and Imaging Methods for Photometry and Radiometry, Bern, Switzerland, August 2010.
3. Parinya Sanguansat, "Principal Component Analysis - Engineering Applications", (publisher: InTech, 2012).
4. Schulz M., Buhr E., Marholdt K., Willemer W. and Bergmann D., "High-definition illuminated table for optical testing", Proceeding SPIE, Singapore 529-538, (September 1999).

Traceable measurement of high laser power in the 1-µm spectral range

Friedhelm Brandt, Holger Lecher, and Stefan Kück

Physikalisch-Technische Bundesanstalt (PTB), Braunschweig, Germany
Corresponding e-mail address: stefan.kueck@ptb.de

The application of high power lasers in industry requires the establishment of a measurement and calibration service for quality management purposes. This paper reports on the traceable laser power measurement for the multi-kilowatt power range, thus allowing the calibration of laser power meters in the 1-µm spectral range. We present the calibration facility, the new standard detector, the calibration chain for the high-power range in the field of laser radiometry as well as the uncertainty budget. The expanded uncertainty (k = 2) of the new standard detector is currently 0.8 % for power levels up to 4.5 kW.

INTRODUCTION

High-power lasers in the power range of a few kW are nowadays widely used in many industrial applications such as cutting, welding, melting and hardening. As part of a research project with several partners from industry, a measuring setup for the calibration of laser power meters up to 2 kW in the wavelength range around 1.06 µm was established. At NEWRAD 2011, we reported on the plans and first results in the realization of the calibration service [1], in this article, we report on the progress in the calibration setup, the standard detectors, the calibration chain for optical radiation power as well as on the uncertainty budget. With this new calibration facility PTB closes the present gap in its customer service, enabling traceability to a national standard for manufacturers and users of Nd:YAG, disc and fiber lasers, as well as for manufacturers of measuring instrumentation and calibration laboratories.

CALIBRATION CHAIN AND SETUP

The calibration chain in laser radiometry for the high-performance range is shown in Figure 1. The characterization of the standard SCT391 has already been described in detail in [2]. The scale of the spectral sensitivity of detectors for high-power laser is transmitted from SCT391 to the new standard detector, the EC-PM (Electrically Calibrated Power Monitor), a modified serial device manufactured by PRIMES [3]. For this purpose, the EC-PM is calibrated with the wavelength of 1.065 µm and a laser power of about 1 kW with the SCT391 standard detector.

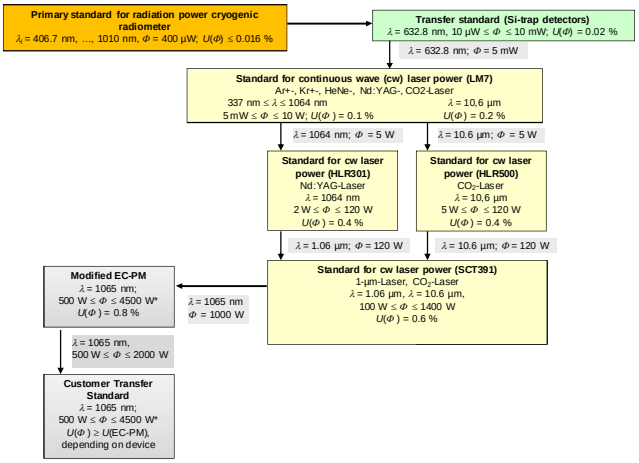

Figure 1. Calibration chain for laser radiometry in the wavelength range of 1.06 µm and laser powers up to 4.5 kW. * By electrical calibration.

The working principle of the EC-PM is as follows: The incident laser radiation is directed through an aperture into a cavity absorber by means of a focusing highly reflective mirror. Within the cavity, the radiation is almost completely absorbed. The absorber is water cooled and the temperature rise ΔT as well as the absolute water flow V_m is measured. The measured laser power Φ is then given by

$$\Phi = V_m c_m \Delta T , \qquad (1)$$

where c_m is the specific heat capacity of water.

From the displayed laser power Φ_{dis} and the previously determined (with the SCT391) laser power Φ, the correction factor f_K of the display for the EC-PM is determined.

$$f_K = \frac{\Phi}{\Phi_{dis}} \qquad (2)$$

The expansion up to 4.5 kW is carried out by means of electrical calibrations of the EC-PM in the power range between 500 W and 4.5 kW. To be able to perform this calibration, an electrical heater is

installed within the EC-PM. Different electrical powers, determined from high-precision current and voltage measurement, are applied to the cooling and sensor system of the EC-PM. From these data, the power correction coefficient is determined for laser powers up to 4.5 kW. The measurements carried out thus far, however, showed a negligible power coefficient.

The optical setup for the calibration of laser power meters in the wavelength range around 1.06 µm and for laser powers up to 2 kW is shown in Figure 2. The laser radiation of the diode laser with the nominal wavelength $\lambda = 1065$ nm is passed through a fiber having a core diameter of 1000 µm to a collimating optic, which also includes a beam splitter to irradiate a monitor detector and a protective window. Behind the optics, the beam has a diameter of approx. 22 mm. In addition, the beam diameter is limited by a subsequent aperture of 22 mm. This aperture is imaged with a lens with focal length $f = 500$ mm to the detection plane, in which alternately the standard detector or the device under test is located.

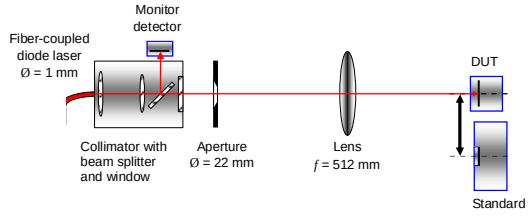

Figure 2. Scheme of the optical setup for the calibration of laser power meters in the power range up to 2 kW ($\lambda = 1.065$ µm).

MEASUREMENT UNCERTAINTY ANALYSYS

The model equation for the determination of the measurement uncertainty is as follows:

$$f_k = f_m \cdot F_{sel} \cdot F_{fk} \cdot F_{VN} \cdot F_{res} \cdot F_H \cdot F_S \cdot F_{\beta\Phi} \cdot F_{Vs}, \qquad (3)$$

The components are listed and described in Table 1, where their values, standard uncertainties, probability distributions, sensitivity coefficients, uncertainty contributions and the fraction to the overall uncertainty are given. Currently, the expanded uncertainty ($k = 2$) is approximately 0.8 %.

SUMMARY/OUTLOOK

A calibration facility for power meters for laser radiation in the multi-kilowatt power range at wavelengths around 1.06 µm was established at PTB. The measurement uncertainty budget has been presented and will be thoroughly discussed in the presentation. Currently calibrations of customer transfer standards up to 2 kW with an expanded uncertainty of at least 0.8 % ($k = 2$) are possible in-house. The power range accessible with the new EC-PM standard detector was expanded by means of electrical calibration up to 4.5 kW. However, for this power range on-site calibrations have to be carried out. Future work will deal with the expansion to the wavelength of 10.6 µm.

REFERENCES

1. F. Brandt, H. Lecher, S. Kück, „Laser Radiometry for High Power Lasers in the 1-µm Spectral Range", 11th International Conference on New Developments and Applications in Optical Radiometry (NEWRAD 2011), Maui, Hawaii, USA, 19. - 23. September 2011.
2. F. Brandt, K. Möstl, Kalibrierung von Leistungsmeßgeräten für Hochleistungslaser, in Laser in Forschung und Technik, edited by W. Waidelich, 730-733, Springer-Verlag, Berlin, 1996.
3. www.primes.de; http://www.primes.de/index.php?lang=de&site=produkte_detail&subnav=produkte&c_id=&p_id=15

Table 1. Measurement uncertainty budget for the calibration of the EC-PM with the SCT391 standard detector.

Measurand	Description	Value	Stand. meas. uncertainty	Distribution	Sens. coeff.	Contribution	Index
F_m	Measured correction factor for the EC-PM	1.023400	$900 \cdot 10^{-6}$	Standard	1.0	$600 \cdot 10^{-6}$	5.2 %
F_{sel}	Factor for the normalized electrical responsivity of the SCT391	1.00000	$1.14 \cdot 10^{-3}$	Standard	1.0	$1.2 \cdot 10^{-3}$	8.7 %
F_{fk}	Factor for the correction factor f_k of the standard	1.00000	$3.38 \cdot 10^{-3}$	Standard	1.0	$3.5 \cdot 10^{-3}$	76.6 %
F_{VN}	Factor for the temperature difference of the standard	1.00000	$577 \cdot 10^{-6}$	Rectangular	1.0	$590 \cdot 10^{-6}$	2.2 %
F_{res}	Factor for the resolution of the EC-PM	1.00000	$57.7 \cdot 10^{-6}$	Rectangular	1.0	$59 \cdot 10^{-6}$	0.0 %

F_H	Factor for the inhomogeneity of the standard	1.00000	$577 \cdot 10^{-6}$	Rectangular	1.0	$590 \cdot 10^{-6}$	2.2 %
F_S	Factor for stray light	1.00000	$577 \cdot 10^{-6}$	Rectangular	1.0	$590 \cdot 10^{-6}$	2.2 %
$F_{\beta\Phi}$	Factor for power dependence of the standard	1.00000	$289 \cdot 10^{-6}$	Rectangular	1.0	$300 \cdot 10^{-6}$	0.6 %
F_{Vs}	Factor for the flow rate dependence of the standard	1.00000	$577 \cdot 10^{-6}$	Rectangular	1.0	$590 \cdot 10^{-6}$	2.2 %
f_c	**Correction factor for the EC-PM**	**1.0234**	**$3.95 \cdot 10^{-3}$**				

Detector-based Radiometry and Reflectometry in the EUV and VUV Spectral Ranges

Alexander Gottwald, Andreas Fischer, Udo Kroth, Christian Laubis, and Frank Scholze

Physikalisch-Technische Bundesanstalt (PTB), Berlin, Germany
Corresponding e-mail address: alexander.gottwald@ptb.de

The Metrology Light Source (MLS) is a synchrotron radiation facility in particular for the wavelength range between 5 nm and 200 nm. This range is completely covered for dedicated use in detector-based radiometry and for reflectometry by two different beamlines. Traceable detector calibration is assured by use of cryogenic electrical substitution radiometers as primary detector standards.

THE EUV AND VUV BEAMLINES

The Metrology Light Source (MLS) of the Physikalisch-Technische Bundesanstalt (PTB) is a low-energy (max. 630 MeV) electron storage ring dedicated for basic radiometry as well as metrological and spectroscopic applications [1]. Its spectral range covers wavelengths from the THz (7 mm) to the extreme ultraviolet (5 nm) regime, thus complementing PTB's (soft-) X-ray instrumentation at the neighbouring BESSY II facility of the Helmholtz Centre Berlin [2].

Monochromatised synchrotron (bending magnet) radiation is used for detector-based radiometry (by use of cryogenic electrical substitution radiometers as primary detector standards) as well as for reflectometry, which is a relative method for the determination of optical properties of materials. At the MLS, two beamlines are in operation for this: the Normal-Incidence ultraviolet (UV)- and vacuum ultraviolet (VUV) Monochromator beamline (NIM) which covers the wavelength range from 400 nm down to 40 nm [3], and the Extreme-Ultraviolet (EUV) beamline for wavelengths between 5 nm and 50 nm [4]. While the first already went into service at the MLS in 2008, so at the very beginning of user operation, the latter started with operation in early 2013. The EUV beamline may be regarded as a counterpart of the still operating PTB SX700 beamline at BESSY II (which has a range from 0,65 nm up to 30 nm). However, it should be noted that it is now possible at the MLS to conduct radiometric measurements in the complete extreme- and vacuum-ultraviolet spectral range without the formerly existing "gap" between 30 nm and 40 nm. Table 1 summarises the main characteristics of these two beam lines.

Both beamlines will receive further improvements in the near future: the EUV grating which currently is a mechanically ruled 1200 mm^{-1} Ru coated grating with 4° blaze angle will be replaced by a laser-holographically manufactured grating which should reduce significantly diffusely scattered light. For the NIM, a new 1200 mm^{-1} SiC laminar grating for the 60 nm to 120 nm wavelength range should improve the available flux there; furthermore, a new primary mirror system should improve thermal and mechanical stability and thus give the possibility for a reduced spot size without affecting the beam stability.

Table 1. Main characteristics for the NIM and EUV beamlines at the MLS.

	NIM	EUV
wavelength range	40 nm to 400 nm	5nm to 50 nm
spot size in focus	1.5 mm (vert.) 2.5 mm (hor.)	adjustable 0.1 mm to 4 mm
beam divergence	10 mrad to 14 mrad	< 4 mrad
grating(s)	2400 mm^{-1} Pt 1200 mm^{-1} SiC 600 mm^{-1} Al	1200 mm^{-1} Ru with 4° blaze angle
typ. radiant power per 100 mA electron current	0.1 µW to 1 µW	0.1 µW to 10 µW
linear polarization	> 86 %	adjustable 50 % to 98 %

THE CRYOGENIC RADIOMETERS

For traceable detector-based radiometric measurements, PTB uses cryogenic radiometers as primary detector standards for monochromatised radiation already since the early 1990's. Today, two different radiometers are in use; SYRES I (synchrotron radiation electrical substitution radiometer) for the EUV and X-ray range, and SYRES II for the UV and

VUV ranges [5]. SYRES II can be seen as upgrade of SYRES I; its design is particularly adapted to the inherent challenges at the NIM beamline, e.g. the relatively low available radiant power and the larger divergence of the beam. While the SYRES II cavity is optimized for minimized (UV-) scattering, the SYRES I cavity was modified regarding optimized X-ray absorption for photon energies up to 60 keV, without losing its usability in the EUV. Recently, smaller updates have been applied to both systems, to ensure state-of-the-art performance.

PTB's scale of spectral responsivity based on these two radiometers is validated by internal and external comparisons [6,7]. Besides routine detector calibrations, the development of semiconductor photodiodes with optimised irradiation stability is in the focus of our work relying on the absolute determination of the spectral responsivity of photo-detectors. Recently, so-called PureB photodiodes [8] have proven their high irradiation stability in combination with still high spectral responsivity in the EUV range (around 13 nm wavelength) as well as in the VUV range around the Lyman-alpha wavelength of 121 nm.

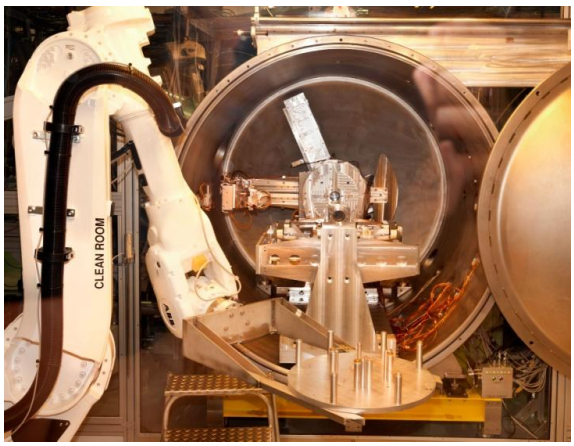

Figure 1. The EUV reflectometer in its new position at the MLS. The sample loading robotic is in the front.

THE REFLECTOMETERS

Reflectometry, i.e. the spectrally dispersed measurement of the reflectance from a surface, is a relative method which sets high demands toward precision metrology. In particular the development of EUV lithography (EUVL), i.e. photolithography with radiation of 13.5 nm wavelength for semiconductor manufacturing, is an outstanding example for a long-lasting, industrial driven methodology development in synchrotron-radiation based metrology. PTB is operating a dedicated EUV reflectometer for optical components up to 650 mm diameter and more than 50 kg weight. It was transferred to the MLS EUV beamline in mid 2013. Besides (specular) reflectance determination, the measurement of non-specular reflection ("scatter") has grown in interest lately. EUV scatterometry is applied to structured surfaces and accompanied by sophisticated mathematical modelling [9]. A dedicated scatterometer instrument was set in operation at PTB's SX700 beamline at BESSY II.

In the UV and VUV range, the typical optical components, mostly used for scientific research, are still much smaller in size. The dedicated VUV reflectometer (in service since 2011) has a load-lock for samples up to 60 mm diameter, its main feature however is the possibility to rotate the plane of reflectance what makes it possible to investigate polarization-dependent reflectances.

REFERENCES

1. A.Gottwald, R. Klein, R. Müller, M. Richter, F. Scholze, R. Thornagel, and G. Ulm, Current capabilities at the Metrology Light Source, Metrologia, 100, S146-S151, 2012.
2. B. Beckhoff, A. Gottwald, R. Klein, M. Krumrey, R. Müller, M. Richter, F. Scholze, R. Thornagel, and G. Ulm, A quarter-century of metrology using synchrotron radiation by PTB in Berlin, Phys. Status Solidi B, 246, 1415-1434, 2009.
3. A. Gottwald, U. Kroth, M. Richter, H. Schöppe, G. Ulm, Ultraviolet and vacuum-ultraviolet detector-based radiometry at the Metrology Light Source, Meas. Sci. Technol., 21, 125101, 2010.
4. C. Laubis, A. Fischer, and F. Scholze, Extension of PTB's EUV metrology facilities, Proc. SPIE, 8322, 832236-1, 2012.
5. A. Gottwald, U. Kroth, M. Krumrey, M. Richter, F. Scholze, G. Ulm, The PTB High-Accuracy Spectral Responsivity Scale in the VUV and X-Ray Range, Metrologia, 43, S125-S129 (2006)
6. A. Gottwald, M. Richter, P.-S. Shaw, Z. Li, U. Arp, Bilateral NIST–PTB comparison of spectral responsivity in the VUV, Metrologia, 48, 02001, 2011.
7. F. Scholze, R. Vest and T. Saito, Report on the CCPR Pilot Comparison: Spectral Responsivity 10 nm to 20 nm, Metrologia, 47, 02001, 2010.
8. F. Sarubbi, T. L. M. Scholtes, and L. K. Nanver, Chemical vapour deposition of α-Boron layers on silicon for controlled nanometer deep p+n junction formation, J. Electron. Mater., 39, 162–173, 2010.
9. V. Soltwisch, S. Burger, and F. Scholze, Scatterometry sensitivity analysis for conical diffraction versus in-plane diffraction geometry with respect to the sidewall angle, Proc. of SPIE, 8789, 878905-1, 2013.

Measurement of the relative spectral radiance responsivity of the three EarthCARE flight model Broad Band Radiometers

E. Theocharous[1] and M Caldwell[2]

[1]*National Physical Laboratory, Hampton Road, Teddington, TW11 0LW, UK*
[2]*STFC Rutherford Appleton Lab Space Dept., DIDCOT, OX11 OQX, UK*
Corresponding e-mail address: e.theo@npl.co.uk

The calibration of the absolute spectral radiance responsivity of the three Broad Band Radiometers (BBRs), which are due to fly on board the EarthCARE mission, consists of measuring the relative spectral radiance responsivity of these instruments over the wavelength range of interest, in combination with the measurement of the absolute spectral radiance responsivity of the same radiometers at certain wavelengths in the UV and visible. This presentation describes how NPL calibrated the relative spectral radiance responsivity of the three Flight Model (FM) BBRs in the 0.24 µm to 24.1 µm wavelength range. The procedures used and the results obtained are summarised. The associated measurement uncertainties are also presented.

INTRODUCTION

The aim of the Broad Band Radiometers (BBRs), which are due to fly on board the EarthCARE mission [1] is to measure the radiance at the top of the atmosphere in two wavebands. A total of three radiometers are to be deployed to measure the radiance from three along track views: forward, nadir, and backwards. The calibration of the absolute spectral radiance responsivity of the BBRs will be done by measuring the relative spectral radiance responsivity of these instruments over the wavelength range of interest, in combination with the measurement of the absolute spectral radiance responsivity of the radiometers at certain wavelengths in the UV and visible. The absolute spectral radiance responsivity is will be measured using an integrating sphere source, in combination with a radiometer whose absolute radiance responsivity is calibrated against the NPL absolute spectral radiance scale. This paper describes the NPL calibration of the relative spectral radiance responsivity of the three Flight Model BBRs in the 0.24 µm to 24.1 µm wavelength range. The paper describes the procedures used and presents the results obtained, together with the associated measurement uncertainties.

METHOD

Figure 1 shows the layout of the experimental arrangement used to calibrate the relative spectral radiance responsivity of the three FM BBRs. Radiation emerging from the exit slit of the double-grating monochromator was collimated using a 300 mm focal length Off Axis Parabolic (OAP) mirror, M1. The collimated beam was steered using a plane mirror, M2, and directed into the vacuum chamber containing the BBR under test using a second plane mirror, M3. A second OAP mirror, M4, and an aperture (not shown in Figure 1) were mounted on a PC-driven linear translation stage and were periodically inserted into the beam so M4 focused the collimated beam onto the active area of a reference detector. The standard software used by NPL for spectral radiant power responsivity calibrations [2] was used.

The FM BBRs had to operate at sub-ambient temperature and in vacuum so they were mounted inside a vacuum chamber and radiation entered the chamber through a CaF_2 window for wavelengths in the 240 nm to 8 µm wavelength range, while a KRS-5 window was used for longer wavelengths (to 24.1 µm). The vacuum enclosure was continuously evacuated during the calibration.

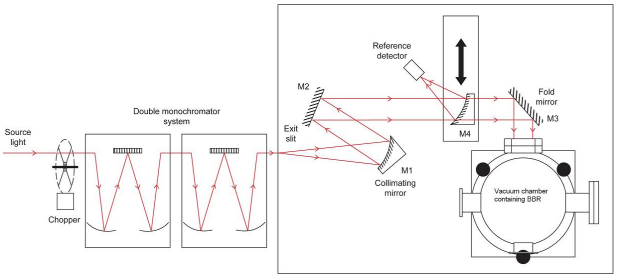

Figure 1. Layout of the arrangement used to calibrate the relative spectral radiance responsivity of the FM BBRs.

The detector used by each BBR is a micro-bolometer array with 30 elements (pixels) on a 0.1 mm pitch, giving a 3 mm total length of the detector array. The effective focal length of the BBR telescope assembly is 67 mm. In the NPL facility, a

300 mm effective focal length OAP mirror was used, resulting in a 4.6 times de-magnification of the monochromator exit slit on the detector. As the detector array is 3 mm in length, a monochromator exit slit of 13.8 mm is required to simultaneously cover all 30 pixels of the array. However, due to limitations in the available spatial uniformity of the optical radiation sources, a 10 mm long exit slit was used, requiring the measurement to be split into two parts, corresponding to the top and bottom of the detector array. The shorter exit slit consequently reduced the aberrations generated by the by the OAP mirrors used to collimate the output of the grating monochromator, thus minimising the non-uniformity in the spatial distribution of the irradiance illuminating the detector array.

The NPL infrared spectral responsivity measurement facility was used to cover the 1.3 μm to 24.1 μm wavelength range, while the NPL UV/Vis/NIR spectral responsivity measurement facility was used to cover the 0.24 μm to 1.55 μm wavelength range. A frequency-stabilised mechanical chopper at 17.4 Hz ± 0.001 Hz was used to modulate the beam entering the monochromator. The chopping frequency used matched that of the BBRs in flight. The temporal profile of the waveform of the chopped beam illuminating the BBR telescope assembly was a near-rectangular trapezoidal. The rise-time of the trapezoid was governed by the width of the beam in the plane of the chopper blade and by the "clear opening" of the chopper blade. The reference signal from the chopper was used to synchronise data acquisition by the BBR data acquisition hardware. A variable time delay was used to ensure that the software logged the output of the BBRs when the chopper blades were fully opened and fully closed. Moreover, the TTL signal controlling the state of the shutter on both facilities was also provided to the BBR data acquisition hardware to ensure that data were acquired at the correct time (when shutter was open/closed).

RESULTS

Figure 2 shows the relative spectral responsivity of the top part of the BBR FM3, normalised at 0.6 μm, as a function of wavelength. A similar profile was measured for the bottom part of the array and for all three BBRs.

DISCUSSION

All three BBRs exhibited similar relative spectral responsivity profiles. These profiles show that the relative spectral responsivity increases with increasing wavelength, except for a reduction in the response around 850 nm due to the reflectance of the aluminium OAP mirrors which form the telescopes of the BBRs. The increasing instrument response with increasing wavelength is likely to be a result of the gold-black coatings with which the detectors of all three BBRs are coated. The coating is quite thick (~30 μm), so the response to short wavelengths (which are absorbed by the top part of the black coating so the generated heat has to travel to the transducer via the body of the coating) is low compared to that at long wavelengths which exhibit a higher penetration into the coating.

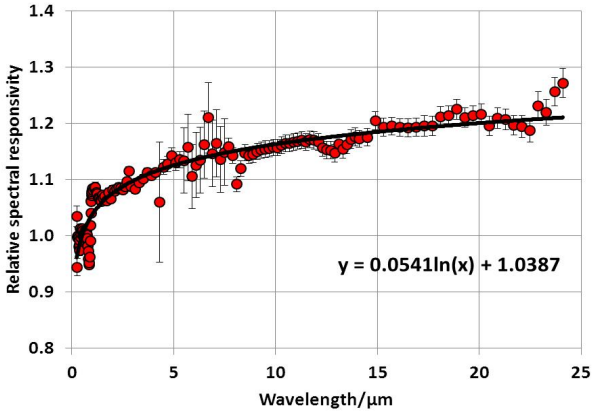

Figure 2. Relative spectral responsivity of the top part of the BBR FM3, normalised at 0.6 μm.

The uncertainty of the measurement of the relative spectral radiance responsivity of the BBRs was calculated by combining the type A uncertainty with a number of type B uncertainty contributions which included the uncertainty due to the following: the NPL relative spectral responsivity scale; the stability of the sources used; differences in the relative reflectance of mirrors M3 and M4 (see Figure 1); the transmittance of the CaF_2 and KRS-5 windows; atmospheric absorption; stray light; the wavelength scale; the non-linear response of the reference detectors and lock-in amplifier used; ambient temperature fluctuations; drifts in the modulation frequency of the chopper; the spatial non-uniformity of response of the reference detectors; the spatial non-uniformity of the output of the grating monochromators; and the splicing of the data generated using different measurement bands. Some

of these uncertainty contributions are strongly dependent on wavelength. The combined uncertainty is shown as error bars in Figure 2.

REFERENCES

1. K. Wallace, N. Wright, K. Ward and M. Caldwell, "The BroadBand Radiometer on the EarthCARE Spacecraft", Proc.SPIE,7453, Infrared Spaceborne Remote Sensing and Instrumentation XVII, 2009.
2. E Theocharous, "The establishment of the NPL infrared relative spectral responsivity scale using cavity pyroelectric detectors", Metrologia, **43**, S115-S119, 2006.

Improving the wavelength accuracy of the Cary 14 prism-grating monochromator

Howard W. Yoon and Vladimir B. Khromchenko

Sensor Science Division, National Institute of Standards and Technology, Gaithersburg, USA
Corresponding e-mail address: hyoon@nist.gov

A Cary 14 monochromator was modified with the installation of a linear, optical encoder for determinations of the angular positions of the prism-grating sine bar. The improvements in the wavelength accuracy and the repeatability of the monochromator are demonstrated using the measurements from a number of atomic spectral emission sources. The resulting expanded wavelength uncertainty is determined to be ± 20 pm in the wavelength range of 250 nm to 1000 nm. Additional measurements of absorption features in rare-earth glass standards are used to validate the wavelength accuracy by comparison to other spectrophotometers at NIST. The monochromator is further be used to calibrate spectrographs which are in-turn used to directly assess the wavelength accuracies of spectrophotometers and spectroradiometers.

INTRODUCTION

Although laser-based facilities are used for the lowest uncertainty measurements in spectroradiometry, in many areas of spectrophotometry or spectroradiometry, a predominance of dispersive grating- or prism-based systems exist. The critical component and a critical parameter in these systems are the monochromator and its wavelength accuracy. If such dispersive systems are to be made comparable in performance to laser-based systems, then the wavelength uncertainties must be made as small as possible [1].

We describe the use of a linear, optical encoder which is attached to the inner wall of the Cary 14* monochromator to measure the angular positions of the prism-grating sine bar. The increased repeatability and the wavelength accuracy are shown. The calibrated monochromator is also used to measure rare-earth doped wavelength standards for comparisons with other standard spectrophotometers. The improved monochromator is also used to calibrate the wavelength scales of spectrographs which can be used in-turn to calibrate other spectroradiometers.

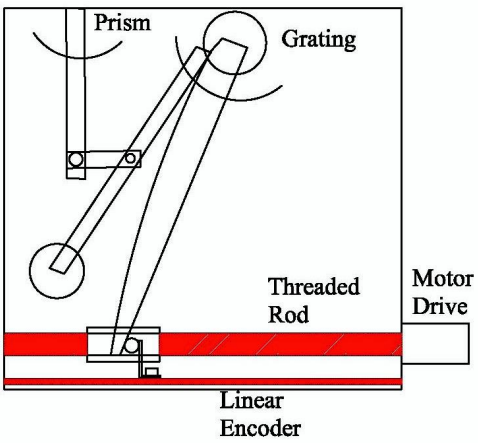

Figure 1. Schematic of the modified wavelength drive compartment of the Cary 14.

EXPERIMENTAL SETUP

A schematic of the modified Cary 14 monochromator wavelength drive is shown in Fig. 1. The prism and the gratings are coupled together and are rotated using a common sine bar. The curvature on one face of the sine bar accounts for the nonlinear refractive index of the fused-silica prism as a function of wavelength and thus the angle. A direct-current servo motor is attached to the end of the threaded rod for movement. The rotational movement of the motor is converted to linear motion by a threaded nut, and the grating is rotated by the arm which is pushed along by the threaded nut. To measure the linear movement, the optical encoder is attached to the internal wall of the monochromator housing, and the optical read head is attached to the threaded nut. The specifications of the optical encoder are shown in Table 1. The encoder is constructed from glass and is attached to the side of the monochromator using metal clips.

Table 1. The specifications of the optical linear encoder.

Total length (cm)	Signal Period (µm)	Interpolation	Interpolated Resolution (nm)	Absolute Position Marker Spacing (mm)
32	4	4096	0.97	20

Since the total spectral measurement range of the Cary 14 is from 200 nm to 3000 nm, the theoretical resolution is calculated to be about 0.01 pm.

WAVELENGTH REPEATABILITY

The initial measurements were performed to determine the repeatability of the wavelength drive. For these measurements, a low pressure Hg lamp was placed inside an integrating sphere, and the output of the integrating sphere was imaged using a spherical mirror which was chosen to match the numerical aperture of the Cary 14. The repeated measurements of the Hg transition at 546.0750 nm [2] are shown in Fig. 2

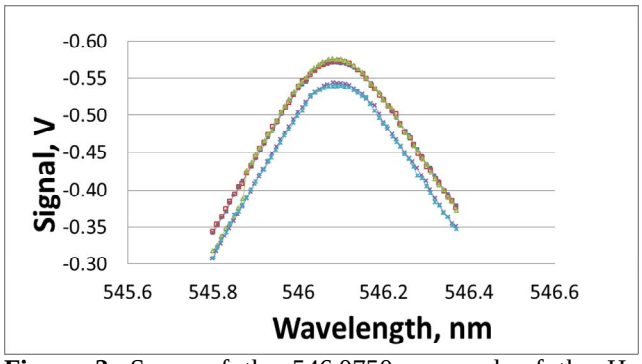

Figure 2. Scans of the 546.0750 nm peak of the Hg emission lamp.

The measurements were performed by always moving the sine bar from the same direction from longer wavelengths to shorter wavelengths so that the sine-bar mechanism was pushed. The repeatability as determined using the spread in the centroid of repeated measurements was ± 1 pm.

WAVELENGTH ACCURACY

Additional atomic emission lamps were used to obtain a fitting function which minimizes the residual differences between the function and the actual values. A plot of the residuals is shown in Fig. 3. The expanded uncertainties from the residuals are determined to be ± 20 pm. The scatter of the residuals is due to the additional uncertainties in the determination of the centroid wavelengths such as the signal-to-noise of the peak measurements which can affect the centroid determinations.

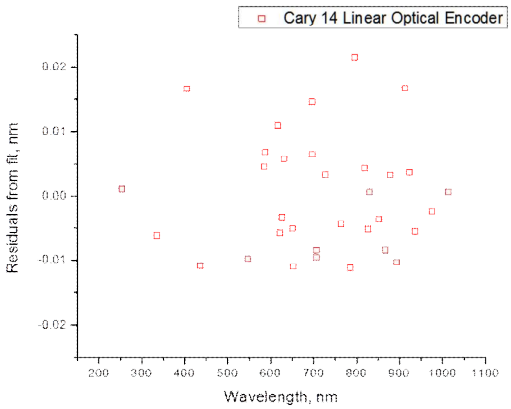

Figure 3. Residuals differences from the 5th order polynomial fitting function.

DISCUSSION

Since the encoder can be read over the entire wavelength range of the Cary 14, the calibrations will be extended from 1000 nm to 2500 nm using an extended InGaAs detector. The monochromator will also be used to calibrate a spectrograph which in-turn will be used to calibrate the monochromatic outputs of spectroradiometers used in the NIST spectral power responsivity and spectral directional reflectance facilities [3].

* Certain commercial equipment, instruments, or materials are identified in this paper to foster understanding. Such identification does not imply recommendation or endorsement by the National Institute of Standards and Technology, nor does it imply that the material or equipment are necessarily the best available for the purpose.

REFERENCES

1. M. White, M. Smid and G. Porrovecchio, Realization of an accurate and repeatable wavelength scale for double subtractive monochromators, Metrologia, 49, 779-784, 2012.
2. C. J Sansonetti, M. L. Salit, J. Reader, Wavelengths of spectral lines in mercury pencil lamps, Applied Optics, 35 Issue 1, 74-77, 1996.
3. P. Y Barnes, E. A. Early and A.C. Parr, Spectral Reflectance, NIST Special Publication 250-48, U.S. Government, Washington, 1998.

Characterization of CCD Detectors for Laser Power Measurement

Takayuki Numata, Minoru Tanabe, Kuniaki Amemiya, Daiji Fukuda, and Tatsuya Zama

National Metrology Institute of Japan (NMIJ), National Institute of Advanced Industrial Science and Technology (AIST)
Tsukuba, Japan
Corresponding e-mail address: t.numata@aist.go.jp

Response character of Si-based CCD image sensors, which is now widely used for laser beam diagnosis, was investigated to explore its capability as a laser power measurement instrument. As a major source of uncertainty, response non-uniformity of test detector was evaluated using laser spot-scanning method and compared with integration sphere-based uniform light source method for wavelengths of 633 nm and 1064 nm. Results from two methods were reasonably consistent and showed response character was significantly varied among devices in near-infrared wavelength region below the band gap energy.

INTRODUCTION

Two-dimensional optical detector, such as charge coupled device (CCD) image sensors, has become rapidly popularized as a laser diagnosis instrument, recently. The device consists of small independent optical detectors laid out in a form of matrix array with particular spacing. This means that radiometric and geometric calibration of the sensor device allows evaluation of local optical power density in a cross section of incident laser beam as well as the total beam power by integrating signals from all pixels in the array. Until now a lot of works about evaluation of CCD's responsivity have been reported [1],[2]. However these works were mainly aimed for application in photometry which deals with relatively small intensity, visible incoherent lights. On purpose of laser beam measurement, evaluation of CCD's responsivity and its uncertainty with optical configuration close to practical measurement, that is, CCD is irradiated by collimated under-fill laser beam, is preferable. So, in this study, response non-uniformity, which is expected to be a major source of uncertainty, was investigated by means of laser spot-scanning technique. The result was compared with a conventional method using uniform light source of integration sphere.

PRINCIPLE

Responsivity of a CCD detector to incident laser power is described as,

$$R_{global} = \frac{\sum_{i=1,j=1}^{m,n} S_{i,j}}{P \cdot t_{exp}} \qquad (1)$$

where, the numerator is the total count signal derived from summation of signals of all m by n pixels in the array, P is the incident "under-fill" laser power, and t_{exp} is the exposure time. CCD driven in video mode generates count signals refreshed with a cycle of exposure time, which is governed by the device itself. Therefore, the responsivity can be defined as ratio of the total amount of count signal per unit time to the incident laser power. As test detector, we have picked up several commercially available Si-CCD-based laser beam profilers manufactured for laser beam measurement equipped with attenuation optics and no cover glass on the sensor surface. As test light source, laser at 1064 nm, which is widely used for laser processing industry, was employed in addition to 488 nm and 633 nm.

EXPERIMENTS AND RESULTS

Response non-uniformity of the test device was first examined by conventional technique using integration sphere-based uniform light source system, shown in Fig.1. Laser sources at 488 nm, 633 nm and 1064 nm are combined in an optical path with dichroic mirrors. For the purpose of speckle reduction, the laser beam which illuminates inner surface of the 12 inch-diam. integration sphere is spatially scanned at the entrance port by a piezoelectric-driven mirror. The speckle contrast detected by array of 4.4 μm x 4.4 μm square pixels of a CCD detector is reduced to less than 2 % at a plane on the 3 inch-diam. exit port. Field non-uniformity, the optical intensity distribution with spatial frequency much smaller than the speckle noise, was also evaluated. A silicon photo detector with ϕ500 μm aperture was scanned in a plane normal to the optical axis in 20 mm x 20 mm

area at 20 mm away from the exit port. Full width of intensity variation was ±0.1 % for each wavelengths.

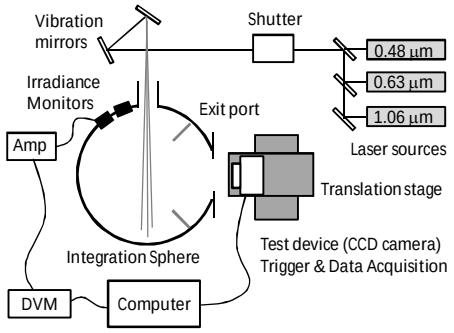

Figure 1. Integration sphere-based uniform light source system.

Using this uniform field, response non-uniformity of test detector was examined. Figure 2 shows the results of response uniformity test for two CCD detectors from different manufacturer. The result indicates response uniformity significantly differs with respect to devices especially in near-infrared (NIR) region. Also, non-uniformity was enhanced in short exposure time. Degradation of uniformity may be originated from non-uniformity of device itself, such as variation in thickness of photodiode structure. In case of CCD (A) at 1064 nm with exposure time of 100 ms, photo response non-uniformity (PRNU), which is defined as ratio of standard deviation of signal counts of all pixels to the average counts, was calculated around 4 %.

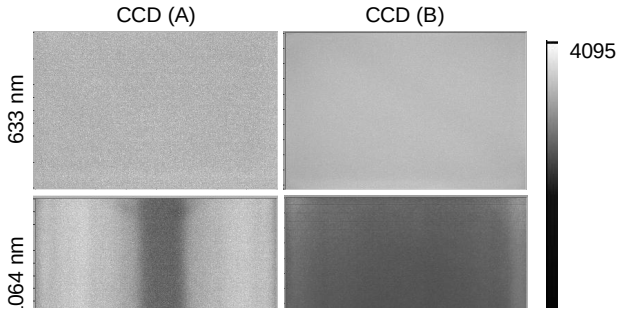

Figure 2. Comparison of response uniformity between two test devices. Sensitive area is about 8 mm x 6 mm for both devices.

Next, the response non-uniformity was investigated by scanning a laser spot. A vertically polarized power-stabilized laser beam with $1/e^2$ diameter of 1 mm was scanned on the test CCD's surface with a pitch (Δx, Δy) of 500 μm with normal incidence. Total count signal from the device was recorded for each illuminating spot. A result for CCD (A) with laser wavelength 1064 nm and exposure time of 100 ms is shown in Fig.3. The values represent relative responsivity normalized to the central value. As seen in the figure response non-uniformity distribution similar to the test using uniform light source was observed. Relative standard deviation without edge region, where laser spot was partially obstructed, was calculated as around 3 % which is reasonably consistent with results of integration sphere method. The difference between two methods may be come from limited solid angle of micro lens structure on the device and smear effect induced by local illumination of laser spot.

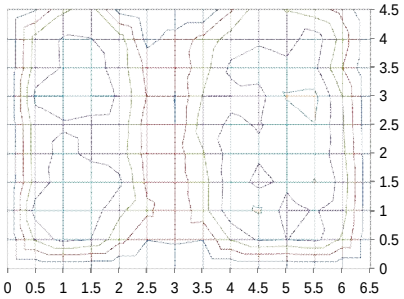

Figure 3. Response non-uniformity investigated about CCD (A) at 1064 nm using laser spot-scanning method. A contour line indicates relative difference of 2 %.

SUMMARY

CCD detector's response non-uniformity was investigated and compared using laser spot scanning method and integration sphere-based uniform light source method in visible and near-infrared wavelength. The results obtained from two different methods were reasonably consistent. The results showed response characteristics in NIR region below band gap energy varied greatly among devices.

ACKNOWLEDGEMENTS

This work has been partially supported by KAKENHI 24760327; Grant-in-Aid for Young Scientists (B) from the Japan Society for the Promotion of Science (JSPS).

REFERENCES

1. A. Ferrero, J. Campos, and A. Pons, Low-uncertainty Absolute Radiometric Calibration of a CCD, Metrologia. 43, S17-S21, 2006.
2. G. Healey, and R. Kondepudy, Radiometric CCD Camera Calibration and Noise Estimation, IEEE Trans. Pat. Anal. Mach. Intel., 16, 267-276, 1994.

Comparison of measured and deconvolved relative spectral responsivities of a CCD-Camera by using the Richardson-Lucy method

L. Bünger, K. Anhalt, R. D. Taubert, S. Eichstädt, and F. Schmähling

Physikalisch-Technische Bundesanstalt, Braunschweig and Berlin, Germany
Corresponding e-mail address: Lars.Buenger@PTB.de

For spectrally resolved detector calibrations a high power level after the spectral selection unit, e.g. monochromator system, is often required. We use an integrating sphere to achieve a uniform radiation field when measuring with different FOV radiometers. The detector signal can be increased by using a brighter radiation source as well as by increasing the spectral bandwidth of the monochromator output. By using a broader bandwidth the resulting "spectral responsivity" is deformed. We model this deformation as a convolution and employ the Richardson-Lucy method for deconvolution. We show that the results are in a good agreement for the relative spectral responsivity of a camera system for different bandwidths of the monochromator.

INTRODUCTION

The determination of the absolute spectral responsivity is based on a spectral radiance/irradiance comparison of an absolutely calibrated trap detector and the test detector (e.g. camera system). Fig. 1 shows the schematic setup of the applied monochromator-integrating sphere based spectral comparator facility at the PTB [1].

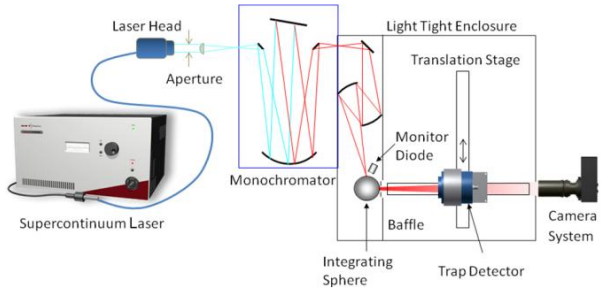

Figure 1. Schematic setup of the PTB monochromator-integrating sphere based spectral comparator facility.

The measurement uncertainty is dominated by the radiance non-uniformity at the integrating sphere exit port. A larger sphere diameter can improve the achievable uniformity but the radiance level at the sphere opening and hence the signal-to-noise ratio of the detectors will decrease. Wider bandwidths of the monochromator allow using a larger integrating sphere for a better sphere uniformity combined with an adequate radiance level for the measurement. However, a spectral deconvolution could be necessary after the measurement to compensate for spectral deformation effects.

For this deconvolution investigation a modified camera system (LMK 98-4 Color by Technoteam GmbH) with a high dynamic range was used [2]. This camera is specially equipped with a 650 nm interference filter for measuring radiation temperature.

BANDPASS FUNCTIONS

A HeNe laser was used to determine the bandpass functions for different slit widths of the monochromator. Using a halogen lamp as the radiation source, the filament is imaged on the entrance slit overfilling the slit width. To determine the bandpass function for this configuration the HeNe laser was combined with a 25 mm diameter integrating sphere to image the homogeneous radiation field of its aperture on the entrance slit.

For the supercontinuum laser (SCL) setup an aperture lens system has been developed to match the f-number of the monochromator. In this case the HeNe laser beam passes the same optical system as the SCL beam to investigate the monochromator slit function.

The resulting bandpass functions for the two setups (lamp and SCL) are significantly different. In lamp configuration, the focussed image of the integrating sphere on the entrance slit irradiates the full width of the entrance slit resulting in a triangular shaped band-pass function. For the SCL setup, the beam is underfilling the slit area, so the laser spot width determines the actual input slit width. As a result, the bandpass function is trapezoidal shaped. This leads to different signal variations, when changing the width of the symmetric monochromator slits.

MEASURED SIGNALS

The responsivity of the camera was measured for different spectral bandwidth settings of the

monochromator in the halogen lamp configuration. For the reference measurement the more powerful SCL was used. For the lamp setup a quadratic dependency while for the laser setup an approximately linear behaviour between the slit widths and the resulting detector signals behind the monochromator was observed. This difference between the measured camera signals for the two radiation source setups depends on the used bandwidth. The difference varies from a factor of 350 at a bandwidth of 0.4 nm to a factor of 17 at a bandwidth of 5 nm. The measurement signals of the camera are corrected with the relative spectral responsivity of the monitor diode located at the integrating sphere to get the relative spectral radiance responsivities of the camera system. Fig. 2 illustrates the influence of the convolution of the measured spectra with the bandpass function.

DECONVOLUTION AND COMPARISON

Different methods for the deconvolution are reported in literature. Here, the Richardson-Lucy method was chosen, due to its robustness with respect to the selected wavelength range and measurement noise [3].

For the deconvolution the relative shape of the bandpass and its exact centroid are important. If the centroid of the bandpass function is not in the center of the selected wavelength range, the deconvolved spectrum shifts by half of this displacement [4, 5]. To correct this wavelength shift the principle of zero-padding before starting the deconvolution procedure was applied.

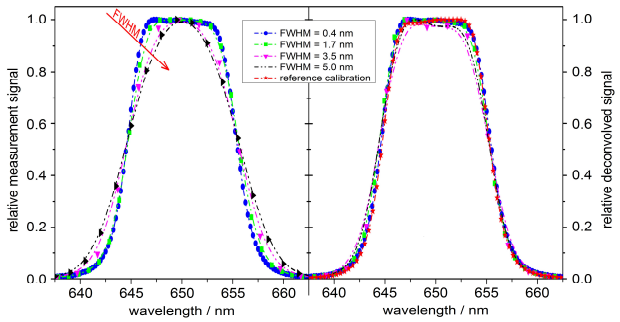

Figure 2. Left: Observed rel. measurement signals for different monochromator bandpass settings (lamp setup). Right: Rel. deconvolved measurement signals (lamp setup) and rel. reference calibration (SCL setup).

The deconvolved spectra show a good agreement to the reference spectrum (Fig. 2). The typical deforming of the spectra is obviously reduced. Only for wider bandwidths and fewer supporting points, appreciable deviations are still noticed. For the convolved and the deconvolved rel. spectral radiance responsivity curves, the effect on the temperature accuracy of the camera system was investigated. The relative spectra were linearly scaled to the total area of the absolutely known reference curve. The calculated temperature deviations with respect to the absolute radiometric temperature are shown in Fig. 3 for the 1.7 nm and for the 5.0 nm bandwidth for the convolved and deconvolved spectra. The temperature deviations for the measured (convolved) spectra increase with increasing temperature. The temperature deviations for the deconvolved spectra are approximately constant, which indicates a good spectral agreement with the reference spectrum. The remaining linear deviation is probably caused by a small centroid wavelength shift due to less supporting points and the used interpolation method. However, there is a good agreement between the deconvolved and the reference temperature calculations.

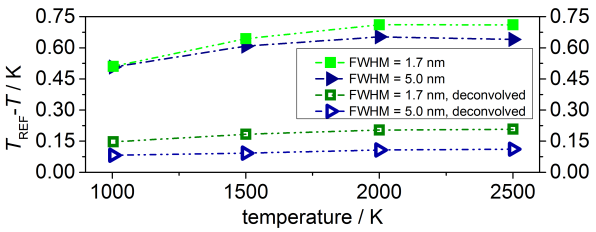

Figure 3. Temperature deviations between the radiometric temperature and the calculated temperature of the scaled relative spectral responsivities and its deconvolved curves.

CONCLUSIONS

The main challenge to realize high signal-to-noise ratios for the absolute spectral radiance responsivity determination of a detector based on a monochromator-integrating sphere setup was discussed. One approach is to apply larger spectral bandwidths in combination with a subsequent spectral deconvolution of the measured data. Combining this method with a more powerful radiation source (SCL) enables much faster calibrations. Especially for camera systems and other large field-of-view detectors, the use of larger integrating spheres with large apertures can significantly improve the spectral radiance responsivity calibration.

REFERENCES

1. T. Keawprasert, Int J Thermophys. 32, 1697-1706, 2011.

2. http://www.technoteam.de/
3. S. Eichstädt, Metrologia, 50, 107–118, 2013.
4. E. Woolliams, "Correcting for bandwidth effects in monochromator measurements." lamp 1, 2005.
5. E. Woolliams, Metrologia, 48, 164–172, 2011.

Investigation of Spectroradiometer Entrance Optics for Characterization of Expanded Radiant Areas

Fabian Plag, Peter Sperfeld, Thomas Fey, Florian Witt, Ingo Kröger, and Stefan Winter

Physikalisch-Technische Bundesanstalt, Braunschweig & Berlin, Germany,
Corresponding e-mail address: fabian.plag@ptb.de

In many radiometric applications the spectral irradiance distribution of non-Lambertian sources, such as the solar spectrum, is determined by using compact array spectroradiometers with different types of entrance optics. The correction of a cosine error has to be considered for measurements of direct and diffuse radiation [1]. The estimation of uncertainties for the irradiance calibration of detectors such as solar cells with a source-based integral measurement method requires a thoroughly radiometric analysis of both the source and the detector [2], [3]. We will present the angular dependence of commonly used entrance optics. Furthermore, their influence on uncertainties in photovoltaic measurements will be discussed.

INTRODUCTION

In order to determine the efficiency of photovoltaic devices under defined conditions, the spectral irradiance distribution of the radiant source has to be well known. In photovoltaic metrology compact array spectroradiometers are widely spread for the purpose of measuring solar spectral irradiance. Indeed, international standards such as IEC 60904-3 ed. 2 define a global (direct & circumsolar/diffuse) reference distribution of solar spectral irradiance. However, a consideration of its angular distribution is not provided in the field of photovoltaic performance rating.

Earlier research on reference solar cells illustrates different cosine errors depending on the type of solar cell and its encapsulation design [3]. Thus, in order to minimize uncertainties assigned to angular dependencies of the radiant source and the detectors, for outdoor calibrations it is required to mathematically correct the cosine errors of the entrance optics and solar cells used. Also for the characterization of the radiation conditions in solar simulators used in the photovoltaic sector for calibrations and quality assurance, angular dependencies should not be neglected. This has particularly to be considered for large illuminated surfaces and short distances to the radiant source.

We will therefore characterize the angular dependence of compact array spectroradiometers' entrance optics as well as integral detectors. The individual cosine correction parameters will be determined for both systems. Finally the spectral and integral homogeneity of a solar simulator will be measured. The impact of the cosine correction on the results will be discussed.

MEASUREMENT METHOD

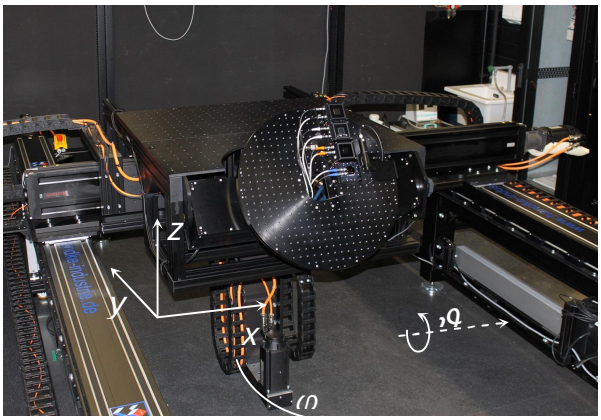

Figure 1. Mounted solar cells on a ϑ-φ-goniometer at PTB's LASER DSR Facility. [4]

The measurement of angular dependencies is performed with a two-axis goniometer mounted on a movable three-axis stage (see Fig. 1).

The load capacity of the goniometer mechanics allows the analysis of large area detectors as well as the rotation of whole array spectroradiometer systems. As a radiant source we use a tungsten halogen lamp. To expand the measurements to the UV spectral range, a xenon arc lamp is used. Possible instabilities of the radiant source are corrected by applying a monitor photodiode. In addition a beam collimation applies direct radiation at defined angles of incidence to the entrance optics and solar cells. By using the inverse square law, the radiometric reference plane of the entrance optics as well as it is rotational axis are determined. With this

configuration the cosine error of integral detectors as well as entrance optics can be measured.

Different types of entrance optics such as integrating spheres and single diffuse reflectors will be evaluated regarding their applicability for expanded radiant area measurements. The use of compact array spectroradiometers allows the determination of spectrally resolved cosine dependencies covering a spectral range from UV-NIR.

The first results using a tungsten halogen lamp as a radiant source and a windowless reference solar cell with WPVS[1] design as a detector are shown in Fig. 2. The solar cell features a cosine error of more than 4 % at angles of incidence $\vartheta > 40°$. Results of a variation in the angle of incidence in φ-direction show a non-symmetric response of the solar cell.

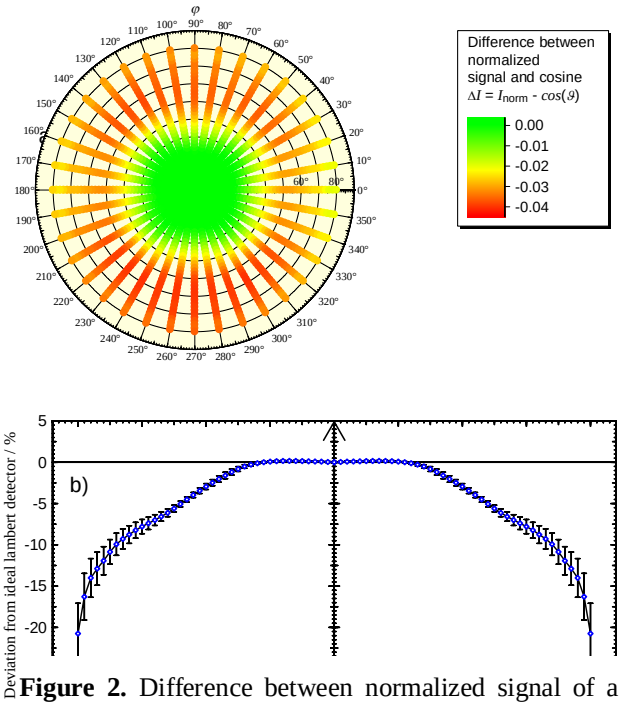

Figure 2. Difference between normalized signal of a solar cell with windowless WPVS design irradiated by a tungsten halogen lamp and cosine a); Deviation from ideal lambert detector averaged over all φ-angles is shown in b).

Finally the homogeneity of solar simulator irradiance will be characterized with the integral detector as well as spectrally with the spectroradiometer. Therefore the irradiated plane will be scanned with both devices.

SUMMARY

Knowledge of the cosine error and its measurement uncertainty of entrance optics allows the estimate of uncertainties in the measurement of expanded radiant areas. A typical application is the measurement of the solar spectrum considering its angular distribution. Uncertainties in the characterization of simulated sunlight in the photovoltaic sector are discussed. By using a cosine correction factor, it is possible to determine the irradiance homogeneity of an illuminated plane with compact array spectroradiometers. In comparison to traditional methods with integral detectors, such as photodiodes or solar cells, uncertainties due to a spectral mismatch can be neglected.

The effect of differences between the angular distribution of natural sunlight and the radiant conditions in solar simulators is estimated. Thus, the determination of measurement uncertainties in photovoltaic devices will be expanded by the implementation of angular dependencies of measurement equipment.

REFERENCES

1. J. Gröbner; M. Blumthaler; W. Ambach, Experimental investigation of spectral global irradiance measurement errors due to a non ideal cosine response. J. Geophys. Res. 1996, 23, 2493-2496.
2. P. Sperfeld, D. Dzafic, F. Plag, F. Haas, et. al., Usability of compact array spectroradiometers for the traceable classification of pulsed solar simulator, Proceedings of 27th PVSEC 2012, Frankfurt, Germany.
3. S. Winter, D. Friedrich, & T. Gerloff (2010), Effect of the Angle Dependence of Solar Cells on the Results of Indoor and Outdoor Calibrations. Proceedings 25th European Photovoltaic Solar Energy Conference and Exhibition, p 4304 – 4306, Valencia.
4. S. Winter, T. Fey, I. Kröger, D. Friedrich, K. Ladner, B. Ortel, S. Pendsa, D. Schlüssel, Laser-DSR Facility at PTB: Realization of a Next Generation High Accuracy Primary Calibration Facility, Proceedings of 27th EUPVSEC 2012, p 3049 – 3051, Frankfurt, Germany.

[1] World Photovoltaic Scale

Measurement of Ambient Contrast Ratio for Curved Displays

Hsueh-Ling Yu[1], Chin-Chai Hsiao[1], Wen-Chun Liu[1], and Richard Young[2]

[1]*Center for Measurement Standards, Hsinchu, Taiwan, R.O.C.,* [2] *Instrument Systems GmbH, Muenchen, Germany*
Corresponding e-mail address: hsuehling.yu@gmail.com

Ambient contrast ratio can be calculated from the reflectance of the display's surface. This article describes how to apply the integrating sphere to measure the reflectance of curved displays. The reasons which may induce measurement error are also discussed.

INTRODUCTION

Flexible or curved displays are expected to be popular in the near future. Ambient contrast ratio (ACR) is the most important parameter to describe the performance of a display when operating under strong ambient light or for outdoor application. The definition of ACR is the luminance ratio of white screen to black screen of a display under uniform diffuse illumination. According to the method recommended in the documentary standards [1-3], ACR can be calculated from the reflectance of the display as shown in Figure 1 by using the integrating sphere. Applying integrating sphere for flat surface d:0 geometry reflectance measurement is a widely used method. However, for curved displays the traditional measurement procedures may not be suitable. This article presents two modified ways to measure the reflectance of a curved surface, one is placing the curved sample outside the sphere as it used to be and the other is placing the sample inside the sphere. As shown in Figure 2, two types of paper with different colors are prepared as the test samples, one type is matte surface and the other type is a little glossy. These samples are bent from flat to convex

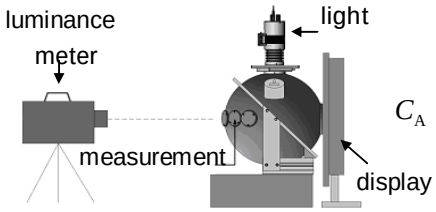

$$C_A = \frac{L_w + \frac{\rho_W}{\pi} E_0}{L_K + \frac{\rho_K}{\pi} E_0}$$

Where L_w: luminance of full-screen white
L_k: luminance of full-screen black
ρ_w: reflectance of full-screen white
ρ_k : reflectance of full-screen black
C_A: ambient contrast

Figure 1. Schematic diagram for ACR measurement.

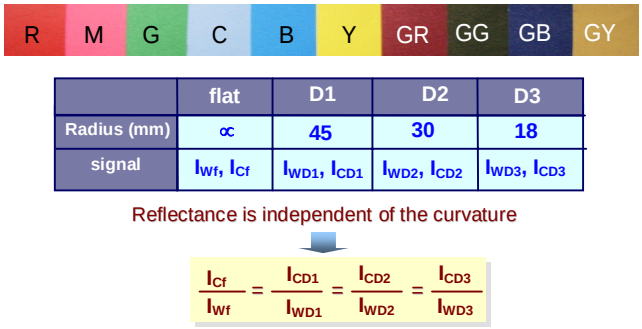

Figure 2. Matte and gloss samples.

with curvature 45 mm, 30 mm, and 18 mm. I_{Wf} ~ I_{WD3} and I_{Cf} ~ I_{CD3} represent the signals for white paper and other color papers, respectively. If the matte papers are perfectly matted, then their reflectance will be independent of the curvature and the ratio of signal for white paper and other color matte paper shall remain the same. Consequently the reflectance of curved surface can be easily measured by using the curved white surface as the standard. The evaluation for the following two measurement methods is based on whether those consistent ratios can be obtained.

METHOD 1: SAMPLE IS OUTSIDE THE SPHERE

The measurement device for Method 1 is Macbeth Color-Eye 7000. As the samples are curved and can not cover the whole sample port of Color-Eye 7000 completely, preventing effects from environmental lighting is extremely important here. Choosing the ratio for flat paper as the reference value, the deviation of the ratios at other curvatures from this reference value for each color are shown in Figure 3.

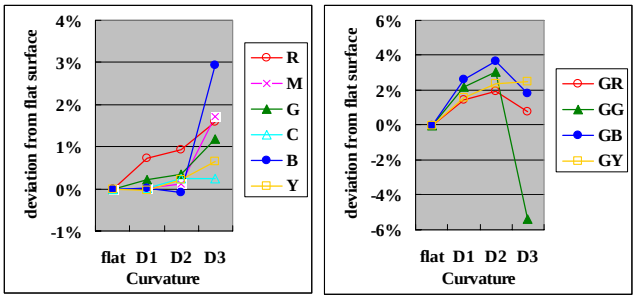

Figure 3. Experimental results of Method 1.

The results show that for matte samples the deviations are within ±2 % for all colors except blue. However for gloss paper, even for samples that are only a little glossy, the deviation is worse. It can be as high as 4%.

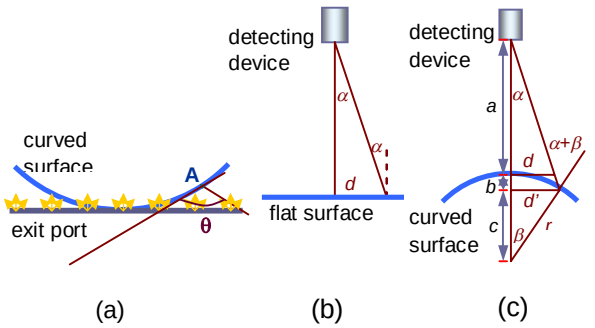

Figure 4. Illumination and observation conditions of d:0 geometry reflectance measurement for curved surface.

There are three reasons that may explain those deviations. The first comes from the diffusion illumination. Since the curved surface is placed outside the sphere, only the vertex is illuminated by the light from all directions. As shown in Figure 4(a), a point such as point A is only illuminated by the light within angle θ. θ is dependent on the curvature and the location of A. The second reason is due to the observation angle. As depicted in Figure 4(b), only the reflected light within α degree is observed by the detecting device for flat surface. Nevertheless for the curved surface, the detecting device can detect the reflected light within α+β degrees as shown in Figure 4(c). Therefore it doesn't meet the condition of "zero" degree observation. This extra angle β is dependent on the viewing angle of the detecting device, the curvature of the surface, and the detecting area. β is big for small curvature and large detecting area. For the matte surface, the effect of β is not so significant since the reflectance from all directions is similar. However for a glossy surface, the effect from β is not negligible. This explains why the deviations for glossy samples are larger than those for matte samples. The third reason is that the matte samples are not perfectly matte, therefore the deviations are affected by the curvature.

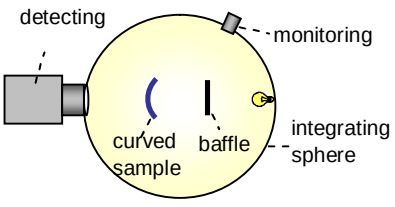

Figure 5. Schematic diagram for method. 2.

Using this traditional d:0 reflectance measurement system as Method 1 to measure curved surface, both the illumination and observation can not meet the conditions of d and 0. In addition, Method 1 is not applicable to measure concave surface. Therefore, Method 2 is adopted as follows.

METHOD 2: SAMPLE IS INSIDE THE SPHERE

Figure 5 shows the schematic diagram of the measurement system for Method 2, and Figure 6 presents the measurement results. The diameter of the sphere is 50 cm. The detecting device is Instrument System CAS 140CT array spectrometer with TOP 100 telescopic optical probe. The monitoring device is Ocean 2000 spectrometer. Although Method 2 uses diffuse illumination, the results are similar to Method 1: the deviations are within ±2% for most matte color paper and the deviation is around 4% for glossy paper. The reason may be due to the incomplete compensation of self-absorption.

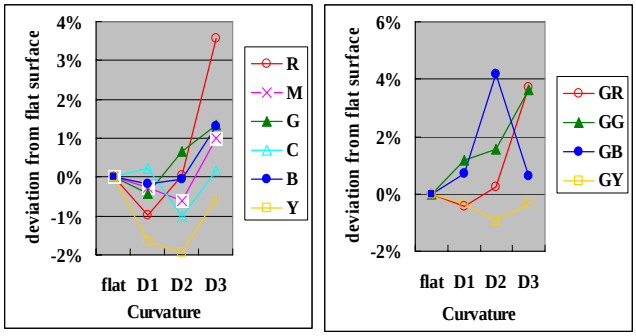

Figure 6. Experimental results of Method 2.

CONCLUSIONS

Two methods of reflectance measurement for curved surfaces are presented in this article. Both methods obtain similar results. The advantage of Method 1 is ease of use, but it is only suitable for convex surfaces. Method 2 is applicable to both convex and concave surfaces but has size limitation. For glossy surfaces, smaller measurement area is recommended for both methods to prevent unwanted reflected light from other directions.

REFERENCES

1. VESA FPDM Version 2.0, Video Electronics Standards Association Display Metrology Committee, 2010.
2. Edward F. Kelley, Diffuse Reflectance and Ambient Contrast Measurements Using a Sampling Sphere, ADEAC, 1-5, October 24-26, 2006.
3. SEMI D56-0310, Measurement Method for Ambient Contrast of Liquid Crystal Displays, 2010.

Establishment of Absolute Diffuse Reflectance Scales in the Near-IR Region at KRISS

Jisoo Hwang, Hehree Cho, Dong-Joo Shin, and Ki Lyong Jeong

Division of Physical Metrology, Korea Research Institute of Standards and Science,
267 Gajeong-ro, Yuseong-gu, Daejeon, 305-340, South Korea
Corresponding e-mail address: jhwang@kriss.re.kr

Absolute scale of diffuse reflectance in the near-IR region has been established at KRISS by using the Sharp-Little method of an integrating sphere-based method. Throughout the spectral range of 360-1600 nm, the diffuse reflectance of spectrally neutral white standards is determined within a relative expanded uncertainty of 0.64% (*k*=2). A detailed instrumentation and an uncertainty evaluation are presented.

INTRODUCTION

Determination of diffuse reflectance is important in various optical applications. At KRISS, the visible absolute diffuse reflectance scale was established about 20 years ago, which has been contributed in disseminating the national standard of diffuse reflectance.[1] Recently, KRISS extended the national scale of absolute diffuse reflectance up to 1600 nm, due to the increasing industrial requirements of near-IR diffuse reflectance standards. Also, a new instrument was developed to replace the old setup. In this paper, we present the new instrument and the experimental results including uncertainty evaluation.

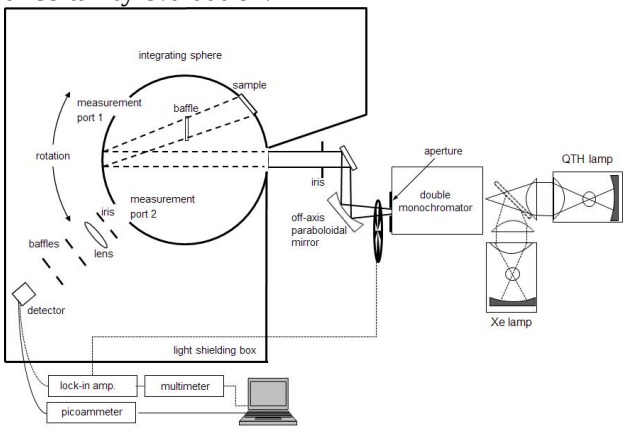

Figure 1. Schematic of the setup for an absolute diffuse reflectance measurement.

MEASUREMENT SETUP

The measurement setup consists of three parts of a source system, an integrating sphere, and a detection system as shown in Figure 1. The source system comprises a quartz-tungsten-halogen lamp, a xenon lamp, and a double monochromator. Two lamps are selectable and the monochromator is used with order sorting filters for the additional removal of heterochromatic stray light.

The detection system is a detector with an imaging system for radiance measurement. The detectors of a Si photodiode and a thermoelectrically cooled InGaAs are used for the radiance measurements in wavelength ranges of 360-1100 nm and 1100-1600 nm, respectively. The InGaAs detector is mounted on a small integrating sphere for uniform detection. A lock-in amplifier measures the voltage of the InGaAs detector and the incident light is chopped.

As shown in Eq. (1) describing the Sharp-Little method, the absolute reflectance is obtained from the ratio of radiance of the sphere wall to that of a sample. [2]

$$\rho_1(\lambda) = G \cdot f(\lambda) \tag{1}$$

Here, $\rho_1(\lambda)$ and $f(\lambda)$ are diffuse reflectance of a sample and the radiance ratio at wavelength of λ, respectively. G is the correction factor on the geometry of the integrating sphere. For the spectral radiance measurements at measurement port 1 and 2 in Figure 1, the detector is mounted on a rotation stage which rotates around an integrating sphere.

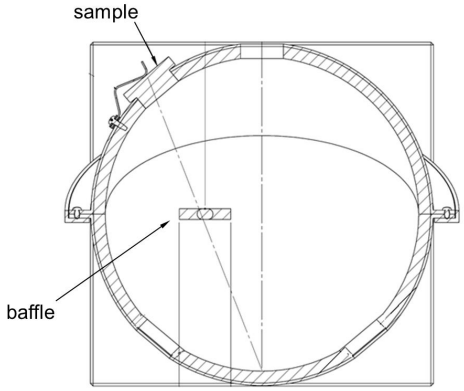

Figure 2. Schematic drawing of the integrating sphere and the white reference sample.

According to the original theory on the Sharp-Little method, G is a correction factor for the

openings, i.e., a ratio of the total surface area of the sphere to the area of the sphere excluding the openings. In this description, the reflection coating of the sphere was assumed to be very thin as well as highly reflective. To employ a real integrating sphere to the Sharp-Little method, we studied the effect of coating thickness of a sphere.[3] Based on the investigation, we designed special white samples which are inserted into a sphere opening.(Figure 2)

Figure 2 shows the integrating sphere with design for realizing the Sharp-Little method. A baffle inside the sphere blocks the firstly diffused light to the sample, which results in the absolute determination of the diffuse reflectance. The sphere was coated with Spectralon (Labsphere) and the white samples were also made of same material.

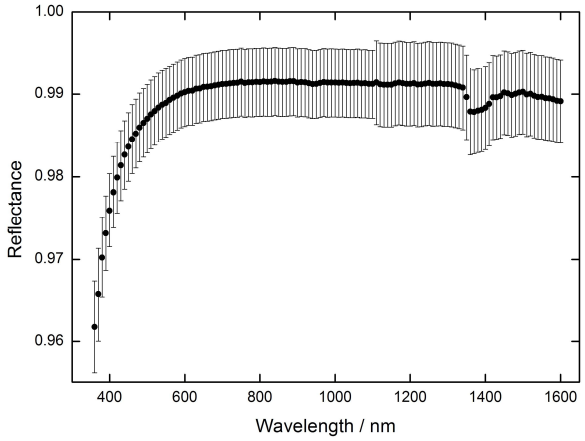

Figure 3. Spectral reflectance of a Spectralon white sample determined with the new Sharp–Little setup.

EXPERIMENTAL RESULTS

Figure 3 shows the measured diffuse reflectance of the Spectralon white standard sample. The circles are the diffuse reflectance values and the error bars correspond to the expanded uncertainties (k=2). According to Eq. (1) of the mathematical model, we evaluated the uncertainty components of a correction factor for the integrating sphere and a radiance ratio measurement of the sphere wall and the sample. In evaluating the uncertainty of the sphere correction factor, we considered the contributions of sphere geometry, port edge reflection, and sample position. For an evaluation of the radiance measurement, we considered the uncertainty terms including non-linearity of a signal, repeatability and reproducibility of a measurement, isochromatic and heterochromatic stray light, polarization, bandwidth effect, wavelength accuracy, and non-uniformity of a sample. In table 1, the uncertainty budget is summarized.

Table 1. Uncertainty budget for the diffuse reflectance measurement using the new instrument.

Uncertainty components	100×Relative standard uncertainty
Radiance ratio measurement	0.31-0.19 (depending on wavelength)
Correction factor for integrating sphere	0.08
Combined uncertainty	0.32~0.21 (depending on wavelength)

CONCLUSION

An integrating sphere-based instrument for an absolute reflectance measurement was developed based on the investigation of the Sharp-Little method. The new instrument was applied to realize an absolute scale of diffuse reflectance in the visible and near-IR region.

REFERENCES

1. C-S Kim and H-J Kong, Rapid absolute diffuse spectral reflectance factor measurements using a silicon-photodiode array, Color Res. Appl., 22, 275–9, 1997.
2. W. Budde and C. X. Dodd, Absolute reflectance measurements in the D/0◦ geometry Die Farbe 19 94–102. 1970.
3. J. Hwang, H. Cho, D.-J. Shin and K. L. Jeong, Correction of port reflection effect for integrating sphere-based reflection measurements, Metrologia, 50, 472-481, 2013.

Imaging spectrophotometer for measuring spectral reflectance 2D distribution

Khaled Mahmoud[1,2], Seongchong Park[1], Seung-Nam Park[1], and Dong-Hoon Lee[1]

[1]*Division of Physical Metrology, Korea Research Institute of Standards and Science (KRISS), Daejeon, Rep. Korea*
[2]*National Institute of Standards (NIS), P. O. Box: 136 Giza, Code No. 12211, Egypt*
Corresponding e-mail address: khaled@kriss.re.kr

We present a novel instrumentation scheme for meausuring the two-dimensional distribution of spectral reflectance based on the spectral imaging technique. It takes digital spectral images of a target sample by using a LED-based monochromatic integrating sphere source and a monochrome CCD camera. We developed a calibration algorithm to assign the digital counts of the images to the reflectance values at each wavelength. By using our proto-type instrument, we demonstrate an agreement with the results of a reference spectrophotometer within 1 % for high reflectance or within 2 % for low reflectance. This new scheme of "imaging spectrophotometer" is promising to measure the spatially resolved spectral reflectance of a complex samples only by single wavelength scan.

MOTIVATION

The standard instrument to measure the reflectance properties of an object is a spectrophotometer. This gives very precise results but the measurements are at one point [1,2]. To measure the spatial variation of the reflectance of non-homogeneous samples, the procedure will be therefore time-consuming and it is difficult to obtain the 2D distribution. Furthermore, it is an expensive instrument.This makes the researchers in the related fields to pay an attention for using imaging cameras in this kind of measurements. The question here is, can these cameras be used as measurement devices to obtain sufficiently accurate information for the target application (e.g. in this paper, measuring with a good accuracy the 2D spatial distribution of reflectance of complex samples?) If this is possible, then in summary, one can say using of imaging devices in radiometric and colorimetric applications can be cost effective, fast, single measurement captures of complete angular performance information for light sources, displays, and scattering materials [3].

MEASUREMENT SETUP

The schematic diagram of the setup is shown in figure 1. The setup comprises two main parts: 1st is the monochromatic light source which provides the monochromatic, stable and uniform illumination on the plane of the sample under test, 2nd is the CCD monochrome camera.

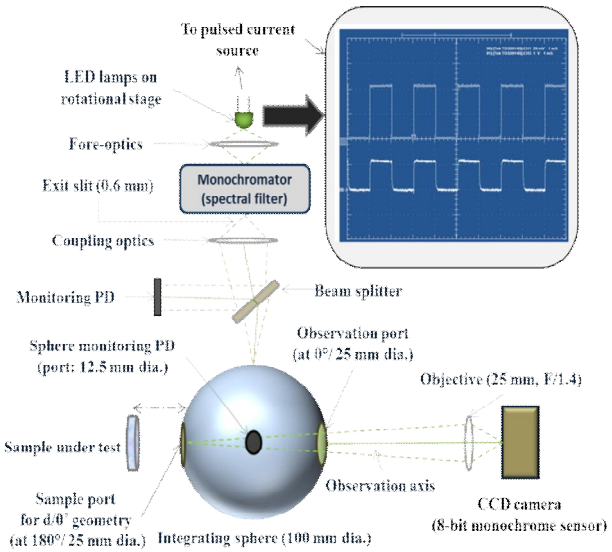

Figure 1. Schematic diagram of the setup. Diagram at the upper right corner represents time trace of light emission as detected by fast-response photodiode for one selected LED showing the temporal behaviour of the output light signal following the electric current pulse (pulse width: 0.1 ms, duty cycle: 50%).

As shown in figure 1, the source part comprises many color LEDs, monochromator used as a spectral tunable bandpass filter, integrating sphere and 2 monitoring photodiodes, first one is used to monitor the power drift just before entering to the sphere using a beam splitter, while the other used on the sphere at a north pole port to monitor the irradiance change of sphere wall for each sample under test. LEDs are driven with pulsed current pulses which provide excellent temporal characteristics and higher brightness by using high-current (much beyond currents in case of CW mode) with short duration pulses. Our sphere is PTFE based (4 inch dia.) with 4 ports each of them has a knife edge to avoid the port effect. For better spatial uniformity of

irradiance inside the sphere, there are no baffles used inside the sphere. The spectral and spatial characteristics of the source (in CW mode operation) have been discussed in details elsewhere [4].

Second part, of the setup is the CCD camera (Thorlabs, Model: DCU224M, monochrome sensor, spatial resolution: 1280×1024 pixels and ADC: 8-bit with 25 mm, F/1.4 objective) as shown in figure 1. The camera is used to capture the spectral 2D-images (frames) during the scan, while the digital pixel data acquisition could be achieved using software which we prepared for the target application using a set of API functions in a VB environment.

MATHEMATICAL MODEL

Here in this section, we will show the basic model for our measurement. Since then, "REF" will be referring to the IS monitoring photodiode and "ref" will refer to the reference white diffused standard used in the measurement with its spectral reflectance data measured by our reference spectrophotometer (Perkin Elmer, Model: Lambda1050.)

$$\rho_{DUT})_{\lambda} = \left[\frac{C_{DUT} / y_{REF-DUT}}{C_{ref} / y_{REF-ref}} \times \rho_{ref} \right]_{\lambda}$$

Where, **C** represents the camera digital counts, y_{REF} represents the monitoring photocurrent, $\boldsymbol{\rho}_{DUT}$ represents the reflectance factors, at the scan wavelength ($\boldsymbol{\lambda}$), to be measured and $\boldsymbol{\rho}_{ref}$ is the reference reflectance data. The digital counts of the camera always obtained from a pre-selected ROI corresponding to the point to be studied at the sample plane.

RESULTS AND CONCLUSION

In this work, the measurement has been made with d/0° geometry. The spectral reflectance factors of the studied samples were measured with the specular components excluded. The measurements were carried out by substitute method using a reference standard traceable to KRISS, Korea. Measurement results has been shown in figure 2, we have measured two sets of samples, one set of grey tiles with different levels of reflectance (shown in figure 2 (a)). In this case, the target scene is only grey sample. Another set of measurements has been made using a multi-color samples in one target scene (shown in figure 2 (b)) and the curves show the measured reflectance factors for different colors in the scene in comparison with the reference curve for each color.

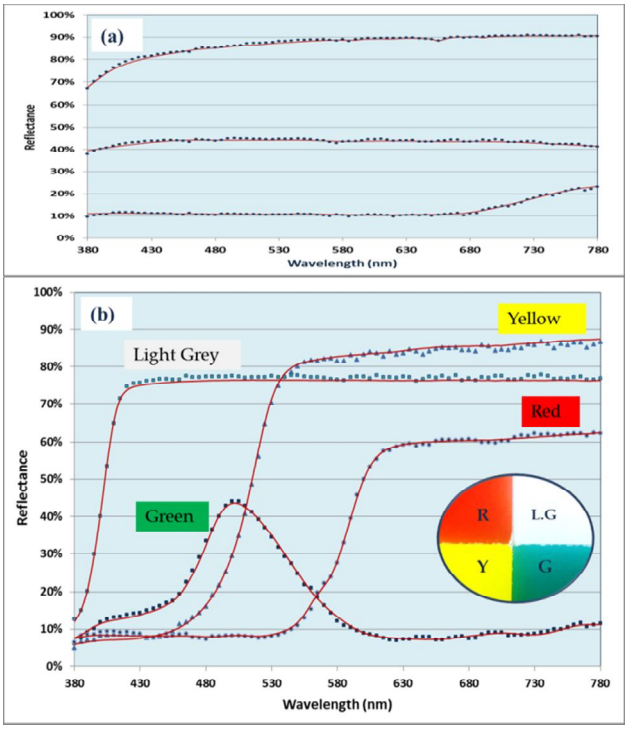

Figure 2. Measurement results of different sets: (a) Shows the measured reflectance spectra of 3 grey diffused sample tiles with different levels of reflectance as one color target, (b) Shows the reflectance of 4 colored samples (red, yellow, grey and green) in multi-color 2D target. In both (a) and (b), blue sets of dots represent the measured values and the red solid lines represent the reference data.

In conclusion, the results show a good agreement with the reference data and measurements showed a high reproducibility. The uncertainty components which are associated with the measurement, e.g. reference standard uncertainty, non-uniformity, non-linearity of the detectors, wavelength scale accuracy, repeatability etc. are under study and the evaluation of uncertainty budget is on progress. The instrument is expected to have a high potential in different related fields.

REFERENCES

1. *International Commission on Illumination*, Practical methods for the measurement of reflectance and transmittance, CIE publication, No. 130, 1998.
2. Budde W et al., Absolute reflectance measurements in the d/0◦ geometry *Die Farbe*, **19,** 94–1022, 1970.

3. Gudrun J. Klinker et al., A physical approach to color image understanding, International Journal of Computer Vision, **4,** 7-38, 1990.
4. K. Mahmoud *et al*., Measurement of normalized spectral responsivity of digital imaging devices by using a LED-based tunable uniform source, Appl. Opt., 52, 1263-1271, 2013.

BRDF Measurements with the NIST Robotic Optical Scatter Instrument (ROSI)

Heather J. Patrick[1], Clarence J. Zarobila[2], and Thomas A. Germer[1]

[1]*National Institute of Standards and Technology, Gaithersburg, MD, USA*
[2]*Jung Research and Development Corp., Washington, DC, USA*
Corresponding e-mail address: heather.patrick@nist.gov

We present spectral bidirectional reflectance distribution function (BRDF) measurements made on ROSI, a recently installed robotic arm-based goniometer at NIST. ROSI is capable of BRDF measurements at nearly any combination of polar and azimuthal incident and scattering angles, at wavelengths tunable from 480 nm to 2500 nm using a supercontinuum-based light source. Progress towards performing BRDF calibrations using ROSI will be discussed.

INTRODUCTION

The Sensor Science Division of NIST currently provides BRDF measurements of spectrally neutral samples using the NIST Spectral Tri-function Automated Reference Reflectometer (STARR).[1] STARR provides angle-resolved BRDF for in-plane geometries at wavelengths from 250 nm to 1100 nm, while measurements from 1100 nm to 2500 nm are presently limited to the normal incidence, 45° viewing (0:45) geometry. In recent years, there has been a growing demand for angle-resolved BRDF measurements at expanded in-plane geometries, as well as for BRDF at out-of-plane geometries, where the viewing direction is not in the plane of incidence.

To address these needs, we have developed ROSI, a robotic arm-based goniometer that enables BRDF measurements at arbitrary in-plane and out-of-plane viewing geometries. As recently demonstrated,[2] robotic arm goniometers allow an unobstructed view of the sample, offer direct programming of the sample face orientation, and feature high reliability and extremely good repeatability. The goniometer has been paired with a powerful supercontinuum-based tunable source, which helps overcome the spectral flux limitations of traditional lamp-based systems. In this paper, we demonstrate spectral- and multi-directional measurements with ROSI.

ROBOTIC GONIOMETER

Figure 1 is a photo of the ROSI goniometer. Linearly polarized light from the tunable source, described in detail elsewhere,[3] illuminates a 1 cm diameter spot at the sample surface. ROSI employs a six-axis robotic arm for rotation and translation of the sample, and a receiver that orbits the robotic arm. The receiver and robot are aligned and the robot programmed to maintain a constant distance between the illuminated area of the sample and a precision aperture on the receiver. As discussed in [3], the ability of the robotic arm to pitch, yaw, and roll the sample face while holding it at a fixed spatial position, along with the rotation of the receiver about the robot, enables the goniometer to reach nearly any combination of incident (θ_i,ϕ_i) and view (θ_r,ϕ_r) angles.

Figure 1. ROSI goniometer holding a white diffuse sample. The path of the incident light is shown by the green arrow. The light source is on the optical table to the left and is not visible in the photo.

The receiver consists of a precision aperture followed by a lens that images the illuminated area of the sample onto the entrance port of an integrating sphere. Two photodiodes, silicon and extended InGaAs, covering a spectral range from below 250 nm up to 2500 nm, are mounted on the sphere. For measurements of incident power, the robot moves the sample clear of the incident beam and the receiver is rotated to capture the incident power.

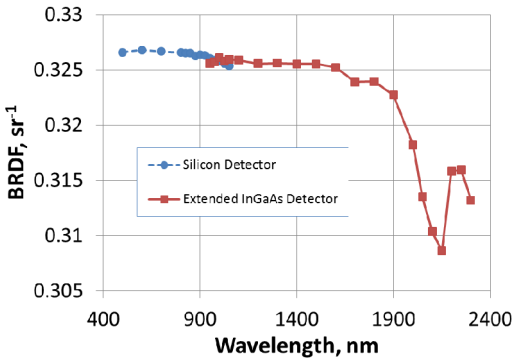

Figure 2. BRDF (unpolarized) versus wavelength. Geometry was 0:45 on a sintered PTFE sample.

MEASUREMENTS

Figure 2 demonstrates the spectral scanning capabilities of ROSI, showing an in-plane BRDF measurement at 0:45 geometry for a sintered polytetrafluoroethylene (PTFE) sample. The data were measured for vertical and horizontal polarization and the results averaged to obtain the BRDF for unpolarized light. The statistical uncertainties are at the 0.1% level or better for both detectors (k=1) over the wavelength range shown in the figure. However, there are numerous systematic error sources that will determine the ultimate accuracy achievable with ROSI. While the geometric accuracy of the ROSI goniometer is very good (repeatability of ± 0.02 mm in positioning), we must also include detector/amplifier gain and linearity uncertainty, corrections due to the finite illumination and aperture area, errors in optical alignment through the goniometer, stray light, wavelength uncertainty, polarization dependence, and others in the total uncertainty budget.[4] More details will be presented at the conference.

In Figure 3, we show the out-of-plane scanning capability of ROSI. The BRDF of sintered PTFE at 69 distinct polar and azimuthal view angles, θ_r and ϕ_r, at a fixed incident angle of θ_i = 60° and ϕ_i = 180° was measured at a wavelength of 550 nm. These data, taken from [4], show significant variation in BRDF with azimuthal angle and demonstrate the need to provide customers who view out-of-plane with calibrations at their geometry. Uncertainty analysis for out-of-plane measurements is ongoing.

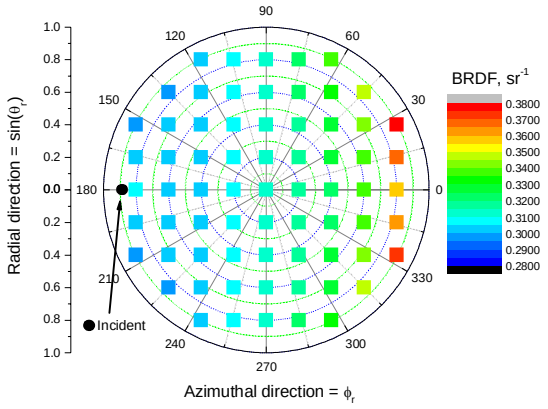

Figure 3. Angle-resolved BRDF of sintered PTFE. Squares: BRDF as a function of sin(θ_r) (radial) and ϕ_r (azimuthal). Black circle: incident angle θ_i = 60°, and ϕ_i = 180° superimposed for reference.

DISCUSSION AND SUMMARY

While we are very encouraged by our initial results using ROSI, we must fully characterize the uncertainty budget and address the need for shorter wavelength measurements in order to perform the measurements currently available in STARR. For the UV to 480 nm range, we are investigating options including coupling a high-brightness laser-induced plasma lamp into the monochromator, or frequency doubling/tripling of a tunable laser. Progress towards extending the wavelength range will be presented.

REFERENCES

1. J.E. Proctor and P.Y. Barnes, “NIST high accuracy reference reflectometer-spectrophotometer”, J.Res. NIST 101, 619-627, 1996.
2. D. Huenerhoff, U. Grusemann, and A. Hoepe, “New robot-based gonioreflectometer for measuring spectral diffuse reflection”, Metrologia, 43, S11-S16, 2006.
3. H.J. Patrick, C.J. Zarobila, T.A. Germer, V.A. Ying, C.A. Cooksey, and B.K. Tsai, “Tunable Supercontinuum Fiber Laser Source for BRDF Measurements in the STARR II Gonioreflectometer”, in Proc. SPIE 8495, Edited by L.M. Hanssen, 84950K-1-13, 2012.
4. H.J. Patrick, C.J. Zarobila, and T.A. Germer, “The NIST Robotic Optical Scatter Instrument (ROSI) and its Application to BRDF Measurements of Diffuse Reflectance Standards for Remote Sensing”, in Proc. SPIE 8866, Edited by J.J. Butler, 886615-1–12 (2013).

xD-Reflect - "Multidimensional Reflectometry for Industry" a research project of the European Metrology Research Program (EMRP)

Andreas Höpe[1], Annette Koo[2], Carsten Forthmann[1], Francisco M. Verdú[3], Farshid Manoocheri[4], Frédéric B. Leloup[5], Gaël Obein[6], Gerd Wübbeler[7], Guillaume Ged[6], Joaquín Campos[8], Kai-Olaf Hauer[1], Li Yang[9], Marek Šmíd[10], Mikhail Langovoy[7], Paola Iacomussi[11], Priit Jaanson[4], and Stefan Källberg[12]

[1]*Physikalisch-Technische Bundesanstalt (PTB), Braunschweig, Germany,*
[2]*Measurement Standards Laboratory, Lower Hutt, New Zealand,*
[3]*Universidad de Alicante, Alicante, Spain,*
[4]*Mittatekniikan Keskus, Espoo, Finland,*
[5]*Katholieke Universiteit Leuven, Gent, Belgium,*
[6]*Conservatoire national des arts et métiers, France,*
[7]*Physikalisch-Technische Bundesanstalt (PTB), Berlin, Germany,*
[8]*Agencia Estatal Consejo Superior de Investigaciones Cientificas, Madrid, Spain,*
[9]*Innventia AB, Stockholm, Sweden,*
[10]*Cesky Metrologicky Institut Brno, Brno, Czech republic,*
[11]*Istituto Nazionale di Ricerca Metrologica, Torino, Italy,*
[12]*SP Sveriges Tekniska Forskningsinstitut AB, Borås, Sweden,*
Corresponding e-mail address: andreas.hoepe@ptb.de

The general objective of the xD-Reflect research project is to meet the demands from European industry to measure the overall macroscopic appearance of modern surfaces by developing and improving methods for optical measurements which correlate with the visual sensation being evoked. In particular, the project deals with different attributes of dedicated artefacts, like "Goniochromatism", "Gloss" and "Fluorescence" properties, which will be investigated in three main work packages. Two additional transversal work packages reinforce the structure: "Modelling and Data Analysis" with the objective to give an irreducible set of calibration schemes and handling methods and "Visual Perception", which will produce perception scales for the different visual attributes.

INTRODUCTION

The appearance of a product is quite important for diverse industries, e.g. automotive, cosmetics, paper, printing, packaging, coatings, plastics, steel industries, etc., as this is frequently one of the most critical parameters affecting customer choice. For this reason, within the last 20 years, significant effort has been made by the manufacturers to produce new and sophis-ticated products which evoke specific visual effects, like metallic colours, goniochromatic pigments

Figure 1. Car painted with a goniochromatic varnishing, according to the visual perspective and the light conditions, the colour impression changes.

(Fig. 1), deep matt finishes or sparkle effects for instance [1].

The EMRP is a metrology-focused program of co-ordinated R&D funded by the European Commission and participating countries within the European Association of National Metrology Institutes (EURAMET).

Current standards and artefacts proposed by the National Metrology Institutes (NMI) to industry to ensure traceability of their measurements are limited to the visual effects they are able to generate. In colour measurements, only two standard configurations, d:0° and 45°:0°, are approved by the CIE (International Commission on Illumination). This is a really insufficient situation and not adapted for all the novel surfaces that show strong directional effects

resulting from metallic, interference or diffractive pigments [2]. The situation is even poorer for the other visual attributes like gloss [3], where the standards have not evolved since 1978 or for fluorescence, where the measurement methods comes from non-fluorescent materials and are today inadequate for application to fluorescent materials.

particular by the development and characterisation of advanced transfer standards.

- Reinforce the link with industry by creating a BRDF/BSDF public domain database for new advanced functional surfaces such as those used in the automotive industry (WP1).

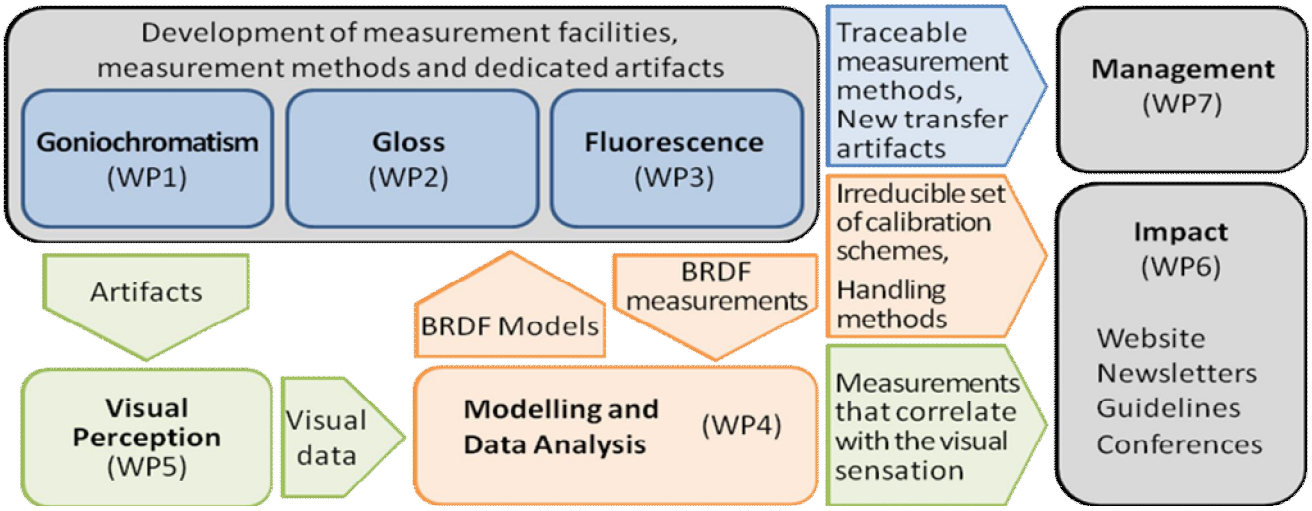

Figure 2. Structure of the project: The technical work packages WP1, WP2, WP3 deal with the describing and determining appearance attributes (Colour, Gloss, Fluorescence), WP4 provides data processing tools and the models. WP5 provides the visual scales. The results will create the impact of this project by knowledge transfer, training & dissemination and exploitation.

SCIENTIFIC AND TECHNICAL OBJECTIVES

The project consortium brings together 7 European NMIs, which have extensive experience and expertise in the field of gonioreflectometry and appearance related measurands. They are complemented by 1 NMI external to the European Community and 3 universities/ research institutes that bring their specific knowledge and experience to the consortium. The Joint-Research-Programme has the following objectives:

- Enhance the spectral and spatial resolution of reference gonioreflectometers developed by each participant, using modern detectors, conoscopic optical designs, CCD cameras, line scan cameras, modern light sources, etc. (WP1, WP2, WP3).
- Reduce the total measurement time that is a significant restriction for calibration capacities (WP1).
- Reduce the measurement uncertainties on BRDF measurements by implementing modern detectors and modern light sources in the concerned facilities and validate the results by a comparison (WP1, WP3).
- Set the optimal geometries for colorimetric measurement of advanced surfaces like metallic colours, or sparkle/graininess effects (WP1 with WP4) and gloss measurement (WP2 with WP4), in
- Propose a new standard and recommendations for gloss measurements taking into account the visual perception, the background and is adapted to modern surfaces (WP2).
- Propose new types of reference artefacts for calibration and characterisation of goniochromatism (WP1), gloss (WP2) and fluorescence (WP3).
- Improve the uncertainties in the measurement of the luminescent radiance factor of fluorescence standards (WP3).
- Propose recommendations for data handling of the large amount of data generated by BRDF measurements (WP4).
- Evaluate uncertainty and sensitivity coefficients for BRDF measurements and psychophysical measurements (WP4).
- Improve in the comprehension and the definition of the visual attributes such as colour, gloss, sparkle, graininess, fluorescence, from a visual point of view (WP5).
- Correlate visual intensity and response stimuli to the advanced BRDF measurements, material characteristics (structural features) and environment attributes (WP4, WP5).

ACKNOWLEDGMENTS

This work has been carried out within EMRP project IND52 "Multidimensional Reflectometry for Industry". The EMRP is jointly funded by the EMRP participating countries within EURAMET and the European Union.

REFERENCES

1. G. Pfaff, Special Effect Pigments: Technical Basics and Applications, 2nd ed., Vincentz Network, Hannover, 2008.
2. CIE 1:2004, "Colorimetry", 3rd ed., International Commission on Illumination, 2004.
3. T. Atamas, K.-O. Hauer, A. Höpe, Appearance measurements of goniochromatic colours, Predicting Perceptions: Proceedings of the 3rd International Conference on Appearance, p. 149 – 154, 2012.
4. G. Obein, K. Knoblauch, F. Viénot, Difference scaling of gloss: Nonlinearity, binocularity, and constancy, J. of Vision 4, 711-720, 2004.

Development of a controlled metrological gloss scale

Guillaume Ged[1], Jérémie Teisseire[2], Emmanuel Garre[2], Marc E. Himbert[1], and Gaël Obein[1]

[1]*Laboratoire Commun de Métrologie LNE-Cnam, Trappes, France,*
[2]*Unité mixte de Recherche Saint-Gobain/CNRS Surface du Verre et interfaces, Aubervilliers, France*
Corresponding e-mail address: guillaume.ged@cnam.fr

Gloss is widely used in a large variety of industrial domains. From a perceptive point of view, most gloss properties are embedded within the specular peak. Eventhough the relation between the morphology of the peak and the sensation is still unclear, there is a need for a gloss scale playing with the shape of the specular peak. We designed samples affecting in various ways the reflective behaviour of a surface. Using sol-gel chemistry processes we managed to change the morphologic parameters of the specular peak on glass artefacts. Those samples are to be characterized, using psychophysical methods in the frame of the European Union funded project Multi-dimensional reflectometry for industry (xD-Reflect). Our aim is to identify which parameters are linked to gloss perception.

THE NEED FOR A DIFFERENT GLOSS SCALE

Gloss has often been described using the notion of a reflected flux measured in various angular configurations.

However, over the last decade, studies have been unveiling a more complex description of this phenomenon. First, the gloss constancy property has implied that whatever the angular configuration in illumination and observation, gloss was intrinsic to a given artefact [1]. Secondly, the visual system does not rely on the mere amount of flux reflected by the sample. This was addressed by studies over he effect of additional diffuse illumination during gloss perception experiments. [2]. Finally, the question of gloss dimension has been asked on several papers, either based on virtual [3] or real [4] artefacts. The data related to gloss should then be embedded within and around the specular peak. We note that present increase in number of multi-angle instruments, both commercial and scientific, is strongly interwoven with such considerations from the industrial point of view.

In order to describe gloss in a way consistent with its visual perception, a morphologic characterization of the specular peak is needed. From this point, one should notice the lack for gloss scales toggling with the various topologic properties of the specular peak. The European Metrology Research Program addresses such considerations through its Joint Research Program on multidimensional reflectometry for industry – xD-Reflect. Amidst a whole work package dedicated to gloss, we aim to produce knowledge on gloss perception and measurement through psychophysical studies.

The first stage of the project consists in the manufacture of a gloss scale representative of various specular peak parameters. Parameters as its height can be adapted by changing the surface optical index, the shape of the peak can be changed by using different roughness geometries and the effect of the diffuse component of the luminous reflexion can be tested by changing the surface hue.

TUNING THE SPECULAR PEAK

We consequently need to design samples through methods affecting the specular peak. One of the possible way to do so is to use sol-gel chemistry. The structure of a sample is shown on figure 1. The substrate of our samples is Saint-Gobain Satinovo® diamond glass depolished on the back side. This glass presents the advantage of having a flat absorption spectrum in the visible range, avoiding thus a greenish coloration. On the depolished back of the sample, we deposit a mineral paint, we thus avoid multiple reflection between the glass interfaces. On the front of the sample is deposited hybrid silica layer. It is then patterned by nanoimprint [5] and turned into pure silica layer by calcination during our process.

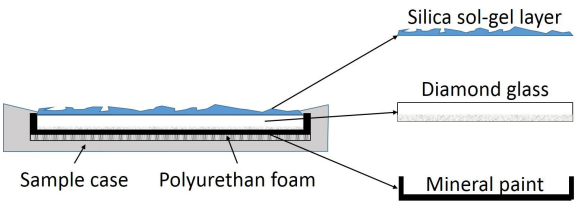

Figure 1. Samples structure.

To obtain four gloss levels, we use an imprint technique that consists in reproducing a pre-existing surface. We chose as masters four gloss levels from a ten-level coated paper scale developed by the company 2C. The result is visible on figure 2.

In order to act upon the height of the specular peak, it is possible to change the Fresnel factor, based on the optical index of the surface. By adding nanoparticles to the sol-gel we can adjust an effective optical index of the layer. On the one hand, when the nanoparticles are titanium dioxide (cristal active S5-300A® by Crystal Global), this index increases. On the other hand, when the nanoparticles are latex, these are destroyed through calcination, leaving air inclusions within the sol-gel layer, thus decreasing the effective optical index value [6].

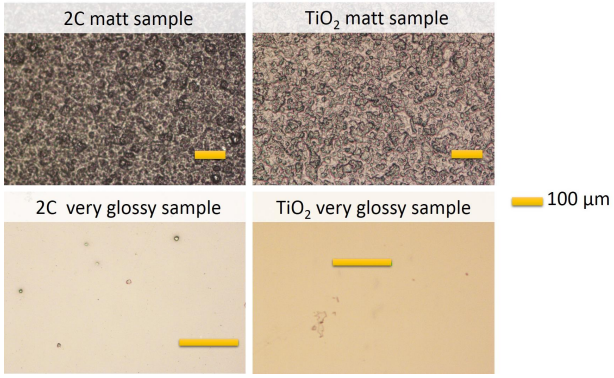

Figure 2. Optical microscope image of the original surface and its replica in high optical index sol-gel.

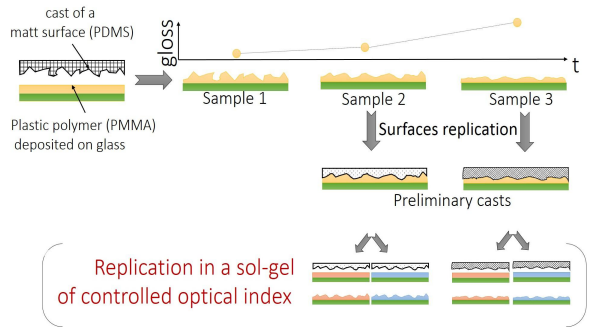

Figure 3. Generating different roughness geometries.

The roughness geometry can be obtained by replication of a matt surface within a plastic polymer. The obtained cast is afterwards, relaxed by heat exposure. The longer the sample is exposed to heat, the more the strains due to the imprinted roughness relax, increasing the sample gloss level [7]. By relaxing a matt surface presenting a microscopic roughness radically different from the mattes sample of the 3C scale, we create another gloss scale similar in terms of specular gloss values but distinct in terms of roughness geometry (Fig. 3)

Finally, we need to test the effect of contrast between the diffuse and specular part of the reflection. The easiest way to do so is to apply different hues, by using black, grey and white mineral paints- to the back of our samples.

SCALE CHARACTERIZATION

During their development, our samples were characterized using a wide panel of techniques such as profilometers, optical roughness meter, optical microscopy, field emission gun microscopy, atomic force microscopy, sprectroradiometer and glossmeter.

Through our design process, we obtained samples dispatched between four gloss levels, three hues, two roughness geometries and two optical indices. We manufactured 48 samples that are to be characterized within the xD-Reflect JRP project. These samples will be studied from both physical (BRDF, roughness…) and perceptive point of view in order to create sound knowledge on gloss perception.

REFERENCES

1. G. Obein et al, Difference scaling of gloss: Nonlinearity, binocularity and constancy, Journal of Vision, august 30, 2004 4(9), 2004.
2. F. Leloup et al, Overall gloss evaluation in the presence of multiple cues to surface, JOSA, 29, 6, 1105-1114, 2012.
3. J.Ferwerda et al, A psychophysically-based model of surface perception, in Proceedings of SPIE 2001, edited by SPIE, 2001.
4. G. Ged et al, Recognizing real materials from their glossy appearance, Journal of Vision, December 21, 2010 10(9), 2010.
5. A. Letailleur et al, Chemorheology of sol-gel silica for patterning high aspect ratio structures by nanoimprint, Chemistry of materials, 22, 10, 3143-3151, 2010.
6. F. Guillemot et al, Latex-templated silica films: tailoring porosity to get a low stable refractive index, Chemistry of Materials,22, 2822-2828, 2010.
7. J. Teisseire et al, Confinement and flow dynamics in thin polymer films for nanoimprint lithography, Applied Physics Letters, 98, 013106, 2011.

High-Resolution Setup for Measuring Photoyellowing of Transparent Materials

Anna Vaskuri[1], Petri Kärhä[1, 2], Ville Mylläri[3], Anu Heikkilä[4], and Erkki Ikonen[1, 2]

[1]*Metrology Research Institute, Aalto University, Espoo, Finland*
[2]*Centre for Metrology and Accreditation (MIKES), Espoo, Finland*
[3]*Department of Material Sciences, Tampere University of Technology, Tampere, Finland*
[4]*Finnish Meteorological Institute, R&D / Climate Change, Helsinki, Finland*
Corresponding e-mail address: anna.vaskuri@aalto.fi

Polystyrene and many other materials turn yellow when exposed to ultraviolet (UV) radiation. The photoyellowing can be quantified with a yellowness index derived from transmittance or reflectance spectrum of the material [1]. In this research, we have constructed a laser-based setup for scanning transmittances spatially from samples. First, eight polystyrene samples were exposed to UV radiation of 276 – 421 nm for different time periods using a spectrograph [2]. Then, the transmittance spectrum of each sample was spatially scanned. Based on the results, the lower exposure wavelengths of 276 – 340 nm caused significant yellowing. In addition, the absorption is higher at the lower measurement wavelengths, as can be expected with yellowing. Using the results, an action spectrum of polystyrene photoyellowing will be derived.

INTRODUCTION

Ultraviolet (UV) radiation damages materials in various ways. In polystyrene and many other materials, the degradation can be seen as the material turning yellow under UV exposure. This photoyellowing can be quantified using a yellowness index [1]. All photodegradation mechanisms including the photoyellowing are functions of the exposure wavelength. This dependence is often described with the action spectrum.

Kärhä *et al* have developed and reported a setup that uses spectrally dispersed light to expose samples, so that the action spectrum can be measured [2]. The setup is a spectrograph that disperses light from a 1 kW xenon lamp spectrally and spatially using a flat-field concave holographic grating. The grating disperses the light at the wavelength range of 276 – 421 nm onto the sample plane of 17×1.5 cm^2. Heikkilä *et al* have further used this facility to measure the UV action spectrum of the photoyellowing of regular newsprint [3]. One of the problems noted was the relatively large measurement beam of the colorimeter used causing convolution, i.e., averaging of colour over large exposure wavelength range.

In this research, we have developed a laser-based setup that can be used to measure transmittance of transparent samples with photoyellowing. A spatial scan with high resolution gives transmittances at regions exposed to different UV wavelengths that can be used to derive the action spectrum. Polystyrene samples were studied by exposing them to UV radiation for different time periods. Transmittance spectra of the samples were then measured with the laser-based measurement setup yielding the action spectrum of the UV degradation of polystyrene.

MEASUREMENT SETUP

The structure of the measurement setup is presented in Fig. 1. Three lasers ($KrAr^+$, HeNe, IR Diode) are used as light sources.

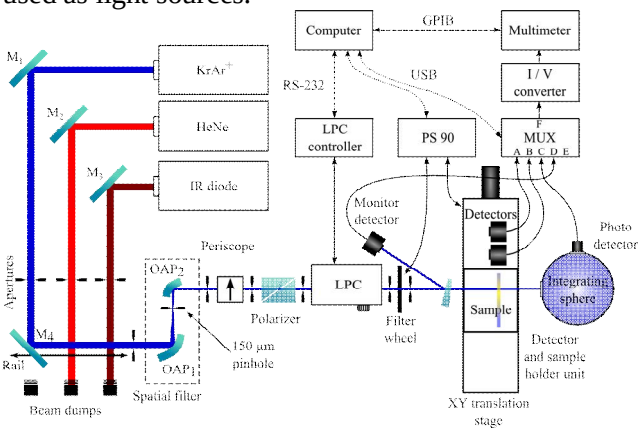

Figure 1. Measurement setup.

The laser beams are directed using mirrors M_1–M_3 towards an optical rail where one beam at a time is selected by a sliding mirror M_4. The unused beams are absorbed by beam dumps. The selected beam travels through a spatial filter constructed from two off-axis parabolic mirrors and a pinhole, for improving the beam profile. The height of the beam is adjusted with a periscope. A laser power controller (LPC) is used to stabilize the beam. The LPC requires

vertically polarized light, and thus a polarizer is mounted in front of its entrance. The material sample is attached on a motorized XY translator. An integrating sphere and a photodiode are used to measure the transmitted beam as can be seen in Fig. 2. The setup is automated and it can be controlled with LabVIEW.

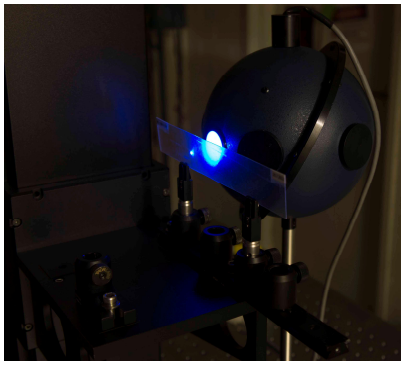

Figure 2. Polystyrene sample being measured.

RESULTS AND DISCUSSION

Eight polystyrene samples were aged under spectrally resolved radiation for time periods of 2, 4, ... , 256 h. The exposed polystyrene samples are shown in Fig. 3.

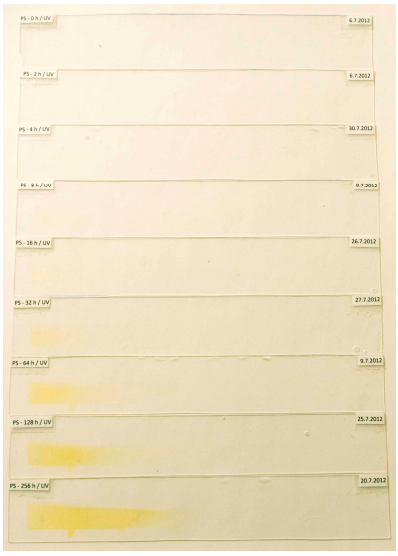

Figure 3. Polystyrene samples exposed to UV radiation.

The samples were attached one at a time to the sample holder in the laser measurement setup. The samples were then scanned horizontally with a 1-mm interval to get transmittances at various locations on the samples. The locations were further converted to corresponding exposure wavelengths using the known dispersion of the spectrograph. The measurements were repeated at seven laser wavelengths.

Figure 4(a) shows an example of the transmittance measurements carried out for the polystyrene sample aged for 256 h. As can be seen, the surface of the sample has scratches which cause systematic deviations in the transmittance level regardless of the measurement wavelength. In Fig. 4(b), the effect of the scratches has been corrected by normalizing the transmittances with respect to the transmittance measured at 676 nm. The effect of the UV-induced photoyellowing can be seen at the exposure wavelength region of 276 – 340 nm where the transmittances drop significantly as compared to longer wavelengths. The transmittance has a clear trend – the lower the measurement wavelength, the higher the absorption, as can be expected with yellowing. Spectral convolution in the data is minimal (~1 nm) due to the sharp laser beams with diameters of 1.0 – 1.6 mm used.

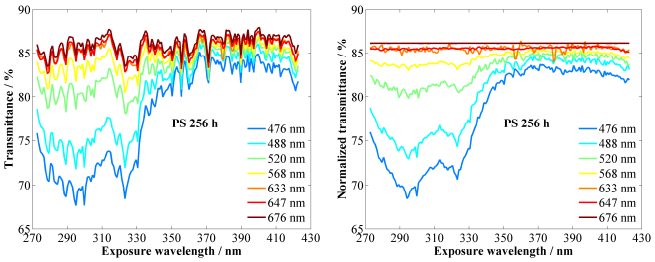

Figure 4. (a) Transmittances and (b) normalized transmittances of the polystyrene sample aged for 256 h.

After measuring all exposed samples with all measurement wavelengths, the yellowness indices [1]

$$YI = \frac{100 \cdot \left(1.28 X_{CIE} - 1.06 Z_{CIE}\right)}{Y_{CIE}} \qquad (1)$$

can be calculated in order to derive the UV action spectrum for polystyrene. In Eq. (1), X_{CIE}, Y_{CIE} and Z_{CIE} are tristimulus values of the XYZ colour space under certain illumination conditions. Interpolation between the laser wavelengths can be carried out using empirical dispersion formulae for the yellowed samples obtained with a lamp-based spectrophotometer.

REFERENCES

1. ASTM D1925–70, *Standard Test Method for Yellowness Index of Plastics*, American Society for Testing and Materials (ASTM), Philadelphia, Reapproved 1988.
2. P. Kärhä, A. Heikkilä, K. Ruokolainen, and M. Kaunismaa, A novel facility for ageing materials with narrow-band ultraviolet radiation exposure, Rev. Sci. Instrum., 82, 023107-1–6, 2011.

3. A. Heikkilä and P. Kärhä, Photoyellowing revisited: Determination of an action spectrum of newspaper, Polym. Degrad. Stab., 99, 190–195, 2014.

DIRECTIONAL REFLECTANCE CHANGES IN PRESSED AND SINTERED PTFE DIFFUSERS FOLLOWING EXPOSURE TO CONTAMINANTION AND IONIZING RADIATION

G.T. Georgiev[1], J.J. Butler[2], L. Ding[1], L.J. Graziani[3], G.A Meadows[3], and K.J. Thome[2]

[1]Sigma Space Corp., Lanham, MD, USA,
[2]NASA Goddard Space Flight Center, Greenbelt, MD, USA, [3]SGT, Greenbelt, MD, USA
Corresponding e-mail address: georgi.t.georgiev@nasa.gov

Changes in the directional reflectance properties of pressed and sintered Polytetrafluoroethylene (PTFE) diffusers induced by exposure to Vacuum UltraViolet (VUV) irradiation before and after controlled contamination are presented in this paper. A 99% reflective optical grade diffuse standards were irradiated with a VUV source. The Bidirectional Reflectance Distribution Functions (BRDF) before and after VUV irradiation were measured and compared at number of scatter geometries and wavelengths. The 8° directional/hemispherical reflectance were also measured and compared from 200nm to 2500nm. Our results indicate a measureable impact of VUV irradiation on pressed and sintered PTFE diffusers in the air-ultraviolet.

INTRODUCTION

The work was performed at Goddard Space Flight Center's (GSFC) Radiometric Calibration Facility, a secondary calibration facility with reflectance measurements traceable to those made by the Spectral Tri-function Automated Reference Reflectometer (STARR) facility at the National Institute of Standards and Technology (NIST). The facility's scatterometer, Fig.1, was used for BRDF measurements and Perkin-Elmer 150 mm integrating sphere was used for 8° directional/hemispherical measurements. This work was done in support of MODIS ongoing on-orbit calibrations. The total combined uncertainty for BRDF and 8° directional/hemispherical measurements is less than 1% (k=1).

EXPERIMENTAL SETUP

The irradiation was performed in a custom built, oil-free vacuum chamber. A McPherson 632 Deuterium VUV lamp was used to irradiate the samples 5 times for duration of 10 hours each. One hour of irradiation time in the facility corresponds to approximately one hour of solar irradiation on orbit. A typical on-orbit diffuser receives approximately 20 to 30 hours of total exposure over a 5-year mission lifetime. If there is no effect at 50 hours it is not likely to affect a sensor's calibration uncertainty budget.

Figure 1. (Right) the BRDF measurement setup; (left bottom) Diffuser mounted in the vacuum chamber; (left top) Vacuum chamber used for VUV irradiation.

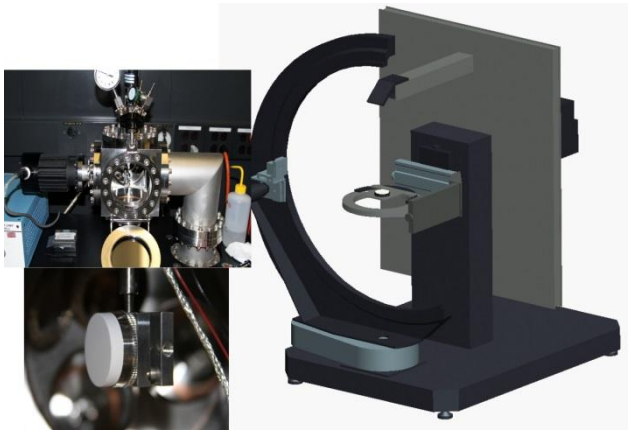

Four diffusers were studied. The BRDF of sample #1 was measured before and after VUV irradiation. Sample #2 and #3 were baked-out at 90 °C and $10E^{-6}$ Torr for duration of 24 hours [1] and measured before and after bake-out. The same samples, #2 and #3, were contaminated with Pennzane in a controlled environment as it is a common lubricant used on satellite spacecraft. Sample #4 is the control sample. We used the BRDF ratio before and after irradiation to characterize directional reflectance changes incurred in the diffusers due to irradiation and contamination.

A 60° irradiation angle was chosen to mimic a typical MODIS on-orbit diffuser solar irradiance geometry. The BRDF was measured at 250nm, 275nm, 300nm, 350nm, 400nm, 500nm, 700nm and 900nm at incident angles of 0°, 45° and 60°, and at viewing angles from 0° to 80°, in 5° steps. The 8° directional-hemispherical reflectance from 250nm to 2.5 µm was also measured and compared pre- and post-irradiation.

RESULTS AND DISCUSSION

The #1 diffuser BRDF changes, Fig.2, show non-isotropic directional effects after irradiation of 50 hours at 250nm, 300nm, 350nm and 400nm at 45° angle of incidence. There are small directional changes in BRDF at longer wavelengths, but they are within the BRDF measurement uncertainty.

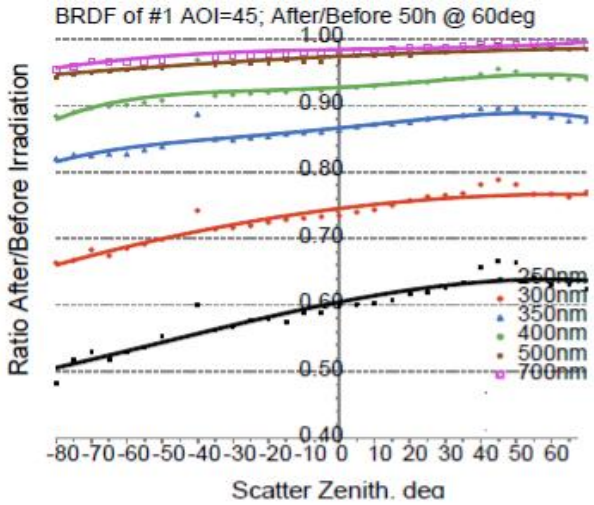

Figure 2. Ratio of BRDF before and after 50 hours irradiation.

The 8° directional/hemispherical reflectance was also measured before and after 10, 20, 30 and 50 hours of VUV irradiation. The change in the reflectance is larger in the UV, but is also seen at visible wavelengths after 50 hours of irradiation.

Our results indicate a measureable impact of VUV irradiation on pressed and sintered PTFE diffusers after controlled contamination as manifested by a directional dependent change in their reflectance in the air-ultraviolet. This effect needs to be considered in the on-orbit deployment of such diffusers. The extent of the reflectance changes depend on the following factors: (i) the irradiation geometry, (ii) the spectrum, intensity, and duration of the irradiation, (iii) the BRDF measurement geometry, and (iv) the spectral band being detected. The irradiation geometry is important because the small distance needed between the lamp source and the diffuser needed to provide the necessary energy levels means that the angle of incidence onto the diffuser varies significantly with position on the diffuser. That angle of incidence variation leads to a variation in the intensity of the irradiation and a variation in the degradation.

Even when the effects for the geometry are taken into account, Fig.3, there is a residual level of degradation that is most likely due to photolysis (or similar process) of organics. The impact on the directionality of the degradation will be larger if photolysis takes place near the surface rather than deeper in the diffuser. The larger irradiation angle should cause more UV degradation near the surface. The results from studies such as the one presented here will be of interest to the remote sensing community both in developing sensor design requirements and in providing constraints for modeling and correction efforts of satellite-based data. For example, current sensors rely on prelaunch characterization of the diffusers for the designed view geometry expected on orbit. The BRDF shape is assumed to be constant with time and the diffuser degradation monitored on orbit for a geometry that is convenient for mission operations but often does not match the sensor-diffuser view geometry. We are expanding the current work to confirm the current results and explain the possible causes of the observed directional dependent change in BRDF due to VUV irradiation in the presence of contamination. The presented data will improve our understanding of processes occurring on-orbit and their impact on the solar diffusers. The data of this study will also be compared to our previous characterization efforts of Roughened Aluminum, QVD and Mie scattering volume diffuser [2].

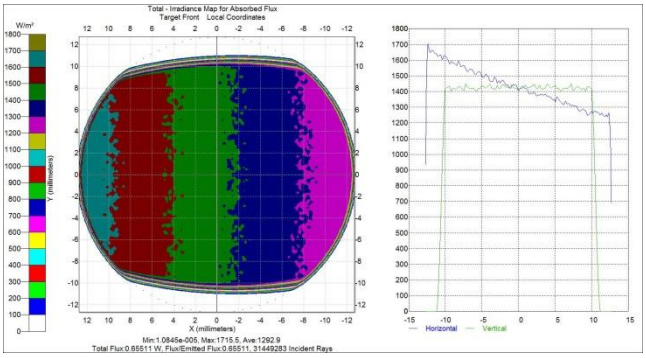

Figure 3. Trace Pro model of Irradiance map of absorbed flux from the UV exposure source.

REFERENCES

1. Haner D.A., McGuckin B.T., Bruegge C.J., "Polarization characteristics of Spectralon illuminated by coherent light", Appl. Optics, 38, 30, 6350-6356, 1999.
2. Heath D.F., Georgiev G.T., "Characteristics of a new type of Mie scattering volume diffuser and its use as a spectral albedo calibration standard for the solar reflective wavelength region", *Proc. SPIE*, vol. 8153, 81530V-1-14, 2011.

Effects of Baffle in Integrating Sphere on Total Luminous Flux Measurement

Kamol Wasapinyokul, Soontorn Chanyawadee, Rojana Leecharoen,
Santhad Chuwongin, and Ajchara Charoensook

Photometry Department, National Institute of Metrology (Thailand), Pathumthani, Thailand
Corresponding e-mail address: kamol@nimt.or.th

The baffle in an integrating sphere was studied to see its effects on the total luminous flux measurement. Effects of three baffle properties – reflectance of the back surface, size, and position, were studied through the spatial correction factor. The results show that the following conditions would make the measured value closer to the accurate one: increasing the back surface reflectance, increasing the baffle diameter, and decreasing the distance between photometer and the baffle. These were due to the difference in the non-uniformity in the sphere the baffle induced in each condition. Optimising these conditions can yield more accurate total luminous flux.

INTRODUCTION

Baffle is a crucial component in an integrating sphere used for the total luminous flux measurement. Its main function is to shield the photometer from direct rays from the light source [1]. However, the presence of a baffle introduces non-uniformity to the sphere. This destroys the ideal characteristics of the sphere and consequently the measurement results are distorted from the accurate value.

In this work, effects of the baffle on the measurement of the total luminous flux of linear-shaped lamps against a standard spherical lamp were studied. Three baffle properties – back surface reflectance, size, and position, were varied and their effects on the total luminous flux were examined through the spatial correction factor.

EXPERIMENTAL

The sphere used in this work was a 2-m LMT integrating sphere. At the centre of the left hemisphere was the photometer, in front of which was a circle baffle. The right hemisphere is movable for sphere access. The sphere inner wall was coated with LMT PHP 80 paint with a reflectance of 80%.

To study the effects of the baffle, the three properties of the baffle – back surface reflectance, size, and position, were varied. At each specific condition, the spatial response distribution function, K, of the sphere was determined as the photo-signal that the photometer could detect when a LED was direct to each position on the sphere wall. For the standard spherical lamp and the test linear-shaped lamps, their luminous intensity distribution, I, was obtained by using a mirror-type gonio-photometer.

Once K and I were obtained, the spatial correction factor, *scf*, of the lamp was consequently calculated by using the follows equation [2]:

$$scf = \frac{1}{\int_{\phi=0}^{2\pi}\int_{\theta=0}^{\pi} I^*(\theta,\phi)\,K^*(\theta,\phi)\sin\theta\, d\theta\, d\phi}, \qquad (1)$$

where $I^*(\theta,\phi)$ and $K^*(\theta,\phi)$ are the normalised I and K at the position on the sphere wall with angular co-ordinate of (θ,ϕ) [1] as shown in Figure 1.

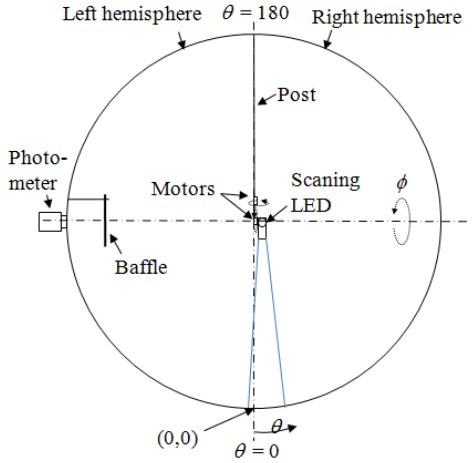

Figure 1. Schematic diagram of the integrating sphere and scanning LED used in this experiment.

The *scf* is a correction factor required in the total luminous flux measurement when the standard and test lamps have different intensity distributions. This was the case for this study where the standard lamp was spherical while the test lamp was linear. The final scf_f of a test lamp was calculated as the ratio of the *scf* of test lamp, scf_t, to that of the standard lamp, scf_s, i.e.:

$$scf_f = \frac{scf_t}{scf_s}. \qquad (2)$$

Due to the normalised nature of I^* and K^*, the value of scf_f is around one. The scf_f of exactly one means that the measured total luminous flux is equal to the accurate value. The value of less than one indicates that the measured value is higher than the accurate value, and vice versa [2].

RESULTS AND DISCUSSIONS

- ***K* of the sphere with default baffle conditions**

Figure 2 shows K of the sphere with default baffle conditions. The result was as expected where K was not uniform all over the sphere due to the presence of the baffle. At the left hemisphere, the signals around the baffle area are higher than the rest due to the reflectance of the rays around the baffle. At the right hemisphere, the signals are lower than the rest due to the shadow produced by the baffle.

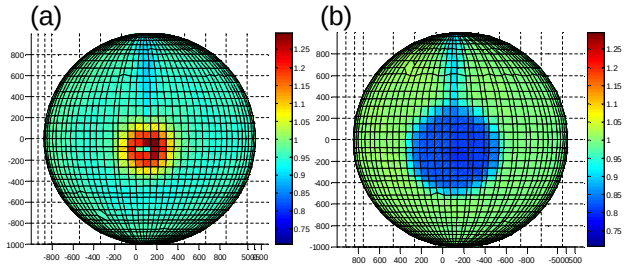

Figure 2. K of (a) left, and (b) right hemisphere, of the integrating sphere with default conditions.

- **Effects of baffle back surface reflectance**

Figure 3 shows the effects of the baffle back surface reflectance on scf_f of five test lamps of different lengths and colour correlated temperatures (CCTs).

The scf_f of all lamps increased, closer to one, with the increase of the reflectance. This means that, when the baffle back surface was higher, the measured total luminous flux would be closer to the accurate value. This was supposed to be because less light was absorbed by the baffle when the reflectance becomes higher, giving more accurate value.

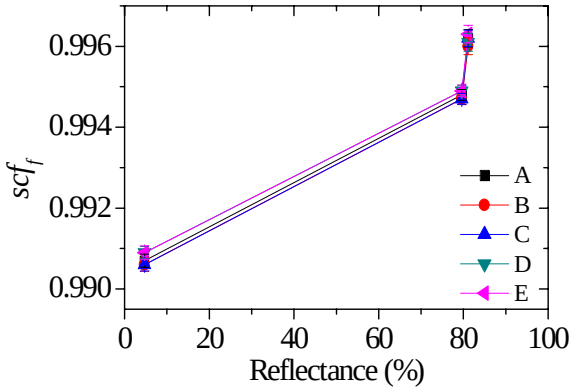

Figure 3. Relation between scf_f and baffle back surface reflectance.

- **Effects of baffle size**

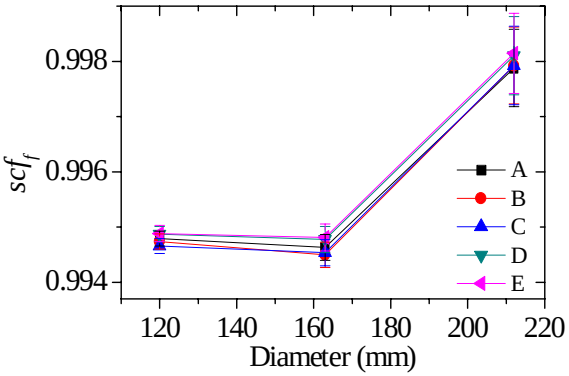

Figure 4. Relation between scf_f and the baffle diameter.

Figure 4 shows the relation between the baffle diameter and scf_f of the test lamps. The results show that scf_f tends to increase closer to one when the baffle is bigger. This is because a bigger baffle would give a bigger shadow area (Figure 2b). This yielded a smaller K^* and hence bigger scf_f, regarding Eq (1).

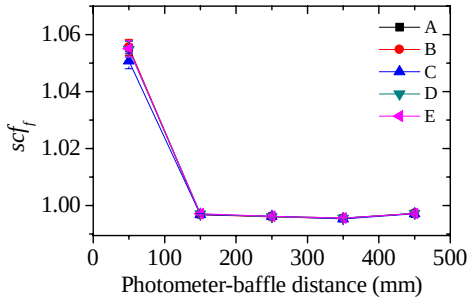

Figure 5. Relation between scf_f and the photometer-baffle distance.

- **Effects of baffle position**

Figure 5 shows the effects of the photometer-baffle distance on scf_f of the test lamps. The results are that scf_f tends to increase closer to one when the baffle was closer to the photometer. When the distance was very close (50 mm), scf_f becomes greater than one.

Effect of the closer baffle to the photometer is similar to that of a bigger baffle as it gives the bigger shadow area, hence a smaller K^* and bigger scf_f.

CONCLUSION

Baffle in an integrating sphere affects the total luminous flux measured to be deviated from accurate. This is due to the non-uniformity it induces. By optimising its conditions, more accurate measured total luminous flux can be achieved.

REFERENCES

1. C. DeCusatis, Handbook of Applied Photometry, Springer, 82-85, (1997).
2. Y. Ohno, Realization of NIST 1995 Luminous Flux Scale using Integrating Sphere Method, J. of Illuminating Engineering Society, 25(1), 13-22, 1996.

Photometric analysis of LEDs by Zernike polynomials

José Luis Velázquez, Alejandro Ferrero, Alicia Pons, Joaquín Campos, and María Luisa Hernanz

Departamento de Imágenes, Visión e Instrumentación Óptica, Instituto de Óptica, CSIC, Madrid, Spain.
Corresponding e-mail address: jl.velazquez@csic.es

The group of optical radiation measurements (GIMRO) is developing a method to characterize photometric properties of the LEDs by using the Zernike polynomials. This new method allows the properties more fundamentals of LEDs, as the divergence, the anisotropy, the optical axis, the total flux and the Lambertianity of the source to be obtained.

INTRODUCTION

Zernike polynomials [1] are used in many cases by its versatility to describe different phenomena. In this work we present a methodology to describe the photometric properties of LEDs with the Zernike polynomials.

These polynomials are a complete set of orthogonal polynomials over the interior of the unit circle and, thus, they allow aberration function to be expanded in a power series.

The Zernike polynomials are defined in polar coordinates (ρ,θ). In our case we have expressed them in spherical coordinates (ϑ,φ), changing [ϑ=asin(ρ), φ=θ] in order to expand the luminous intensity and luminance distribution in power series. Using this transformation of the Zernike polynomials it is possible to express the angular emission of LEDs as a summation of well-known polynomials, whose corresponding weights allow the photometric properties and quantities of the LED emission to be interpreted and estimated in a straightforward way.

METHOD

The angular distribution of the luminous intensity of 18 LEDs from different manufacturers (6 LUXEON REBEL, 7 CREE XLAMP and 5 OSRAM GOLDEN DRAGON high-power LEDs) and with different spectral distributions (blue, red, green, polar white, warm white and neutral white) has been measured. Measurements were carried out using the goniophotometer [2] developed for this purpose in the IO-CSIC, consisting of two stages of rotation to vary the polar angle and azimuth angle and four stages of linear displacement for centering the LEDs.

From these measurements, the most important Zernike terms to fit the angular distribution of the luminous intensity were determined: the constant term (with weight C_{Cons}), the defocus function (C_{Def}), the primary spherical (C_{Sph}), the vertical coma (C_{ComaV}), the horizontal coma (C_{ComaH}), the vertical tilt (C_{TiltV}), the horizontal tilt (C_{TiltH}), the vertical astigmatism (C_{AstigV}) and the oblique astigmatism (C_{AstigO}), as they are usually referred in optics..

By fitting the Zernike polynomials to the measured luminous intensity, coefficients (or weights) are obtained which allow the angular distribution to be described with a few parameters. Some intrinsic properties of the LEDs emission have been matched by using these coefficients: the divergence, the optical axis, the anisotropy (obtained by the standard deviation), the total luminous flux and the Lambertianity of the source. These parameters will be obtained using the following expressions:

Divergence:

$$\vartheta = \arcsin\left(\sqrt{\frac{-\sqrt{\frac{3}{5}}C^I_{def} + 3C^I_{Sph} \pm \frac{\sqrt{3C^{I\ 2}_{\mathrm{Def}} - 3\sqrt{5}C^I_{\mathrm{Cons}}C^I_{\mathrm{Sph}} + 3\sqrt{15}C^I_{\mathrm{Def}}C^I_{\mathrm{Sph}} + 30C^{I\ 2}_{\mathrm{Sph}}}}{\sqrt{5}}}{6C^I_{\mathrm{Sph}}}}\right) \quad (1)$$

Optical Axis:

$$\vartheta_0 = \arccos\left(\frac{1}{\sqrt{\left(2\frac{C^I_{\mathrm{TiltV}}}{C^I_{\mathrm{Cons}}}\right)^2 + \left(2\frac{C^I_{\mathrm{TiltH}}}{C^I_{\mathrm{Cons}}}\right)^2 + 1}}\right) \quad (2)$$

Total flux

$$\Phi^I = \int_0^{\pi/2}\int_{-\pi}^{\pi} R^I_{teory}[\vartheta,\varphi]\sin(\vartheta)\,d\vartheta\,d\varphi = 2\pi\left(C^I_{Cons} + \frac{C^I_{Def}}{\sqrt{3}} + \frac{C^I_{Sph}}{\sqrt{5}}\right) \quad (3)$$

Lambertianity

$$Lamb = \frac{C^L_{Cons}}{\sum_{i=1}^{36} C^L_i} \quad (4)$$

RESULTS

Results for some CREE XLAMP LEDs are shown in this section. These results can be compared with the manufacturer's values only in the case of the divergence and the total flux. For the rest of the intrinsic properties, the manufacturer doesn't provide any information.

The divergences of every LED, estimated as the full width at half maximum (FWHM) is shown in Table 1. The manufacturer provides a divergence of 90º for all the LEDs. The value of the green LED is the closest to the value given by the manufacturer.

Table 1. Divergence values (and their expanded uncertainties) obtained for some of the CREE XLamp LEDs.

	Divergence coef. / º
White	81.827 (0.001)
Blue	82.953 (0.001)
Red	73.381 (0.001)
Green	92.353 (0.001)

The spherical coordinates of the direction of the optical axis are shown in Table 2, the first column corresponds to the azimuthal angle (φ_0) and the second one to the polar angle (ϑ_0).

Table 2. Spherical coordinates of the direction of the optical axis (and their expanded uncertainties) obtained for some of the CREE XLamp LEDs .

	Azimuthal optical axis / º	Polar optical axis / º
White	187.68 (0.02)	2.46 (0.03)
Blue	99.01 (0.06)	2.85 (0.03)
Red	124.15 (0.01)	8.32 (0.01)
Green	160.98 (0.01)	6.27 (0.01)

The anisotropy of the emission of the studied LEDs is shown in Table 3. This parameter gives insight of the variation of the emission of the source across different directions. It is observed that the emission of the blue LED is the most isotropous, since it presents the lower anisotropy coefficient value.

Table 3. Anisotropy coefficient obtained for some of the CREE XLamp LEDs .

	Anisotropy coef.
White	0.646
Blue	0.082
Red	0.905
Green	0.688

Calculated and manufacturer's total flux are shown in Table 4.

Table 4. Total flux (and their expanded uncertainties) obtained for some of the CREE XLamp LEDs.

	Experimental Total Flux coef. / Lm	Theoretical Total Flux coef. / Lm
White	72.4684 (0.0021)	73.9
Blue	20.1307 (0.0005)	18.1
Red	38.1167 (0.0011)	39.8
Green	64.0868 (0.0018)	51.7

Lastly, a coefficient to account the Lambertianity, which should be 1 for the Lambertian radiator, is given in Table 5.

Table 5. Lambertianity coefficients (and their expanded uncertainties) obtained for some of the CREE XLamp LEDs .

	Lambertianity coef.
White	0.58 (0.02)
Blue	0.61 (0.03)
Red	0.54 (0.02)
Green	0.50 (0.02)

CONCLUSION

We have proposed a method to characterize photometric properties of the LEDs using the Zernike polynomials, which allow the angular emission of LEDs to be expressed as a summation of well-known polynomials.

By fitting the Zernike polynomials to the measured luminous intensity, coefficients (or weights) are obtained which allow the angular distribution to be described with a few parameters. Some intrinsic properties of the LEDs emission have been defined and calculated using these coefficients: the divergence, the optical axis, the anisotropy, the total luminous flux and the Lambertianity of the source.

One of the advantages of the proposed method is that it allows us to generate a model to reconstruct the emission of the angular distribution with a few parameters.

REFERENCES

1. A. Khotanzad, Y. H. Hong, Invariant Image Recognition by Zernike Moments, IEEE, 12-5, 489-497, 1990.
2. J. L. Velázquez, A. Ferrero, M. López, A. Pons, A. Villamarín, J. Campos y A. Sperling, Angular distribution of the averaged luminous intensity of low power LEDs transfer standards, SPIE, 8785-87858W, 2013.

Natural and Accelerated Ageing of Solid State Lamps

Petri Kärhä[1,2], Hans Baumgartner[1], Anna Vaskuri[1], Dominique Renoux[3], and Erkki Ikonen[1,2]

[1]Metrology Research Institute, Aalto University, Espoo, Finland, [2]Centre for Metrology and Accreditation (MIKES), Espoo, Finland, [3]Laboratoire National de Métrologie et d' Essais, Trappes Cedex, France

Corresponding e-mail address: petri.karha@aalto.fi

We present results on natural ageing of solid state lamps based on LEDs for nearly three years of burning time. These results are compared to ageing of similar lamps at two elevated temperatures. Raising the temperature to 45 °C reduces the life times on the average by a factor of 3.2. For heating to 60 °C, the corresponding acceleration factor is 4.6. A lamp type was found that is a promising candidate as a reference standard lamp with fluctuation of 0.2 % in luminous flux during 20,000 burn hours.

INTRODUCTION

Due to banning incandescent lamps, general lighting will gradually turn into using solid state lamps (SSL) based on light emitting diodes (LED). In some cases, it is natural to replace with SSLs also the standard lamps used for calibrating measurement equipment. In such use, stability, both short and long term, is an important issue.

Generally SSLs age rather fast when taken into use but after approximately 100 h of use, degradation slows down. The expected life times are long, tens of thousands of hours. Thus ageing the lamps throughout their expected life time to predict their behaviour is extremely time consuming. Methods to predict life time behaviour in significantly shorter time frames are needed.

We have studied possibilities to predict long term behaviour of SSLs from their behaviour under accelerated ageing, and from the short term ageing, according to [1,2]. Predictions are compared with results of long term natural ageing.

MEASUREMENTS

Five types of SSLs, four from Osram and one from Philips, have been studied for their ageing both naturally and accelerated.

Four specimens of each lamp type are ageing naturally under room conditions since May 2011, already for almost three years (Fig. 1). Photometric properties of the lamps are characterised approximately every three months to see how the lamps degrade. The tests include measurements of luminous flux, electrical power, luminous efficacy and colorimetric properties. The expanded uncertainty of luminous efficacy measurements is 1.2% – 2.9% depending on the electrical and geometrical properties of the lamps [3]. The uncertainty in luminous flux is 1.1% – 2.2%.

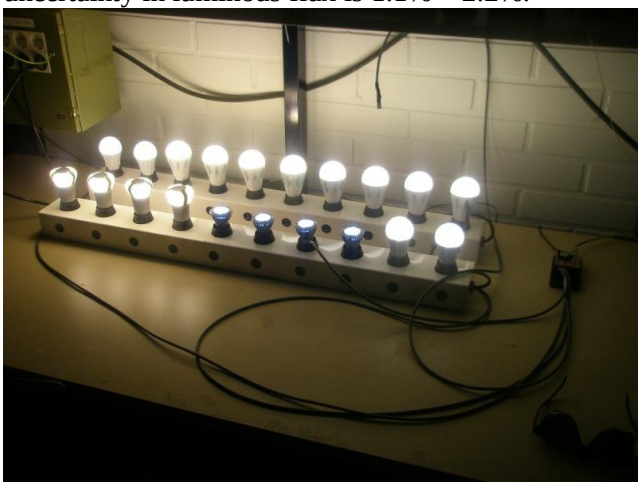

Figure 1. Four specimens of five lamp types undergoing natural ageing in room conditions.

Specimens of the same lamp types were aged under accelerating conditions as well. The acceleration was accomplished by using the lamps for 6 months at the elevated temperatures of 45 °C and 60 °C. The same photometric properties as with the natural ageing were measured every two months.

RESULTS AND DISCUSSION

Only three of the lamp types studied aged in the classical sense, i.e., their luminous flux decreased, as can be seen in Fig. 2. With lamp type D, the luminous flux has remained constant for 20,000 h, and with lamp type A, it even increased for 8,000 h. Similar trends were observed in luminous efficacy measurements. The electrical currents drawn by the lamps varied significantly less as compared to the photometric properties.

The accelerated tests show similar behaviour but faster, which is demonstrated in Fig. 3 for lamp type B. Three specimens of the lamp were aged at 45 °C and three specimens were aged at 60 °C. The figure

presents the averages of the decaying luminous fluxes and the corresponding natural ageing from Fig. 2. The acceleration can be seen in the derivatives of the exponential decays.

Raising the temperature to 45 °C accelerates ageing by a factor of 3.2, as defined by the ratios of the expected lifetimes L_{70} or L_{50} [1] at room temperature divided by the expected lifetimes at the raised temperature. For heating to 60 °C, the acceleration factor is 4.6.

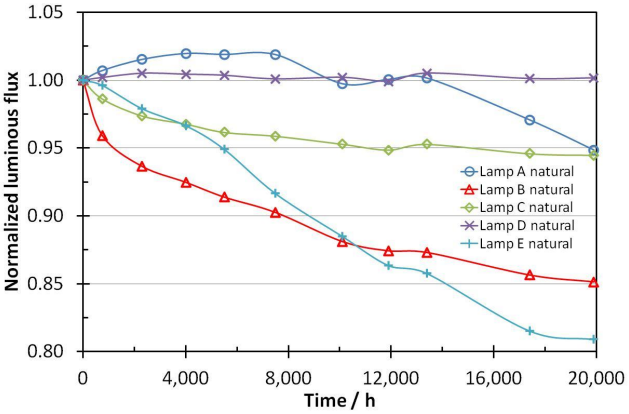

Figure 2. Average change of luminous flux under natural ageing as a function of time for five lamp types. The expanded uncertainty is of the order of 1.1% – 2.2%.

Ageing can also be analyzed by multiplying the time scales of the accelerated results so that the shapes of the curves overlap. This results in lower accelerating factors of 1.3 and 3.0 on the average for the 45 °C and 60 °C temperatures, respectively. The difference is explained by the way the data are treated. In the IESNA method for predicting lifetimes [2], the lifetime is predicted using the last 50% of the measurement points only, if ageing time exceeds 10,000 h. By looking at Figs. 2 and 3, it is quite obvious that an exponential fit to the early data or to the late data produces different lifetime estimates.

The lamps not showing classical ageing were omitted from the lifetime analysis, although e.g. the increase in the luminous flux noted for the lamp type A seemed to be accelerated by raising the temperature as well.

The standard deviation of the luminous flux values for lamp type D is 0.2% during the 20,000 burn hours. For individual lamp specimens, the standard deviations were 0.2% – 0.5%. This lamp type would be an excellent candidate as a reference standard lamp due to its stability.

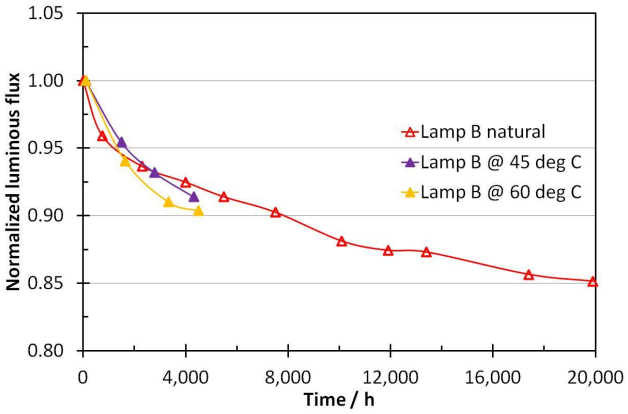

Figure 3. Decay in the luminous flux of one lamp type at room temperature (red open triangles), at 45 °C (purple closed triangles), and at 60 °C (orange closed triangles).

More details on the results and further analysis will be presented in the conference. Possibilities to predict long term behaviour from short term measurements will be discussed

ACKNOWLEDGMENT

The work leading to this study was partly funded by the European Metrology Research Programme (EMRP) ENG05 Project "Metrology for Solid state Lighting." The EMRP is jointly funded by the EMRP participating countries within EURAMET and the European Union.

REFERENCES

1. IES LM-80-08, *IES Approved Method for Measuring Lumen Maintenance of LED Light Sources*, Illuminating Engineering Society of North America, New York, 2008.
2. IES TM-21-11, *Projecting Long Term Lumen Maintenance of LED Light Sources*, Illuminating Engineering Society of North America, New York, 2011.
3. T. Poikonen, T. Pulli, A. Vaskuri, H. Baumgartner, P. Kärhä, and E. Ikonen, Luminous efficacy measurement of solid-state lamps, Metrologia, 49, S135–S140 (2012).

Characterization of thin films for thickness non-uniformity

S. Pourjamal[1], H. Mäntynen[1], P. Jaanson[1,2], F. Manoocheri[1,2], and E. Ikonen[1,2]

[1] *Metrology Research Institute, Aalto University, Espoo, Finland*
[2] *Centre for Metrology and Accreditation (MIKES), Espoo, Finland*

Here the characterization methods and instrumentation for obtaining experimental results for the optical parameters and thickness profile of SiO_2 thin-film samples are presented. These results are based on spectral reflectance data at multiple sample spots and angles of incidence including 6°, 15°, and 30°. The optical parameters of the SiO_2 coatings derived from the reflectance results are compared with those determined from the near-normal and oblique incidence of the central spot of the samples. Preliminary results indicate that the characterizations are consistent and agree within 1 nm and 17 nm for the nominal film thicknesses of 300 and 6000 nm, respectively.

INTRODUCTION

As technology grows towards smaller and thinner devices, there is a need for accurate measurements of surface properties. Therefore the accurate measurement and analysis of thin film non uniformity are necessary for establishing appropriate film quality control methodologies. This requires reliable methods to measure optical properties of different parts of thin film materials with a high degree of accuracy. This contribution discusses the non-uniformity effects of SiO_2 thin films on the optical properties measured by a gonioreflectometer [1] and an industrial spectrometer [2] which are described in the next section.

CHARACTERIZATION METHOD OF OPTICAL THIN FILM COATING

The optical parameter results obtained during the analysis are compared with those of published refractive-index values for the silicon substrate [3]. The reflectance measurements were performed with an absolute gonioreflectometer that has been built at Aalto University and with the Perkin-Elmer spectrophotometer at 6° and 30° incident angle. The effect of the systematic factors in the measurements is discussed in [4]. In the analysis of SiO_2 thin-film samples, we use a mathematical model that considers a thin homogeneous layer of a dielectric material deposited on a macroscopically thick plane-parallel substrate [5]. We mostly use the Cauchy formula to describe the refractive index of the SiO_2 thin-film layer.

The gonioreflectometer instrument has a double monochromator-based source system providing a collimated beam. The polarization state of the beam is defined by the Glan–Taylor polarizing prism. The linearly polarized beam is incident on the test sample mounted in a sample holder that consists of a rotary turntable and a linear translator. The intensity of the incident and the reflected beams is measured alternately by a detector mounted on another turntable that has a common axis of rotation with that of the sample holder unit. Silicon and InGaAs photodiodes are used as the detector for the measurements in the wavelength ranges from 300 to 900 nm and from 900 to 1480 nm, respectively. The estimated standard uncertainty in the reflectance measurements for the wavelengths from 300 to 700 nm is 0.2% and varies between 0.5% and 1% at the longer wavelengths.

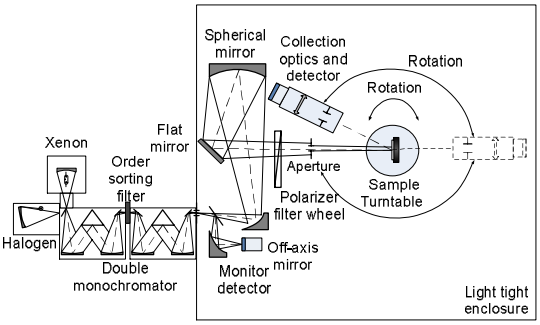

Figure 1. Schematic of gonioreflectometer's optical system.

The optical parameters of the SiO_2 layer are determined from the measured reflectance spectra separately for each angle of incidence by fitting simultaneously the results obtained with s and p-polarization over the wavelength range of interest.

PRELIMINARY RESULTS

The analysis of the determined refractive indices for each set of the reflectance data did not reveal any reasonable absorption in the SiO_2 layer. Thickness

measurement results of Si wafer 3 are presented in Figure 2. The layered model which is used to describe the sample is Si/roughness/SiO_2/roughness/air. Mean relative difference between modeled and measured data for 6° angle of incidence is 0.18%, which proves good compatibility between the results. Roughness layers were modeled as Bruggeman EMA layers with 50 % of each material of the surrounding layers [6]. Fitted surface roughness thickness is 5.1± 1.5 nm.

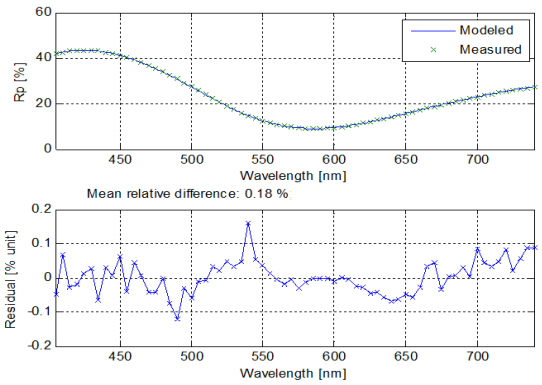

Figure 2. Thickness fitting results of the central spot of Si wafer 3at 6° angle of incidence.

Results of the thickness fits for measurements at 6° and 30° incidence angles for Si wafer 3 are presented in Table 1. The results indicate small thickness nonuniformities in the *x* direction of the wafer. However, there is a slope in *y* direction. As it's clear from the results, there is a good agreement in thickness slope results for different angles of incidence. The wavelength dependence of the residual between the measured and fitted results increases when fixed index of refraction is used for the thin film material in the model. This issue will be addresses in detail during the conference.

ACKNOWLEDGEMENT

This research was performed under the European Metrology Research Program project Thin Films (Metrology for the manufacturing of thin films).

Table 1. Fitted spot thicknesses of Si wafer 3 in the measurement coordinates for 6° and 30° angles of incidence. *u*(*t*) indicates the standard uncertainty of film thickness.

x [mm]	*y* [mm]	Angle of Incidence (°)	thickness [nm]	*u*(*t*) [nm]
0	0	6	298.1	0.35
-20	0	6	298.1	0.36
20	0	6	298.0	0.36
0	-20	6	297.6	0.79
0	20	6	299.2	0.89
0	0	30	299.1	0.18
-20	0	30	299.1	0.17
20	0	30	299.0	0.19
0	-20	30	298.2	0.20
0	20	30	300.2	0.22

REFERENCES

1. S. Nevas, F. Manoocheri, and E. Ikonen, "Gonioreflectometer for measuring spectral diffuse reflectance," Appl. Opt. 43, 6391–6399, 2004.
2. Lambda 900 UV/VIS/NIR spectrometer, fixed angle reflectance accessory, Perkin Elmer corporation, USA.
3. C. M. Herzinger *et al*, "Ellipsometric determination of optical constants for silicon and thermally grown silicon dioxide via a multi-sample, multi-wavelength, multi-angle investigation" J. Appl. Phys. 83, 3323-3336, 1998.
4. A. V. Tikhonravov, M. K. Trubetskov, M. A. Kokarev, T. V.Amotchkina, A. Duparré, E. Quesnel, D. Ristau, and S. Günster, "Effect of systematic errors in spectral photometric data on the accuracy of determination of optical parameters of dielectric thin films," Appl. Opt. 41, 2555–2560, 2002.
5. J. A. Dobrowolski, F. C. Ho, and A. Waldorf, "Determination of optical constants of thin film coating materials based on inverse synthesis," Appl. Opt. 22, 3191–3200, 1983.
6. S. Bosch, J. F. Borrull, N.Leinfellner, A. Canillas, "Effective dielectric function of mixtures of three or more materials: a numerical procedure for computations," Surface Science 453, 9–17, 2000.

Improving the Traceability of Fluorescence Measurements for Practical Applications in Colorimetry

Joanne C. Zwinkels, William Neil, and Mario Noël

National Research Council of Canada, Ottawa, Canada)
Corresponding e-mail address: joanne.zwinkels@nrc-cnrc.gc.ca

The traceability of absolute fluorescence calibrations for colorimetric applications has been a concern for several years because this traceability is to a fluorescence scale realized using the CIE two-monochromator reference method with a bidirectional geometry (45°:0 or 0:45°) whereas for many important applications of fluorescence colorimetry, e.g. for paper and textiles, the measurement geometry is hemispherical using an integrating sphere. To address this need for more direct traceability, the National Research Council of Canada (NRC) is developing a new versatile fluorescence instrument that can be configured for measurements under different geometries, including bidirectional and hemispherical. This paper will discuss the characterization of this new instrument and its performance validation by measurement comparisons with the NRC well-established reference facilities for diffuse reflectance and bidirectional fluorescence.

INTRODUCTION

The CIE recommended method for high-accuracy fluorescence measurements for colorimetric applications [1] is the two-monochromator method with a bidirectional geometry (45:0 or 0:45). For this reason, reference instruments that are used to realize radiometric scales for fluorescence measurements are based on this geometry. However, the recommended test methods for many practical applications in colorimetry, e.g. the measurement of paper [2] and textiles [3], specify a hemispherical geometry. This problem of transferring this scale from a directional geometry to a hemispherical geometry has been a concern for the past several years and different methods have been used to reduce this transfer error. In particular, the authorized laboratories for optical property measurements in accordance with ISO standards for the paper industry have developed a harmonized procedure for this geometric correction. This involves calculating a constant geometric correction factor to the reflected component only of the bidirectional calibration result for the fluorescent paper standard so that it agrees with the average measured reflectance of this paper in an ISO-conforming instrument (d:0 geometry) over the wavelength range which is not affected by emission (620-700 nm). While this empirical approach has provided satisfactory measurement precision, it has compromised the traceability of these fluorescence measurements.

GONIOSPECTROFLUORIMETER

The NRC has been providing traceable fluorescence calibration services for more than 15 years [4] using the NRC Reference Spectrofluorimeter (RS) which has been recently extended for measurements in the NIR range [5]. However, this traceability is strictly to a fixed bidirectional geometry (45a:0) and the illuminated sample area is ~10 mm diameter.

To address the need for traceable fluorescence calibrations for practical colorimetric applications, requiring different measurement geometries and larger sampling areas, the NRC is developing a new reference goniospectrofluorimeter (GSF). This instrument uses scanning monochromators in both the excitation and emission paths. The source illumination is a 400 W Xe arc lamp and a portion of this incident beam is directed by means of a quartz beamsplitter to a Si diode monitor detector. The monochromator gratings and optics have been optimized for excitation that extends in the UV to 240 nm and a measurement range that spans the visible from 380 - 800 nm, which is needed for high-accuracy colorimetric evaluation of materials containing fluorescent whitening agents. The analysing detector is a thermoelectrically cooled PMT and the instrument has been made light-tight to allow operation in DC mode which has significantly improved its noise performance. The large sample compartment can accommodate the following sampling accessories: 1) an 8 sample gonio-stage to investigate the angular distribution of sample fluorescence; 2) a 300 mm diameter integrating sphere for hemispherical fluorescence calibrations;

and 3) an annular reflector ring for bidirectional (45°a:0) fluorescence calibrations. Another highly desirable feature of this instrument is a large sample beam which measures 25 mm in diameter and therefore provides a more representative calibration result for real samples which exhibit spatial non-uniformity.

RESULTS

The GSF has been well-characterized for its wavelength uncertainty, degree of polarization, bandpass error, stray light, and noise. To obtain traceability to radiometric scales, the instrument has been calibrated using physical transfer standards (calibrated source, detector, diffusing reflector) to technically correct and normalize the excitation and emission spectra to obtain data on an absolute reflectance scale.

The accuracy of this instrument is being evaluated by comparison of measurements results for both non-fluorescent and fluorescent standards calibrated using NRC's well-characterized reference and calibration facilities for diffuse reflectance [6] and bidirectional fluorescence [4,5]. Figure 1 shows an example of the reflected-only radiance factors of a fluorescent white paper measured in 0:45 geometry on the GSF and compared with the result measured on the RS.. It can be seen that these early results show agreement of 0.4-1.5% depending upon wavelength.. Work is continuing to further reduce stray light errors and correct for polarization effects.

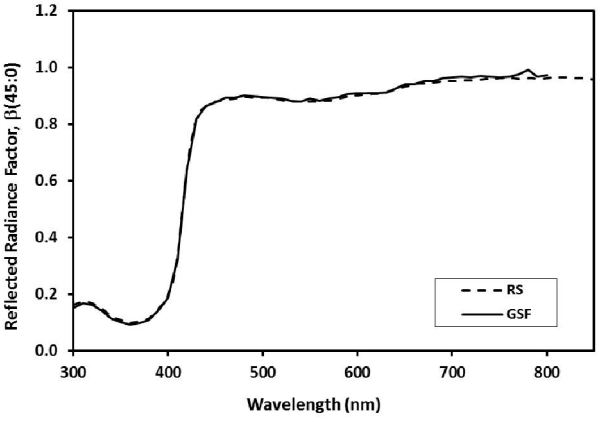

Figure 1. Comparison of bidirectional (0:45) reflected radiance factor of a fluorescent white paper standard measured on the NRC Reference Goniospectrofluorimeter (GSP) and the NRC Reference Spectrofluorimeter (RS).

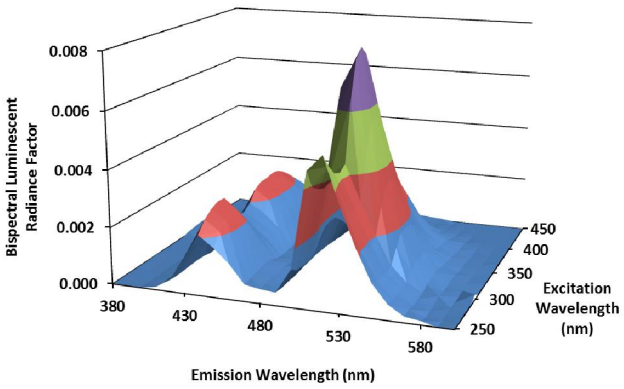

Figure 2. Measured hemispherical (0:d) bispectral luminescent radiance factor of a fluorescent plastic standard measured on the GSP using the sphere accessory.

Shown in Figure 2 is an example of hemispherical (0:d) bispectral luminescent radiance factor measurements on the GSF. These data are for a fluorescent blue-green plastic standard which has been corrected for most instrument effects. We will present updated results which further correct this data for various sphere-related errors.

CONCLUSIONS

The characterization and validation of a new NRC reference instrument for fluorescence measurements is well-advanced for both bidirectional and sphere geometries. Preliminary measurement comparison results show good agreement with other NRC reference instruments. This new facility will support NRC fluorescence calibration services for several measurement geometries and thus provide improved traceability for important applications in practical colorimetry.

REFERENCES

1. CIE Publication 182:2007 "Calibration methods and photoluminescent standards for total radiance factor measurements".
2. International Standard ISO 2469:2007 Paper board and pulps – Measurement of diffuse reflectance factor.
3. American Association of Textile Chemist and Colorists (AATCC) Evaluation Procedure 6 (2008) Instrumental Color Measurement.
4. J.C.. Zwinkels, D.S. Gignac, M. Nevins, I. Powelll and A. Bewsher, "Design and testing of a two-monochromator reference spectrofluorimeter for high-accuracy total radiance factor measurements", Appl. Opt., 36, 892-902, 1997.
5. J.C. Zwinkels, M. Noël and S. Hillman, "Near-infrared photoluminescence of orange color standards – then and now", J. Mod. Opt., 60, 1115-1123, 2013.
6. J.C. Zwinkels and W. Erb, "Comparison of absolute d/0 diffuse reflectance factor scales of the NRC and the PTB", Metrologia, 34, 357-363, 1997.

New Developments in the NIST Infrared Optical Properties of Materials Program

Leonard Hanssen[1], Sergey Mekhontsev[1], Jinan Zeng[2], and John Burnett[1]

[1]*National Institute of Standards and Technology (NIST), Gaithersburg, MD, USA*
[2]*Space Dynamics Laboratory (SDL), Logan UT, USA*
Corresponding e-mail address: hanssen@nist.gov

The Infrared Optical Properties of Materials Program in the Sensor Science Division at the National Institute of Standards and Technology (NIST) continues to upgrade its capabilities to provide comprehensive coverage of measurable infrared optical properties as well as to provide multiple paths for traceability to its scales for the user community. Upgrades include new and improved measurement instrumentation, new measurement methods, and the establishment of a quality system, supported by intercomparisons with other leading National Measurement Institutes (NMIs). Support for the community include the development of a new NIST calibration service, an intercomparison among users, and new Standard Reference Materials (SRMs).

INTRODUCTION

The Sensor Science Division at NIST has established scales for infrared spectral transmittance, reflectance, absorptance, emittance, bi-directional reflectance distribution function (BRDF), and index of refraction of solid materials. Recent developments have included expansion of the wavelength ranges for both the spectral and laser-based systems, addition of new instrumentation including integrating spheres and a hemi-ellipsoidal collecting mirror system, replacement of the Fourier transform spectrometers (FTS) with higher performance instruments optimized to the tasks, upgrades to existing custom accessories, automation of measurement processes and the establishment of a high accuracy refractive index measurement system. Of equal importance are the establishment of a quality system and a NIST Calibration Service, with uncertainties validated by a range of intercomparisons, including the Consultative Committee on Temperature (CCT-S1) Supplementary Comparison of infrared spectral emittance. Other recent user support was the organization of a reflectance comparison among 21 laboratories and the development of new SRMs calibrated for spectral reflectance.

NEW CALIBRATION SERVICE

A new NIST Calibration Service #38075S for *Infrared Spectral Transmittance, Reflectance and Emittance* is available to customers for the calibration of material samples of any type of solid material including windows, filters, mirrors, specular and diffuse samples or coated substrates. [1] The spectral range for all properties is 1 µm to 18 µm. The properties include regular transmittance $\tau_{\square}$, reflectance $\rho_{\square}$, absorptance α, and emittance ε, are measured with *s*- and *p*-polarized light over angular ranges of 0° ($\tau_{\square}$) or 8° ($\rho_{\square}$) to 80°, as well as near-normal directional-hemispherical transmittance τ_{dh}, and reflectance ρ_{dh}. Depending on the property, measurements can be made over ranges of temperatures varying up to 4 K to 300 K. Examples demonstrating the range of reflectance level capability is shown in Fig. 1. In addition, ε (and hence α) can be measured up to 1150 K for non-oxidizing opaque materials. BRDF can be measured using laser sources at wavelengths of 1.32 µm, 1.55 µm, 3.9 µm to 4.1 µm, 4.9 µm to 5.1 µm, and

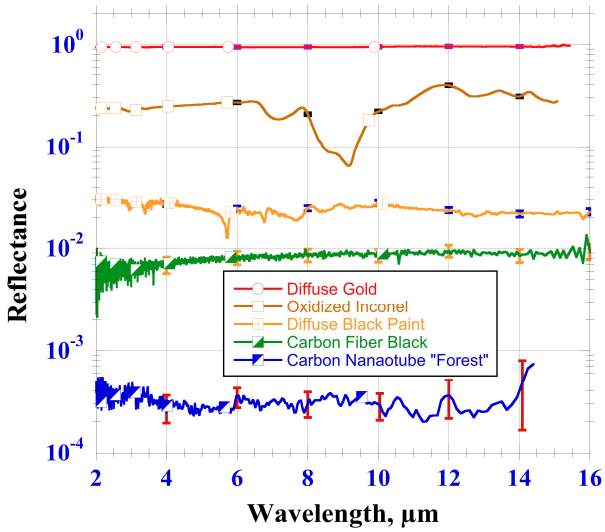

Figure 1. Reflectance results of a variety of diffuse samples showing the range of measurement capability. Error bars represent expanded uncertainties (k=2).

9.2 µm to 11.2 µm. Finally, index of refraction *n*, can be measured on prism samples using the minimum deviation method from 1 µm to 14 µm.

NEW MEASUREMENT INSTRUMENTATION AND METHODS

To meet the demand for extending the spectral coverage up to 50 µm to support programs such as climate change research, we are establishing a pair of new devices, interfaced to our Fourier transform spectrometer spectral source, for both specular and diffuse samples. The first is a high-reflectance gold-coated arc-sprayed aluminum integrating sphere coupled to a blocked-impurity-band (BIB) detector with spectral coverage up to ~ 30 µm. The second employs a diamond-turned aluminum hemi-ellipsoidal mirror instrument (HEMI), with the sample and a custom black-coated pyroelectric detector placed at the two foci in the mirror's baseplane, with spectral coverage to □ 100 µm. Fig. 2 shows a photo of the HEMI setup.

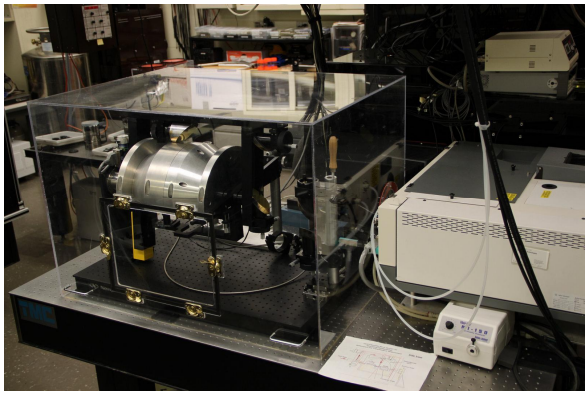

Figure 2. HEMI accessory for directional-hemispherical reflectance.

REFLECTANCE INTERCOMPARISON

A comprehensive intercomparison of infrared spectral reflectance was recently completed. 21 participants in the United States and Canada, representing government agencies and contractors, equipment manufacturers, measurement service laboratories, and standards laboratories, each completed measurements of individual sets of 5 different transfer standard samples: both specular and diffuse types, high and low reflectance, as well as with spectral structure. A photo of one sample set is shown in Fig. 3. Near-normal spectral reflectance, over the infrared spectral range of from 2.5 µm to 14 µm, was the measured quantity. NIST prepared, measured and delivered a set of transfer standard samples to each participant. After measurements by the participants, the sets were returned to NIST for repeated measurement, as a check against any change due to contamination, shipping damage, or other sample degradation. Results from each participant, which included measured values and uncertainties, were analyzed and compared to the NIST measurements.

Figure 3. Reflectance sample set for intercomparison.

As might be expected, the level of agreement, relative to the combined uncertainties varied among the participants. In some cases, the results indicated a significant underestimation of the participant uncertainties, whereas in others case, the opposite was the case. Individual reports were provided to the participants along with the opportunity to purchase the set.

NEW STANDARD REFERENCE MATERIALS

The results of the intercomparison provided an ideal test of the samples as potential standards, including stability and uniformity. This has led to the opportunity to develop new reflectance standards as an additional traceability path for the entire measurement community. Over the next few years, high reflectance specular (both 25 mm and 51 mm dia.) and near-Lambertian diffuse (25 mm dia.) SRMs will become available for purchase from NIST. These will be spectrally calibrated from 2 µm through 18 µm.

FUTURE DEVELOPMENTS

We are replacing the Fourier transform spectrometers (FTSs) with new instruments and rebuilding each system to optimize measurement efficiency and improve measurement accuracies. A chamber-contained system for high temperature emittance measurements of powders and liquids to support additive manufacturing needs is also planned.

REFERENCES

1. http://www.nist.gov/calibrations/opticalproperties.cfm

Investigation of spectral diffuse transmittance standards

Annette Koo and John Hamlin

[1]*Measurement Standards Laboratory of New Zealand, Callaghan Innovation, Lower Hutt, New* Zealand
Corresponding e-mail address: Annette.koo@callaghaninnovation.govt.nz

The lack of reference standards for spectral diffuse transmittance has resulted in large uncertainties for this type of measurement as well as difficulty in achieving comparable results from different instruments. In this work we identify potential reference materials, make measurements of diffuse transmittance and reflectance using an integrating sphere, and investigate the use of goniospectrophotometric methods to calibrate them.

INTRODUCTION

It is widely acknowledged that for best results when making reflectance measurements using an integrating sphere, the reference should have similar scattering properties to the material under test. This is done to account for sphere non-uniformities as well as light loss at the sides of the port. Reference materials are therefore available with both gloss and matte finishes. The same however cannot be said for transmittance measurements in which an unobstructed beam, (generally highly directional) is used as a reference regardless of the sample being measured.

The lack of reference materials for spectral diffuse transmittance, noted by Verrill in 1985 [1] has persisted through to today despite the wide range of industries and researchers regularly making diffuse transmittance measurements such as photobiological materials [2], food packaging [3] and sunscreens [4]. In fact an inter-laboratory comparison of spectrophotometric properties of glazing products found the greatest discrepancy in the measurement of diffuse transmittance of scattering samples [5].

Several sources of error found in the use of integrating spheres for spectrophotometric measurements are exacerbated when making transmittance measurements due to the nature of the samples. Samples are often translucent and of thickness up to several mm. The measurement result is therefore sensitive to the port size [6, 7] and incident beam properties in addition to the usual sensitivities to sphere uniformity.

In this work we report an ongoing investigation into the absolute calibration of spectral diffuse transmittance standards by the goniospectrophotometric methods used to calibrate reflectance standards [8, 9].

METHOD

The first samples investigated were an acid etched, 1 mm thick piece of Suprasil 300 [6] in which absorption in the visible range of wavelengths is negligible as well as thin PTFE sheeting and wafers of sintered halon. Measurements of diffuse reflectance plus diffuse transmittance showed divergences from the expected values, particularly at the shorter wavelengths. Figure 1 shows the result for Suprasil 300, for example, where the expected value is unity across the wavelength range. In order to investigate the origin of this discrepancy, goniospectrophotometric measurements are planned as well as 4π sphere measurements.

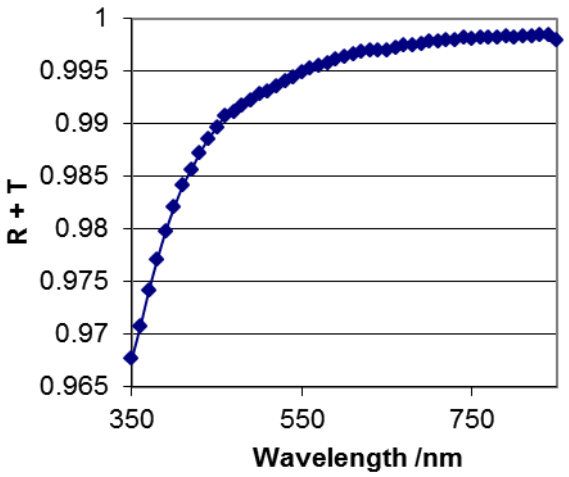

Figure 1. Sum of diffuse reflectance and diffuse transmittance measurements on acid etched Suprasil 300.

The MSL goniospectrophotometer, designed to accommodate both reflectance and transmittance geometries, will be used to measure the bi-directional scattering distribution function (BSDF) for normal incidence of the set of potential specular diffuse transmittance reference materials already mentioned. It is expected that suitable materials for reference

samples will have cylindrical symmetry in their scattering properties so that measurements are only required for one value of the detection azimuthal angle, ϕ_d. To obtain total diffuse transmittance or reflectance the BSDF must then be integrated over the appropriate detection hemisphere.

Other suitable reference materials to be investigated may include commercially available haze standards and opal glass.

This work has been funded by the MSL contract for the provision of measurement standards in New Zealand.

REFERENCES

1. J.F. Verrill, Physical standards in absorption and reflection spectrophotometry, in *Advances in standards and methodology in spectrophotometry*, edited by C. Burgess and K. D. Mielenz, 111-124, Elsevier, Amsterdam, 1987.
2. H. L. Gorton, C. R. Broderson, W. E. Williams, T. C. Vogenlmann, Measurement of the optical properties of leaves under diffuse light. *Photochemistry and photobiology* **86**, 1076-1083, 2010.
3. J. O. Bosset, P. U. Gallmann and R. Sieber, Influence of light transmittance of packaging materials on the shelf-life of milk and dairy products – a review, in Food Packaging and preservation, edited by M. Mathlouthi, 222-265, Aspen Publishers, New York, 1994.
4. A. Springsteen, R Yurek, M. Frazier and K. F. Carr, Measurement of sun protection factor of sunscreens by diffuse transmittance. *Anal. Chim. Acta* **380**, 155-164, 1999.
5. J. C. Jonsson and C. Curcija, Inter-laboratory comparison using integrating sphere spectrophotometers to measure reflectance and transmittance of specular, diffuse and light-redirecting glazing products, *Proc. of SPIE* **8495**, 849509-1 – 849509-15, 2012.
6. J. J. Hsia, The translucent blurring effect – method of evaluation and estimation, NBS technical note 594-12, 1976.
7. J. C. Jonsson and M. Rubin, Light-loss when measuring transmittance of thick scattering samples with an integrating sphere, Proc of SPIE **6670**, 667007-1 -1 667007-8, 2007.
8. C. J. Chunnilall, A. J. Deadman, L. Crane and E. Usadi, NPL scales for radiance factor and total diffuse reflectance, *Metrologia* **40**, S192-S195, 2003.
9. S. Nevas, F. Manoochers and E. Ikonen, Gonioreflectometer for measuring spectral diffuse reflectance, *Appl. Opt.* **43**, 6391-6399, 2004.
10. Hereaus, Quartz glass for optics, Printed in Germany.

Emissivity measurement of high-temperature piezoelectric ceramics

Maksim Shpak[1,2], Martti Heinonen[1], Tim Stevenson[3], Jacques Hameury[4], Maija Ojanen[1], and Erkki Ikonen[1,2]

[1]MIKES, Espoo, Finland, [2]Aalto University, Espoo, Finland, [3]University of Leeds, Leeds, UK, [4]LNE, Trappes, France
Corresponding e-mail address: maksim.shpak@aalto.fi

Emergence of new piezoelectric materials capable of operating at high temperatures requires new metrological approaches for their traceable characterization. The aim of this work is measurement of spectral emissivity of a piezoelectric ceramic material as a function of temperature. Our method combines a direct spectral radiance measurement with a reflectance measurement to obtain emissivity at temperatures above 500 °C.

INTRODUCTION

Piezoelectric ceramics are indispensable in numerous consumer and industry applications as sensors and actuators. Most of these devices are based on the ubiquitous (Pb,Zr)TiO_3 material, which loses its functional properties at temperatures around 200 °C, but many potential applications would require operation at much higher temperatures. New types of piezoelectric ceramic materials are being developed to answer this demand. At the same time this poses new challenges for measurements of their properties. As part of a pan-European effort to establish a new metrological infrastructure for traceable characterization of electro-thermal-mechanical coupling of piezoelectric materials at high temperatures, this work concentrates on investigation of optical properties of a high Curie temperature piezoelectric ceramic material $0.5(Bi_{0.95}La_{0.05})FeO_3$-$0.5PbTiO_3$ (BFPT), aiming at characterizing its emissivity at temperatures up to 1000 °C.

Emissivity of a material is required for performing non-contact temperature measurements. Emissivity also affects radiative heat exchange, and its influence is increased at higher temperatures. Emissivity is therefore needed for successful thermodynamic modelling.

Emissivity of a material typically varies with temperature and wavelength. To determine the spectral emissivity of BFPT we use a furnace to heat the sample to a known temperature and measure its spectral radiance. Emissivity is obtained as the ratio of the measured radiance and the calculated radiance for a blackbody at the same temperature. Due to difficulties of accurate surface temperature measurement at high temperatures, additional reflectance measurements are performed to obtain the emissivity at a single wavelength and to establish the temperature scale for spectral measurements.

MATERIALS AND METHODS

BFPT is a synthesised high-temperature piezoelectric ceramic material [1]. The sample used in these measurements is a 2-mm-thick disk of 15 mm in diameter. The front surface of the sample is highly polished. The sample positioned in the holder is shown in Fig. 1(a).

The sample disk was mounted in an Inconel holder placed inside a furnace, as shown in Fig. 1(b). The temperature of the sample surface was monitored with a type S thermocouple. Spectral radiance of the exposed sample surface was measured with a spectroradiometer. The measurement area was approximately 5 mm in diameter at the centre of the surface.

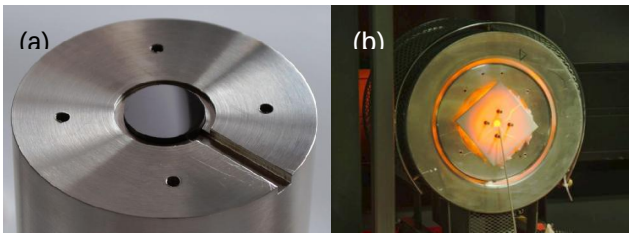

Figure 1. (a) A BFPT disk sample with polished surface in the sample holder made of Inconel. The diameter of the disk sample is 15 mm. (b) Sample in the furnace and heated to a high temperature.

Spectral emissivity of the surface at a specific temperature was measured directly by comparing its spectral radiance to the spectral radiance of a blackbody at the same temperature [2]. The spectral radiance of the blackbody is obtained from the Planck's radiation law. Measurements were performed in the temperature range of 500–800 °C and the wavelength range of 400–2000 nm.

It turned out to be difficult to make a good thermal contact between the thermocouple and the sample surface. When combined with large temperature gradients the poor contact caused systematically lower temperature readings. Another

method for obtaining emissivity of the surface is indirectly via the reflectance measurement. The sum of directional hemispherical reflectance, directional hemispherical transmittance and directional emissivity is equal to one. Therefore for opaque samples spectral directional emissivity can be obtained by subtracting spectral directional hemispherical reflectance from unity. Additionally, if the diffuse reflectance of the surface is negligibly small, the specular reflectance alone can be used.

Spectral directional emissivity of the BFPT was measured with a reflectometer for temperatures between 23 °C and 500 °C. For temperatures above 500 °C, we plan to measure specular reflectance of the sample surface with 633 nm and/or 1523 nm He-Ne lasers, while simultaneously recording radiance of the surface at the same wavelength, as illustrated in Fig. 2. Detectors are recording the intensity of both the incident laser beam and the reflected beam. The laser beam is chopped, and detectors are connected to two lock-in amplifiers. With simultaneous measurement of radiance and emissivity the temperature of the surface is obtained from the Plank's radiation law.

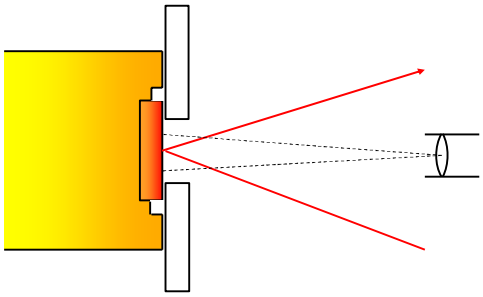

Figure 2. Simultaneous specular reflectance and radiance measurement of a sample at a high temperature.

The described measurement gives the temperature dependence of emissivity at a single wavelength. Fixing the emissivity at a single wavelength allows the calculation of the actual surface temperature for direct spectral radiance measurements, and obtaining the spectral emissivity in the full wavelength range.

RESULTS

Spectral emissivities of BFPT for temperatures between 23 °C and 500 °C are shown in Fig. 3. Preliminary results of direct spectral emissivity measurements are presented in Fig. 4. Based on the measurement results below 500 °C, the emissivity was assumed to be temperature-independent around the wavelength of 800 nm, and equal to 0.79.

BFPT appears to have low temperature dependence of emissivity in the visible wavelength range, and increasing emissivity trend with temperature in the near-infrared region (Fig. 3). Emissivity results at temperatures above 500 °C will be validated at 633 nm and/or 1523 nm by measurements using the laser reflectance.

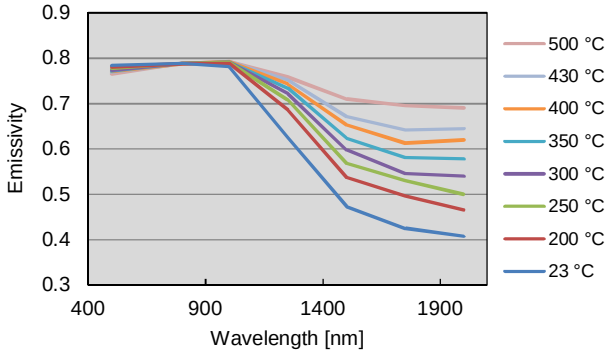

Figure 3. Directional (8°) spectral emissivity of BFPT as a function of wavelength for temperatures 23–500 °C.

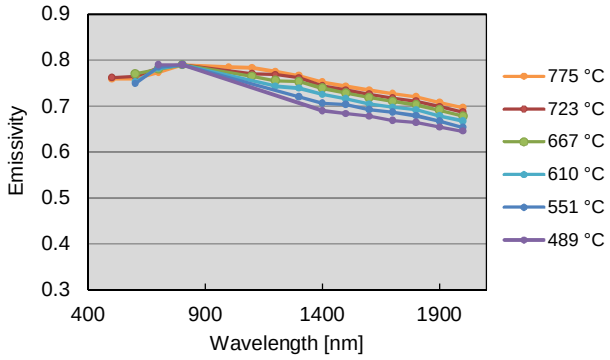

Figure 4. Preliminary results on spectral emissivity of BFPT at temperatures above 500 °C.

ACKNOWLEDGEMENTS

This work was funded through the European Metrology Research Programme (EMRP) Project NEW09 METCO. The EMRP is jointly funded by the EMRP participating countries within EURAMET and the European Union.

REFERENCES

1. T.P. Comyn, T. Stevenson, A.J. Bell, Piezoelectric properties of $BiFeO_3$-$PbTiO_3$ ceramics, J. Phys. IV, 128, 13–17, 2005.
2. M. Shpak, L. Sainiemi, P. Kärhä, M. Heinonen, S. Franssila, E. Ikonen, Refractive index of silicon with various doping levels at high temperatures, in Proc. of NEWRAD 2011, pp. 144–145.

0°:45°a Radiance Factor Measured by a BRDF System

Wen-Chun Liu, Hsueh-Ling Yu, and Yi-Chen Chuang

Center for Measurement Standards, Industrial Technology Research Institute (CMS, ITRI), Hsinchu, Taiwan
Corresponding e-mail address: sveta.liu@gmail.com

Radiance factor under the *0°:45°a* geometric condition can be simply obtained by a commercial spectrophotometer using substitution method. This is acceptable only if the measured surface and/or the responsivity of the optical detecting system is uniform. This article intends to show that it is necessary to measure the bidirectional reflectance distribution function (BRDF) in order to obtain the *0°:45°a* radiance factor accurately, especially for non-uniform surfaces and optical detecting system.

INTRODUCTION

Spectral radiance factor ($\beta(\lambda)$) is defined as the ratio of reflected spectral radiant flux of a test sample ($\Phi_r(\lambda)$) to that of a perfect Lambertian surface ($\Phi_{0r}(\lambda)$) under the same measurement conditions. Spectral radiance factor can be described as follows.

$$\beta(\lambda) = \Phi_r(\lambda) / \Phi_{0r}(\lambda) \tag{1}$$

In a commercial spectrophotometer, the reflected *0°:45°a* spectral radiant flux is collected by an annulus where the radiant flux can be assumed a summation of radiant flux from many small sections with the same area in the annulus. Based on this assumption, the *0°:45°a* radiance factor can be described as in equation (2) and (3), where the subscript *0°:45°a* denotes the geometric condition and the subscript *i* denotes the corresponding property in individual section.

$$\begin{aligned} \beta_{0/45a}(\lambda) &= \Phi_{r,0/45a}(\lambda) / \Phi_{0r,0/45a}(\lambda) \\ &= \sum \Phi_{ir,0/45a}(\lambda) / \sum \Phi_{i0r,0/45a}(\lambda) \end{aligned} \tag{2}$$

Ideally, $\Phi_{i0r,0/45a}(\lambda)$ of each section should be the same. Thus the equation (2) can be further rewritten as equation (3), assuming there are *N* sections.

$$\begin{aligned} \beta_{0/45a}(\lambda) &= (\sum(\beta_{i,0/45}(\lambda) \times \Phi_{i0r,0/45}(\lambda))) / (N \times \Phi_{i0r,0/45}(\lambda)) \\ &= (\Phi_{i0r,0/45}(\lambda) \times \sum \beta_{i,0/45}(\lambda)) / (N \times \Phi_{i0r,0/45}(\lambda)) \\ &= \sum \beta_{i,0/45}(\lambda) / N = \overline{\beta_{i,0/45}(\lambda)} \end{aligned} \tag{3}$$

According to equation (3), $\beta_{0/45a}(\lambda)$ can be obtained by averaging radiance factors of all the sections in the annulus.

The BRDF system in CMS-ITRI uses a 5-axis-robot as the sample holder to allow the sample spinning around the surface normal and to measure $\beta_{i,0/45}$, as shown in Figure 1(a).

In the experiment, the sample is the reflection plate of a solar cell shown in Figure 1(b). Experimental results of $\beta_{0/45a}$ were obtained using our BRDF system by spinning the sample from -180° to 180° at an interval of 10°. For comparison, a spectrophotometer (Cary500) with *0°:45°a* geometry accessory was used to obtain $\beta_{0/45a}$ independently.

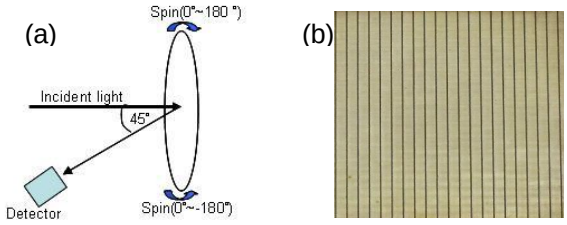

Figure 1. (a) Schematic diagram of the BRDF System for $\beta_{0/45a}$ measurement (b) The sample used in the experiment (reflection plate of a solar cell).

RESULTS AND DISCCUSIONS

In our experiments, we chose a spacially non-uniform and non-isotropic sample purposely to show the necessity of using BRDF system to obtain $\beta_{0/45a}$ accurately.

The *0°:45°* reflected signal versus the spin angle at 600 nm are shown in Figure 2. Based on Figure 2, the reflected signal of the chosen sample is angle-dependent, indicating this sample is not isotropic. Similar trends have been observed at other wavelengths. The results are listed in Table 1. In Table 1, it is noticed that $\beta_{0/45a}$ measured by commercial spectrophotometer ($\beta_{0/45a\_sp}$) is close to the averaged results of spinning the sample from -180° to 180° from BRDF ($\overline{\beta_{i,0/45}(\lambda)}$) but not comparable to $\beta_{i,0/45}$ at an arbitrary orientation, indicating radiance factor at any particular spin angle cannot represent the radiance factor of the sample as a whole.

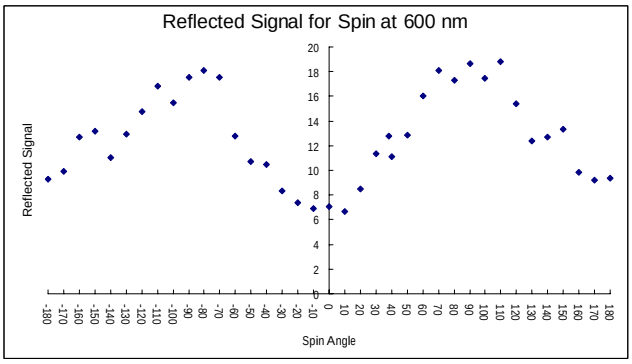

Figure 2. Reflected signal vs. spin angle at 600 nm.

Table 1. Deviation of (i) $\overline{\beta_{i,0/45}(\lambda)}$; (ii) and (iii) $\beta_{i,0/45}$ relative to $\beta_{0/45a}$ measured by spectrophotometer.

wavelength (nm)	(i) Average $\frac{\overline{\beta_{i,0/45}(\lambda)}-\beta_{0/45\_sp}(\lambda)}{\beta_{0/45\_sp}(\lambda)}$	(ii) Spin Angle 110° $\frac{\beta_{110°,0/45}(\lambda)-\beta_{0/45\_sp}(\lambda)}{\beta_{0/45\_sp}(\lambda)}$	(iii) Spin Angle 10° $\frac{\beta_{10°,0/45}(\lambda)-\beta_{0/45\_sp}(\lambda)}{\beta_{0/45\_sp}(\lambda)}$
380	0.59 %	10.37 %	-8.74%
420	0.96 %	14.15 %	-12.45 %
460	0.47 %	16.89 %	-16.68 %
500	-0.35 %	18.93 %	-20.78 %
540	-0.82 %	20.84 %	-23.72 %
580	-0.98 %	22.54 %	-25.71 %
620	-0.60 %	25.59 %	-26.62 %
660	-0.49 %	26.20 %	-27.20 %
700	-0.49 %	25.04 %	-28.02 %
740	-0.22 %	24.08 %	-28.19 %
780	0.00 %	24.28 %	-28.21 %

Radiance factor of the samples measured at *0°:45°a* geometric condition ($\beta_{0/45a\_sp}$) are shown in equation (6), where β_s and β_t are the radiance factor of the standard and the sample respectively, and I_t and I_s are measured signals from the standard and the sample correspondingly. Mostly, the surface of the standard is considered uniform. The ratio of the signals should be proportional to reflected radiant flux and the responsivity (k_i) of the optical detecting system, including collecting annulus, and detector.

$$\beta_t = \frac{I_t}{I_s}\times\beta_s = \frac{\sum\left(k_i\Phi_{it,0/45}\right)}{\sum\left(k_i\Phi_{is,0/45}\right)}\times\beta_s \qquad (6)$$

When the surfaces of the sample and the standard are both uniform, the reflected radiant flux in each small detecting section should be very close, and the measured signals would be proportional to the ratio of the reflected radiant flux at *0°:45°a*. As a result, equation (6) can be rewritten as equation (7) below.

$$\beta_t = \frac{\Phi_{it,0/45}\sum k_i}{\Phi_{is,0/45}\sum k_i}\beta_s = \frac{Nk\Phi_{it,0/45}}{Nk\Phi_{is,0/45}}\beta_s = \frac{\Phi_{t,0/45a}}{\Phi_{s,0/45a}}\beta_s \quad (7)$$

On the other hand, assume the sample is not uniform but the responsivity of the optical detecting system is uniform, k_i in each detecting section is almost the same, then the obtained radiance factor is proportional to the ratio of the reflected radiant flux shown in equation (8). If the system is very uniform, the deviation in column 2 of Table 1 would be smaller. However, uniformity of the detecting system in a spectrophotometer is not easy to be verified.

$$\beta_t = \frac{k_i\sum\Phi_{it,0/45}}{k_i\sum\Phi_{is,0/45}}\beta_s = \frac{\Phi_{t,0/45a}}{\Phi_{s,0/45a}}\times\beta_s \qquad (8)$$

In the case that the sample and the optical detecting system in spectrophotometer are not uniform, the obtained reflectance factor would not be proportional to the ratio of the reflected radiant flux at *0°:45°a*. Equation (6) is then rewritten as equation (9) which implies radiance factor cannot be obtained using *0°:45°a* accessory. Radiance factor of a non-uniform sample is essentially needed to be obtained using a BRDF system instead of using a spectrophotometer with built-in *0°:45°a* accessory.

$$\beta_t = \frac{\sum\left(k_i\Phi_{it,0/45}\right)}{\Phi_{is,0/45}\sum k_i}\times\beta_s \qquad (9)$$

CONCLUSION

Commercial spectrophotometer at *0°:45°a* may use a standard calibrated at *0°:45°*, which is assumed to have good uniformity and non-directive reflectance. In case the standard has some defects, it is expected to result in measurement errors when the standard is used under *0°:45°a* geometric condition.

It is also shown that either the responsivity of the annulus or the sample has to be uniform, or the $\beta_{0/45a}$ obtained by spectrophotometer based on substitution method will result in measurement errors. It is highly commended that BRDF method is used to obtain *0°:45°a* spectral radiance factor if possible.

REFERENCES

1. D. Huenerhoff, U. Grusemann & A. Hoepe, "New robot-based gonioreflecometer for measuring spectral diffuse reflection", Metrologia, 43, S11-S16, 2006.

Development of Ultra-Low Reflectance Optical Absorber Using Etched Ion Tracks

Kuniaki Amemiya[1], Hiroshi Koshikawa[2], Yasunari Maekawa[2], Takayuki Numata[1], Kenichi Kinoshita[1], Hiroshi Shitomi[1], Yoshiro Ichino[1], and Tatsuya Zama[1]

[1]*National Metrology Institute of Japan, Tsukuba, Japan*
[2]*Japan Atomic Energy Agency, Takasaki, Japan*
Corresponding e-mail address: k.amemiya@aist.go.jp

High aspect ratio conical micro pores with black layer like nickel phosphorous black surface is expected to show ultra-low reflectance of 0.1 % level. We have been developing a novel broadband ultra-black material using ion track etch pits deposited with amorphous carbon absorber. A prototype showed low reflectance of 1% level in the visible wavelength range. This promising optical absorber will contribute to an absolute photothermal detector for optical power standard.

INTRODUCTION

Low reflectance black materials are widely used for broadband photothermal detectors. Nickel-phosphorous (NiP) black surface [1], which has high aspect ratio conical micro pores with black layer, shows ultra-low reflectance of 0.1 % level in the visible and near-infrared range [2]. Although carbon nanotube black also shows quite low reflectance [3], NiP black can be used for absolute optical calorimeters [4] with high thermal equivalence [5].

For longer wavelength, however, NiP black is not so perfect absorber due to its composition [2], which can be hardly customized for mid-infrared use.

We have been developing a novel broadband ultra-black material by ion track etching technique [6], which is a kind of ion beam lithography. In this paper we describe the first demonstration of the fabrication of quite low reflectance materials using etched ion tracks deposited with optical absorption layer.

MATERIALS AND METHODS

Figure 1 summarises the fabrication processes of the black material. We used a CR-39 plastic track detector as an ion track registration material [6]. The CR-39 plate irradiated by energetic heavy ions forms conical shaped pores on its surface through etching process. We irradiated CR-39 plates, BARYOTRAK (Fukuvi Chemical Industry, Japan), with oxygen ion beam of 335 MeV at 10^6 /cm^2 from AVF Cyclotron (930, Sumitomo Heavy Industry, Japan), and then etched the plates in 6.5 mol/l NaOH solution at 70 ^{o}C for 12 h.

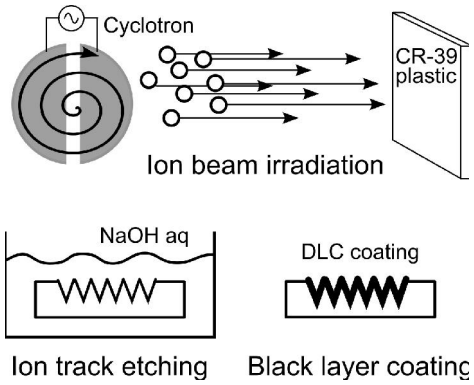

Figure 1. Procedures of the black material fabrication.

The etched surface was coated with 5 μm-thick diamond like carbon (DLC), a kind of amorphous carbon, since amorphous carbon has broadband absorption spectrum [7] expected to be used for longer wavelength range. The total reflectance of the DLC-coated surface was measured using LAMBDA 900 spectrophotometer (PerkinElmer, USA) in the visible wavelength range comparing with a SPECTRALON diffuse reflectance standard of 2% reflectance level (Labsphere, USA).

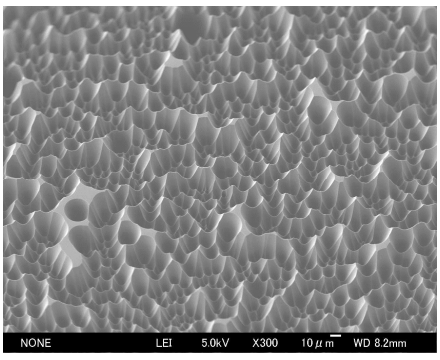

Figure 2. SEM image of the surface structures of the etched CR-39 plate.

RESULTS

Figure 2 shows the SEM image of the surface structures of the etched CR-39 plates. Conical shaped etch pits cover almost all area of the surface. The aspect ratio of the etch pits was about 3. DLC has similar value of complex refractive index with the NiP black surface (nickel oxide) in the visible wavelength range, therefore the previous simulation for NiP black [2] predicts that the DLC coated etch pits also show the total reflectance of well below 1%.

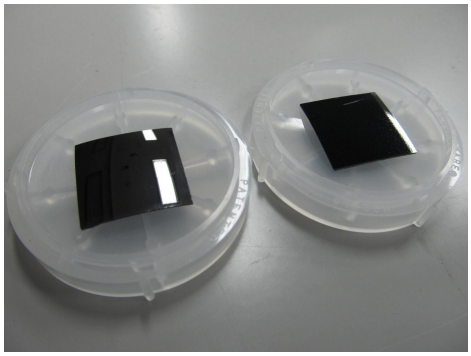

Figure 3. Picture of the DLC coated CR-39 plate (left) and the DLC coated CR-39 with etched ion tracks (right). A part of the sample with ion tracks was not irradiated by ion beam, where seems like flat plate.

Figure 3 is the picture of the DLC coated samples. DLC on a flat plate shows black colour but has large specular reflection. On the other hand, DLC-coated conical pits have optically diffusive surface and show low reflectance. Measured total reflectance of those samples in the visible wavelength range is shown in Figure 4. The total reflectance of DLC-coated etched ion tracks was about one order smaller than that of flat DLC surface. This indicates that the conical pits work as optical traps, where incident light experiences multiple reflection and iterative absorption.

The total reflectance of about 1%, however, was larger than the expected value of well below 1%. One reason is that the DLC is deposited roundly on the steep “ridgeline” between the etch pits, which prevents incident light from optically trapping into the conical pores. Some post-processing to avoid this and characterization in the infrared region are future work.

CONCLUSIONS

We developed a novel broadband low reflectance material using ion track etch pits deposited with amorphous carbon absorber. The prototype showed total reflectance as low as 1% level in the visible wavelength range. Customization of the microstructure will give lower total reflectance materials towards 0.1% level. This promising optical absorber will contribute to an absolute photothermal detector for optical power standard.

ACKNOWLEDGEMENTS

This work was partially supported by KAKENHI 24760326 [Grant-in-Aid for Young Scientists (B)] from the Japan Society for the Promotion of Science (JSPS). The ion beam irradiation experiment was performed at Takasaki Ion Accelerators for Advanced Radiation Application (TIARA) of Japan Atomic Energy Agency, Takasaki, Japan, which was also supported by the University of Tokyo.

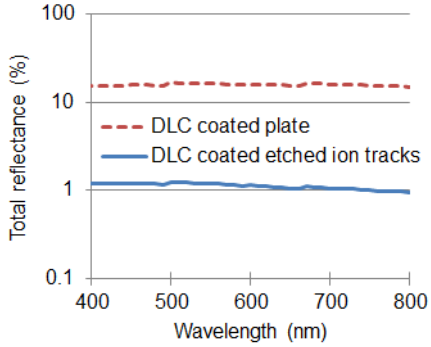

Figure 4. Measured total reflectance of the DLC coated CR-39 plate (red dashed line) and the DLC coated CR-39 with etched ion tracks (blue solid line).

REFERENCES

1. S. Kodama, et al., Ultra-black nickel-phosphorus alloy optical absorber, IEEE IM, 39, 230-232, 1990.
2. K. Amemiya, et al., Comprehensive characterization of broadband ultralow reflectance of porous nickel–phosphorus black surface by numerical simulation, Appl. Opt., 51, 6917-6925, 2012.
3. J. H. Lehman, et al., Carbon multi-walled nanotubes grown by HWCVD on a pyroelectric detector, Infrared Phys. Technol., 47, 246–250, 2006.
4. K. Amemiya, et al., Final report on APMP.PR-S4: comparison of fiber optic power meter responsivity, Metrologia 48, 02004, 2011.
5. K. Amemiya, et al., Thermally optimized design of a laser calorimeter by finite element calculation for higher thermal equivalence and absorber uniformity, in Proceedings of the 10th International Conference on New Developments and Applications in Optical Radiometry (NEWRAD, 2008), 71-72, 2008.
6. S. Kodaira, et al., Detection threshold control of CR-39 plastic nuclear track detectors for the selective measurement of high LET secondary charged particles, Radiat. Meas., 46, 1782-1785, 2011.
7. N. Maron, Optical properties of fine amorphous carbon grains in the infrared region, Astrophys. Space Sci., 172, 21-28, 1990.

BRDF measurements at 254 nm for the LISA Pathfinder satellite mission

Andreas Höpe[1], Kai-Olaf Hauer[1], Patrick Bergner[2], and Tobias Ziegler[2]

[1]*Physikalisch-Technische Bundesanstalt (PTB), Braunschweig, Germany*
[2]*Airbus Defence and Space, Friedrichshafen, Germany*
Corresponding e-mail address: andreas.hoepe@ptb.de

With the robot-based gonioreflectometer of PTB the BRDF (Bidirectional Reflectance Distribution Function) of a gold/titanium coated molybdenum sample was measured at a wavelength of 254 nm. Hereunto the diffuse reflection was measured in 1821 distinct directional geometries in 3D-space around the specular angle for a total of 10 different incidence angles in the angular range 0° to 85°. The characterised sample was an artefact with identical surface properties as the inner surface coating of the electrode housing for the test masses of the LISA (Laser Interferometer Space Antenna) Pathfinder satellite mission. The angular dependent reflection values at 254 nm are essential for radiation transport calculations, since special UV-lamps are applied for the in-orbit discharge of the test masses.

INTRODUCTION

The LISA Pathfinder-Mission is a dedicated technology demonstrator for the Evolved Laser Interferometer Space Antenna (eLISA) mission of the European Space Agency (ESA), which will be the first gravitational wave observatory in space [1, 2]. The LISA Pathfinder mission essentially emulates one arm of the eLISA constellation by shrinking the prospected 10^6 km armlength down to 35 cm, giving up the sensitivity to gravitational waves, but keeping the principle of the measurement technology, where the distance between two test masses is measured using a laser interferometric technique. The launch for the LISA Pathfinder-Mission is currently planned for 2015.

One important component of the mission is the inertial sensor subsystem, which consists of two test masses and all systems interacting directly with these masses, among all others the electrode housing. The capacitive sensor comprises a hollow cubic molybdenum housing with gold coated electrodes mounted in the faces. As there is no physical contact between the test masses and the surrounding environment, one issue that must be dealt with is charging of the test mass due to cosmic ray and solar energetic particle impacts. A build up of charge on the test mass, coupled with the potentials on the electrodes, will lead to additional noise in the test mass position. The charge is controlled using a non-contact discharge system based on the photo-electric effect, where UV light at 254 nm from Mercury lamps is channelled to the electrode housing via fibre optics. For computer based radiation transport calculations of this procedure angular dependent reflection values of the electrode housing surface at 254 nm are needed [3].

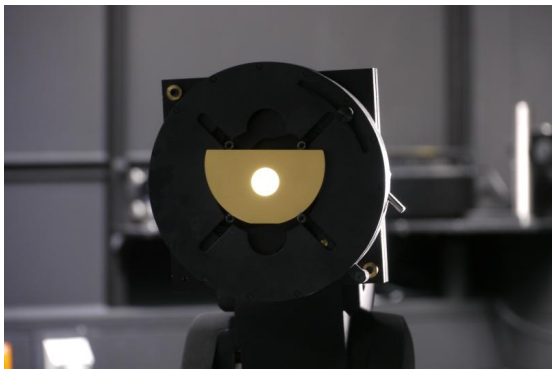

Figure 1. Photo showing the gold-titanium coated molybdenum sample mounted to the robot-based gonioreflectometer of PTB. The highlighted circle indicates the given measurement area for a reflection under 0°.

PERFORMED MEASUREMENTS

For the characterisation of the electrode housing material angular resolved measurements of the surface reflection properties were performed. Subject of the measurement was a sample given as a gold-titanium coated segment of a circle made of molybdenum with a diameter of approx. 90 mm, a height of approx. 56 mm and a thickness of about 6 mm (see Fig.1) with identical surface properties to the original electrode housing material of the LISA Pathfinder.

Measured was the BRDF f_r at a total of 1821 measuring points in the half space above the sample surface at a wavelength of λ = 254 nm [4]. The measuring points consists of 10 different incidence angles θ_i in the range of θ_i = 0° to 85° (0°, 5°, 15°, 25°, 35°, 45°, 55°, 65°, 75°, 85°). The BRDF was determined in spherical shells centred around the specular angle with zenith angles of (0°, 2°, 4°, 6°, 8°, 10°, 14°, 18°, 22°, 26°, 30°, 34°, 38°), see Fig. 2.

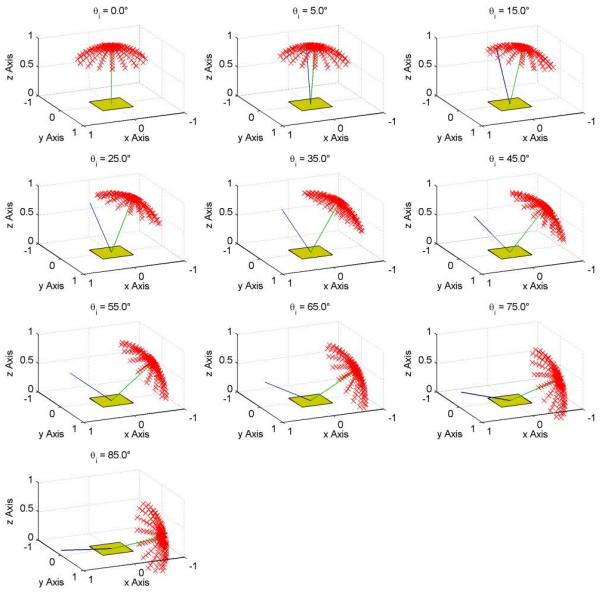

Figure 2. Visualisation of the 1821 measurement geometries. Red crosses: position of the detector, blue line: incidence, green line: direction of the specular reflection.

The robot-based gonioreflectometer facility uses two-stage mirror-based 10:1 imaging optics to map a 20 mm circular area on the sample onto the 2 mm wide entrance slit of the monochromator [5]. For the presen-ted measurements a so-called solar blind channel photo-multiplier (CPM) with a wavelength range of 165 nm to 320 nm was attached to the monochromator. The signals are detected with a picoamperemeter and transferred to a computer for data storage and analysis.

The time required for the measurement of one single data point was about 6 minutes. This time includes the proper alignment of the sample to the required geometrical configuration in 3D-space with the robot, the measurement of the reflection signal (with an average determination over 10 readings) and the subsequent positioning to a position where, for normalisation purposes in order to calculate the BRDF value f_r, the radiance signal of the irradiating lamp can be measured. The normalized BRDF data measured around the specular directions for incidence angles θ_i = 0° to 45° are illustrated in Fig. 3 in false colour representation. The open structure on top of the BRDF graphics for θ_i = 0° and at the right side for θ_i = 5°, 15° comes from the angular range where the irradiating lamp blocks the detection path (values around $\theta_r = \theta_i$ and $\phi_r = \phi_i$ = 0°). The full angular dimension of shading due to the lamp is 14°.

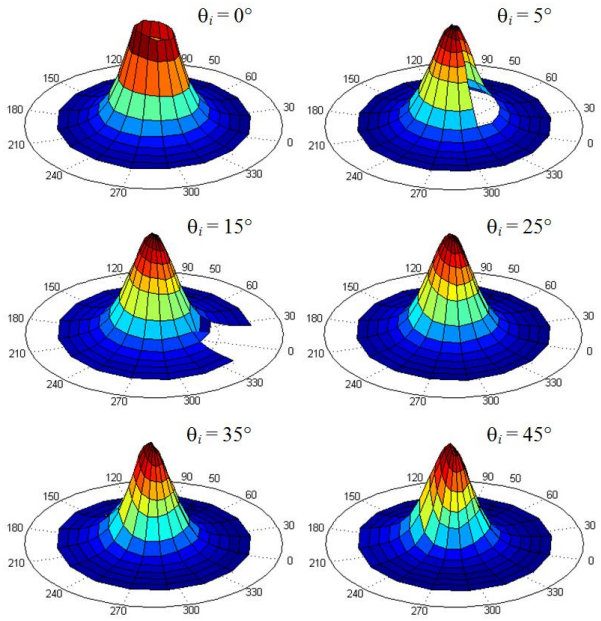

Figure 3. Normalized BRDF at 254 nm data measured around the specular direction in false colour representation for incidence angles θ_i = 0° to 45°.

Due to the considerably large number of data points of roughly two thousand it was not possible to carry out repetitive measurements for minimizing the uncertainty. For the BRDF f_r at 254 nm of the gold/titanium coated molybdenum surface values in the range 0.01 to 544.12 were measured, with a standard coverage factor of the expanded uncertainty in most of the cases of k = 2.36, with some positive outliers going down to k = 2.13.

ACKNOLEDGMENTS

The authors thank G. Santoruvo, Compagnia Generale per lo Spazio, Milano, Italy, for the construction and manufacturing of the gold/titanium coated molybdenum sample.

REFERENCES

1. P. McNamara, G. Racca, Introduction to LISA Pathfinder, (LISA-LPF-RP-0002), http://sci.esa.int/lisa-pathfinder/45819-introduction-to-lisa-pathfinder/#, 2009.

2. Pau Amaro-Seoane et al., Doing science with eLISA: Astrophysics and cosmology in the millihertz regime, arXiv:1201.3621v1 [astro-ph.CO], 2012.
3. T. Ziegler, P. Bergner, G. Hechenblaikner, N. Brandt, W. Fichter, Modeling and Performance of Contact-Free Discharge Systems for Space Inertial Sensors, arXiv:1207.0394v2 [physics.ins-det], 2012, accepted for publication in IEEE Transactions on Aerospace and Electronic Systems.
4. A. Höpe, K.-O. Hauer, Three-dimensional appearance characterisation of diffuse standard reflection materials, Metrologia, 47, 295-304, 2010.
5. D. Hünerhoff, U. Grusemann, A. Höpe, New robot-based gonioreflectometer for measuring spectral diffuse reflection, Metrologia, 43, S11-S16, 2006.

The new NPL infrared gonio-reflectometer

E. Theocharous, R. Mole, C. L. Greenwell, and C. J. Chunnilall

National Physical Laboratory, Hampton Road, Teddington, TW11 0LW, UK
Corresponding e-mail address: e.theo@npl.co.uk

A new Infrared Gonio-Reflectometer (IGR) was assembled at the National Physical Laboratory (NPL). The IGR is a goniometric (multi-angle) instrument capable of measuring the specular and diffuse reflectance and diffuse transmittance of materials for angles of incidence and reflectance/transmittance from 6° to 85°. Measurements can be made in the 2.5 µm to 50 µm wavelength region with the aid of an FT spectrometer. The design and construction of the instrument is described, as well as its characterisation and use for specular and diffuse reflectance measurements.

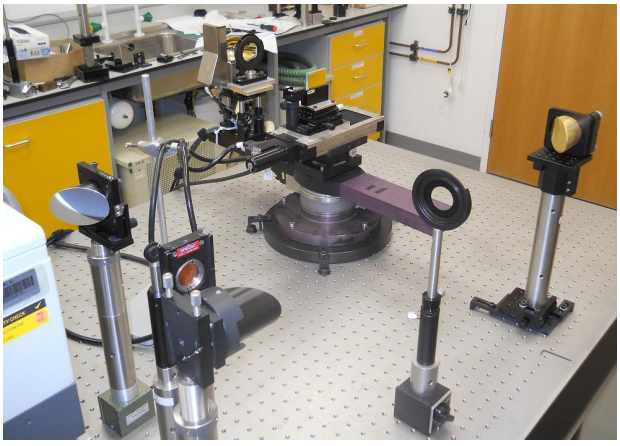

Figure 1. Photo of the IGR without the light-tight enclosure.

INTRODUCTION

The reflectance and transmittance properties of optical materials are essential to understand in order to optimise an optical design. Although there are a large number of gonio-reflectometers which operate in the visible and NIR wavelength ranges, gonio-reflectometers which operate in the infrared region are rather rare due to the issues of alignment, low source spectral radiance and poor detector detectivity. The new NPL Infrared Gonio-Reflectometer (IGR) utilises a direct specular reflectance measurement method, by measuring the radiant power in a beam before and after it is reflected by the test sample, for any particular angle of incidence. The test sample is mounted on a turntable which enables it to be positioned at the required angle of incidence with respect to the incident beam. The photodetector is mounted on a second turntable to allow measurements at the required angle of reflection. Finally a translation stage is used to slide the test sample out of the incident beam and allow the detector to measure the radiant power of the incident beam. The incident beam is the recombined beam at the output of an FT Michelson interferometer, and the detected signal is Fourier-transformed to obtain a spectrum as a function of wavelength.

DESCRIPTION OF THE IGR

The NPL IGR uses two rotary tables, with a common vertical rotation axis, driven by stepper motors (see Figure 1). The upper table carries the sample, mounted vertically in a holder which is itself mounted on a linear horizontal stepper-motor-driven translation stage. The lower table carries the detector module which comprises of an aperture/baffle, an ellipsoid mirror and a DLATGS pyroelectric detector. The detector module is located at a distance of approximately 250 mm from the axis of rotation. This enables the test sample to be positioned at any angle to the incident light beam, and the light reflected in any direction in the horizontal plane to be measured, all under computer control. Measurements can be made for any angle of incidence and reflectance/transmittance from 6° to 85°. The angular positions of both turntables are read with a resolution of 0.01°.

The linear slide on which the sample is located enables the sample to be moved laterally, out of the incoming beam, so the radiant power of the incident light can be measured. Translation of the sample within the incoming beam allows some characterisation of the sample reflectance/ transmittance uniformity in the horizontal direction. By rotating the sample, it is possible to characterise the uniformity of reflectance and/or transmittance of the test sample in other orientations. The sample can also be moved out-of-plane via a manual linear translation stage in order to ensure that its surface is coincident with the axes of rotation of the two main

rotation stages. The sample can also be tilted about a horizontal axis in order to ensure the surface of the test sample is perpendicular to the incident beam. The entire assembly is housed in a light-tight cabinet made from panels of black Perspex which can be purged with dry CO_2-free air. Figure 1 shows a photo of the IGR without the light-tight enclosure.

A Fourier Transform (FT) spectrometer equipped with KBr and multi-layer mylar beam splitters allows measurements to be done over the 2.5 µm to 50 µm wavelength range. A silica beam splitter allows the gonio-reflectometer to be aligned using visible radiation. Infrared radiation is generated by the FT spectrometer's own internal infrared source. The source output is collimated before it passes through the Michelson interferometer. Modulated collimated radiation leaving the FT spectrometer is focused using an off- axis parabolic (OAP) mirror onto a variable diameter circular aperture which acts as a spatial filter. The diameter of this aperture is usually set to approximately 1 mm. An infrared polariser located after the aperture, allows the plane of polarisation illuminating the sample to be selected. The beam is then re-collimated using a second OAP mirror. The collimated radiation passes through a large diameter variable circular aperture, which determines the diameter of the collimated beam, before being focused in the plane of the surface of the test sample using a third OAP mirror. The optical axis of this beam is set parallel to the surface defined by the rotation of the photodetector, with the beam focused in the plane normal to the beam axis and parallel to the common axis of the two turntables. The two-turntable assembly is able to move transversely relative to the beam axis so that the axis of rotation of the two turntables bisects the focussed incident beam.

A commercially-available DLATGS pyroelectric detector, sensitive over the 2.5 µm to 50 µm wavelength range, is incorporated in the detector module of the IGR. DLATGS detectors are known to be highly temperature sensitive [1], hence the IGR detector is actively temperature stabilized using thermoelectric cooling to eliminate drifts in the detector responsivity due to ambient temperature fluctuations. The DLATGS detector has a 1.5 mm diameter active area. An ellipsoidal mirror is used to image the spot formed on the surface of the test sample onto the active area of the DLATGS detector and thus improve the collection efficiency. A circular aperture is used in front of the ellipsoidal mirror. In specular reflectance and transmittance measurements this aperture acts as a baffle and reduces the amount of stray light reaching the detector. In diffuse reflectance and transmittance measurements, this aperture acts as the limiting aperture to define the solid angle over which radiation is collected. An amplifier housed in the detector housing amplifies the detector output before it is sent back to the FT spectrometer for processing.

RESULTS

The IGR has been used to measure the specular reflectance of metal-coated mirrors and other optical components at different angles of incidence and different incident states of polarisation. As an example, Figure 2 shows the specular reflectance of BK7 glass in the 2.5 µm to 18 µm wavelength range corresponding to unpolarised light incident at a 10^o angle of incidence. The IGR has also been used to measure the regular transmittance of a number of infrared optical materials including the transmittance of the filter used by the Flight Model Broad Band Radiometers [2]. These measurements, along with measurements of diffuse reflectance, will be reported at the meeting.

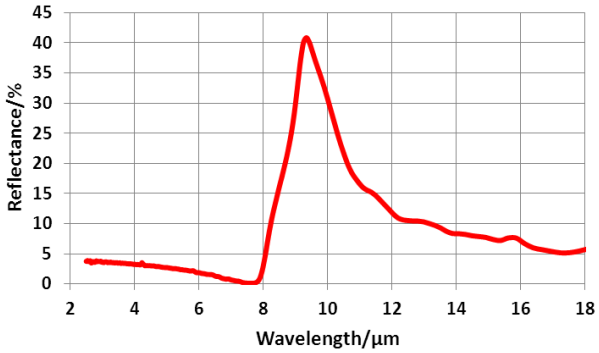

Figure 2. Specular reflectance of BK7 glass for a 10^o angle of incidence.

Support from the National Measurement Office of the UK Department of Business, Innovation and Skills is gratefully acknowledged.

REFERENCES

1. E. Theocharous, "Absolute linearity measurements on a gold-black-coated deuterated L-alanine-doped triglycine sulphate pyroelectric detector" Applied Optics, 47, 3731-3736, 2008.
2. K. Wallace, N. Wright, K. Ward and M. Caldwell, "The BroadBand Radiometer on the EarthCARE Spacecraft", Proc.SPIE,7453, Infrared Spaceborne Remote Sensing and Instrumentation XVII, 2009.

Characterization of Encircled Flux Source For Multimode Fiber Measurements

Jing Zhang[1], Eric Jun Hao Cheung[2], Nigel Guohong Ter [3], and Ravi Doddavaram[4]

[1]*National Metrology Centre (NMC), Agency for Science, Technology and Research (A*STAR), Singapore*
[2]*Engineering Science Programme, Faculty of Engineering, National University of Singapore*
[3]*School of Electrical and Electronic Engineering, Nanyang Technological University*
[4]*Psiber Data Pte. Ltd., Singapore*
Corresponding e-mail address: zhang_jing@nmc.a-star.edu.sg

The encircled flux (EF) measurement was setup in NMC. Insertion loss of a multimode fiber was evaluated with the EF compliant source and compared with non-EF compliant source. The measurement uncertainty was discussed.

INTRODUCTION

With increasing adoption of high speed fiber networks, qualifying the infrastructure becomes imperative before deployment. Be it Ethernet standards or the Fiber Channel standards, the primary performance metric has always been the insertion loss (attenuation) of the channel. The performance specifications are usually defined by standards bodies like IEEE, ISO, TIA etc. With higher speeds, the requirement has become very stringent and the accuracy/uncertainty of loss measurements plays a vital part in qualifying the channel meaningfully. For instance, the insertion loss requirement for an OM3 Fiber for a 40GBase-SR4 standard is about 1.9 dB/Km. Measurements of loss and bandwidth in multimode fibers highly depend upon the launching conditions of the light source. As such, the launch conditions of the light source play a key role in determining the accuracy of measurement.

Encircled flux (EF), defines the integral of power output of the fiber over the radius of the fiber. It is being adopted as a more precise method of defining mode fill for bandwidth simulation and loss testing and has become part of several new multimode fiber testing standards. It sets limits for the amount of optical power included within a specified radius of the fiber core. It is intended to create a more reproducible modal condition for multimode fiber testing. Since EF is new, testing sources for EF are not easily available. EF measurement has yet been demonstrated to be well correlated between labs or manufacturers.

G. He et al. presented a near-field scanning system for evaluating conformity to the encircled flux (EF) standard of a measurement source used for MMF loss/attenuation characterization [1]. In this paper, we studied CCD based EF measurement and analyzed the uncertainty in the EF measurement. The insertion loss of multimode fiber was measured by using an EF compliant source. The uncertainty in MMF loss measurement was discussed.

EF MEASUREMENT

We set up a near field imaging system to have a magnified image of the near field beam profile. A 20X objective lens and a 6.5X zoom lens were combined in the imaging system to obtain the near field image with enough magnification. A near infrared CCD camera (laser profiler) was used to capture the magnified image. A stage micrometer was used to measure the dimension of the near field beam profile by replacing the multimode fiber in the imaging system at the same setting to obtain the image of the scale in the same field of viewing as the image of near field beam profile. Co-axial illumination was at the same wavelength as the light source under test to avoid the alignment error caused by the chromatic dispersion of the imaging system.

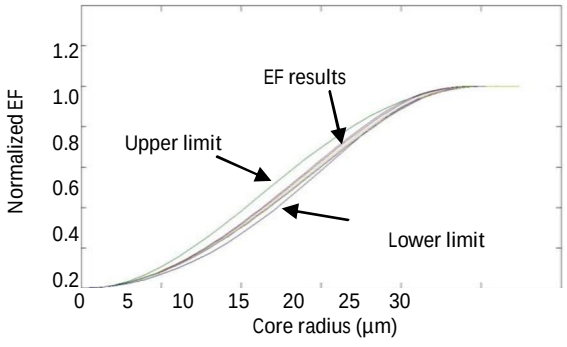

Figure 1. Plots of normalized EF of the LED based EF compliant MMF source from five times of measurements.

A sample of LED based EF compliant 50/125 μm MMF source was measured. The centre of the beam was then determined by our program. The intensity at the cross-section is a function $I(r)$ of radius r away from the optical centre of the core. The EF function is expressed as

$$EF(r) = \int_0^r xI(x)dx / \int_0^R xI(x)dx \quad (1)$$

where the integration limit R is defined in IEC-61280-1-4 [2] and TIA-455-203 [3] as equal to 1.15 times of the nominal core radius of the MMF-under-test. Figure 1 shows the calculated EF of the sample with EF template specified by IEC 61280-4-1 [4] for 850 nm and 50/125 μm fiber.

EF MEASUREMENT ERROR ANALYSIS

The encircled flux measurement involves the intensity measurement and dimension measurement. The errors in the two measurements contribute to the EF calculation result. The sources of dimensional uncertainty are listed in table 1 and the combined standard uncertainty is 0.4 %. The expanded uncertainty of the dimensional measurement is 0.9 %, estimated at a level of confidence of approximately 95 % with a coverage factor k = 2.2.

Table 1. Dimensional uncertainty analysis.

Source of uncertainty	*Ui* (%)	*DOF*
Scale standard uncertainty	1.5E-3	infinity
Uncertainty due to alignment of the stage micrometer	1.0E-3	5
Uncertainty due to alignment of fiber source	2.0E-3	5
Uncertainty due to scale imagin g processing	2.9E-3	5
Combined standard uncertainty	4.0E-3	14
Expanded uncertainty	9E-3	

The uncertainty of the intensity measurement is mainly from the linearity of the CCD camera which is ±1%. As EF is the integral of the pixels within a radius, the error of EF due to intensity error is much less than the intensity error at individual pixels. The error in locating the centre of the beam contributed to the error in EF calculation, which was found to be very small in our cases.

COMPARISON OF MMF MEASUREMENT BY USING EF AND NON-EF SOURCE

The insertion loss of MMF is very modal dependant. We measured the insertion loss of a 200 m long 50/125 μm MMF fiber with SC connectors. The light source and the standard photodetector had FC connectors. FC – SC fiber patch cords (50/125 μm) were used to connect the light source to MMF, and MMF to standard photodetector. By using the EF compliant MMF source, the insertion loss of the 200 m MMF patch cord was measured to be 0.96 dB with 0.008 dB standard deviation. The sources of uncertainty of the insertion loss measurement are listed in Table 2. The combined standard uncertainty was 0.042 dB. The expanded uncertainty of the 200 m MMF patch cord insertion loss measurement was 0.12 dB, estimated at a level of confidence of approximately 95 % with a coverage factor k = 2.87. By using a normal VCSEL MMF source, the insertion loss of the same set was measured to be 0.84 dB with 0.012 dB standard deviation. The combined standard uncertainty was 0.048 dB. The expanded uncertainty was 0.12 dB, estimated at a level of confidence of approximately 95 % with a coverage factor k = 2.43. The measured insertion loss by using normal VCSEL source was 0.12 dB smaller than by using EF compliant source.

Table 2. Insertion loss uncertainty analysis.

Source of uncertainty	*Ui* dB	*DOF*
Measurement uncertainty of the R.S. detector	7.50E-3	infinity
Light source power stability	3.00E-3	4
Reproducibility of SC/SC fiber connectors' linkage	4.00E-2	4
Repeatability of MMF IL	8.00E-3	4
Combined standard uncertainty	4.16E-2	4.66E+00
Expanded uncertainty	1.19E-1	

CONCLUSION

The encircled flux measurement of 50/125 μm multimode fiber light source at 850 nm wavelength was set up. The error and uncertainty in the EF measurement were discussed. The insertion loss of a 200 m MMF patch cord was measured by using an EF compliant source. The insertion loss was 0.96 dB with expanded uncertainty of 0.12 dB.

REFERENCES

1. G. He, et al., "Improved near-field scanning system for encircled flux measurement", Optoelectronics, IET, Vol. 5 No. 1, pp. 46-49 (2009).
2. IEC 61280-1-4 Ed. 2.0: Fibre-optic communication subsystem test procedures – Part 1-4: General communication subsystems – light source encircled flux measurement method.
3. TIA-455-203-A: Light source encircled flux method.
4. IEC 61280-4-1 Ed. 2.0: Fibre-optic communication subsystem test procedures – Part 4-1: Installed cable plant – multimode attenuation measurement.

Effective Refractive-Index Differences Measurement for Few-Mode Fibers

Jing Zhang[1], Nigel Guohong Ter[2], Xuguang Shao[2], Tianye Huang[2,3], Zhifang Wu[2,3], Yunxu Sun[2], Huy Quoc Lam[4], and Ping Shum[2,3]

[1] *National Metrology Centre, Agency for Science, Technology and Research (A*STAR), Singapore*
[2] *School of Electrical and Electronics Engineering, Nanyang Technological University, Singapore*
[3] *CINTRA CNRS/NTU/THALES, Singapore*
[4] *Temasek Laboratories, Nanyang Technological University, Singapore*
Corresponding e-mail address: Zhang_jing@nmc.a-star.edu.sg

A method for measuring and analyzing the effective refractive index differences in a few-mode fiber is described. From the analysis, the interferences between the excited modes can be observed. The effective refractive index differences Δn_{eff} in the fiber can be calculated.

INTRODUCTION

Few-mode fibers have been a hot research area in the past few years. Mode-division multiplexed transmission in few-mode fibers has attracted great attention as it can increase the transmission capacity of a single optical fiber [1]. The characterization of few-mode fibers is of interest and important to the manufacturers and users of the fibers.

Menashe et al. developed an interferometric technique for measuring the dispersion of high order mode in optical fibers [2]. The method was based on measuring the interference pattern in a short distance of fiber. The dispersion is measured using the wavelength dependence of the interference signal between the basic mode and the hgh order mode. Savolainen et al. presented a method for measuring the effective refractive-index differences in a few-mode fiber by applying axial fiber stretching[3].

The effective refractive-index difference is an important property for few-mode fibers. In this paper we present the method by using inversion Fourier transform to analyze the spectrum and get the differences in effective refractive indexes.

THE METHOD

The interferometer configuration in [2] and [3] is used in our method. The fundamental mode and higher order modes are excited in the few-mode fiber by launching the light from a single mode fiber with lateral offset. As a result of propagation constant difference, phase differences between these modes accumulate in the few mode fiber. At the end of the few mode fiber, a second single mode fiber collects the light from the different modes in few mode fiber offset. As the second single mode fiber only supports one mode, inter-modal interferences happen.

Assuming two modes (LP01 and LP11) exist in the few mode fiber, at a given wavelength, the two modes interfering in the second single mode fiber can be expressed as

$$\begin{aligned} E &= E_1 + E_2 \\ &= \sin\left(\omega t + Ln_{eff1}/\lambda\right) + \sin\left(\omega t + Ln_{eff2}/\lambda\right) \\ &= 2\sin\left(\omega t + L\frac{n_{eff1}+n_{eff2}}{2\lambda}\right)\cos\left(L\frac{n_{eff1}-n_{eff2}}{2\lambda}\right) \end{aligned} \quad (1)$$

where E1 and E2 are the interfering light waves from mode LP01 and LP11, respectively, ω is the frequency of the propagating wave, λ is the wavelength L is the length of few mode fiber, and n_{eff1} and n_{eff2} are the effect refractive index of the two guided modes. The intensity detected by a photodetector is

$$\begin{aligned} I &\propto \cos\left(L\left(n_{eff1}-n_{eff2}\right)/\lambda\right) = \cos\left(L\frac{\Delta n_{eff}}{\lambda}\right) \\ &= \cos\left(\omega\frac{L\Delta n_{eff}}{2\pi c}\right) \end{aligned} \quad (2)$$

where Δn_{eff} is the difference in effective refractive indexes, c is the speed of light. The spectrum of the intensity is determined by the difference between the two interfering modes. By doing inverse Fourier transform, a peak will appear in the time response, at $t = \frac{L\Delta n_{eff}}{2\pi c}$. Δn_{eff} can be calculated from *t*.

When there are other modes existing in the fiber, interference may happen with those modes [3]. The spectrum of the intensity will have more components. By doing inverse Fourier transform, more peaks due to interferences between the modes will appear in the time response. By analyzing all peaks in the time response, differences between the interfering modes will be solved.

EXPERIMENTAL SETUP AND MEASUREMENTS

The experimental setup consists of a tunable laser source and an optical spectrum analyzer (OSA). A piece of few-mode fiber is spliced with normal single mode fibers at the both ends. Large lateral offset are made at joints between few-mode fiber and the single mode fibers in order to excite the higher order modes considerably. Two fiber samples are measured in our study. Fiber Sample 1 is a 50 cm-long ~5.2 µm-core-diameter fiber doped with ~35 mol.% Ge. Figure 1 shows the measured spectrum in the range from 1520 nm to 1620 nm. Figure 2 shows the analyzed time response of Fiber Sample 1. There is only one peak in the time response of Fiber Sample 1, which indicates that there are only two modes (LP01 and LP11) excited in the fiber. The effective refractive index difference Δn_{eff} between the two modes is calculated to be 0.0099.

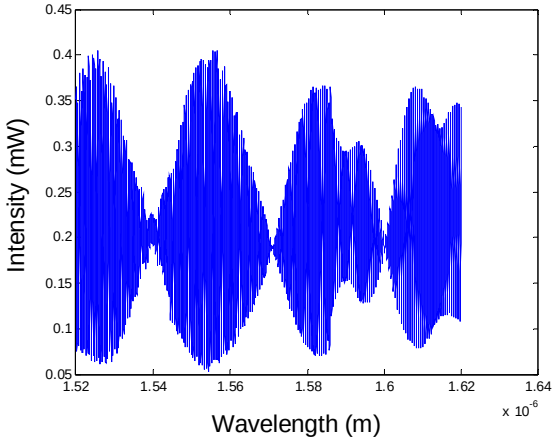

Figure 1. Measured spectrum of Fiber Sample 1.

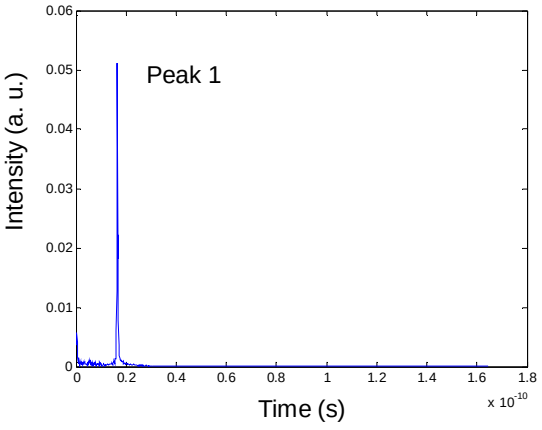

Figure 2. Time response of Fiber Sample 1.

Fiber Sample 2 is a 30.5cm-long ~7.6µm-core-diameter fiber doped with ~35 mol.% Ge. Figure 3 shows the analyzed time response from Fiber Sample 2. Two peaks appear in the time response. Peak 1 is the interference between LP01 and LP11. Peak 1 may be the interference between LP11 and LP12. Δn_{eff} is calculated and shown in table 1. Simulations are carried out to find out all the modes in the two fibers.

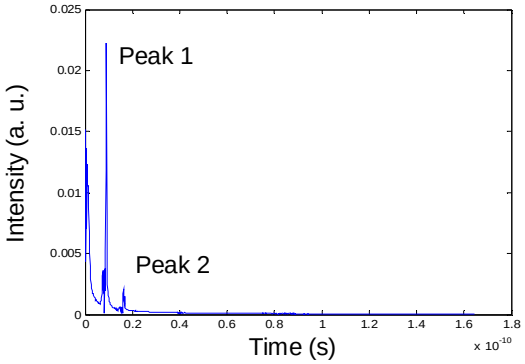

Figure 3. Time response of Fiber Sample 2.

Table 1. Calculation of Δn_{eff}.

Fiber sample	Peak	Time (s)	Δn_{eff}
Fiber Sample 1	Peak 1	1.643E-11	0.0099
Fiber Sample 2	Peak 1	9.035e-12	0.0089
Fiber Sample 2	Peak 2	1.626e-11	0.016

CONCLUSION

The method for measuring and analyzing the effective refractive index differences in a few-mode fiber was presented. The modes interferences in the fiber can be observed in the analysis. The measurement results agree well with theoretical predictions for the fiber under investigation.

REFERENCES

1. R. Ryf, S. Randel, A. H. Gnauck, C. Bolle, A. Sierra, S. Mumtaz, M. Esmaeelpour, E. C. Burrows, R. J. Essiambre, P. J. Winzer, D. W. Peckham, A. H. McCurdy, and R. Lingle, "Mode-division multiplexing over 96km of few-mode fiber using coherent 6 x 6 MIMO processing," J. Lightwave Technol. 30(4), 521–531 (2012).
2. D. Menashe, M. Tur, and Y. Danziger, "Interferometric technique for measuring dispersion of high order modes in optical fibres," Electron. Lett. 37(24), 1439–1440 (2001).
3. Juha-Matti Savolainen, Lars Grüner-Nielsen, Poul Kristensen, and Peter Balling, "Measurement of effective refractive-index differences in a few-mode fiber by axial fiber stretching", OPTICS EXPRESS, Vol. 20(17), 18646-18651 (2012).

New Apparatus for Fluorescence Spectrophotometer Calibration

Hsueh-Ling Yu[1], Chin-Chai Hsiao[1], Daniel Ting[2], and Chung-Wen Hung[1]

[1]*Center for Measurement Standards, Hsinchu, Taiwan, R.O.C.,*
[2]*Agilent Tech. Taiwan Ltd., Taipei, Taiwan, R.O.C.*
Corresponding e-mail address: hsuehling.yu@gmail.com

Traditionally the fluorescence spectrophotometer is calibrated using chemical-made fluorescence reference materials for the ultraviolet (UV) to visible ranges and tungsten lamp for the near infrared (IR) range. Besides the inconvenience of using tungsten lamp, the common problem of many reference materials is the overlapping of the excitation and emission spectra which may induce calibration error in some wavelength rages. This article presents a LED reference source which is designed to have the same form as the sample cell usually used for the fluorescence spectro-photometer and is able to cover the whole range from UV to near IR to take the place of the inconvenient tungsten lamp and increase the measurement accuracy by avoiding the overlapping spectra problems.

INTRODUCTION

Fluorescence spectrophotometer is widely used for qualitative or quantitative analysis for many organic and some inorganic compounds. As shown in Figure 1, when the sample is stimulated by $S(\lambda_{ex})$, $E_{em}(\lambda_{em})$ is proportional to $S(\lambda_{ex})\times A(\lambda_{ex})\times y(\lambda_{ex}, \lambda_{em})$ and the output signal $M(\lambda_{em})$ is equal to $E_{em}(\lambda_{em})\times D(\lambda_{em})$. Usually the fluorescence spectro-photometer performs three measurements. The first is illuminating the fluorescence sample by fixing the excitation monochromator at wavelength λ_{ex} and measuring the fluorescence spectrum $E_{em}(\lambda)$ emitted from the sample by scanning the emission monochromator. Assuming the output signal is $M_1(\lambda)$, then $E_{em}(\lambda) = M_1(\lambda)/D(\lambda)$. The second measurement is fixing the emission monochromator at wavelength λ_{em} and scanning the excitation monochromator to measure the excitation spectrum $E_{ex}(\lambda)$ of the sample. Assuming the signal is $M_2(\lambda)$, then $E_{ex}(\lambda) = M_2(\lambda)/S(\lambda)$. The third measurement is synchronous scanning of the sample with a wavelength difference $\Delta\lambda$ between the excitation monochromator and emission monochromator. Assuming the output signal is $M_3(\lambda)$, then $E_{em}(\lambda) \propto M_3(\lambda)/S(\lambda+\Delta\lambda)/D(\lambda)$. Therefore $S(\lambda)$ and $D(\lambda)$ shall be calibrated to get consistent fluorescence spectrum $E_{ex}(\lambda)$ and $E_{em}(\lambda)$, no matter by which fluorescence spectrophotometer they are measured.

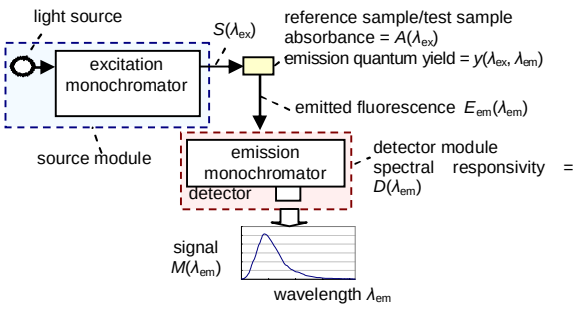

Figure 1. Schematic diagram of the fluorescence spectrophotometer.

TRADITIONAL CALIBRATION METHODS

Applying fluorescence reference material is one of the most popular methods for fluorescence spectrophotometer calibration [1]. Figure 2 [2] shows the excitation (blue curves) and emission (red curves) spectra of the reference materials Anthracene and Rhodamine B (RhB). Usually, the excitation spectrum is applied to calibrate $S(\lambda)$ of the source module and the emission spectrum is used to calibrate $D(\lambda)$ of the detector module. However many fluorescence reference materials have the problem of spectrum overlap as shown in Figure 2. The re-absorption effect may induce measurement deviation for certain wavelength range due to the calibration error within the overlap region. Besides the problem of spectrum overlap, currently there is no suitable IR fluorescence reference material. A reference light source like tungsten lamp is needed for IR calibration. This increases the expense and inconvenience of calibration.

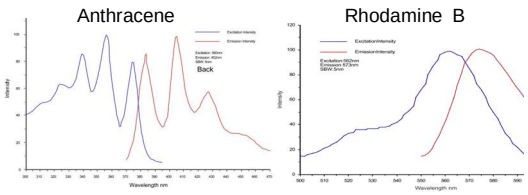

Figure 2. The emission and excitation spectra of the reference materials.

NEW APPARATUS FOR CALIBRATION

To reduce the inconvenience of current calibration method and increase the measurement accuracy, a new type of reference source is designed in this article. To take the place of the reference materials, the primary consideration of the reference source is ease of use. As shown in Figure 3, considering user habits and also in response to the space and measurement range of the fluorescence spectrophotometer, the reference source is composed of 9 SDM LEDs which are welded on the printed circuit board and placed inside the sample cell. Therefore this LED reference source can be easily inserted into the cell holder while calibrating the fluorescence spectrophotometer. The composite spectrum of the LED reference source covers the range from 340 nm to 1000 nm. The spectrum can be adjusted easily by choosing different LEDs.

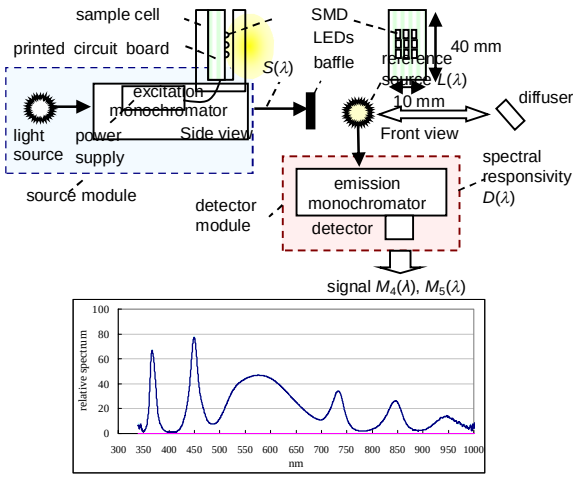

Figure 3. Design of the LED reference source and its relative spectrum.

Figure 4 depicts the calibration procedures by using the reference source. First, block $S(\lambda)$ and place the reference source with known spectrum $L(\lambda)$ at the same position used for placing the sample cell. Measure $L(\lambda)$ with the detector module and assume the output signal is $M_4(\lambda)$. Then $M_4(\lambda)$ is proportional to $L(\lambda)\times D(\lambda)$. As $L(\lambda)$ is known, the relatively spectral responsivity $D(\lambda)$ of the detector module can be calculated from $M_4(\lambda)/L(\lambda)$. Afterward, replace the reference source with the diffuser and illuminate the diffuser which reflectance is known as $R(\lambda)$ by $S(\lambda)$ and scan synchronously with both monochromators. The signal $M_5(\lambda)$ is proportional to $S(\lambda)\times R(\lambda)\times D(\lambda)$. Since $R(\lambda)$ and $D(\lambda)$ are known, the relative spectrum of $S(\lambda)$ is then equal to $M_5(\lambda)/D(\lambda)/R(\lambda)$.

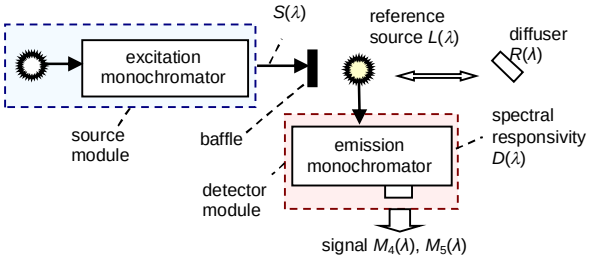

Figure 4. The schematic diagram for measuring $D(\lambda)$ and. $S(\lambda)$by using the LED reference source.

EXPERIMENTAL RESULTS

To check the performance of the new apparatus, a fluorescence spectrophotometer is calibrated by using the LED reference source to obtain the output spectrum S(λ) of the source module and the spectral responsivity D(λ) of the detector module. Afterward use RhB as the test sample and apply this calibrated fluorescence spectrophotometer to measure the excitation and emission spectra of RhB. If the calibration works well, the measured excitation and emission spectra shall be the same as the spectra shown in Figure 2. Figure 5 shows the results of $E_{ex}(\lambda)$ and $E_{em}(\lambda)$ measured by the fluorescence spectrophotometer which are the same as the reported values of RhB as depicted in Fig. 2. The results verify that the LED reference source has excellent performance in fluorescence spectrophotometer calibration.

CONCLUSIONS

Compared with reference materials, using LED reference source can increase measurement accuracy since there are no problems like the excitation and emission spectra overlapping, the emission magnitude being affected by the wavelength and polarization of the excitation light, and so on. Other advantages of the LED reference source include the long lifetime of LEDs, the signal is much stronger

than the emission light from the reference materials, and the wavelength range can be modified simply by choosing different LEDs rather than changing the formula of the reference materials by chemical methods. The experiment verified that applying this LED reference source can obtain satisfying results for fluorescence spectrophotometer calibration.

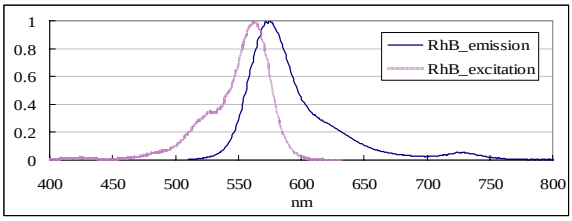

Figure 5. The emission and excitation spectra of RhB measured by the fluorescence spectrophotometer calibrated by the LED reference source.

REFERENCES

1. Standard Guide for Fluorescence-Instrument Calibration and Qualification, ASTM E2719-09.
2. Reference Materials for Molecular Fluorescence Spectrophotometry, Starna Scientific Ltd.

Bilateral Comparison of Diffuse Reflectance

Wen-Chun Liu[1], Yu Ma[2], Hsueh-Ling Yu[1], and Ruoduan Sun[2]

[1]*Center for Measurement Standards, ITRI, Hsinchu, Taiwan*
[2]*National Institute of Metrology, Beijing, China*
Corresponding e-mail address: sveta.liu@gmail.com

This paper presents the bilateral comparison of diffuse reflectance between CMS and NIM. The results show that the difference is larger at around 380 nm and 780 nm, and there are more uncertainty sources at beginning and ending of the measurement. The incident angle within 8° has limited effect on the diffuse reflectance.

INTRODUCTION

Diffuse reflectance comparison is key comparison, and APMP will hold the comparison in the near future. To reduce the problems during measurement and to find out the reasons caused the measurement difference, a bilateral comparison between Center for Measurement Standards (CMS) and National Institute of Metrology (NIM) was taken before the formal APMP spectral diffuse reflectance comparison. Another reason for the bilateral comparison is the closer and closer interaction between Taiwan and China, and thus the measurement consistency becomes more and more important.

The comparison was completed in the end of 2013. CMS was responsible for preparing the artefact for this comparison. The diffuse reflectance comparison was performed under de:8° or 8°:de geometry condition.

METHOD OF THE COMPARISON

A white plate with gloss and matt surfaces was used as the artefact for this comparison. The artefact was calibrated by NIM and CMS, respectively. The comparison is to measure the spectral diffuse reflectance of the white plate. For the gloss surface, two geometry conditions, 8^o:de and 8^o:di were performed in this comparison, and for the matt surface, only 8^o:de geometry condition was measured. The spectral diffuse reflectance of the transfer standard was measured at wavelength range from 380 nm to 780 nm in suitable laboratory accommodation maintained at a temperature of 20°C to 25°C. To understand the effect of the incident angle, the artefact was also measured with 0^o:de geometry accessory whose incident angle is 3.5^o in CMS.

Diffuse reflectance in the comparison was measured by using spectrometer through substitution method. The standard in CMS was traced to National Research Council (NRC), and that in NIM was traced to an absolute system realized by an auxiliary integrating sphere method.

The results of the diffuse reflectance from CMS were S_{CMS} and those from NIM were S_{NIM}. The difference was shown as equation (1).

$$\Delta = \left(S_{CMS} - S_{NIM}\right) \quad (1)$$

COMPARISON RESULTS

Figures 1 to 3 show the difference of the diffuse reflectance between CMS and NIM.

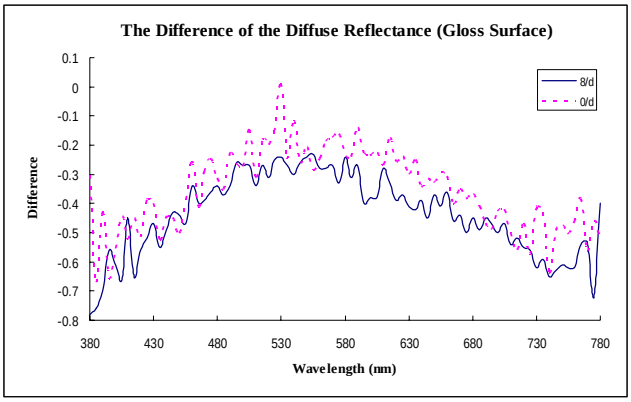

Figure 1. The difference of the diffuse reflectance at 8°:di and 0°:di on the gloss surface.

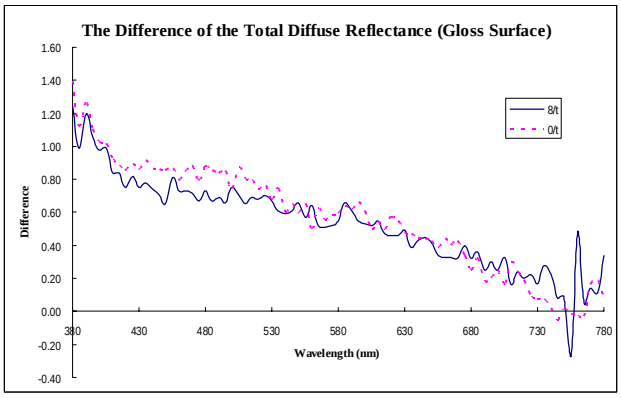

Figure 2. The difference of the diffuse reflectance at 8°:de and 0°:de on the gloss surface.

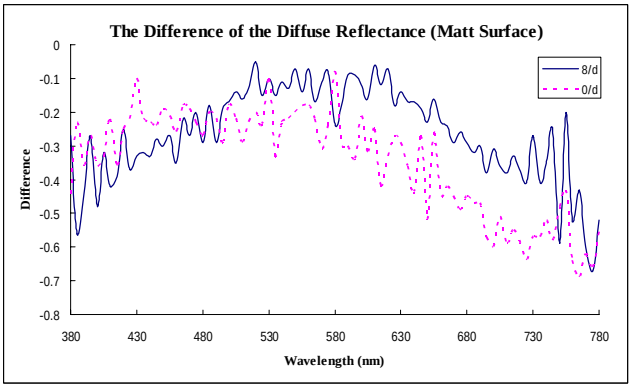

Figure 3. The difference of the diffuse reflectance at 8°:de and 0°:de on the matt surface.

The uncertainty in NIM is 0.6 % from 400 nm to 760 nm, and 0.8 % from 380 nm to 395 nm and from 765 nm to 780 nm. The uncertainty in CMS is 0.6 % from 380 nm to 780 nm. From Figure 1 to Figure 3, larger uncertainty was found at beginning and ending of the diffuse reflectance measurement, so Figure 4 to 6 show the results of the spectral reflectance at 8°:de and 8°:di at 380 nm and 780nm on the gloss and matt surface.

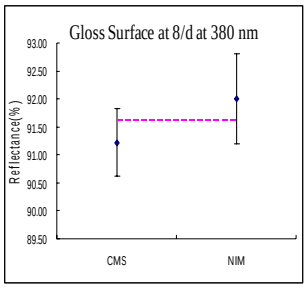

Figure 4(a)

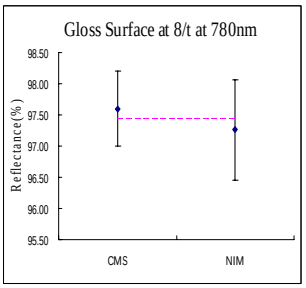

Figure 4(b)

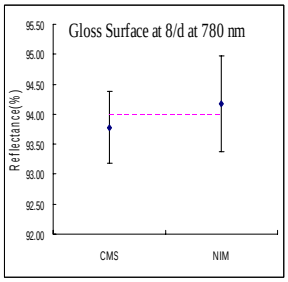

Figure 5(a)

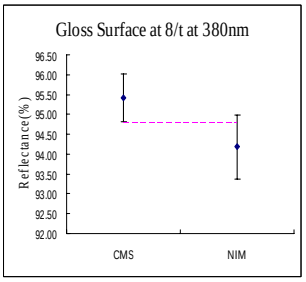

Figure 5(b)

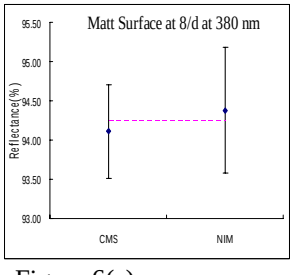

Figure 6(a)

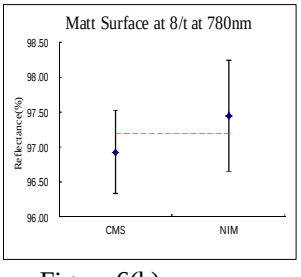

Figure 6(b)

DISCUSSION AND CONCLUSIONS

The comparison shows that the difference becomes smaller for longer wavelengths at 8°:di and 0°:di. The general trends at 8°:de and 0°:de are larger difference at around 380 nm and 780 nm. The difference at 8°:de and 8°:di from 750 nm to 780 nm changes more dramatically than that at 0°:de and 0°:di shows that the spectrophotometer with 8°:de accessory is not stable at those wavelengths. There should be more uncertainty sources at beginning and ending of the measurement.

The results on the gloss surface at 0°:de and 0°:di are smaller than those at 8°:de and 8°:di but the results on the matt surface at 0°:de are larger than those at 8°:de at longer wavelengths. The roughness of the surface also influences the measurement results.

The difference between 8°:de and 0°:de or between 8°:di and 0°:di is close. The incident angle within 8° has limited effect on the diffuse reflectance.

REFERENCE

1. Colorimetry, 3rd Edition, CIE 15-2004, 2004.

Absolute linearity measurements on three InSb detectors in the infrared

E. Theocharous[1] and S. P. Theocharous[2]

[1]*National Physical Laboratory, Teddington, UK,*
[2]*Blackett Laboratory, Imperial College, London, UK*
Corresponding e-mail address: e.theo@npl.co.uk

The non-linearity characteristics of three InSb detectors of different active areas and supplied by three different detector manufacturers were experimentally investigated using the NPL detector linearity or response characterization facility. All three InSb detectors exhibited a linear response for incident radiant powers ranging from below 1 nW to about 100 µW at 4.7 µm and 3.8 µm. Linearity measurements at 2.2 µm and 1.6 µm indicate that the response of all three detectors is linear for incident radiant powers ranging from below 1 nW to about 50 µW but becomes non-linear for radiant powers higher than 50 µW. The deviation from linearity was shown to be independent of the area of the detector being illuminated. Outside the linear regime, two non-linearity regimes were identified at high radiant powers, the first characterized by the level of incident radiant power alone, with the second showing a dependence on the wavelength of incident radiation.

INTRODUCTION

The absolute linearity characteristics of a number of infrared detectors, including photoconductive (PC) HgCdTe, photovoltaic (PV) HgCdTe, PbS, PbSe and pyroelectric detectors have already been reported [1–4]. The responsivity of the infrared photon detectors which were investigated (PC and PV HgCdTe, PbS and PbSe) were shown to exhibit strong non-linearity [1- 4], even when relatively low optical signals were being detected. Moreover, the deviations from linearity of all infrared photon detectors evaluated to date have been shown to be dependent on the illuminating irradiance, rather than the total radiant power incident on the detectors.

The photo-detectors offering the highest specific detectivity (D*) in the 3 µm to 5 µm atmospheric window are the PV InSb detectors. Previous studies of the linearity of response of InSb detectors were restricted to wavelengths below 2.1 µm, well away from the 3 µm to 5 µm atmospheric window where InSb detectors are expected to operate. The purpose of this paper is to report the results of an experimental investigation carried out at NPL into the characterization of the linearity of response of three cryogenically-cooled PV InSb detectors. Special care was paid to the identification of the true dependence of the deviation from linearity of these detectors on parameters such as the wavelength of radiation illuminating the detector as well as the area of the detector being illuminated.

METHOD

The linearity of a photo-detection system describes its ability to generate an electrical output signal which is directly proportional to the input optical signal. Radiometrists quantify the deviation from linearity of photodetection systems using a parameter called the "linearity factor", $L(V_{A+B})$ [1]. The linearity characteristics of the three InSb detectors were evaluated on the NPL linearity of response characterisation facility. Full details of this facility can be found in [1]. This facility measures the linearity factor of photodetection systems using the "flux-superposition" method [2]. This method was adopted because it is an absolute linearity measurement method.

RESULTS

Figure 1 shows the plot of the linearity factor of a 5 mm diameter InSb detector "A" at 2.2 µm as a function of incident radiant power, measured using a 2 mm diameter spot of quasi-monochromatic radiation. This shows that the detector is linear for radiant powers ranging from 0.1 nW to about 50 µW. However, for radiant powers exceeding 50 µW, the response of the test detector becomes non-linear, with the deviation from linearity increasing monotonically with increasing incident radiant power (see Figure 1). Figure 2 shows a plot of the linearity factor of the same InSb detector (detector "A") as a function of incident radiant power, measured using a 2 mm diameter spot of quasi-monochromatic radiation

peaking at 1.6 µm, 2.2 µm and 3.8 µm. For radiant powers lower than 800 µW, there is good overlap between the three sets of results, indicating that the deviation from linearity is independent of the wavelength with which the detector is illuminated and only depends on the total radiant power illuminating the test detector. However, Figure 2 also indicates that the slope of the plots increases sharply above a certain level of incident radiant power, and this value is wavelength dependent.

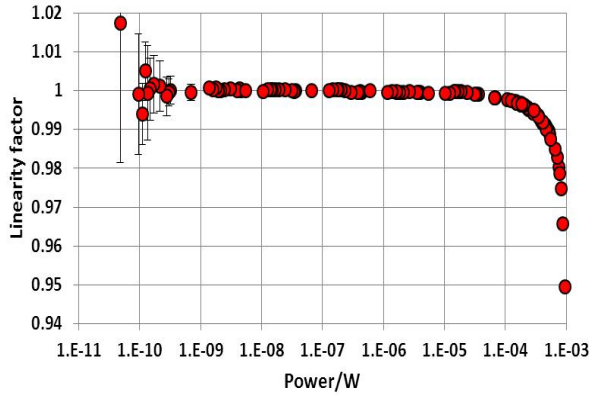

Figure 1. Plot of the linearity factor of the InSb detector "A" at 2.2 µm as a function of incident radiant power, measured using a 2 mm diameter spot.

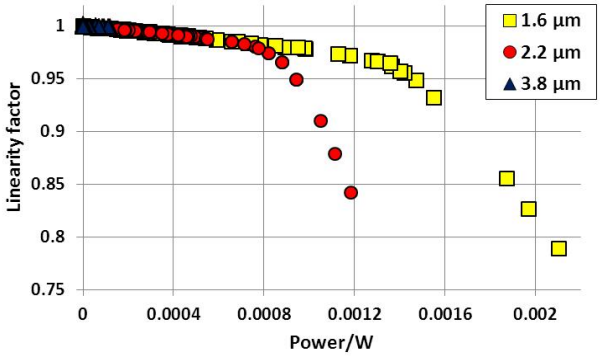

Figure 2. Plot of the linearity factor of the InSb detector "A" as a function of incident radiant power, measured using a 2 mm diameter spot of radiation peaking at 1.6 µm, 2.2 µm and 3.8µm. The maximum radiant power available at 3.8 µm was 100 µW.

DISCUSSION

The linearity of response characteristics of all three InSb detectors which were evaluated showed no deviation from linearity when the detectors were illuminated with quasi-monochromatic radiation peaking at 3.8 µm and 4.7 µm for incident radiant powers ranging from below 1 nW up to 100 µW, the maximum radiant power which was available using glowbar source, the 3.8 µm and 4.7 µm bandpass filters and a 2 mm diameter pinhole, see Figure 2.

Higher radiant powers were available at shorter wavelengths so measurements were repeated at 2.2 µm and 1.6 µm. For radiant powers higher than about 50 µW, all three InSb detectors which were evaluated exhibited a non-linear response. The deviation from linearity for all three test detectors was independent of the area of the detector being illuminated, indicating that the deviation from linearity depends on the total radiant power illuminating the detectors, not the incident irradiance as was seen in previous linearity measurements on other infrared photon detector technologies.

Our measurements at the short wavelengths (1.6 µm and 2.2 µm), where high radiant powers were available, also indicate that there are three regimes in the linearity characteristics of the InSb test detectors. In the first regime, the response of the test detectors is linear for incident radiant powers below 50 µW. Beyond this level of radiant power, the response of all three test detectors becomes nonlinear, with the deviation from linearity increasing linearly with increasing incident radiant power. In this regime the deviation from linearity is largely independent of the wavelength of the incident radiation. Beyond a certain level of incident radiant power, the slope of the plot of the linearity factor versus radiant power increases sharply, and this defines the start of the third regime (see Figure 2). This indicates that beyond this level of radiant power, the deviation from linearity is caused by a different mechanism which is able to give rise to a stronger non-linearity. Moreover, the radiant power at the boundary between the second and third regimes (which is defined by the increase in the slope of the plots) appears to be strongly dependent on wavelength, with the shorter the wavelength, the higher the radiant power at which the last regime comes into play.

Support from the National Measurement Office of the UK Department of Business, Innovation and Skills is gratefully acknowledged.

REFERENCES

1. E. Theocharous, "Absolute linearity measurements on a PV HgCdTe detector in the infrared", *Metrologia*, **49**, S99-S105, 2012.

2. E Theocharous, “Absolute linearity measurements on PbS detectors in the infrared”, *Applied Optics*, **45**, 2381-2386, 2006.
3. E. Theocharous, J. Ishii and N. P. Fox, “Absolute linearity measurements on HgCdTe detectors in the infrared”, *Applied Optics*, **43**, 4182-4188, 2004.
4. E. Theocharous, “Absolute linearity measurements on a PbSe detector in the infrared”, *Infrared Physics and Technology*, **50**, 63-69, 2007.

Assembly and evaluation of a pyroelectric detector bonded to vertically aligned multiwalled carbon nanotubes over thin silicon

E. Theocharous[1], S. P. Theocharous[2], and J. H. Lehman[3]

[1]*National Physical Laboratory, Teddington, UK*
[2]*Physics Department, Imperial College, London, UK*
[3]*National Institute of Standards and Technology, Boulder, Colorado, USA*
Corresponding e-mail address: e.theo@npl.co.uk

A novel pyroelectric detector consisting of a vertically aligned nanotube array on thin silicon (VANTA/Si) bonded to a 60 µm thick crystal of $LiTaO_3$ was fabricated and its performance was evaluated using NPL's detector-characterisation facilities. The relative spectral responsivity of the detector was found to be spectrally flat in the 0.8 µm to 24 µm wavelength range, in agreement with directional-hemispherical reflectance measurements of witness samples of the VANTA coatings. The test detector exhibited good spatial uniformity of response as well as a small super-linear response, which is similar to that of pyroelectric detectors coated with good quality goldblack coatings.

INTRODUCTION

The choice of the absorptive coating is very important in determining the performance of a thermal detector. The addition of a black coating to the active area of the thermal detector increases the fraction of incident radiation which is absorbed and converted into heat, but also increases the heat capacity and hence reduces the temperature rise of the detector-coating composite. It is important that black coatings have high absorptivity, and also intrinsically low thermal capacity. These requirements are all satisfied by VANTA coatings which have been shown to combine very high absorptivity values and very low thermal capacities. Absorptive coatings applied to thermal detectors should also have high thermal conductivities. This condition is also satisfied by VANTA coatings which have been shown to have high thermal conductivity axially as well as transverse to the nanotube forest.

Despite the potential advantages of VANTA coatings over other black coatings, they have yet to be widely applied as absorptive coatings for thermal detectors because VANTA coatings have only been reliably grown on high-mass super alloys and on thermally stable materials such as silicon. The main obstacle to putting a VANTA coating on a pyroelectric transducer is that VANTA coatings are grown at substrate temperatures of about 750 ^{o}C in a reducing atmosphere. The growth temperature is well above the Curie point of pyroelectric materials such as $LiTaO_3$ (~660 ^{o}C) and the growth conditions modify the dielectric properties of the crystal by diffusion of oxygen from the surface.

This paper describes the evaluation of a pyroelectric detector having a novel composite VANTA-on-silicon absorber. The thin silicon substrate on which the VANTA coating was grown was bonded to a 60 µm thick $LiTaO_3$ pyroelectric crystal, which acts as the detector transducer. The paper summarises the fabrication of the new detector and the evaluation of its radiometric characteristics. Full details of the fabrication and evaluation of this detector can be found elsewhere [1]

METHOD

A variety of methods have been used to apply carbon nanotubes to a thermal detector, including bulk nanotubes sprayed on pyroelectric materials [2] and a freestanding forest transferred from a silicon substrate to a pyroelectric or thermopile detector [3]. These approaches all come with compromises with respect to cost, detector performance and fabrication yield. In the present work, rather than removing the nanotube forest from a silicon growth substrate and transferring it to the pyroelectric substrate, the nanotubes are left on the silicon substrate. In order to minimize the heat capacity, the nanotube forest was grown on relatively thin silicon (this subassembly is referred to as VANTA/Si) and the VANTA/Si was bonded directly to the pyroelectric detector electrode. Figure 1 shows a flow chart which summarises the process which was used to fabricate the pyroelectric detector with the VANTA/Si coating. The nanotubes were grown by chemical vapour deposition (CVD).

The pyroelectric detector element was constructed from a 60 µm thick, 12 mm diameter,

lithium tantalate ($LiTaO_3$) crystal. Circular electrodes, 10 mm in diameter, were deposited on each face of the crystal, which consisted of 50 nm of gold on top of 25 nm of chromium on the back face and 25 nm of chromium on the front face (the face to which the VANTA/Si was attached).

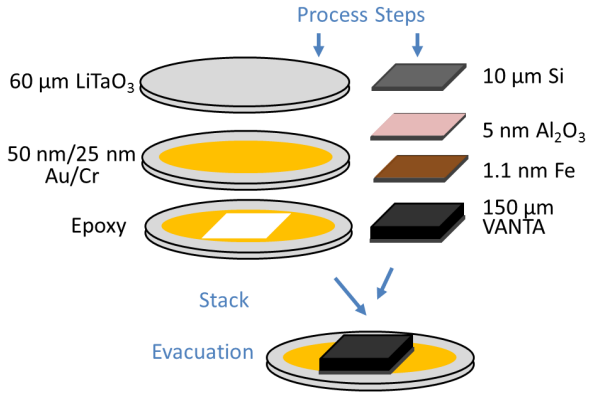

Figure 1. Flow chart summarising the process which was used to fabricate the pyroelectric detector with the VANTA-on-silicon coating (from reference 1).

The VANTA/Si was attached to the front electrode with silver-filled, two part electrically-conducting epoxy. The composite VANTA/Si/$LiTaO_3$ stack was assembled into a detector package such that the front electrode was the electrical "earth ground" while the back electrode was the "signal electrode." The front face of the detector was defined by a 3 mm aperture placed in front of the area defined by the VANTA/Si coating.

RESULTS

The test detector offers superior Signal-to-Noise Ratio (SNR) characteristics compared to previous VANTA-coated pyroelectric detectors, allowing the spectral responsivity measurements to be extended to 24 µm. Figure 2 shows the relative spectral responsivity of the VANTA/Si-coated pyroelectric detector in the 0.8 µm to 24 µm wavelength range, normalised at a wavelength of 1 µm. The error bars shown represent the standard uncertainty of the measurements. Figure 2 shows that the spectral responsivity of the test detector is spectrally flat (within the uncertainty of the measurements) over the entire wavelength range of measurements. Since the absorption characteristics of the VANTA/Si coating govern the detector relative spectral responsivity characteristics, it can be concluded that the VANTA coating deposited on the test detector has a spectrally flat absorbance over the 0.8 µm to 24 µm wavelength range. This, in combination with absolute directional-hemispherical reflectance measurements made at NPL on witness VANTA samples [4], indicate that the VANTA coating deposited on the test detector combines high absorptivity with spectral flatness. This confirms the suitability of VANTA coatings for a number of applications, including thermal detectors in the infrared.

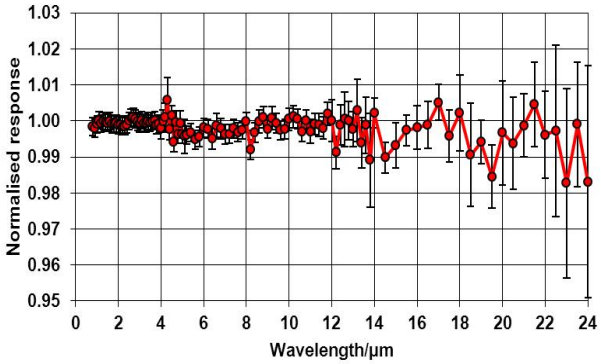

Figure 2. Relative spectral responsivity of the pyroelectric detector with the VANTA/Si coating, normalised at 1 µm (from reference 1).

The DC equivalent radiant power responsivity of the VANTA/Si test detector operated in photo-current mode for a modulation frequency of 80 Hz was measured to be 5.9 x 10^{-7} A W^{-1} at 1.5 µm. This is 30 % higher than the corresponding absolute spectral responsivity of an uncoated $LiTaO_3$ pyroelectric detector of similar crystal thickness (60 µm thick). However, in radiometry, the real benefit of the black VANTA/Si coating is not provided by the 30 % higher absolute responsivity but lies in the fact that the presence of the black coating gives the pyroelectric detector a spectrally flat response. The full results of the evaluation of this detector, including the linearity, spatial uniformity, frequency of response characteristics can be found elsewhere [1].

Support from the National Measurement Office of the UK Department of Business, Innovation and Skills is gratefully acknowledged.

REFERENCES

1. E. Theocharous, S. P. Theocharous and J. H. Lehman, "Assembly and evaluation of a pyroelectric detector bonded to vertically aligned multiwalled carbon nanotubes over thin silicon", Applied Optics, **52**, 8054-8059, 2013.

2. E. Theocharous and J. Lehman, “The evaluation of a pyroelectric detector with a sprayed carbon multi-wall nanotube black coating in the infrared”, Infrared Physics & Technology, **54**, 34-38, 2011.
3. S. P. Theocharous, E. Theocharous and J. H. Lehman, “The evaluation of the performance of two pyroelectric detectors with vertically aligned multi-walled carbon nanotube coatings”, Infrared Physics & Technology **55**, 299–305, 2012.
4. C. J. Chunnilall, J. H. Lehman, E. Theocharous and A. Sanders, “Infrared hemispherical reflectance of carbon nanotube mats and arrays in the 5–50 μm wavelength region” Carbon, **50**, 5348-5350, 2013.

Economic Impact Measurement by CMC, and CCPR Strategy

Takashi Usuda[1]

[1] *National Metrology Institute of Japan (NMIJ), Advanced Industrial Science and Technology (AIST)*
Tsukuba, Japan
Corresponding e-mail address: takashi.usuda@aist.go.jp

Economic impact studies related to measurement are becoming important in, for example, the dialogue between National Metrology Institutes (NMIs) and governmental funding bodies. In this regard, a new methodology employing loss parameters (false positive, false negative, and loss function) due to the deviation of measurement standards is proposed. The economic impact of inconsistencies in a measurement standard associated with the quality distribution of its instruments is illustrated. The example suggests that the open access database for measurement standards namely CMC (Calibration Measurement Capabilities) maintained under the Mutual Recognition Arrangement (CIPM MRA) is invaluable for assessing economic impact. The CCPR (Consultative Committee for Photometry and Radiometry under metre convention) activities are also mentioned.

ECONOMIC IMPACT BY MEASUREMENT STANDARDS

The benefits of measurement standards to the economy are unquestionable. However, assessments of the cost to maintain measurement standards are becoming important in dialogue between National Metrology Institutes (NMIs) and governmental funding bodies.

Any measurement is a comparison process in which the value of a quantity is expressed as the product of a value and a unit; that is,

Quantity = {numerical value} X [unit]

If the quantity has unit price, it can be directly converted to economic impact; that is,

Economic value = Quantity X {unit price}

Consequently, the uncertainty of measurement standard maintained by a national metrology institute (NMI) directly affects to the economic value. This is quite obvious for example in mass (daily transaction of goods), flow (petrol and gas), electricity (electric power) measurements. However, it is not easy to assess economic impact which quantity cannot identify its unit price such as luminance, illuminance, etc.

MODELING OF THE METHODOLOGY

All industrial products exhibit a distribution in terms of quality, designated here $D(x)$, where x is a measurand of the product quality (see Fig. 1(a)). The products that fit within the testing limits ($\pm\Delta$) are selected as suitable by the manufacturer/exporter (Fig. 1(a)), and delivered to the user/importer (Fig. 1(b)). The user/importer in turn verifies the quality of the products against its own measurement standards (Fig. 1(c)). If there are no deviations between the metrology standards of the exporter and the importer, all is well and no additional losses arise. However, if there is a deviation ε between the measurement standards of the exporter and those of the importer, additional losses will arise.

These financial losses are caused by “false positive” results, meaning those exported products that will nonetheless be rejected by the importer, and “false negative” results, caused by the products previously rejected by the exporter that would in fact have been accepted by the importer (see Fig. 1(c)). Mathematically, the number of products recognized as “false positive” is given by, and as “false negative” by. The financial losses resulting from these false positive and false negative results can then be calculated given the unit price of the product.

Needless to say, the false positive fraction causes more significant economic loss and could also damage the exporting company’s reputation. So this evaluation of false positive results represents a minimum estimate of the economic consequence of a difference between the measurement standards.

Since the implementation of the CIPM MRA[1], peer-reviewed results of comparisons of measurement standards have been collated as CMC in the BIPM key comparison database (KCDB)[2]. Using the equivalence demonstrated in this database together with data on the quality distribution of products (information usually held confidential by production companies), it is possible to estimate the economic

loss caused by deviations between measurement standards. The CMC thus makes it possible to quantitatively assess the economic impact associated with the distribution of the products and the deviation of measurement standards, which was not possible before. Employing the model and methodology, the author reported the economic impact due to deviation of measurement standards using weighing scale instruments supplied from Japan [3]. In this presentation, some other examples in photometry and radiometry measurements will be reported.

FURTHER DISCUSSION

Recently, effectiveness of the CMC andmaintaining costs fo r the CMC are also requested to be examined. With this regards, the strategy of the CCPR (Consultative Committee for Photometry and Radiometry) under the Metre Convention [4] will be also discussed.

REFERENCES

1. CIPM Mutual Recognition Arrangement http://www.bipm.org/en/cipm-mra/
2. The BIPM key comparison database http://kcdb.bipm.org/appendixB/KCDB_ApB_search.asp
3. T. Usuda and A. Henson, Economic Impact of Equivalence of Measurement Standards, NCSLI Measure, Vol. 7 No. 1, 62-70, 2012.
4. CCPR Strategy Summary, http://www.bipm.org/utils/en/pdf/CCPR-strategy-summary.pdf

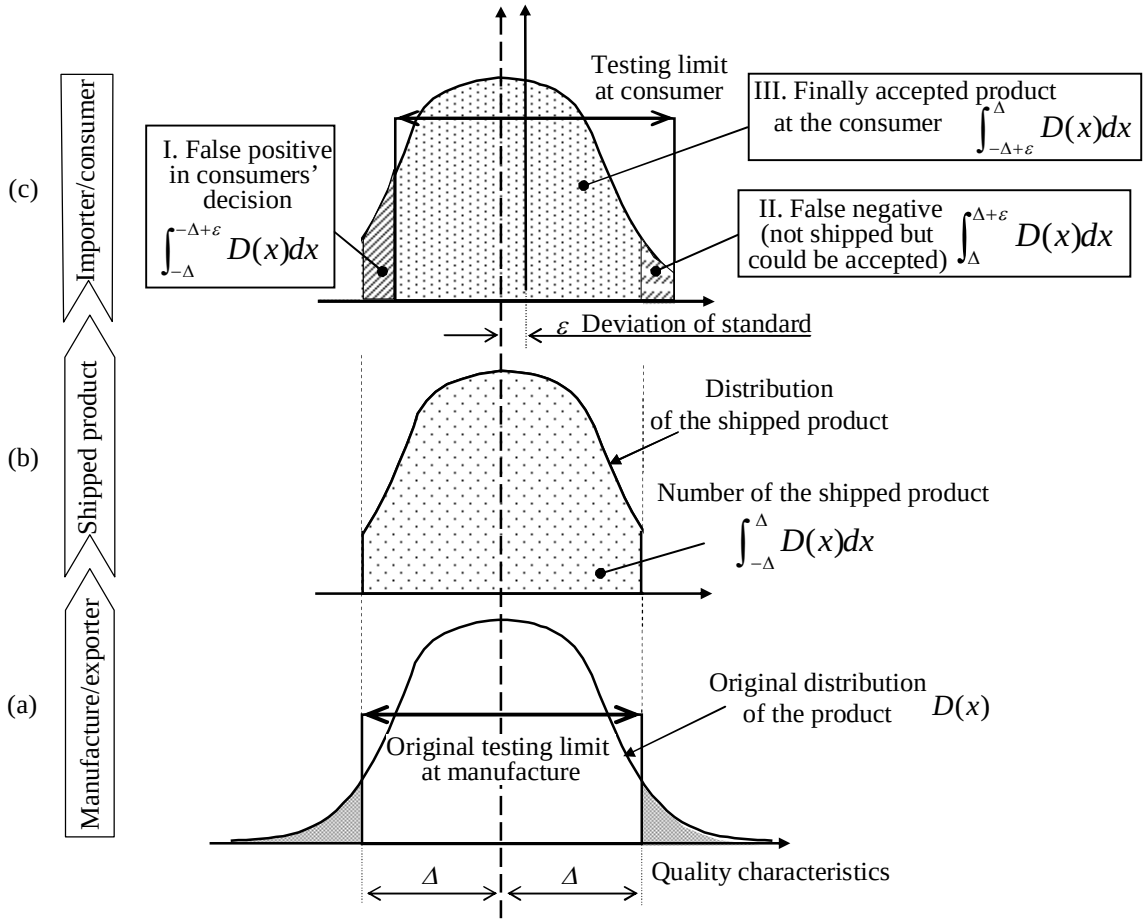

Figure 1. Economic losses due to a deviation between the metrology standards maintained by two trading partners.

Adjustable Power Line Impedance Emulator for Characterization of Energy-Saving Lamps

Tuomas Poikonen[1], Teemu Koskinen[2], Hans Baumgartner[2], Petri Kärhä[1,2], and Erkki Ikonen[1,2]

[1]*Centre for Metrology and Accreditation (MIKES), Espoo, Finland*
[2]*Metrology Research Institute, Aalto University, Espoo, Finland*
Corresponding e-mail address: tuomas.poikonen@mikes.fi

We have developed an adjustable power line impedance emulator (APLIE) for characterization of electrical power consumption of AC-operated energy-saving lamps. The device is connected in series with the AC voltage source and the lamp in order to reduce the sensitivity of the lamp electronics to the output impedance of the AC voltage source. Test measurements conducted for a group of energy-saving lamps showed that some lamp electronics are very sensitive to changes in the source impedance. A difference of 1.2 % was measured for the efficacy of a compact fluorescent lamp (CFL), when using different impedance settings. The APLIE can be used for developing a fixed impedance stabilization network for measurements of energy-saving lamps.

INTRODUCTION

Electrical power measurement of AC-operated energy-saving light sources, such as LED lamps or CFLs, is challenging because they contain built-in power converters that draw distorted current waveforms from the electrical network [1]. Tools for electrical power characterization of energy-saving lamps are thus highly important. Furthermore, testing laboratories use regulated AC voltage sources for operating the lamps in the efficacy measurements. Depending on the manufacturer, the output impedance of the AC voltage source can be different at two different testing laboratories. The problem arises, when the impedance of the AC voltage source is coupled with the power converter circuit of the energy-saving lamp. As a result, the operation of the lamp electronics may change, and differences of several percents in the measured luminous efficacy (lm/W) can occur for some lamp types [2].

In order to obtain comparable measurement results for energy-saving lighting products at different testing laboratories, a device needs to be developed that stabilizes the impedance of the measurement configuration so that different types of AC voltage sources can be reliably used for supplying lamps of different types in the measurements. Stabilization networks for measurement of electromagnetic compatibility (EMC) are commercially available, but they are not directly suitable for measurements of energy-saving lamps, for which the most interesting frequency range is 50 Hz – 200 kHz [2,3].

IMPEDANCE EMULATOR

We have developed an adjustable power line impedance emulator (APLIE) for characterization of energy-saving lamps. The passive single-phase LCR network can emulate various impedance curves found in typical low-voltage power distribution networks, to which the lamps are connected in normal operation. A photograph of the device is presented in Figure 1.

Figure 1. Adjustable power line impedance emulator.

The model of the LCR circuit used in the APLIE was developed on the basis of the data published on power line impedances measured in several different countries around the world [4–9]. In addition, the impedance of wall sockets in the campus area of Aalto University was measured at the fundamental frequency of 50 Hz. The data were then combined, and used to calculate average, minimum and maximum curves for the power line impedances to be simulated. The circuit proposed by Zhao and Rietveld [2] was simulated as well, and was found to produce an impedance curve close to the calculated average.

Therefore, we decided to use the circuit model by Zhao and Rietveld as the basis to further develop the circuit used in our device. The component values were selected to closely produce the aforementioned average, minimum and maximum impedance curves. Some of the filter components were removed from the actual circuit to avoid unusually large reactive power requirement for the AC voltage source. The APLIE consumes only 4 W of active power, and 100 var of reactive power from the AC voltage source, when no load is connected.

Special care was taken in the selection of components to obtain characteristics close to the simulated model. The resistances of the wiring and switches were minimized. Air gapped coils and capacitors designed for high-speed switched mode applications were used. The impedance responses of the APLIE were successfully characterized in the frequency range of DC – 1 MHz. At the average setting, the impedance is approximately 0.5 Ω at 50 Hz, and gradually increases to 100 Ω at 1 MHz. The impedances of the minimum and maximum setting deviate from the average by up to one order of magnitude. In addition to the three basic curves, the impedance can be adjusted at three different frequency bands using switches in the front panel.

TEST MEASUREMENTS

Test measurements were carried out for 5 LED lamps, a CFL, and an incandescent lamp using our luminous efficacy measurement facility [3]. The electrical power consumptions of the lamps were measured and the waveforms were sampled for analysis. As expected, the efficacy measured for the incandescent lamp was found to be insensitive to changes in the impedance. For the CFL, the largest difference obtained in the efficacy with different impedance settings was 1.2 %. The shapes of current waveforms and harmonic contents of three LED lamps changed significantly with different impedance settings, although the changes in the efficacy were less than 0.1 %. A larger group of lamps needs to be tested to make general conclusions on the behaviour of various lamp electronics. It was also found that when the APLIE was in use and configured for the average impedance, the output of the AC voltage source was stable and some of the sporadic phenomena found without the APLIE disappeared.

CONCLUSIONS

The developed impedance emulator can be used as a versatile tool in the research of electrical power characterization of AC-operated energy-saving lamps In addition, it can be used for developing a fixed impedance stabilization network that, in the future, could be used by testing laboratories. The preliminary test measurements support the need to develop such a network, as the difference of 1.2 % in the luminous efficacy measured for the CFL with different source impedance settings is as large as the expanded uncertainty reported earlier for luminous efficacy measurement of LED lamps [3]. Measurement results for a larger group of energy-saving lamps will be presented at the conference.

REFERENCES

1. Z. Ye, F Greenfield, and Z. Liang, A topology study of single-phase offline AC/DC converters for high brightness white LED lighting with power factor pre-regulation and brightness dimmable, in Proceedings of Industrial Electronics Conference, 1961–1967, IEEE, 2008.
2. D. Zhao and G. Rietveld, The influence of source impedance in electrical characterization of solid state lighting sources, in Proceedings of Precision Electromagnetic Measurements Conference, 300-301, IEEE, 2012.
3. T. Poikonen, T. Pulli, A. Vaskuri, H. Baumgartner, P. Kärhä, and E. Ikonen, Luminous efficacy measurement of solid-state lamps, Metrologia, 49, S135–S140, 2012.
4. J. R. Nicholson and J. A. Malack, RF impedance of power lines and line impedance stabilization networks in conducted interference measurements, in Proceedings of Transactions on Electromagnetic Compatibility Conference, 84-86, IEEE, 1973.
5. J. A. Malack and J. R. Engstrom, RF impedance of united states and european power lines, Transactions on Electromagnetic Compatibility Conference, 36-38, IEEE, 1976.
6. J. P. L. Neto, S. Tsuzuki, Y. Kawakami, and Y. Yamada, In-door power-line impedance measurement up to high frequency (10 KHz – 70 MHz), in Proceedings of 7th International Symposium on Power-Line Communications and Its Applications, 243-247, IEEE, 2003.
7. A. Knop and F. W. Fuchs, High frequency grid impedance analysis with three-phase converter and FPGA based tolerance band controller, in Proceedings of Compatibility and Power Electronics Conference, 286-291, IEEE, 2009.
8. I. U. Marcus, A. E. Nestor, and P. Clarkson, The influence of the network impedance on the nonsinusoidal (harmonic) network current and flicker measurements, in Proceedings of Transactions on Instrumentation and Measurement Conference, 60, 2202-2210, IEEE, 2011.
9. M. Sigle, W. Liu, and K. Dostert, On the impedance of the low-voltage distribution grid at frequencies up to 500 kHz, in Profeedings of International Symposium on Power Line Commmunications and Its Applications, 30-34, IEEE, 2012.

Setup for measurement of the optical characteristics of UV-NIR solid-state light sources emission

S.V. Nikanenka, A.V. Danilchyk, V.A. Dlugunovich, V.A. Zhdanovskii, A.V. Kreidzich, A.A. Liplianin, M.V. Rzheutski, and E.V. Lutsenko

B. I. Stepanov Institute of Physics National Academy of Sciences of Belarus, Minsk, Belarus
Corresponding e-mail address: s.nikonenko@dragon.bas-net.by

In this paper, we present the setup for the measurement of the optical characteristics of the solid-state light sources, e.g. light emitting diodes and laser diodes, in the range from 200 to 900 nm, recently installed at B. I. Stepanov Institute of Physics NAS of Belarus.

Key words: spectral, radiometric and photometric characteristics, SSL sources, LED, LD, UV-NIR.

1. INTRODUCTION

For the last years, an essential progress in development of semiconductor light sources, i.e. laser diodes (LDs) and light emitting diodes (LEDs), operating in UV spectral range, was made. As expected, low cost at mass production and high efficiency of such UV light sources will cause their wide usage in many applications such as water and air purification, chemical and biology analisys, communication, etc. Thereafter, a development of equipment and methods for a proper certification of such light sources is necessary. Moreover, the UV emission, even being of low power, is harmful to human health, which imposes a serious requirements of precise control of its characteristics. The main ones from the characteristics are spatial distribution of light intensity, spectral radiance and irradiance, average optical power. The characteristics are essential for designing, manufacturing and maintenance of the products, containing UV light sources.

Though the both LEDs and LDs are solid-state light (SSL) sources, the standard methods of measurement of characteristics and parametres of their radiations have essential differences. At certification of laser products, usually the standards ISO 11554, ISO 13694 and ISO 11146 are used. For the measurement of the optical characteristics of LEDs, methods of measurements recommended in CIE-127 [1] is applied. At the same time, the ISO standards don't give specified instructions for measurement of spatial distribution of laser radiation intensity with big divergence, that is critical for semiconductor laser having radiation divergence of up to ~60°. At that recommendations [1] are not enough for measurement of radiometric characteristics of UV and NIR LEDs, especially a spectral radiance.

2. MEASUREMENT SETUP

A setup for the measurement optical characteristics of UV-NIR SSL sources emission was developed and built in the Institute of Physics National Academy of Sciences of Belarus [2, 3].

The setup is used for measurement of the following optical characteristics of LEDs and LED-based products emission, based on recommendations [1]: luminous intensity, illuminance, averaged LED intensity, spatial distribution of luminous intensity, spectral radiance and irradiance. And also for the measurement of LDs radiation optical characteristics, on a recommendations basis of ISO 11554: average power of laser radiation, power density of laser radiation and power density spatial distribution of laser radiation.

The setup operates in six modes: the measurement of the LEDs luminous intensity, averaged intensity and illuminance; the measurement of average power and power density of radiation; the measurement of the spatial distribution of luminous intensity of LEDs (LED-lamps); the measurement of the spatial distribution of radiation power density of LDs and LEDs; the measurement of spectral irradiance of LDs and LEDs; the measurement of spectral radiance of LEDs. It should be noted, that other light sources (e. g. lamps) can also be tested using the setup.

The photometric part of setup is based on the photometer LMT 520B. The radiometric part of setup uses radiometer with head OPHIR PD300-UV-SH.

At measurement the photometric and radiometric quantities, the following sequence of operations is used: LD *2* , LED (LED-lamp) *3* or lamp *4* in the holder of goniometric system 5 is mounted. By means of alignment system *7* [4], the

position of the centre of a source of radiation and the centre of a photosensitive area of photometric or radiometric *9* heads are adjusted to the optical axis at the required distance. After that, a necessary conditions for sources of radiation is established using block of powering and control of sources *6* which consists of the high-precision power supplies, temperature controllers and multimeters. All components of the setup can work independently or under control of the personal computer (PC) *10*. Software was developed to provide all the necessary algorithms of the setup's operation. The obtained measurement results are saved in a file on the PC. For the spatial distribution of intensity of an emission source power density a representation in graphical form (2D and 3 D) is possible.

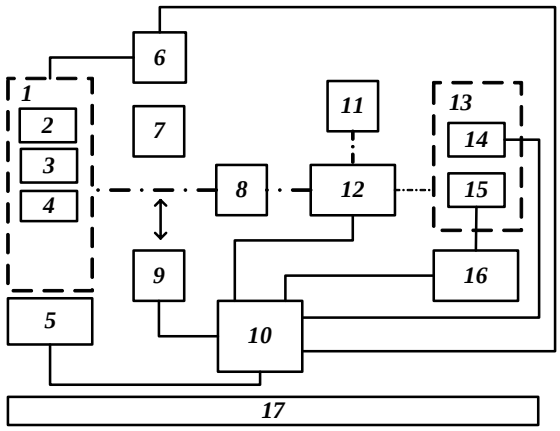

The spectral radiometric part of the setup consists of a block of input optics *8*, a block of rapid analysis *11*; monochromator *12*; block of detectors *13*. The block of input optics consists of an integrating sphere FOIS-1 and toroidal mirror. The registration system consists of a picoammeter Keithley 6485 and lock-in amplifier Ametec 7265. If PMT used, then registration system is integrated photon counter directly connected to PC.

1 – block of sources; *2* – sub-block of laser sources; *3* – sub-block of LED sources; *4* – sub-block of lamp sources; *5* – goniometric system; *6* – block of powering and control of sources; *7* – alignment system; *8* – block of input optics; *9* – photometer (radiometer); *10* – computer; *11* – block of rapid analysis; *12* – monochromator; *13* – block of detectors; *14* – trap-detector (UV, NIR detector); *15* – PMT with photon counter; *16* – registration system; *17* – optical table

Figure 1. Block scheme of setup.

For the measurement of spectral irradiance and spectral radiance the spectral radiometric system is calibrated by deuterium CL7-H and quartz-halogen BN-LH250-BC standard lamps.

For measurement of spectral radiance we used a specially made reference monochrome UV LEDs [5] with wavelength 365 nm and 385 nm which provided homogeneous radiance of emission across their apertures. The UV sources demonstrated excellent time stability of the radiance and light intensity. Therefore they are perspective as standard UV radiation sources.

3. METROLOGICAL CHARACTERISTICS OF THE SETUP

The following metrological characteristics of the measurement setup were established: the range of the measurement of LEDs luminous intensity and the averaged intensity for CIE standard condition A (B) is from 0,01 to 60 kd, with the relative expanded uncertainty less than 2,0 %; the spectral range of the measurement of the radiation power is from 200 to 1100 nm; the relative expanded uncertainty of measurement of laser radiation power density in the range from 300 nW to 300 mW is less than 2,0 %; the deviation angles in two perpendicular planes are ± 110° and 360°; the relative expanded uncertainty of the reproduction range of the rotation angle is 0,08 %; the relative combined uncertainty of measurement spatial distribution of luminous intensity is 1,04 %; the relative expanded uncertainty of spatial distribution measurement of laser radiation power density in range from 300 nW to 300 mW is less than 3,4 %; the relative combined uncertainty of LEDs spectral irradiance measurement in the spectral range from 250 to 900 nm is less than 2,8 %; the range of measurement of LEDs spectral irradiance is from 10^2 до 10^{10} $W \cdot m^3$; the relative combined uncertainty of LEDs spectral radiance measurement in spectral range from 250 to 500 nm is less than 3,5 %; the range of measurement of LEDs spectral radiance is from 10^2 до 10^{12} $W \cdot m^3 sr^{-1}$.

REFERENCES

1. CIE, Technical Report CIE Publication 127, 2nd Ed., Measurement of LEDs, 2007.
2. Patent RU114151.
3. Patent RU115469.
4. Patent RU123984.
5. Patent RU115889.

Dimensional Accuracy for Multi-element Photodetector

K. Dhoska[1], V. Vabson[2], A. Hermaste[1], and T. Kübarsepp[1,2]

[1]*Tallinn University of Technology, Tallinn, Estonia*
[2]*AS Metrosert, Tallinn, Estonia*
Corresponding e-mail address: klodian.dhoska@ttu.ee

An optical photodetector composed of several photodiodes can be a complex geometrical object. In the tests of manufactured mechanical parts for 12-photodiode transmission trap detector, we have used TESA MICRO-HITE 3D Coordinate Measuring Machine (CMM). In this paper, the measurement method and repeatability results of the dimensional measurements of a body part holding three photodiodes are briefly described.

INTRODUCTION

A multi-photodiode detector is a complex geometrical object whose performance depends on dimensional accuracy of manufactured parts. For example, the construction of twelve-element transmission trap detector, which can also be operated as an attenuator [1], relays on the accurate machining of the mechanical details to provide coaxiality of the incoming and out-coming beams as shown in Fig. 1.

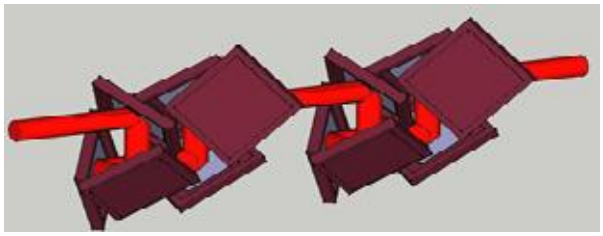

Figure 1. Scheme of the photodiodes configured in twelve-element photodetector.

The design of the 12-photodiode transmission trap can be found elsewhere [2]. It is important that all photodiodes are mounted under radiation incidence angle close to 45°. For the best performance declination angle between the incoming and the outcoming beams after each 3-photodiode module should be less than ±0.2°. Thus, before assembling of photodiodes to the modules, it is necessary to test agreement between specifications and manufactured item with utmost accuracy.

MEASUREMENT METHOD

Our aim was to determine the angle between reference and manufactured 45° tilted plane of photodiode mounting. In the measurement of angles TESA MICRO-HITE 3D CMM was used.

Figure 2. Configuration of angle measurements realized by using TESA MICRO-HITE 3D CMM.

Measurement setup is illustrated in Fig. 2. In the measurements, first the reference plane I was fixed and the angle between reference plane and tilted plane II was measured by using the touching probe head with diameter 2 mm. Distributed points across the plane II were measured to cover the entire plane. The same measurement procedure was conducted for the planes III (reference) - IV and for the planes V (reference) – VI, as there are three locations in the module for assembling photodiodes.

RESULTS

Repeatability of the measurement results is shown in Fig. 3. As can be seen, the deviation from 45°-angle between the measured planes is within ±0.2° at most measurement points.

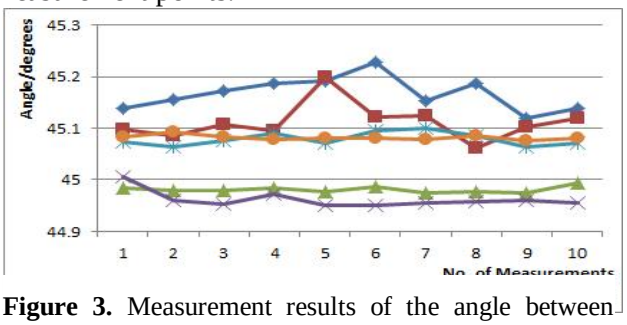

Figure 3. Measurement results of the angle between reference and tilted planes of a test 3-photodiode module.

1. S. Kück et al, "The SIQUTE-project – first results towards single-photon sources for quantum technologies", submitted to NEWRAD 2014, Espoo, Finland.
2. T. Kübarsepp et al, "High-attenuation tunnel-type detector for calibration of single-photon devices", submitted to NEWRAD 2014, Espoo, Finland.

Measurement and Calibration Facilities at the Metrology Light Source

Alexander Gottwald, Burkhard Beckhoff, Andreas Fischer, Rolf Fliegauf, Peter Hermann, Arne Hoehl, Andrea Hornemann, Hendrik Kaser, Roman Klein, Michael Kolbe, Udo Kroth, Christian Laubis, Ralph Müller, Wolfgang Paustian, Mathias Richter, Frank Scholze, Reiner Thornagel, and Gerhard Ulm

Physikalisch-Technische Bundesanstalt (PTB), Berlin, Germany
Corresponding e-mail address: alexander.gottwald@ptb.de

In April 2008 the Metrology Light Source (MLS) of the Physikalisch-Technische Bundesanstalt (PTB) started its regular user operation. The MLS is a 630 MeV electron storage ring dedicated to synchrotron-radiation based metrology in the far-IR/THz, IR, UV, VUV and EUV spectral ranges. Since then, new instrumentation was stepwise put into operation to improve measurement capabilities.

STATUS OF THE RING FACILITY

The MLS is designed for a highly flexible operation adapted to metrological purposes [1]. It is capable of being operated at any electron energy between 105 MeV and 630 MeV and at any current between about 1 pA (i.e. 1 electron stored) and 200 mA ($2 \cdot 10^{11}$ electrons stored). Furthermore, the electron optics can be tuned to special modes, e.g. for short electron bunch lengths ("low-α mode") to produce enhanced emission of THz radiation [2].

Many improvements have been achieved since the beginning of operation. From the hardware side, by the end of 2012 the former U180 electromagnetic undulator insertion device was replaced by an U125 permanent magnet device. Optimization of feedback systems for the electron beam led to a higher beam stability for a variety of beam conditions, which include the full range of accessible electron energies, low-α mode, single-bunch operation, and different vertical beam sizes (by tuning of the radio-frequency excitations). By optimisation of the low-α mode, average THz power of 60 mW (corresponding to 35 W peak power) had been achieved.

THE MLS AS PRIMARY SOURCE STANDARD

The most basic use of an electron storage ring in radiometry is as a primary source standard for radiation particular in the spectral regions of the near-infrared, visible, ultraviolet, and vacuum- and extreme ultraviolet ranges [3]. For the use as calculable source of radiation, all relevant parameters (i.e. electron energy, magnetic field strength, electron current, geometry of the electron beam and the observation geometry) must be determined. Recently, the instrumentation for counting the number of electrons in the regime of electron beam currents in the pA and nA range was improved. This electron current range is important for the traceable calibration of counting detectors [4].

Transfer standard sources can be calibrated traceable to the MLS as the primary source standard. For this task, a new transfer station was put into operation, covering the spectral range from 7 nm to 400 nm (beamline # 2a in Fig. 1). The core of this source calibration facility is a monochromator with six gratings in normal and gracing incidence geometry which are exchangeable under vacuum. The station can be moved to either be illuminated by the primary source or the source under test, in such a way that either source has the same distance to the transfer station.

NEW INSTRUMENTATION FOR THE EUV, VUV AND IR/THZ RANGES

Table 1. Beamlines with related wavelength ranges (in brackets) at the MLS. Beamline numbering corresponds to Fig. 1.

No.	Description
1	U125 undulator radiation #a,b,e: deflected undispersed radiation #c: direct undispersed radiation #d: IDB beamline (4 nm to 400 nm)
2	#a: source calibration (7 nm to 400 nm) #b: direct bending magnet radiation
3	EUV beamline (5 nm to 50 nm)
4	UV/VUV NIM beamline (40 nm to 400 nm)
5	IR beamline (0.6 µm to 7 mm)
6	THz beamline (100 µm to 7 mm)
7	Diagnostics front-end

The radiation from the bending magnets and the undulator of the storage ring is brought to the experimental stations by different beamlines (Fig. 1 and Tab. 1).

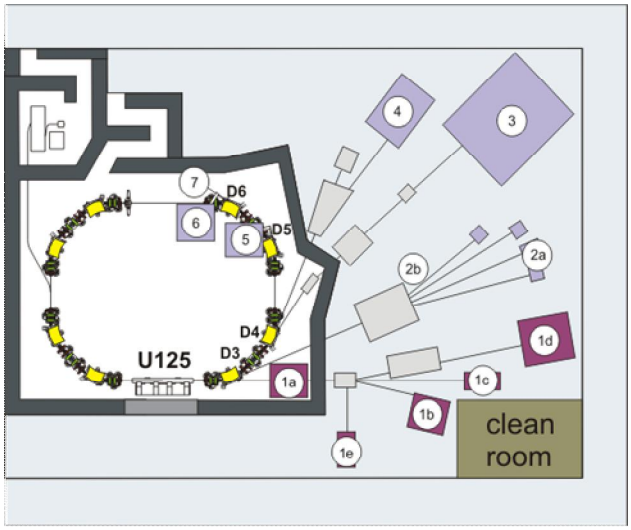

Figure 1. Scheme of the MLS and the experimental hall.

The beamlines themselves and the instrumentation for measurements have been set up sequentially over the past years, and are still under completion. For the THz and infrared beamlines (#5 and #6), the focus lies on spectromicroscopic instrumentation, in particular on a infrared microscope in combination with a rapid scan Fourier-transform infrared spectrometer (FTIR) and a scanning near-field optical microscope (SNOM), the latter operated in collaboration with the FU Berlin [5]. The scientific cases cover nano-structured surfaces, solid-state interfaces, and molecular biology.

The EUV beamline (#3) went into full service in 2013. It is mainly used with PTB's large EUV reflectometer facility in the frame of optics metrology for the development of EUV lithography techniques [6]. For reflectometry in the UV and VUV range at the Normal Incidence Monochromator (NIM) beamline, a dedicated reflectometer is in operation since 2011. The EUV as well as the NIM beamline are also used for detector-based radiometry, i.e. characterisation and calibration of photodetectors using cryogenic radiometers as primary detector standards [7].

PTB has used synchrotron radiation also for the characterisation and calibration of space-based instruments in particular for solar research for more than 20 years now. A dedicated facility with a large-sized vacuum vessel, which can accommodate complete space instruments up to 1.2 m in length, and an appropriate clean-room installation was available at the MLS in early 2014 [8]. It can be operated at the direct bending magnet as well as at the NIM (#4) and undulator (#1d) beamlines.

The U125 undulator delivers tuneable, highly intensive, and directional radiation over a spectral range from EUV to IR. The Insertion Device Beamline (IDB) is equipped with a normal incidence-grazing incidence hybrid monochromator (NIGI) capable to uniformly cover this broad spectral range. It makes the IDB well suited in particular for applied (spectroscopic) methods. A VUV ellipsometer is operated in collaboration with the Institute of Analytical Sciences (ISAS). The VUV spectral range enables the investigation of, e.g., wide band-gap semiconductor materials. Furthermore, a hemispherical photoelectron analyzer is used in co-operation with the Technische Universität Berlin for ultraviolet photoelectron spectroscopy Here, the scientific work is currently focusing on organic molecules for photovoltaic applications [9].

REFERENCES

1. A.Gottwald, R. Klein, R. Müller, M. Richter, F. Scholze, R. Thornagel, and G. Ulm, Current capabilities at the Metrology Light Source, Metrologia, 49, S146-S151, 2012.
2. J. Feikes, M. von Hartrott, M. Ries, P. Schmidt, G. Wüstefeld, A. Hoehl, R. Klein, R. Müller, and G. Ulm, Metrology Light Source: The first electron storage ring optimized for generating coherent THz radiation, Phys. Rev. STAB, 14, 030705, 2011.
3. R. Klein, G. Brandt,R. Fliegauf, A. Hoehl, R. Müller, R. Thornagel, G. Ulm, M. Abo-Bakr, J. Feikes, M. v. Hartrott, K. Holldack, and G. Wüstefeld, Operation of the Metrology Light Source as a primary radiation source Standard Phys. Rev. Special Topics - Accelerators and Beams (PRST-AB), 11, 110701, 2008.
4. I. Müller, R. M. Klein, J. Hollandt, G. Ulm, and L. Werner, Traceable calibration of Si avalanche photodiodes using synchrotron radiation, Metrologia, 49, S152-S155, 2012.
5. P. Hermann, A. Hoehl, P. Patoka, F. Huth, E. Rühl, and G. Ulm, Near-Field Imaging and Nano-Fourier-Transform Infrared Spectroscopy using Broadband Synchrotron Radiation, Optics Express, 21, 1094-4087, 2013.
6. Ch. Laubis, A. Barboutis, M. Biel, Ch. Buchholz, B. Dubrau, A. Fischer, A. Hesse, J. Puls, Ch. Stadelhoff, V. Soltwisch, and F. Scholze, Status of EUV Reflectometry at PTB, Proc. SPIE, 8679, 867921-1, 2013
7. A. Gottwald et al., this conference.
8. R. Klein et al., this conference.
9. F. Roth, C. Lupulescu, T. Arion, E. Darlatt, A. Gottwald, and W. Eberhardt, Electronic properties and morphology of Cu-phtalocyanine-C60, J. Appl. Phys., 115, 033705 (2014).

Virtual experiment uncertainty analysis of robot-based gonioreflectometers

Andreas Höpe[1], Carsten Forthmann[1], Kai-Olaf Hauer[1], Mikhail Langovoy[2], Franko Schmähling[2], and Gerd Wübbeler[2]

[1]*Physikalisch-Technische Bundesanstalt (PTB), Braunschweig, Germany*
[2]*Physikalisch-Technische Bundesanstalt (PTB), Berlin, Germany*
Corresponding e-mail address: andreas.hoepe@ptb.de

The Physikalisch-Technische Bundesanstalt (PTB) is meanwhile operating two robot-based gonioreflectometer facilities for research and calibration purposes related to the Bidirectional Reflectance Distribution Function (BRDF). In the recent years new materials with new sophisticated reflection effects, like goniochromatism, sparkle and graininess, emerged into industrial application, requiring extended physical explanation using for instance the BRSSDF (Bidirectional Scattering Surface Reflectance Distribution Function), where also the position dependent reflection properties on a reflecting surface are taken into account. Due to the increase in complexity of the BRSSDF measurement, it is not feasible any more to apply the standard mathematical methods of the GUM (Guide to the Expression of Uncertainty in Measurement) which thus need to be extended by Monte Carlo Methods (MCM) and Virtual Experiments.

INTRODUCTION

The characterisation of diffuse reflecting surfaces in full 3D-space by means of the BRDF or even the BRSSDF (Fig. 1) is gaining more and more interest in industry, driven by increased requirements concerning the visual appearance of commercial products, [1, 2].

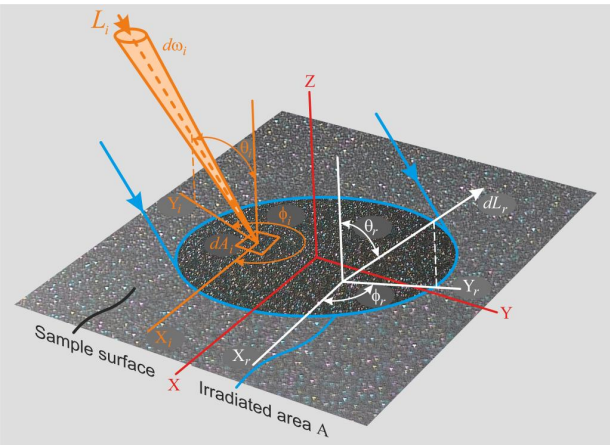

Figure 1. Geometry of incident and reflected beams according to a description of a surface via the BRSSDF.

The BRSSDF is given by a function S with a dependency upon the location of the point at which the incident flux strikes, upon the location of the point which the ray of radiance dL_r emerges and upon the directions involved, i.e.:

$$S = S(\theta_i, \phi_i, x_i, y_i; \theta_r, \phi_r, x_r, y_r) \quad (1)$$

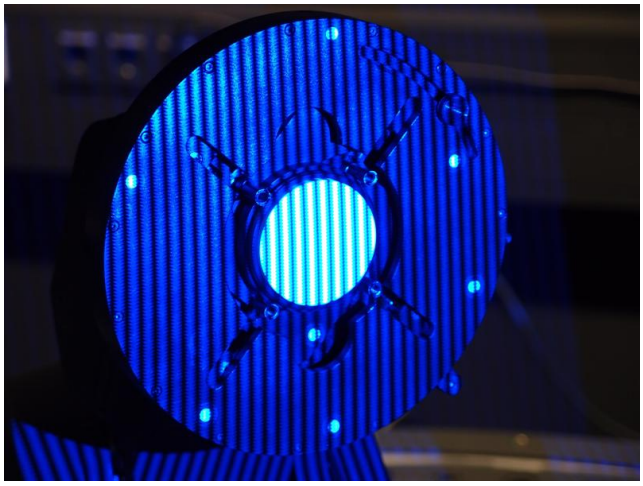

Figure 2. Alignment of a diffuse reflection standard attached to the robot-based gonioreflectometer with a 3D-scanner stripe-projection system.

Within the European Metrology Research Program (EMRP) of the European Commission a special project of coordinated R&D named "Multidimensional Reflectometry for Industry" was approved in the last year. The short name of the project is xD-Reflect, indicating the multi-dimensional aspects (x > 3) of modern reflectometry.

The project is divided into 5 scientific work packages entitled "Goniochromatism", "Gloss", "Fluorescence", "Modelling and Data Analysis" and "Visual Perception". PTB has the leadership of the "Goniochromatism" and "Modelling and Data Analysis" work packages. One important common task of the conjoint PTB-work within the 3-year work program of the project are computer-based virtual experiments in order to carry out sensitivity analysis by taking into account possible errors related to the geometric, spectrometric and optical setup of the real gonioreflectometers. Figure 2 shows part of the alignment

procedure of a diffuse reflection standard with a 3D-scanner stripe-projection system. These types of reflection standards are used for the transfer of the absolute diffuse reflection scale in directional geometries (spectral radiance factor) of PTB to customers in research and industry. Proper alignment of the sample orientation in relation to the incident and detection beam paths is essential in order to obtain small uncertainties.

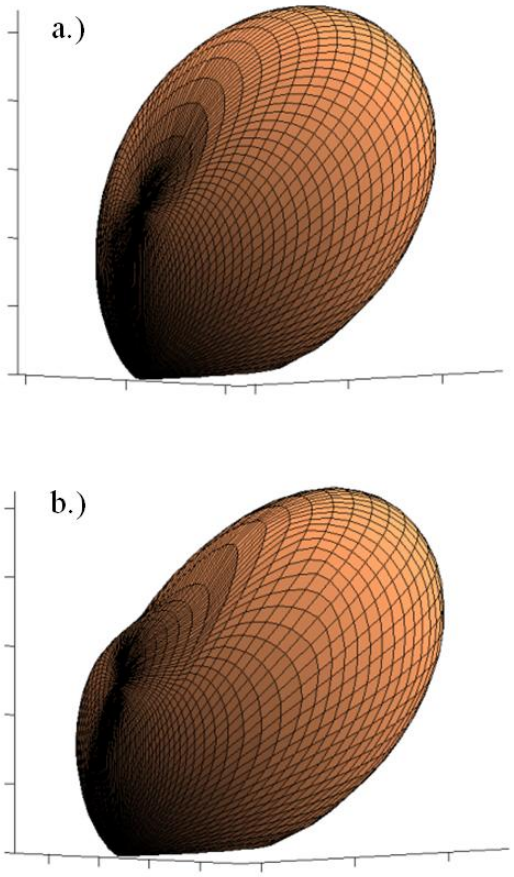

Figure 3. First simulated BRDF using a Phong-type BRDF-model for an incident angle of 45°, a.) perfect aligned gonioreflectometer, b.) gonioreflectometer with a misaligned detector.

SCIENTIFIC AND TECHNICAL OBJECTIVES

The evaluation of reliable uncertainties for complex measurements such as in robot-based gonio-reflectometry requires an appropriate mathematical modelling. On the basis of mathematical models also virtual computer experiments can be developed which can be employed to gain insight into the measurement system and to enable a characterisation of the whole measurement setup. Virtual computer experiments can especially be utilized to study the impact of certain misalignments within the measurement setup or to carry out sensitivity analyses in order to identify dominant uncertainty contributions.

For the robot-based gonioreflectometers of PTB [3, 4] the virtual computer experiment is designed by different interacting modules describing the light source, the goniometer setup with all the degrees of freedom for the movement, the surface under test and the detector. The surface under test is modelled by analytical BRDF functions and the simulation of the whole experiment is carried out via ray tracing techniques [5]. Figure 3 shows two simulated BRDF measurements for an angle of 45° of the incident beam obtained via virtual experiments. Figure 3b illustrates a first result of the impact of a misalignment in the detection beam path of the gonioreflectometer setup, inducing distortions in the resulting BRDF measurement.

ACKNOWLEDGMENTS

This work has been carried out within EMRP project IND52 "Multidimensional Reflectometry for Industry". The EMRP is jointly funded by the EMRP participating countries within EURAMET and the European Union.

REFERENCES

1. A. Höpe, K.-O. Hauer, Three-dimensional appearance characterisation of diffuse standard reflection materials, Metrologia, 47, 295-304, 2010.
2. T. Atamas, K.-O. Hauer, A. Höpe, Appearance measurements of goniochromatic colours, Predicting Perceptions: Proceedings of the 3rd International Conference on Appearance, p. 149-154, 2012.
3 D. Hünerhoff, U. Grusemann, A. Höpe, New robot-based gonioreflectometer for measuring spectral diffuse reflection, Metrologia, 43, S11-S16, 2006.
4. A. Höpe, T. Atamas, D. Hünerhoff, S. Teichert, K.-O. Hauer, ARGon^3 - "3D Appearance Robot-based Gonio-reflectometer" at PTB, Rev. Sci. Instrum. 83(4), 045102-1-045102-8, 2012.
5. F. Schmähling, G. Wübbeler, M. Lopez, F. Gassman, U. Krüger, F. Schmidt, A. Sperling, C. Elster, A virtual experiment for near-field goniophotometric measurements", Appl. Opt., in press, Doc. ID: 200819.

Use of an array spectroradiometer for monitoring solar radiation at a mid-latitude site.

R Kift[1], ARD Smedley[1], and AR Webb[1]

[1]*University of Manchester, Manchester, UK*

Corresponding e-mail address: richard.kift@manchester.UK

The array spectrometer shows great potential for making solar measurements. They can record spectral data whilst being as fast as broadband instruments, allowing for a range of retrievals using different weighting functions. But they have several limitations, (e.g. low quantum efficiency in UV and stray light). The results presented here show that when stray light correction is used in the UVA and visible array spectrometers can provide data within 3% of those obtained from scanning spectrometers. Whilst in the UVB results are similar down to a cut-off wavelength (dependent on solar zenith angle) caused by the drop in solar irradiance.

INTRODUCTION

As part of the EMRP project two array spectrometers are being deployed long term in Manchester to monitor the direct and global solar irradiance. There are several advantages in using array spectrometers which have a large wavelength range which can be measured simultaneously in a short period (seconds) and stability due to having no moving parts. They are also less expensive but due to limitations inherent in the layout of the monochromator and the detectors used these instruments suffer from poor quantum efficiency in the UV and problems due to stray light. This means that calibration and analysis of measurements is not as straightforward as for the more common scanning spectroradiometers used[1].

To assess the quality and accuracy of the data obtained during the deployment a Bentham DTM300 has been used to make co-located measurements over several weeks in each season. For this poster data obtained on a clear day (16/7/2013) has been used to examine the absolute calibration and effectiveness of the stray light correction procedure[2] over the widest range of solar zenith angles at a mid-latitude site for one of these array spectrometers (an Ocean Optics S2000).

Table 1. Instrument parameters.

Instrument parameter	Ocean Optics S2000	Bentham DTM300
Spectral range(nm)	200-850	290-550
Slit function FWHM (nm)	1.2	0.6
Dynamic range	$4x10^3$	$> 10^6$
Time for 1 spectra (sec)	55	180

METHODS

The S2000 array spectrometer used has been fitted into a temperature stabilised box to minimise changes in the dark signal. Also to improve the signal to noise ratio the instrument averages over an interval of 55s, saving data each minute with each individual measurement taking 4 ms. The Bentham DTM300 measures global irradiance every 15 minutes (at 0, 15, 30 and 45 minutes) from 290 to 550 nm with a 1 nm step taking 3 minutes to complete (Fig 1.). A clear day was chosen to minimise discrepancies due to the differing data acquisition times, as the S2000 spectral values were an average over 55 seconds whilst the Bentham DTM300 provided a single data point for each wavelength during the S2000 scan.

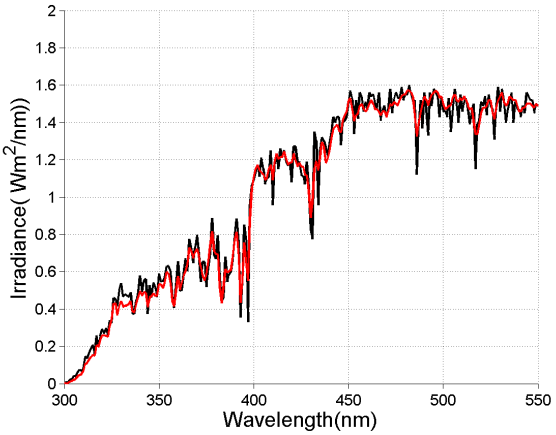

Figure 1. Plot of Bentham DTM300 and Ocean Optics S2000 12 UT spectra on 16/7/2013.

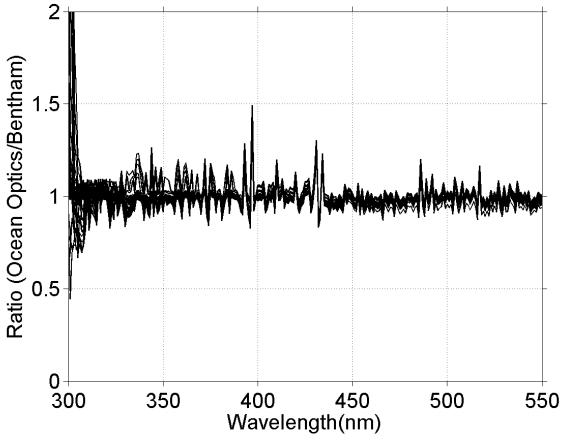

Figure 2. Ratio of 40 Bentham DTM300 and Ocean Optics S2000 spectra on 16/7/2013 with stray light corrected.

Both spectrometers used global heads, with good cosine responses with the Bentham having a Schreder head (f2 < 5%) and the S2000 a Bentham D7 sma head (f2 < 3%) to reduce differences due to cosine errors.

The instrument input optics were mounted and levelled next to each other to ensure that the same view of the horizon was obtained.

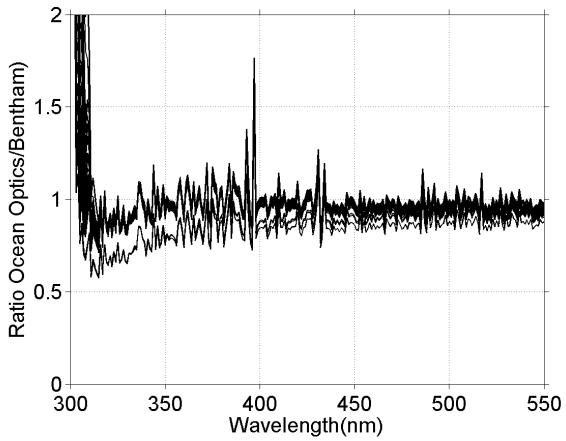

Figure 3. .Ratio of 40 Bentham DTM300 and Ocean Optics S2000 spectra on 16/7/2013 with no stray light correction.

RESULTS AND CONCLUSION

The absolute ratio of the S2000 to Bentham for the whole of day 197 (16/7/2013) was found to be 0.98 (±0.06) for the UVB, UVA and visible wavelength ranges, when stray light correction is used (fig 2). A lower wavelength limit of 310nm in the UVB was used as the signal is approaching the detection limit of the instrument. This ratio compares to values of 2.23 (±2.24), 0.97 (±0.05) and 0.96 (±0.023), in the UVB, UVA and visible respectively when no stray light correction applied (fig 2).

The stray light correction is also seen to flatten the ratio and remove the distortion in the UVA and UVB due to incorrect removal of the dark signal without taking account of the stray light. The structure remaining in the ratios is due to the difference in slit functions and wavelength sampling in the original instruments.

ACKNOWLEDGEMENT

This research was undertaken within the EMRP ENV03 Solar UV project. The EMRP is jointly funded by the EMRP participating countries within EURAMET and the European Union.

REFERENCES

1. M. Blumthaler J. Gröbner L. Egli S. Neva. A guide to measuring solar UV spectra using array spectroradiometers, 2011.
2. Kreuter A, Blumthaler M. Stray light correction for solar measurements using array spectrometers. Review of Scientific Instruments 80, 096108A, R2009.

Heat-Pipe Temperature Controller System for the Room Temperature Predictable Quantum Efficient Detector

Kathryn Nield[1], Ross Mason[1], Bernard Rougie[2], Dominique Renoux[3], Hamish Edgar[1], and Marek Šmíd[4]
[1]Measurements Laboratory of New Zealand, Callaghan Innovation, Lower Hutt, New Zealand,

[2]*Conservatoire National des Arts et Métiers*
[3]*Laboratoire national de métrologie et d'essais, Paris, France*
[3]*Czech Metrology Institute, Praha, Czech Republic.*
Corresponding e-mail address: Kathryn.nield@callaghaninnovation.govt.nz

A temperature control system has been designed for the predicatable quantum efficient detector (PQED). The PQED requires temperature stabilisation at a set point to within ±0.05 °C and operability over the temperature range -20.0 °C to 30 °C. In addition, a gas simple purging system been designed to prevent condensation and ice formation in the device when stabilised below the ambient dew point temperture.when operated at lower temperatures.

INTRODUCTION

The PQED is a solid state silicon detector with reported accuracy in the predictability of its quantum efficiency at the part per million level when operated at liquid nitrogen temperature and 100 parts per million when operated at room temperature [1, 2].

In the case of the room temperature PQED (RT-PQED) it is necessary to stabilise the device to a set temperature to within ±0.05 ℃ to minimise the influence of temperature on response and on dark current fluctuations. Furthermore, to facilitate measurements of temperature sensitivity of response, and other activities of the EMRP Newstar project (SIB 57), the control system should function from -20.0 °C to 30.0 °C.

As the RT-PQED has been promoted as a simple and easy to operate device it would be advantageous that the temperature and gas purging systems are also easy to operate. This would then open up the opportunity to use the RT-PQED at lower than ambient temperature with advantage of reducing thermal electronic noise and associated dark current.

HEAT-PIPE TEMPERATURE CONTROLLER

Previously, a temperature control system has been developed and implemented at MSL based upon dual-heat-pipes and a commercially available thermoelectric control system [3]. These devices have been used to stabilise a number of artefacts such as photodetectors and standard resistors. In previous work this type of temperature control system achieved stability better than 0.01 °C over periods of up to 12 hours.

MECHANICAL REQUIREMENTS

Although the RT-PQED is not operated under vacuum, it is equipped with a Brewster window to minimize the impact of dust and other contaminates onto the detector surface. As the RT-PQED consists of both the detector and Brewster window housing, the foot-print and volume of the system under temperature control are key factors in the design.

INITIAL CONCEPT

The first prototype of the temperature controller consisted of:

- 6 acetone filled heat pipes
  - 4 (350 × 50) mm heat pipes arranged in an annular fashion along the length of the PQED housing, with 60 mm of heat pipe length protruding perpendicularly to the PQED device
  - 2 (200 × 50) mm heat pipes to act as heat spreaders (for uniformity)
- 1 peltier device – located on the upper heat spreading heat pipe
- 1 additional heat pipe cooler, connected to the hot side of the peltier.
- Lengths of Perspex – to act as insulation to this assembly which is external to the annular heat pipes around the PQED.
- Expanded polystyrene moulded around the length of the annular heat pipe assembly.
- PRT to control the system, mounted in the groove formed by the protruding sections of the annular heat pipe assembly.

Figure 1. Temperature control prototype alongside model of RT-PQED.

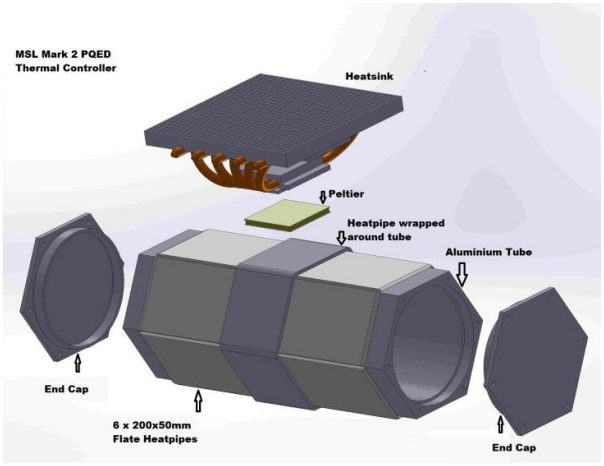

Figure 2. Schematic of proposed second temperature control system.

To assess the lowest temperature of operation for the prototype a simple dry air purging system was built to prevent condensation occurring below the dew point temperature. In this way the system was able to operate down to -15 °C and remain stable for an extended period. The sources of loss and their magnitude are given in Table 1. It is estimated that with better insulation that the thermal losses in this current design could be significantly reduced from 17 W to 6 W.

Table 1. Heat-pipe temperature controller - sources of thermal loss.

Source of thermal loss	Size of loss
Annular heat pipes	4.5 W
Flat heat pipe	12 W
PQED rear side	0.03 W
PQED window side	0.07 W
Mounting rods	0.6 W
Total loss	17.2 W

A second version of this system has been designed with the main improvements being the use of a cylindrical sleeve for the PQED around which the heat-pipes can be arranged (figure 2). In this way the surface area of the system can be reduced with aim of extending the temperature range of the system to. -20.0 °C.

Gas purging, also considered in this second version, will used to prevent condensation within the detector system when operated below the ambient de point temperature., and to minimize contamination by dust for operation of the detector without the Brewster window. For this purpose, commercial compressed argon or nitrogen gas with to remove dust particles larger than 1 µm will be supplied to the PQED; the purging gas will be pre-conditioned to the operating temperature of the system.

CONCLUSION

A prototype temperature control system has been developed for the PQED. This device has been tested and is capable of temperature control from -15 °C to room temperature.

Work is progressing to improve the initial concept so that the -20.0 °C temperature limit can be achieved as well as to incorporate effective gas purging to facilitate both lower than dew point temperature control and to prevent contamination of the detector surface when operated without the Brewster window..

REFERENCES

1. M.Sildoja, Predictable quantum efficient detector: I Photodiodes and predicted responsivity, Metrologia, 50, 385, 2013.
2. I Muller et al, Predictable quantum efficient detector: II Characterization and confirmed responsivity, Metrologia, 50, 395, 2013.
3. R Mason et al, A dual heat-pipe temperature controller system for detectors and other calibration artefacts, Newrad 2011 Conference Abstracts, Maui Hawaii, September 2011.

This work has been funded in part by the EMRP contract SIB57 and in part by the MSL contract for the provision of measurement standards in New Zealand.

Performances of the innovative portable spectroradiometer: rapid wide-range tunability and high reproducibility.

Achour Sadouni, Olga Kozlova, Daniel Truong, Frédéric Bourson Mohamed Sadli, and Stéphan Briaudeau

Laboratoire Commun de Métrologie LNE-Cnam, La Plaine St Denis, France.
Corresponding e-mail address: stephan.briaudeau@cnam.fr

We have developed and characterized an innovative portable spectroradiometer. The key feature of the developed spectroradiometer is a combination of wide-range tunability and high performances in a relatively compact device (90cm x 30cm x 20cm). The main performances are the following: rapid wide-range tunability over 300 nm; 10 nm detection spectral width; detectivity ~ 100 fW at 1 Hz; wavelength stability 5 pm over 24 hours; signal stability 0.05% over 24 hours; The spectroradiometer was calibrated with an Ar spectral lamp with wavelength reproducibility better than 10 pm.

INTRODUCTION

In order to prepare the "mise-en-pratique" (practical realisation) of the new definition of kelvin LCM-LNE-CNAM is involved in the development of high-temperature fixed points (HTFPs) and on the determination of their thermodynamic temperature. To assign a thermodynamic temperature to the HTFPs made in our laboratory [1] we designed, developed and characterised an innovative spectroradiometer.

Figure 1. Tuneable portable spectroradiometer.

SPECTROMETER'S MAIN CHARACTERISTICS

This device fits in 90-cm-long, 30-cm-width and 20-cm-heigth dimensions and its weight is about 20 kg (Fig. 1). It is therefore transportable.

The developed device allows an easy, rapid and continuous adjustment the working wavelength in a wide range (650 nm – 950 nm). The spectral bandwidth is about 10 nm.

Contrary to the interference filter based devices the spectral responsivity of the developed spectroradiometer can be easily characterised with a tuneable laser source. No optical interferences occur.

We have characterized the performances of the developed spectroradiometer. Its detectivity is of order of 100fW at 1 Hz. The signal is stable at the level of 0.05% over 24 hours and can be improved by with better thermal control. The working wavelength is stable at the level of 5 pm over 24 hours.

The working wavelengths of the spectroradiometer were calibrated with an Ar spectral lamp (Fig. 2). The whole spectrum can be recorded within one minute. The repeatability of such calibration is better than 10 pm.

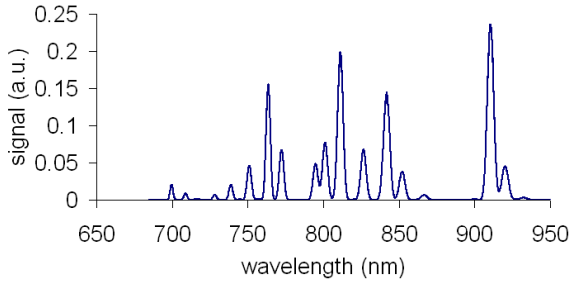

Figure 2. Ar lamp spectrum registered with spectroradiometer.

CONCLUSION

We have developed and characterized an innovative tuneable portable spectroradiometer, which shows a high reproducibility. This device is relatively

compact and its dimensions are comparable to an interference-filter-based one, but it spectral responsivity can be easily characterised with a tuneable laser source. The wavelength stability of the developed device is comparable to a radiance comparator [2], but it is still a transportable device.

REFERENCES

1. M.Sadli, O. Pehlivan, F. Bourson, A. Diril, K. Ozcan, "Collaboration Between UME and LNE-INM on Co–C Eutectic Fixed-Point Construction and Characterization", Int J Thermophys (2009) 30:36–46.
2. Self study manual on optical radiation measurement, edited by Fred Nicodemus, http://www.nist.gov/pml/div685/pub/studymanual.cfm